A Generalized Pyrolysis Model for Combustible Solids

by

Christopher William Lautenberger

B.S. (Worcester Polytechnic Institute) 2000
M.S. (Worcester Polytechnic Institute) 2002

A dissertation submitted in partial satisfaction of the
requirements for the degree of

Doctor of Philosophy

in

Engineering – Mechanical Engineering

in the

Graduate Division

of the

University of California, Berkeley

Committee in charge:

Professor A. Carlos Fernandez–Pello, Chair
Professor Patrick J. Pagni
Professor Scott L. Stephens

Fall 2007

A Generalized Pyrolysis Model for Combustible Solids

by Christopher William Lautenberger

Abstract

A Generalized Pyrolysis Model for Combustible Solids

by

Christopher William Lautenberger

Doctor of Philosophy in Engineering – Mechanical Engineering

University of California, Berkeley

Professor Carlos Fernandez–Pello, Chair

This dissertation presents the derivation, numerical implementation, and verification/validation of a generalized model that can be used to simulate the pyrolysis, gasification, and burning of a wide range of solid fuels encountered in fires. The model can be applied to noncharring and charring solids, composites, intumescent coatings, and smolder in porous media. Care is taken to make the model as general as possible, allowing the user to determine the appropriate level of complexity to include in a simulation. The model considers a user–specified number of gas phase and condensed phase species, each having its own temperature–dependent thermophysical properties. Any number of heterogeneous (gas–solid) or homogeneous (solid–solid or gas–gas) reactions can be specified. Both in–depth radiation transfer through semi–transparent media and radiation transport across pores are considered. Volume change (surface regression or swelling/intumescence) is handled by allowing the size of grid points to change as dictated by mass conservation. All volatiles generated inside the solid escape to the ambient with no resistance to mass transfer unless a pressure solver is invoked; the resultant flow of volatiles is then calculated according to Darcy's law. A gas phase

convective–diffusive solver can be invoked to determine the composition of the volatiles. Oxidative pyrolysis is simulated by modeling diffusion of oxygen from the ambient into the pyrolyzing solid where it may participate in reactions. Consequently, the mass flux and composition of volatiles escaping from the solid can be calculated. To aid in determining the required input parameters, the model is coupled to a genetic algorithm that can be used to estimate the required input parameters from bench–scale fire tests or thermogravimetric analysis.

Standalone model predictions are compared to experimental data for the thermo–oxidative decomposition of non–charring and charring solids, as well as the gasification and swelling of an intumescent coating and forward smolder propagation in polyurethane foam. Genetic algorithm optimization is used to extract the required input parameters from the experimental data, and the optimized model calculations agree well with the experimental data. Blind simulations indicate that the predictive capabilities of the model are generally good, particularly considering the complexity of the problems simulated.

ACKNOWLEDGEMENTS

First, I would like to thank Nikki for her patience, encouragement, and unwavering support during this long process. To my parents, family, and friends "back east"–thank you for making me feel that little has changed every time I visit! The road to UC Berkeley is largely due to my MS thesis advisors, Prof. N.A. Dembsey at WPI and Dr. J.L. de Ris at FM Global Research, and I am indebted to them for making me realize that I like doing research. At UC Berkeley, Prof. A.C. Fernandez–Pello was an excellent advisor and friend, I thank him for providing the opportunity to conduct this research and the many suggestions he has given over the years. I would also like to thank Prof. P.J. Pagni and Prof. S.L. Stephens for reading through this manuscript and providing valuable comments. MaryAnne Peters provided important assistance and support over the years!

My lab–mates are a great group of people, and they certainly helped make graduate work quite enjoyable if sometimes noisy due to frequent "discussions" (arguments) over anything and everything, thanks in particular to David Rich, Mark Mikofski, Guillermo Rein, and Amnon Bar–Ilan for that. I would also like to acknowledge my many less–noisy lab–mates over the years including Bennett Sprague, Olivier Putzeys, Sang Park, David Sadeli, Kevin Macko, Ronda Ropes, Jorge Hernandez, Sara McAllister, Jaime Herren, Amanda Dodd, Hector Mendoza, Jay James, Sonya Ferreres, and anyone else I forgot. I would like to specifically thank my FIST project–mates (David Rich, Sara McAllister, Jorge Hernandez and the many undergraduate students who helped out over the years) for running many experiments so I could remain in front of the computer. I am particularly thankful to the fire group at Arup in San Francisco (Jim Quiter, Armin Wolski, Andrew Coles, Geza Szakats, Toby White, and

Susan Lamont) for allowing me to work there part–time, and putting up with my sporadic availability! I would also like to thank Prof. A.C. Fernandez–Pello, N.J. Alvares, and Prof. P.J. Pagni for involving me in their fire–related consulting.

Discussions with Simo Hostikka of VTT Finland regarding his development of the FDS5 pyrolysis model have helped shape this work. Similarly, this work was molded by discussions with Profs. J. Torero, G. Rein, and J. Quintiere. At NIST, Kevin McGrattan has always responded quickly to my many FDS–related questions. Esther Kim at WPI struggled with running beta versions of the pyrolysis model, but never complained, and her input helped me clarify (hopefully!) confusing aspects of the model.

Many people contributed experimental data that was used as part of this work, even if there wasn't space to include it in this thesis. In particular, Prof. N.A. Dembsey and Esther Kim at WPI provided a large amount of cone calorimeter and Fire Propagation Apparatus data for FRP composites; G.J. Griffin (CSIRO) provided experimental data for intumescent coatings in electronic form; Pedro Reszka (University of Edinburgh) provided large amounts of cone calorimeter data for wood, and P.A. Beaulieu (FM Global Research) provided PMMA ignition data in electronic form.

This research was supported largely by NASA under the umbrella of the FIST (Forced–flow Ignition and flame Spread Test) project. Zeng–Guang Yuan served as technical monitor of the FIST project (Grant NNC–05GA02G), as well as the advisor for the separate NASA Graduate Student Researcher Program project (Grant NNC–04HA08H) that grew out of FIST and made most of this work possible. David Urban, Gary Ruff, and Fletcher Miller were strong advocates of the FIST project. The last three months of this work were supported by NSF under Award 0730556.

TABLE OF CONTENTS

LIST OF FIGURES

LIST OF TABLES

NOMENCLATURE

Letters

a	Coefficients in discretized equations or Thomas algorithm
A	Area or reactant species
A	Parameter in Equation 3.98
b	Coefficient in discretized equations or Thomas algorithm
b	Exponent in Equation 3.67
B	Product species or parameter in Equation 3.98
c	Specific heat capacity (J/kg–K)
c	Coefficient in Thomas algorithm
C	Parameter in Equation 3.98
d	Coefficient in Thomas algorithm or pore diameter (m)
D	Diffusivity (m^2/s) or parameter in Equation 3.98
$\mathcal{D}$	Coefficient in discretized Equations, see e.g. Equation 3.84c
E	Activation energy (J/mole) or parameter in Equation 3.98
F	Coefficient in convective diffusive equation, see e.g. Equation 3.77 or parameter in Equation 3.98
F	Radiative exchange factor (Equation 2.41)
G	Parameter in Equation 3.98
h	Enthalpy (J/kg)
h_c	Convective heat transfer coefficient (W/m^2–K)
h_{cr}	Inverse contact resistance (W/m^2–K)
h_{cv}	Volumetric heat transfer coefficient (W/m^3–K)
ΔH	Change in enthalpy (J/kg)
$\dot{j}_j''$	Diffusive mass flux (kg/m^2–s)
J	Coefficient in convective–diffusive equation, see e.g. Equation 3.77
k	Thermal conductivity (W/m–K)
k	Reaction rate (s^{-1}), e.g. Equation 2.22
k_b	Boltzmann constant (J/K)
K	Permeability (m^2)
K	Number of condensed phase reactions
K_g	Number of homogeneous gas phase reactions
L	Thickness (m)
m	Mass (kg)
m''	Mass per unit area (kg/m^2)
$\dot{m}''$	Mass flux (kg/m^2–s)
M	Number of condensed phase species
M	Molecular mass (g/mol or kg/mol)
M	Moisture content on an oven–dry basis (Equation 2.32)
n	Exponent (reaction order, Equation 3.58; Property exponent, Equation 3.3)
N	Number of gaseous species
p	Exponent in Equation 3.67
P	Pressure (Pa)

P	Cell Peclet number, e.g. Equation 3.84e
P	Coefficient in Thomas algorithm, Equation 3.122
Pr	Prandtl number
q	Exponent in Equation 3.67
$\dot{q}''$	Heat flux (W/m^2). $\dot{q}''$ is conductive, $\dot{q}_r''$ is radiative, $\dot{q}_e''$ is external radiative
Q	Coefficient in Thomas algorithm, Equation 3.122
$\dot{Q}'''$	Volumetric rate of heat release or absorption (W/m^3)
r	Reaction rate (kg/m^3–s)
R	Universal gas constant (J/mole–K)
s	Position of solidification front in Stefan problem (m)
S	Source term
Sc	Schmidt number
t	Time (s)
T	Temperature (K)
Δt	Time step (s)
w	Condensed phase velocity (m/s)
X	Volume fraction (–)
y	Yield
Y	Mass fraction (–)
z	Distance (m)
Z	Condensed phase pre–exponential factor (s^{-1})
Z	Gas phase pre–exponential factor, Equation 3.67 (units of m, mole, K, s)
δz	Distance from center of grid one grid cell to center of adjacent grid cell (m)
Δz	Size (height) of grid cell (m)

Greek symbols

α	Relaxation parameter
α	Conversion
α	Thermal diffusivity (m^2/s), e.g. Equation 3.133a
β	Heating rate (K/min or K/s)
γ	Length scale (m) controlling radiant conductivity, see Equation 3.4
Γ	Effective diffusion coefficient in discretized equations
δ	Thickness (m)
ε	Emissivity (–)
ε	Energy of attraction between two molecules, Equation 3.9 (J)
ε	Small value
κ	In–depth radiation absorption coefficient (m^{-1})
λ	Eigenvalue, e.g. Equation 3.136b, Equation 3.138d
λ	Wavelength (m), e.g. Equation 2.37
λ	Decay coefficient (s^{-1}), e.g. Equation 2.4
ν	Viscosity (m^2–s)
ρ	Density (kg/m^3)
σ	Stefan–Boltzmann constant ($W/m^2–K^4$)
σ	Collision diameter of molecular species, Equation 3.9 (Å)
σ_m^2	Parameter in Equation 3.5c (K^2)
ϕ	Generic variable
χ	Parameter controlling swelling, see Equation 3.61 and 3.62
ψ	Porosity (–)
Ω	Function of dimensionless temperature
$\dot{\omega}'''$	Volumetric reaction rate (kg/m^3–s)
θ	Stretched time, see Equation 2.5
ξ	See Equation 2.5

Subscripts

A	Species A
b	Baseline or bottom (interface value)
B	Species B
B	Bottom (cell center value)
c	Combustion
d	Destruction, datum, or bond dissociation (as in ΔH_d)
D	Diffusivity
e	East (interface value)
e	External (as in $\dot{q}''_e$)
exp	Experimental
E	East (cell center value)
f	Formation
g	Gaseous, gas phase, or gasification
i	Condensed phase species i
ig	Ignition
j	Gaseous species j
k	Heterogeneous reaction k
ℓ	Homogeneous gas phase reaction ℓ
ℓ	Liquid (in Stefan problem)
m	Melting
mod	Model
nb	No blowing
O_2	Oxygen
p	Pyrolysis
P	Point P
r	Reference sample (Equation 2.30)
r	Reference (as in T_r), radiative (as in k_r), or reaction (as in ΔH_r)
s	Solid phase (really, condensed phase) or surface (e.g. Equation 2.1)
s	Sample of interest (Equation 2.30)
sol	Solid
t	Top (interface value)
T	Top (cell center value)
v	Vaporization, volatile, or virgin (Section 2.1.5)
vol	Volatilization
w	West (interface value)
W	West (cell center value)
0	Initial (as in T_0)
0	At $z = 0$ (as in $\dot{m}''_0$)
∞	Ambient or at the end of an experiment (Equation 2.19)
δ	At $z = \delta$
λ	At wavelength λ
Σ	Integrated (summation)

Superscripts

$+$	Positive part of source term
$-$	Negative part of source term
$\bar{(\,)}$	Weighted or averaged
$\circ$	Value at present time
∞	Ambient

1.0 INTRODUCTION

Most fire modeling performed to date should probably be called "fire consequence modeling" because rarely is the fire itself modeled in detail. Instead, the fire is specified *a priori* as a time–history of heat and chemical species generation rates (usually, a heat release rate and associated product yields). A fire model then predicts the effects, or consequences, of this particular fire on the space under consideration. This approach is suitable for designing a building's egress and life safety systems to mitigate the threat from a specific fire, but it cannot be used to estimate how a fire would develop given a certain initiating fire.

Due in part to increases in computer power, fire modeling has reached the point that fire development can actually be predicted. Though these prediction techniques are not yet mature, property–based first principles fire modeling of the end–use configuration is considered an appropriate long–term goal of fire research [1, 2]. Such an endeavor involves the coupling of a gas phase model to handle fluid mechanics, heat transfer, radiation, and combustion to a condensed phase "pyrolysis model" that simulates the heating and pyrolysis (sometimes called decomposition, gasification, or volatilization) of condensed phase fuels.

At the present time, our predictive capabilities for condensed phase phenomena relevant to fires lag those of the gas phase significantly. The Navier–Stokes equations govern fire–induced gas phase fluid flow, and considerable progress has been made in turbulence modeling and numerical methods. Sophisticated non–premixed combustion models have been developed (largely by the combustion community), and combustion is now understood in terms of elementary reactions for simple fuels (methane, hydrogen).

Work is underway to better understand the radiative characteristics of flames, in particular soot formation and oxidation.

In comparison, most of the condensed phase pyrolysis modeling work conducted to date has focused on a few materials (thermoplastics and wood), often applying simplified single–step decomposition mechanisms or infinitely–fast kinetics approximations and ignoring oxidative reactions. While a simple model should not necessarily be viewed in a negative light, highly simplified pyrolysis models perform well only over a narrow range of range of experimental conditions (heat flux levels, oxygen concentrations). Furthermore, simplified models usually cannot be applied to complex solid fuels that have layered or laminated composition, non–simple decomposition kinetics, or to those that exhibit volume change (swelling, surface regression) or sensitivity to oxygen concentration during pyrolysis. Since a wide variety of solid fuels are encountered in fires, and most of them exhibit some of the complex characteristics mentioned above, a generalized pyrolysis model that could be used to accurately simulate the large number of solid fuels encountered in fires is needed.

The biggest challenge of pyrolysis modeling for application to real–world fires is not formulating a comprehensive set of governing equations and then coding a computer program that solves those equations. Instead, the challenge is making enough simplifications and approximations (without compromising generality or neglecting relevant physical phenomena) that there are a manageable number of empirical or adjustable parameters, all of which can be estimated from laboratory experiments.

The primary contributions of this dissertation are: 1) Formulation of a simplified generalized pyrolysis model that can be applied to a wide variety of combustible solids;

2) Initial development and testing of a material property estimation technique that can be used to estimate the needed model input parameters from existing laboratory experiments using parallel processing; 3) Numerical implementation (coding) of all equations and making the subsequent software, source code, executable files, and associated documentation available electronically.

Although several pyrolysis simulations of combustible solids are presented and model calculations are compared to available experimental data, it is not the objective of this dissertation to identify controlling mechanisms, delve deep into the physics occurring at the microscale, or develop detailed models for any particular material. Indeed, these are all important tasks worthy of study, and it is hoped that this dissertation will enable future workers to make much needed progress in these areas by providing a generalized framework that can be used as–is or extended to include additional phenomena.

The work reported in this dissertation was conducted as part of the NASA–funded Forced–flow Ignition and flame Spread Test (FIST) project and a NASA Graduate Student Researcher Program (GSRP) extension to FIST. The overall aim of the FIST project is to develop a normal–gravity flammability apparatus that provides a good assessment of material flammability characteristics in reduced–gravity exploration atmospheres and to develop modeling tools that can provide a better understanding of flammability (particularly ignition and flame spread) in such environments.

Since 2003, a large amount of modeling work has been conducted as part of the FIST project (and related endeavors). The numerical pyrolysis model described here and its predecessors have been coupled to NIST's Fire Dynamics Simulator (FDS) Version 4.07 [3] and used to simulate both ignition [4] and flame spread [5, 6]. The concept of a

critical mass loss rate at ignition was explored theoretically [7], and a theory was developed to explain the experimentally–observed increase in surface temperature at piloted ignition with applied heat flux [8]. The 1D numerical pyrolysis model described in this dissertation has recently been extended to two dimensions and used to simulate two–dimensional smolder structure with complex kinetics [9]. However, to focus the scope of this dissertation and limit its length, none of this work is discussed here; only 1D standalone numerical pyrolysis modeling and a related parameter estimation methodology are presented.

The dissertation is organized as follows: Chapter 1 introduces the research topic and discusses the motivation for this work. Chapter 2 presents a literature review and background information. Various aspects of the condensed phase processes that affect a material's overall reaction to fire are reviewed and the different modeling strategies that have been used to simulate the burning of solids are summarized. An overview of condensed phase decomposition kinetics and thermodynamics is given due to their importance for the burning of solids. Conduction, radiation, convection, and momentum transfer within combustible solids are discussed.

Chapter 3 presents the generalized pyrolysis model developed as part of this work, beginning with the derivation of a self–consistent set of one–dimensional transient governing equations. These equations are general and can be used to simulate the pyrolysis of most combustible solids. Next, the numerical solution methodology is described in detail, and its implementation (coding) is verified through comparison of numerical calculations with several analytical solutions. Chapter 4 investigates the effects

of various input parameters on the model calculations and highlights some of the physics that can be included in calculations.

Chapter 5 presents a genetic algorithm–based optimization technique that can be used to extract the required input parameters from laboratory experiments, including traditional flammability tests and small–scale thermal analysis. This algorithm is needed because a major obstacle impeding real world application of pyrolysis modeling is the difficulty associated with determining the input parameters (or material properties) required to characterize different materials.

In Chapter 6, the generalized pyrolysis model is used to simulate the pyrolysis and gasification of several combustible solids, with model input parameters determined by genetic algorithm optimization. Four experiments are simulated: thermo–oxidative decomposition of polymethylmethacrylate (PMMA), thermo–oxidative decomposition of white pine, gasification and swelling of an intumescent coating, and smolder propagation in polyurethane foam. Good agreement between the model predictions and the experimental data was obtained, particularly considering that the model was not developed specifically to simulate a particular material or class of materials.

Finally, concluding remarks are presented in Section 7. The dissertation concludes with two appendices: Appendix A gives the derivation of an exact solution to the heat conduction equation that is used for model verification in Chapter 3, and Appendix B is a rudimentary user's guide to the code that was used for all calculations in this dissertation. This code (standalone pyrolysis model and parallelized genetic algorithm–based parameter optimization technique) is freely available, see Appendix B for details. Continued development is planned under National Science Foundation Award 0730556.

2.0 BACKGROUND – PYROLYSIS MODELING

This chapter aims to provide an overview of the heat transfer, mass transfer, and kinetics processes that control a material's overall pyrolysis behavior. As it is currently used by the fire community, "pyrolysis" refers generically to the liberation of gaseous volatiles from a solid fuel, regardless of the presence or absence of oxygen. However, in the chemical engineering literature, pyrolysis generally refers to the anaerobic thermal decomposition of solids. In this work, the terms pyrolysis, gasification, degradation, and decomposition are used throughout to refer to the generation of gaseous components (pyrolysate) from a condensed phase fuel. Pyrolysate refers to the gaseous mixture of compounds that are released when a solid material is thermally stimulated, and may include hydrocarbons, alcohols, water vapor, carbon monoxide, and carbon dioxide. For most fuels, little is known about the detailed composition of the pyrolysate vapors that are released during pyrolysis.

Generically, a pyrolysis model is an algorithm that quantifies the rate at which solid combustible surfaces heat up and generate gaseous pyrolysate when thermally stimulated. It may be a standalone computer program, or a boundary condition in a computer fire model. The pyrolysis models proposed to date range from very simple empirical formulations that rely heavily on fire test data to highly complex models that attempt to simulate microscale physical and chemical processes in exhaustive detail. Some of these are reviewed in the following section. This short chapter cannot due justice to the large body of literature related to pyrolysis modeling, and the reader is referred to several reviews that have been published since 1993 [10–17].

2.1 Types of pyrolysis models

Most pyrolysis models intended for fire applications fit into one of two main categories. The first category comprises semi–empirical or material fire property–based formulations that relate burning and flame spread rates directly to bench–scale fire test data. This class of model provides a macro–scale description of the burning process without considering the individual micro–scale physical and chemical processes that collectively contribute to a material's overall reaction to fire. The next category includes comprehensive models that consider (with a widely varying level of detail) the actual small–scale processes and transport phenomena occurring within the solid.

All pyrolysis models begin (explicitly or implicitly) with universally applicable statements of conservation of mass, energy, species, and sometimes momentum. However, the approach taken by most authors when postulating a model is to make approximations and simplifications that reduce these general conservation laws to a simplified set of governing equations that are applicable only to one class of materials. Therefore, most comprehensive pyrolysis models can be further divided into thermoplastic polymer, charring, or intumescent formulations.

In the remainder of Section 2.1, semi–empirical material fire property based pyrolysis models and comprehensive pyrolysis models for thermoplastic, charring, and intumescent materials are reviewed. The emphasis here is on the modeling strategy; later the controlling kinetics (Section 2.2) and transport phenomena (Section 2.3) are examined in greater detail.

2.1.1 Semi–empirical and fire property–based pyrolysis/gasification models

The fire scientist's primary tools for quantifying the fire behavior of combustible solids are bench–scale laboratory tests that measure the mass loss rate (MLR) and heat release rate (HRR) of small–scale (~ 0.01 m^2) fuel samples exposed to a well–characterized thermal stimulus, usually radiant heating. These experiments provide an overall measure of a material's fire behavior or "reaction to fire"—and can provide insight into the transport phenomena that affect the decomposition of combustible solids. Although effective material fire properties such as the thermal inertia and heat of gasification can be estimated from these tests, fundamental material properties (e.g. temperature–dependent thermal conductivity and specific heat capacity) cannot.

Some of the earliest fire growth modeling studies were motivated by the possibility that the outcome of standardized full–scale fire tests could be predicted with a model formulated in terms of property data that can be obtained directly from existing bench–scale fire tests. Since the cost of obtaining this bench–scale fire test data is a fraction of that associated with full–scale fire testing, this approach has been advocated as cost–effective alternative to full–scale fire testing.

Several simple models have been postulated that require input data that can be directly measured or inferred from widely–used bench–scale fire tests such as the cone calorimeter [18] or LIFT apparatus [19]. One modeling approach [20 – 22] assumes that a material's burning rate is zero until its surface is heated to its pyrolysis temperature T_p, sometimes taken as equal to the ignition temperature, T_{ig}. The reason for this equivalence is that a solid's pyrolysis rate is very sensitive to temperature so small increases in temperature can cause large increases in the pyrolysis rate. The time at which a material

element reaches T_p is determined by solution of the transient heat conduction equation. This can be accomplished many different ways, e.g. by assuming that the material is a one–dimensional constant–property semi–infinite inert solid and applying Duhamel's theorem [20]:

$$T_s(t) = \begin{cases} T_0 + \dfrac{1}{\sqrt{\pi k\rho c}} \displaystyle\int_{\tau=0}^{t} \frac{\dot{q}''_{net,mod}(\tau)}{\sqrt{t-\tau}}\,\mathrm{d}\tau & \text{for } t < t_p \\ T_p & \text{for } t \geq t_p \end{cases} \tag{2.1}$$

In Equation 2.1, T_s is the calculated surface temperature, T_0 is the initial solid temperature, $k\rho c$ is the apparent thermal inertia, and t_p is the time at which the surface first reaches T_p. $\dot{q}''_{net,mod}$ is the net heat flux to the material's surface calculated by the model (accounting for convective and radiative losses) and may include contributions from an ignition burner and hot smoke layer. Throughout this section, the subscript "mod" is used to differentiate a modeled quantity from an experimentally measured quantity (denoted with a subscript "exp") as in Equation 2.3 below.

Ignition and subsequent burning are assumed to occur after the material's surface is heated to T_p. After ignition, it is assumed that the surface temperature remains constant and equal to T_p [20]. However, it should be emphasized that this is an approximation because experimental measurements show that the surface temperature of burning solids is generally higher than the pyrolysis (or ignition) temperature [23, 24]. For thermally thick non–charring solids burning under steady–state conditions [25], the mass loss rate per unit area is proportional to the net heat transfer to the solid surface divided by the effective heat of gasification ΔH_g. For now, we will consider ΔH_g as a material fire property. As will be discussed in further detail in Section 2.2, ΔH_g is the quantity of heat required to generate unit mass of volatiles at temperature T_p from unit mass of solid

initially at T_0. Thus, the heat release rate of a solid element after it ignites can be calculated from the net heat flux to the surface multiplied by $\Delta H_c/\Delta H_g$ [20, 22].

$$\dot{Q}''_{mod}(t) = \begin{cases} 0 & \text{for } t < t_p \\ \dfrac{\Delta H_c}{\Delta H_g} \dot{q}''_{net,mod}(t) & \text{for } t \geq t_p \end{cases} \tag{2.2}$$

Here, $\dot{Q}''_{mod}$ is the heat release rate per unit area calculated by the model. ΔH_c is the heat of combustion, and the ratio $\Delta H_c/\Delta H_g$ is another material fire property sometimes called the combustibility ratio [26] or heat release parameter [27]. Equation 2.2 is strictly valid only for noncharring ablative thick solids burning under steady state (thermally thick) conditions, but it has been applied to other burning regimes [20, 22] with good results.

As an alternative to Equation 2.2, a solid's heat release rate is sometimes related directly to transient heat release rate or mass loss rate measurements obtained from small–scale fire tests [28, 29] or an approximate curve fit to this data [30]:

$$\dot{Q}''_{mod}(t) = \dot{Q}''_{exp}(t) \tag{2.3}$$

$$\dot{Q}''_{mod}(t) = \dot{Q}''_{peak,exp} \exp(-\lambda t) \tag{2.4}$$

In Equation 2.3, used by Brehob *et al.* [28] and Tsai and Drysdale [29], the modeled heat release rate history ($\dot{Q}''_{mod}(t)$) of a burning element is assumed identical to the measured heat release rate history ($\dot{Q}''_{exp}(t)$) from the cone calorimeter. In Equation 2.4, proposed by Karlsson [30], $\dot{Q}''_{peak,exp}$ is the peak heat release rate measured experimentally, e.g. in the cone calorimeter, and λ is a fitting parameter that controls the assumed exponential decay in heat release rate.

The primary shortcoming of Equations 2.3 and 2.4 is that they implicitly assume that the net heat flux history which the material in the model "feels" is identical to its thermal exposure in the laboratory test. Therefore, this type of model technically cannot accommodate any difference in heat flux history between the experiment and the model, such as an increase in the burning rate due to external heating (for example, from hot layer radiation). Additionally, it has been shown experimentally that the mass loss rate is affected by the total (cumulative) heat absorbed by the solid [31]. It may be possible to obtain reasonable results by performing fire tests at multiple irradiance levels and developing some sort of an interpolation scheme to extend the data to an arbitrary heating history, but this type has not yet been widely demonstrated. As an attempt to remedy this deficiency, an "acceleration" function has been introduced [32, 33] where the modeled heat release rate is related essentially to the total heat flux absorbed by the solid, summarized in Equation 2.5:

$$\xi(t) = \frac{\dot{q}''_{net,mod}(t)}{\dot{q}''_{net,exp}(t)} \tag{2.5a}$$

$$\theta(t) = \int_{t'=0}^{t} \xi(t')\,\mathrm{d}t' \tag{2.5b}$$

$$\dot{Q}''_{mod}(t) = \xi(t)\dot{Q}''_{exp}(\theta(t)) \tag{2.5c}$$

Although the above modeling approaches are crude in comparison to some of the more refined treatments of the solid phase, this simple description of solid phase processes has been successful at predicting full–scale fire behavior. The primary advantage of these modeling approaches is that all required input parameters ($k\rho c$, T_{ig}, ΔH_g, ΔH_c, and $\dot{Q}''_{exp}(t)$) can be obtained from existing bench–scale fire tests using well–established data reduction techniques. As greater levels of complexity are added, establishing the required

input parameters (or "material properties") for different materials becomes a much more onerous task.

2.1.2 Comprehensive pyrolysis models: thermoplastics

Thermoplastic materials include many of the widely used commodity polymers such as polyethylene (PE), polypropylene (PP), polystyrene (PS), and polymethylmethacrylate (PMMA). Unless fire retardants are added, thermoplastics usually do not char. Instead, they burn completely and leave minimal residue. Thermoplastics melt to various degrees, and the models considered in this section do not explicitly consider melting; however, melting and related phenomena will be discussed further in Section 2.3.5. Laboratory–scale combustion experiments show that after an initial transient period, noncharring thermoplastics exhibit a quasi–steady–state burning rate that depends primarily on the applied irradiance level. However, this steady–state burning period is observed only for thermally thick materials that are not affected by heat losses from the back (unexposed) face of the sample. Figure 2.1, adapted from Babrauskas [34], shows the heat release rate of PMMA samples having different thicknesses measured in cone calorimeter [18] combustion experiments. It can be seen that steady–state burning is not achieved, except for the thicker samples. This indicates that a material's burning behavior is affected by heat transfer at the unexposed side of the sample, i.e. the insulating effect of the substrate is a factor. There is no mechanism included in Equations 2.1 – 2.2 above (since they are developed for a semi–infinite solid) to account for this behavior, but it can be captured with comprehensive pyrolysis models that treat the heat transfer aspect of the problem in greater detail.

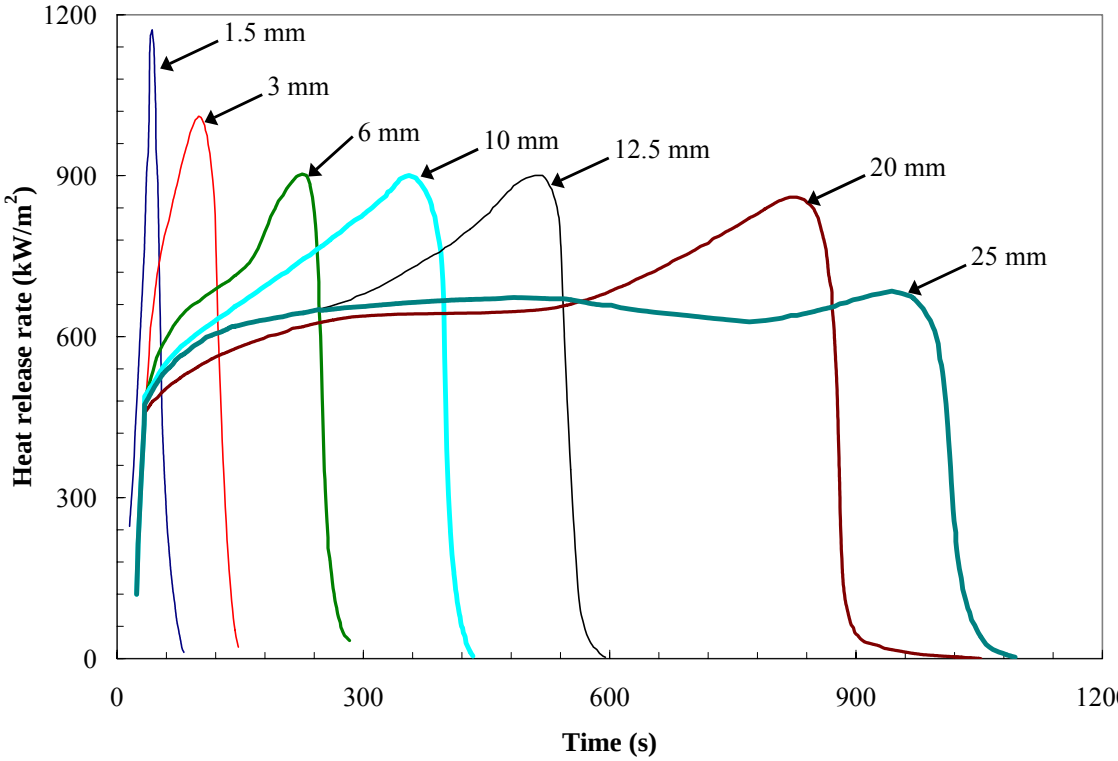

Figure 2.1. PMMA burning in the cone calorimeter–effect of thickness. Adapted from Babrauskas [34].

The simplest class of comprehensive pyrolysis models for polymers is ablation models [35 – 39] that are basically refinements to Equations 2.1 – 2.2. Rather than using Duhamel's theorem to calculate the surface temperature of a semi–infinite inert solid (Equation 2.1), the temperature profile of the finite–thickness solid is determined either by a numerical finite difference solution [38, 39] or integral methods [35–37] wherein a functional form of the temperature profile is assumed *a priori*. This makes it possible to handle materials that do not exhibit thermally thick behavior. With ablation models, the pyrolysis rate is zero until T_p is reached at the surface, at which point the surface temperature is maintained at T_p (as in Equation 2.2). Thus, it is assumed that the pyrolysis kinetics are much faster than heat diffusion, and that the latter is the limiting process. The rate of mass loss is calculated from a heat balance at the sample surface where it is

assumed that all mass loss occurs. The temperature distribution in the solid $T(z, t)$ is calculated by solving the one–dimensional heat conduction equation for an opaque constant density inert solid:

$$\rho c \frac{\partial T}{\partial t} = \frac{\partial}{\partial z}\left(k \frac{\partial T}{\partial z} \right) \tag{2.6}$$

Solution of Equation 2.6 requires specification of one initial condition and two boundary conditions. The initial condition describes the temperature profile in the solid at time $t = 0$, and the "back face" boundary condition describes the rate of heat transfer from the back face as a function of temperature. This back face boundary condition makes it possible to capture the upturn in the HRR after most of the material has been consumed, e.g. Figure 2.1. The remaining boundary condition is applied at the front face, and it takes a slightly different form depending on whether or not the material has ignited (started to gasify). Denoting t_p as the time at which the surface temperature reaches T_p, the front face boundary condition at $z = 0$ is [38]:

$$-k \frac{\partial T}{\partial z} = \dot{q}''_{net} \qquad \text{for } t < t_p \tag{2.7a}$$

$$T = T_p \qquad \text{for } t \geq t_p \tag{2.7b}$$

$$-k \frac{\partial T}{\partial z} = \dot{q}''_{net} - \dot{m}'' \Delta H_{vol} \qquad \text{for } t \geq t_p \tag{2.7c}$$

The primary quantity of interest is usually the fuel generation rate (equivalent to the mass loss rate), $\dot{m}''$, which is determined from Equation 2.7c. ΔH_{vol} is the heat of volatilization, often called the heat of vaporization by the fire community (see Section 2.2.2 for further explanation), and is not the same as ΔH_g, the heat of gasification. ΔH_{vol} is the quantity of heat required to generate unit mass of volatiles at T_p from unit mass of solid at T_p and is

positive for an endothermic process. As will be discussed in Section 2.2.2, ΔH_g is equal to ΔH_{vol} plus the sensible enthalpy required to raise unit mass of solid from its initial temperature T_0 to its pyrolysis temperature T_p.

The primary advantage of this approach compared with more detailed models discussed later is its simplicity, being not much more complicated than Equations 2.1 – 2.2 above. The decomposition process is characterized by a single parameter (T_p), making approximate analytical solutions possible [35]. Finite thickness materials that are influenced by the back face boundary condition can be readily handled. With a finite–difference solution method, temperature–dependent material properties (k, ρ, c) can be incorporated. Despite its simplicity, this approach is capable of accurately reproducing burning rates in bench–scale combustion experiments [37, 39], as shown in Figure 2.2.

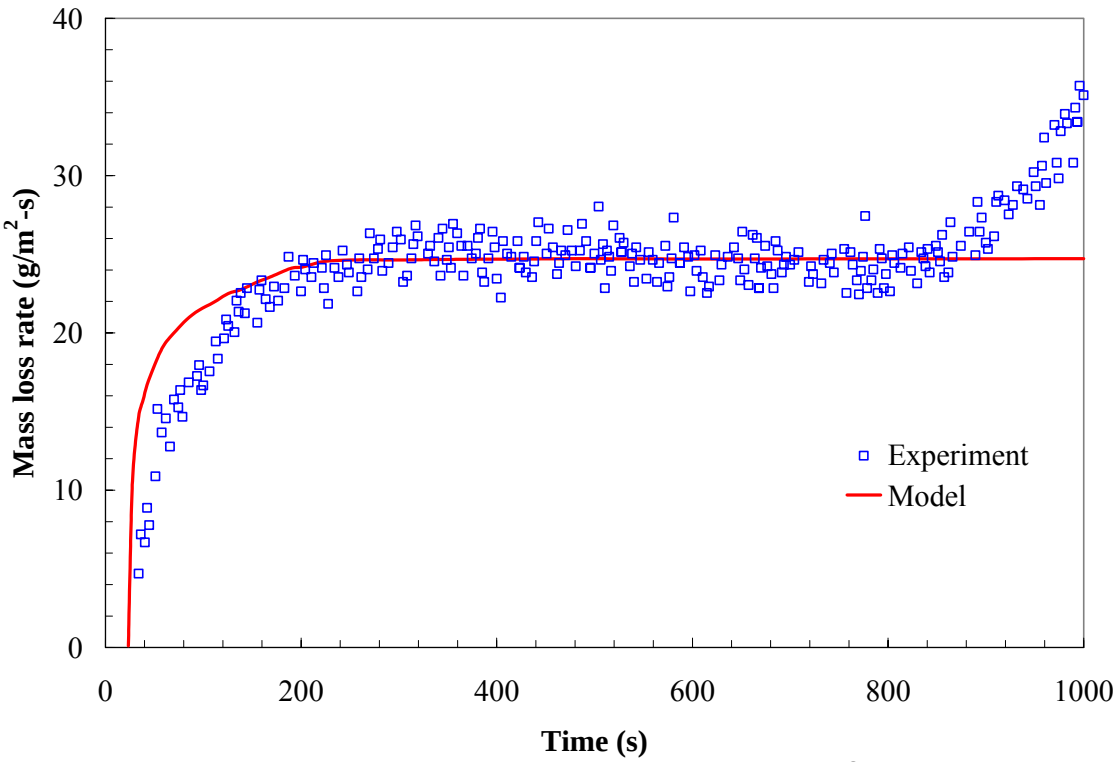

Figure 2.2. PE burning in cone calorimeter at 70 kW/m^2 irradiance. Comparison of measured MLR and integral ablation model [37] calculation.

One disadvantage of the ablation approach compared with the semi–empirical models discussed earlier is that the properties required to characterize a particular material cannot be directly determined from bench–scale fire tests. Individual values of k, ρ, and c are needed rather than the product $k\rho c$ (which can be estimated from fire tests [19]). Furthermore, the heat of volatilization ΔH_{vol} is also needed; it cannot be easily estimated from bench–scale fire test data (only ΔH_g can). Related to the physics, disadvantages include the assumption that ignition occurs when the solid surface temperature reaches T_p and then remains constant. In actuality, the surface temperature at ignition depends on the environmental conditions and pilot strength/location. As mentioned above, the temperature of a burning solid does not remain constant at its ignition temperature [23, 24]. Unless an advective term is added to Equation 2.6 to accommodate surface regression, there is no mechanism to account for a change in thickness as the sample burns away. Since the calculations in Figure 2.2 are based on a model that does not account for surface regression, the model calculations deviate from the experimental data after ~800 s due to the insulating effect of the substrate and the decreasing thickness of the solid.

Finite rate pyrolysis models, which usually involve a single–step n^{th}–order Arrhenius reaction, represent the next level of complexity. Pyrolysate generation has been treated as occurring only at the surface [3**,** 40] or more frequently, as a distributed in–depth reaction [41–51] to account for sub–surface fuel generation. With ablation models [35–39] or finite–rate kinetics models that relate the fuel generation rate to the surface temperature [3**,** 40], all fuel generation occurs at the surface. However, once a finite–rate distributed reaction is introduced (see Equations 2.8 – 2.10 below), fuel

generation also occurs in–depth. The decomposition or pyrolysis process is characterized by three parameters: pre–exponential factor (Z), activation energy (E), and reaction order (n), although n is frequently assumed to be 1. The volumetric decomposition rate (kg of volatiles generated per unit volume of condensed phase per second) is a function of temperature and the "conversion" α which can be thought of as the reaction progress (discussed in greater detail in Section 2.2.1, see Equation 2.19). This type of model can be summarized briefly as:

$$\rho c \frac{\partial T}{\partial t} + \rho w c \frac{\partial T}{\partial z} = \frac{\partial}{\partial z}\left(k \frac{\partial T}{\partial z} \right) - \dot{\omega}'''_{fg} \Delta H_{vol} - \dot{Q}'''_{s-g} \tag{2.8}$$

$$\dot{\omega}'''_{fg} = \rho Z (1-\alpha)^{n-1} \exp\left(-\frac{E}{RT} \right) \tag{2.9}$$

$$\dot{m}''_g(z) = \int_{\delta}^{z} \dot{\omega}'''_{fg} \, \mathrm{d}\zeta \tag{2.10}$$

It has been assumed in writing Equations 2.8 and 2.10 that all fuel generated in–depth escapes instantaneously and no pyrolysate vapor is stored as bubbles in the molten polymer. Quantities without a subscript refer to the condensed phase, and a subscript g denotes the gaseous volatiles. The second term on the LHS of Equation 2.8 includes the advective velocity w because as the condensed phase is volatilized, it is assumed that the molten polymer instantaneously fills the voids, thereby giving rise to surface regression. Here, $\dot{m}''_g(z)$ is the local mass flux of gaseous fuel, taken as negative when flowing toward the surface since the $+z$ direction points into the solid. It is assumed that the condensed phase density is constant (i.e., density invariant with temperature), so from mass conservation the advective mass flux of the molten polymer is related to the mass flux of gaseous fuel as $\rho w(z) = -\dot{m}''_g(z)$. The divergence of the volatile mass flux is the

local volumetric fuel generation rate, i.e. $\frac{\partial \dot{m}''_g}{\partial z} = \dot{\omega}'''_{fg}$. Due to temperature gradients, the temperature at which pyrolysate is generated in–depth is generally different from the temperature of the condensed phase material through which it must pass to reach the surface. Thus, there will be heat transfer between the gaseous and condensed phases. This is accounted for through the term $\dot{Q}'''_{s-g}$, the volumetric rate of heat transfer from the solid phase to the gas phase. This term is sometimes modeled by assuming thermal equilibrium between the gaseous and condensed phases, giving rise to a convective term of the form $\dot{m}''_g c_{pg} \frac{\partial T_g}{\partial z}$. However, this term is sometimes omitted [3, 51] on the basis that it is small except at high heat flux levels with steep temperature gradients. One challenge is simulating the mechanism through which pyrolysate vapors generated in–depth escape from the solid. Although it is usually assumed that the vapors instantaneously escape with no flow resistance, a few studies have included the effect of bubbling, ranging from simplified [48] to detailed [52–54] treatments.

One shortcoming of this modeling approach is that the effect of oxygen concentration on the decomposition rate is not explicitly included. In general, the decomposition kinetics and thermodynamics (as well as the composition of the volatiles generated) are sensitive to oxygen concentration. In a fire, combustible solids can be exposed to oxygen concentrations ranging from those of the ambient oxidizer to close to zero.

The sensitivity of solid decomposition to oxygen has been demonstrated by Kashiwagi and Ohlemiller [55]. They measured the mass loss rate of PMMA irradiated (under nonflaming conditions) at 17 and 40 kW/m^2 in atmospheres ranging from pure

nitrogen to 40% oxygen by volume. Their results are reproduced in Figure 2.3. It can be seen that the mass loss rate increases with the oxygen content of the atmosphere, but the oxygen sensitivity is more noticeable at 17 kW/m^2 irradiance (Figure 2.3a) than 40 kW/m^2 (Figure 2.3b). This observation can be explained as follows: the oxygen concentration in the vicinity of the sample surface is reduced as the mass loss rate increases because gas phase oxygen from the oxidizer stream is displaced by the gaseous pyrolysate "blowing" from the sample surface. Since the mass loss rates are higher at 40 kW/m^2, the surface is better protected by blowing and it is more difficult for oxygen to penetrate into the polymer. This reveals some of the transport phenomena affecting solid decomposition: oxygen must be making its way into the molten polymer by either molecular diffusion or penetration into burst pores created by bubbling. As will be discussed in Section 2.2.1, we still have a limited quantitative understanding of these phenomena.

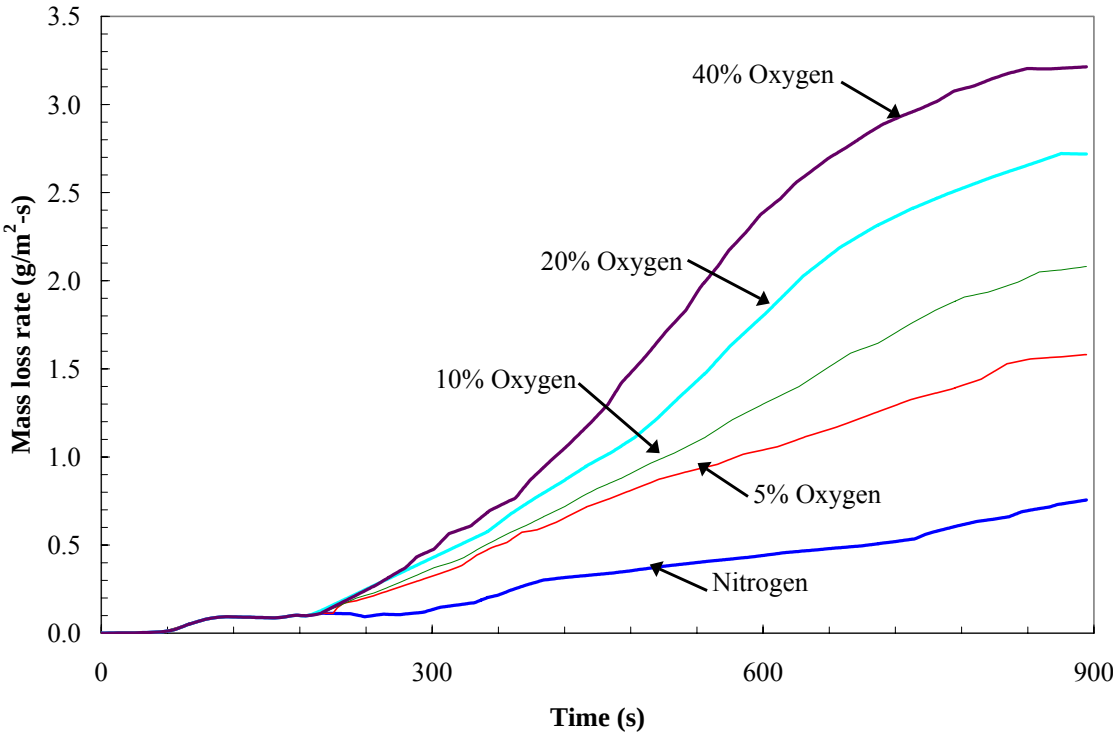

(a)

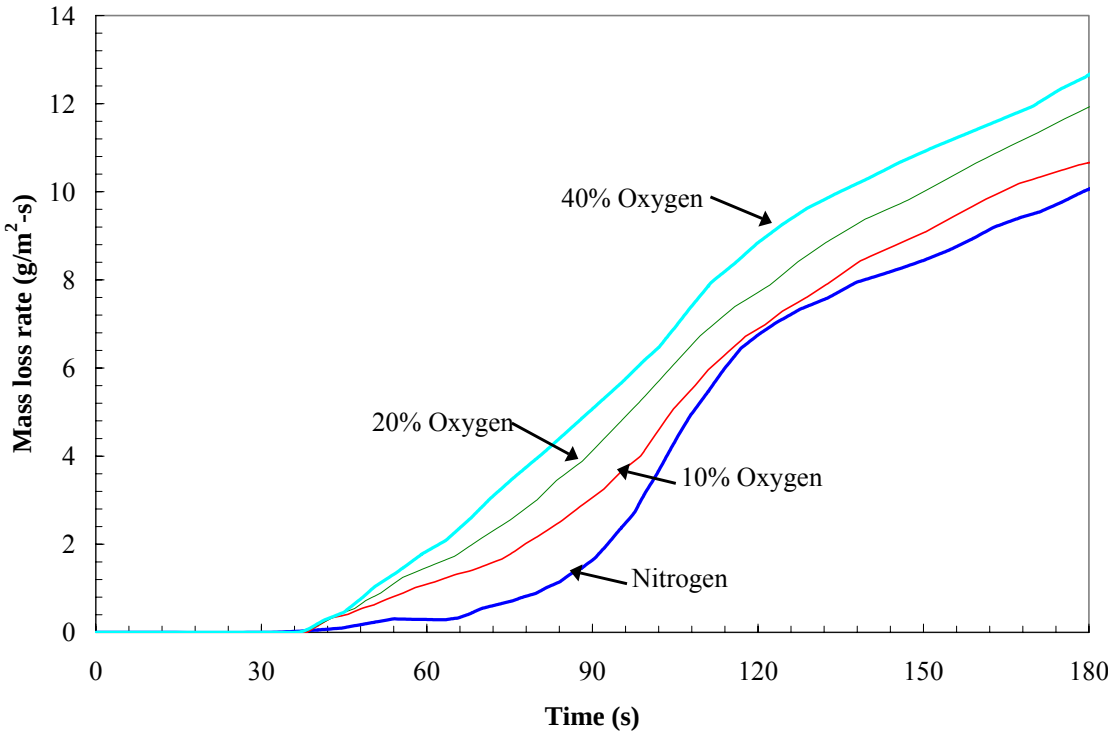

(b)

Figure 2.3. Effect of ambient oxygen concentration on gasification rates of PMMA. From Kashiwagi and Ohlemiller [55]. (a) 17 kW/m^2; (b) 40 kW/m^2.

2.1.3 Comprehensive pyrolysis models: charring materials

A large number of materials encountered in practice exhibit charring, either naturally (wood, thermoset polymers, phenolic composites) or due to addition of fire retardants. In contrast to thermoplastic materials where most of the fuel generation occurs near the surface (even for a distributed reaction), the primary fuel generation zone in charring materials can be located well below the surface at a reaction front that separates the char layer from the virgin layer. For a fixed thermal exposure, thermoplastics show an increasing or steady–state MLR/HRR until the material is consumed. However, charring materials generally show a decaying MLR/HRR after an initial peak is reached. This is because a low–density porous char helps protect the virgin material from further heat transfer (char can be quite effective at limiting carbon transfer from the condensed phase). Some materials show a second peak if the reaction zone "feels" the insulating effects of the underlying substrate. This dual–peak shape is characteristic of charring materials, but it is not always observed—whether or not two peaks occur depends on the thickness, heat flux, and substrate material. Figure 2.4 shows the mass loss rate of particleboard measured in nitrogen when irradiated at six heat flux levels between 14 and 39 kW/m^2 [56]. At higher heat flux levels the distinctive two–peak curve becomes apparent, but it does not occur at the lower heat flux levels. The change in shape of the mass loss rate curve with heat flux is the combined effect of several phenomena: heat transfer in the virgin and char layers and to the underlying substrate as well as chemical kinetics, which control the rate at which the virgin material is converted to char.

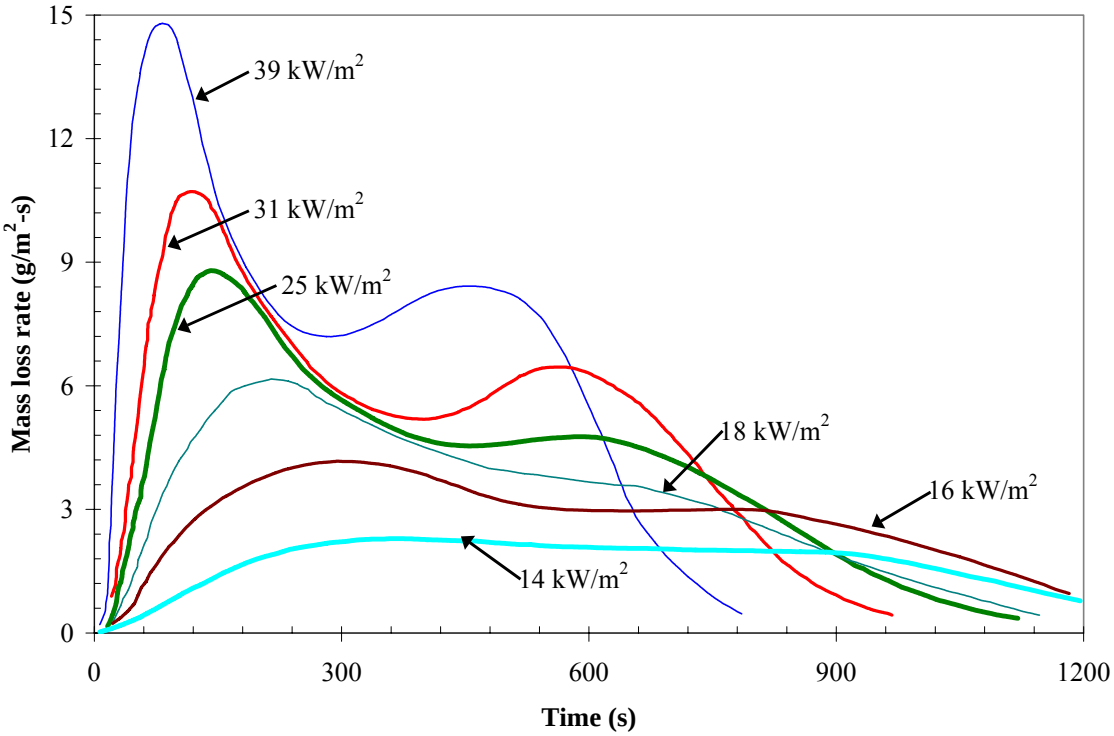

Figure 2.4. Mass loss rate of particleboard in nitrogen (from [56]).

In addition to general reviews that cover some aspects of modeling charring degradation [10–12, 14], modeling the fire behavior of charring materials has been specifically covered in review papers published in 2000 [13] (wood and polymers), 2005 [15] (lignocellulosic fuels), and 2007 [17] (biomass). These papers provide a good assessment of the current status of modeling the decomposition of charring solids.

Models of charring pyrolysis usually use numerical solution of the governing equations. An exception is the asymptotic analysis of Wichman and Atreya [57] wherein approximate formulas are developed for the mass loss rate of a charring solid in the limit of large activation energy. In the simplest class of numerical models for charring pyrolysis, it is assumed that an infinitely thin reaction zone (or pyrolysis front) separates the char layer from the virgin material [58–68], analogous to the Stefan problem where phase change occurs at a thin interface. This is a reasonable approximation at high heat

flux levels, but can become questionable at lower heat fluxes. A single reaction is considered, and infinitely fast or finite rate kinetics can be used. In some models, the conversion of virgin material to char is assumed to occur at a fixed pyrolysis temperature [58–63, 66–67] and the velocity at which the front propagates into the solid is determined by a heat balance at the pyrolysis front. Thus, the kinetics are infinitely fast, analogous to the thermoplastic ablation models discussed earlier. In other formulations, finite rate kinetics are used, and the propagation velocity follows the usual Arrhenius form [3, 64, 65]. A recent paper [68] compared the infinite–kinetics (fixed pyrolysis temperature) approach to the finite kinetics approach. Integral models [58, 59, 61, 62, 66, 67, 69] have the advantage that the governing partial differential equations are transformed to ordinary differential equations, but numerical solution is generally still required.

Several models have been postulated that do not rely on the assumption of an infinitely–thin pyrolysis front separating the char layer from the virgin material (see e.g. [51, 70–80]). When a single global reaction is considered, they are all essentially variations of Kung's 1972 model [70], originally developed for wood. Although this model is quite simple compared to some of the more recent modeling efforts, it illustrates the main characteristics of the newer models that generally include more sophisticated submodels for transport phenomena or reaction chemistry. Kung's model [70] describes the decomposition process as a single–step endothermic Arrhenius reaction where virgin wood is converted to char and volatiles, with the volatiles escaping instantaneously. The density, thermal conductivity, and volumetric heat capacity are assumed to vary linearly with the extent of conversion between virgin wood and char. Heat transfer due to

movement of volatiles through the char layer is accounted for by assuming that thermal equilibrium exists between the solid and gas phases.

Kung originally posed the model in terms of an "active material" generated from a virgin material. However, a slightly different formulation is presented here wherein the mass fraction of each solid phase "species" (i.e. virgin material or char) is tracked. This makes it straightforward to extend the model to more detailed cases where multiple species are tracked. For simplicity, the moisture content is assumed to be negligible. Let Y_c and Y_v designate the local mass fractions of char and virgin material in the solid (X_c and X_v are the analogous volume fractions). The bulk density of the virgin material is denoted ρ_v, and the bulk density of the fully–reacted char is ρ_c. It is assumed here that ρ_v and ρ_c are constant for a particular material, i.e. they do not depend on temperature. The sensible specific enthalpies of the virgin and char are denoted h_v and h_c. Then, the weighted bulk density and specific enthalpy are defined as:

$$\overline{\rho} = X_v \rho_v + X_c \rho_c \tag{2.11a}$$

$$\overline{h} = Y_v h_v + Y_c h_c \tag{2.11b}$$

Consider a single reaction that converts virgin fuel to char and volatiles. It is assumed to be first order in the remaining virgin material, with the reaction rate following the usual Arrhenius dependency on temperature:

$$\dot{\omega}''' = \overline{\rho} Y_v Z \exp\left(-\frac{E}{RT}\right) \tag{2.12}$$

The volumetric formation rate of gaseous pyrolysate ($\dot{\omega}'''_{fg}$) and solid char ($\dot{\omega}'''_{fc}$) are determined from Equation 2.12 and the ratio of the char and virgin bulk densities as:

$$\dot{\omega}'''_{fg} = \left(1 - \frac{\rho_c}{\rho_v}\right)\dot{\omega}''' \tag{2.13a}$$

$$\dot{\omega}'''_{fc} = \frac{\rho_c}{\rho_v}\dot{\omega}''' \tag{2.13b}$$

Assuming there is no net shrinkage or swelling during the charring process and that the storage of gaseous pyrolysate in the char pores is negligible in comparison with its formation rate, conservation of mass, species, and energy can be summarized as:

$$\frac{\partial \overline{\rho}}{\partial t} = -\frac{\partial \dot{m}''_g}{\partial z} = -\dot{\omega}'''_{fg} \tag{2.14}$$

$$\frac{\partial\left(\overline{\rho} Y_c\right)}{\partial t} = \dot{\omega}'''_{fc} = \frac{\rho_c}{\rho_v}\dot{\omega}''' \tag{2.15}$$

$$\overline{\rho}\frac{\partial \overline{h}}{\partial t} = \frac{\partial}{\partial z}\left(\overline{k}\frac{\partial T}{\partial z}\right) - \dot{\omega}'''_{fg}\Delta H_p - \dot{Q}'''_{s-g} \tag{2.16}$$

In Equation 2.14, $\dot{m}''_g$ is the mass flux of volatiles, taken as negative when flowing toward the surface (because the $+z$ direction points into the solid). It has been assumed that the volatiles escape instantaneously with no flow resistance and that no net shrinkage or swelling occurs. For clarity of presentation, Equation 2.16 has been written assuming that both solid species have equal specific heat capacities; the more general case gives rise to terms having the form of a volumetric reaction rate multiplied by enthalpy differences between species (see Section 3.1.7) but is not instructive. The $\dot{Q}'''_{s-g}$ term in Equation 2.16 accounts for heat transfer from the solid phase to the gas phase, analogous to Equation 2.8. ΔH_p is the "heat of pyrolysis", the analogous quantity to the heat of volatilization ΔH_{vol} discussed earlier with reference to thermoplastic materials. As with ΔH_{vol}, ΔH_p is positive if the reaction is endothermic. Note that the conservation equation

for the virgin mass fraction is obtained from solution of Equation 2.15 since $Y_c + Y_v = 1$. In Equation 2.16, $\bar{k}$ is the effective thermal conductivity. It depends on the local state of the material (i.e., Y_c and Y_v) and temperature, particularly due to radiative transfer across pores (these issues are discussed further in Section 2.3). Although it is difficult to accurately estimate the thermal properties of partially degraded materials, the simplest approach is to assume that $\bar{k}$ varies linearly with the local mass fractions and is independent of temperature:

$$\bar{k} = X_v k_v + X_c k_c \tag{2.17}$$

where k_v and k_c are constants corresponding to the thermal conductivity of the virgin material and the completely charred material respectively. Similarly, the mass–weighted specific heat capacity is:

$$\bar{c} = Y_v c_v + Y_c c_c \tag{2.18}$$

Even for this relatively simple model, ten model constants are required to characterize a particular material: k_v, ρ_v, c_v, k_c, ρ_c, c_c, Z, E, ΔH_p, and c_{pg}. Of these, only ρ_v is readily attainable by direct measurement. Recognizing this difficulty, de Ris and Yan [81] developed an optimization method that determines a set of "equivalent properties" which maximize the agreement between the predictions of a linearized version of Kung's model and experimental data. This methodology for determining the model constants has been applied infrequently [82], and only a few sets of parameter values were found in the literature. Some of those are listed in Table 2.1.

Table 2.1. Literature values of Kung [70] char model parameters.

	Pacific maple [74]	Particle board [74]	White pine [75]	Red oak[†] [82]
k_v [W/m–K]	0.16	0.126	$0.157 + 0.0003(T–T_0)$	0.15–0.21
ρ_v [kg/m^3]	530	663	–	660–700
c_v [J/kg–K]	2420	2520	$2140 + 4.19\ (T–T_0)$	1400–1800
k_c [W/m–K]	$0.16 + 8.2\times10^{-5}\ (T–T_0)$	0.126	$0.084 + 0.002(T–T_0)$	0.18–0.27
ρ_c [kg/m^3]	106	133	–	170–200
c_c [J/kg–K]	1.0	2520	$1928 + 1.98(T–T_0)$	2500–3000
c_g [J/kg–K]	–	–	2000	–
Z [s^{-1}]	5.25×10^8	5.25×10^7	7.49×10^9	–
E [kJ/mol]	110	125.6	145[‡]	–
ΔH_p [J/kg]	0	0	3.0×10^5	$1.0 – 6.8 \times 10^5$
ε [–]	–	0.9	–	0.88 – 1.0

[†] Z and E given for linearized pyrolysis reaction, see Refs. 81–82.
[‡] Listed as "1.45E8 J/(mol K)"

More complex analyses of charring pyrolysis usually use a basic modeling approach similar to that embodied in Equations 2.11 – 2.18. What differs from model to model is the reaction mechanism (i.e., multi–step, reaction order other than unity), the number of condensed phase species, and treatment of the transport phenomena, i.e. calculation of the effective thermal properties, inclusion of an internal flow–resistance, swelling/shrinkage, or description of bubbling and related phenomena. For example, the influence of the porous char structure on flow of volatiles has been investigated by adding solution of the momentum equation using Darcy's law [71, 72]. Fredlund [72] formulated a detailed two–dimensional model (most models are one–dimensional) that included flow of both liquid and gaseous water, with Darcy's law for flow through the porous components. The model also included a surface reaction. The model predictions were compared to extensive experimental data, including temperature, density, and pressure measured at several in–depth locations with generally good results. This set of experimental data [72] remains one of the most comprehensive available in the literature. These more complex models have rarely been applied to fire situations, although they are

used extensively in chemical engineering for purposes of optimizing energy conversion techniques, particularly from biomass.

The mass loss rate of charring materials generally increases with oxygen concentration. Oxidative reactions occurring near the surface of the char layer may substantially increase the surface temperature above that in inert environments, and under some circumstances char oxidation may account for ~10% of the heat release rate under flaming conditions [83]. As with the thermoplastic model above, when using Equations 2.11 – 2.18 there is no way to account for the influence of oxygen on the pyrolysis reaction, unless Z, E, and ΔH_p are made explicit functions of the ambient oxygen concentration or an additional oxidative reaction is added. To illustrate the importance of oxygen concentration on the decomposition of charring materials, the mass loss rate and surface temperature of white pine irradiated at 40 kW/m^2 at three different oxygen concentrations [84] is shown in Figure 2.5. It can be seen from Figure 2.5a that the mass loss rate in air is approximately double that in nitrogen. The effect of char oxidation is evident in Figure 2.5b where it can be seen that the surface temperature of the sample tested in air is approximately 150 ºC greater than that of the sample tested in nitrogen. Related to fundamental transport phenomena, these data indicate that the decomposition kinetics and/or thermodynamics (endothermic vs. exothermic reactions) are affected by oxygen concentration. Surface heating due to char oxidation is a critical factor affecting autoignition because gas phase combustion reactions are initiated by the hot surface. The surface temperature of decomposing solids is very difficult to measure accurately, and measurements are scarce, but recent work using optical methods is promising [24, 85].

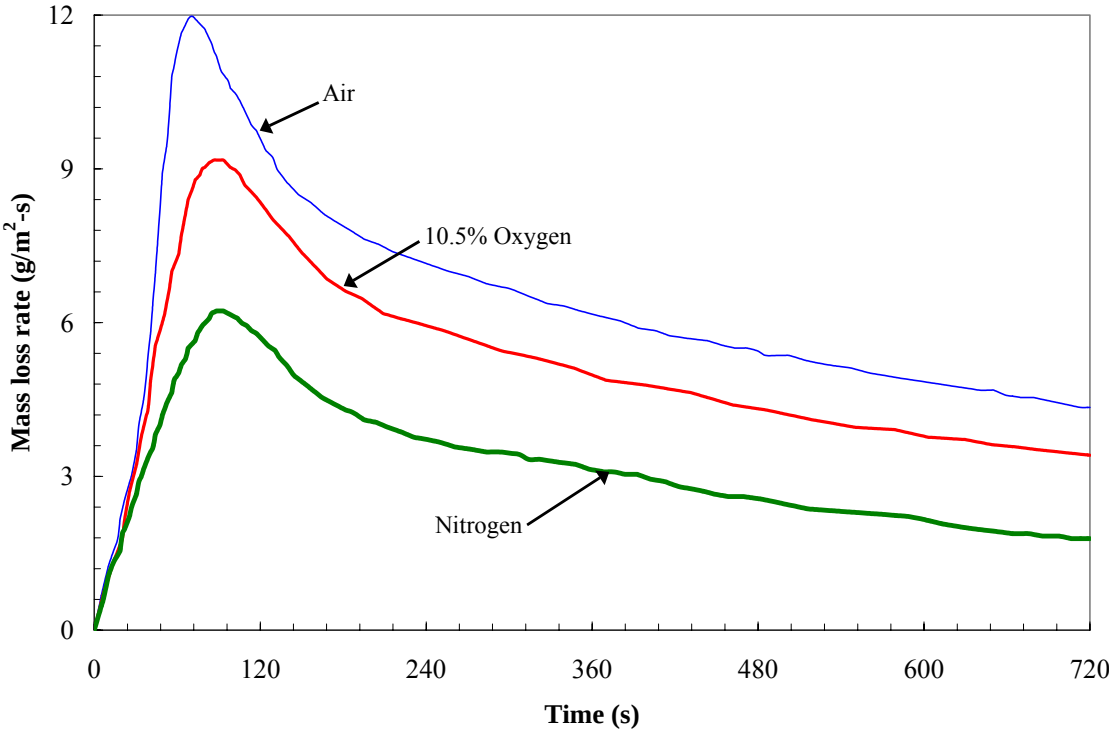

(a)

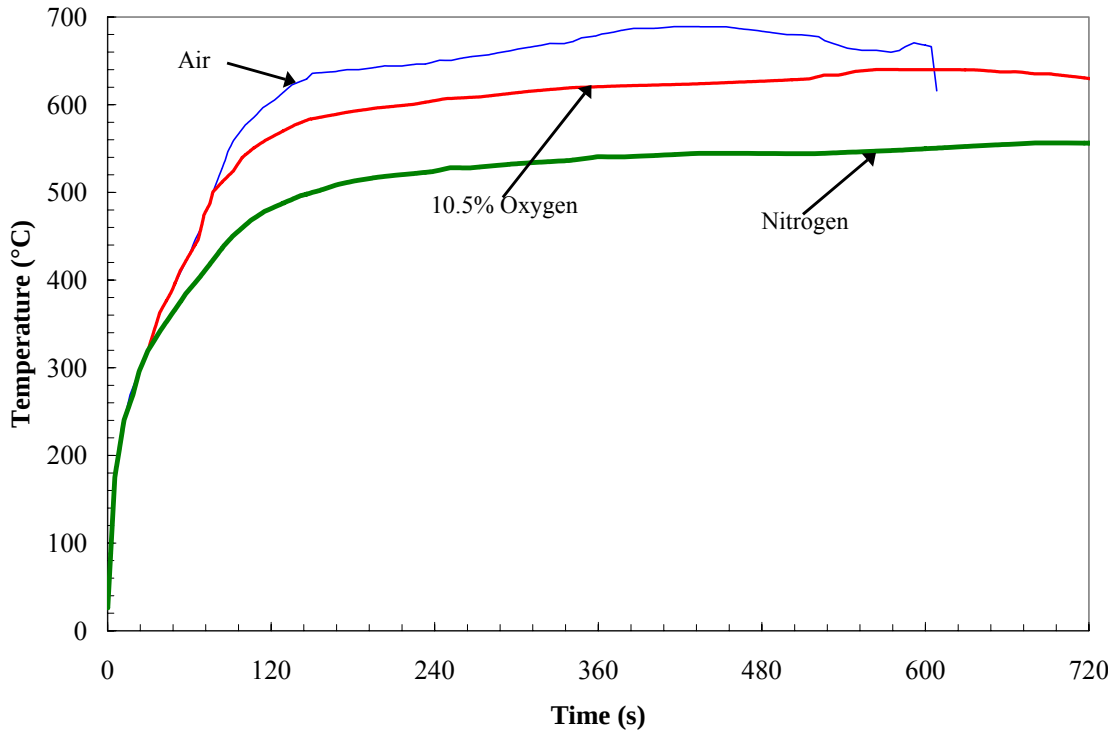

(b)

Figure 2.5. Experimental measurements of white pine irradiated at 40 kW/m^2 under three different oxygen concentrations. Adapted from Ref. [84].
(a) Mass loss rate; (b) Surface temperature.

2.1.4 Comprehensive pyrolysis models: intumescent coatings

An intumescent material or coating swells when heated to form a porous low–density char, thereby reducing heat transfer to the underlying virgin material. Intumescence is an effective mechanism for providing a high degree of thermal resistance while minimizing thickness of the protective skin. Intumescent coatings are sometimes applied to steel structural members to achieve the fire resistance ratings required by building codes, although the US Navy has concluded that intumescent coatings do not provide a level of fire resistance equivalent to traditional insulation, largely due to poor adhesion characteristics [89]. In addition to being applied as a coating, intumescents are sometimes grafted into composite materials to improve fire performance. Given the environmental problems associated with traditional halogenated fire retardants, ecological concerns may lead to an increased usage of intumescence or char promoters, which are thought of as ecologically friendly processes [90].

Modeling intumescence is considerably more complicated than modeling thermoplastic or charring pyrolysis due to large changes in density and volume. The earliest model for the thermal response of an intumescent material in the open literature was presented by Cagliostro and Riccitiello [91] to help develop design guidelines for a NASA coating. The semi–empirical model used measured temperature–dependent property data where available. When quantitative data were not available, "reasonable values" were chosen. Decomposition was modeled by a three–step Arrhenius reaction. Since the emphasis was on the ability of the intumescent coating to insulate a substrate from thermal insult, the only quantitative comparison of prediction and experiment was for the measured substrate temperature.

Anderson and Wauters [92] used an approach similar to Cagliostro and Riccitiello [91] to model a different intumescent coating used by the US Navy. Thermogravimetric (TG) and Differential Scanning Calorimetry (DSC) data (see Sections 2.2.1 and 2.2.2) were used to establish the kinetics and thermodynamics of the decomposition process. An interesting feature of their approach is that the TGA experiments were modeled with a 31 term Fourier series rather than the traditional Arrhenius approach. A Lagrangian formulation was adopted, and the change in volume of an element was related directly to its change in mass. They compared model predictions to experimental data for the substrate temperature and expansion factor. They found that the model was able to capture the main features of the experiments, but there were quantitative discrepancies between the measured and calculated substrate temperature.

Buckmaster *et al.* [93] later argued based on experimental observation that intumescence occurs at a thin front. Adopting an Eulerian description, they modeled the reaction as occurring at fixed temperature at an infinitely–thin interface between the intumescent char layer and the unreacted material, reducing their model to a Stefan problem. The results were compared only qualitatively with experimental data because their emphasis was on the mathematical description of the problem rather than making quantitative predictions.

Henderson and Wicek [94] developed a detailed model of an expanding phenolic composite that included gas flow by Darcy's law. Temperature dependent thermal properties were used, along with an Arrhenius decomposition reaction in which the activation energy, pre–exponential factor, and reaction order varied with the extent of conversion. The only quantitative comparison between the model predictions and

experimental data was for temperatures measured at four different locations within the solid, and very good agreement was obtained. An interesting feature of their model is that it predicted internal overpressures greater than 40 atm.

Shih *et al.* [95] extended the model developed earlier by Buckmaster *et al.* [93] and treated intumescence as a phase change occurring over a finite temperature range using the concept of a "pseudo latent heat" to account for the endothermicity of the intumescent reaction. Their model was capable of reproducing the "bending" behavior seen in the experimentally measured substrate temperature profiles. Similar to Shih *et al.* [95], Bourbigot *et al.* [96] treated the intumescent process in a polypropylene intumescent material as a phase change process, but with an Arrhenius reaction rate.

The most detailed models to date are probably due to Di Blasi and Branca [97] and Di Blasi [98]. They simulated the experiments of Cagliostro and Riccitiello [91] with a three–step reaction mechanism. The model predictions were very sensitive to the submodel used to calculate the effective thermal conductivity of the char. Quantitative agreement between the model predictions and the substrate temperature measurements [91] was possible only when using a thermal conductivity model developed specifically for intumescent coatings with a modification to account for radiation heat transfer across pores.

The model of Wang *et al.* [99] is notable because the three–dimensional problem was considered (all other models are one–dimensional). However, their model was not "fully" three dimensional because gas flow and swelling were permitted only in one direction.

Most authors simulating the decomposition of intumescent materials have used substrate temperature measurements as the only metric against which the predictive capabilities are judged. This is partly due to the dearth of available experimental data. However, it can be misleading to conclude that a particular model "works" on the basis of a comparison of a single temperature measurement. Also important are the mass loss rate or heat release rate and the degree of swelling predicted by the model. The paper by Griffin *et al.* [100] gives thermogravimetric and Differential Thermal Analysis (DTA) data for three different intumescent coatings as well as measurements of substrate temperature, expansion factor (degree of swelling), and heat release rate in the cone calorimeter. This may prove to be a useful source of validation data for modelers.

2.2 Decomposition kinetics and thermodynamics

Many of the pyrolysis models discussed above either treat the decomposition as being infinitely fast or use a single lumped reaction that approximates the "global" decomposition behavior. In actuality, the production of gaseous volatiles from a heated combustible solid is the macroscopic net result of multiple elementary reactions occurring simultaneously. Oxygen is involved in some reactions, as in the case of char oxidation, whereas other reactions can occur in the absence of oxygen, as in pyrolysis under nitrogen. As a result, both exothermic and endothermic reactions occur, sometimes simultaneously. Although techniques exist for measuring the rate constants of elementary gas phase reactions, analogous techniques have not yet been developed for kinetics in solids. Nonetheless, some fairly advanced diagnostic tools are used in the field of thermal analysis to investigate the kinetics and thermodynamics of decomposing solids. Experimental techniques that aim to study the decomposition kinetics and

thermodynamics of solids use very small samples (on the order of a few milligrams) to reduce heat and mass transfer effects. The assumption is that all gradients become negligible and the degrading sample can be treated as homogeneous (isothermal).

2.2.1 Thermal and thermooxidative stability

One of the most important factors contributing to a combustible solid's overall fire hazard is its thermal decomposition kinetics. Since ignition of solid materials is usually kinetically controlled (i.e., very sensitive to temperature near the heated surface), ignitability is strongly influenced by thermal stability. By viewing the flame spread process as a sequence of piloted ignitions, it can be seen that a material's propensity to propagate a flame is also affected by its thermal stability.

Thermogravimetric analysis (TGA) is the most widely used experimental technique for quantifying the thermal stability of solids. A high–precision scale is used to measure the mass of a small sample (usually no more than a few mg) as it is exposed to an atmosphere with specified temperature and composition. TGA experiments may be isothermal or, more frequently, expose the sample to an atmosphere having a temperature that increases linearly with time. Due to the small sample size, the sample temperature is taken as equal to the temperature of the atmosphere (low Biot number).

For a sample with initial mass m_0, the conversion α is defined as:

$$\alpha = \frac{m_0 - m}{m_0 - m_\infty} \tag{2.19}$$

where m_∞ is the sample mass at the end of the experiment. For materials that leave no residue (such as noncharring polymers), $m_\infty = 0$ and therefore $\alpha = 1 - m/m_0$. TGA data are usually analyzed within the framework of a kinetic model of the form:

$$\frac{\mathrm{d}\alpha}{\mathrm{d}t} = k(T) f(\alpha) \tag{2.20}$$

In Equation 2.20, $k(T)$ is a function carrying the temperature–dependency of the reaction rate and $f(\alpha)$ is the "reaction model", often assumed to be:

$$f(\alpha) = (1-\alpha)^n \tag{2.21}$$

where n is called the "reaction order" (in the remaining solid mass). With few exceptions [92, 101], the function $k(T)$ is assumed to take an Arrhenius form:

$$k(T) = Z \exp\left(-\frac{E}{RT}\right) \tag{2.22}$$

where Z is the frequency factor, or pre–exponential factor (often denoted A), and E is the activation energy. After combining Equations 2.20 – 2.22, the time rate of change of α becomes:

$$\frac{\mathrm{d}\alpha}{\mathrm{d}t} = Z \exp\left(-\frac{E}{RT}\right)(1-\alpha)^n \tag{2.23}$$

In nonisothermal experiments, the atmosphere temperature increases linearly with time at a constant heating rate (e.g., 20 ºC/min) denoted β. By assuming that the sample temperature is equal to the atmosphere temperature, the transformation $\mathrm{d}t = \mathrm{d}T/\beta$ can be made, and Equation 2.23 can be written as:

$$\frac{\mathrm{d}\alpha}{\mathrm{d}T} = \frac{Z}{\beta} \exp\left(-\frac{E}{RT}\right)(1-\alpha)^n \tag{2.24}$$

The three model parameters (Z, E, and n, sometimes called the "kinetic triplet") are determined from a plot of α or $\mathrm{d}\alpha/\mathrm{d}T$ as a function of T. A thermogravimetric (TG) curve is a plot of α vs. T, whereas a differential thermogravimetric (DTG) curve is a plot of $\mathrm{d}\alpha/\mathrm{d}T$ vs. T. Several techniques have been proposed for extracting the three model

parameters (Z, E, and n) from TG and DTG curves. They are all essentially nonlinear curvefitting exercise that seek to minimize the residual error between Equation 2.24 (or its integral) and experimental data. As an example, Figure 2.6 shows the experimentally measured $d\alpha/dT$ for high density polyethylene compared with the calculation of Equation 2.24 using $Z = 3.85 \times 10^{15}$ s^{-1}, $E = 252.8$ kJ/mol, and $n = 0.582$ [102]. Ideally, kinetic parameters should be determined for variable thermal conditions (heating rates).

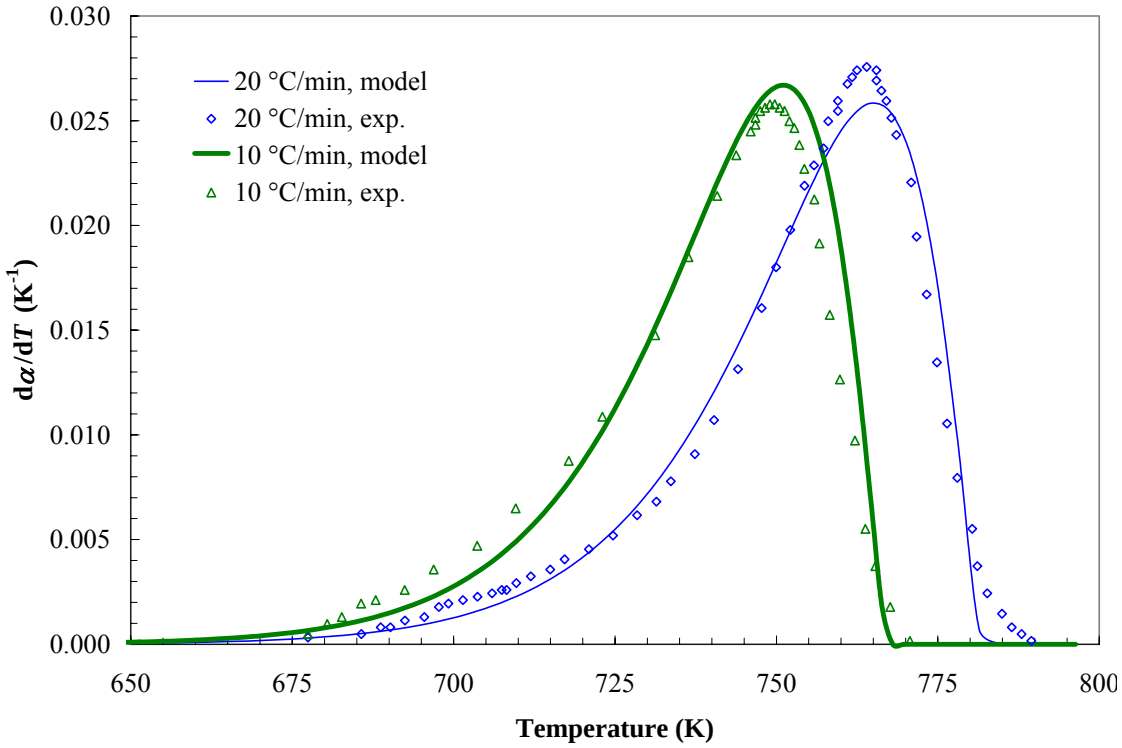

Figure 2.6. Single step decomposition of high density polyethylene [102]. Points are experimental data and solid line is calculated with Equation 2.24.

There is some debate regarding the interpretation of the parameters Z and E as well as the physical correctness of modeling the rate constant using an Arrhenius form. Vyazovkin and Wight [103] suggest that the physical interpretation of the Arrhenius function as applied to solid decomposition is supported by a sound theoretical foundation. Taking the opposite view, Agrawal [104] states, "Although the Arrhenius equation has

little physical significance in solid–state reactions, it may be assumed as a two–parameter model to correlate the data thereby minimizing the number of adjustable parameters." Ŝimon [101, 105] has also suggested that Z and E have no physical meaning and should be interpreted merely as adjustable model parameters. Similarly, Parker [106] wrote that for complex materials "not much physical significance should be attached to such parameters".

Regardless of the physical significance of the parameters in the single–step Arrhenius equation, it is capable of adequately reproducing experimental TG data for a variety of materials that exhibit single–step decomposition. Values of Z, and E and n that have been reported in the literature for a few representative materials are listed in Table 2.2.

Table 2.2. Literature values of kinetic triplet for single–step decomposition.

Material	Ref.	Atmosphere	β [ºC/min]	n	ln Z [ln (s^{-1})]	E [kJ/mol]
Cellulose	[107]	N_2	5	1	54.0	317
Cellulose	[107]	Air	5	1	47.6	277
PE	[107]	N_2	5	1	25.2	203
PE	[107]	Air	5	1	29.7	181
PE	[108]	5% O_2/95% N_2	5–20	1.3	18.4	138
PE (HD)	[109]	N_2	–	1	30.6	220
PE (LD)	[109]	N_2	–	1	34.5	241
PE (LD)	[109]	N_2	–	1	27.6	201
PET	[108]	Air	5–20	0.9	32.1	222
POM	[110]	N_2	4	1	26.0	118
PP	[107]	N_2	5	1	26.4	205
PP	[107]	Air	5	1	18.8	127
PP	[109]	N_2	–	1	35.7	244
PP	[109]	N_2	–	1	26.1	188
PS	[107]	N_2	5	1	35.3	240
PS	[107]	Air	5	1	11.7	110
PS	[109]	N_2	–	1	31.1	204

The atmosphere under which the experiments were conducted is listed in Table 2.2 because the decomposition kinetics of many materials are sensitive to oxygen concentration. One must be careful when applying literature values of thermokinetic parameters. For ignition studies, it is more appropriate to use values obtained in an oxidative environment (e.g., air) than under nitrogen. For estimating burning rates, values obtained under nitrogen are probably more appropriate because during flaming combustion the oxygen concentration near the solid surface is low since most oxygen is consumed at the diffusion flame front. Modeling flame spread and fire growth is more complicated because mass burning occurs in a largely inert environment (pyrolysis zone) but preheating and flame spread occur under oxidative conditions.

Due to the sensitivity of decomposition kinetics to oxygen concentration and the wide range of oxygen concentrations encountered in fires, a kinetic equation that explicitly accounts for the presence of oxygen on the decomposition rate could be useful. However, this has not yet been applied to fire scenarios and has only been used in research environments. Esfahani [111] modeled the thermo–oxidative degradation of a PMMA slab using a kinetic equation of the form:

$$\frac{\mathrm{d}\alpha}{\mathrm{d}t} = Z \exp\left(-\frac{E}{RT}\right)\left(0.8 + X_{O_2}^{\infty}\right)^8 \tag{2.25}$$

where $X_{O_2}^{\infty}$ is the freestream oxygen concentration. Other workers [108, 112] have used a similar equation:

$$\frac{\mathrm{d}\alpha}{\mathrm{d}t} = Z \exp\left(-\frac{E}{RT}\right)(1-\alpha)^n X_{O_2}^{\infty\, m} \tag{2.26}$$

where m is an exponent characterizing the material's decomposition sensitivity to oxygen. Senneca *et al.* [108] determined the constants m and n for PE and PET. Jun *et al.*

[112] used Equation 2.26 to study the thermooxidative decomposition of polypropylene. However, n varied with heating rate for a fixed value of m, and the activation energy and pre–exponential factor varied with oxygen concentration and heating rate.

One shortcoming of using Equation 2.25 or 2.26 to model the decomposition of thick solids is that the reaction rate within the solid should depend on the local oxygen concentration within the decomposing solid, not the freestream value. However, modeling the penetration of oxygen into a solid to determine the local oxygen concentration is a difficult task. Additionally, a material's decomposition kinetics may not change monotonically with oxygen concentration, as implied by Equations 2.25 and 2.26. For example, below ~270 ºC the decomposition of PMMA is actually faster in nitrogen than in air, but it becomes faster in air at higher temperatures [113].

The decomposition process of many solids is too complex to be characterized by a single–step reaction because multiple reactions become active over different temperature ranges. As an example, an experimental DTG curve for flexible polyurethane foam is shown in Figure 2.7, along with the calculation of a five step reaction mechanism developed by Rein *et al.* [114]. Table 2.3 lists a few references where multiple–step reactions have been developed for various materials.

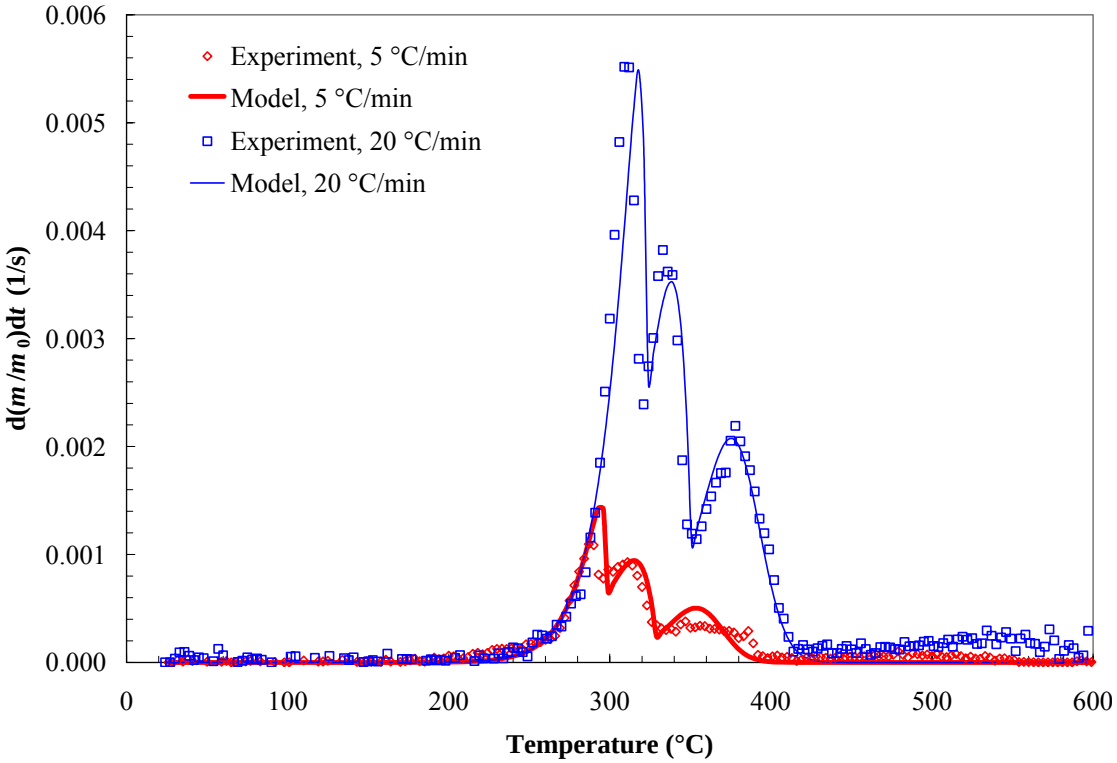

Figure 2.7. Decomposition of polyurethane foam in air.
Points are TG data and solid lines are reaction mechanism of Rein *et al.* [114].

Table 2.3. Literature sources for multi–step reaction decomposition mechanisms.

Material	Ref.	Atmosphere	# Steps
Douglas fir	[106]		4+
PMMA	[115]	Argon	4
PVC	[116]	He:O_2 (variable)	3 or 7
Intumescent coatings	[100]	Air, N_2	3+
Polyurethane	[117]	Air	3
Polyurethane	[114]	Air, N_2	5
Epoxy resin	[118]	Air	2
Chestnut wood	[119]		7
Lodgepole pine	[120]		5
Pine (wet)	[121]		6
FR white pine	[122]	Nitrogen	3

Interestingly, many examples exist in the literature where different workers have found that the same generic material (i.e., PMMA or PE) shows a different number of reaction steps. As an example, the decomposition of PMMA under nitrogen has been observed to proceed as a single step [123] and four steps [115]. These differences are

probably attributed to differences in polymer synthesis or sample preparation. Lyon and Walters [124] point out that the "heat release capacity" of polymers (as determined by pyrolysis combustion flow calorimetry) can vary by $\pm 20\%$, depending on the source of the sample.

As with the number of decomposition steps, it is common for different values of reaction order to be reported for the same generic material and there is much discussion in the thermal analysis literature regarding how to determine reaction order. Gao *et al.* [123] show that reaction order can be estimated by the value of α at the maximum reaction rate. So–called "model–free" or "isoconversional" methods have been developed [105, 125] which permit the activation energy to be estimated independent of the reaction order. However, the activation energy depends on the extent of conversion, and the pre–exponential factor cannot be estimated without assuming a reaction order.

While thermogravimetric analysis is a useful tool for quantifying a solid's thermal stability, it has several limitations. TGA's relevance to fires has been questioned [118] because typical TGA heating rates (between 0.1 K/min and 30 K/min) are much lower than can be encountered in fires (sometimes 500 K/min or greater). One difficulty associated with using higher heating rates in TGA is that the thermal lag between the sample temperature and the atmosphere temperature increases with heating rate, especially if the decomposition process is endothermic. The magnitude of this thermal lag is difficult to accurately quantify.

Undetected thermal lag may be responsible for the "compensation effect", which refers to linear dependence of ln Z on E frequently found in thermogravimetric studies [123, 126]. Consequently, the thermokinetic parameters found by TGA are a function of

the heating rate. Carrasco and Pagès [127] found that the pre–exponential factor depends only on the heating rate (compensation effect) but also on the mass of the sample, indicating that the effects of heat and mass transfer are not completely absent from the TGA experiments.

2.2.2 Reaction enthalpies

Whereas the rate at which a material burns once ignited is usually not strongly sensitive to its thermal decomposition kinetics, it is quite sensitive to the enthalpies of reaction. At solid temperatures typical of flaming combustion, the decomposition kinetics of most solids become so fast that they are no longer the limiting factor in the gasification process. Instead, the mass burning rate is determined by a balance between the applied heat flux, surface heat losses, heat conduction to the interior of the solid, and the heat absorbed or released in chemical reactions within the solid. However, since decomposition kinetics affect this heat balance, they do have a secondary effect on mass burning rates. This heat balance is the basis for the semi–empirical pyrolysis models discussed in Section 2.1.1. More specifically, the steady–state mass loss rate can be related to the heat (or enthalpy) of gasification (ΔH_g) as:

$$\dot{m}'' = \frac{\dot{q}''_{net}}{\Delta H_g} \tag{2.27}$$

where $\dot{q}''_{net}$ is the net rate of heat transfer to the material's surface. It can be seen from Equation 2.27 that (under steady state conditions) $\dot{m}''$ plotted against $\dot{q}''_{net}$ should have slope $1/\Delta H_g$, provided ΔH_g does not depend on $\dot{q}''_{net}$. This permits ΔH_g to be measured directly from bench–scale combustion experiments [25], and ΔH_g is widely viewed as a

material fire property. Experimental values of ΔH_g for different fuels have been tabulated elsewhere [14, 27] and are not reproduced here.

Equation 2.27 was originally applied to the steady burning of polymers [25]. Following Lyon and Janssens [14], ΔH_g can be defined more precisely as:

$$\Delta H_g = \int_{T_0}^{T_p} c(T)\,\mathrm{d}T + \Delta H_m + \Delta H_d + \Delta H_v \tag{2.28}$$

where ΔH_m is the latent heat of melting (if melting occurs between T_0 and T_p), ΔH_d is the bond dissociation energy, and ΔH_v is the heat of vaporization of the decomposition products. ΔH_d can be thought of as the heat required to break a polymer molecule into fragments by thermal decomposition, and ΔH_v is the heat required to subsequently vaporize those decomposition products. Thus, the heat of gasification is the difference between the enthalpy of the solid fuel at T_0 and the enthalpy of its volatiles at T_p. In other words, ΔH_g is the quantity of heat required to generate unit mass of volatiles at temperature T_p from unit mass of solid initially at T_0.

Although ΔH_g is usually treated as an effective value that is constant for a particular material, there are several reasons that ΔH_g is technically not constant. Due to the upper bound of the integral on the RHS of Equation 2.28, ΔH_g depends on the temperature at which volatilization occurs (T_p). As discussed earlier, real materials do not instantaneously volatilize at a fixed temperature, but rather over a finite temperature range. Additionally, a spectrum of decomposition products is formed during thermal degradation. The composition of these volatiles depends on temperature, atmospheric composition, and perhaps heating rate. As an example, the monomer yield decreases with temperature for PMMA and PS, but increases with temperature for PP [128]. Partially

oxidized fuel fragments may appear in the decomposition products for decomposition under air, but not inert environments unless the solid contains oxygen. Since the heat required to break large molecules into fragments and then vaporize these fragments depends on their chemical composition, ΔH_d and ΔH_v are expected to vary with the volatile composition. In the context of Equation 2.28, ΔH_d and ΔH_v will vary with the atmospheric composition, and they should be interpreted as average values over the range of temperatures at which decomposition occurs in that environment. For these reasons, strictly speaking a material cannot be assigned a single value of ΔH_g [129]. However, this is more of a technicality than a practical consideration because the effective heat of gasification measured from combustion experiments has been shown to be a good predictor of steady state burning rates [37].

Consistent terminology and nomenclature have not yet been adopted for discussing the various terms in Equation 2.28. In the fire safety literature, the term "heat of vaporization" is frequently used [25, 37, 3, 129]. In the above context, this is approximately equal to $\Delta H_d + \Delta H_v$. Less frequently, the terms "heat of volatilization" [128] and "heat of decomposition" [130] have been used. Particularly for wood, the terms "heat of pyrolysis" [131] or the more general "heat of reaction" [70, 121, 132, 133] have been used, but rarely precisely defined. References [107, 134] report experimental values for the "heat of pyrolysis" of several materials. Since the solid phase energy conservation equation includes a source term that generally appears as a reaction rate multiplied by a heat of reaction / pyrolysis / vaporization / volatilization / decomposition, it is important to be sure that values from the literature are not misinterpreted.

The field could benefit from some consensus in this area because it is difficult to interpret literature values from different workers that may or may not be referring to the same basic quantity. Following Frederick and Mentzer [128], this work will use the term "heat of volatilization". This quantity is defined for a polymer that decomposes according to a single–step reaction (see Equations 2.8 – 2.9) as:

$$\Delta H_{vol} \approx \Delta H_d + \Delta H_v \tag{2.29}$$

The "heat of pyrolysis" ΔH_p is the analogous quantity for a charring material that decomposes by a single step reaction (see Equations 2.12 and 2.16). Both ΔH_{vol} and ΔH_p are global values that apply to the decomposition process as a whole. They imply a single–step reaction and do not include a sensible enthalpy contribution. A positive value designates an endothermic reaction and a negative value designates an exothermic reaction. When multiple reactions are considered, the term "heat of reaction" (ΔH_r) is recommended. For example, Alves and Figueiredo [121] developed a six–step reaction mechanism for wood, with each reaction carrying its own heat of reaction.

In the discussion above, the units of ΔH_{vol} and ΔH_p are Joules per kilogram of gases liberated from the condensed phase. However, there exists some confusion regarding the units of ΔH_r. The reason for this is that some authors use a heat of reaction that implies units of Joules per kilogram of reactants consumed, while others use a ΔH_r having units of Joules per kilogram of gases liberated from the condensed phase. Viewing ΔH_r as an empirical quantity rather than one defined strictly from a thermodynamic basis, both definitions are acceptable. In fact, one can be converted to the other given knowledge of the reaction stoichiometry. However, care must be taken when interpreting literature values of the heat of reaction.

For practical applications of comprehensive solid pyrolysis models, it is the values of ΔH_{vol}, ΔH_p, or ΔH_r that are needed, as opposed to ΔH_g. While the heat of gasification ΔH_g can be estimated from bench–scale combustion experiments conducted at multiple heat flux levels, ΔH_{vol}, ΔH_p, or ΔH_r cannot. For this reason, these quantities are usually treated as adjustable parameters [135] or estimated experimentally from techniques similar to TGA such as Differential Thermal Analysis (DTA) or Differential Scanning Calorimetry (DSC) [136].

DSC is a thermal analysis technique that can be used to measure the enthalpy of reaction (due to glass transition, phase change, etc.) in a constant mass solid. Similar to TGA, DSC exposes milligram size samples to a programmed atmospheric composition and temperature, usually increasing linearly with time. DSC devices measure the difference in the rate of heat flow to the sample of interest and a reference sample with well–known thermal properties. Then, the apparent specific heat capacity of the sample can be calculated as [136]:

$$c_s = \frac{1}{m_s}\left[c_r m_r + \frac{\dot{Q}_s - \dot{Q}_r}{\beta} \right] \tag{2.30}$$

Here, a subscript s denotes the sample of interest and a subscript r denotes the reference sample. Mass is denoted by m, rate of heat flow by $\dot{Q}$, and the linear heating rate by β. Glass transitions, phase change, and chemical reactions all affect the apparent specific heat capacity. Thus, the apparent specific heat measured by DSC is not the "real" specific heat capacity, which is attributed to heat storage by molecular vibrations. The heat associated with a physical change or chemical reaction is determined from a DSC plot of c_s vs. T as the area under a "peak" minus the "baseline" specific heat. The latter is the

specific heat capacity that would have been recorded in the absence of the glass transition, phase change, or chemical reaction of interest [136]. It cannot be exactly determined, and must be estimated. As an example, Figure 2.8 shows a simulated DSC curve (converted to apparent specific heat capacity) for a hypothetical material with a reaction centered at 650 K. The hatched area represents the heat of reaction.

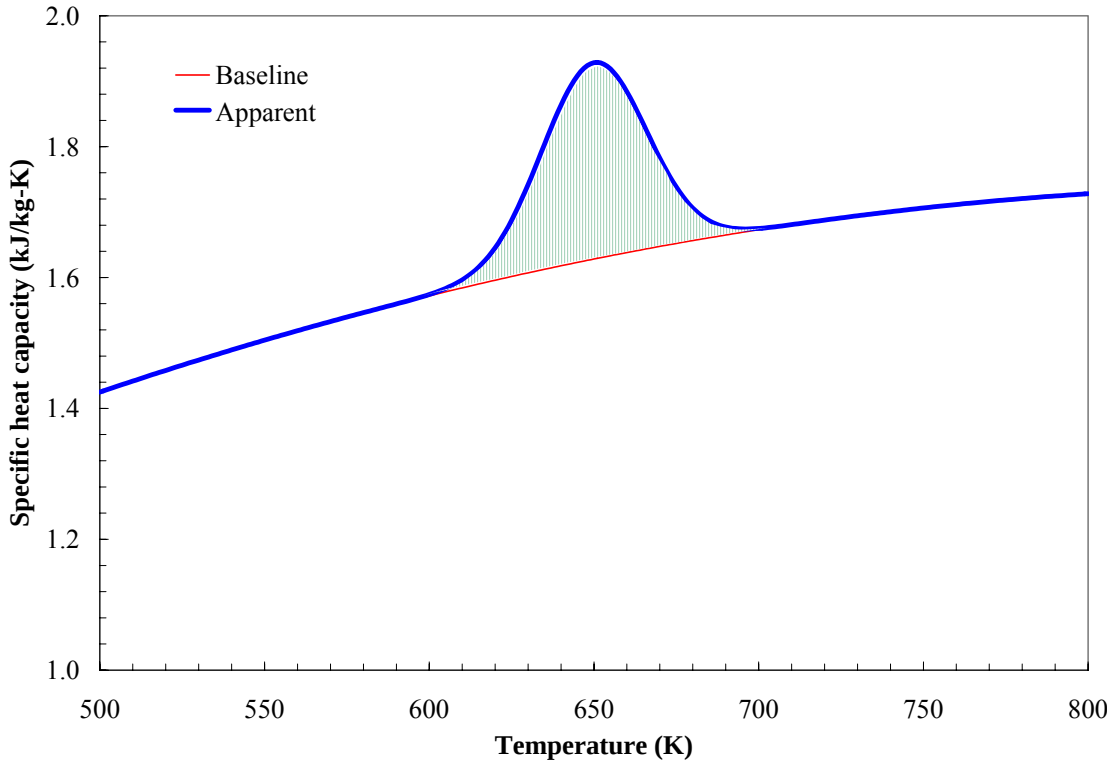

Figure 2.8. Sample DSC curve showing endothermic reaction centered at 650K.

With DSC, the sample mass is not monitored unless it is implemented as part of a Simultaneous Thermal Analysis (STA) device. Therefore, non–STA DSC is well–suited for quantitatively measuring heats of reaction or heats of transition that do not involve volatilization, but its accuracy is reduced when volatilization occurs [136]. Few values of ΔH_{vol} or ΔH_p for different materials were located in the literature, and this search was confounded by the inconsistent terminology mentioned above. In fire applications, the

heat of pyrolysis of wood is frequently assumed to be zero [106, 137]. Table 2.4 lists some heats of volatilization obtained for different materials from DSC and STA.

Table 2.4. Literature values of heat of volatilization (See Equation 2.29).

Material	Ref.	Atmosphere	β [ºC/min]	ΔH_{vol} [kJ/kg]
PE	[128]	Nitrogen	10	665
PE	[25]		–	961
PP	[128]	Nitrogen	10	631
PP	[130]	Nitrogen	10	370
PMMA	[128]	Nitrogen	10	803
PMMA	[25]			1007
PMMA	[130]	Nitrogen	10	687
PMMA	[113]	Nitrogen	20	1080
PMMA	[113]	Air	20	550
PS	[128]	Nitrogen	10	819
PS	[25]			1012
PS	[130]	Nitrogen	10	683
POM	[25]			1720
POM	[130]	Nitrogen	10	937
Nylon 66	[25]			564
Nylon 66	[130]	Nitrogen	10	140
Nylon 6	[128]	Nitrogen	10	786
Polychloral	[130]	Nitrogen	10	380
P(α–M–S)	[130]	Nitrogen	10	443
PVC	[130]	Nitrogen	10	140
PAN	[130]	Nitrogen	10	–444
PBT	[130]	Nitrogen	10	281
BPC II–polyarylate	[130]	Nitrogen	10	–302
PET	[130]	Nitrogen	10	174
PPO	[130]	Nitrogen	10	150
HDPE	[130]	Nitrogen	10	256
PTFE	[130]	Nitrogen	10	447
PC	[130]	Nitrogen	10	111
PI	[130]	Nitrogen	10	62
Kevlar	[130]	Nitrogen	10	228
PBZT	[130]	Nitrogen	10	338

As mentioned earlier, it is expected that ΔH_{vol} will change with atmospheric composition. Peterson *et al.* [113] found that for PMMA, ΔH_{vol} decreases from approximately 1080 J/g under nitrogen to 550 J/g under air (both endothermic). Dakka

[138] presented DTA data suggesting the decomposition reaction for PMMA is endothermic under nitrogen, but exothermic in the presence of oxygen. However, in a later paper [139] the same author presents additional DTA data using smaller particles indicating the PMMA decomposition reaction is endothermic.

2.3 Heat, mass, and momentum transfer

The preceding sections emphasized the pyrolysis modeling strategies used by different workers as well as solid phase decomposition kinetics and thermodynamics. This section takes a closer look at the relevant transport phenomena occurring within the solid.

2.3.1 Solid phase heat conduction

Thermophysical properties of real materials generally vary with temperature. Numerical methods can easily accommodate temperature–dependent thermal properties. Room temperature values of k, ρ, and c have been tabulated for most polymers [14, 140], with simple scaling relations suggested for the variation of these properties with temperature. The density of polymers generally decreases with temperature, by as much as 20% between room temperature and 350ºC (close to typical ignition temperatures). Temperature–dependent densities of several polymers have been compiled by Orwoll [141]. The temperature–dependent specific heat of most polymers can be found in the series of papers by Gaur *et al.* [142–149]. However, the data generally do not extend much above 300ºC. Temperature–dependent thermal conductivities of polymers are scattered throughout the literature. The papers by Zhang *et al.* [150, 151] are a good source of data (k and ρc) for commodity polymers. Since PMMA is widely used in

flammability studies, Steinhaus [152] conducted a detailed investigation of its thermophysical properties. A few experimental measurements for the temperature dependency of density, specific heat capacity, and thermal conductivity of common polymers are listed in Tables 2.5, 2.6, and 2.7 (temperature in units of °C).

Table 2.5. Temperature–dependent density of several polymers.

Material	Ref.		$\rho(T)$ [kg/m^3]						
Rubber (natural)	[141]	T	0	20					
		ρ	921	909					
Nylon 6	[141]	T	240	260	280	300			
		ρ	1176	1165	1154	1143			
Nylon 6,6	[141]	T	260	280	300				
		ρ	1100	1086	1071				
PC	[141]	T	40	80	120	160	200	240	280	340
		ρ	1192	1180	1167	1150	1123	1095	1067	1025
PE (branched)	[141]	T	120	140	160	180	200	220		
		ρ	801	790	780	769	759	749		
PE (linear)	[141]	T	140	160	180	200				
		ρ	785	774	762	751				
PET	[141]	T	140	160	180	200				
		ρ	1172	1156	1140	1125				
PMMA	[141]	T	40	80	120	160	200	220	240	260
		ρ	1181	1171	1153	1126	1097	1082	1067	1052
POM	[141]	T	100	120	140	160	180	200	220	
		ρ	1063	1048	1033	1018	1004	990	976	
PP (atactic)	[141]	T	80	100	120					
		ρ	827	816	802					
PP (isotactic)	[141]	T	180	200	220	240	260	280	300	
		ρ	764	754	744	734	724	714	705	
Polystyrene	[141]	T	40	80	120	160	200	240	280	320
		ρ	1040	1026	1005	984	961	939	916	893
PTFE	[141]	T	360	380						
		ρ	1548	1504						
PVC	[141]	T	100	120	140					
		ρ	1352	1338	1322					

Table 2.6. Temperature–dependent specific heat capacity of several polymers.

Material	Ref.		$c(T)$ [J/kg–K]							
PE (c)	[142]	T	17	47	77	107	137	157	177	187
		c	1515	1639	1804	2151	2585	2889	3213	3382
PE (a)	[142]	T	17	27	77	127	177	227	277	327
		c	2176	2206	2361	2516	2670	2824	2979	3134
PP (c)	[144]	T	17	47	77	107	127	147	167	187
		c	1563	1756	1970	2197	2354	2514	2679	2850
PP (a)	[144]	T	17	27	77	127	177	227	277	327
		c	2067	2103	2284	2464	2643	2824	3005	3183
PMMA	[152]	T	17	47	77	97	107	167	227	277
		c	1434	1564	1694	1781	2180	2333	2486	2613
PS	[145]	T	17	47	77	127	177	227	277	327
		c	1179	1317	1460	1935	2063	2190	2317	2445
PTFE	[147]	T	7	37	107	187	247	327	367	447
		c	976.4	1023	1109	1236	1357	1328	1379	1475
PVC	[147]	T	17	37	57	77	81	87	97	107
		c	922.2	978.2	1038	1102	1424	1457	1513	1569
Nylon 6,6	[148]	T	17	47	50	127	177	227	277	327
		c	1416	1566	2223	2383	2486	2590	2693	2797
Nylon 6	[148]	T	17	37	40	87	147	207	267	327
		c	1451	1559	2404	2468	2549	2630	2711	2792
PET	[148]	T	17	67	69	107	147	197	257	317
		c	1136	1322	1736	1792	1851	1924	2013	2101
POM	[143]	T	–3	17	27	47	67	87	107	117
		c	1152	1237	1284	1387	1500	1619	1740	1800
PC	[149]	T	17	57	107	145	147	187	237	287
		c	1168	1328	1534	1695	1891	1982	2096	2210

(c) crystalline
(a) amorphous

Table 2.7. Temperature–dependent thermal conductivity of several polymers.

Material	Ref.		$k(T)$ [W/m–K]							
PC	[150]	T	28	83	119	146	169	204	225	248
		k	0.24	0.25	0.26	0.26	0.26	0.25	0.23	0.23
PE	[150]	T	17	45	107	118	129	139	160	214
		k	0.34	0.31	0.23	0.22	0.22	0.22	0.22	0.21
PP	[150]	T	71	105	116	138	146	156	222	234
		k	0.25	0.24	0.23	0.2	0.19	0.13	0.13	0.13
PS	[150]	T	35	44	89	108	115	163	216	238
		k	0.16	0.16	0.17	0.17	0.16	0.16	0.16	0.16
PMMA	[152]	T	0	105	275					
		k	0.2	0.2	0.16					

Whereas moisture content has only a minor effect on the thermal properties of polymers, it can affect the thermal properties of wood significantly. A further

complication is that the thermal properties of wood also vary with temperature and grain orientation; a good deal of information is contained in Refs. [153–159].

Most experimental measurements indicate that the specific heat of wood is fairly independent of species. The following relation has been suggested for the specific heat capacity of generic oven dry virgin wood [154]:

$$c_{v0}(T) = 1160 + 3.87T \tag{2.31}$$

where T has units of °C and c_{v0} has units of J/kg–K. The variation of wood's specific heat capacity with moisture content and temperature can be estimated as [154]:

$$c_v(M,T) = \frac{c_{v0}(T) + 4186M}{1+M} + \Delta c_v(M,T) \tag{2.32a}$$

$$\Delta c_v(M,T) = M(23.6T - 1326M + 238) \tag{2.32b}$$

In Equations 2.31 and 2.32 the subscript v denotes virgin wood, and M is the moisture content on an oven dry mass basis, defined as:

$$M = \frac{m}{m_0} - 1 \tag{2.33}$$

where m is the mass of a wood sample at a given moisture content and m_0 is the oven dry mass of that same wood sample.

Equations 2.31 – 2.33 apply below approximately 200°C. At higher temperatures, thermal decomposition begins and the wood is transformed to a carbonaceous char generally having properties different from the virgin wood. The rate at which the virgin wood is converted to char depends on the kinetics of the decomposition reactions (see Section 2.2.1). The temperature dependency of wood char specific heat (c_c) is similar to that of amorphous graphite, increasing with temperature [159]:

$$c_c \approx 714 + 2.32T - 0.0008T^2 - 3.69\times10^{-7}T^3 \tag{2.34}$$

In Equation 2.34, T has units of °C and c_c has units of J/kg–K. Little information is available regarding the specific heat capacity of partially degraded wood, but the temperature–dependent analogue of Equation 2.18 (i.e., linear interpolation between the c_v and c_c) can be used as a first approximation.

The thermal conductivity of wood depends primarily on oven dry density and moisture content. The following relation was found to provide a good correlation to experimental thermal conductivity measurements [154]:

$$k_v \approx 0.019 + \frac{\rho_0}{1000}\left(0.194 + 0.406M\right) \tag{2.35}$$

In Equation 2.35, ρ_0 is the oven dry density (kg/m^3). Temperature has a relatively minor effect on the thermal conductivity of wood [153]. It has been suggested that the thermal conductivity increases by approximately 10% for each 50 °C increase in temperature [154].

Little information is available regarding the thermal conductivity of charred wood, particularly partially degraded wood. Alves and Figueiredo [121] experimentally measured the thermal conductivity of pine char between 30 °C and 220 °C, recommending the following correlation:

$$k_c \approx 0.113 + 8.2\times10^{-5}T \tag{2.36}$$

where T has units of °C. It is unlikely that Equation 2.36 applies at all temperatures because, as will be discussed in Section 2.3.2, radiation transport across char pores increases the "effective" or "apparent" thermal conductivity at high temperatures. Several models for the effective thermal conductivity in porous materials such as chars have been proposed [96, 157, 160–163]. However, the predictive capabilities of these models have

not been rigorously evaluated, particularly due to the difficulties associated with accurately measuring the temperature–dependent thermal conductivity of chars. For example, Cagliostro and Riccitiello [91] generated four different samples of intumescent char under identical furnace conditions and found inter–sample variations of +/– 100% in the measured thermal conductivity.

2.3.2 Radiation

Radiation is the dominant mode of heat transfer through the gas phase in large fires [164]. Since radiation drives burning rates, it is important to understand the radiative characteristics of solid materials. A fraction of the radiation incident upon a material may be reflected from the surface. The remainder can be absorbed by or transmitted through the material.

In a fire, one of the most important radiative characteristics of a material is its absorptivity, defined as the fraction of the incident radiation that is absorbed by the material. The absorptivity is strongly wavelength–dependent. For example, at wavelengths below 1 μm the absorptivity of clear PMMA is close to zero, but at wavelengths above 3 μm it approaches unity. The absorptivity at a single wavelength λ is denoted α_λ. However, in a fire we are usually interested in the integrated absorptivity α:

$$\alpha = \frac{\int_0^\infty \alpha_\lambda \dot{q}''_{e,\lambda} \mathrm{d}\lambda}{\int_0^\infty \dot{q}''_{e,\lambda} \mathrm{d}\lambda} \tag{2.37}$$

It can be seen from Equation 2.37 that the integrated absorptivity depends on the spectral energy distribution of the radiation source. Therefore, a material technically cannot be assigned a single value of integrated absorptivity because the spectral distribution of the

incoming radiation depends on the temperature of the emitter. This is true even if the emitter behaves as a blackbody due to Wien's displacement law. In fires, the temperature of radiation sources ranges from approximately ~600 K (smoke layer, hot surfaces) to ~2000 K (flames). Additionally, certain bench–scale fire tests use tungsten–filament heaters that operate at temperatures near 3000 K. Thus, the effect of source temperature on the integrated (or effective) absorptivity has relevance for both real fires and bench–scale fire testing.

Hallman's 1971 Ph. D. dissertation [165] and subsequent publications [166, 167] remain some of the best sources of information on the change of polymers' integrated surface absorptivity with the temperature of the emitter. Hallman measured the spectral absorptivity of several solids and then determined the integrated surface absorptivity of different solids irradiated by hexane flames, blackbodies between 1000 K and 3500 K, and solar energy. His absorptivity data are reproduced in Table 2.8. Note that the integrated absorptivity of some materials is relatively insensitive to the temperature of the radiation source (black PMMA) but others are quite sensitive. For example, the absorptivity of clear PMMA decreases from 0.85 for a 1000 K blackbody to 0.25 for a 3500 K blackbody.

Similar measurements were made by Wesson *et al.* [168] for undegraded wood. Their results are reproduced in Table 2.9.

Table 2.8. Integrated surface absorptivities for polymers from Hallman [166].

Generic name	Trade name	Blackbody emitter temperature (K)						
		1000	1500	2000	2500	3000	3500	Flame
Acrylonitrile butadien styrene	Cycolac®	0.91	0.86	0.77	0.71	0.65	0.61	0.92
Cellulose acetate butyrate	Uvex®	0.84	0.71	0.56	0.43	0.34	0.27	0.88
Cork		0.64	0.56	0.49	0.46	0.44	0.44	0.60
Melamine/formaldehyde	Formica®	0.91	0.88	0.85	0.82	0.80	0.79	0.91
Nylon 6/6		0.93	0.90	0.86	0.82	0.75	0.71	0.93
Phenolic	Bakelite	0.90	0.86	0.81	0.77	0.75	0.75	0.91
Polycarbonate (rough surface)	Lexan®	0.87	0.83	0.78	0.75	0.72	0.71	0.88
Polyethylene (low density)		0.92	0.88	0.82	0.77	0.72	0.68	0.93
Polymethylmethacrylate (black)	Plexiglas®	0.94	0.94	0.95	0.95	0.95	0.95	0.94
Polymethylmethacrylate (clear)	Plexiglas®	0.85	0.69	0.54	0.41	0.31	0.25	0.89
Polymethylmethacrylate (white)	Plexiglas®	0.91	0.86	0.78	0.70	0.62	0.56	0.92
Polyoxymethylene	Delrin®	0.92	0.86	0.78	0.71	0.64	0.59	0.93
Polyphenylene oxide		0.86	0.78	0.70	0.63	0.57	0.53	0.88
Polypropylene		0.87	0.83	0.78	0.74	0.70	0.68	0.86
Polystyrene (clear)	Styrolux®	0.75	0.60	0.46	0.35	0.28	0.22	0.78
Polystyrene (white)		0.86	0.75	0.63	0.53	0.45	0.40	0.88
Polyurethane thermoplastic	Texin®	0.92	0.89	0.83	0.77	0.72	0.68	0.93
Polyvinyl chloride (clear)		0.81	0.65	0.49	0.38	0.30	0.24	0.85
Polyvinyl chloride (gray)		0.90	0.90	0.89	0.89	0.89	0.89	0.91
PVC/acrylic (gray, rolled)	Kydex®	0.88	0.87	0.86	0.85	0.84	0.83	0.88
PVC/acrylic (red cast)	Kydex®	0.91	0.90	0.89	0.88	0.87	0.86	0.92
Rubber (Buna–N)		0.92	0.93	0.93	0.93	0.93	0.93	0.92
Rubber (Butyl IIR)		0.92	0.93	0.94	0.94	0.95	0.95	0.92
Rubber (natural, gum)		0.88	0.82	0.76	0.72	0.69	0.68	0.89
Rubber (neoprene)		0.91	0.92	0.93	0.93	0.93	0.93	0.91
Rubber (silicone)		0.79	0.66	0.58	0.54	0.52	0.53	0.79

Table 2.9. Integrated surface absorptivity for wood from different emitters. From Wesson *et al.* [168].

Wood	Flame radiation	Tungsten lamp radiation	Solar radiation
Alaskan cedar	0.76	0.44	0.36
Ash	0.76	0.46	0.36
Balsa	0.75	0.41	0.35
Birch	0.77	0.47	0.39
Cottonwood	0.76	0.48	0.40
Mahogany	0.76	0.49	0.52
Mansonia	0.76	0.47	0.51
Maple	0.76	0.49	0.44
Oak	0.77	0.56	0.49
Redgum	0.77	0.52	0.56
Redwood	0.77	0.51	0.55
Spruce	0.76	0.45	0.35
White pine	0.76	0.49	0.43
Masonite	0.75	0.52	0.61

During a fire, a material's radiative characteristics may change. Although the integrated absorptivities from Wesson *et al.* [168] (reproduced in Table 2.9) are relatively low, the absorptivity of charred wood is generally not the same as that of virgin wood. Janssens [169] suggested that blackening causes the absorptivity of wood to increase from ~0.76 (based on Reference [168]) to approximately unity as the surface temperature approaches the ignition temperature. He therefore used an average value of 0.88 in his ignition analyses, and recommends using an integrated absorptivity of 1.0 during flaming combustion [159].

Wood is not the only class of materials that exhibits a change in radiative characteristics during a fire. Under nonflaming conditions, low density polyethylene has been observed to change from visually opaque to transparent, eventually followed by a darkening of the surface [55]. This indicates that a change in the material's radiative characteristics occurred (at least in the visible range). Modak and Croce [170] reported that for clear PMMA, 39% of flame radiation is transmitted through the surface, but for "charred" PMMA (previously exposed to a fire environment and then cooled) no radiation penetrates in depth. Bubbling occurring near the surface of polymers can change their radiative characteristics, but this effect is has not yet been reliably quantified. In a real fire, materials may become coated in soot from flames or a smoke layer, causing their absorptivities to approach unity.

For a material that is opaque to thermal radiation, almost all absorption occurs within a micron of the surface, and absorption can be treated as a surface phenomenon. This is the usual assumption in fire problems, but at certain wavelengths some solids are semi–transparent and absorb radiation in–depth. This diathermancy is usually modeled

using an absorption coefficient κ_λ (sometimes also denoted a_λ) that describes the rate of attenuation of radiation at a particular wavelength:

$$\frac{\partial \dot{q}''_{r,\lambda}}{\partial z} = -\kappa_\lambda \dot{q}''_{r,\lambda} \tag{2.38}$$

where for simplicity, incident radiation applied normal to the surface and "one way" radiation transport have been assumed. More complicated treatments of in–depth radiation absorption than Equation 2.38 have also been used [171–174]. As with surface absorptivity, the absorption coefficient is strongly wavelength–dependent. Similar to the integrated surface absorptivity, an integrated absorption coefficient can be defined as:

$$\kappa = \frac{\int_0^\infty \kappa_\lambda \dot{q}''_{e,\lambda} \mathrm{d}\lambda}{\int_0^\infty \dot{q}''_{e,\lambda} \mathrm{d}\lambda} \tag{2.39}$$

Compared to measurements of surface absorptivity, there is less information available regarding the in–depth absorption of thermal radiation in combustible solids. At wavelengths greater than 2.5 μm, the radiative absorption depth is less than 2 mm in PE and less than 1 mm in PMMA [55]. Several workers have included the effects of in–depth radiation absorption in pyrolysis models [49, 50, 111, 171–174]. Obtaining accurate property data that characterizes the in–depth absorption (normally, the "gray" absorption coefficient) can be difficult. Modak and Croce [170] reported that the gray absorption coefficient of clear PMMA for its flame radiation is 124 m^{-1}. Progelhof *et al.* [175] give band–mean absorption coefficients for PMMA and poly(4–methylpentene–1) as a function of wavelength (and developed exact solutions for the temperature profiles resulting in semi–transparent solids). Table 2.10 gives the absorption coefficient and

absorptivity for PMMA as determined experimentally by Manohar *et al.* [174] over 14 different wavelength "bands".

Table 2.10. Absorption coefficient and surface absorptivity for clear PMMA over 14 wavelength bands. From Manohar *et al.* [174].

λ_1 (μm)	λ_2 (μm)	κ_λ (m^{-1})	α_λ (–)
1.59	1.67	268	0.994
1.67	1.77	555	0.991
1.77	1.87	274	0.990
1.87	1.99	170	0.990
1.99	2.13	226	0.987
2.13	2.29	1277	0.770
2.29	2.47	2407	0.927
2.47	2.68	870	0.981
2.68	2.93	2165	0.385
2.93	3.24	2453	0.957
3.24	3.62	2474	0.436
3.62	4.09	2864	0.976
4.09	4.71	3585	0.934
4.71	5.56	3895	0.670

Reduction in the effective surface absorptivity or in–depth absorption coefficient both increase the time to ignition. Therefore, ignition times at the same applied heat flux level from different thermal radiation sources are not necessarily the same. Figure 2.9 shows Hallman's data [165] for the ignition time of PE and PS from benzene flames and a tungsten lamp. At a given heat flux, the ignition times are generally longer using the tungsten lamp because the integrated surface absorptivity is lower for the tungsten lamp than for the benzene flame (see Table 2.8).

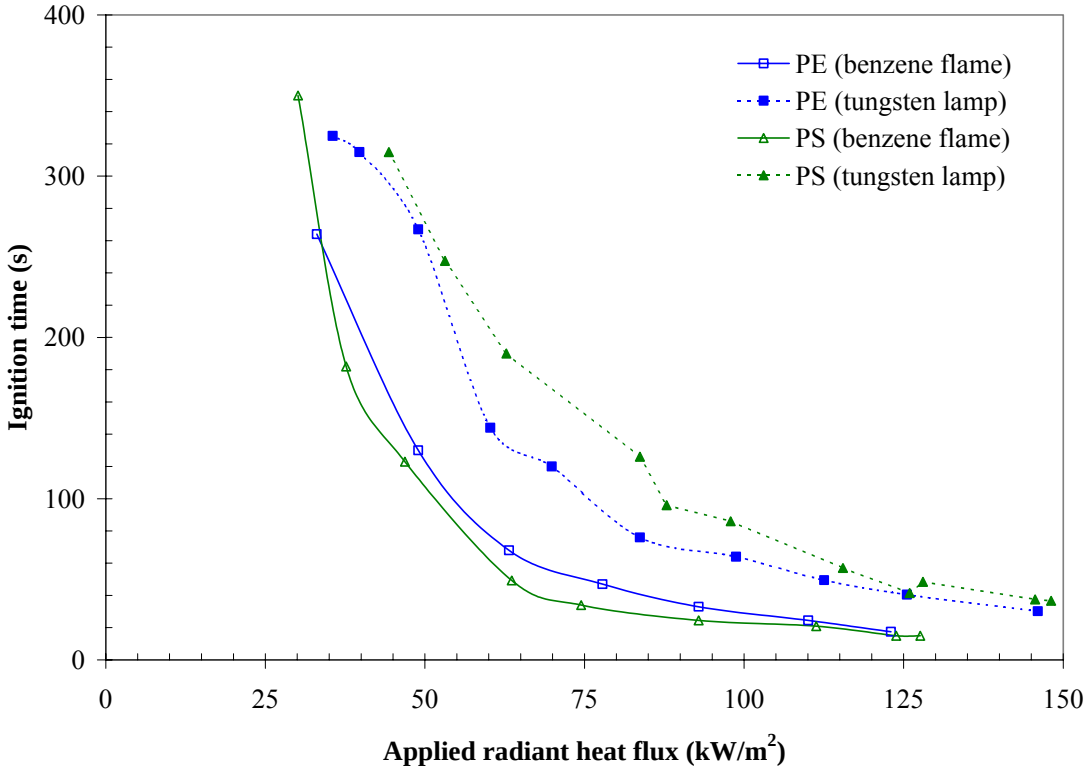

Figure 2.9. Effect of heater type on time to ignition for PE and PS [165].

Thomson and Drysdale [177] also found differences in the ignition times of PMMA and PP at the same heat flux level (as measured with a Gardon heat flux gauge) depending on whether the heat flux was varied by holding the heater temperature constant and changing its position, or by holding the heater position constant and changing its temperature. These spectral effects have not been extensively studied by fire researchers, although it appears to be important, particularly when interpreting experimental data from bench–scale flammability tests. In some standardized tests, the irradiated surface is coated with a thin layer of carbon black or paint to ensure that the applied radiant heat flux is absorbed at the surface. For example, the specimen preparation protocol in ASTM E2058–03 [178] requires that ignition/combustion samples are sprayed with a single coat of high temperature flat black paint. Babrauskas (pg. 306

of Reference [179]) has cautioned that a surface coating of graphite powder may affect ignition times.

It may be possible to improve a material's fire performance with additives that reduce its surface absorptivity or in–depth absorption coefficient. It has been found that addition of a small amount of carbon nanotubes to polypropylene reduces its ignition time because the in–depth radiation absorption coefficient was increased [180].

Radiation may be an important or even dominant mode of heat transfer in a porous medium even if the solid material itself is effectively opaque ($\kappa \to \infty$). Consider a single pore embedded in a porous material in which a temperature gradient exists. Energy is transferred by thermal radiation through the gas filling the pore from the hotter side of the pore to the colder side. The magnitude of this heat transfer depends on the temperature gradient, the size and shape of the pore, its absorptivity, and radiation attenuation by any participating gases contained in the pore. See Refs. [181, 182] for comprehensive reviews of radiative transfer in porous media.

The simplest engineering treatment of radiative transfer in porous media involves the concept of a "radiant conductivity". The heat transfer due to radiation is calculated as:

$$\dot{q}_r'' = -k_r \frac{\partial T}{\partial z} \tag{2.40}$$

where the radiant conductivity k_r varies with the third power of temperature:

$$k_r = 4Fd\sigma T^3 \tag{2.41}$$

In Equation 2.41 d is the pore diameter and F is the radiative exchange factor [182] which, for the purposes of this chapter, can be considered an empirical parameter related primarily to the pore structure. Both are difficult to determine theoretically or experimentally, although the pore diameter may be estimated by high–resolution

microscopy. Most workers have used some variation of Equation 2.41 to calculate radiant conductivities, and a few of the expressions that have been used are listed in Table 2.11 (where ε is emissivity and ψ is porosity):

Table 2.11. Radiant conductivity expressions.

Ref.	Material	k_r	d
[117]	PU foam	$\frac{16}{3}\sigma d T^3$	virgin: 50 μm charred: 1300 μm
[120]	Lodgepole pine	$\frac{13.5\sigma d T^3}{\varepsilon}$	40 μm
[183]	Intumescent coating	$\varepsilon^2 \sigma d T^3$	~100 μm
[97]	Intumescent coating	$\frac{13.5\sigma d T^3}{\varepsilon\psi}$	unreacted: 5 μm reacted: 325 μm

The radiant thermal conductivity calculated with Equation 2.41 is plotted in Figure 2.10 for F = 4/3 and pore diameters of 100 μm and 10 μm. For comparison, a typical solid phase thermal conductivity for many polymers and cellulosic materials is ~0.1 – 0.3 W/m–K.

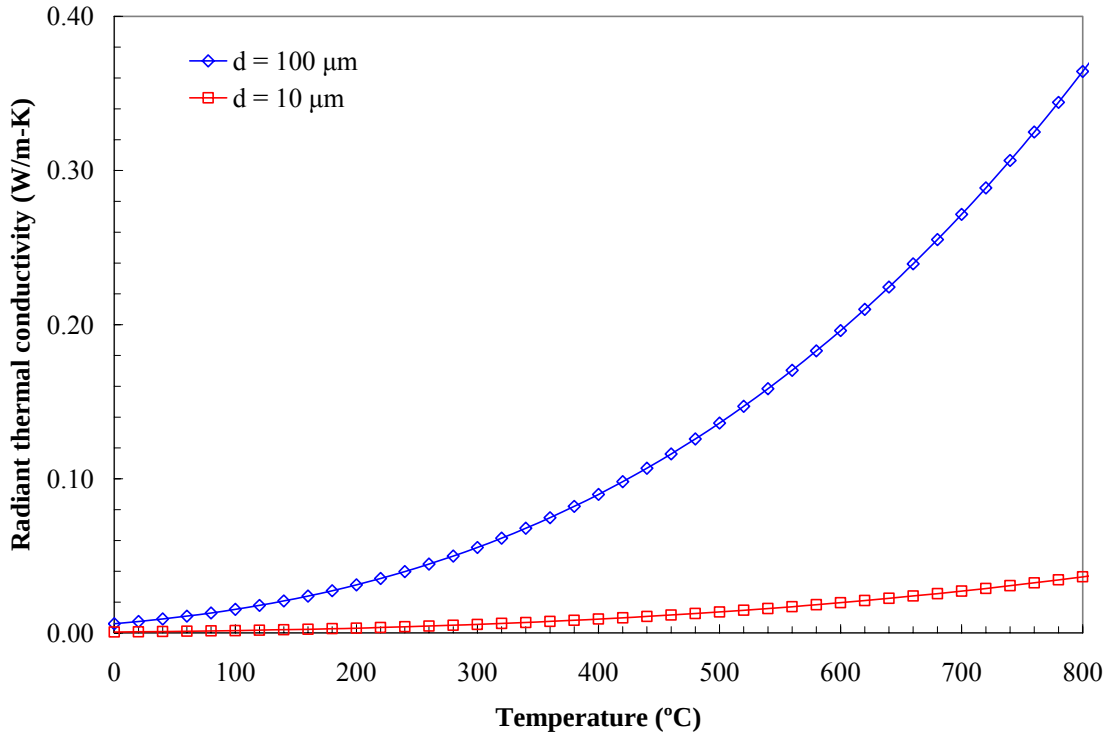

Figure 2.10. Radiative conductivity calculated with Equation 2.41 for F = 4/3.

Figure 2.10 suggests that the radiant thermal conductivity may become of comparable magnitude to the solid thermal conductivity at relatively low temperatures, particularly for the case of 100 μm pore diameter. Di Blasi and Branca [97] found that radiation transfer through a porous char was the dominant mode of heat transfer in simulation of an intumescent coating, but Kantorovich and Bar–Ziv [161] have suggested that the radiant contribution to the thermal conductivity can be neglected for temperatures lower than 1000 K. Based on the limited information available in the literature, it is difficult to draw any conclusions regarding when the radiant conductivity should be included in calculations and what the "correct" values of F and d to use for a particular material or class of materials. An alternative to rigorously attempting to establish F and d independently is to lump them together into a fitting parameter γ, i.e. $k_r = \gamma\sigma T^3$ where γ is approximately in the range 10^{-5} m < γ < 10^{-2} m.

2.3.3 Convection, advection, and diffusion

For the purposes of this chapter, the distinction will be made between convection and advection in the interior of a decomposing solid as follows: advection is bulk motion of the condensed phase, and convection is heat transfer between the gaseous and condensed phases within the solid. The difference between the two can be illustrated by considering a pyrolyzing slab of a non–charring solid material. As volatiles escape from the interior of the condensed phase to the ambient atmosphere, the condensed phase (e.g., molten polymer) instantaneously fills the voids left by escaping volatiles. This causes surface regression, i.e. the thickness of the solid decreases with time due to the resultant advection. The same effect occurs due to a change in bulk density with temperature (swelling or shrinkage) or due to an intumescent reaction. This bulk motion of the condensed phase is advection. In comparison, convection occurs when volatiles generated in–depth move toward the surface and pass through condensed phase material that is not necessarily at the same temperature as the volatiles. This temperature difference gives rise to convective heat transfer between the volatiles and the condensed phase.

For the case of a solid irradiated at its surface, the temperature in the region where volatiles are produced in–depth is lower than the temperature closer to the surface (unless there is in–depth radiation absorption, heating at the back face, or exothermic reactions occurring in–depth). Consequently, as the volatiles flow toward the surface, heat is transferred from the solid to the volatiles, in effect cooling the solid. The temperature difference between the condensed and solid phases ("thermal non–equilibrium") and its effect on the heat transfer rates have been investigated extensively in the field of heat transfer in porous media, e.g. Refs. [184, 185]. However, in most fire–related studies it is

assumed that the solid and gaseous phases are in thermal equilibrium due to the much smaller volumetric heat capacity of the volatiles [70–72]. One exception is Florio *et al.* [186], who investigated the effect of thermal non–equilibrium during the degradation of an ablative composite. They assumed that the rate of heat transfer between the condensed and gaseous phases was proportional to a volumetric heat transfer coefficient multiplied by the temperature difference. The authors [186] found differences of as much as 200 K between the gaseous and condensed phases. However, the applied heat flux was 280 kW/m^2, considerably greater than typical fire–level heat fluxes. Florio *et al.* [186] also considered the case where the solid and condensed phases were in thermal equilibrium. Although there were not drastic differences between the temperature profiles calculated with the thermal equilibrium or non–equilibrium models, Florio *et al.* [186] advocate using thermal non–equilibrium for similar materials and boundary conditions. However, at boundary conditions imposed by typical fire–level heat fluxes, the assumption of thermal equilibrium between the gaseous and condensed phases is probably acceptable, and this eliminates one adjustable model parameter (the internal volumetric heat transfer coefficient) from the problem. The convection term is sometimes omitted from models altogether on the basis that it is small [73].

Diffusion of ambient oxygen into a decomposing solid may be an important effect to consider if the reactions in the solid are sensitive to the local oxygen concentration. To date, there has been little work investigating the consequences of oxygen diffusion into decomposing solids. However, gaseous diffusion inside decomposing solids probably becomes less important at high heating rates or high heat flux levels where transport of volatiles takes place primarily by convection and blowing from the surface limits

penetration of ambient oxygen into the decomposing solid. Diffusion of gases due to concentration gradients inside a decomposing solid is sometimes modeled using the dusty gas flux equation developed for multi–component gas transport in porous media (such as a char layer). This approach has been used to simulate energy recovery processes such as flash pyrolysis [187], but it has not yet been applied to simulate practical fire problems. It is difficult to justify the inclusion of such complexity in fire modeling at the present time given the lack of knowledge regarding the composition of gaseous pyrolysate and secondary gas–solid reactions inside the char layer.

2.3.4 Momentum

By invoking the assumption that the decomposition products move from the condensed phase to the adjacent gas phase with negligible internal resistance, the momentum equation is usually not solved. However, the empirical Darcy's law is sometimes used to model the internal pressure distribution and the resultant velocity of the escaping decomposition products (e.g., Refs. [71, 72, 94, 186]). With this approach, the velocity of the volatiles is proportional to the internal pressure gradient and the material's permeability divided by the dynamic viscosity of the gas. This implies a Stokes flow where inertial terms are negligible. Any accumulation of gases inside the solid results in an increase in the internal pressure, and the pressure evolves according to a transient diffusion equation similar to the heat conduction equation.

The model of Henderson and Wicek [94] predicted overpressures of as much as 50 atm in an expanding polymer composite. Overpressures of this magnitude could have a significant effect on the structural integrity of a material. Lee *et al.* [188] measured overpressures of 0.3 atm in wood when heated perpendicular to the grain, but only 0.003

atm when heated parallel to the grain. Under most fire scenarios, unless one is interested in estimating the structural response of a material, the assumption of instantaneous escape of volatiles is advantageous because it can reduce the solution complexity.

2.3.5 Special topics: melting, bubbling, and related phenomena

Crystalline solids have a well–defined melting temperature, a common example is ice. Amorphous materials, such as glass, generally soften when heated and melt over a range of temperatures rather than at a single temperature. Most thermoplastic polymers are semi–crystalline, containing a mixture of amorphous and crystalline components. Many polymers begin softening or melting at temperatures lower than typical piloted ignition temperatures. Therefore, melting usually occurs prior to ignition and becomes even more pronounced during flaming combustion. Melting influences the combustion behavior of polymers through latent heat absorption (i.e. ΔH_m in Equation 2.28) and changes in thermal properties (thermal conductivity and specific heat capacity) in the vicinity of the melting temperature. From a practical standpoint, polymers that are rigid at room temperature may melt, flow, and drip. Pool fires formed by melt flow at the base of vertical walls have been observed to dominate upward flame spread rates [189], and efforts are underway to model this phenomenon [190].

Melting allows for increased penetration of oxygen into the polymer by molecular diffusion and also makes bubbling possible. One of the best descriptions of the bubbling process in polymers is given by Kashiwagi and Ohlemiller [55] who studied the behavior of PE and PMMA irradiated at two heat flux levels and several ambient oxygen concentrations. PMMA irradiated in a nitrogen atmosphere at 17 kW/m^2 formed ~1 mm diameter bubbles at depths as much as 3 mm below the surface. Bubbles that formed

within 1 mm of the surface were seen to vent through small holes; bubbles that formed deeper below the surface occasionally burst through necklike holes to the gas phase, violently ejecting vapor and molten polymer. This violent bursting process has also been observed in microgravity [191]. The presence of gas phase oxygen reduces the viscosity of the molten polymer, leading to higher bubbling frequency and a less–violent bursting process. The ~1 mm holes formed by the bubbles allow oxygen to penetrate as much as 1 mm into the polymer, thereby increasing the depth of the oxygen affected region beyond that which is possible by diffusion. At higher heat fluxes, the bubbles are smaller and closer to the surface.

Despite the importance of melting and bubbling to polymer flammability, there has been only a handful of modeling studies aimed at better understanding these phenomena. A model that includes melting has been developed and used to successfully predict the time to ignition of a polypropylene/glass composite [192]. More recently, polymer melt flow behavior in laboratory–scale experiments has been modeled with encouraging results [190]. However, modeling of bubbling is still a research topic. Wichman [52] developed a model that describes the effect of bubbling on the transport of volatiles under steady–state conditions. No direct comparison with experimental data was possible since experiments are inherently transient, but the model is in qualitative agreement with experimental observations. In Butler's model [53], the bubble layer is assumed to be perfectly mixed. The model predicted a MLR that was approximately constant with time, whereas experimental data showed an increasing mass loss rate. A more recent model [54] includes a more detailed description of bubbling, but the author concludes that a better representation of the bursting process is still needed.

3.0 GENERALIZED PYROLYSIS MODEL

Drawing from the concepts discussed in Chapter 2, a broadly applicable pyrolysis model is formulated in this chapter. Rather than developing separate model equations for different classes of materials (noncharring, charring, intumescent), the model is kept as general as possible. A particular material is simulated by specifying a set of model parameters (thermophysical properties, reaction mechanisms, etc.), and a particular experimental configuration is simulated by specifying of initial and boundary conditions. The flexibility to invoke or omit submodels for various transport phenomena is retained because there may be little consequence to omitting a particular phenomenon from a simulation other than reducing the computational expense and the number of adjustable parameters that must be specified to characterize a material. An underlying theme is that the user decides on the level of complexity (and number of degrees of freedom) to include in a simulation. Consequently, the model is extremely flexible.

Separate conservation equations are solved for gaseous and condensed phase mass, species, and energy as well as gas phase momentum using the empirical Darcy's law approximation (Stokes flow). An arbitrary number of gas phase and condensed phase species can be accommodated, each having its own thermophysical properties. The user may specify any number of heterogeneous (solid/gas) or homogeneous (gas/gas) reactions. Both in–depth radiation absorption in a semi–transparent medium as well as radiation transport across pores are considered. Melting is modeled using an apparent specific heat capacity. All volatiles generated inside the solid escape to the ambient with no resistance to flow unless the pressure solver is invoked to solve for the pressure distribution in the solid, in which case the resultant flow of volatiles is calculated

according to Darcy's law. Similarly, the user may invoke a gas phase convective–diffusive solver that determines the composition of the volatiles, including diffusion of gaseous species from the ambient into the decomposing porous solid. Thus, in addition to calculating the mass–flux of volatiles escaping from the solid, the actual composition of these vapors is calculated.

General aspects of the model formulation and derivation of the governing equations are presented in Section 3.1. The model's treatment of reaction rates and the associated source terms are discussed separately in Section 3.2, and details of the numerical solution methodology are given in Section 3.3. Model verification exercises are presented in Section 3.4 where model calculations are compared to available exact solutions. Appendix B is a user's guide to the model.

3.1 Model formulation

As described in Chapter 2, many previously developed pyrolysis models have simplifications built in their model equations that limit their applicability to a single class of materials (charring, noncharring, etc.) or even to a specific material. However, since the most general forms of the conservation equations for mass, energy, species, and momentum apply universally, it is possible to formulate a generalized pyrolysis model that can be applied to most solid combustibles. The biggest challenge associated with this task is making enough simplifications and approximations that the number of empirical or adjustable parameters is kept manageable without compromising the generality of the model or neglecting relevant physical phenomena.

Rather than hardcoding a certain level of complexity, the user determines how much complexity or detail to include in a simulation. For example, thermophysical

properties may be temperature–dependent or invariant with temperature; decomposition mechanisms can be single–step or multi–step; thermal radiation can be absorbed only at the surface or in–depth, and so on. Some of the physics embedded in the governing equations may be superfluous for practical engineering applications; however, they can simply be omitted from a calculation if desired.

3.1.1 Preliminaries and definitions

Consider a condensed phase combustible material that may contain as many as M chemically distinct condensed phase species. Examples of different condensed phase species include pure polymer, fiber reinforcements in a composite, char, and ash. Within the material, the initial concentrations of each species may be uniform (as in the case of a homogeneous blended composite) or vary spatially (as in the case of laminated composites). As the solid is heated, it may degrade to form N chemically distinct gaseous species. These species include hydrocarbon fragments, water vapor, carbon monoxide, etc.

Throughout this work, the index i is used to denote condensed phase species and the index j is used to denote gaseous species. Thus, Y_i is the mass of condensed phase species i divided by the total mass of all condensed phase species, and Y_j is the mass of gaseous species j divided by the mass of all gaseous species. Note that Y_j is not the mass of gaseous species j divided by the mass of all gaseous and condensed phase species. As implied in the previous paragraph, M is the number of condensed phase species and N is the number of gaseous species.

Since the condensed phase is composed of M distinct species, each having its own thermophysical properties, the effective properties appearing in the conservation

equations presented later must be calculated from the appropriately weighted local composition. Some quantities are weighted by the local volume fraction, and others are weighted by the local mass fraction. The relation between mass fraction and volume fraction is:

$$X_i = \overline{\rho}\frac{Y_i}{\rho_i} \tag{3.1}$$

Here $\overline{\rho}$ is the weighted bulk density, ρ_i is the bulk density of condensed phase species *i*, X_i is the volume fraction of condensed phase species *i*, and Y_i is the mass fraction of condensed phase species *i*. The convention used here is that quantities with an overbar denote averaged quantities, i.e. the weighted bulk density is defined as:

$$\overline{\rho} = \sum_{i=1}^{M} X_i \rho_i \tag{3.2}$$

The bulk density of each condensed phase species is assumed to vary with temperature according to the relation:

$$\rho_i(T) = \rho_{0,i}\left(\frac{T}{T_r}\right)^{n_{\rho,i}} \tag{3.3}$$

where T_r is a user–specified reference temperature, often (but not necessarily) taken as the ambient temperature.

Note that in Equations 3.1 to 3.3, ρ_i is the bulk density of species *i* in a vacuum if it is porous. Bulk density is defined as total mass divided by total volume, not the density of a pure nonporous solid. The designation of the bulk density of species *i* as ρ_i is different from the nomenclature used in other pyrolysis models where ρ_i is usually the mass of species *i* per unit volume of mixture (which would instead be represented here as $\overline{\rho}Y_i$). Also, it should be emphasized that ρ_i is the bulk density, which is related to the

density of the solid nonporous species ($\rho_{s,i}$) as $\rho_i = (1-\psi_i)\rho_{s,i}$ where ψ_i is the porosity of condensed phase species *i*.

To simplify the model, it is assumed that porosity is a "property" of each condensed phase species. That is, the porosity of species *i* is calculated as $\psi_i(T) = 1 - \rho_i(T)/\rho_{s0,i}$. The user specifies $\rho_{s0,i}$ (the density of solid nonporous species *i* a particular temperature) and $\rho_i(T)$ (the bulk density of species *i* as a function of temperature). Note that the small density contribution from the gases that fill the voids ($\psi\rho_g$) is ignored because, as mentioned above, the bulk density is formally defined under vacuum. However, this is more of a technical than a practical consideration because $\psi\rho_g << \rho_{s,i}(1-\psi_i)$ except under special circumstances.

The primary advantage of making the approximation that porosity is a property of a condensed phase species is that the weighted porosity can be calculated from the local composition as $\overline{\psi} = \sum X_i\psi_i$. This eliminates the need to solve a separate equation for the porosity evolution. It was felt that this advantage outweighs the primary disadvantage brought by this approach, illustrated by the following example: Consider a polymer composite comprised of glass fiber reinforcements and a thermoplastic matrix that pyrolyzes through a noncharring reaction that leaves no residue. After the matrix has completely pyrolyzed, a porous structure (the inert glass fiber reinforcements) remains. From a modeling perspective, the porous glass "species" that remains would be different for composite systems with different glass concentrations. The reason for this is that the bulk density (and porosity) of the porous glass structure that remains after the resin has pyrolyzed depends on the initial glass concentration in the composite. Since bulk density

is specified for each species by Equation 3.3, it is not possible for a particular condensed phase species to have two different bulk densities at a particular temperature. Thus, the porous glass that remains after pyrolysis of two composites with 30% glass and 70% glass by mass must be treated as two different species, even though in actuality the porous glass structure is comprised of the same solid material (glass fibers) at different porosities. This is the biggest disadvantage of assuming that each species has a unique bulk density. Solving a separate equation for the porosity evolution could eliminate this shortcoming, but the resultant formulation would be much more complicated than the present treatment. Pursuit of this more complicated approach is recommended in Chapter 7 for future work.

The effective thermal conductivity of a condensed phase material is affected by its density, porosity, moisture content, microstructure, and orientation of wood grain or composite reinforcements. There are several models in the literature that can be used to estimate effective thermal conductivities on the basis of these considerations. However, as with the presumed temperature dependency of the condensed phase bulk density, a simple temperature–dependency of the effective thermal conductivity is assumed here. Consequently, it is inherently assumed that the user–specified thermal conductivity takes into account bulk density, porosity, etc. This is commensurate with the spirit of the present work, which aims to formulate a generalized model and code the governing equations in a self–consistent manner rather than consider detailed submodels for thermophysical properties of specific materials. Nonetheless, if desired, the user is free to use such models as the basis for specifying $k_{0,i}$ $n_{k,i}$ and γ_i in Equation 3.4 which gives the effective thermal conductivity of condensed phase species i:

$$k_i(T) = k_{s,i}(T) + k_{r,i}(T) = k_{0,i}\left(\frac{T}{T_r}\right)^{n_{k,i}} + \gamma_i \sigma T^3 \tag{3.4}$$

In Equation 3.4, the effective thermal conductivity of each condensed phase species is broken into a solid and a radiative component ($k_{s,i}$ and $k_{r,i}$ respectively). The latter is attributed to radiation heat transfer across pores and may become a dominant mode of heat transfer in porous media at high temperature. The parameter γ_i controls this radiative contribution. It has units of length and depends on the pore structure and other considerations (see Section 2.3.2 for details). It is emphasized that the thermal conductivity of each species as calculated with Equation 3.4 should be interpreted as an effective value that includes the effects of the bulk density, porosity, moisture content, microstructure, etc. As with bulk density and porosity, the averaged effective thermal conductivity is weighted by condensed phase species volume fractions ($\bar{k} = \sum X_i k_i$).

The temperature–dependent specific heat capacity of species *i* is assumed to be the sum of a "baseline" specific heat ($c_{b,i}$) and (for polymers that melt) the apparent increase in the specific heat capacity due to the latent heat of melting ($c_{m,i}$):

$$c_i(T) = c_{b,i}(T) + c_{m,i}(T) \tag{3.5a}$$

$$c_{b,i}(T) = c_{0,i}\left(\frac{T}{T_r}\right)^{n_{c,i}} \tag{3.5b}$$

The latent heat of melting is assumed to be distributed via a Gaussian peak centered at T_m, the melting temperature:

$$c_{m,i}(T) = \frac{\Delta H_{m,i}}{\sqrt{2\pi\sigma_{m,i}^2}} \exp\left(-\frac{(T - T_{m,i})^2}{2\sigma_{m,i}^2}\right) \tag{3.5c}$$

In Equation 3.5c, σ_m^2 is a model parameter having units of K^2 that controls the "width" of the Gaussian specific heat peak. Inherent in Equation 3.5c is the assumption that a condensed phase species melts over a range of temperatures rather than at a single temperature. This is not necessarily a shortcoming of the model because only crystalline solids have a well–defined melting temperature. Most polymers are a mixture of crystalline and amorphous components so that melting (or softening of the amorphous components) usually occurs over a finite temperature range.

The sensible enthalpy of condensed phase species *i* at temperature *T* is determined by integration of Equation 3.5a using the definitions from Equations 3.5b and 3.5c:

$$\begin{aligned} h_i(T) &= \int_{T_d}^{T} \left(c_{b,i}(\theta) + c_{m,i}(\theta) \right) \mathrm{d}\theta \\ &= \frac{c_{0,i}}{n_{c,i}+1} \left(T \left(\frac{T}{T_r} \right)^{n_{c,i}} - T_d \left(\frac{T_d}{T_r} \right)^{n_{c,i}} \right) + \frac{\Delta H_{m,i}}{2} \left(\mathrm{erf}\left(\frac{T - T_{m,i}}{\sqrt{2\sigma_{m,i}^2}} \right) - \mathrm{erf}\left(\frac{T_d - T_{m,i}}{\sqrt{2\sigma_{m,i}^2}} \right) \right) \end{aligned} \quad (3.6)$$

Note that T_d is the temperature datum used to establish an absolute value of enthalpy (it is not necessarily the same as the ambient, initial, or reference temperature). The averaged enthalpy and specific heat capacity are determined as mass–weighted quantities, i.e. $\bar{c} = \sum_{i=1}^{M} Y_i c_i$ and $\bar{h} = \sum_{i=1}^{M} Y_i h_i$.

The above formulation is general, and it is designed to allow the user to decide on the level of complexity (or number of degrees of freedom) to include in a simulation. For example, if a condensed phase species with constant specific heat capacity is desired, then the user sets $n_{c,i} = 0$ and $\Delta H_{m,i} = 0$. Similarly, radiative transport across pores can be eliminated by setting $\gamma_i = 0$.

In addition to the condensed phase properties described above, the user must also specify for each species an emissivity (ε_i, dimensionless), radiative absorption coefficient (κ_i, m^{-1}), and permeability (K_i, m^2). The averaged quantities are calculated by volume weighting, i.e. $\bar{\varepsilon} = \sum X_i \varepsilon_i$, $\bar{\kappa} = \sum X_i \kappa_i$, and $\bar{K} = \sum X_i K_i$.

As described above, temperature–dependent condensed phase properties are incorporated in a simplified way and the functional form of this temperature dependency for k, ρ, and c is assumed *a priori*. Thus, the model can accommodate general trends such as an increase in c with temperature. However, detailed temperature dependencies of the underlying thermophysical properties cannot be included. This is not necessarily a drawback because rarely are accurate temperature–dependent measurements of $k(T)$, $c(T)$, or $\rho(T)$ available, particularly at temperatures above 300 ºC that are most relevant to mass burning. Additionally, very few detailed property measurements are available for intermediate species such as char or ash. It was felt that the simplicity of a two–parameter model (which, as seen later, works well with property estimation via genetic algorithm optimization) for thermophysical properties outweighs any potential drawbacks associated with the inability to specify detailed temperature dependent properties.

In addition to condensed phase properties, several gas phase properties are needed. The gas phase density is calculated from the ideal gas law:

$$\rho_g = \frac{P\bar{M}}{RT_g} \tag{3.7}$$

In Equation 3.7, $\bar{M}$ is calculated from the local volume fractions of all gaseous species ($\bar{M} = \sum_{j=1}^{N} X_j M_j$) and R is the universal gas constant.

It is assumed that all gaseous species have equal specific heat capacities that are independent of temperature. This approximation is justified given that very little is known about the composition of the gaseous volatiles produced during the gasification of practical materials. As with the condensed phase enthalpy, the gas phase sensible enthalpy is weighted by mass:

$$\overline{h}_g = \sum_{j=1}^{N} Y_j h_{g,j} = c_{pg}\left(T_g - T_d\right) \tag{3.8}$$

where c_{pg} denotes the (constant) gaseous specific heat capacity.

Gaseous diffusion coefficients are calculated from Chapman–Enskog theory. The binary diffusion coefficient (m^2/s) for species A diffusing into species B is:

$$D_{AB} = 0.018829 \frac{\sqrt{T^3\left(\frac{1}{M_A} + \frac{1}{M_B}\right)}}{P\sigma_{AB}^2 \Omega_{D,AB}} \tag{3.9a}$$

In Equation 3.9a, M_A and M_B have units of g/mol, σ_{AB} is a weighted collision diameter of species A and B (Å), k_b is the Boltzmann constant, and ε_{AB} is the maximum energy of attraction between molecules A and B. Thus, σ_{AB} and $(\varepsilon/k_b)_{AB}$ are model parameters that describe the binary diffusion coefficient of species A into species B. These parameters are tabulated for several gases by Bird *et al.* [193], along with $\Omega_{D,AB}$ is a function of $T/\left(\varepsilon_{AB}/k_b\right)$. Note that σ_{AB} and ε_{AB} are weighted averages between molecules A and B:

$$\sigma_{AB} = \frac{1}{2}\left(\sigma_A + \sigma_B\right) \tag{3.9b}$$

$$\varepsilon_{AB} = \sqrt{\varepsilon_A \varepsilon_B} \tag{3.9c}$$

Since little is known about the composition of gaseous volatiles for practical materials, several approximations are made to simplify the gas phase calculations. It is

assumed that all gaseous species have the same diffusivity, taken as that of oxygen into the primary pyrolysate species. Unit Lewis number is assumed (Pr = Sc = 1) and it follows from these approximations:

$$k_g \approx \rho_g D c_{pg} \tag{3.10a}$$

$$\nu \approx D \tag{3.10b}$$

As shown later, Equation 3.10a allows for considerable simplification of the gas phase energy equation.

To summarize, in addition to molecular weight, there are five gas phase properties: k_g, ρ_g, D, c_{pg}, and ν. ρ_g is calculated from Equation 3.7, c_{pg} is a user–specified constant, D is calculated from Equation 3.9, and the remaining two properties (k_g and ν) are calculated from the relations in Equation 3.10.

3.1.2 Control volume system

The governing equations are solved using a fully implicit finite volume formulation, and the control volume system for which the governing equations are derived is shown schematically in Figure 3.1. Cell P ("point") has neighboring cells T ("top") and B ("bottom"). The interface between cell P and T is denoted t, and the interface between cell P and B is denoted b. The notation ϕ_T indicates the value of variable ϕ in cell T and ϕ_t indicates the value of variable ϕ at the interface between P and T. $(\delta z)_t$ is the distance from P to T and $(\delta z)_b$ is the distance from P to B. The size (height) of cell P is $(\Delta z)_P$. For the purpose of calculating source terms, it is assumed that the value of ϕ at the center of a particular cell prevails over the entire cell, but for calculating gradients at cell boundaries it is assumed that ϕ varies in a piecewise linear manner

between cell centers. The z dimension increases with depth into the solid, i.e. $z = 0$ corresponds to the surface and $z = \delta$ corresponds to the back face. Note that P is located at the center of each cell, except for the two boundary nodes where P is at the edge (because these are "half" cells). The convention used is that ϕ° denotes the value of ϕ at time t and ϕ denotes the value of ϕ at time $t + \Delta t$.

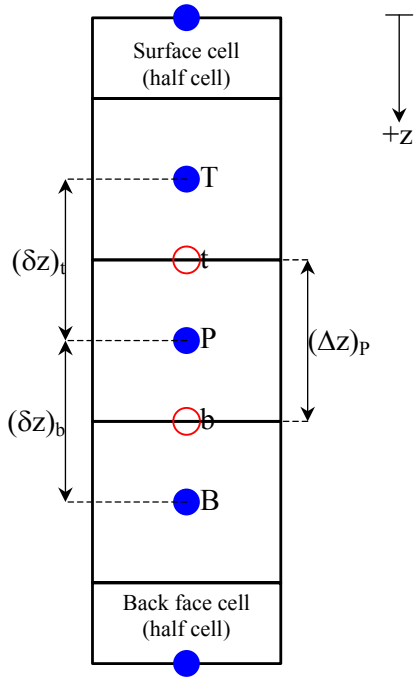

Figure 3.1. Control volume system used for discretization.

In the following sections, the conservation equations are derived for a single one–dimensional control volume. Formally, this involves application of the Reynolds Transport Theorem. For the present simple 1D system of Cartesian control volumes, the conservation equations are derived from physical considerations by setting the sum of the inflow, outflow, and generation terms equal to the storage term. The end result is identical to formal application of the Reynolds Transport Theorem.

Although the governing equations are one–dimensional, each control volume is drawn as a 2D square, just as the 1D control volume system indicated in Figure 3.1 is drawn with a finite width. The convention adopted is that red arrows into the "top" and out of the "bottom" of the control volume indicate fluxes (of mass, species, and energy), i.e. the flow of some quantity per unit area per unit time. Blue arrows into or out of the "sides" are used to indicate volumetric processes due either to source terms (formation or destruction of some quantity per unit volume per unit time) or transfer of some quantity from the condensed phase to the gaseous phase (or vice versa). This convention is indicated schematically in Figure 3.2.

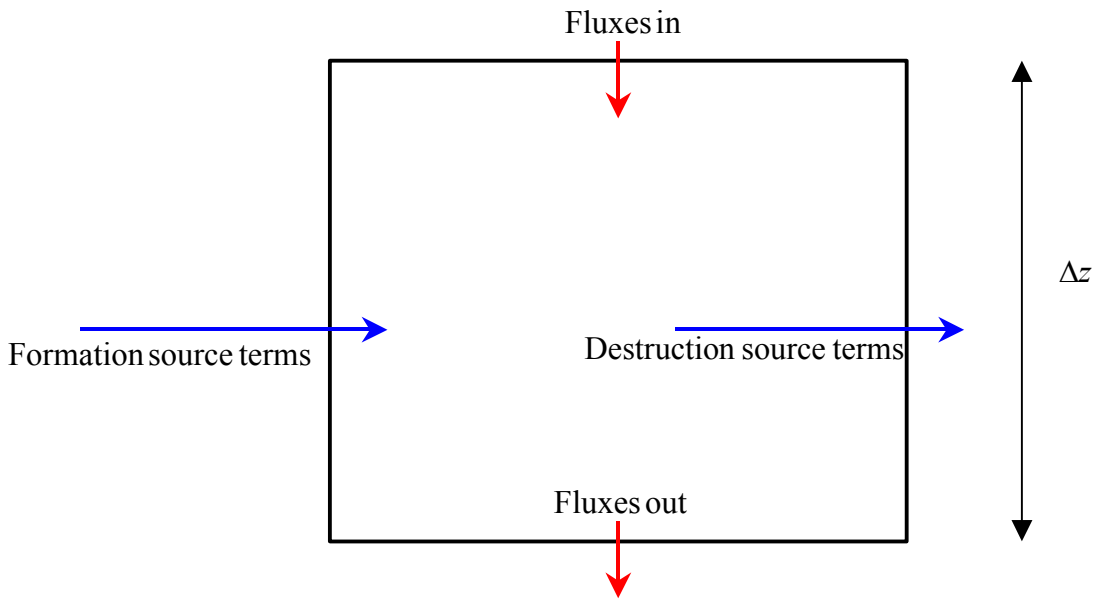

Figure 3.2. General convention used in conservation equation derivation schematic.

3.1.3 Condensed phase mass conservation

A key aspect of this model is that it is specifically designed to accommodate volume change, either due to material consumption (surface regression) or swelling (attributed to intumescence or a condensed phase bulk density that decreases with temperature). This is accomplished by assuming that each grid cell, having height Δz, is

permeable to gaseous mass transfer but is impermeable to condensed phase mass transfer, and that bulk density is a property of a condensed phase species. Thus, if the condensed phase bulk density remains constant but gases escape (e.g., due to pyrolysis) then Δz decreases to conserve mass. The same occurs if no gases escape but the bulk density increases. Conversely, Δz must increase if the bulk density decreases while no gases escape. It is possible to have a release of gases occur simultaneously with a change in bulk density; in this case, the change in Δz, if any, depends on mass conservation considerations. An increase in porosity (decrease in bulk density) can occur with no change in Δz, and this is the usual approach for modeling pyrolysis of charring solids. Due to this formulation, the grid spacing Δz appears in the conservation equations that will be presented below.

The control volume used for deriving the condensed phase mass conservation equation is shown schematically in Figure 3.3:

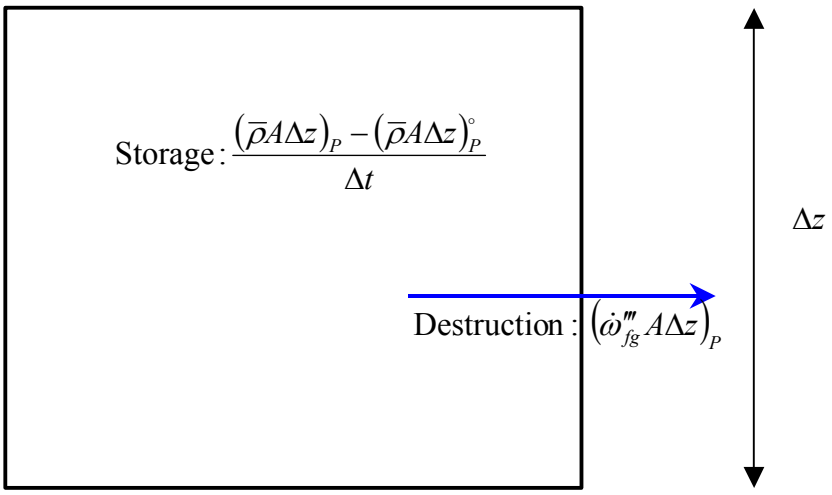

Figure 3.3. Condensed phase mass conservation schematic.

Recall that $\bar{\rho}$ is the weighted bulk density under vacuum. The destruction (consumption) term accounts for the conversion of condensed phase mass to gas phase

mass. Thus, it consists of the total volumetric formation rate of all gases from the condensed phase ($\dot{\omega}'''_{fg}$, kg/m^3–s) multiplied by the cell volume, taken as $A\Delta z$ where A is an appropriate cross–sectional area. The term $\dot{\omega}'''_{fg}$ is defined on a per unit volume of gas plus solid (i.e. per unit volume of mixture) basis. It will be explained in Section 3.2.1 how $\dot{\omega}'''_{fg}$ is calculated. The precise definition of A is unimportant because, as will be shown below, it cancels due to the one–dimensionality of the governing equations. The storage term is the time rate of change of mass contained in the control volume.

Summing the contributions shown in Figure 3.3 gives:

$$-\left(\dot{\omega}'''_{fg} A\Delta z\right)_P = \frac{\left(\bar{\rho} A\Delta z\right)_P - \left(\bar{\rho} A\Delta z\right)_P^{\circ}}{\Delta t} \tag{3.11}$$

There are no "in" and "out" contributions because it is assumed that condensed phase mass does not cross cell boundaries. Assuming A is constant, the condensed phase mass conservation equation becomes:

$$\frac{\left(\bar{\rho}\Delta z\right)_P - \left(\bar{\rho}\Delta z\right)_P^{\circ}}{\Delta t} = -\left(\dot{\omega}'''_{fg}\Delta z\right)_P \tag{3.12}$$

Thus, it can be seen that the grid spacing Δz appears in the condensed phase mass conservation equation, which contains only two terms: generation (RHS) and storage (LHS). No convective terms are present because, as mentioned above, an assumption of this model is that condensed phase mass does not cross cell boundaries (only gaseous mass is permitted to cross cell boundaries). The source term on the RHS is the formation rate of gases from the condensed phase and does not include the formation rate of condensed phase species. This is by design since the formation of one condensed phase

species from another, in the absence of gas formation, does not change the quantity $(\overline{\rho}\Delta z)_P$. Although both $\overline{\rho}$ and Δz could change, their product would be unaffected.

Physically, Equation 3.12 says that the product of the condensed phase density in a cell and the size of that cell will decrease due to the formation of gases in that cell. For an idealized charring material, the formation of gases will result in a reduction of $\overline{\rho}$ (due to an increase in porosity). Similarly, for an idealized thermoplastic material, the formation of gases will result in a reduction of Δz, i.e. the cell shrinks. For "real" (non–idealized) materials, a reduction of $\overline{\rho}$ may occur simultaneously with a reduction of Δz. As will be discussed below, both $\overline{\rho}$ and Δz can be uniquely determined by solving the condensed phase species conservation equation. For the special case where Δz is fixed, as occurs for charring fuels with no shrinkage or swelling, one can take the limit of Equation 3.12 as $\Delta t \to 0$ to obtain $\frac{\partial \overline{\rho}}{\partial t} = -\dot{\omega}'''_{fg}$.

Equation 3.12 reduces to an ordinary differential equation for the quantity $\overline{\rho}\Delta z$ in each cell *P* (see Section 3.3.1 for details). Thus, a single initial condition is required in each cell:

$$\left(\overline{\rho}\Delta z\right)_P^{\circ}\Big|_{t=0} = \left(\left(\Delta z\right)_0 \sum_{i=1}^{M}\left(X_{i0}\rho_{i0}\right)\right)_P \tag{3.13}$$

3.1.4 Condensed phase species conservation

The condensed phase species conservation equation is similar to the condensed phase mass conservation equation in that it is assumed that no condensed phase species cross cell boundaries. Thus, the only terms that must be considered are storage, formation, and destruction, as shown schematically in Figure 3.4:

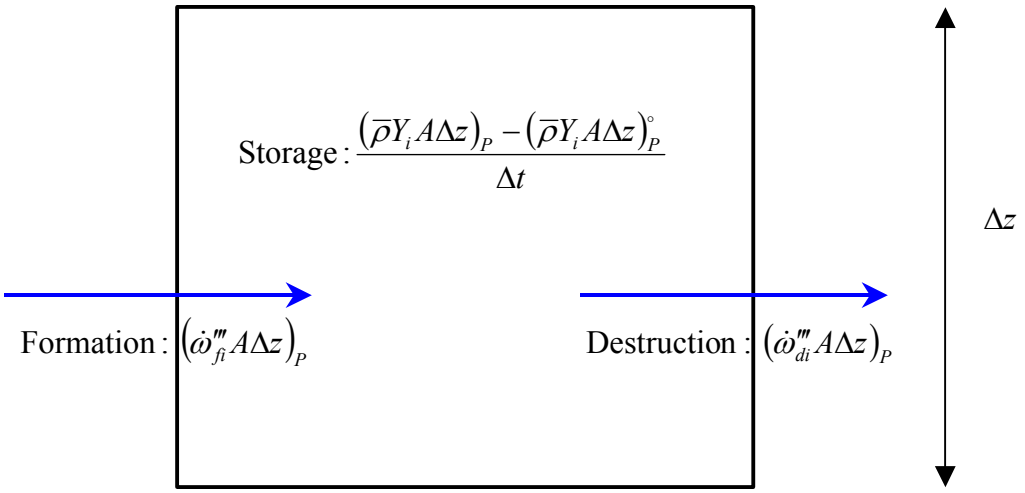

Figure 3.4. Condensed phase species conservation schematic.

Here, $\dot{\omega}'''_{fi}$ and $\dot{\omega}'''_{di}$ are respectively the volumetric total formation rate and volumetric total destruction rate of condensed phase species *i*. They are defined on a per unit volume of gas plus solid (per unit volume of mixture) basis. It will be explained in Section 3.2.1 how these source terms are calculated. Summing the individual contributions shown in Figure 3.4 gives:

$$(\dot{\omega}'''_{fi} A\Delta z)_P - (\dot{\omega}'''_{di} A\Delta z)_P = \frac{(\bar{\rho}Y_i A\Delta z)_P - (\bar{\rho}Y_i A\Delta z)_P^\circ}{\Delta t} \tag{3.14}$$

The final form of the conservation equation is obtained after assuming *A* is constant:

$$\frac{(\bar{\rho}Y_i \Delta z)_P - (\bar{\rho}Y_i \Delta z)_P^\circ}{\Delta t} = (\dot{\omega}'''_{fi} \Delta z)_P - (\dot{\omega}'''_{di} \Delta z)_P \tag{3.15}$$

Although it may seem unusual that the grid spacing Δz appears in Equations 3.12 and 3.15, these conservation equations are well–posed. Equations 3.12, 3.15, and the auxiliary relation $\bar{\rho} = \left(\sum (Y_i / \rho_i)\right)^{-1}$ are $M + 2$ equations for $M + 2$ unknowns in each grid cell: the M species' mass fractions, $\bar{\rho}$, and Δz. For the special case where Δz is fixed, one can take the limit of Equation 3.15 as $\Delta t \to 0$ to obtain $\frac{\partial(\bar{\rho}Y_i)}{\partial t} = \dot{\omega}'''_{fi} - \dot{\omega}'''_{di}$.

The condensed phase species conservation equation also reduces to an ODE for the quantity $\overline{\rho} Y_i \Delta z$ in each cell *P*. The single required initial condition is:

$$\left(\overline{\rho} Y_i \Delta z\right)_P^{\circ}\Big|_{t=0} = \left(\overline{\rho} \Delta z\right)_P^{\circ}\Big|_{t=0} \left(Y_{i0}\right)_P \tag{3.16}$$

3.1.5 Gas phase mass conservation

The control volume used to derive the gas phase mass conservation equation is shown schematically in Figure 3.5:

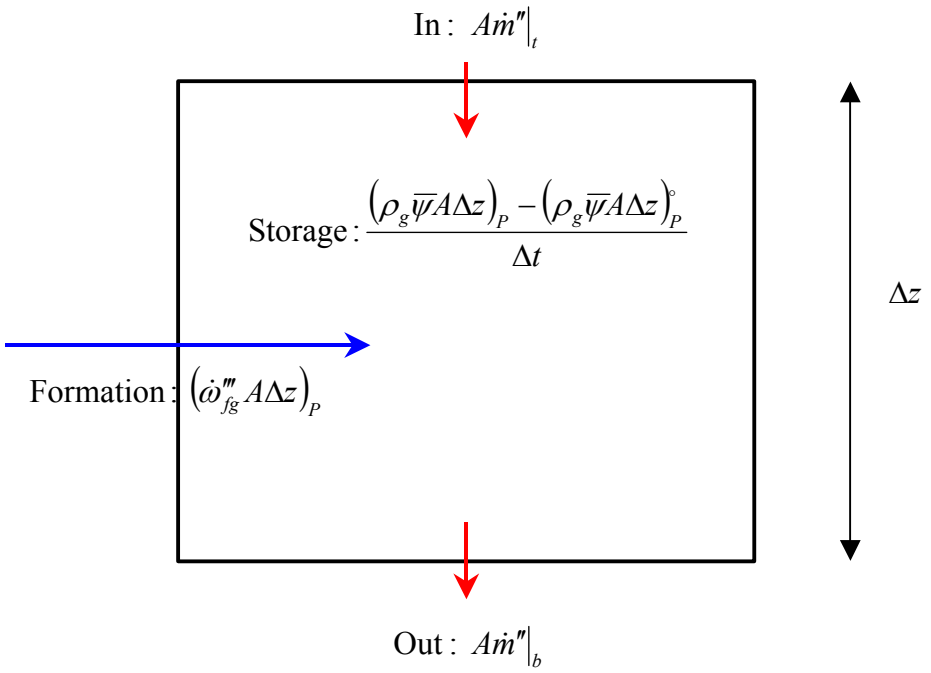

Figure 3.5. Gas phase mass conservation schematic.

The storage term is similar to that for the condensed phase mass conservation equation, except the density is that of the gas phase (ρ_g), and the weighted porosity ($\overline{\psi}$) appears. Note that the formation (or source) term is attributed to the conversion of condensed phase mass to gas phase mass. It is equal in magnitude to, but has the opposite sign of, the source term that appears in the condensed phase mass conservation equation. Porosity

does not appear in the source term because, as mentioned above, it is calculated on a per unit volume of mixture (solid plus gas) basis. The only inflow and outflow terms are due to convective mass transfer ($\dot{m}''$) because the diffusive mass transfer terms cancel. Summing the terms shown in Figure 3.5 gives:

$$A\dot{m}''\big|_t - A\dot{m}''\big|_b + \left(\dot{\omega}'''_{fg} A\Delta z\right)_P = \frac{\left(\rho_g \overline{\psi} A\Delta z\right)_P - \left(\rho_g \overline{\psi} A\Delta z\right)_P^\circ}{\Delta t} \tag{3.17}$$

Divide both sides by A:

$$\frac{\left(\rho_g \overline{\psi}\Delta z\right)_P - \left(\rho_g \overline{\psi}\Delta z\right)_P^\circ}{\Delta t} + \dot{m}''\big|_b - \dot{m}''\big|_t = \left(\dot{\omega}'''_{fg}\Delta z\right)_P \tag{3.18}$$

Unlike Equation 3.12 (the condensed phase mass conservation equation), Equation 3.18 contains convective terms to account for the flow of volatiles. For the special case where Δz is fixed, one can take the limit of Equation 3.18 as $\Delta t \to 0$ and $\Delta z \to 0$ to obtain $\dfrac{\partial\left(\rho_g \overline{\psi}\right)}{\partial t} + \dfrac{\partial \dot{m}''}{\partial z} = \dot{\omega}'''_{fg}$.

Equation 3.18 requires one initial condition and one boundary condition. The initial condition in each cell P is:

$$\left(\rho_g \overline{\psi}\Delta z\right)_P^\circ\Big|_{t=0} = \left((\Delta z)_0 \sum_{j=1}^{N} \left(X_{j0}\rho_{g,j}\right) \sum_{i=1}^{M} \left(X_{i0}\psi_i\right) \right)\Bigg|_{t=0} \tag{3.19a}$$

A single boundary condition is required. Normally, this is specification of the mass flux at the back face, which is zero for a negligibly permeable substrate. However, in a simulation of smoldering combustion, the back face mass flux may be nonzero due to the contribution from an internal forced flow. Thus, a more general back face boundary condition is:

$$\dot{m}''\big|_{z=\delta} = \dot{m}''_\delta \tag{3.19b}$$

3.1.6 Gas phase species conservation

In the gas phase species conservation equation, both convective and diffusive transport across cell boundaries must be considered. The convective flux of gaseous species j is $\dot{m}''Y_j$ and the diffusive flux of gaseous species j is denoted $\dot{j}_j''$. The control volume used for deriving the gas phase mass conservation equation is shown schematically in Figure 3.6:

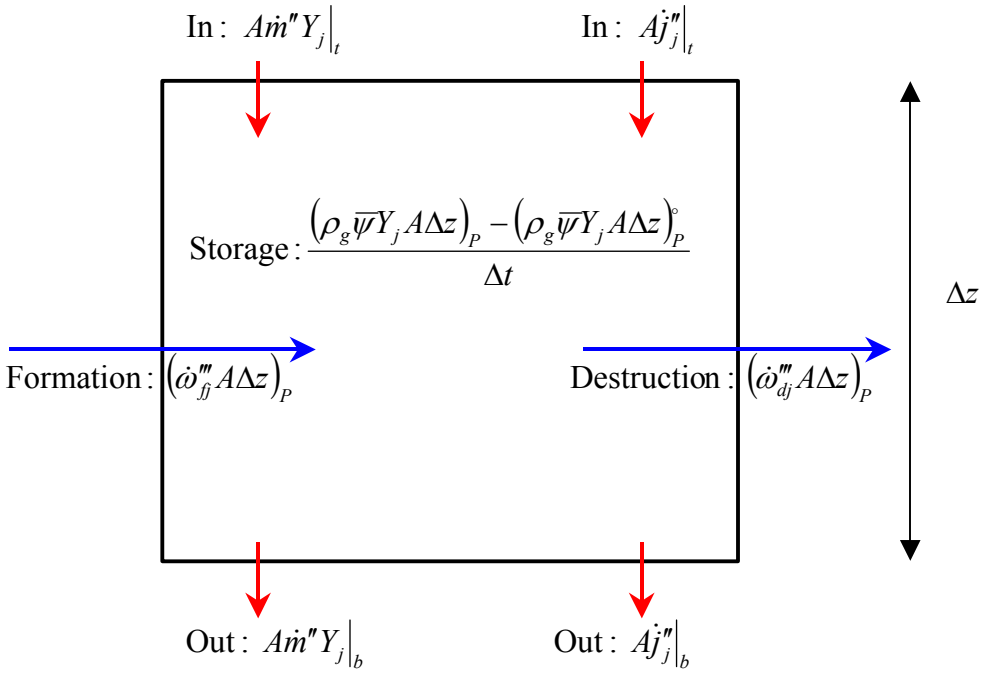

Figure 3.6. Gas phase species conservation schematic.

The source terms $\dot{\omega}_{fj}'''$ and $\dot{\omega}_{dj}'''$ are defined on a per unit volume of solid plus gas basis, i.e. on a per unit volume of mixture basis. Summing the terms shown in Figure 3.6 gives:

$$A\dot{m}''Y_j\big|_t+A\dot{j}_j''\big|_t-A\dot{m}''Y_j\big|_b-A\dot{j}_j''\big|_b+\left(\dot{\omega}_{fj}'''A\Delta z\right)_P-\left(\dot{\omega}_{dj}'''A\Delta z\right)_P=\frac{\left(\rho_g\overline{\psi}Y_jA\Delta z\right)_P-\left(\rho_g\overline{\psi}Y_jA\Delta z\right)_P^\circ}{\Delta t} \tag{3.20}$$

Divide both sides by A and regroup:

$$\frac{\left(\rho_g \overline{\psi} Y_j \Delta z\right)_P - \left(\rho_g \overline{\psi} Y_j \Delta z\right)_P^\circ}{\Delta t} + \dot{m}'' Y_j\Big|_b - \dot{m}'' Y_j\Big|_t = -\dot{j}_j''\Big|_b + \dot{j}_j''\Big|_t + \left(\dot{\omega}_{fj}''' \Delta z\right)_P - \left(\dot{\omega}_{dj}''' \Delta z\right)_P \quad (3.21)$$

For the special case where Δz is fixed, one can take the limit of Equation 3.21 as $\Delta t \to 0$ and $\Delta z \to 0$ to obtain $\frac{\partial\left(\rho_g \overline{\psi} Y_j\right)}{\partial t} + \frac{\partial\left(\dot{m}'' Y_j\right)}{\partial z} = -\frac{\partial \dot{j}_j''}{\partial z} + \dot{\omega}_{fj}''' - \dot{\omega}_{dj}'''$. To facilitate numerical solution, the final form of the gas phase species conservation equation solved by the code is obtained by multiplying the gas phase mass conservation equation (Equation 3.18) by $Y_{j,P}$ and subtracting the result from Equation 3.21:

$$\begin{aligned}&\left(\rho_g \overline{\psi} \Delta z\right)_P^\circ \frac{Y_{j,P} - Y_{j,P}^\circ}{\Delta t} + \dot{m}'' Y_j\Big|_b - \dot{m}'' Y_j\Big|_t - Y_{j,P}\dot{m}''\Big|_b + Y_{j,P}\dot{m}''\Big|_t = \\ &-\dot{j}_j''\Big|_b + \dot{j}_j''\Big|_t + \left(\dot{\omega}_{fj}''' \Delta z\right)_P - \left(\dot{\omega}_{dj}''' \Delta z\right)_P - \left(\dot{\omega}_{fg}''' Y_j \Delta z\right)_P\end{aligned} \quad (3.22)$$

Similar to the condensed phase species conservation equation, $\dot{\omega}_{fj}'''$ is the total formation rate of gaseous species j and $\dot{\omega}_{dj}'''$ is the total destruction rate of gaseous species j. These source terms include contributions from both heterogeneous (gas/solid) and homogeneous (gas/gas) reactions. It will be explained how these source terms are calculated in Section 3.2. Although the diffusive term in Equation 3.22 is written in its general form ($\dot{j}_j''$), Fickian diffusion is assumed when Equation 3.22 is solved numerically:

$$\dot{j}_j'' = -\overline{\psi}\rho_g D \frac{\partial Y_j}{\partial z} \quad (3.23)$$

For each gaseous species j, Equation 3.22 requires one initial and two boundary conditions. The initial conditions in each cell P are the gaseous species mass fraction at time $t = 0$:

$$Y_j^\circ\Big|_{t=0} = Y_{j0} \quad (3.24a)$$

Two boundary conditions are required for each gaseous species j. Normally, the back face ($z = \delta$) is impermeable so there is no flow of volatiles across the back face and the species mass fraction gradient is set to zero:

$$\left.\frac{\partial Y_j}{\partial z}\right|_{z=\delta} = 0 \tag{3.24b.1}$$

The main exception is smoldering combustion with an internal forced flow where the mass fractions of the species in the incoming gas (if any) must be specified:

$$Y_j\big|_{z=\delta} = Y_{j\delta} \tag{3.24b.2}$$

No boundary condition is required for gaseous species at an outflow boundary if the Peclet number is sufficiently high [194]. However, this condition is not always met, so the diffusive mass flux of gaseous species into or out of the decomposing solid at the front face is approximated using the heat/mass transfer analogy:

$$-\overline{\psi}\rho_g D\left.\frac{\partial Y_j}{\partial z}\right|_{z=0} \approx \frac{h_c}{c_{pg}}\left(Y_j^{\infty} - Y_j\big|_{z=0}\right) \tag{3.24c}$$

If the user desires, the effect of blowing on the heat transfer coefficient can be simulated using a Couette flow approximation [195]:

$$h_c = \frac{\dot{m}_0'' c_{pg}}{\exp\left(\dot{m}_0'' c_{pg} / h_{c,nb}\right) - 1} \tag{3.25}$$

where $h_{c,nb}$ is the heat transfer coefficient with no blowing, and $\dot{m}_0''$ is the mass flux of gases at the surface. The user specifies whether the heat transfer coefficient is fixed at $h_{c,nb}$, or whether it is reduced due to blowing according to Equation 3.25.

3.1.7 Condensed phase energy conservation

The control volume used for deriving the condensed phase energy conservation equation is shown schematically in Figure 3.7:

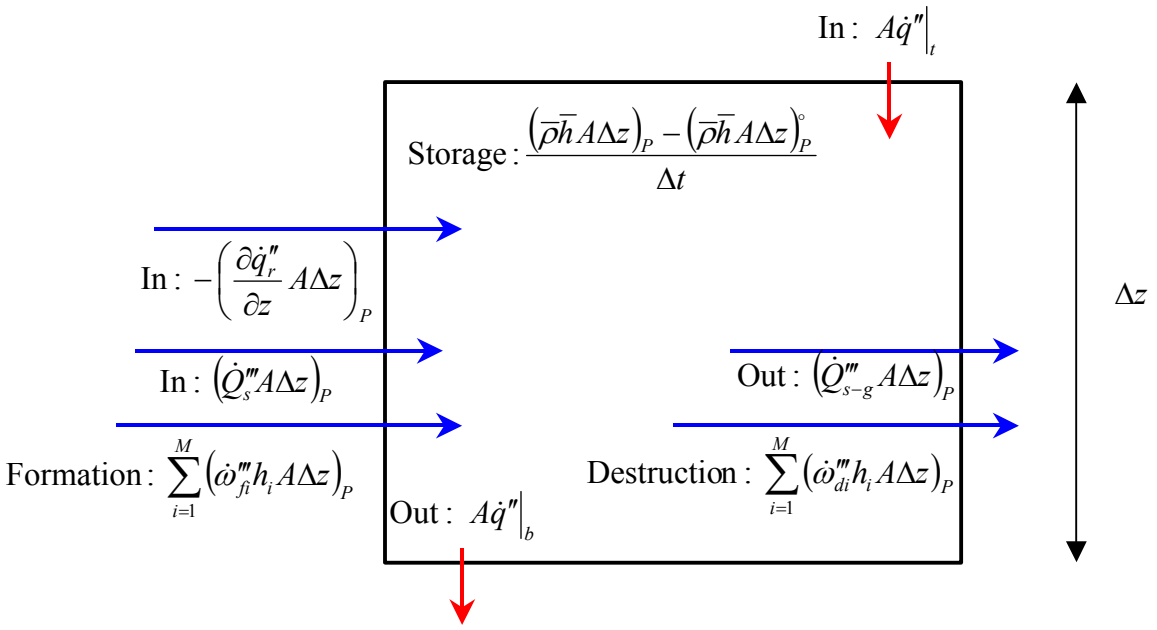

Figure 3.7. Condensed phase energy conservation schematic.

Changes in kinetic energy, potential energy, and work done on the surroundings are neglected. All source terms are defined on a per unit volume of gas plus solid (i.e. per unit volume of mixture) basis. In Figure 3.7, the term $\dot{Q}_s'''$ is the volumetric rate of heat release (or absorption) due to condensed phase reactions (see Equation 3.64), and $\dot{Q}_{s-g}'''$ is the volumetric rate of heat transfer from the condensed phase to the gas phase, modeled as:

$$\dot{Q}_{s-g}''' = h_{cv}\left(T - T_g\right) \tag{3.26}$$

where h_{cv} is the volumetric heat transfer coefficient (W/m^3–K), assumed for simplicity to be constant (independent of Reynolds number and pore characteristics). For radiation applied only normal to the surface, the in–depth radiative heat flux is:

$$\dot{q}_r''(z) = \bar{\varepsilon}\dot{q}_e'' \exp\left(-\int_0^z \bar{\kappa}(\zeta)\mathrm{d}\zeta\right) \tag{3.27}$$

Therefore, its divergence (shown as an "in" term in Figure 3.7) is:

$$\frac{\partial \dot{q}_r''}{\partial z} = -\bar{\varepsilon}\dot{q}_e''\bar{\kappa}(z)\exp\left(-\int_0^z \bar{\kappa}(\zeta)\mathrm{d}\zeta\right) \tag{3.28}$$

This simple formulation only accounts for "one–way" radiation, meaning the penetration of radiation into the solid is calculated, but the emission from interior parts of the solid is not (surface radiant emission is still considered, see Equation 3.33b). This treatment is slightly different from the solid phase model in NIST's Fire Dynamics Simulator Version 5.0 [51] which accounts for two–way radiation and radiation applied other than normal to the surface. Note that if $\bar{\kappa}$ is not a function of z, then Equation 3.28 simplifies to $\partial \dot{q}_r'' / \partial z = -\bar{\varepsilon}\dot{q}_e''\bar{\kappa}\exp(-\bar{\kappa}z)$.

In Figure 3.7, $\dot{q}''$ is the conductive heat flux through the condensed phase:

$$\dot{q}'' = -\bar{k}\frac{\partial T}{\partial z} \tag{3.29}$$

A decomposing solid frequently consists of a single "layer". However, the model can also accommodate materials with a layered or laminated composition. For layers that are not in perfect thermal contact, the rate of heat transfer between layers calculated as $h_{cr}\Delta T$ where h_{cr} is an inverse contact resistance (W/m^2–K) and ΔT is the temperature difference between the "back" of one layer and the "front" of the layer that it abuts. At the interface between two layers that are not in perfect thermal contact, the thermal conductivity $\bar{k}$ in Equation 3.29 is replaced with $h_{cr}\times\delta z$ where δz is the appropriate distance between cell centers (see Figure 3.1).

Summing the terms indicated in Figure 3.7 gives:

$$A\dot{q}''\Big|_t - A\dot{q}''\Big|_b - \left(\dot{Q}'''_{s-g} A\Delta z\right)_P + \left(\dot{Q}'''_s A\Delta z\right)_P - \left(\frac{\partial \dot{q}''_r}{\partial z} A\Delta z\right)_P + \sum_{i=1}^{M}\left(\dot{\omega}'''_{fi} h_i A\Delta z\right)_P - \sum_{i=1}^{M}\left(\dot{\omega}'''_{di} h_i A\Delta z\right)_P = \frac{\left(\overline{\rho}\overline{h} A\Delta z\right)_P - \left(\overline{\rho}\overline{h} A\Delta z\right)^{\circ}_P}{\Delta t} \tag{3.30}$$

Assuming A is constant:

$$\frac{\left(\overline{\rho}\overline{h}\Delta z\right)_P - \left(\overline{\rho}\overline{h}\Delta z\right)^{\circ}_P}{\Delta t} = -\dot{q}''\Big|_b + \dot{q}''\Big|_t - \left(\dot{Q}'''_{s-g}\Delta z\right)_P + \left(\dot{Q}'''_s \Delta z\right)_P - \left(\frac{\partial \dot{q}''_r}{\partial z}\Delta z\right)_P + \sum_{i=1}^{M}\left(\left(\dot{\omega}'''_{fi} - \dot{\omega}'''_{di}\right) h_i \Delta z\right)_P \tag{3.31}$$

For the special case where Δz is fixed, one can take the limit of Equation 3.31 as $\Delta t \to 0$ and $\Delta z \to 0$ to obtain $\frac{\partial\left(\overline{\rho}\overline{h}\right)}{\partial t} = -\frac{\partial \dot{q}''}{\partial z} - \dot{Q}'''_{s-g} + \dot{Q}'''_s - \frac{\partial \dot{q}''_r}{\partial z} + \sum_{i=1}^{M}\left(\dot{\omega}'''_{fi} - \dot{\omega}'''_{di}\right) h_i$. To facilitate numerical solution, the final form of the condensed phase energy equation that is solved by the code is obtained by multiplying the condensed phase mass conservation equation (Equation 3.12) by $\overline{h}_P$ and subtracting the result from Equation 3.31:

$$\left(\overline{\rho}\Delta z\right)^{\circ}_P \frac{\overline{h}_P - \overline{h}^{\circ}_P}{\Delta t} = -\dot{q}''\Big|_b + \dot{q}''\Big|_t - \left(\dot{Q}'''_{s-g}\Delta z\right)_P + \left(\dot{Q}'''_s \Delta z\right)_P - \left(\frac{\partial \dot{q}''_r}{\partial z}\Delta z\right)_P + \sum_{i=1}^{M}\left(\left(\dot{\omega}'''_{fi} - \dot{\omega}'''_{di}\right) h_i \Delta z\right)_P + \overline{h}_P\left(\dot{\omega}'''_{fg}\Delta z\right)_P \tag{3.32}$$

One initial and two boundary conditions are required. The initial condition in each cell P is:

$$T^{\circ}_P(z)\Big|_{t=0} = T_0 \quad \Rightarrow \overline{h}^{\circ}_P\Big|_{t=0} = \sum_{i=1}^{M}\left(Y_{i0} h_{i0}\right)_P \tag{3.33a}$$

The front face boundary condition is:

$$-\overline{k}\frac{\partial T}{\partial z}\Big|_{z=0} = \varepsilon \dot{q}''_e - h_c\left(T\Big|_{z=0} - T_\infty\right) - \varepsilon\sigma\left(T^4\Big|_{z=0} - T^4_\infty\right) \quad \text{(for } \overline{\kappa}\Big|_{z=0} \to \infty\text{)} \tag{3.33b}$$

$$-\bar{k}\left.\frac{\partial T}{\partial z}\right|_{z=0} = -h_c\left(T\big|_{z=0} - T_\infty\right) - \varepsilon\sigma\left(T^4\big|_{z=0} - T_\infty^4\right) \quad \left(\text{for } \bar{\kappa}\big|_{z=0} \neq \infty\right) \tag{3.33b}$$

The back face boundary condition is:

$$-\bar{k}\left.\frac{\partial T}{\partial z}\right|_{z=\delta} = h_{c\delta}\left(T\big|_{z=\delta} - T_\infty\right) \tag{3.33c}$$

3.1.8 Gas phase energy conservation

The control volume used to derive the gas phase energy conservation equation is shown schematically in Figure 3.8:

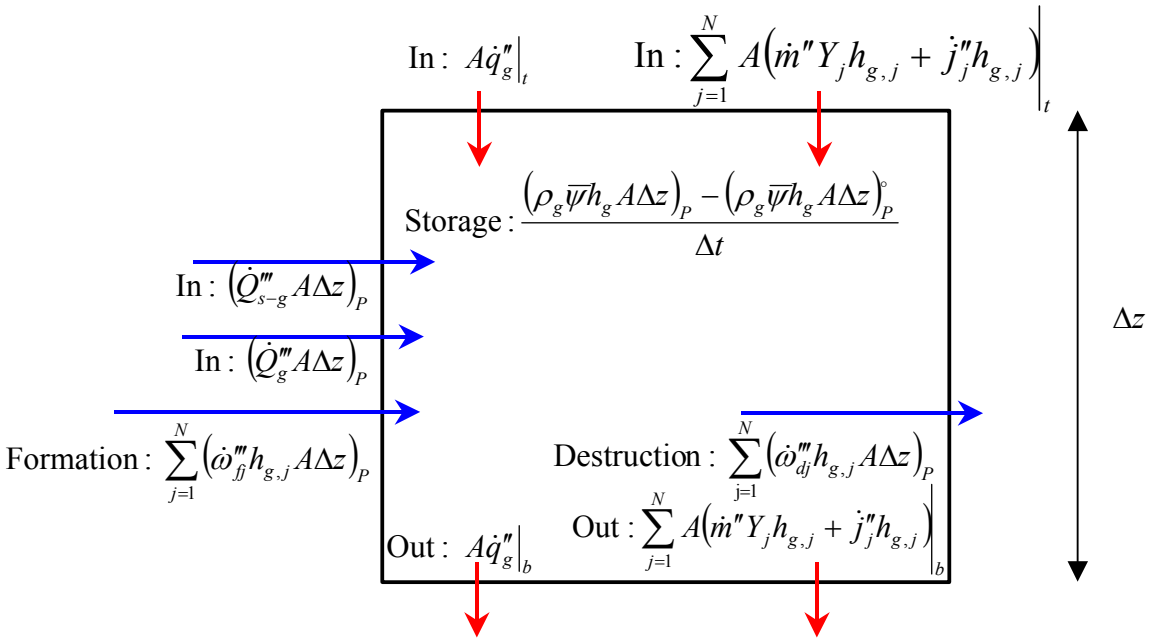

Figure 3.8. Gas phase energy conservation schematic.

All source terms are defined on a per unit volume of solid plus gas basis, i.e. on a per unit volume of mixture basis. Note that gas phase conduction ($\dot{q}_g''$), convection ($\sum \dot{m}'' Y_j h_{g,j}$), and diffusion ($\sum \dot{j}_j'' h_{g,j}$) are considered. The term $\dot{Q}_{s-g}'''$ is the volumetric rate of heat

transfer from the condensed phase to the gas phase (Equation 3.26). Summing the terms shown in Figure 3.8 gives:

$$A\dot{q}''_g\Big|_t + \sum_{j=1}^{N} A\left(\dot{m}'' Y_j h_{g,j} + \dot{j}''_j h_{g,j}\right)\Big|_t + \left(\dot{Q}'''_{s-g} A\Delta z\right)_P + \sum_{j=1}^{N}\left(\dot{\omega}'''_{fj} h_{g,j} A\Delta z\right)_P - A\dot{q}''_g\Big|_b -$$
$$\sum_{j=1}^{N} A\left(\dot{m}'' Y_j h_{g,j} + \dot{j}''_j h_{g,j}\right)\Big|_b - \sum_{j=1}^{N}\left(\dot{\omega}'''_{dj} h_{g,j} A\Delta z\right)_P + \left(\dot{Q}'''_g A\Delta z\right)_P = \tag{3.34}$$
$$\frac{\left(\rho_g \overline{\psi} h_g A\Delta z\right)_P - \left(\rho_g \overline{\psi} h_g A\Delta z\right)^{\circ}_P}{\Delta t}$$

Assume A is constant:

$$\frac{\left(\rho_g \overline{\psi} h_g \Delta z\right)_P - \left(\rho_g \overline{\psi} h_g \Delta z\right)^{\circ}_P}{\Delta t} + \dot{m}'' h_g\Big|_b - \dot{m}'' h_g\Big|_t = -\dot{q}''_g\Big|_b + \dot{q}''_g\Big|_t - \sum_{j=1}^{N} \dot{j}''_j h_{g,j}\Big|_b + \sum_{j=1}^{N} \dot{j}''_j h_{g,j}\Big|_t \tag{3.35}$$
$$+\left(\dot{Q}'''_{s-g}\Delta z\right)_P + \sum_{j=1}^{N}\left(\dot{\omega}'''_{fj} h_{g,j}\Delta z\right)_P - \sum_{j=1}^{N}\left(\dot{\omega}'''_{dj} h_{g,j}\Delta z\right)_P + \left(\dot{Q}'''_g \Delta z\right)_P$$

Equation 3.35 can be simplified by noting that the sum of the conductive and diffusive heat flux is:

$$\begin{aligned}
\dot{q}''_g + \sum_{j=1}^{N} \dot{j}''_j h_{g,j} &\equiv -\overline{\psi} k_g \frac{\partial T}{\partial z} - \sum_{j=1}^{N} \overline{\psi}\rho_g D_j h_{g,j} \frac{\partial Y_j}{\partial z} \\
&\equiv -\frac{\overline{\psi} k_g}{c_{pg}}\left(\frac{\partial h_g}{\partial z} - \sum_{j=1}^{N} h_{g,j}\frac{\partial Y_j}{\partial z}\right) - \sum_{j=1}^{N} \overline{\psi}\rho_g D_j h_{g,j}\frac{\partial Y_j}{\partial z} \\
&\equiv -\frac{\overline{\psi} k_g}{c_{pg}}\frac{\partial h_g}{\partial z} + \sum_{j=1}^{N}\left(\frac{\overline{\psi} k_g}{c_{pg}} h_{g,j}\frac{\partial Y_j}{\partial z} - \overline{\psi}\rho_g D_j h_{g,j}\frac{\partial Y_j}{\partial z}\right) \\
&\equiv -\frac{\overline{\psi} k_g}{c_{pg}}\frac{\partial h_g}{\partial z} + \sum_{j=1}^{N}\left(\overline{\psi}\left(\frac{k_g}{c_{pg}} - \rho_g D_j\right) h_{g,j}\frac{\partial Y_j}{\partial z}\right)
\end{aligned} \tag{3.36}$$

Fickian diffusion has been assumed when calculating the diffusive flux term. By making the approximation that all gases have the same diffusion coefficient ($D_j = D$) the summation term in Equation 3.36 will drop out if $\rho_g D = k_g/c_{pg}$, i.e. by assuming that $k_g = \rho_g c_{pg} D$ (which implies unit Lewis number, Pr = Sc = 1). As mentioned in Section 3.1.1, this approximation is made here, allowing for considerable simplification:

$$\dot{q}''_g + \sum_{j=1}^{N} \dot{j}''_j h_{g,j} \approx -\overline{\psi}\rho_g D \frac{\partial h_g}{\partial z} \tag{3.37}$$

Substituting Equation 3.37 into Equation 3.35 gives:

$$\begin{aligned} &\frac{\left(\rho_g \overline{\psi} h_g \Delta z\right)_P - \left(\rho_g \overline{\psi} h_g \Delta z\right)_P^\circ}{\Delta t} + \dot{m}'' h_g\Big|_b - \dot{m}'' h_g\Big|_t = \overline{\psi}\rho_g D \frac{\partial h_g}{\partial z}\Big|_b - \overline{\psi}\rho_g D \frac{\partial h_g}{\partial z}\Big|_t \\ &+ \left(\dot{Q}'''_{s-g}\Delta z\right)_P + \sum_{j=1}^{N}\left(\dot{\omega}'''_{fj} h_{g,j}\Delta z\right)_P - \sum_{j=1}^{N}\left(\dot{\omega}'''_{dj} h_{g,j}\Delta z\right)_P + \left(\dot{Q}'''_g \Delta z\right)_P \end{aligned} \tag{3.38}$$

For the case where Δz is fixed, one can take the limit of Equation 3.38 as $\Delta t \to 0$ and $\Delta z \to 0$ to obtain $\frac{\partial\left(\rho_g \overline{\psi} h_g\right)}{\partial t} + \frac{\partial}{\partial z}\left(\dot{m}'' h_g\right) = \frac{\partial}{\partial z}\left(\overline{\psi}\rho_g D \frac{\partial h_g}{\partial z}\right) + \dot{Q}'''_{s-g} + \sum_{j=1}^{N}\left(\left(\dot{\omega}'''_{fj} - \dot{\omega}'''_{dj}\right)h_{g,j}\right) + \dot{Q}'''_g$.

To facilitate numerical solution, the final form of the gas phase energy equation that is solved by the code is obtained by multiplying the gas phase mass conservation equation (Equation 3.18) by $(h_g)_P$ and subtracting the result from the gas phase energy equation (Equation 3.38):

$$\begin{aligned} &\left(\rho_g \overline{\psi}\Delta z\right)_P^\circ \frac{h_{g,P} - h_{g,P}^\circ}{\Delta t} + \dot{m}'' h_g\Big|_b - \dot{m}'' h_g\Big|_t - h_{g,P}\dot{m}''\Big|_b + h_{g,P}\dot{m}''\Big|_t = \\ &\overline{\psi}\rho_g D \frac{\partial h_g}{\partial z}\Big|_b - \overline{\psi}\rho_g D \frac{\partial h_g}{\partial z}\Big|_t + \left(\dot{Q}'''_{s-g}\Delta z\right)_P + \\ &\sum_{j=1}^{N}\left(\left(\dot{\omega}'''_{fj} - \dot{\omega}'''_{dj}\right)h_{g,j}\Delta z\right)_P + \left(\dot{Q}'''_g \Delta z\right)_P - \left(\dot{\omega}'''_{fg} h_g \Delta z\right)_P \end{aligned} \tag{3.39}$$

One initial and two boundary conditions are required. The initial condition is:

$$T_P^\circ(z)\Big|_{t=0} = T_0 \qquad \Rightarrow \overline{h}_P^\circ\Big|_{t=0} = \sum_{j=1}^{N}\left(Y_{j0} h_{g,j0}\right)_P \tag{3.40a}$$

The front face boundary condition is:

$$-\overline{\psi}\rho_g D \frac{\partial h_g}{\partial z}\Big|_{z=0} = h_c\left(T_\infty - T_g\Big|_{z=0}\right) \tag{3.40b}$$

The back face boundary condition is:

$$-\overline{\psi}\rho_g D\left.\frac{\partial h_g}{\partial z}\right|_{z=\delta} = h_{c\delta}\left(T_g\big|_{z=\delta} - T_\infty\right) \tag{3.40c}$$

3.1.9 Gas phase momentum conservation

An equation describing the evolution of the pressure profile inside the decomposing solid is derived beginning with the gas phase mass conservation equation (Equation 3.18):

$$\frac{\left(\rho_g\overline{\psi}\Delta z\right)_P - \left(\rho_g\overline{\psi}\Delta z\right)_P^\circ}{\Delta t} + \dot{m}''\big|_b - \dot{m}''\big|_t = \left(\dot{\omega}'''_{fg}\Delta z\right)_P$$

Assuming Darcian flow with no buoyancy contribution, the mass fluxes are calculated as:

$$\dot{m}''\big|_b = -\left(\frac{\overline{K}}{\nu}\right)_b \left.\frac{\partial P}{\partial z}\right|_b \tag{3.41a}$$

$$\dot{m}''\big|_t = -\left(\frac{\overline{K}}{\nu}\right)_t \left.\frac{\partial P}{\partial z}\right|_t \tag{3.41b}$$

A pressure evolution equation is obtained by replacing ρ_g with P using the ideal gas law ($P = \rho_g R T_g / \overline{M}$) and substituting Equation 3.41 into Equation 3.18:

$$\frac{\left(\frac{P\overline{M}}{RT_g}\overline{\psi}\Delta z\right)_P - \left(\frac{P\overline{M}}{RT_g}\overline{\psi}\Delta z\right)_P^\circ}{\Delta t} - \left(\frac{\overline{K}}{\nu}\right)_b \left.\frac{\partial P}{\partial z}\right|_b + \left(\frac{\overline{K}}{\nu}\right)_t \left.\frac{\partial P}{\partial z}\right|_t = \left(\dot{\omega}'''_{fg}\Delta z\right)_P \tag{3.42}$$

Equation 3.42 can be solved for P because all other quantities are known (calculated elsewhere).

One initial and two boundary conditions are needed. The initial condition states that the pressure in each cell is atmospheric:

$$P^{\circ}\Big|_{t=0} = P_{\infty} \tag{3.43a}$$

The boundary condition at the front face sets the pressure equal to the atmospheric value:

$$P\Big|_{z=0} = P_{\infty} \tag{3.43b}$$

The pressure gradient at the back face is set to give the desired mass flux:

$$-\left(\frac{\overline{K}}{\nu}\frac{\partial P}{\partial z}\right)\Bigg|_{z=\delta} = \dot{m}''_{\delta} \tag{3.43c}$$

3.1.10 Zero–dimensional transient simulations (TGA)

In Sections 3.1.3 through 3.1.9, one–dimensional transient governing equations were presented. Such equations are appropriate for simulating the pyrolysis and gasification of a finite–thickness slab having gradients in temperature, mass, pressure, etc. However, a zero–dimensional transient mode may also be invoked. This formulation is intended to represent lumped systems with negligible gradients of temperature and species as occurs in ideal thermogravimetric experiments. Zero–dimensional transient forms of the governing equations are presented below.

Condensed phase mass conservation:

$$\frac{\left(\overline{\rho}\Delta z\right) - \left(\overline{\rho}\Delta z\right)^{\circ}}{\Delta t} = -\dot{\omega}'''_{fg}\Delta z \tag{3.44}$$

Condensed phase species conservation:

$$\frac{\left(\overline{\rho}Y_i\Delta z\right) - \left(\overline{\rho}Y_i\Delta z\right)^{\circ}}{\Delta t} = \dot{\omega}'''_{fi}\Delta z - \dot{\omega}'''_{di}\Delta z \tag{3.45}$$

Gas phase mass–conservation:

$$\frac{\left(\rho_g\overline{\psi}\Delta z\right) - \left(\rho_g\overline{\psi}\Delta z\right)^{\circ}}{\Delta t} = \dot{\omega}'''_{fg}\Delta z \tag{3.46}$$

Gas phase species conservation:

$$Y_j = Y_j^{\infty} \tag{3.47}$$

Condensed phase energy conservation:

$$T = T_0 + \beta t \tag{3.48}$$

Gas phase energy conservation:

$$T_g = T_0 + \beta t \tag{3.49}$$

Gas phase momentum conservation:

$$P = P_{\infty} \tag{3.50}$$

Here, β is the linear ramp rate in K/s. The temperature and gas phase mass fractions are taken as the ambient values. Thus, for the 0D transient formulation T and Y_j are specified by the user rather than calculated. Note that Equations 3.44 and 3.45 are essentially the same as the condensed phase mass and species conservation equations presented earlier for cell P in the 1D transient model. Thus, in the 1D transient model, each cell behaves as if it was a single thermogravimetric sample. Note that the gas phase

The above governing equations can be used to calculate both differential thermogravimetric curves ($\mathrm{d}/\mathrm{d}t\left(m/m_0\right)$) and thermogravimetric curves (m/m_0). To do so, it is not necessary to explicitly solve Equation 3.46. The initial conditions on Equations 3.44 and 3.45 are the same as those presented earlier with reference to condensed phase mass and species conservation in the 1D transient formulation. A differential thermogravimetric curve is calculated as:

$$\frac{\mathrm{d}}{\mathrm{d}t}\left(\frac{m''}{m_0''}\right) = -\frac{\dot{\omega}_{fg}'''\Delta z}{m_0''} = -\frac{\dot{\omega}_{fg}'''\Delta z}{\left(\overline{\rho}\Delta z\right)\big|_{t=0}} \tag{3.51}$$

Integrating the differential thermogravimetric curve gives the thermogravimetric curve:

$$\frac{m''}{m_0''}(t) = 1 - \frac{1}{m_0''}\int_0^t \dot{\omega}_{fg}'''(\tau)\Delta z(\tau)\mathrm{d}\tau \tag{3.52}$$

Equations 3.51 and 3.52 are used primarily for simulating TGA experiments, in particular for extracting decomposition kinetics from TGA data using genetic algorithm optimization.

3.2 Reaction rates and source terms

The governing equations were derived in the previous sections. However, these equations contain several source terms attributed to reactions that must be quantified. In the model, two types of reactions are considered: homogeneous and heterogeneous. Homogeneous gas phase reactions involve only gases and do not involve the condensed phase. Examples of such reactions include tar cracking (where large tar molecules are broken into smaller hydrocarbon molecules) and the oxidation of gaseous pyrolysate. These reactions are discussed in Section 3.2.2 after reactions involving the condensed phase are first described in Section 3.2.1.

Condensed phase reactions may be homogeneous or heterogeneous. Solid–solid phase change or glass transition could be modeled as homogeneous reactions provided they do not involve the release of gases. More common in pyrolysis modeling, heterogeneous reactions involve the destruction of a condensed phase species to form gases and/or additional condensed phase species. An example is char formation wherein one condensed phase species (e.g., wood) is converted to a second condensed phase species (char) with the release of gases (pyrolysate). Some heterogeneous reactions may also involve the consumption of gases. For example, in heterogeneous char oxidation, oxygen is consumed and partially oxidized gaseous species are produced. Catalytic

reactions are a special case of heterogeneous reactions and can be simulated with the present model.

3.2.1 Heterogeneous and homogeneous condensed phase reactions

In the discussion that follows, a particular condensed phase reaction is denoted by the index k, and the total number of condensed phase reactions is designated K (not to be confused with permeability). It is assumed that each condensed phase reaction k consumes a single condensed phase species (A_k) and forms a distinct condensed phase species (B_k) plus gases, i.e. the reaction is of the form $A_k \rightarrow B_k + \text{gases}$. Thus, A_k denotes the condensed phase reactant species (the condensed phase species consumed by reaction k) and B_k denotes the condensed phase product species (the condensed phase species generated by reaction k). Although it is assumed that each condensed phase reaction k transforms a single condensed phase species (A_k) into at most one additional condensed phase species (B_k) plus gases, the user may specify multiple reactions that transform condensed phase species A to different species. Consequently, reactions of the type $A \rightarrow B + C + \text{gases}$ can be accommodated with the present code through specification of multiple reactions.

In the combustion literature, stoichiometry of gas phase reactions is usually expressed using molar "ν" coefficients. The same is often done for condensed phase pyrolysis reactions, with the important difference that the ν coefficients are given on a mass basis. For example, a reaction k that transforms condensed phase species A_k to condensed phase species B_k plus gases can be represented as:

$$1\,\text{kg}\ A_k \rightarrow \nu_{B,k}\ B_k + \nu_{g,k}\ \text{gases}$$

As will be described in detail below, the ν coefficients are related to the "solid fraction" (SF) of reaction *k*. The solid fraction of reaction *k* is the fraction of condensed phase species A_k's mass that is converted to condensed phase species B_k. Extending this terminology, 1 – SF could be called the "gas fraction". The solid fraction is related to the bulk densities of condensed phase species A_k and B_k as:

$$\mathrm{SF}_k = 1 + \left(\frac{\rho_{B_k}}{\rho_{A_k}} - 1 \right) \chi_k \tag{3.53}$$

In Equation 3.53, the parameter χ_k is the fraction of the bulk density difference between condensed phase species A_k and B_k that is converted to gases (more on this later). Note that since the bulk densities may depend on temperature, SF may be a function of temperature for a particular reaction.

The simplified reaction given above ($1\,\mathrm{kg}\ A_k \rightarrow \nu_{B,k}\ B_k + \nu_{g,k}\ \mathrm{gases}$) represents the conversion of one condensed phase species (A_k) to another condensed phase species (B_k), with an accompanying release of gases. It follows directly from mass conservation that $\nu_{B,k} \equiv \mathrm{SF}_k$. Consequently, $\nu_{g,k} \equiv 1 - \mathrm{SF}_k$. However, reactions may also occur wherein gaseous species are both consumed and generated, i.e. oxygen is consumed and partially oxidized products are produced during heterogeneous char oxidation. Representing this type of a reaction in a general form is quite cumbersome. Thus, for illustrative purposes, a specific case will first be presented before generalizing the result.

Consider the heterogeneous oxidation of condensed phase species A_k by reaction *k* to form condensed phase species B_k plus gases:

$$1\,\mathrm{kg}\ A_k + \nu_{O_2,k}\mathrm{O}_2 \rightarrow \nu_{B,k}\ B_k + \nu_{g,k}\ \mathrm{gases}$$

As before, it follows directly from mass conservation that $\nu_{B,k} \equiv \mathrm{SF}_k$, and consequently $\nu_{g,k} \equiv 1 - \mathrm{SF}_k + \nu_{O_2,k}$. However, this simplified reaction assumes that only oxygen is consumed, and gives no information about the composition of the gases that are generated. In reality, there may be gases other than oxygen that are consumed by a reaction (e.g., CO and CO_2 sometimes serve as the oxidizer in heterogeneous char oxidation) and a mixture of several gases may be produced from a particular reaction. Thus, some generalization is required. A heterogeneous pyrolysis reaction may be represented in general form as:

$$1\,\text{kg } A_k + \sum_{j=1}^{N} \nu'_{j,k}\ \text{kg gas } j \rightarrow \nu_{B,k}\ \text{kg } B_k + \sum_{j=1}^{N} \nu''_{j,k}\ \text{kg gas } j \tag{3.54a}$$

$$\nu_{B,k} = \mathrm{SF}_k \tag{3.54b}$$

$$\nu'_{j,k} = -(1 - \mathrm{SF}_k)\min(y_{s,j,k}, 0) \tag{3.54c}$$

$$\nu''_{j,k} = (1 - \mathrm{SF}_k)\max(y_{s,j,k}, 0) \tag{3.54d}$$

In Equation 3.54a, $\nu'_{j,k}$ is the net mass of gaseous species *j* consumed by reaction *k* and $\nu''_{j,k}$ is the net mass of gaseous species *j* produced by reaction *k* per unit mass of A_k reacted. Note the use of single vs. double primes to differentiate between reactants and products. In order to generalize and simplify the specification of $\nu'_{j,k}$ and $\nu''_{j,k}$, a user–defined "species yield matrix" is introduced. This *N* by *K* matrix is denoted $y_{s,j,k}$ and appears in Equations 3.54c and 3.54d (recall that *N* is the total number of gaseous species). Its entries may be positive or negative, with a positive entry corresponding to net production of a gaseous species, and a negative entry corresponding to net consumption of a gaseous species. The physical meaning of each entry in the species

yield matrix is the net mass of gas phase species j consumed or generated by reaction k per unit mass of the condensed phase that is converted to gases by reaction k (which is equivalent to $1 - \mathrm{SF}_k$). The sum of all entries in any column of the species yield matrix must add to 1 to conserve mass, and this must be strictly adhered to or nonphysical results will occur. Substitution of Equations 3.54b, 3.54c, and 3.54d into Equation 3.54a results in a balanced equation (conserves mass) only if $\sum_{j=1}^{N} y_{s,j,k} = 1$. Given a pyrolysis mechanism in the literature of the form of Equation 3.54a, it is possible to convert it to the present treatment of reactions using the relations in Equations 3.53 and 3.54.

The stoichiometry of pyrolysis reactions is given in Equation 3.54, but the rate at which the reactions occur (kinetics) must also be calculated. Equation 2.23 (used to analyze TGA experiments) serves as the starting point for the treatment of the condensed phase decomposition kinetics:

$$\frac{\mathrm{d}\alpha}{\mathrm{d}t} = Z \exp\left(-\frac{E}{RT}\right)(1-\alpha)^n \tag{2.23}$$

See the text surrounding Equation 2.23 for an explanation of the meaning of α, Z, E, and n. Since Equation 2.23 implies a single–step reaction, several changes are required before it can be generalized to accommodate multi–step reactions. Define α_i as the conversion of condensed phase species i. This quantity is tracked locally in each cell, so $1 - \alpha_i$ can be calculated in a cell having size Δz as:

$$1 - \alpha_i = \frac{m_i''}{m_{i\Sigma}''} = \frac{\overline{\rho} Y_i \Delta z}{\left(\overline{\rho} Y_i \Delta z\right)_\Sigma} \tag{3.55}$$

In Equation 3.55, the numerator is the mass per unit area of condensed phase species i in a particular cell; the denominator is the initial (i.e., at $t = 0$) mass per unit area of

condensed phase species i in that same cell plus the cumulative formation of species i through time t in that cell:

$$\left(\bar{\rho} Y_i \Delta z\right)_\Sigma \equiv \left(\bar{\rho} Y_i \Delta z\right)\Big|_{t=0} + \int_0^t \dot{\omega}_{fi}'''(\tau)\Delta z(\tau)\mathrm{d}\tau \tag{3.56}$$

The subscript Σ serves as a reminder that $\left(\bar{\rho} Y_i \Delta z\right)_\Sigma$ includes an integral (evaluated numerically as a summation). Note that $\dot{\omega}_{fi}''' \geq 0$ because $\dot{\omega}_{fi}'''$ is the formation rate of condensed phase species i (not the formation rate minus the destruction rate). Thus, the quantity $\left(\bar{\rho} Y_i \Delta z\right)_\Sigma$ increases monotonically or remains constant; it can never decrease. Since the conversion given in Equation 3.55 is tracked separately in each cell, from a kinetics standpoint each cell behaves as if it was a TGA sample.

Defining $1 - \alpha_i$ per Equations 3.55 and 3.56 ensures that $0 \leq \alpha_i \leq 1$, even for intermediate species (such as char) that are formed during the decomposition process but are not initially present in an unreacted material. That is, the conversion of an intermediate species i may fall anywhere in the range from 0 to 1. This is different from the conventional approach wherein $\left(\bar{\rho} Y_i \Delta z\right)_\Sigma$ in Equation 3.56 would be replaced with $\left(\bar{\rho}\Delta z\right)\Big|_{t=0}$. This approach is included as an option in the code, but was not chosen as the default reaction order model because it places a lower limit on the numerical value of conversion for intermediate species.

To illustrate this point, consider a reaction mechanism with two steps occurring in series. In the first step, condensed phase species A having bulk density ρ_A and initial mass fraction of 1 is completely converted to gases plus condensed phase species B having bulk density ρ_B. In the second step, condensed phase species B is converted to condensed

phase species *C*. If $\left(\overline{\rho} Y_i \Delta z\right)_\Sigma$ in Equation 3.55 is replaced with $\left(\overline{\rho}\Delta z\right)\big|_{t=0}$, then for constant Δz the conversion of species *A* is:

$$\alpha_A = 1 - \frac{\overline{\rho} Y_A \Delta z}{\left(\overline{\rho} Y_A \Delta z\right)_\Sigma} = 1 - \frac{\overline{\rho} Y_A \Delta z}{\left(\overline{\rho}\Delta z\right)\big|_{t=0}} = 1 - \frac{\overline{\rho} Y_A}{\rho_A}$$

At $t = 0$, $Y_A = 1$ and consequently $\overline{\rho} = \rho_A$. It follows from the above equation that $\alpha_A = 0$ at $t = 0$, i.e. the "conversion" of species *A* is initially 0. If species *A* is fully converted to species *B* before the onset of the reaction that volatilizes species *B*, then from the above equation $Y_A = 0$ and $\alpha_A = 1$ after species *A* has been completely converted to species *B*. Thus, the conversion of species *A* ranges from 0 to 1, as one would expect.

However, the situation is different for species *B*. If $\left(\overline{\rho} Y_i \Delta z\right)_\Sigma$ in Equation 3.55 is replaced with $\left(\overline{\rho}\Delta z\right)\big|_{t=0}$ and Δz is constant, the conversion of species *B* is given by the expression:

$$\alpha_B = 1 - \frac{\overline{\rho} Y_B \Delta z}{\left(\overline{\rho} Y_B \Delta z\right)_\Sigma} = 1 - \frac{\overline{\rho} Y_B \Delta z}{\left(\overline{\rho}\Delta z\right)\big|_{t=0}} = 1 - \frac{\overline{\rho} Y_B}{\rho_A}$$

The maximum value of α_B occurs after species *B* has been converted fully converted to species *C* and $Y_B = 0$, so $\alpha_B = 1$. The minimum value of α_B occurs when species *A* has been fully converted to species *B*, but before species *B* has started to react to form species *C*. This means that $Y_B = 1$, and consequently $\overline{\rho} = \rho_B$. From the above equation, the minimum possible value of α_B is $1 - \rho_B / \rho_A$. For wood, the char density may be ~20% of the virgin density. This means that $\rho_B / \rho_A = 0.2$, and α_B could be no lower than 0.8. In other words, the char conversion value could be no lower than 0.8, even though no part of the char has yet been converted to gases. To eliminate this inconsistency, and give a

greater importance to the reaction order, the treatment embodied in Equations 3.55 and 3.56 was selected as the default approach because it ensures that the conversion value of any intermediate species can approach zero. However, as will be shown in Section 4.7, calculated mass loss rates may not be sensitive to the reaction order treatment (conventional approach vs. this work's default approach).

Equation 2.23 gives the reaction rate in units of 1/s. However, the governing equations derived earlier contain volumetric reaction rate source terms such as $\dot{\omega}_{fi}'''$ and $\dot{\omega}_{di}'''$ that have units of kg/m^3–s. Some manipulation of Equation 2.23 and 3.55 is required to obtain these volumetric source terms. Attention is focused on a single reaction *k*, which destroys condensed phase species *i*. In particular, an expression for the volumetric destruction rate of condensed phase species *i* by reaction *k* ($\dot{\omega}_{di,k}'''$) is sought. Substituting Equation 3.55 into Equation 2.23 and replacing the total derivative with a partial derivative (since an expression that applies at every point in a slab is desired) gives:

$$\frac{\partial \alpha_{i,k}}{\partial t} = -\frac{\partial}{\partial t}\left(\frac{\overline{\rho} Y_i \Delta z}{\left(\overline{\rho} Y_i \Delta z\right)_\Sigma} \right) = Z_k \exp\left(-\frac{E_k}{RT} \right)\left(1-\alpha_i\right)^{n_k}$$

where $\partial \alpha_{i,k} / \partial t$ is the contribution to species *i*'s conversion time rate of change attributed to reaction *k*. Apply the quotient rule for differentiation and multiply by $\left(\overline{\rho} Y_i \Delta z\right)_\Sigma$:

$$\frac{\partial\left(\overline{\rho} Y_i \Delta z\right)_k}{\partial t} - \frac{\overline{\rho} Y_i \Delta z}{\left(\overline{\rho} Y_i \Delta z\right)_\Sigma} \frac{\partial\left(\overline{\rho} Y_i \Delta z\right)_{\Sigma,k}}{\partial t} = -Z_k \exp\left(-\frac{E_k}{RT} \right)\left(1-\alpha_i\right)^{n_k} \left(\overline{\rho} Y_i \Delta z\right)_\Sigma$$

It follows from condensed phase species conservation (Equation 3.15) that $\frac{\partial\left(\overline{\rho} Y_i \Delta z\right)_k}{\partial t} = \dot{\omega}_{fi,k}''' \Delta z - \dot{\omega}_{di,k}''' \Delta z$, and making this substitution gives:

$$\dot{\omega}'''_{fi,k}\Delta z - \dot{\omega}'''_{di,k}\Delta z - \frac{\overline{\rho}Y_i\Delta z}{\left(\overline{\rho}Y_i\Delta z\right)_\Sigma}\frac{\partial\left(\overline{\rho}Y_i\Delta z\right)_{\Sigma,k}}{\partial t} = -Z_k\exp\left(-\frac{E_k}{RT}\right)\left(1-\alpha_i\right)^{n_k}\left(\overline{\rho}Y_i\Delta z\right)_\Sigma$$

The term $\dot{\omega}'''_{fi,k}$ on the LHS is identically zero since by definition reaction *k* destroys condensed phase species *i*; therefore, it does not form condensed phase species *i*. From Equation 3.56, $\frac{\partial\left(\overline{\rho}Y_i\Delta z\right)_{\Sigma,k}}{\partial t} = \frac{\partial}{\partial t}\left(\left(\overline{\rho}Y_i\Delta z\right)\Big|_{t=0} + \int_0^t \dot{\omega}'''_{fi,k}(\tau)\Delta z(\tau)\mathrm{d}\tau\right) = \dot{\omega}'''_{fi,k}(t)\Delta z(t) = 0$ where the last equality on the RHS results from $\dot{\omega}'''_{fi,k} = 0$. Making these substitutions, dividing by Δz, and solving for $\dot{\omega}'''_{di,k}$ gives:

$$\dot{\omega}'''_{di,k} = \left(1-\alpha_i\right)^{n_k}\frac{\left(\overline{\rho}Y_i\Delta z\right)_\Sigma}{\Delta z}Z_k\exp\left(-\frac{E_k}{RT}\right) \tag{3.57}$$

After using Equation 3.55 to replace $1-\alpha_i$ with $\overline{\rho}Y_i\Delta z/\left(\overline{\rho}Y_i\Delta z\right)_\Sigma$, Equation 3.57 is used as the basis for the treatment of reaction rate source terms in this work, although a slightly different nomenclature is used hereafter for clarity. As described earlier, reaction *k* destroys condensed phase species A_k and forms condensed phase species B_k. Gases may be both consumed and produced by the reaction. The k^{th} reaction rate (r_k) is the destruction rate of condensed phase species A_k by condensed phase reaction *k* and is denoted $\dot{\omega}'''_{dA_k}$. Using Equation 3.57 as the basis for the reaction rate treatment, r_k is calculated either as a thermal pyrolysis or a thermo–oxidative decomposition depending on whether or not the exponent $n_{O_2,k} = 0$:

$$r_k = \dot{\omega}'''_{dA_k} = \left(\frac{\overline{\rho}Y_{A_k}\Delta z}{\left(\overline{\rho}Y_{A_k}\Delta z\right)_\Sigma}\right)^{n_k}\frac{\left(\overline{\rho}Y_{A_k}\Delta z\right)_\Sigma}{\Delta z}Z_k\exp\left(-\frac{E_k}{RT}\right)\ (\text{for } n_{O_2,k}=0) \tag{3.58a}$$

$$r_k = \dot{\omega}'''_{dA_k} = \left(\frac{\overline{\rho}Y_{A_k}\Delta z}{\left(\overline{\rho}Y_{A_k}\Delta z\right)_\Sigma}\right)^{n_k}\frac{\left(\overline{\rho}Y_{A_k}\Delta z\right)_\Sigma}{\Delta z}\left[\left(1+Y_{O_2}\right)^{n_{O_2,k}}-1\right]Z_k\exp\left(-\frac{E_k}{RT}\right)(\text{for } n_{O_2,k}\neq 0) \tag{3.58b}$$

For each reaction *k*, the index of the condensed phase reactant species (A_k) and the index of the condensed phase product species (B_k) are specified by the user. In Equation 3.58, the oxygen mass fraction (Y_{O_2}) is the local value inside the decomposing solid as determined by solution of the gaseous species conservation equations. It is not the freestream value (except for TGA simulations, i.e. 0D transient formulation). Each reaction's kinetics are characterized by four parameters: 1) n_k (reaction order in remaining mass of condensed phase species A_k, see Section 2.2), 2) $n_{O_2,k}$ (reaction order in gaseous oxygen mass fraction), 3) Z_k (pre–exponential factor), and 4) E_k (activation energy).

Equation 3.58a is applied to reactions for which $n_{O_2,k} = 0$, and Equation 3.58b is applied when $n_{O_2,k} = 0$. The exponent $n_{O_2,k}$ describes the oxygen sensitivity of reaction *k,* so a value of $n_{O_2,k} = 0$ is specified for reactions that are not sensitive to oxygen. By design, Equation 3.58b approaches zero as the oxygen concentration goes to zero or as $n_{O_2,k}$ approaches zero. The oxygen dependency in Equation 3.58b is slightly different from the conventional approach where the reaction rate is proportional to $Y_{O_2}^{n_{O_2,k}}$. The presence of oxygen can be conveniently treated as promoting an otherwise anaerobic reaction, i.e. a decomposition mechanism in a non–oxidative atmosphere can be used as the starting point for an analogous oxidative reaction mechanism. Additionally, the products (both condensed– and gas phase) generated by a reaction may change in the presence of oxygen. Thus, different reaction products can be tracked by specifying two separate reactions (a thermal pyrolysis with $n_{O_2,k} = 0$ and a thermo–oxidative decomposition with $n_{O_2,k} \neq 0$).

Equation 3.58 looks somewhat complicated due to its generality, but it can be simplified considerably for a few special cases. When $n_k = 1$ and $n_{O_2,k} = 0$, Equation 3.58 reduces to the following familiar form:

$$r_k = \dot{\omega}'''_{dA_k} = \overline{\rho} Y_{A_k} Z_k \exp\left(-\frac{E_k}{RT}\right) \tag{3.59}$$

It can be seen that the simplified version of Kung's charring pyrolysis model presented in Section 2.1.5 is a specialized case of the present treatment (e.g., compare Equation 2.12 with Equation 3.59). Also, for $n_{O_2,k} = 0$, $\left(\overline{\rho} Y_i \Delta z\right)_\Sigma$ in Equation 3.56 replaced with $\left(\overline{\rho}\Delta z\right)\big|_{t=0}$ (conventional reaction order approach), and no volume change (Δz = constant), Equation 3.58 reduces to:

$$\frac{r_k}{\overline{\rho}\big|_{t=0}} = \frac{\dot{\omega}'''_{dA_k}}{\overline{\rho}\big|_{t=0}} = \left(\frac{\overline{\rho} Y_{A_k}}{\overline{\rho}\big|_{t=0}}\right)^{n_k} Z_k \exp\left(-\frac{E_k}{RT}\right) \tag{3.60}$$

Equation 3.60 is the same reaction rate treatment used in NIST's Fire Dynamics Simulator Version 5 [51]. Thus, it can be seen that the treatment of pyrolysis reactions in FDS is a special case of the more generalized treatment used in this work. For simplified cases, comparison of this model's calculations to those of the FDS pyrolysis model shows near exact agreement if solid/gas heat transfer (which is not included in the FDS pyrolysis model) is eliminated from the present formulation.

Note that Equation 3.58 gives the destruction rate of species A_k by reaction k. However, it does not give the formation rate of condensed phase species B_k by reaction k, nor the rate at which the mass of condensed phase species A_k is volatilized (converted to gases) by reaction k. These quantities are calculated, respectively, by Equations 3.61 and 3.62:

$$\dot{\omega}'''_{fB_k} = \mathrm{SF}_k \dot{\omega}'''_{dA_k} = \left(1 + \left(\frac{\rho_{B_k}}{\rho_{A_k}} - 1\right)\chi_k\right)\dot{\omega}'''_{dA_k} \tag{3.61}$$

$$\dot{\omega}'''_{fg_k} = (1 - \mathrm{SF}_k)\dot{\omega}'''_{dA_k} = \left(1 - \frac{\rho_{B_k}}{\rho_{A_k}}\right)\chi_k \dot{\omega}'''_{dA_k} \tag{3.62}$$

The solid fraction of reaction k (SF_k) that appears in Equations 3.61 and 3.62 is defined in Equation 3.53. Recall that SF is the fraction of the mass of condensed phase species A that is converted to condensed phase species B; the remainder of the mass of condensed phase species A is volatilized, i.e. converted to gases (Equation 3.62). As mentioned earlier, the parameter χ_k is the fraction of the bulk density difference between condensed phase species A and B that is converted to gases. For SF_k to fall between 0 and 1, the parameter χ_k must be in the range $0 \le \chi_k \le \rho_{A,k} / (\rho_{A,k} - \rho_{B,k})$. The upper limit is obtained by setting $\mathrm{SF}_k = 0$ in Equation 3.53 and solving for χ_k.

Note that $\dot{\omega}'''_{fg_k}$ is the rate at which the mass of condensed phase species A_k is volatilized (converted to gases) by reaction k. This is not necessarily the same as the total production rate of gases. For example, consider a char oxidation reaction where gaseous oxygen is consumed at a rate of 2 kg/m^3–s and solid char is consumed at a rate of 1 kg/m^3–s to produce 3 kg/m^3–s of product gases. In this case, $\dot{\omega}'''_{fg_k}$ would be 1 kg/m^3–s (not 3 kg/m^3–s) because although a total of 3 kg/m^3–s of product gases are being produced, only 1 kg/m^3–s of this originated in the condensed phase as the mass of species A_k.

For a noncharring reaction, no residue remains and the reaction completely transforms condensed phase species A_k to gases, so the specification of B_k is irrelevant

and we set $\rho_{B_k} = 0$ and χ_k = 1. Then, SF_k in Equation 3.61 (the solid fraction) becomes zero so the formation rate of condensed phase species B_k is also zero. At the same time, the quantity 1 – SF_k in Equation 3.62 (one minus the solid fraction) becomes 1, meaning that only gases are generated from the reaction. This type of reaction will cause surface regression because Δz will shrink according to the condensed phase mass conservation equation.

Equations 3.61 and 3.62 can also be used to model a charring reaction with no volume change. If $\chi_k = 1$ and $0 < \rho_{B_k} < \rho_{A_k}$, it can be seen from Equations 3.61 and 3.62 that the formation rate of condensed phase species B and gases are both nonzero. This is very similar to the traditional approach to modeling the pyrolysis of charring materials.

Equations 3.61 and 3.62 can also be used to model an intumescent reaction with volume change by setting $0 \le \chi_k < 1$. Then, provided $\rho_{B_k} < \rho_{A_k}$, a lower density solid is formed from a higher density solid and swelling occurs to conserve mass. Essentially, the decrease in $\overline{\rho}$ is compensated for by an increase in Δz through the condensed phase mass conservation equation, leading to swelling. In the extreme case of $\chi_k = 0$, the material swells without any escape of gases. Values of χ_k between 0 and 1 cause intumescence (swelling) to occur simultaneously with the release of gaseous vapors. The relative amounts of swelling and volatilization are dictated by the value of χ_k (closer to 0 means more swelling, and closer to 1 means more volatilization).

Values of χ_k between 1 and $\rho_{A,k}/\left(\rho_{A,k} - \rho_{B,k}\right)$ can be used to simulate a charring reaction that results in shrinkage (provided $\rho_{B_k} < \rho_{A_k}$). Essentially, the decreased formation rate of condensed phase species B_k (see Equation 3.61 and note that the term in

parentheses is negative) caused by a value of χ_k greater than 1 leads to a decrease in Δz (shrinkage) through the condensed phase mass conservation equation. Finally, values of χ_k greater than $\rho_{A,k}/(\rho_{A,k}-\rho_{B,k})$ can be used to simulate condensation reactions where gas phase mass is converted to condensed phase mass.

Note that adding Equations 3.61 and 3.62 gives:

$$\dot{\omega}'''_{fB_k} + \dot{\omega}'''_{fg_k} = \dot{\omega}'''_{dA_k} \tag{3.63}$$

Equation 3.63 says that for reaction k, the rate at which condensed phase species A_k is converted to condensed phase species B_k plus the rate at which condensed phase species A_k is converted to gases equals the destruction rate of condensed phase species A_k.

As discussed in Section 2.2.2 there really is no agreement among researchers as to how to treat heats of reaction. In this work, to allow for maximum flexibility, the heat of reaction is calculated as the sum of two separate contributions. One part of the heat of reaction applies only to the generation of condensed phase species and is denoted $\Delta H_{sol,k}$ (where *sol* is for *solid*); the other part applies only to the generation of volatiles from the condensed phase and is denoted $\Delta H_{vol,k}$ (where *vol* is for *volatiles*). Specifically, the volumetric rate of heat release or absorption to the solid phase due to reaction k is:

$$\dot{Q}'''_{s,k} = -\dot{\omega}'''_{fB_k}\Delta H_{sol,k} - \dot{\omega}'''_{fg_k}\Delta H_{vol,k} \tag{3.64}$$

The units of $\Delta H_{sol,k}$ are J/kg of B_k produced. $\Delta H_{sol,k}$ is the latent (not sensible) specific enthalpy difference between condensed phase species B_k and A_k (recall that reaction k converts condensed phase species A_k to condensed phase species B_k). Positive values of $\Delta H_{sol,k}$ correspond to an endothermic reaction, and negative values correspond to an exothermic reaction. $\Delta H_{sol,k}$ is often set to zero, unless reaction k represents a solid–solid

or solid–liquid phase change with an associated change in latent enthalpy. The change in sensible enthalpy is accounted for by the $\sum\left(\dot{\omega}_{fi}''' - \dot{\omega}_{di}'''\right)h_i$ term in Equation 3.32. As will be explained below, $\Delta H_{sol,k}$ may also be nonzero if it is desired to use a heat of reaction having units Joules per kilogram of condensed phase reactant consumed.

The term $\Delta H_{vol,k}$ is the quantity of heat required to convert unit mass of condensed phase species A_k to gases at whatever temperature the reaction occurs. This quantity is analogous to the heat of pyrolysis or heat of volatilization discussed in Section 2.2.2. It is sometimes called the heat of vaporization or heat of volatilization, usually implying an endothermic reaction (and a positive value of $\Delta H_{vol,k}$). However, for exothermic reactions $\Delta H_{vol,k}$ would be negative. For negative values of $\Delta H_{vol,k}$, the terminology heat of reaction is preferred but the nomenclature $\Delta H_{vol,k}$ is retained. Regardless of what $\Delta H_{vol,k}$ is called, it is important to note that it has units of J/kg of gas volatilized from the condensed phase. It is different from the heat of gasification (sometimes denoted ΔH_g or L_g), which includes a contribution for the sensible enthalpy required to heat the condensed phase from its initial temperature to its volatilization temperature (see Equation 2.28).

Both $\Delta H_{sol,k}$ and $\Delta H_{vol,k}$ have units of J/kg, but some clarification is needed regarding Joules per kg of what. These quantities are defined in this work on a per unit mass of product that originated in the condensed phase basis. That is, the units of $\Delta H_{sol,k}$ are J per kg of condensed phase species B_k generated from condensed phase species A_k. Similarly, the units of $\Delta H_{vol,k}$ are J per kg of gases generated by volatilizing condensed phase species A_k (or equivalently, J per kg of gaseous mass generated that originated in the condensed phase). Note that any mass that originated in the gas phase is not included in this heat of reaction. For example, assume a noncharring reaction converts 1 kg of

condensed phase species A and 1 kg of gaseous oxygen to 2 kg of product gases, releasing 1 MJ of sensible enthalpy in the process. The value of $\Delta H_{vol,k}$ for this reaction is –1 MJ/kg, not –1/2 MJ/kg.

In the literature, heats of reaction are sometimes given on a J per kg of *reactant consumed* basis. Using the present terminology, such a heat of reaction would have units of J per kg of species A_k destroyed by reaction k. This treatment of the heats of reaction can be recovered by setting $\Delta H_{sol,k} = \Delta H_{vol,k} = \Delta H_k$, and the flexibility that this affords is one of the primary motivations for splitting the heat of reaction into two separate components in this model. It then follows from Equation 3.64 after making use of Equation 3.63 that ΔH_k has units of J per kg of condensed phase species A_k consumed by reaction k, as shown step by step below:

$$\begin{aligned}
\dot{Q}'''_{s,k} &= -\dot{\omega}'''_{fB_k}\Delta H_{sol,k} - \dot{\omega}'''_{fg_k}\Delta H_{vol,k} \\
&= -\left(\dot{\omega}'''_{fB_k}\Delta H_{sol,k} + \dot{\omega}'''_{fg_k}\Delta H_{vol,k}\right) \\
&= -\left(\dot{\omega}'''_{fB_k}\Delta H_{k} + \dot{\omega}'''_{fg_k}\Delta H_{k}\right) \\
&= -\left(\dot{\omega}'''_{fB_k} + \dot{\omega}'''_{fg_k}\right)\Delta H_{k} \\
&= -\dot{\omega}'''_{dA_k}\Delta H_{k}
\end{aligned}$$

Note that Equation 3.32 (condensed phase energy conservation equation) contains a source term $\dot{Q}'''_s$ that is obtained by summing the $\dot{Q}'''_{s,k}$ in Equation 3.64 over all reactions. Thus, any heat release or absorption due to Equation 3.64 is distributed to the condensed phase (the subscript s denotes "solid" although "condensed" would be more accurate). Whether the heat released or absorbed by a heterogeneous reaction is distributed to the condensed phase or the gas phase is somewhat inconsequential since these phases are usually in a state close to thermal equilibrium on account of the much lower volumetric heat capacity of the gas phase.

Equation 3.62 above gives the formation rate of all gases by reaction k ($\dot{\omega}'''_{fg_k}$). However, it does not contain any information regarding the production/destruction rates of individual gas species (or equivalently, the composition of the gases that are generated or consumed by that reaction). This is specified through the user–specified species yield matrix $y_{s,j,k}$ mentioned earlier. The net generation rate of gaseous species j from condensed phase reaction k is calculated as:

$$\dot{\omega}'''_{s,j,k} = \dot{\omega}'''_{fg_k} y_{s,j,k} \tag{3.65}$$

where $y_{s,j,k}$ is the N by K species yield matrix. See the text following Equation 3.54 for additional discussion about $y_{s,j,k}$. Note that the subscript s seen on both sides of Equation 3.65 stands for "solid" as a reminder that gaseous species may also be formed or destroyed by homogeneous gas phase reactions. This type of reaction is discussed in the following section.

3.2.2 Homogeneous gas phase reactions

The modeling of condensed phase reactions and heterogeneous reactions involving both the gas phase and the condensed phase have been described in Section 3.2.1. However, the user may also specify any number of homogeneous gas phase reactions. Such reactions can be used to account for tar cracking where large hydrocarbon molecules are broken into smaller hydrocarbon molecules or the oxidation of pyrolysate as it flows through a char layer toward the surface where both the oxygen concentration and temperature are highest.

Just as there are K condensed phase reactions and individual condensed phase reactions are indicated by the index k, there are L homogeneous gas phase reactions and

individual reactions are indicated by the index ℓ. Each homogeneous gas phase reaction ℓ converts two gas phase reactants (A_ℓ and B_ℓ) to gaseous products. Since only the gas phase is involved, these reactions are termed "homogeneous" to differentiate them from the heterogeneous reactions discussed earlier.

Although the stoichiometry of gas phase reactions is usually expressed on a molar basis, little is known about many of the gaseous species produced during pyrolysis, so the stoichiometry of homogeneous gas phase reactions is expressed here on a mass basis as:

$$1\,\text{kg } A_\ell - y_{g,B_\ell,\ell}\,\text{kg } B_\ell \rightarrow \sum_{j=1}^{N} \max\left(y_{g,j,\ell},0\right)\text{kg gas } j \tag{3.66}$$

In Equation 3.66, $y_{g,j,\ell}$ is the N by L "homogeneous gaseous species yield matrix", analogous to the gaseous species yield matrix ($y_{s,j,k}$) discussed earlier with reference to heterogeneous reactions. The physical meaning of individual entries in $y_{g,j,\ell}$ is the mass of gaseous species j produced by reaction ℓ (for positive entries) or consumed by reaction ℓ (for negative entries) per unit mass of gaseous species A_ℓ consumed. Note that in writing Equation 3.66, it is assumed that $y_{g,A_\ell,\ell} = -1$, i.e. the yield corresponding to gas phase species A_ℓ is –1. It is also assumed that for reaction ℓ the only other negative entry in the $y_{g,j,\ell}$ matrix is the yield corresponding to gas phase species B_ℓ (denoted $y_{g,B_\ell,\ell}$ in Equation 3.66). All entries in a column of the homogeneous gaseous species yield matrix must add to 0 for mass to be conserved, and this must be strictly obeyed or nonphysical results will occur.

The reaction rate of the ℓ^{th} homogeneous gas phase reaction is the destruction rate of gas phase species A_ℓ:

$$r_\ell = \dot{\omega}'''_{dA_\ell} = \left[A_\ell\right]^{p_\ell}\left[B_\ell\right]^{q_\ell} T^{b_\ell} Z_\ell \overline{\psi} \exp\left(-\frac{E_\ell}{RT_g}\right) \tag{3.67}$$

Porosity ($\overline{\psi}$) appears in Equation 3.67 because a reaction rate defined on a per unit volume of solid plus gas (i.e. per unit volume of mixture) basis is needed. For dimensional consistency in Equation 3.67, the units of Z vary with the specified values of p, q, and b. For $p = 1$, $q = 1$, and $b = 0$, the units of Z are kg–m^3/mole^2–s. $\dot{\omega}'''_{dA_\ell}$ is the destruction rate of gaseous species A_ℓ due to homogeneous gas phase reaction ℓ, and [A] denotes the molar concentration of gaseous species A:

$$\left[A\right] = \frac{\rho_g Y_A}{M_A} \tag{3.68}$$

The creation or destruction of gaseous species j by homogeneous gaseous reaction ℓ is calculated from the homogeneous gaseous species yield matrix ($y_{g,j,\ell}$) as:

$$\dot{\omega}'''_{g,j,\ell} = r_\ell y_{g,j,\ell} \tag{3.69}$$

Note that the entry corresponding to species A_ℓ in the $y_{g,j,\ell}$ matrix must be –1 for the first equality in Equation 3.67 to be true, and this is consistent with the discussion following Equation 3.66.

The volumetric rate of heat release (or absorption) to the gas phase by homogeneous gaseous reaction ℓ is:

$$\dot{Q}'''_{g,\ell} = -\dot{\omega}'''_{dA_\ell} \Delta H_\ell \tag{3.70}$$

where ΔH_ℓ is the heat of reaction associated with homogeneous gas phase reaction ℓ. Its units are J of heat released per unit mass of gas phase species A_ℓ consumed by homogeneous gas phase reaction ℓ. As with the condensed phase reactions, positive values of ΔH_ℓ correspond to an endothermic reaction, and negative values correspond to

an exothermic reaction. The subscript *g* in Equation 3.70 indicates that any heat absorbed or released is distributed to the gas phase.

3.2.3 Total source terms obtained by summing over all reactions

In the preceding two subsections, source terms due to individual reactions were presented. However, the terms that appear in the conservation equations are the total source terms, which are obtained by summing over all reactions. For example, the total formation rate of all gases by volatilization of the condensed phase ($\dot{\omega}'''_{fg}$) is calculated by summing over all condensed phase reactions as:

$$\dot{\omega}'''_{fg} = \sum_{k=1}^{K} \dot{\omega}'''_{fg_k} \tag{3.71}$$

Similarly, the total destruction rate of condensed phase species *i* is formally obtained as:

$$\dot{\omega}'''_{di} = \sum_{k=1}^{K} \delta_{i,A_k} \dot{\omega}'''_{dA_k} \tag{3.72}$$

where A_k denotes the index of condensed phase species A_k and δ_{i,A_k} is the Kronecker delta having properties $\delta_{i,A_k} = \begin{cases} 1 & \text{if } i = A_k \\ 0 & \text{if } i \neq A_k \end{cases}$. Additional source terms appearing in the conservation equations are obtained by analogous summations. These are indicated below in Table 3.1.

Table 3.1. Conservation equation source terms obtained by summation.

Quantity	Description	Obtained by summation from equation
$\dot{\omega}_{di}'''$	Total destruction rate of condensed phase species *i*	3.58
$\dot{\omega}_{fi}'''$	Total formation rate of condensed phase species *i*	3.61
$\dot{\omega}_{fg}'''$	Total formation rate of all gases from volatilization of the condensed phase	3.62
$\dot{Q}_{s}'''$	Rate of heat release or absorption to the condensed phase due to condensed phase reactions	3.64
$\dot{\omega}_{dj}'''$	Total destruction rate of gas phase species *j* due to both condensed phase and homogeneous gas phase reactions	3.65 and 3.69
$\dot{\omega}_{fj}'''$	Total formation rate of gas phase species *j* due to both condensed phase and homogeneous gas phase reactions	3.65 and 3.69
$\dot{Q}_{g}'''$	Rate of heat release or absorption to the gas phase due to gas phase reactions	3.70

3.3 Solution methodology

In the previous sections, the governing conservation equations were derived and the treatment of the source terms was presented. In this section, it is explained how these equations are simultaneously solved numerically.

3.3.1 Condensed phase mass conservation

The condensed phase mass conservation equation has been given as Equation 3.12 and is repeated below:

$$\frac{\left(\overline{\rho}\Delta z\right)_P - \left(\overline{\rho}\Delta z\right)_P^{\circ}}{\Delta t} = -\left(\dot{\omega}_{fg}'''\Delta z\right)_P$$

Note that this is essentially an ODE for the quantity $\overline{\rho}\Delta z$. Thus, no boundary conditions are required; only an initial condition in each cell (essentially the specification of $\overline{\rho}$ and Δz) is required, see Equation 3.13. To ensure that the quantity $\overline{\rho}\Delta z$ remains positive, the condensed phase mass conservation equation is integrated in time as:

$$\left(\overline{\rho}\Delta z\right)_P = \frac{\frac{\left(\overline{\rho}\Delta z\right)_P^\circ}{\Delta t}}{\frac{1}{\Delta t} + \frac{\left(\dot{\omega}_{fg}'''\Delta z\right)_P}{\left(\overline{\rho}\Delta z\right)_P}} \tag{3.73}$$

The rationale for Equation 3.73 is explained in Section 3.3.3 in the context of condensed phase species conservation.

To prevent numerical problems that occur as $\Delta z \to 0$ (as occurs when a slab of a noncharring polymer burns completely away), if a cell's thickness decreases below a user–specified value, perhaps 0.1 Å (0.01 nm) then all reaction rates in that cell are set to zero and that cell behaves as if it was inert. This distance is less than one tenth of the diameter of a single atom and the temperature drop across such a small distance is very small, perhaps 10^{-6} K, so this approximation is considered reasonable. Although no numerical problems are encountered as the cell size gets large, the solution is not necessarily accurate if gradients are not well–resolved due to large grid sizes.

3.3.2 Gas phase mass conservation

The gas phase mass conservation equation has been given as Equation 3.18:

$$\frac{\left(\rho_g\overline{\psi}\Delta z\right)_P - \left(\rho_g\overline{\psi}\Delta z\right)_P^\circ}{\Delta t} + \dot{m}''\big|_b - \dot{m}''\big|_t = \left(\dot{\omega}_{fg}'''\Delta z\right)_P$$

It is not explicitly solved unless the pressure solver is not used to calculate $\dot{m}''$. If this is the case, then the gas phase mass conservation equation is used to calculate $\dot{m}''$ assuming that all volatiles generated in–depth escape instantaneously with no resistance to mass transfer, i.e. the mass flux at the top of cell *P* is calculated as:

$$\dot{m}''\big|_t = \dot{m}''\big|_b - \left(\dot{\omega}_{fg}'''\Delta z\right)_P + \frac{\left(\rho_g\overline{\psi}\Delta z\right)_P - \left(\rho_g\overline{\psi}\Delta z\right)_P^\circ}{\Delta t} \tag{3.74}$$

Thus, provided that $\dot{m}''$ is known at the back face, $\dot{m}''$ can be determined at any point in the decomposing material by applying Equation 3.74 in every cell starting at the back face and moving toward the front face. Note that due to the coordinate system used (z increases with depth into the decomposing solid) $\dot{m}''$ is negative when the flow direction is toward the surface.

3.3.3 Condensed phase species conservation

The condensed phase species conservation equation has been given as Equation 3.15:

$$\frac{\left(\overline{\rho} Y_i \Delta z\right)_P - \left(\overline{\rho} Y_i \Delta z\right)_P^\circ}{\Delta t} = \left(\dot{\omega}_{fi}''' \Delta z\right)_P - \left(\dot{\omega}_{di}''' \Delta z\right)_P$$

This is essentially an ODE for the quantity $\overline{\rho} Y_i \Delta z$ in each cell *P*. Thus, no boundary conditions are required, and only an initial condition (the specification of $\overline{\rho}$, Y_i, and Δz) in each cell is required, see Equation 3.16.

Physical considerations require $\overline{\rho} Y_i \Delta z \geq 0$. However, without special treatment it is possible for this quantity to become negative during numerical solution. This erroneous result can be prevented by splitting the source term into its positive and negative components (see Patankar [194] pg. 145) as will be described below. Consider a source–dominated conservation equation of the same form as Equation 3.15 where the total source term $\left(S_\phi\right)_P$ is filtered into its positive and negative components:

$$\frac{\phi_P - \phi_P^\circ}{\Delta t} = \left(S_\phi^+\right)_P - \left(S_\phi^-\right)_P$$

Here, $\left(S_\phi^+\right)_P \geq 0$, $\left(S_\phi^-\right)_P \geq 0$, and $\left(S_\phi\right)_P = \left(S_\phi^+\right)_P - \left(S_\phi^-\right)_P$. Now multiply the second term on the RHS by ϕ_P/ϕ_P and rearrange:

$$\phi_P = \frac{\dfrac{\phi_P^\circ}{\Delta t} + \left(S_\phi^+\right)_P}{\dfrac{1}{\Delta t} + \dfrac{\left(S_\phi^-\right)_P}{\phi_P}}$$

In practice, this should be implemented as:

$$\phi_P = \frac{\dfrac{\phi_P^\circ}{\Delta t} + \left(S_\phi^+\right)_P}{\dfrac{1}{\Delta t} + \dfrac{\left(S_\phi^-\right)_P}{\max\left(\phi_P, \varepsilon\right)}}$$

where ε is a very small number (e.g. 10^{-30}) to prevent division by zero. Note that all quantities on the RHS are greater than or equal to zero. Thus, ϕ_p can approach zero, but it can never become negative. This treatment of mass and species conservation was found to be critical for ensuring a stable solution.

To ensure that $\overline{\rho} Y_i \Delta z$ remains positive, numerical solution of the condensed phase species conservation equation is implemented as:

$$\left(\overline{\rho} Y_i \Delta z\right)_P = \frac{\dfrac{\left(\overline{\rho} Y_i \Delta z\right)_P^\circ}{\Delta t} + \left(\dot{\omega}_{fi}''' \Delta z\right)_P}{\dfrac{1}{\Delta t} + \dfrac{\left(\dot{\omega}_{di}''' \Delta z\right)_P}{\max\left(\left(\overline{\rho} Y_i \Delta z\right)_P, \varepsilon\right)}} \tag{3.75}$$

Here $\dot{\omega}_{fi}'''$ is the total formation rate of condensed phase species *i* (obtained by summing over all reactions *k*) and is positive. Similarly, $\dot{\omega}_{di}'''$ is the total destruction rate of condensed phase species *i* (obtained by summing over all reactions *k*) and is also positive. Since all quantities on the right hand side are greater than or equal to zero, this treatment ensures that the quantity $\overline{\rho} Y_i \Delta z$ does not become negative.

In each grid cell, Equation 3.73 is solved for $\overline{\rho}\Delta z$. Similarly, each of the M values of $\overline{\rho}\Delta z Y_i$ are determined from Equation 3.75. Then, each Y_i is obtained by dividing $\overline{\rho}\Delta z Y_i$ by $\overline{\rho}\Delta z$. The weighted density is then calculated from the relation:

$$\overline{\rho} = \left(\sum_{i=1}^{M} \left(Y_i / \rho_i \right) \right)^{-1} \tag{3.76}$$

which is obtained by summing both sides of Equation 3.1 over M and solving for $\overline{\rho}$. With $\overline{\rho}$ known, Δz can be determined by dividing $\overline{\rho}\Delta z$ by $\overline{\rho}$. Thus, it can be seen how Y_i, $\overline{\rho}$, and Δz are independently determined from solution of Equations 3.73 and 3.75 using the auxiliary relation in Equation 3.76.

3.3.4 Gas phase species conservation

Due to the convective and diffusive terms, solution of the gas phase species conservation equation is much more involved than solution of the condensed phase species conservation equation. The gas phase species conservation equation has already been given as Equation 3.22:

$$\begin{aligned} &\left(\rho_g \overline{\psi} \Delta z \right)_P^{\circ} \frac{Y_{j,P} - Y_{j,P}^{\circ}}{\Delta t} + \dot{m}'' Y_j \Big|_b - \dot{m}'' Y_j \Big|_t - Y_{j,P} \dot{m}'' \Big|_b + Y_{j,P} \dot{m}'' \Big|_t = \\ &- \dot{j}_j'' \Big|_b + \dot{j}_j'' \Big|_t + \left(\dot{\omega}_{fj}''' \Delta z \right)_P - \left(\dot{\omega}_{dj}''' \Delta z \right)_P - \left(\dot{\omega}_{fg}''' Y_j \Delta z \right)_P \end{aligned}$$

The discretization of and numerical solution of Equation 3.22 follows Patankar [194]. Begin by defining the following:

$$J_b = \dot{m}'' Y_j \Big|_b + \dot{j}_j'' \Big|_b \tag{3.77a}$$

$$J_t = \dot{m}'' Y_j \Big|_t + \dot{j}_j'' \Big|_t \tag{3.77b}$$

$$F_b = \dot{m}'' \Big|_b \tag{3.77c}$$

$$F_t = \dot{m}''\big|_t \tag{3.77d}$$

$$a_P^\circ = \frac{\left(\Delta z \rho_g \overline{\psi}\right)_P^\circ}{\Delta t} \tag{3.77e}$$

Substituting Equation 3.77 into Equation 3.22 (and multiplying $\left(\dot{\omega}_{dj}'''\Delta z\right)_P$ by $Y_{j,P}/Y_{j,P}$) gives:

$$\begin{aligned} &a_P^\circ\left(Y_{j,P} - Y_{j,P}^\circ\right) + \left(J_b - Y_{j,P}F_b\right) - \left(J_t - Y_{j,P}F_t\right) = \\ &\left(\dot{\omega}_{fj}'''\Delta z\right)_P - \frac{\left(\dot{\omega}_{dj}'''\Delta z\right)_P}{Y_{j,P}} Y_{j,P} - Y_{j,P}\left(\dot{\omega}_{fg}'''\Delta z\right)_P \end{aligned} \tag{3.78}$$

Following Patankar [194] Equation 5.54–5.55:

$$J_b - Y_{j,P}F_b = a_B\left(Y_{j,P} - Y_{j,B}\right) \tag{3.79a}$$

$$J_t - Y_{j,P}F_t = a_T\left(Y_{j,T} - Y_{j,P}\right) \tag{3.79b}$$

where the coefficients a_B and a_T will be defined below. Substituting Equation 3.79 into Equation 3.78 gives:

$$\begin{aligned} &a_P^\circ\left(Y_{j,P} - Y_{j,P}^\circ\right) + a_B\left(Y_{j,P} - Y_{j,B}\right) - a_T\left(Y_{j,T} - Y_{j,P}\right) = \\ &\left(\dot{\omega}_{fj}'''\Delta z\right)_P - \frac{\left(\dot{\omega}_{dj}'''\Delta z\right)_P}{Y_{j,P}} Y_{j,P} - Y_{j,P}\left(\dot{\omega}_{fg}'''\Delta z\right)_P \end{aligned} \tag{3.80}$$

Multiplying through and combining like terms gives:

$$\left(a_P^\circ + a_B + a_T + \frac{\left(\dot{\omega}_{dj}'''\Delta z\right)_P}{Y_{j,P}} + \left(\dot{\omega}_{fg}'''\Delta z\right)_P\right) Y_{j,P} - a_B Y_{j,B} - a_T Y_{j,T} = a_P^\circ Y_{j,P}^\circ + \left(\dot{\omega}_{fj}'''\Delta z\right)_P \tag{3.81}$$

Define:

$$b = a_P^\circ Y_{j,P}^\circ + \left(\dot{\omega}_{fj}'''\Delta z\right)_P \tag{3.82a}$$

$$a_p = a_P^\circ + a_B + a_T + \frac{\left(\dot{\omega}_{dj}'''\Delta z\right)_P}{Y_{j,P}} + \left(\dot{\omega}_{fg}'''\Delta z\right)_P \tag{3.82b}$$

The final form of the discretized equation is obtained by substituting Equation 3.82 into Equation 3.81:

$$a_p Y_{j,P} = a_B Y_{j,B} + a_T Y_{j,T} + b \tag{3.83}$$

The gas phase species conservation equation is purposely cast in the form of Equation 3.83 because it can be efficiently solved by the Thomas (or tridiagonal matrix) algorithm as will be described in Section 3.3.8. In Equation 3.83, the a_B and a_T coefficients are:

$$a_B = \mathcal{D}_b A(|P_b|) + \max(-F_b, 0) \tag{3.84a}$$

$$a_T = \mathcal{D}_t A(|P_t|) + \max(-F_t, 0) \tag{3.84b}$$

$$\mathcal{D}_b = \Gamma_b / (\delta z)_b \tag{3.84c}$$

$$\mathcal{D}_t = \Gamma_t / (\delta z)_t \tag{3.84d}$$

$$P_b = F_b / \mathcal{D}_b \tag{3.84e}$$

$$P_t = F_t / \mathcal{D}_t \tag{3.84f}$$

In Equation 3.84, P is the cell Peclet number (not pressure), and F is the convective mass flux (Equation 3.77). The function $A(P)$ is given by Patankar [194] in Table 5.2 and repeated below in Table 3.2:

Table 3.2. The function $A(|P|)$ from Patankar [194].

	Scheme	Formula for $A(\|P\|)$
1	Central difference	$1 - 0.5\|P\|$
2	Upwind	1
3	Hybrid	$\max(0, 1 - 0.5\|P\|)$
4	Power law	$\max(0, (1 - 0.1\|P\|)^5)$
5	Exponential	$\|P\| / [\exp(P) - 1]$

Fickian diffusion is assumed, so in Equation 3.84c and 3.84d $\Gamma = \rho_g \psi D$. Since the diffusion coefficient is required at the interface between cells, the interface value is calculated using the harmonic mean between cell *P* and the adjacent cells (*B* or *T*):

$$\Gamma_t = \frac{\Gamma_P \Gamma_T}{\Gamma_T + \frac{(\Delta z)_T (\Gamma_P - \Gamma_T)}{(\Delta z)_P + (\Delta z)_T}} \tag{3.85a}$$

$$\Gamma_b = \frac{\Gamma_P \Gamma_B}{\Gamma_B + \frac{(\Delta z)_B (\Gamma_P - \Gamma_B)}{(\Delta z)_P + (\Delta z)_B}} \tag{3.85b}$$

The front face and back face boundary conditions have already been given as Equations 3.24b and 3.24c. Their numerical implementation is discussed in greater detail in Section 3.3.8.

3.3.5 Condensed phase energy conservation

The condensed phase energy equation has already been given as Equation 3.32:

$$(\overline{\rho}\Delta z)_P^\circ \frac{\overline{h}_P - \overline{h}_P^\circ}{\Delta t} = -\dot{q}''\Big|_b + \dot{q}''\Big|_t - \left(\dot{Q}'''_{s-g}\Delta z\right)_P + \left(\dot{Q}'''_s \Delta z\right)_P$$
$$-\left(\frac{\partial \dot{q}''_r}{\partial z}\Delta z\right)_P + \sum_{i=1}^{M}\left(\left(\dot{\omega}'''_{fi} - \dot{\omega}'''_{di}\right)h_i \Delta z\right)_P + \overline{h}_P\left(\dot{\omega}'''_{fg}\Delta z\right)_P$$

Equation 3.32 can be written as:

$$(\overline{\rho}\Delta z)_P^\circ \frac{\overline{h}_P - \overline{h}_P^\circ}{\Delta t} = \dot{q}''\Big|_t - \dot{q}''\Big|_b + (S\Delta z)_P \tag{3.86a}$$

$$(S)_P = -h_{cv}\left(T - T_g\right)_P + \left(\dot{Q}'''_s\right)_P - \left(\frac{\partial \dot{q}''_r}{\partial z}\right)_P + \sum_{i=1}^{M}\left(\left(\dot{\omega}'''_{fi} - \dot{\omega}'''_{di}\right)h_i\right)_P + \overline{h}_P\left(\dot{\omega}'''_{fg}\right)_P \tag{3.86b}$$

For numerical convenience, the source term (Equation 3.86b) is split into positive and negative components:

$$S_P = \left(S^+\right)_P - \left(S^-\right)_P \tag{3.87a}$$

$$\left(S^+\right)_P = h_{cv} T_{g,P} - \left(\frac{\partial \dot{q}_r''}{\partial z}\right)_P + \sum_{i=1}^{M}\left(\dot{\omega}_{fi}''' h_i\right)_P + \bar{h}_P\left(\dot{\omega}_{fg}'''\right)_P + \sum_{k=1}^{K}\max\left(\dot{Q}_{s,k}''', 0\right) \tag{3.87b}$$

$$\left(S^-\right)_P = h_{cv} T_P + \sum_{i=1}^{M}\left(\dot{\omega}_{di}''' h_i\right)_P - \sum_{k=1}^{K}\min\left(\dot{Q}_{s,k}''', 0\right) \tag{3.87c}$$

To facilitate use of the efficient Thomas algorithm/TDMA solver to solve Equation 3.86, the heat conduction terms must be expressed in terms of enthalpy, i.e.:

$$\begin{aligned} \dot{q}''\big|_t &= -\bar{k}_t \frac{\partial T}{\partial z}\bigg|_t \equiv -\left(\frac{\bar{k}}{\bar{c}}\right)_t \left(\frac{\partial \bar{h}}{\partial z}\bigg|_t - \sum_{i=1}^{M}\left(h_i \frac{\partial Y_i}{\partial z}\right)_t\right) \\ &\approx -\left(\frac{\bar{k}}{\bar{c}}\right)_t \frac{\bar{h}_P - \bar{h}_T}{(\delta z)_t} + \sum_{i=1}^{M}\left[\left(\frac{\bar{k}}{\bar{c}} h_i\right)_t \frac{Y_{i,P} - Y_{i,T}}{(\delta z)_t}\right] \end{aligned} \tag{3.88a}$$

$$\begin{aligned} \dot{q}''\big|_b &= -\bar{k}_b \frac{\partial T}{\partial z}\bigg|_b \equiv -\left(\frac{\bar{k}}{\bar{c}}\right)_b \left(\frac{\partial \bar{h}}{\partial z}\bigg|_b - \sum_{i=1}^{M}\left(h_i \frac{\partial Y_i}{\partial z}\right)_b\right) \\ &\approx -\left(\frac{\bar{k}}{\bar{c}}\right)_b \frac{\bar{h}_B - \bar{h}_P}{(\delta z)_b} + \sum_{i=1}^{M}\left[\left(\frac{\bar{k}}{\bar{c}} h_i\right)_b \frac{Y_{i,B} - Y_{i,P}}{(\delta z)_b}\right] \end{aligned} \tag{3.88b}$$

Substituting Equations 3.87 and 3.88 into Equation 3.86 gives:

$$\begin{aligned} &\frac{\left(\bar{\rho}\Delta z\right)_P^\circ}{\Delta t}\left(\bar{h}_P - \bar{h}_P^\circ\right) = -\left(\frac{\bar{k}}{\bar{c}}\right)_t \frac{\bar{h}_P - \bar{h}_T}{(\delta z)_t} + \sum_{i=1}^{M}\left[\left(\frac{\bar{k}}{\bar{c}} h_i\right)_t \frac{Y_{i,P} - Y_{i,T}}{(\delta z)_t}\right] + \\ &\left(\frac{\bar{k}}{\bar{c}}\right)_b \frac{\bar{h}_B - \bar{h}_P}{(\delta z)_b} - \sum_{i=1}^{M}\left[\left(\frac{\bar{k}}{\bar{c}} h_i\right)_b \frac{Y_{i,B} - Y_{i,P}}{(\delta z)_b}\right] + \left(S^+ \Delta z\right)_P - \left(S^- \Delta z\right)_P \end{aligned} \tag{3.89}$$

Define:

$$a_P^\circ = \frac{\left(\bar{\rho}\Delta z\right)_P^\circ}{\Delta t} \tag{3.90a}$$

$$a_T = \frac{\left(\bar{k}/\bar{c}\right)_t}{(\delta z)_t} \tag{3.90b}$$

$$a_B = \frac{\left(\overline{k}/\overline{c}\right)_b}{\left(\delta z\right)_b} \tag{3.90c}$$

$$a_{Th_i} = \frac{\left(\overline{k}h_i/\overline{c}\right)_t}{\left(\delta z\right)_t} \tag{3.90d}$$

$$a_{Bh_i} = \frac{\left(\overline{k}h_i/\overline{c}\right)_b}{\left(\delta z\right)_b} \tag{3.90e}$$

The values in the numerator of Equations 3.90b – 3.90e are calculated using harmonic means (see Equation 3.85). Substitute Equation 3.90 into Equation 3.89:

$$\begin{aligned} a_P^\circ\left(\overline{h}_P - \overline{h}_P^\circ\right) &= -a_T\left(\overline{h}_P - \overline{h}_T\right) + \sum_{i=1}^{M}\left[a_{Th_i}\left(Y_{i,P} - Y_{i,T}\right)\right] + \\ a_B\left(\overline{h}_B - \overline{h}_P\right) &- \sum_{i=1}^{M}\left[a_{Bh_i}\left(Y_{i,B} - Y_{i,P}\right)\right] + \left(S^+\Delta z\right)_P - \left(S^-\Delta z\right)_P \end{aligned} \tag{3.91}$$

Distribute multiplication and multiply the negative part of the source term by $\overline{h}_P/\overline{h}_P$ to ensure that all coefficients remain positive:

$$\begin{aligned} a_P^\circ\overline{h}_P - a_P^\circ\overline{h}_P^\circ &= -a_T\overline{h}_P + a_T\overline{h}_T + \sum_{i=1}^{M}\left[a_{Th_i}Y_{i,P} - a_{Th_i}Y_{i,T}\frac{\overline{h}_P}{\overline{h}_P} - a_{Bh_i}Y_{i,B}\frac{\overline{h}_P}{\overline{h}_P} + a_{Bh_i}Y_{i,P}\right] + \\ a_B\overline{h}_B - a_B\overline{h}_P &+ \left(S^+\Delta z\right)_P - \left(S^-\Delta z\right)_P\frac{\overline{h}_P}{\overline{h}_P} \end{aligned} \tag{3.92}$$

Combine like terms:

$$\begin{aligned} &\left(a_P^\circ + a_T + a_B + \frac{\left(S^-\Delta z\right)_P + \sum_{i=1}^{M}\left[a_{Th_i}Y_{i,T} + a_{Bh_i}Y_{i,B}\right]}{\overline{h}_P}\right)\overline{h}_P = a_P^\circ\overline{h}_P^\circ + \\ &a_T\overline{h}_T + a_B\overline{h}_B + \sum_{i=1}^{M}\left[\left(a_{Th_i} + a_{Bh_i}\right)Y_{i,P}\right] + \left(S^+\Delta z\right)_P \end{aligned} \tag{3.93}$$

Define:

$$a_P = a_P^\circ + a_T + a_B + \frac{\left(S^- \Delta z\right)_P + \sum_{i=1}^{M}\left[a_{Th_i} Y_{i,T} + a_{Bh_i} Y_{i,B}\right]}{\overline{h}_P} \tag{3.94a}$$

$$b = a_P^\circ \overline{h}_P^\circ + \left(S^+ \Delta z\right)_P + \sum_{i=1}^{M}\left[\left(a_{Th_i} + a_{Bh_i}\right) Y_{i,P}\right] \tag{3.94b}$$

Substitute Equation 3.94 into Equation 3.93:

$$a_P \overline{h}_P = a_T \overline{h}_T + a_B \overline{h}_B + b \tag{3.95}$$

Equation 3.95 is of the form needed to apply the Thomas algorithm. The two required boundary conditions have already been given as Equations 3.33b and 3.33c. Their numerical implementation is discussed in greater detail in Section 3.3.8.

At the end of a time step or iteration, the mass–weighted enthalpy ($\overline{h} = \Sigma Y_i h_i$) is known. Newton's method is used to extract the temperature from the mass weighted enthalpy. Essentially, the following equation is solved for the unknown temperature *T*:

$$\sum_{i=1}^{M} Y_i h_i(T) = \overline{h} \tag{3.96}$$

where Y_i and $\overline{h}$ are known. From Equation 3.6, the sensible enthalpy of species *i* is:

$$\begin{aligned} h_i(T) &= \int_{T_d}^{T} \left(c_{b,i}(\theta) + c_{m,i}(\theta)\right) \mathrm{d}\theta \\ &= \frac{c_{0,i}}{n_{c,i}+1}\left(T\left(\frac{T}{T_r}\right)^{n_{c,i}} - T_d\left(\frac{T_d}{T_r}\right)^{n_{c,i}}\right) + \frac{\Delta H_{m,i}}{2}\left(\mathrm{erf}\left(\frac{T - T_{m,i}}{\sqrt{2\sigma_{m,i}^2}}\right) - \mathrm{erf}\left(\frac{T_d - T_{m,i}}{\sqrt{2\sigma_{m,i}^2}}\right)\right) \\ &= \frac{c_{0,i} T^{n_{c_i}+1}}{T_r^{n_{c_i}}\left(n_{c,i}+1\right)} - \frac{c_{0,i} T_d^{n_{c_i}+1}}{T_r^{n_{c_i}}\left(n_{c,i}+1\right)} + \frac{\Delta H_{m,i}}{2}\left(\mathrm{erf}\left(\frac{T - T_{m,i}}{\sqrt{2\sigma_{m,i}^2}}\right) - \mathrm{erf}\left(\frac{T_d - T_{m,i}}{\sqrt{2\sigma_{m,i}^2}}\right)\right) \end{aligned} \tag{3.97}$$

Equation 3.97 can also be written as:

$$h_i(T) = A_i T^{B_i} - C_i + D_i \mathrm{erf}\left(\frac{T - E_i}{F_i}\right) - G_i \tag{3.98a}$$

$$A_i = \frac{c_{0,i}}{\left(n_{c,i}+1\right)T_r^{n_{c,i}}} \tag{3.98b}$$

$$B_i = n_{c,i} + 1 \tag{3.98c}$$

$$C_i = \frac{c_{0,i}}{\left(n_{c,i}+1\right)} \frac{T_d^{n_{c,i}+1}}{T_r^{n_{c,i}}} \tag{3.98d}$$

$$D_i = \frac{\Delta H_{m,i}}{2} \tag{3.98e}$$

$$E_i = T_{m,i} \tag{3.98f}$$

$$F_i = \sqrt{2\sigma_{m,i}^2} \tag{3.98g}$$

$$G_i = \frac{\Delta H_{m,i}}{2} \text{erf}\left(\frac{T_d - T_{m,i}}{\sqrt{2\sigma_{m,i}^2}} \right) \tag{3.98h}$$

Thus, the following equation must be solved for the unknown temperature T:

$$\sum_{i=1}^{M} Y_i \left(A_i T^{B_i} - C_i + D_i \text{erf}\left(\frac{T - E_i}{F_i} \right) - G_i \right) = \overline{h} \tag{3.99}$$

or putting the unknown temperature on the LHS and the known terms on the RHS:

$$\sum_{i=1}^{M} \left(Y_i A_i T^{B_i} + Y_i D_i \text{erf}\left(\frac{T - E_i}{F_i} \right) \right) = \overline{h} + \sum_{i=1}^{M} Y_i \left(C_i + G_i \right) \tag{3.100}$$

For the special case of no melting, Equation 3.100 becomes:

$$\sum_{i=1}^{M} Y_i A_i T^{B_i} = \overline{h} + \sum_{i=1}^{M} Y_i C_i \tag{3.101}$$

Note that for the special case of all species having constant (temperature invariant) specific heat (i.e. $n_{c,i} = 0 \ \forall \, i$) and no melting, Equation 3.101 can be simplified by substituting Equations 3.98b and 3.98d:

$$\sum_{i=1}^{M} Y_i \left(\frac{c_{0,i}}{\left(n_{c,i}+1\right) T_r^{n_{c,i}}} \right) T^{B_i} = \bar{h} + \sum_{i=1}^{M} \frac{c_{0,i}}{\left(n_{c,i}+1\right)} \frac{T_d^{n_{c_i}+1}}{T_r^{n_{c,i}}}$$

$$\sum_{i=1}^{M} Y_i \left(\frac{c_{0,i}}{\left(0+1\right) T_r^{0}} \right) T^{0+1} = \bar{h} + \sum_{i=1}^{M} \frac{c_{0,i}}{\left(0+1\right)} \frac{T_d^{n_{c_i}+1}}{T_r^{0}}$$

$$\sum_{i=1}^{M} Y_i c_{0,i} T = \bar{h} + \sum_{i=1}^{M} c_{0,i} T_d$$

$$\sum_{i=1}^{M} Y_i c_{0,i} \left(T - T_d\right) = \bar{h}$$

This leads to the following simple equation to extract the temperature from the enthalpy:

$$T - T_d = \frac{\bar{h}}{\sum_{i=1}^{M} Y_i c_{0,i}} \tag{3.102}$$

3.3.6 Gas phase energy conservation

The gas phase energy conservation equation has been given as Equation 3.39:

$$\begin{aligned}
&\left(\rho_g \overline{\psi} \Delta z\right)_P^{\circ} \frac{h_{g,P} - h_{g,P}^{\circ}}{\Delta t} + \dot{m}'' h_g \Big|_b - \dot{m}'' h_g \Big|_t - h_{g,P} \dot{m}'' \Big|_b + h_{g,P} \dot{m}'' \Big|_t = \\
&\overline{\psi} \rho_g D \frac{\partial h_g}{\partial z}\Bigg|_b - \overline{\psi} \rho_g D \frac{\partial h_g}{\partial z}\Bigg|_t + \left(\dot{Q}_{s-g}''' \Delta z\right)_P + \\
&\sum_{j=1}^{N} \left(\left(\dot{\omega}_{fj}''' - \dot{\omega}_{dj}''' \right) h_{g,j} \Delta z \right)_P + \left(\dot{Q}_g''' \Delta z \right)_P
\end{aligned}$$

Equation 3.39 can be written as:

$$\begin{aligned}
&\left(\rho_g \overline{\psi} \Delta z\right)_P^{\circ} \frac{h_{g,P} - h_{g,P}^{\circ}}{\Delta t} + \dot{m}'' h_g \Big|_b - \dot{m}'' h_g \Big|_t - h_{g,P} \dot{m}'' \Big|_b + h_{g,P} \dot{m}'' \Big|_t = \\
&\overline{\psi} \rho_g D \frac{\partial h_g}{\partial z}\Bigg|_b - \overline{\psi} \rho_g D \frac{\partial h_g}{\partial z}\Bigg|_t + \left(S \Delta z\right)_P - \left(\dot{\omega}_{fg}''' h_g \Delta z \right)_P
\end{aligned} \tag{3.103a}$$

$$\left(S\right)_P = \left(\dot{Q}_{s-g}'''\right)_P + \sum_{j=1}^{N} \left(\dot{\omega}_{fj}''' h_{g,j} \right)_P - \sum_{j=1}^{N} \left(\dot{\omega}_{dj}''' h_{g,j} \right)_P + \left(\dot{Q}_g''' \right)_P \tag{3.103b}$$

Now split the source term into positive and negative parts:

$$\left(S\right)_P = \left(S^+\right)_P - \left(S^-\right)_P \tag{3.104a}$$

$$\left(S^+\right)_P = h_{cv}T + \sum_{j=1}^{N}\left(\dot{\omega}'''_{fj}h_{gj}\right)_P + \left(\dot{Q}'''_g\right)_P \tag{3.104b}$$

$$\left(S^-\right)_P = h_{cv}T_g + \sum_{j=1}^{N}\left(\dot{\omega}'''_{dj}h_{gj}\right)_P \tag{3.104c}$$

It has been assumed in writing Equations 3.104b and 3.104c that $\dot{Q}'''_g$ has only positive components, i.e. there are no endothermic homogeneous gas phase reactions. Substituting Equation 3.104 into Equation 3.103 gives:

$$\begin{aligned}&\left(\rho_g\overline{\psi}\Delta z\right)^{\circ}_P\frac{h_{g,P}-h^{\circ}_{g,P}}{\Delta t}+\dot{m}''h_g\Big|_b-\dot{m}''h_g\Big|_t-h_{g,P}\dot{m}''\Big|_b+h_{g,P}\dot{m}''\Big|_t=\\&\overline{\psi}\rho_g D\frac{\partial h_g}{\partial z}\Bigg|_b-\overline{\psi}\rho_g D\frac{\partial h_g}{\partial z}\Bigg|_t+\left(S^+\Delta z\right)_P-\left(S^-\Delta z\right)_P-\left(\dot{\omega}'''_{fg}h_g\Delta z\right)_P\end{aligned} \tag{3.105}$$

As with the gaseous–species conservation equation, the discretization and numerical solution of Equation 3.105 follows Patankar [194]. Begin by defining the following:

$$J_b = \dot{m}''h_g\Big|_b - \overline{\psi}\rho_g D\frac{\partial h_g}{\partial z}\Bigg|_b \tag{3.106a}$$

$$J_t = \dot{m}''h_g\Big|_t - \overline{\psi}\rho_g D\frac{\partial h_g}{\partial z}\Bigg|_t \tag{3.106b}$$

$$F_b = \dot{m}''\Big|_b \tag{3.106c}$$

$$F_t = \dot{m}''\Big|_t \tag{3.106d}$$

$$a^{\circ}_P = \frac{\left(\rho_g\overline{\psi}\Delta z\right)^{\circ}_P}{\Delta t} \tag{3.106e}$$

Substituting Equation 3.106 into Equation 3.105 gives:

$$a_P^\circ \left(h_g - h_g^\circ\right)_P + J_b - J_t - F_b\left(h_g\right)_P + F_t\left(h_g\right)_P = \left(S^+ \Delta z\right)_P - \left(S^- \Delta z\right)_P - \left(\dot{\omega}_{fg}''' h_g \Delta z\right)_P \quad (3.107)$$

Following Patankar [194] Equation 5.54–5.55:

$$J_b - h_{g,P} F_b = a_B \left(h_{g,P} - h_{g,B}\right) \quad (3.108a)$$

$$J_t - h_{g,P} F_t = a_T \left(h_{g,T} - h_{g,P}\right) \quad (3.108b)$$

where the coefficients a_B and a_T will be defined below. Substitute Equation 3.108 into Equation 3.107, and multiply the negative part of the source term by $h_{g,P}/h_{g,P}$:

$$\left(a_P^\circ + a_B + a_T + \frac{\left(S^- \Delta z\right)_P}{h_{g,P}} + \left(\dot{\omega}_{fg}''' \Delta z\right)_P\right) h_{g,P} = a_P^\circ h_{g,P}^\circ + a_B h_{g,B} + a_T h_{g,T} + \left(S^+ \Delta z\right)_P \quad (3.109)$$

Define:

$$a_P = a_P^\circ + a_B + a_T + \frac{\left(S^- \Delta z\right)_P}{h_{g,P}} + \left(\dot{\omega}_{fg}''' \Delta z\right)_P \quad (3.110a)$$

$$b = a_P^\circ h_{g,P}^\circ + \left(S^+ \Delta z\right)_P \quad (3.110b)$$

After substituting Equation 3.110 into Equation 3.109, the final form of the discretized equation becomes:

$$a_P h_{g,P} = a_B h_{g,B} + a_T h_{g,T} + b \quad (3.111)$$

Again, Equation 3.111 is of the form that can be solved by the Thomas algorithm. The two required boundary conditions have been given as Equations 3.40b and 3.40c, and their numerical implementation is described in Section 3.3.8.

3.3.7 Gas phase momentum conservation

Begin with Equation 3.42:

$$\frac{\left(\frac{P\overline{M}}{RT_g}\overline{\psi}\Delta z\right)_P - \left(\frac{P\overline{M}}{RT_g}\overline{\psi}\Delta z\right)_P^\circ}{\Delta t} - \left(\frac{\overline{K}}{\nu}\right)_b \left.\frac{\partial P}{\partial z}\right|_b + \left(\frac{\overline{K}}{\nu}\right)_t \left.\frac{\partial P}{\partial z}\right|_t = \left(\dot{\omega}'''_{fg}\Delta z\right)_P$$

Replace the pressure gradient with its discrete approximation:

$$-\left(\frac{\overline{K}}{\nu}\right)_b \left.\frac{\partial P}{\partial z}\right|_b \approx -\left(\frac{\overline{K}}{\nu}\right)_b \frac{P_B - P_P}{(\delta z)_b} \tag{3.112a}$$

$$-\left(\frac{\overline{K}}{\nu}\right)_t \left.\frac{\partial P}{\partial z}\right|_t \approx -\left(\frac{\overline{K}}{\nu}\right)_t \frac{P_P - P_T}{(\delta z)_t} \tag{3.112b}$$

Expand the first term on the LHS as:

$$\frac{\left(\frac{P\overline{M}}{RT_g}\overline{\psi}\Delta z\right)_P - \left(\frac{P\overline{M}}{RT_g}\overline{\psi}\Delta z\right)_P^\circ}{\Delta t} \equiv \left(\frac{\overline{M}\overline{\psi}\Delta z}{RT_g\Delta t}\right)_P^\circ \left(P_P - P_P^\circ\right) + P_P\left(\left(\frac{\overline{M}\overline{\psi}\Delta z}{RT_g\Delta t}\right)_P - \left(\frac{\overline{M}\overline{\psi}\Delta z}{RT_g\Delta t}\right)_P^\circ\right) \tag{3.113}$$

Substituting Equations 3.112 and 3.113 into Equation 3.42 gives:

$$\left(\frac{\overline{M}\overline{\psi}\Delta z}{RT_g\Delta t}\right)_P^\circ \left(P_P - P_P^\circ\right) + P_P\left(\left(\frac{\overline{M}\overline{\psi}\Delta z}{RT_g\Delta t}\right)_P - \left(\frac{\overline{M}\overline{\psi}\Delta z}{RT_g\Delta t}\right)_P^\circ\right) - \left(\frac{\overline{K}}{\nu}\right)_b \frac{P_B - P_P}{(\delta z)_b} + \left(\frac{\overline{K}}{\nu}\right)_t \frac{P_P - P_T}{(\delta z)_t} = \left(\dot{\omega}'''_{fg}\Delta z\right)_P \tag{3.114}$$

Define:

$$a_P^\circ = \left(\frac{\overline{M}\overline{\psi}\Delta z}{RT_g\Delta t}\right)_P^\circ \tag{3.115a}$$

$$a_T = \frac{\left(\overline{K}/\nu\right)_t}{(\delta z)_t} \tag{3.115b}$$

$$a_B = \frac{\left(\overline{K}/\nu\right)_b}{(\delta z)_b} \tag{3.115c}$$

Substitute Equation 3.115 into Equation 3.114:

$$a_P^\circ\left(P_P - P_P^\circ\right) - a_B\left(P_B - P_P\right) + a_T\left(P_P - P_T\right) = \left(\dot{\omega}_{fg}'''\Delta z\right)_P - P_P\left(\left(\frac{\overline{M}\,\overline{\psi}\Delta z}{RT_g\Delta t}\right)_P - a_P^\circ\right) \quad (3.116)$$

Distribute multiplication and combine like terms:

$$\left(a_P^\circ + a_B + a_T\right)P_P = a_P^\circ P_P^\circ + a_B P_B + a_T P_T + \left(\dot{\omega}_{fg}'''\Delta z\right)_P - P_P\left(\left(\frac{\overline{M}\,\overline{\psi}\Delta z}{RT_g\Delta t}\right)_P - a_P^\circ\right) \quad (3.117)$$

Define:

$$a_P = a_P^\circ + a_B + a_T \quad (3.118a)$$

$$b = a_P^\circ P_P^\circ + \left(\dot{\omega}_{fg}'''\Delta z\right)_P - P_P\left(\left(\frac{\overline{M}\,\overline{\psi}\Delta z}{RT_g\Delta t}\right)_P - a_P^\circ\right) \quad (3.118b)$$

Substituting Equation 3.118 into Equation 3.117 gives:

$$a_P P_P = a_B P_B + a_T P_T + b \quad (3.119)$$

Equation 3.119 can be solved by the Thomas algorithm. The two required boundary conditions have been given as Equations 3.43b and 3.43c, and their numerical implementation is described in the following section.

3.3.8 Tri–diagonal matrix (Thomas) algorithm

As shown above, wherever possible the governing equations are discretized in the general form:

$$a_P\phi_P = a_B\phi_B + a_T\phi_T + b \quad (3.120)$$

This makes it possible to use the efficient recursive algorithm known as the Thomas (or tri–diagonal matrix) algorithm. First, rewrite Equation 3.120 as:

$$a_i\phi_i = b_i\phi_{i+1} + c_i\phi_{i-1} + d_i \quad (3.121)$$

i.e., a_i is a_P, b_i is a_B, c_i is a_T, and d_i is b. Next, define:

$$P_i = \frac{b_i}{a_i - c_i P_{i-1}} \tag{3.122a}$$

$$Q_i = \frac{d_i + c_i Q_{i-1}}{a_i - c_i P_{i-1}} \tag{3.122b}$$

The Thomas algorithm begins by calculating P_1 and Q_1 (where the subscript 1 denotes that these values refer to the first cell):

$$P_1 = \frac{b_1}{a_1} \tag{3.123a}$$

$$Q_1 = \frac{d_1 + c_1 \phi_0}{a_1} \tag{3.123b}$$

In Equation 3.123b, ϕ_0 is the ambient value of ϕ (the subscript 0 denotes the 0^{th} cell). Next, Equations 3.122a and 3.122b are used to calculate P_i and Q_i for i = 2 to n where n is the number of cells. The value of ϕ in cell n is calculated as:

$$\phi_n = Q_n + \frac{b_n \phi_{n+1}}{a_n - c_n P_{n-1}} \tag{3.124}$$

In Equation 3.124, ϕ_{n+1} represents the value of ϕ flowing into the back face (or the ambient value of ϕ at the back face). With ϕ_n known, the remaining $n-1$ ϕ values are calculated using the relation:

$$\phi_i = P_i \phi_{i+1} + Q_i \tag{3.125}$$

Some clarification is warranted regarding the coefficients in cell 1 and cell n. Since the TDMA solver is used to solve four separate conservation equations (gaseous species, condensed and gaseous energy, and gaseous momentum) the meaning of the boundary coefficients for each of these conservation equations is discussed separately below.

In the gaseous momentum conservation equation, the front face pressure is equal to the ambient value. Therefore, the following values are set for the gaseous momentum equation: $a_1 = 1$, $b_1 = 0$, $c_1 = 0$, $d_1 = P_\infty$ (here, P is pressure, not the P defined in Equation 3.122a). Substituting these values into Equation 3.121, it can be seen that this ensures $\phi_1 = P_\infty$, the desired result. At the back face, a specified mass flux is desired. This can be achieved by setting the pressure gradient to a desired value. Note that the back face boundary condition (Equation 3.43c) is discretized as:

$$\dot{m}''_\delta = -\left(\frac{\overline{K}}{\nu}\frac{\partial P}{\partial z}\right)\Bigg|_{z=\delta} \approx c_n\left(P_{n-1} - P_n\right) \tag{3.126}$$

It follows from Equation 3.126 that $P_n = P_{n-1} - \dot{m}''_\delta / c_n$. Note that flow into the back face corresponds to a negative value of $\dot{m}''_\delta$. The discretized pressure evolution equation at the back face is:

$$a_n P_n = b_n P_{n+1} + c_n P_{n-1} + d_n \tag{3.127}$$

Setting $b_n = 0$ and substituting Equation 3.126 into Equation 3.127 gives an expression for a_n:

$$a_n = \frac{c_n P_{n-1} + d_n}{P_{n-1} - \dfrac{\dot{m}''_\delta}{c_n}} \tag{3.128}$$

The back face pressure boundary condition is implemented by setting the value of a_n per Equation 3.128.

In the condensed phase energy equation, the convective and radiative losses (or gains) are converted to volumetric source terms by dividing a flux by the boundary node grid size. For example, the convective loss or gain at the front face is accounted for by

adding a source term of magnitude $\dot{q}_c''/(\Delta z)_1$ to the source term in cell 1, where $\dot{q}_c'' = h_c(T_\infty - T_1)$. Rather than explicitly setting the temperature gradient at the front and back faces, the coefficients c_1 and b_n are set to zero, and volumetric source terms are added to cells 1 and n. Numerically, this is equivalent to explicitly specifying the gradient at the front and back faces, but it is conceptually easier to implement.

In the gas phase species conservation equation, boundary conditions at both the front and the back face are required. At the front face, Equation 3.123b is applied directly, where ϕ_0 corresponds to the ambient gaseous mass fractions. However, the value of c_1 requires careful interpretation. Tracing backward from Equation 3.121 to Equation 3.120 to Equation 3.84b and Equation 3.84d, it is seen that $c_1 \equiv a_{T,1} \equiv \mathscr{D}_{t,1} A(|P_{t,1}|) + \max(-F_{t,1}, 0)$. The usual definition of $\mathscr{D}_t$ is $\mathscr{D}_t = \rho_g \overline{\psi} D/(\delta z)_t$. However, in cell 1 the heat/mass transfer analogy is used to calculate the value of $\mathscr{D}_t$ as:

$$\mathscr{D}_{t,1} \approx \frac{h_c}{c_{pg}} \tag{3.129}$$

Equation 3.129 allows the front face boundary condition to be implemented via Equation 3.123b.

At the back face, the only special treatment required is that the mass flux and gaseous mass fractions of the incoming flow (if any) must be specified. It is assumed that $\mathscr{D}_{b,n} = 0$ and Equation 3.124 can be applied directly, where ϕ_{n+1} represents the gaseous mass fractions of the incoming flow. If there is no incoming flow, as is the usual case except for smoldering combustion with an internally–forced flow, then this no–flux boundary condition is implemented by setting $b_n = 0$.

The boundary conditions on the gas phase energy conservation equation are implemented in a way that is directly analogous to the gas phase species conservation equation.

3.3.9 Relaxation and convergence criteria

Due to the strong nonlinearity in the governing equations, a fully–implicit iterative numerical solution is used. Convergence is achieved when the solution in every grid cell chances by less than some pre–determined tolerance. Relative tolerances are used to establish convergence of the gas phase and condensed phase species equations. For example, the condensed phase species conservation equation is converged when the following is true in every grid cell:

$$\frac{Y_i - Y_{i,old}}{\min\left(Y_{i,old}, \varepsilon\right)} < rtol \tag{3.130}$$

where *rtol* is a user–specified relative tolerance (perhaps 10^{-5}), and ε is a small number (e.g. 10^{-7}) to prevent division by zero. Note that $Y_{i,old}$ is the mass fraction at the previous iteration (not the previous time step).

For the other equations, an absolute tolerance is used as the convergence criterion. For example, the pressure evolution equation is converged when the following is true in every grid cell:

$$P - P_{old} < atol \tag{3.131}$$

where *atol* is a user–specified absolute convergence criterion, perhaps 10^{-7} Pa. Again, P_{old} is the pressure at the previous iteration, not the previous time step.

In order to reduce the possibility of divergence between iterations, solution relaxation is implemented by replacing the coefficients a_P and b in the discretized governing equations with $a_{P,relax}$ and b_{relax}, as shown in Equation 3.132:

$$a_{P,relax}\phi_P = a_B\phi_B + a_T\phi_T + b_{relax} \tag{3.132a}$$

$$a_{P,relax} = \frac{a_P}{\alpha} \tag{3.132b}$$

$$b_{relax} = b + \left(\frac{1-\alpha}{\alpha}\right)a_P\phi_{P,old} \tag{3.132c}$$

where α is the user–specified relaxation parameter ($0 < \alpha \leq 1$) and $\phi_{P,old}$ is the value of ϕ from the previous iteration (not the previous time step). Note that when $\alpha = 1$, $a_{P,relax} = a_P$ and $b_{relax} = b$. For simplicity, the same value of α is applied to all equations and α is static, meaning that it is not dynamically determined during a simulation. Normally, $\alpha = 1$ and solution relaxation via Equation 3.132 would be invoked only when the solution fails to converge within a pre–determined number of iterations.

3.4 Model Verification

In this section, the numerical calculations of the model are compared to several analytical solutions to verify that the governing equations have been correctly implemented. As will be shown in the following sections, the model calculations compare well with available analytical solutions. In addition to this exercise, overall balances for mass, energy, and species conservation have been verified for several different scenarios but are not presented here to limit the length of this dissertation.

3.4.1 Semi–infinite solid

Consider a constant property inert homogeneous semi–infinite solid initially at temperature T_0. It is exposed to a constant radiative heat flux at $z = 0$. The solid is perfectly opaque so radiation is absorbed immediately at the surface. The solid loses heat by convection to the ambient at temperature T_0. This problem can be stated mathematically as:

$$\frac{1}{\alpha}\frac{\partial T(z,t)}{\partial t} = \frac{\partial^2 T(z,t)}{\partial z^2} \quad \text{for } 0 \le z < \infty \tag{3.133a}$$

$$T\big|_{z\to\infty} = T_0 \tag{3.133b}$$

$$-k\frac{\partial T}{\partial z}\bigg|_{z=0} = \dot{q}_e'' - h_c\left(T - T_0\right)\big|_{z=0} \tag{3.133c}$$

$$T\big|_{t=0} = T_0 \tag{3.133d}$$

The solution to this problem is well–known:

$$\frac{T - T_0}{\dot{q}_e''/h_c} = \text{erfc}\left(\frac{z}{\sqrt{4\alpha t}}\right) - \exp\left(\frac{z}{k/h_c} + \frac{t}{k\rho c/h_c^2}\right)\text{erfc}\left(\frac{z}{\sqrt{4\alpha t}} + \sqrt{\frac{t}{k\rho c/h_c^2}}\right) \tag{3.134}$$

The model calculations are compared to this analytical solution using the following parameters: k = 0.2 W/m–K, ρ = 1000 kg/m^3, c = 1400 J/kg–K, $\dot{q}_e''$ = 25 kW/m^2, h_c = 20 W/m^2–K, and T_0 = 300 K. A grid spacing of 0.1 mm is used, with a constant time step of 0.1 s. A region 4 cm in thickness is simulated to approximate semi–infinite behavior over 180 s. A comparison of the exact solution and that calculated numerically is given in Figure 3.9. It can be seen that there is almost an exact match between the analytical solution and that calculated numerically.

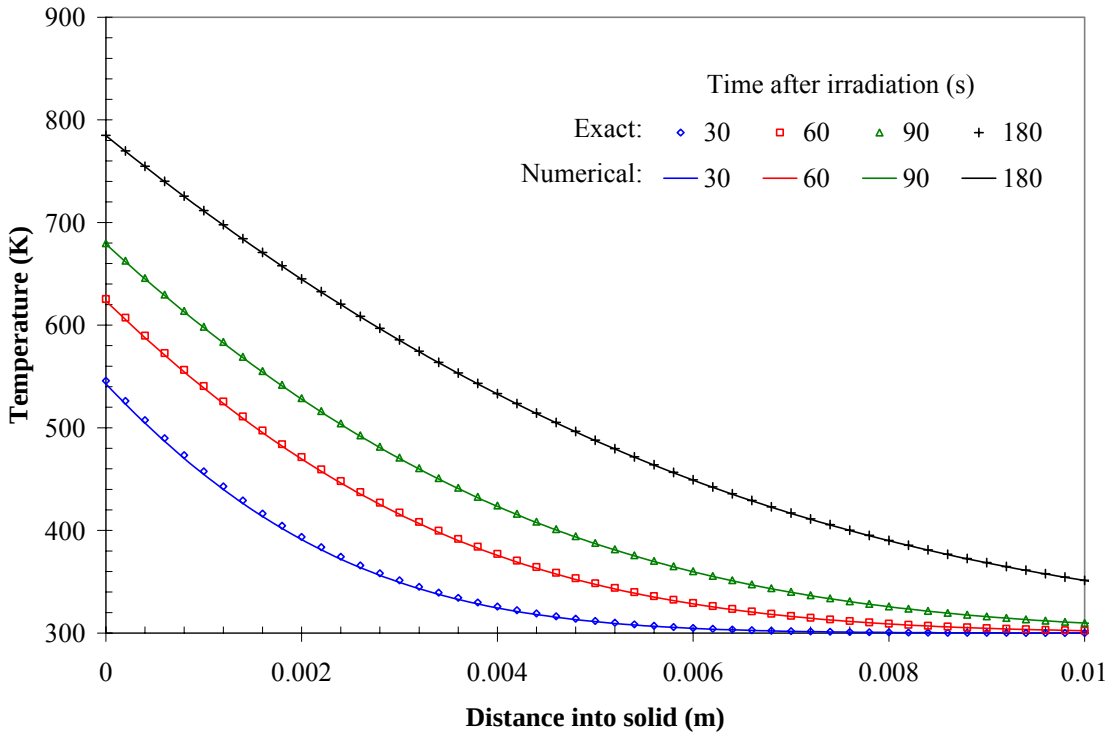

Figure 3.9. Comparison of exact solution and numerical model calculation for semi–infinite solid with surface radiation absorption and convective heat losses.

3.4.2 In–depth radiation absorption

Consider a constant property inert homogeneous solid of thickness δ. It is exposed to a constant radiative heat flux at $z = 0$ and insulated at its back face ($z = \delta$). Instead of the radiation being absorbed at the surface, it is attenuated in–depth. Heat losses from the irradiated surface are by convection only to the ambient at temperature T_0. The solid is initially at temperature T_0. The problem may be stated mathematically as:

$$\frac{1}{\alpha}\frac{\partial T(z,t)}{\partial t} = \frac{\partial^2 T(z,t)}{\partial z^2} + \frac{\dot{q}''_e \kappa \exp(-\kappa z)}{k} \quad \text{for } 0 \le z \le \delta \tag{3.135a}$$

$$\left.\frac{\partial T}{\partial z}\right|_{z=\delta} = 0 \tag{3.135b}$$

$$-k\left.\frac{\partial T}{\partial z}\right|_{z=0} = -h_c\left(T - T_0\right)\Big|_{z=0} \tag{3.135c}$$

$$T\big|_{t=0} = T_0 \tag{3.135d}$$

Appendix A shows how the exact solution to this problem is obtained via Green's function. The exact solution is:

$$T - T_0 = \frac{2\dot{q}''\kappa^2}{k} \times \sum_{m=1}^{\infty} \frac{1}{\lambda_m\left(\kappa^2 + \lambda_m^2\right)} \frac{\cos\left(\lambda_m\delta\right) + \frac{\lambda_m}{\kappa}\sin\left(\lambda_m\delta\right) - \exp\left(-\kappa\delta\right)}{\lambda_m\delta + \frac{1}{2}\sin\left(2\delta\lambda_m\right)} \cos\left(\lambda_m\left(\delta - z\right)\right)\left(1 - \exp\left(-\alpha\lambda_m^2 t\right)\right) \tag{3.136a}$$

with eigenvalues given by the relation:

$$\cot\left(\lambda_m\delta\right) = \frac{k}{h_c}\lambda_m \tag{3.136b}$$

The same properties are used as for the semi–infinite solid (Section 3.4.1), except that the thickness of the solid is δ = 1 cm and its absorption coefficient is κ = 1000 m^{-1}. A comparison of the exact and numerical temperature profiles are given in Figure 3.10. It can again be seen that there is excellent agreement between the numerical calculations and the exact solution. Due to in–depth radiation absorption, the peak temperature does not occur at the surface.

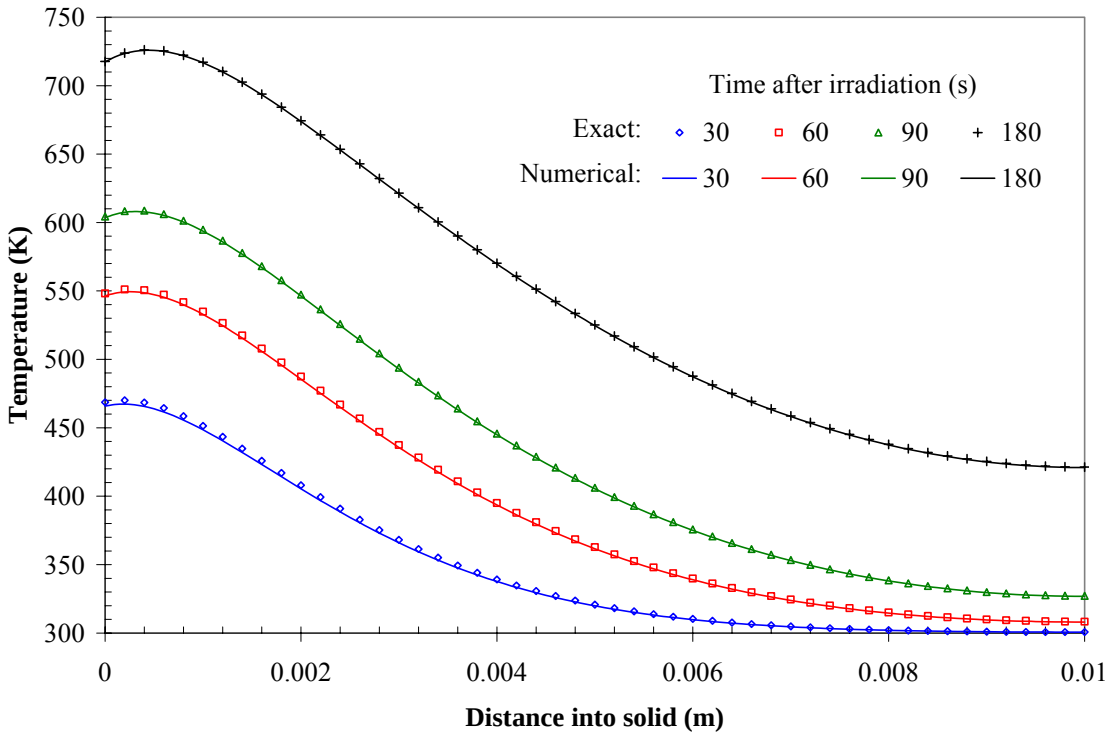

Figure 3.10. Comparison of exact solution and numerical calculation for finite thickness solid with in–depth radiation absorption and surface heat losses by convection.

3.4.3 Freezing: Stefan problem

The classical Stefan problem describes the propagation of a solidification front into a semi–infinite medium initially at temperature T_0 above its melting temperature T_m. At time $t = 0$ the solid's surface (at $z = 0$) is instantaneously dropped to temperature T_∞ (below its melting temperature). When the solid temperature at a given location is lowered to T_m, it solidifies and releases the latent heat of melting (ΔH_m). A solidification front with position $s(t)$ begins to propagate into the solid. This front separates the semi–infinite medium into two separate regions: the solid ($z \le s(t)$) and the melt ($z > s(t)$). The governing equations are:

$$\frac{1}{\alpha_s}\frac{\partial T_s}{\partial t} = \frac{\partial^2 T_s}{\partial z^2} \text{ for } 0 \le z \le s(t) \qquad (3.137a)$$

$$\frac{1}{\alpha_\ell}\frac{\partial T_\ell}{\partial t} = \frac{\partial^2 T_\ell}{\partial z^2} \quad \text{for } s(t) < z < \infty \tag{3.137b}$$

with boundary and initial conditions:

$$T_s\big|_{z=0} = T_\infty \tag{3.137c}$$

$$T_\ell\big|_{z\to\infty} = T_0 \tag{3.137d}$$

$$T_\ell\big|_{t=0} = T_0 \tag{3.137e}$$

and interface conditions:

$$T_s\big|_{s(t)} = T_\ell\big|_{s(t)} = T_m \tag{3.137f}$$

$$k_s \left.\frac{\partial T_s}{\partial z}\right|_{s(t)} - k_\ell \left.\frac{\partial T_\ell}{\partial z}\right|_{s(t)} = \rho \Delta H_m \frac{ds}{dt} \tag{3.137g}$$

The solution to this problem is as follows:

$$s(t) = \lambda\sqrt{4\alpha_s t} \tag{3.138a}$$

$$T_s(z,t) = T_\infty + \frac{T_m - T_\infty}{\operatorname{erf}(\lambda)} \operatorname{erf}\left(\frac{z}{\sqrt{4\alpha_s t}}\right) \tag{3.138b}$$

$$T_\ell(z,t) = T_0 + \frac{T_m - T_0}{\operatorname{erfc}\left(\lambda\sqrt{\alpha_s/\alpha_\ell}\right)} \operatorname{erfc}\left(\frac{z}{\sqrt{4\alpha_\ell t}}\right) \tag{3.138c}$$

Where λ is an eigenvalue that must be calculated implicitly from the following relation:

$$\frac{\exp\left(-\lambda^2\right)}{\operatorname{erf}(\lambda)} - \sqrt{\frac{\alpha_s}{\alpha_\ell}}\frac{k_\ell}{k_s}\frac{T_0 - T_m}{T_m - T_\infty}\frac{\exp\left(-\lambda^2\alpha_s/\alpha_\ell\right)}{\operatorname{erfc}\left(\lambda\sqrt{\alpha_s/\alpha_\ell}\right)} = \frac{\sqrt{\pi}\lambda\Delta H_m}{c_s\left(T_m - T_\infty\right)} \tag{3.138d}$$

A comparison of the exact solution and that calculated numerically is given in Figure 3.11. The parameters used in the calculation are selected to approximate polypropylene, a common melting thermoplastic: $k_s = k_\ell$ = 0.20 W/m–K, $\rho_s = \rho_\ell$ = 900

kg/m^3, $c_s = c_\ell$ = 1700 J/kg–K, T_m = 433 K, and ΔH_m = 50,000 J/kg. The initial temperature is T_0 = 438 K, and the surface temperature is T_∞ = 428 K. These parameters give an eigenvalue of λ = 0.2317 from Equation 3.138d. In the model $\sigma_m^2 = 0.1$ was used with a grid spacing of 0.05 mm and a time step of 0.02 s. It can be seen from Figure 3.11 that there is good agreement between the numerical calculations and the exact solution. Discrepancies most likely stem from a slight inconsistency between the exact solution and the numerical simulation: the exact solution assumes a well–defined melting temperature, whereas in the numerical calculations the latent heat of melting is distributed over a narrow temperature window (see Equation 3.5c).

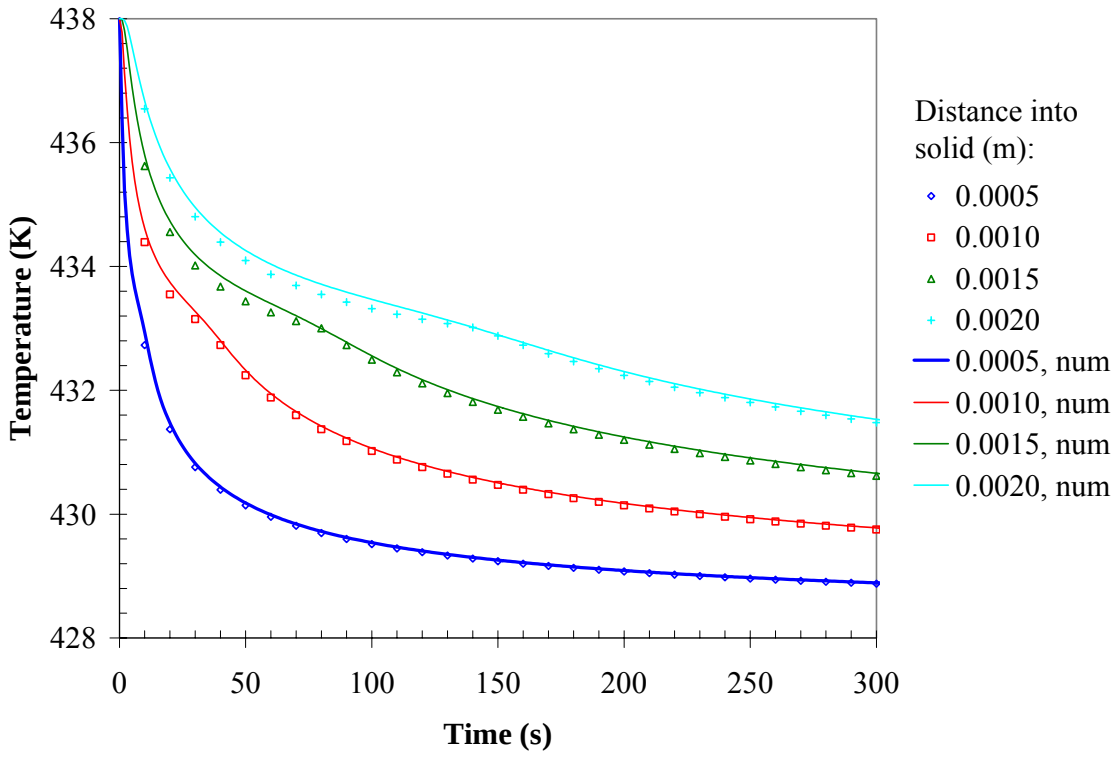

Figure 3.11. Stefan problem. Comparison of exact solution and model calculation. Solid lines are model calculations and individual points are exact solution.

3.4.4 Decomposition kinetics

This section simulates the decomposition kinetics of a two–step reaction involving three species, e.g. the conversion of a virgin solid to char followed by the subsequent oxidation of the char to form ash. Consider the following coupled ordinary differential equations and initial conditions:

$$\frac{\mathrm{d}Y_A}{\mathrm{d}t} = -Y_A k_{AB} \;\; ; \;\; Y_A(0) = 1 \tag{3.139a}$$

$$\frac{\mathrm{d}Y_B}{\mathrm{d}t} = Y_A k_{AB} - Y_B k_{BC} \;\; ; \;\; Y_B(0) = 0 \tag{3.139b}$$

$$\frac{\mathrm{d}Y_C}{\mathrm{d}t} = Y_B k_{BC} \;\; ; \;\; Y_C(0) = 0 \tag{3.139c}$$

The solution to this problem is:

$$Y_A(t) = \exp(-k_{AB}t) \tag{3.140a}$$

$$Y_B(t) = \frac{k_{AB}}{k_{BC} - k_{AB}}\left[\exp(-k_{AB}t) - \exp(-k_{BC}t)\right] \tag{3.140b}$$

$$Y_C(t) = \frac{k_{AB}\left(1 - \exp(-k_{BC}t)\right) + k_{BC}\left(\exp(-k_{AB}t) - 1\right)}{k_{AB} - k_{BC}} \tag{3.140c}$$

The exact solution in Equation 3.140 is compared to that calculated numerically (using the lumped equations presented in Section 3.1.10) for $k_{AB} = 0.389\,\mathrm{s}^{-1}$ and $k_{BC} = 0.262\,\mathrm{s}^{-1}$. The results are shown in Figure 3.12. It can be seen that there is excellent agreement between the model calculations and the exact solution.

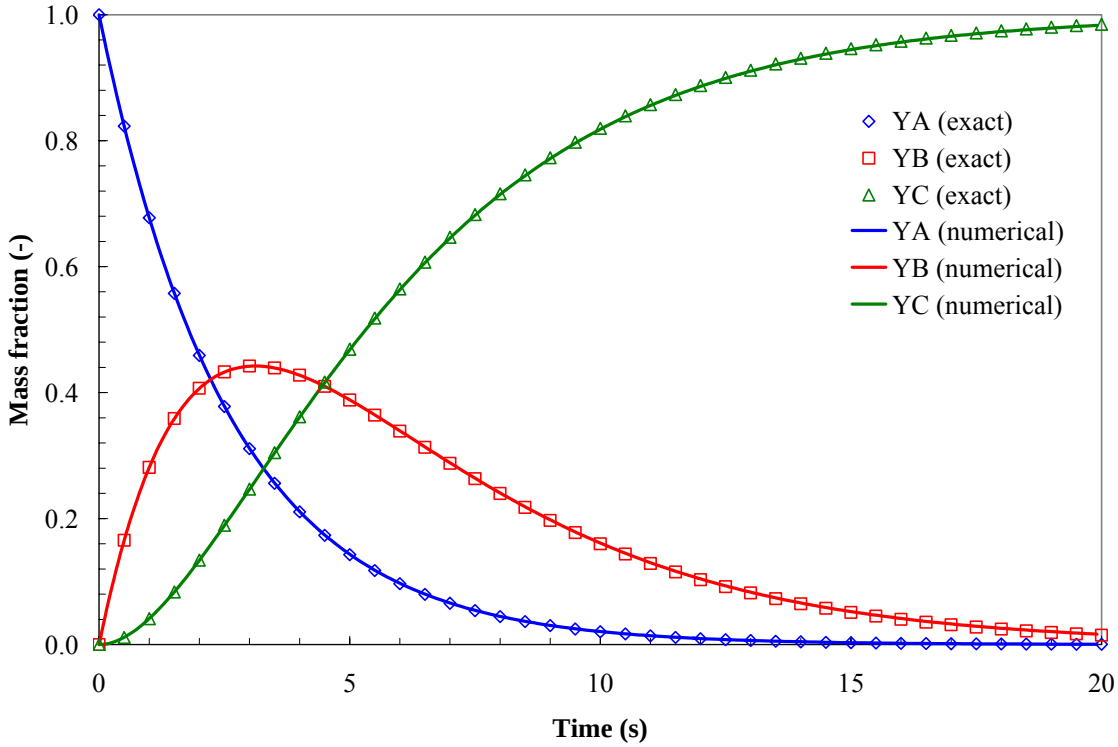

Figure 3.12. Comparison of exact solution and numerical model calculation for coupled ordinary differential equations.

4.0 MODEL RESPONSE TO CHANGES IN INPUT PARAMETERS

In Section 3 the pyrolysis model formulation is presented and its implementation is verified by comparing numerical calculations to analytical solutions. In this section, the effects of various input parameters are investigated as part of an informal sensitivity study before it is used in the following section to simulate actual solids. These parameters that are investigated include: grid spacing, time step, heat of volatilization/pyrolysis, activation energy, reaction order, reaction order treatment, radiative characteristics, thermal conductivity, specific heat capacity, density, front face heat transfer coefficient, back face heat transfer coefficient, and permeability.

The pyrolysis model has not been non–dimensionalized because it is intended for application as a boundary condition in CFD–based simulations of flame spread. Consequently, is difficult to generalize make a sensitivity/parameter effects study general. Therefore, the simulations presented below are conducted for two hypothetical, but representative, materials. One material represents a noncharring polymer such as PMMA, and the other represents a charring solid such as wood. Although their properties were selected to be of the same order of magnitude of real–world fuels, these two hypothetical materials do not directly correspond to any real–world fuels. This informal sensitivity study is by no means exhaustive; it is intended to provide a qualitative idea of the effect that various parameters have on the model calculations while demonstrating some of the model's features and physics that can be included in calculations.

The hypothetical fuels have constant thermal properties, i.e. independent of temperature. No melting occurs, there is no radiation transfer across pores, and radiation is absorbed only at the surface. Each material is assumed to volatilize according to a

single–step first–order global reaction that is unaffected by the presence of oxygen. For the thermoplastic material, a noncharring reaction converts the virgin polymer to pyrolysate gases, leaving no residue and causing surface regression. For the charring solid, the virgin fuel (loosely, wood) is converted to a porous char plus volatiles.

The simulations represent a cone calorimeter experiment conducted in nitrogen (no flame heat flux). The fuel, having a thickness of 1 cm, is exposed to thermal radiation (50 kW/m^2 incident flux) at its front face, and is perfectly–insulated at its back face. A convective heat transfer coefficient of 10 W/m^2–K is assumed at the front face. The baseline thermophysical properties of the three condensed phase species (polymer, wood, and char) are listed in Table 4.1. Similarly, Table 4.2 lists the reaction kinetics (assumed identical for both reactions). The baseline grid spacing and time step are 0.1 mm and 0.1 s, respectively.

Table 4.1. Thermophysical properties of condensed phase species in hypothetical materials.

Property	Condensed phase species		
	polymer	wood	char
k (W/m–K)	0.2	0.2	0.1
ρ (kg/m^3)	1200	500	50
c (J/kg–K)	1500	1500	1500
ε (–)	1	1	1
κ (m^{-1})	∞	∞	∞
γ (m)	0	0	0

Table 4.2. Reaction kinetics for decomposition of hypothetical materials three condensed phase species.

Property	Reaction	
	polymer $\rightarrow$ gases	wood $\rightarrow$ char + gases
Z (s^{-1})	1×10^9	1×10^9
E (kJ/mol)	130	130
χ (–)	1	1
n (–)	1	1
n_{O2} (–)	0	0
ΔH_{sol} (J/kg)	0	0
ΔH_{vol} (J/kg)	1×10^6	1×10^6

4.1 Grid spacing

Grid spacing is an important practical consideration because both storage and CPU time increase as the number of grid points is increased. It should be small enough that the solution does not change significantly with further grid refinement, but not much finer than is required for a grid–independent solution. The effect of grid spacing on the calculation results is investigated below. Holding the time step constant at 0.1 s, the grid spacing is varied over two orders of magnitude: 1 mm, 0.1 mm, and 0.01 mm.

The calculated surface temperature and mass loss rate are shown in Figure 4.1 for the thermoplastic and in Figure 4.2 for the charring solid. Although only two traces are visible in each plot, there are actually three plotted traces. The calculations for grid spacings of 0.1 mm and 0.01 mm fall visibly on the same curve. Thus, the present calculations are grid–independent at a spacing of 0.1 mm or finer. However, this is not a general conclusion, and applies only to these two hypothetical materials at the applied heat flux. Note that nonphysical oscillations in both the mass loss rate and temperature are observed for a grid spacing of 1 mm, indicating that a spacing of 1 mm is too coarse for the present simulations.

Due to surface regression, the thickness of the thermoplastic material approaches zero and the material is completely consumed. This causes the downturn in the calculated mass loss rate seen after 500 s. Comparing this behavior with the experimental measurements of PMMA HRR in the cone calorimeter shown in Figure 2.1, it can be seen that this behavior is qualitatively consistent with experimental observations. A reduction in the mass loss rate leads to an increase in surface temperature since the pyrolysis reaction is endothermic ($\Delta H_{vol} = +1 \times 10^6$ J/kg).

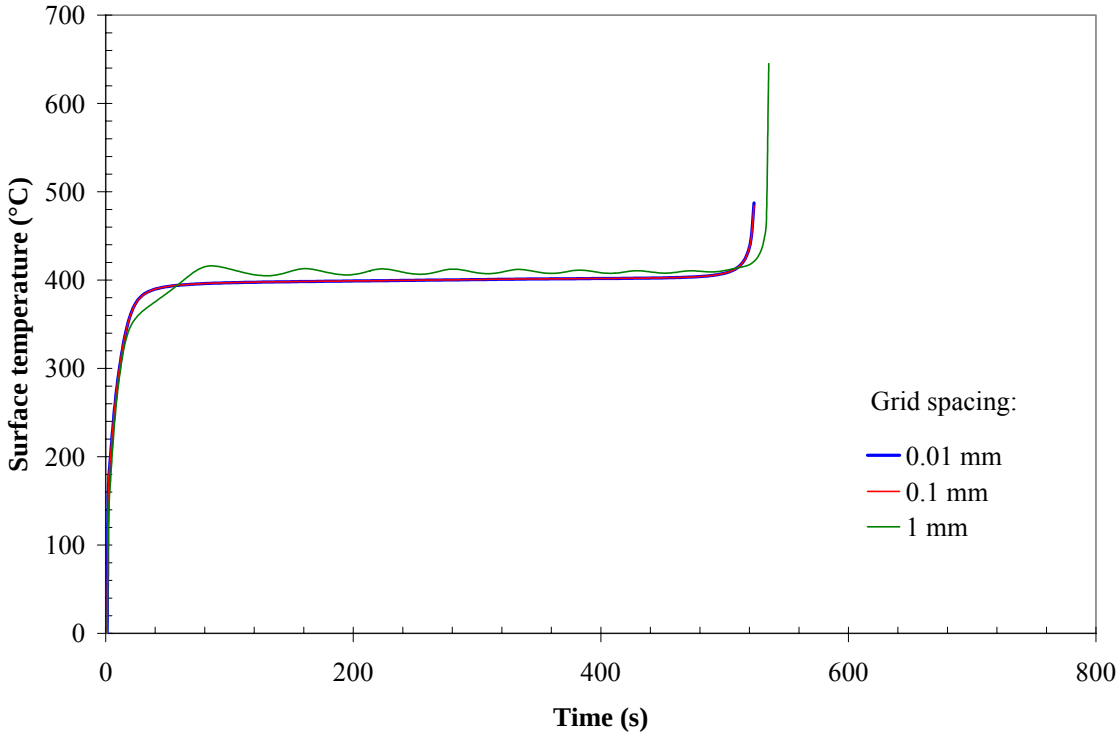

(a)

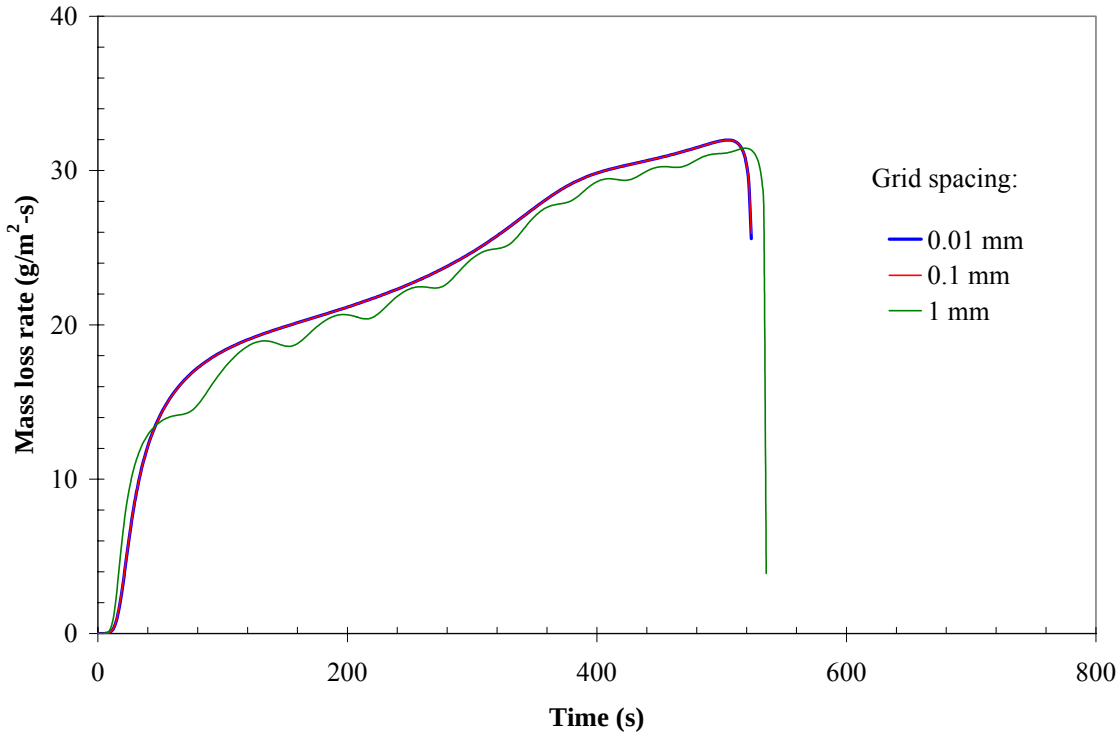

(b)

Figure 4.1. Effect of grid spacing on thermoplastic pyrolysis. (a) Surface temperature; (b) Mass loss rate.

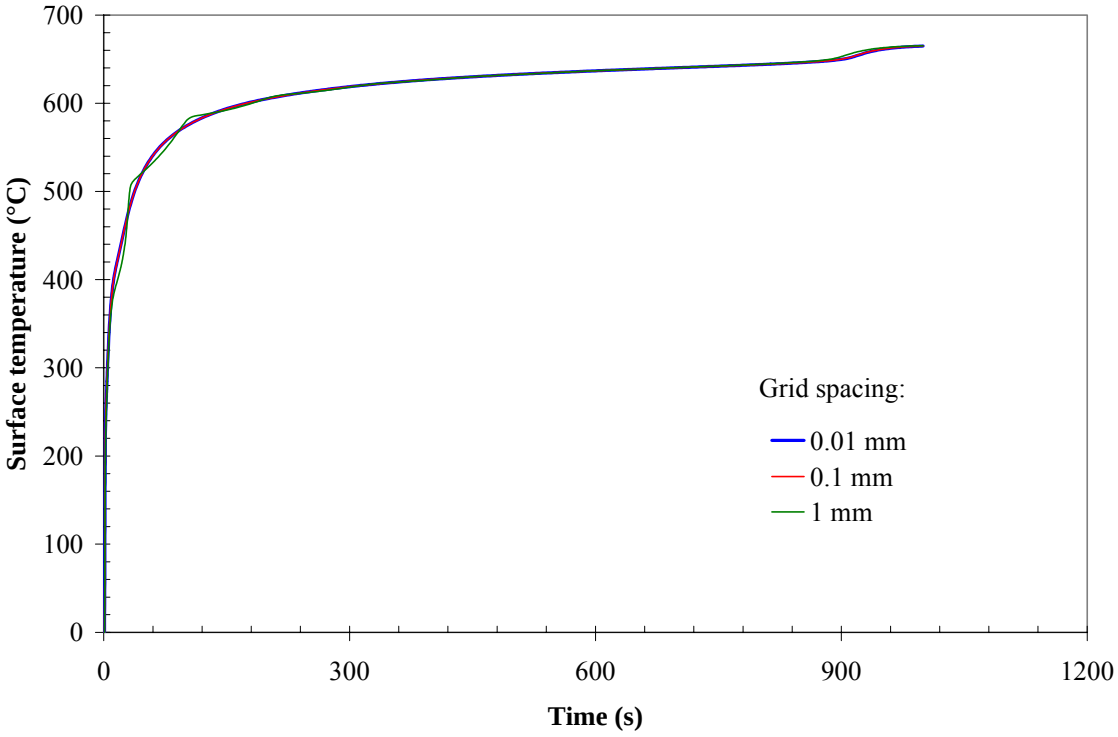

(a)

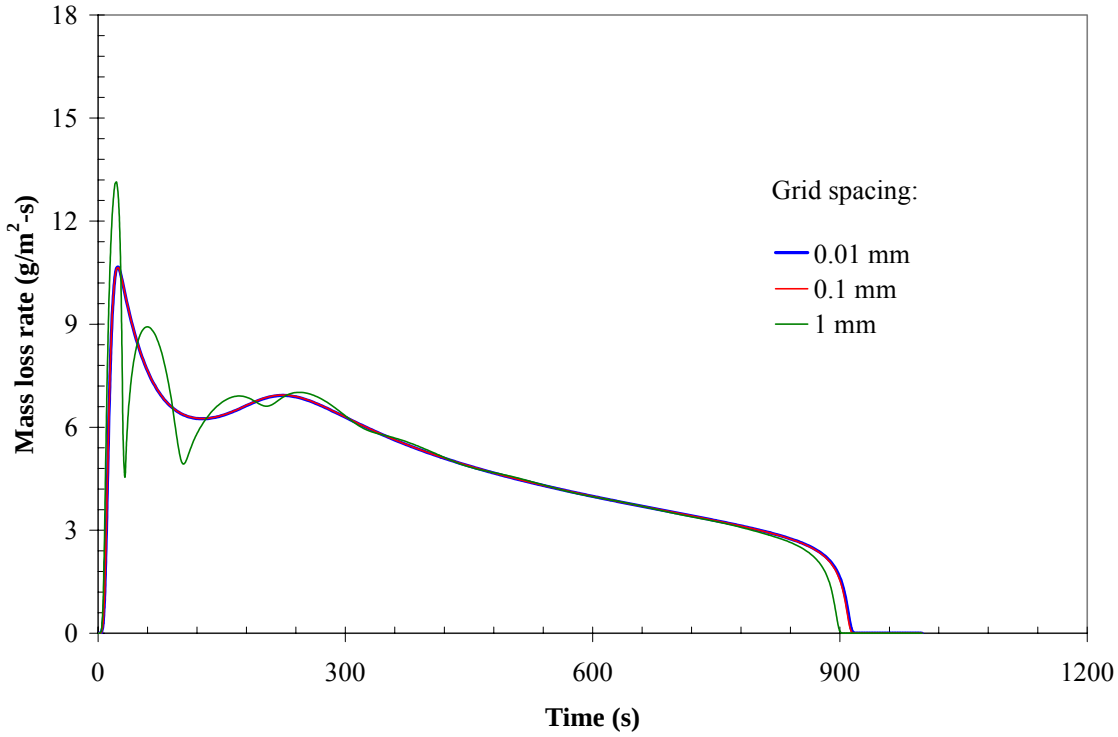

(b)

Figure 4.2. Effect of grid spacing on charring solid pyrolysis. (a) Surface temperature; (b) Mass loss rate.

4.2 Time step

As with grid spacing, the time step was also varied over two orders of magnitude. Holding the grid spacing constant at 0.1 mm, three time steps were investigated: 1 s, 0.1 s, and 0.01 s. The calculated surface temperature and mass loss rates are shown in Figure 4.3 (thermoplastic) and Figure 4.4 (charring solid). With a time step of 1 s, the charring simulation became unstable approximately 20 s into the calculation. The simulation results are not affected by the time step provided it is approximately 0.1 s or smaller. Again, this finding is specific only to this particular combination of thermal properties, reaction kinetics, and applied heat flux level.

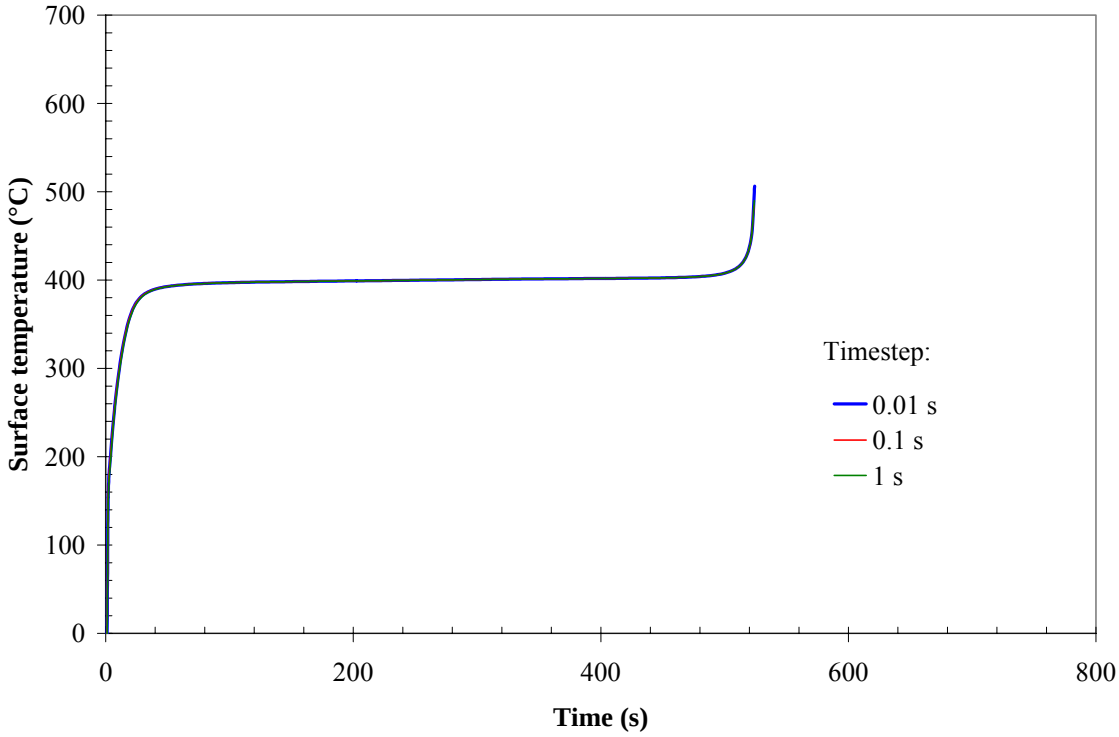

(a)

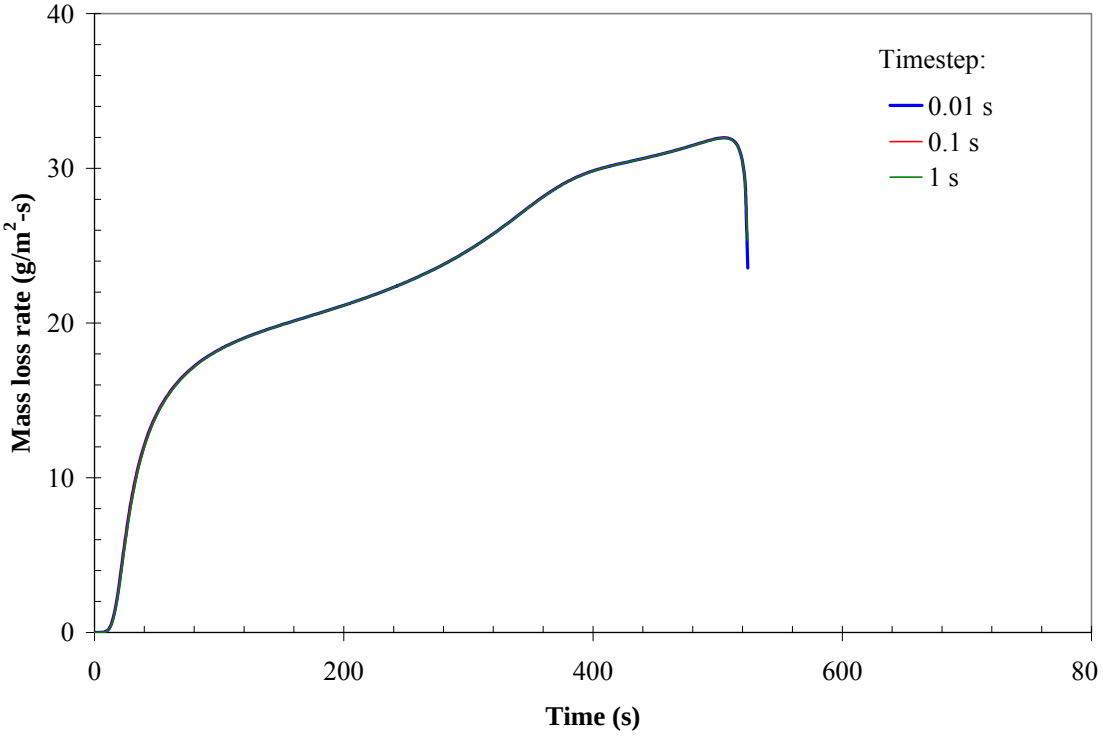

(b)

Figure 4.3. Effect of time step on thermoplastic pyrolysis.
(a) Surface temperature; (b) Mass loss rate.

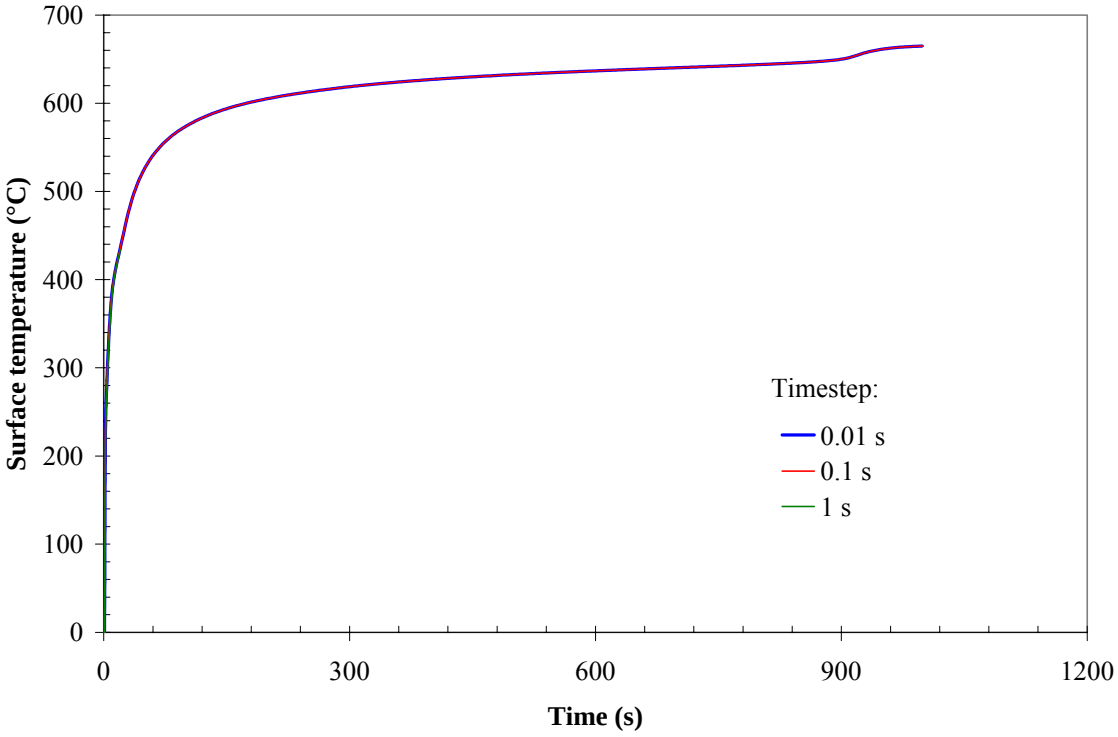

(a)

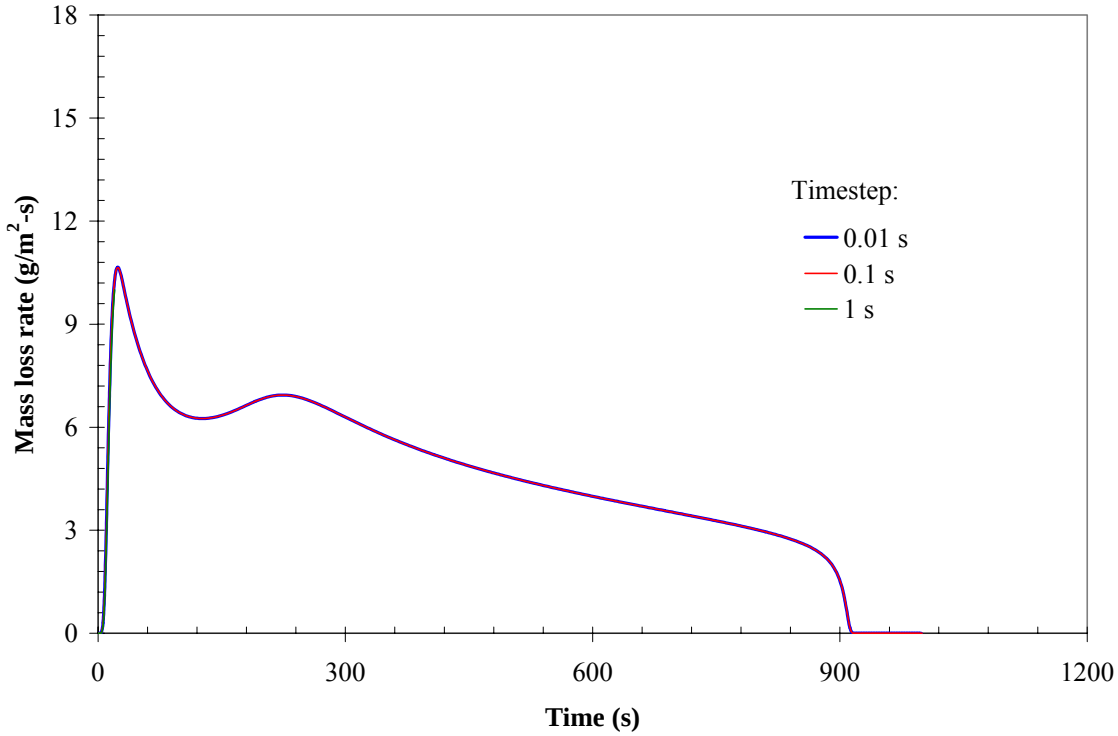

(b)

Figure 4.4. Effect of time step on charring solid pyrolysis. (a) Surface temperature; (b) Mass loss rate.

4.3 Heat of volatilization or pyrolysis

Three different values for ΔH_{vol} are investigated: 0 kJ/kg, 1000 kJ/kg, and 2000 kJ/kg. For the thermoplastic, ΔH_{vol} is considered the heat of volatilization, and for the charring material it is considered the heat of pyrolysis. Literature values for the heat of volatilization/pyrolysis are often in the range 0 – 2000 kJ/kg (see Table 2.4). Recall that a positive value of ΔH_{vol} indicates an endothermic reaction.

The results are shown in Figure 4.5 for the hypothetical thermoplastic, and Figure 4.6 for the hypothetical charring solid. It can be seen that the surface temperature and particularly the mass loss rate are sensitive to ΔH_{vol}, especially at later times. At short times (less than ~20 s) the mass loss rate is not strongly sensitive to ΔH_{vol}. This is because the mass loss rate is initially limited by the decomposition kinetics. Viewing the piloted ignition time as the time required to achieve a critical mass loss rate, it can be seen that piloted ignition times are a strong function of decomposition kinetics but are relatively insensitive to ΔH_{vol}. In comparison, burning rates are strongly sensitive to ΔH_{vol} because the mass loss rate is controlled primarily by a heat balance and ΔH_{vol} can absorb a large amount of thermal energy. However, since the decomposition kinetics also affect the heat balance, burning rates are also somewhat sensitive to decomposition kinetics, as will be illustrated more clearly in Sections 4.4 to 4.6.

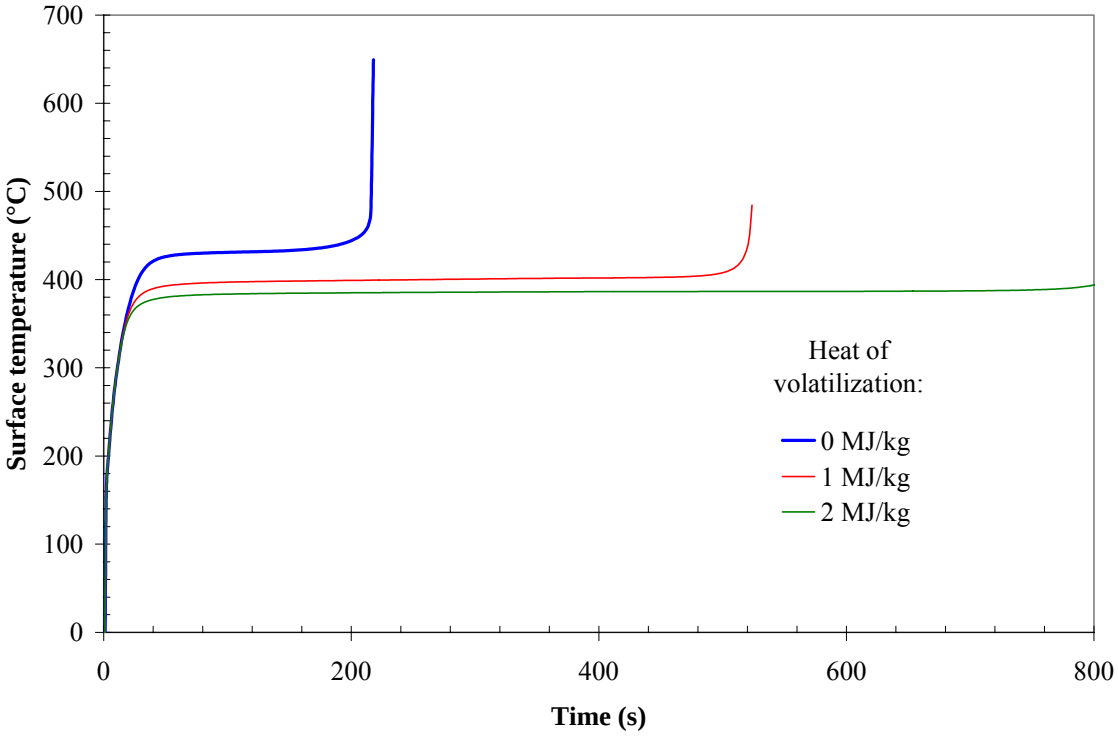

(a)

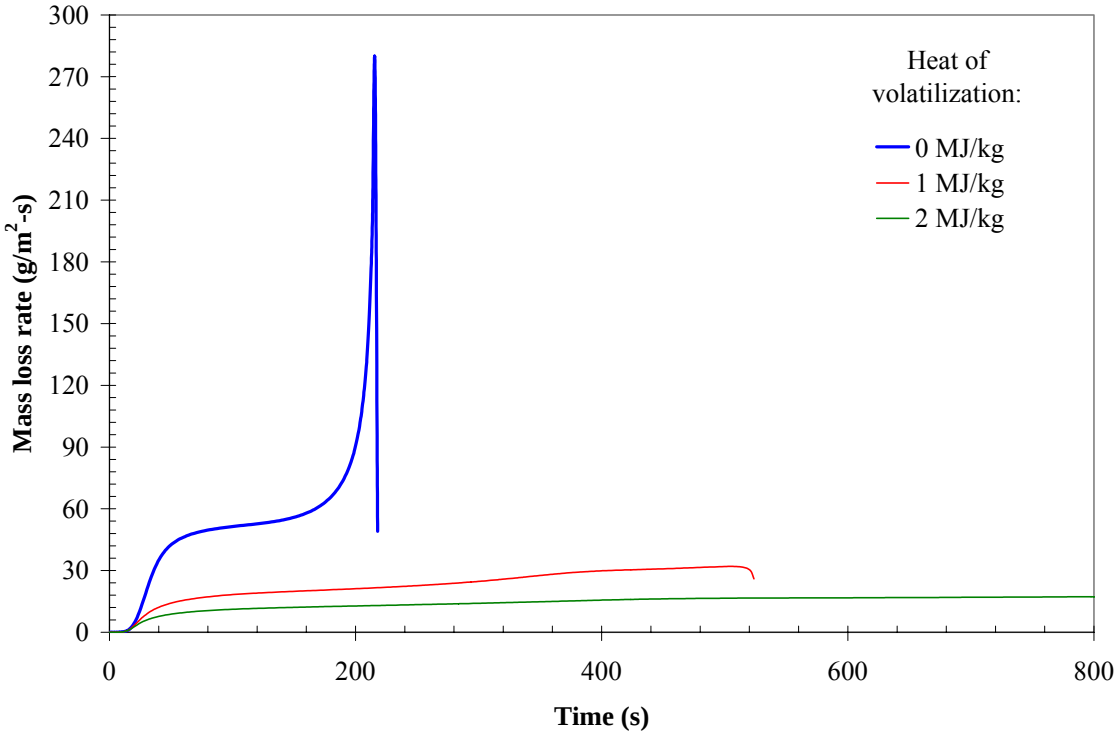

(b)

Figure 4.5. Effect of heat of volatilization on thermoplastic pyrolysis. (a) Surface temperature; (b) Mass loss rate.

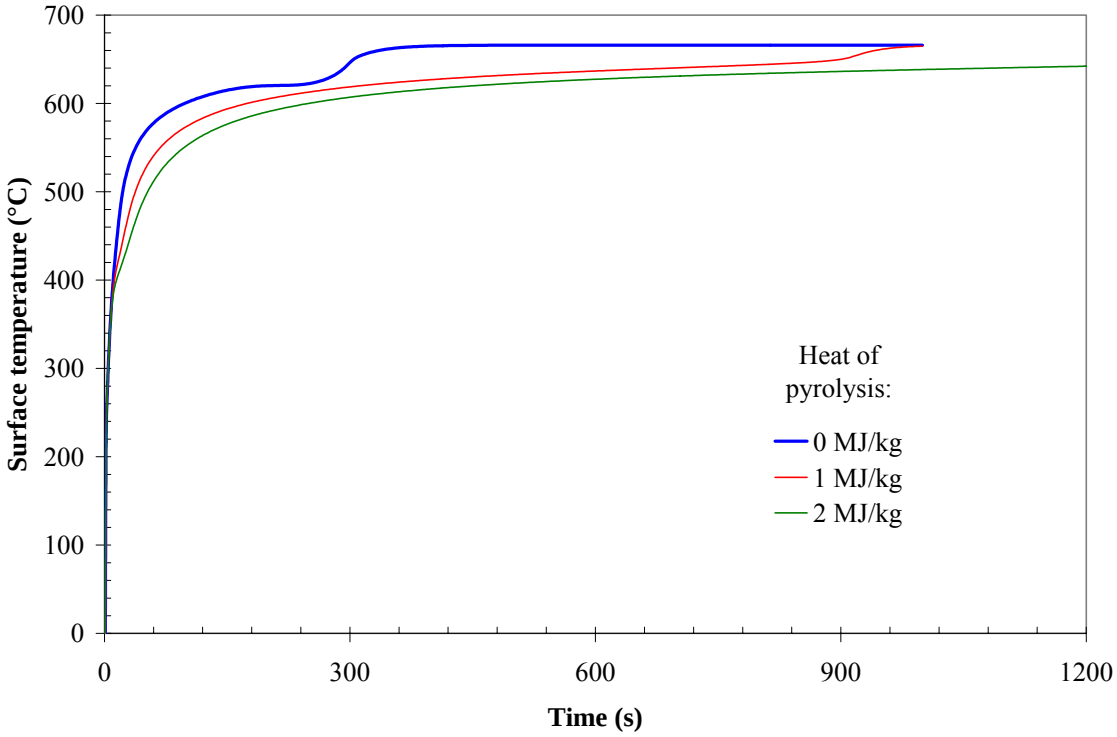

(a)

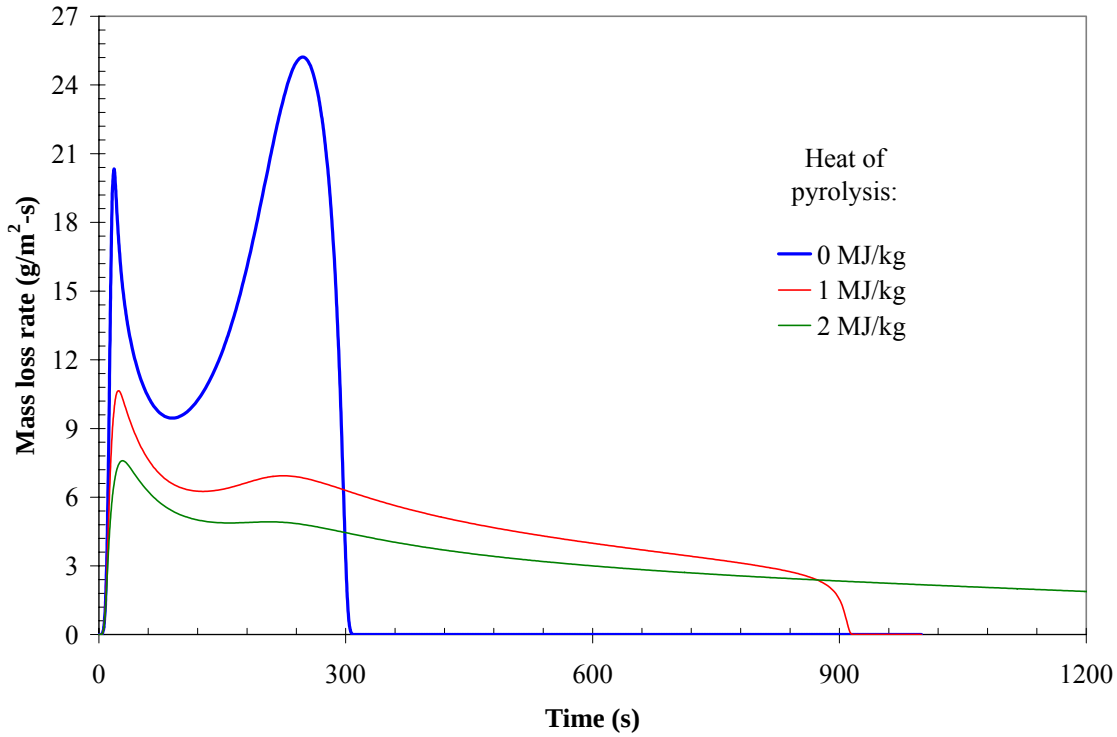

(b)

Figure 4.6. Effect of heat of pyrolysis on charring solid pyrolysis. (a) Surface temperature; (b) Mass loss rate.

4.4 Activation energy

The effect of the activation energy on the calculated surface temperature and mass loss rate is shown in Figure 4.7 (thermoplastic) and Figure 4.8 (charring solid). For the thermoplastic, both the surface temperature and the mass loss rate are quite sensitive to the activation energy. Specifically, the mass loss rate increases as the activation energy decreases. Since the pyrolysis reaction is endothermic (ΔH_{vol} = +1000 kJ/kg), the surface temperature decreases as the mass loss rate is increased, i.e. as the activation energy is decreased. It is interesting to note that as the surface temperature is decreased, the net heat flux to the solid increases since both convective and radiative surface losses are reduced.

Similar trends are seen for the charring solid: a decrease in activation energy results in an increase in the mass loss rate. The surface temperature also increases with an increase in the activation energy, but this effect is subtle in comparison to the large effect seen with the thermoplastic solid.

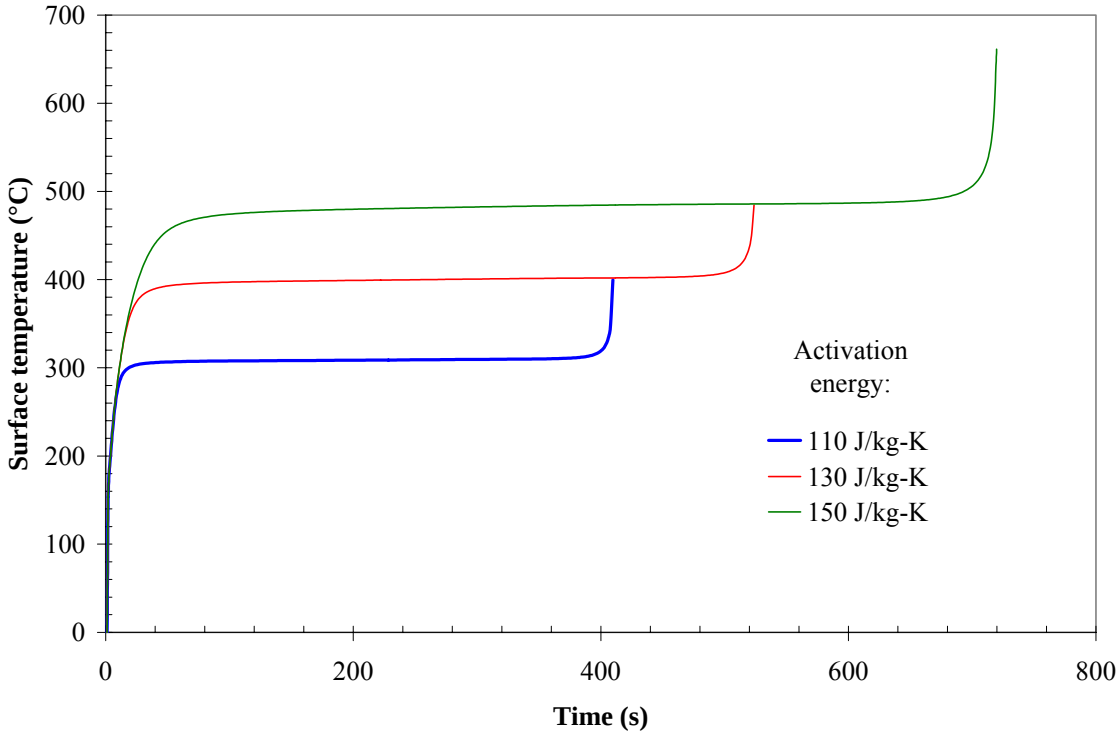

(a)

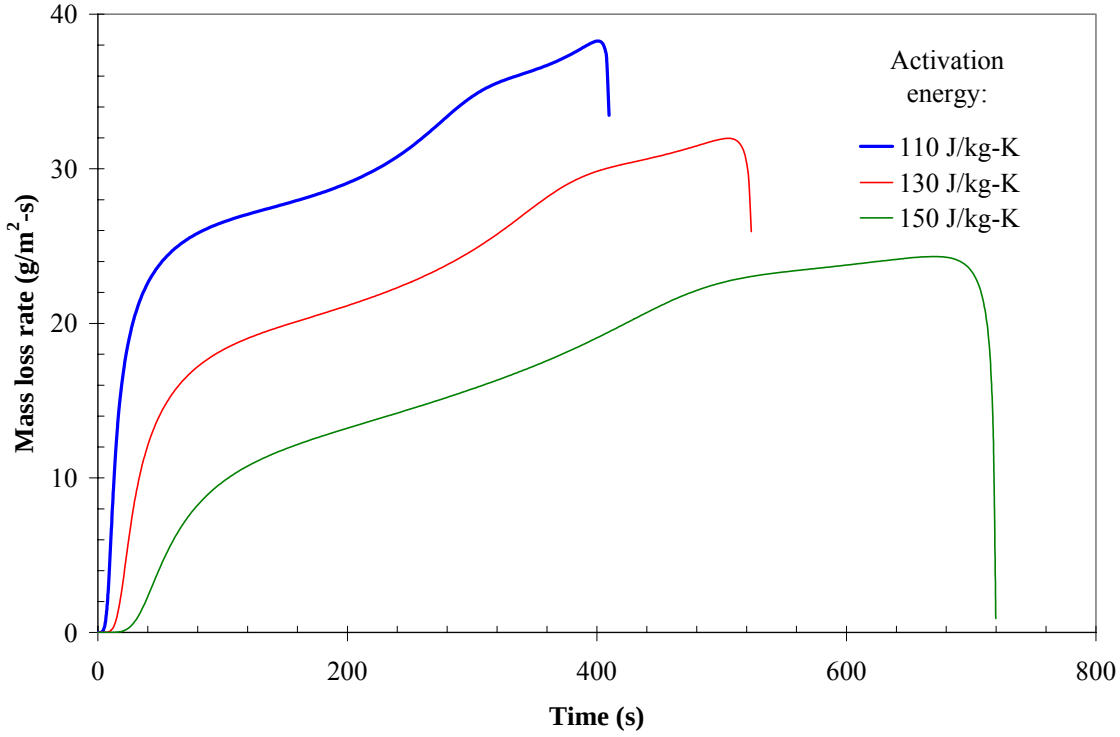

(b)

Figure 4.7. Effect of activation energy on thermoplastic pyrolysis. (a) Surface temperature; (b) Mass loss rate.

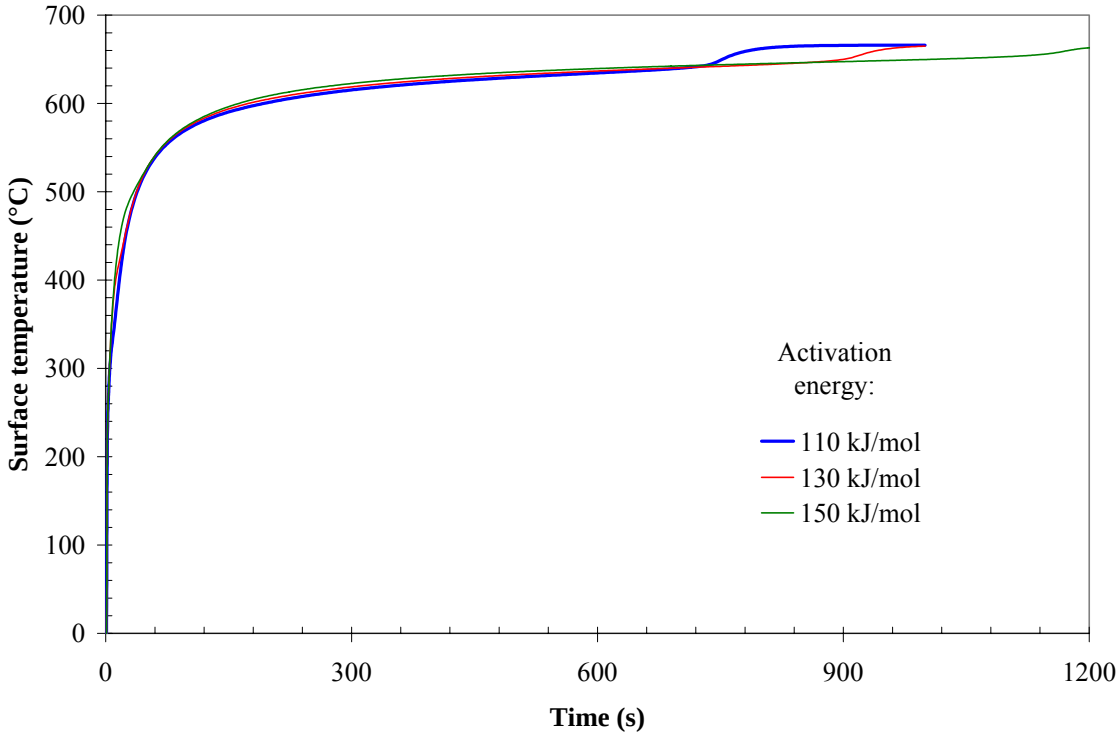

(a)

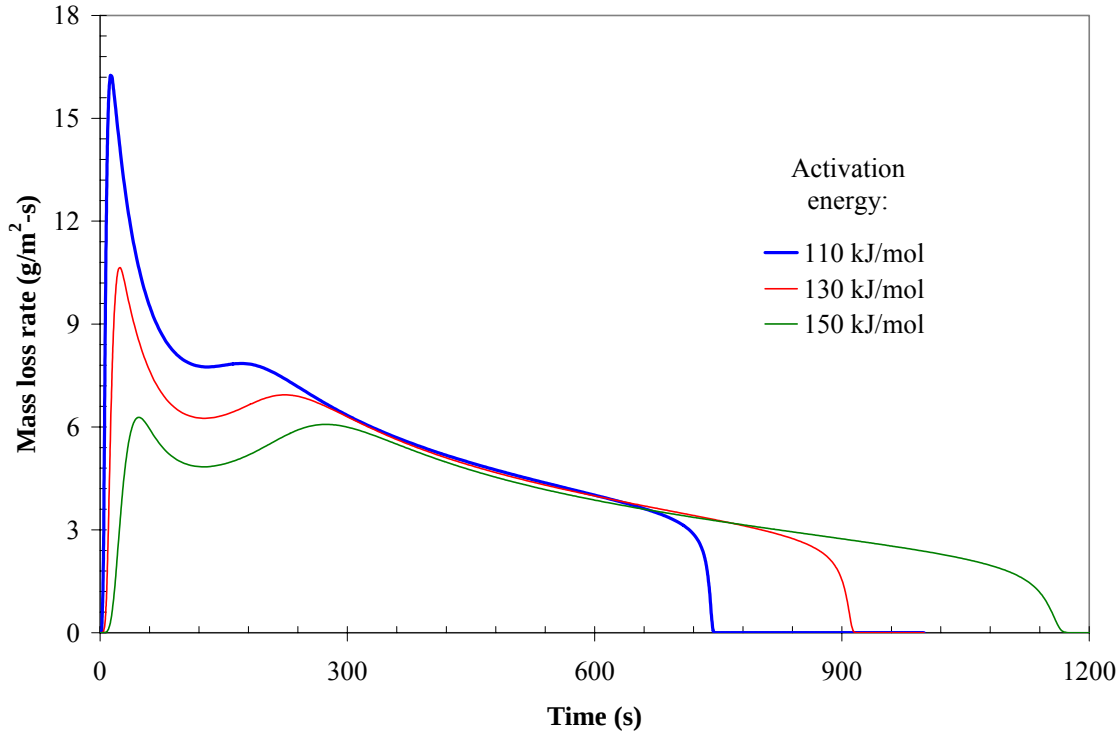

(b)

Figure 4.8. Effect of activation energy on charring solid pyrolysis. (a) Surface temperature; (b) Mass loss rate.

4.5 Pre–exponential factor

The effect of the pre–exponential factor is similar to the activation energy. Figure 4.9 shows the calculated surface temperature and mass loss rate of the thermoplastic solid, and Figure 4.10 shows the same for the charring solid. Interestingly, varying the pre–exponential factor by +/– 1 order of magnitude has a smaller effect than varying the activation energy by +/– 20 kJ/mol.

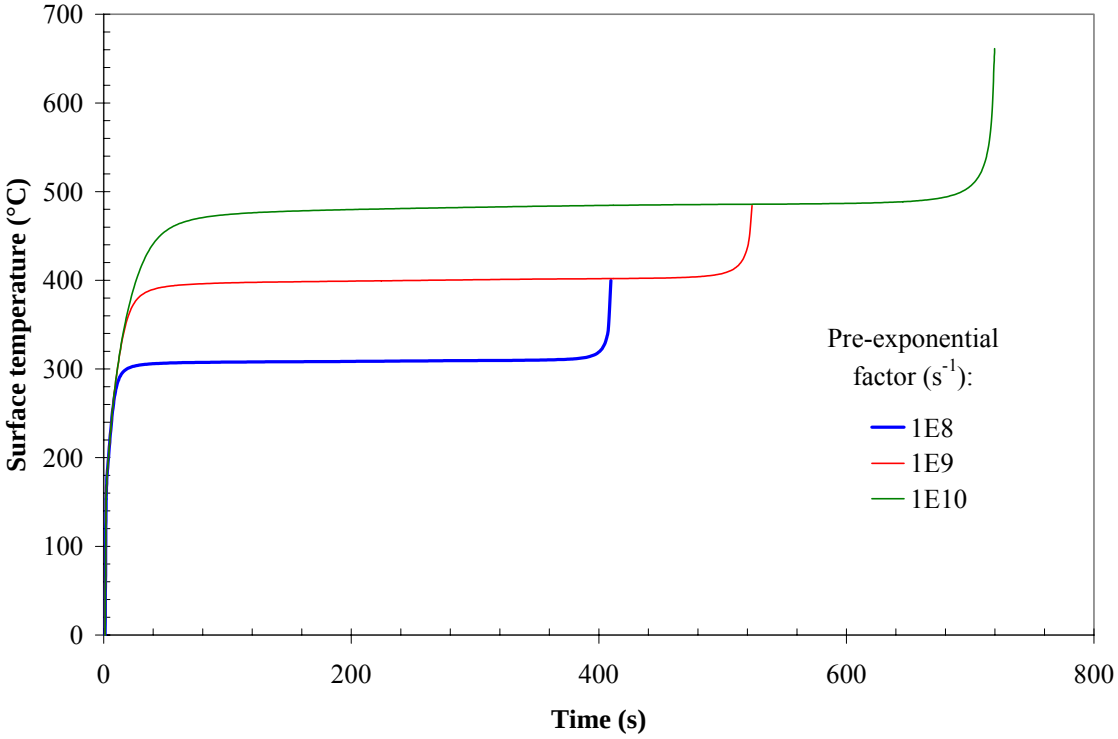

(a)

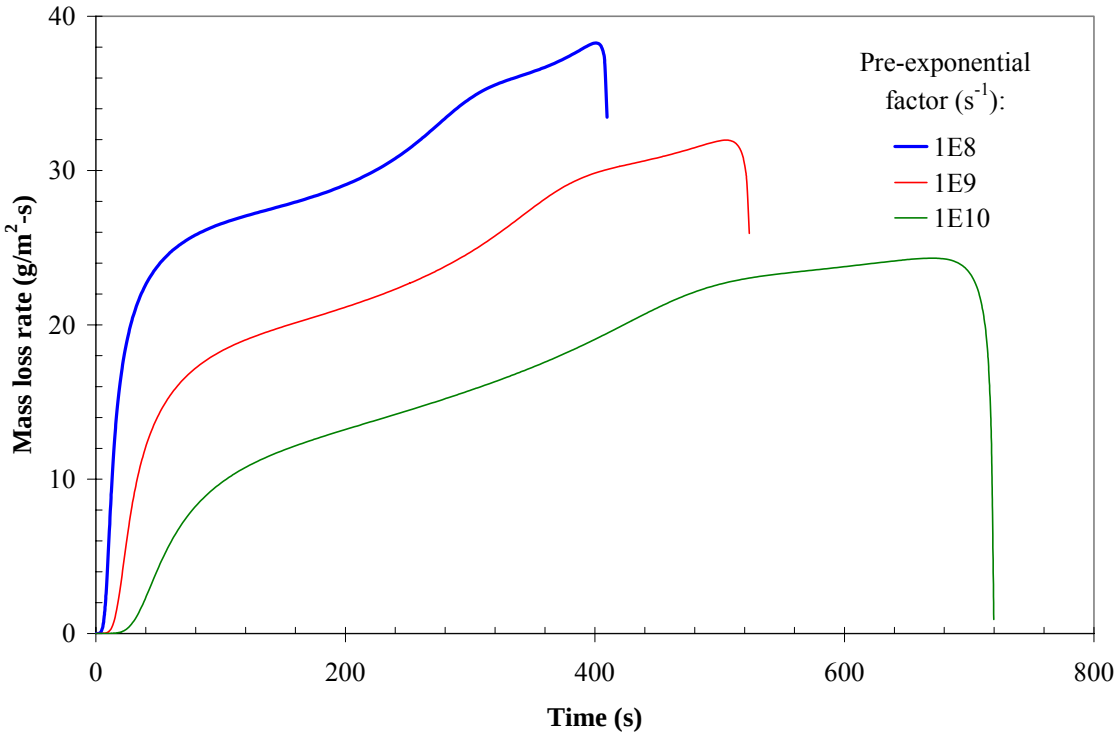

(b)

Figure 4.9. Effect of pre–exponential factor on thermoplastic pyrolysis. (a) Surface temperature; (b) Mass loss rate.

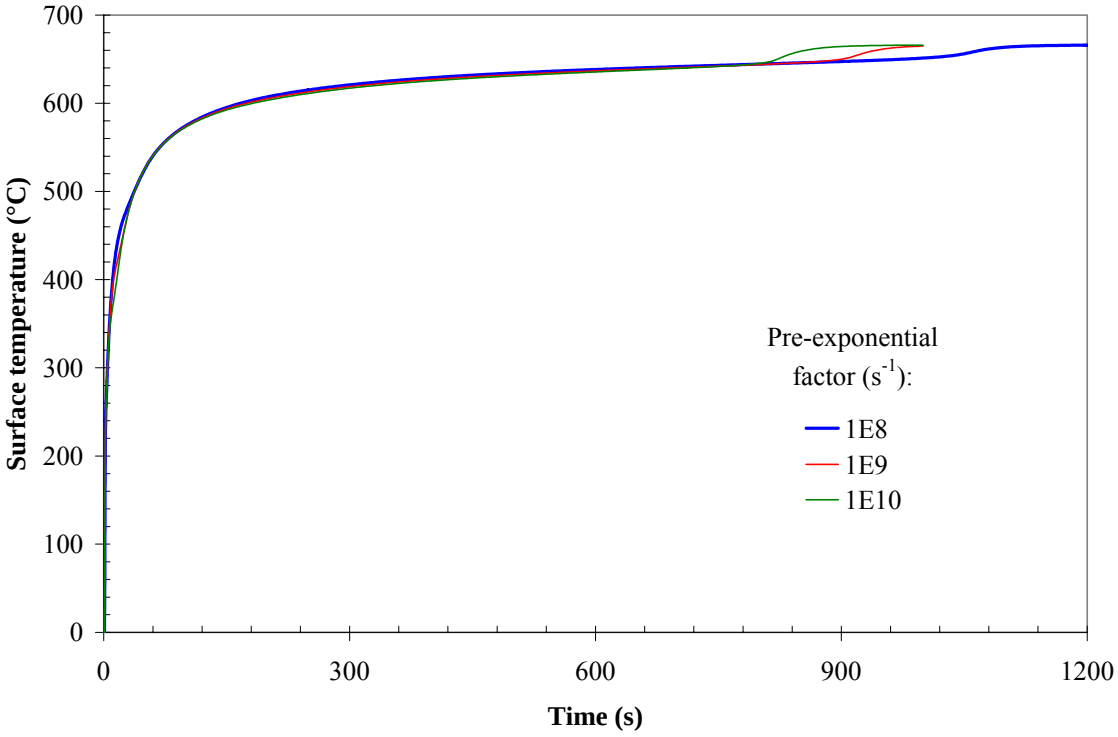

(a)

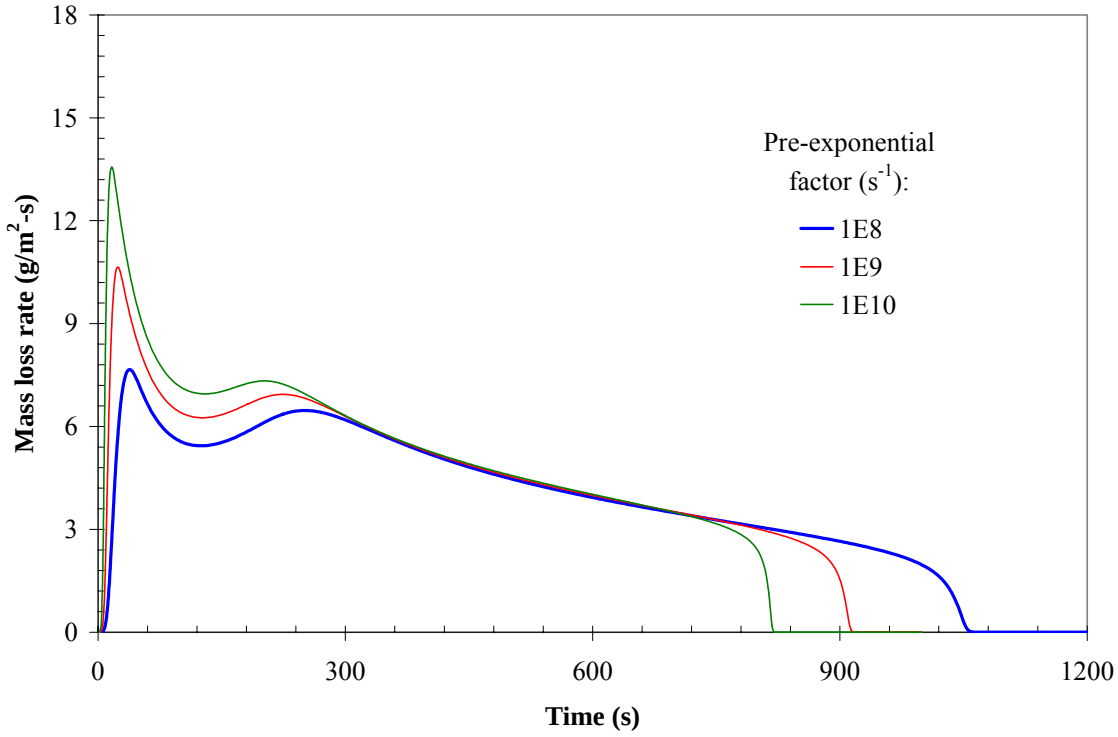

(b)

Figure 4.10. Effect of pre–exponential factor on charring solid pyrolysis. (a) Surface temperature; (b) Mass loss rate.

4.6 Reaction order

The effect of the reaction order is shown in Figures 4.11 (thermoplastic) and 4.12 (charring solid). It can be seen from Figure 4.11 that for the thermoplastic the mass loss rate increases as the reaction order is decreased. Consequently, the surface temperature decreases as the reaction order decreases. The reaction order also affects the overall shape of the mass loss rate curve. At higher reaction orders, the features of the mass loss rate curve are somewhat "softened", e.g. the drop off in the mass loss rate curve as the material is almost completely consumed is not as sharp at higher reaction orders. The reason for this is that from Equation 3.58, the destruction rate of condensed phase species A is proportional to $\left(\frac{\bar{\rho} Y_A \Delta z}{\left(\bar{\rho} Y_A \Delta z \right)_\Sigma} \right)^n$ where n is the reaction order. When the numerator of this quantity is smaller than the denominator (as happens in the later stages of pyrolysis) the reaction rate is smaller for higher values of n, explaining why the mass loss rate decreases as the reaction order increases.

The effect of the reaction order is more apparent for the thermoplastic than for the charring solid. In fact, the reaction order does not have a significant effect on the surface temperature or mass loss rate curves for the charring solid (Figure 4.12). However, it can be seen from the first peak in the mass loss rate curve (around 40 s) that the mass loss rate increases with decreasing reaction order, as it does for the thermoplastic solid. For a reaction order of 0.5, the mass loss rate curve shows non–physical oscillations, but the magnitude of these oscillations is so small that this is probably not a practical concern.

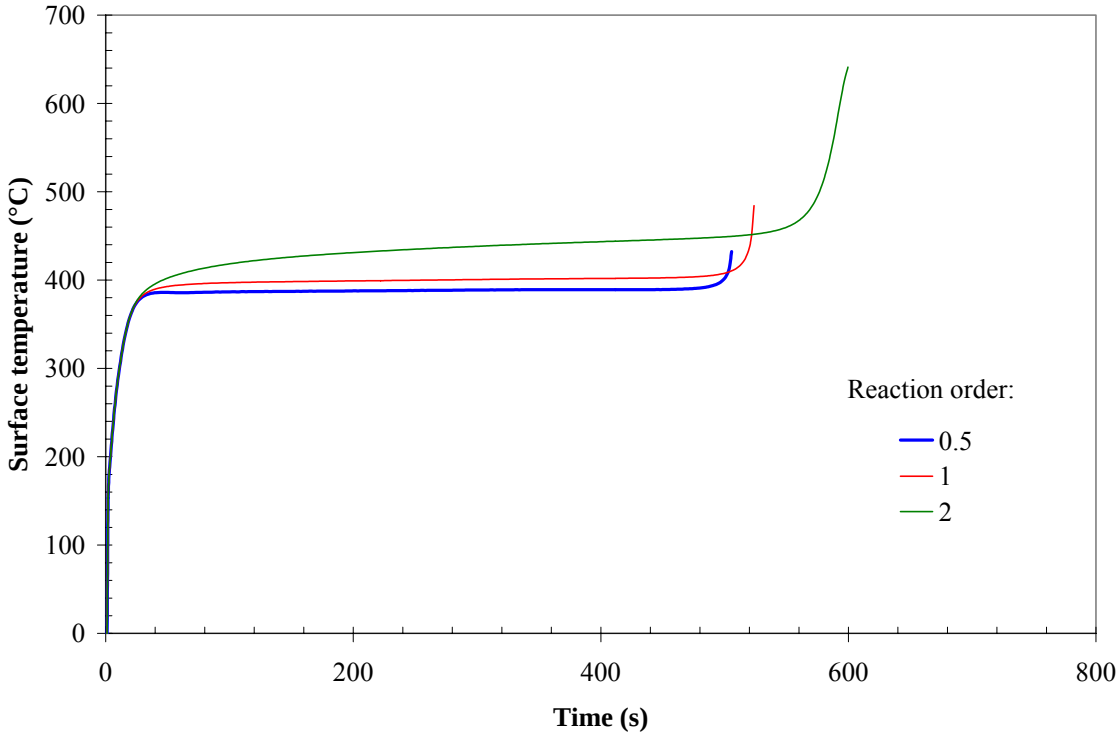

(a)

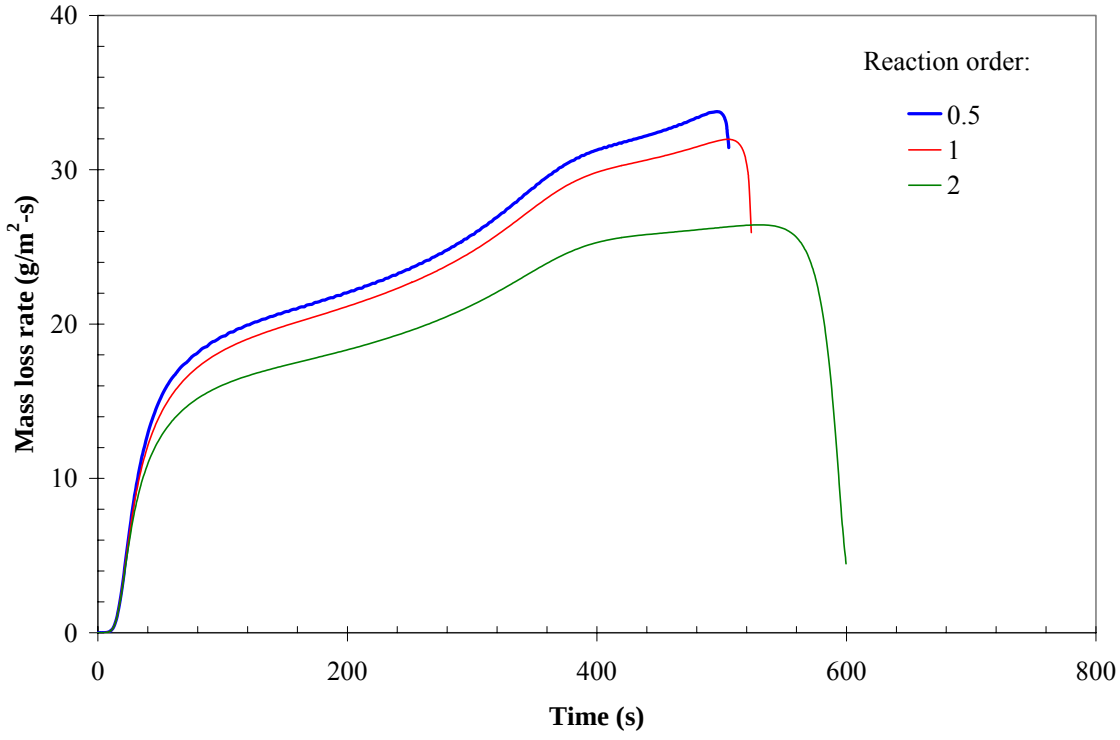

(b)

Figure 4.11. Effect of reaction order on thermoplastic pyrolysis. (a) Surface temperature; (b) Mass loss rate.

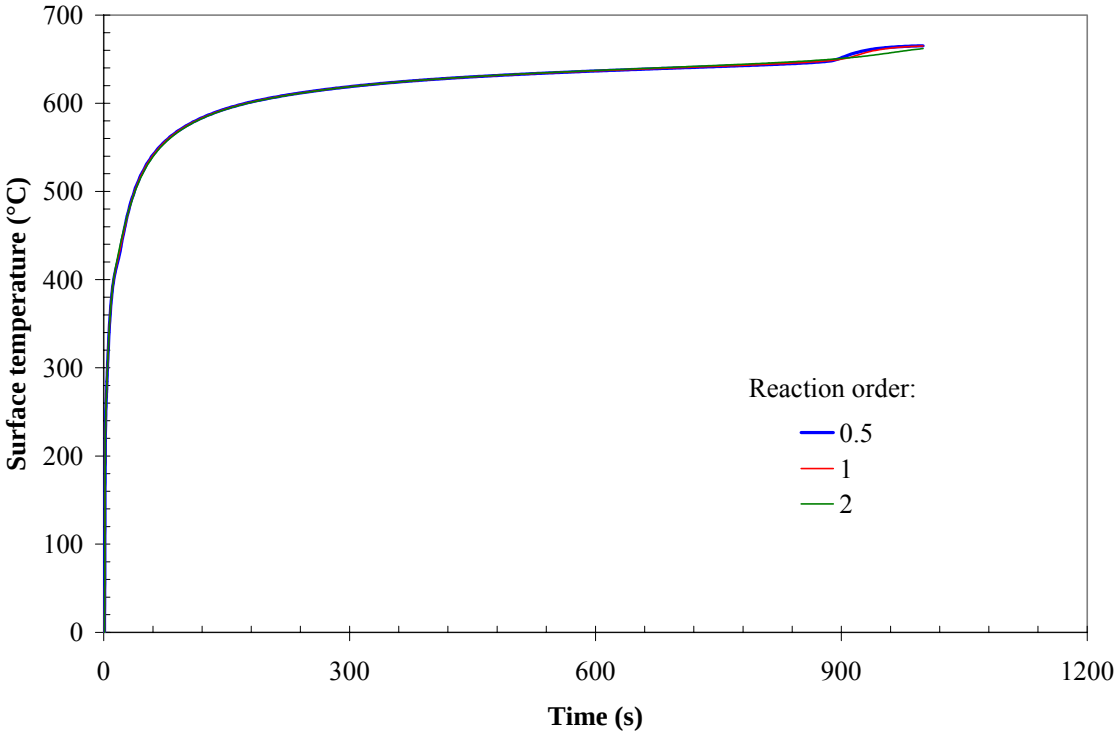

(a)

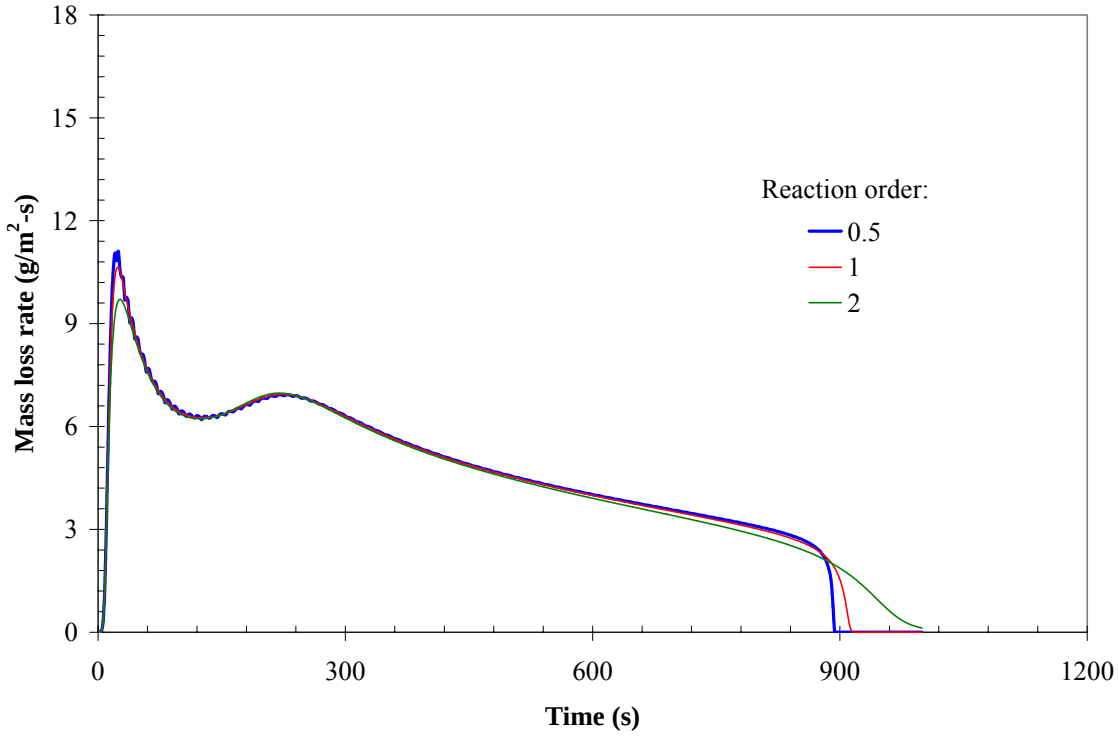

(b)

Figure 4.12. Effect of reaction order on charring solid pyrolysis. (a) Surface temperature; (b) Mass loss rate.

4.7 Reaction order treatment

Two different treatments of reaction order are presented in Section 3.2.1. The default treatment in this work is slightly different than the conventional approach, and is referred to below as the "unconventional" treatment. From Equations 3.55 and 3.56, the conversion of condensed phase species *i* (α_i) is calculated here as:

$$1-\alpha_i = \frac{m_i''}{m_{i\Sigma}''} = \frac{\overline{\rho} Y_i \Delta z}{\left(\overline{\rho} Y_i \Delta z\right)_\Sigma}$$

$$\left(\overline{\rho} Y_i \Delta z\right)_\Sigma \equiv \left(\overline{\rho} Y_i \Delta z\right)\Big|_{t=0} + \int_0^t \dot{\omega}_{fi}'''(\tau)\Delta z(\tau)\mathrm{d}\tau$$

Doing so ensures that the conversion may fall in the range $0 \le \alpha_i \le 1$. The "conventional" treatment involves replacing $\left(\overline{\rho} Y_i \Delta z\right)_\Sigma$ with $\left(\overline{\rho} Y_i \Delta z\right)\Big|_{t=0}$. As explained earlier, this effectively places a lower limit on the value of α_i for intermediate species, and the conversion cannot approach 0.

To investigate the effect of the conventional vs. unconventional treatment of reaction order, a second reaction was added to the hypothetical charring material. This reaction converts char to ash (having a bulk density of 5 kg/m^3). It is assumed to be a second order reaction with pre–exponential factor $Z = 1 \times 10^{11}$ s^{-1} and activation energy E = 150 kJ/mol. A comparison of the conventional and the unconventional approach to reaction order treatment is shown in Figure 4.13. It can be seen that, for this hypothetical material, there is almost no difference between the two approaches. However, this is not necessarily a general conclusion.

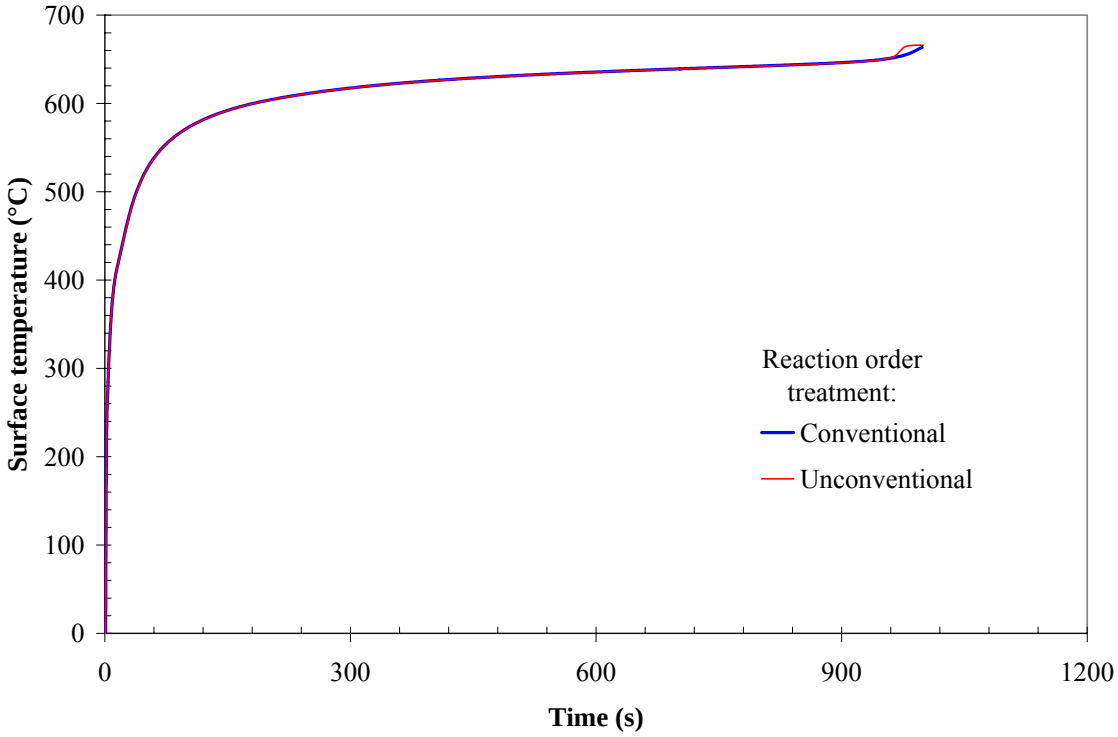

(a)

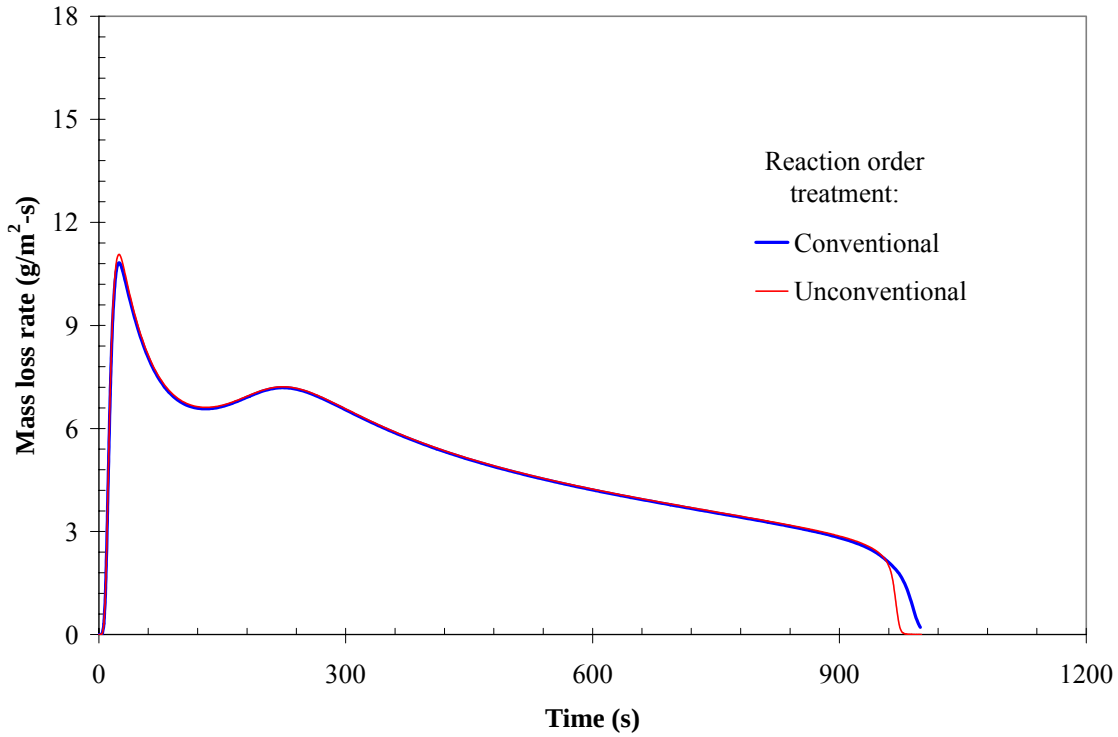

(b)

Figure 4.13. Effect of reaction order treatment on charring solid pyrolysis. (a) Surface temperature; (b) Mass loss rate.

4.8 Radiative characteristics

Real–world solids often absorb radiation in–depth. Although the wavelength–dependency of this process is beyond the scope of the present work, the model does include the ability to specify a band mean radiation absorption coefficient (κ, m^{-1}, see Equations 3.27 and 3.28). Similarly, in porous solids at high temperatures, radiation can transport heat across pores. This is simulated with a radiant conductivity that depends on the third power of temperature. As indicated in Equation 3.4, the parameter that controls this radiant conductivity is denoted γ and has units of m. In this section, the effect of κ is investigated for the thermoplastic, and the effect of γ is investigated for the charring solid. Note that γ for the "wood" was assumed to be zero, but the "char" had a nonzero value of γ.

Figure 4.14 shows the effect of κ on the calculated surface temperature and mass loss rate for the thermoplastic. As κ is decreased, more radiation is absorbed in–depth, leading to a reduction in the surface temperature. Initially, the mass loss rate is kinetically limited and strongly sensitive to the temperature near the surface, so lower values of κ correspond to lower mass loss rates. At later times, the mass loss rate increases with a reduction in κ because the net heat flux to the solid is higher due to the reduced surface temperature.

Figure 4.15 shows the effect of γ on the calculated surface temperature and mass loss rate for the charring solid. Since higher values of γ increase the effective thermal conductivity of the char layer, the surface temperature decreases as γ is increased because more heat is conducted away from the surface to the interior of the solid. This increases the mass loss rate because more heat reaches the interior reaction zone.

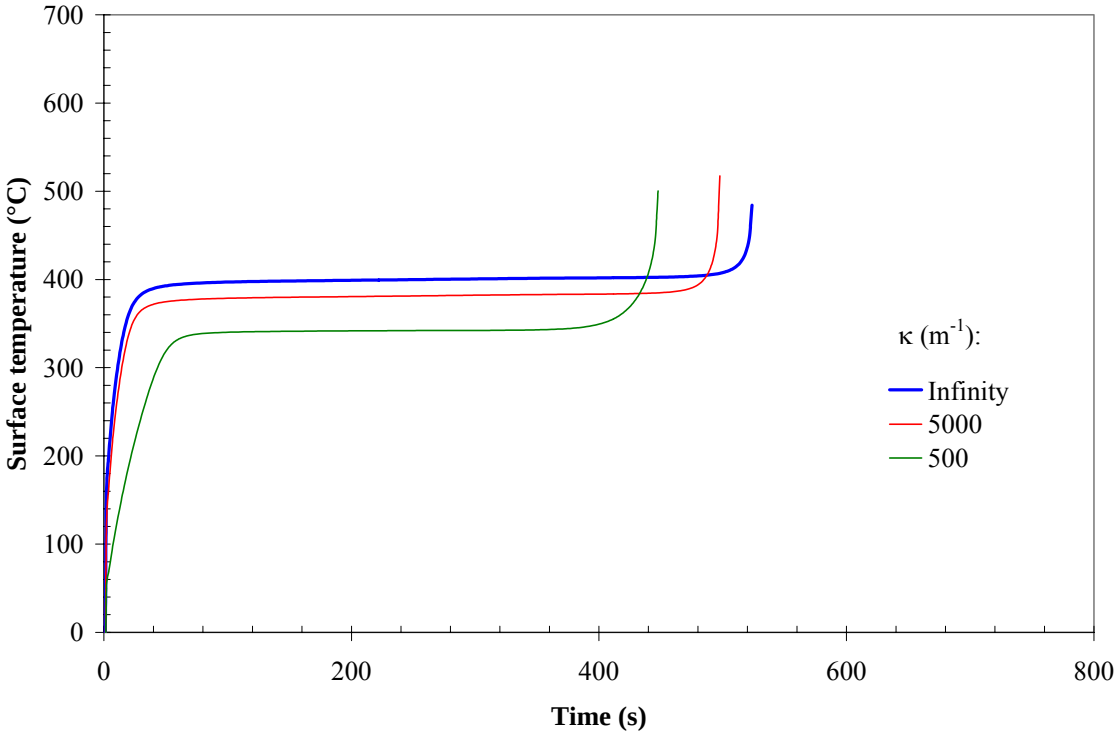

(a)

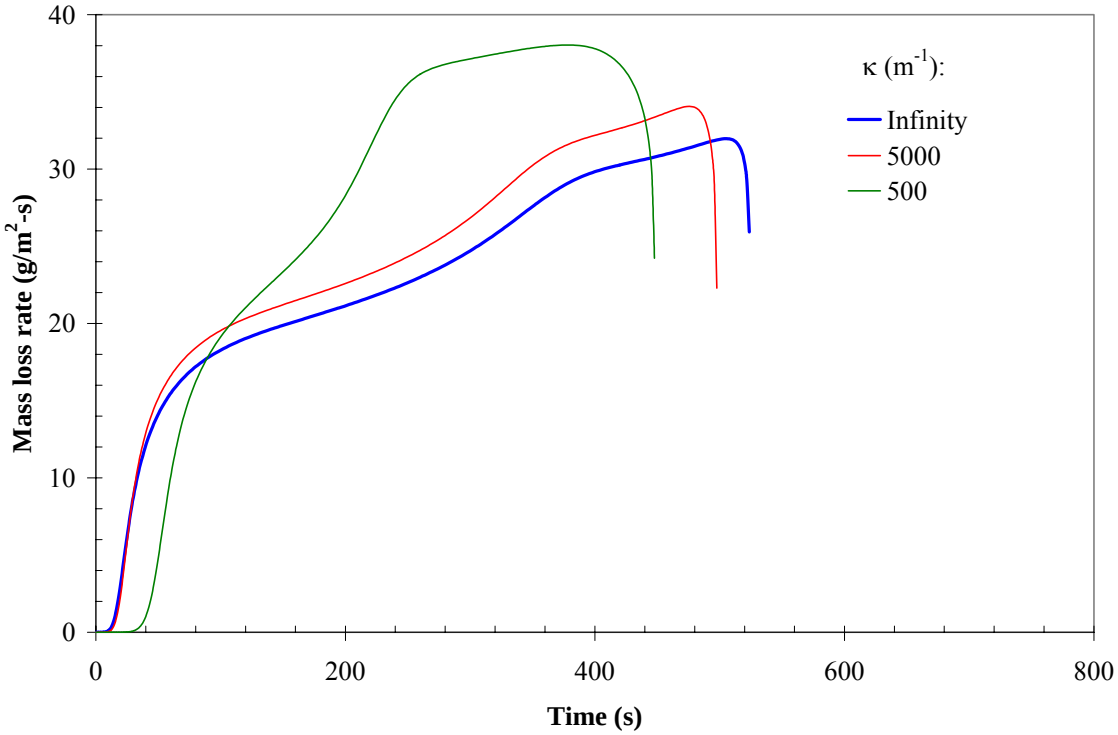

(b)

Figure 4.14. Effect of in–depth absorption coefficient on thermoplastic pyrolysis. (a) Surface temperature; (b) Mass loss rate.

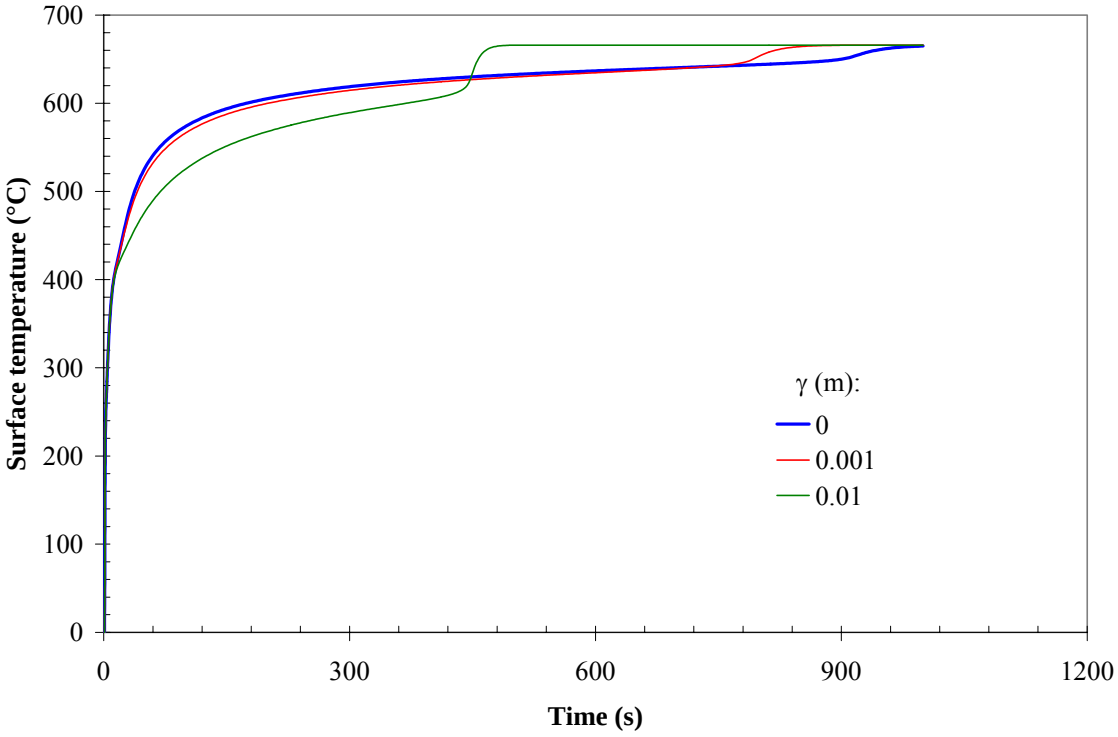

(a)

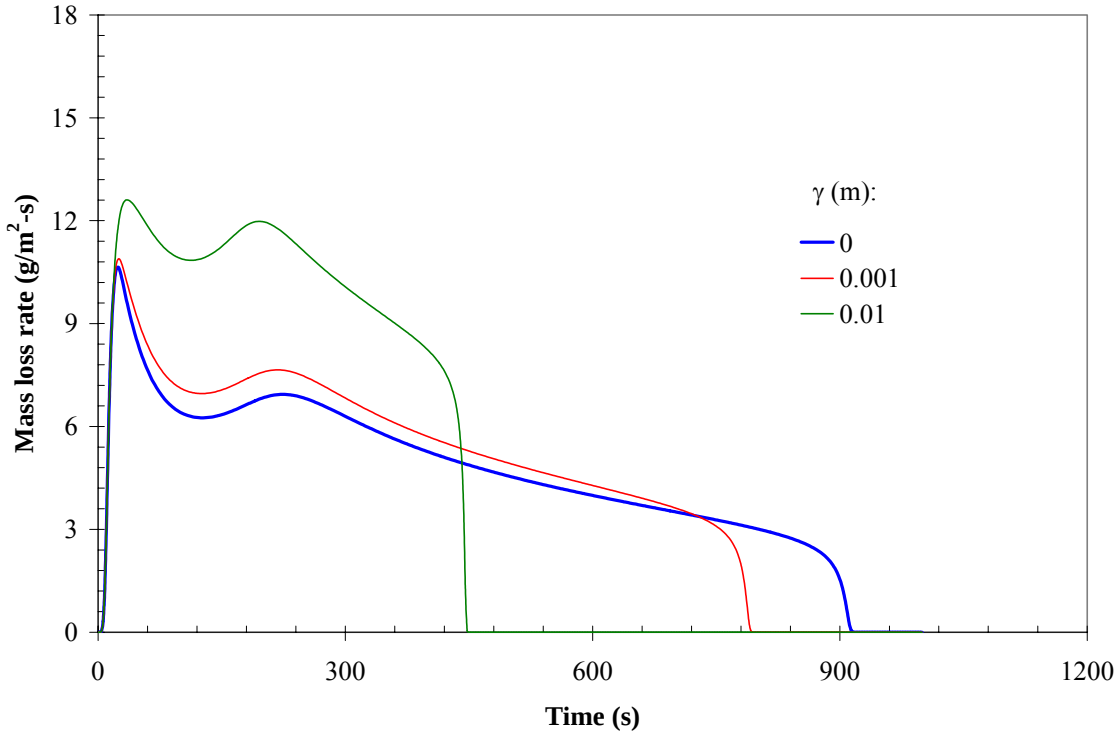

(b)

Figure 4.15. Effect of γ on charring solid pyrolysis.
(a) Surface temperature; (b) Mass loss rate.

4.9 Thermal conductivity

The effect of the thermal conductivity on the calculated surface temperature and mass loss rate is shown in Figure 4.16 for the thermoplastic and Figure 4.17 for the charring solid. As shown in Figure 4.16a, the surface temperature decreases as the thermal conductivity is increased. This is because more heat is conducted to the interior of the material as the thermal conductivity is increased. Figure 4.16b shows that mass loss rates are initially higher for lower values of thermal conductivity (for $t < \sim 150$ s). The initial mass loss rates are kinetically limited, meaning that they are strongly sensitive to the temperature near the surface, which is higher for lower values of thermal conductivity. At later stages, the mass loss rates are controlled more by a heat balance than by kinetics. Since a higher thermal conductivity translates to a lower surface temperature, the radiative and convective heat losses are smaller and therefore more of the incident radiant heat flux is available to pyrolyze the solid. For long times, this leads to an increase in the mass loss rate with increasing thermal conductivity.

The effect of the thermal conductivity on the calculated surface temperature and mass loss rate for the charring solid (Figure 4.17) show similar trends as those for the thermoplastic. The surface temperatures increase as the thermal conductivity decreases. Initially, the mass loss rate is higher for the lower thermal conductivities, but at long times it is higher. Note that the thermal conductivities listed in the legend of Figure 4.17 correspond to the "wood" and the "char", i.e. the blue line corresponds to the case where wood has a thermal conductivity of 0.1 W/m–K, and the char has a thermal conductivity of 0.05 W/m–K.

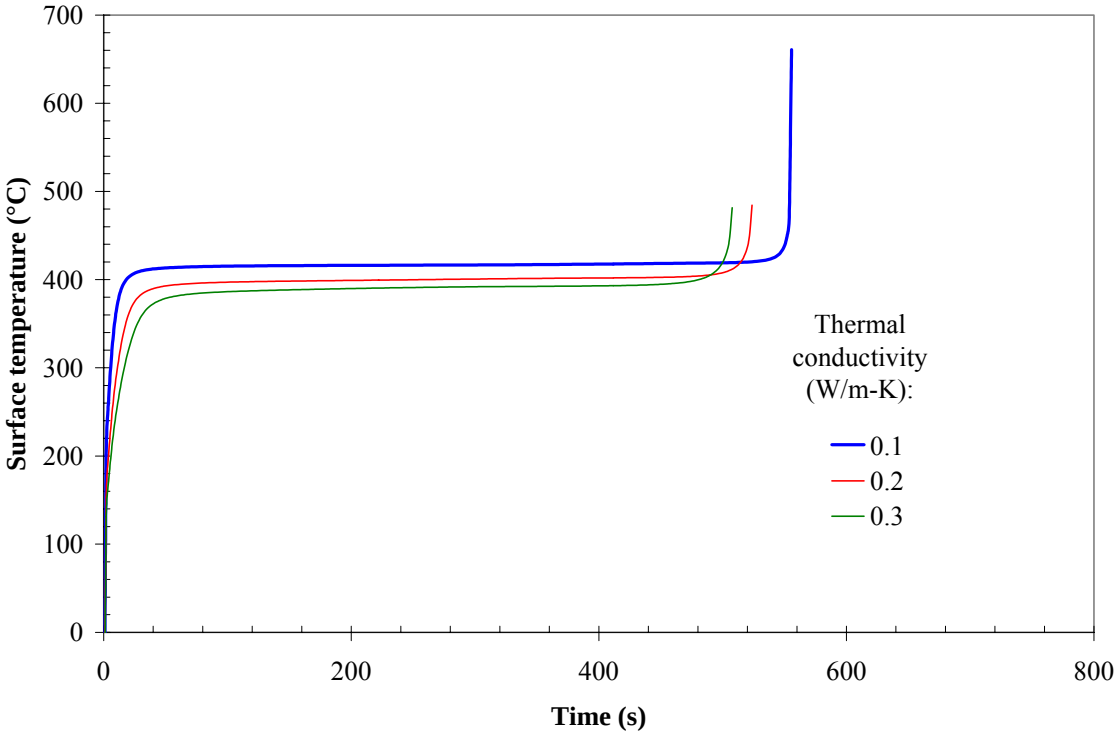

(a)

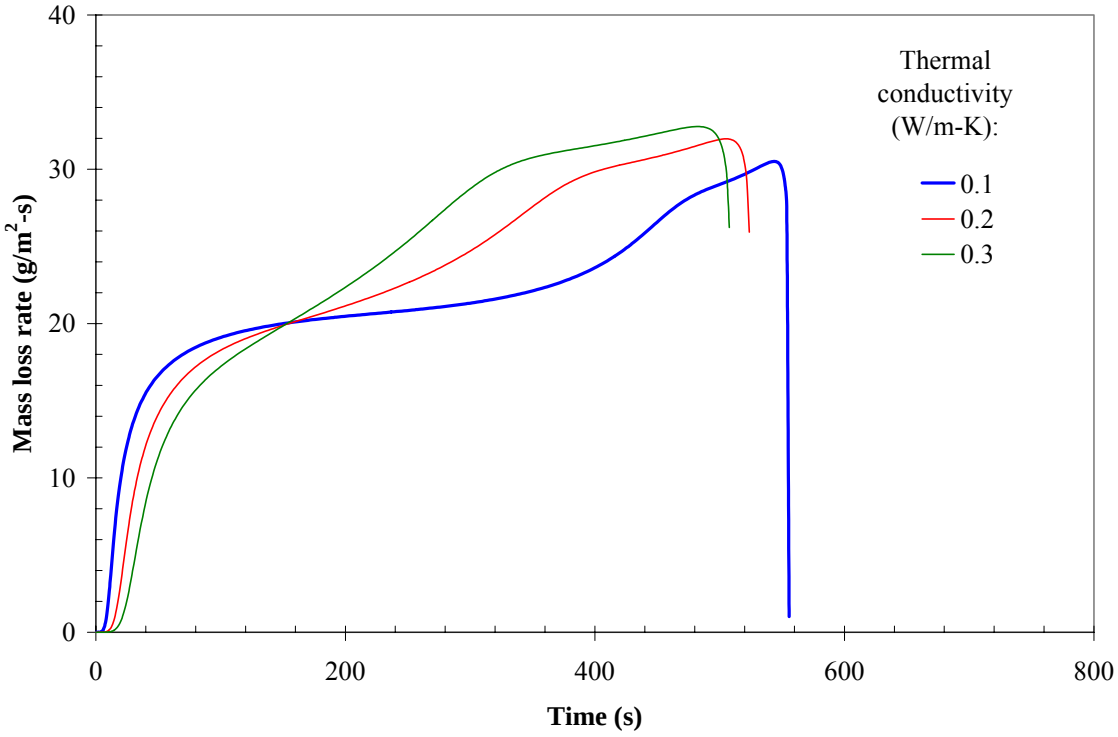

(b)

Figure 4.16. Effect of thermal conductivity on thermoplastic pyrolysis. (a) Surface temperature; (b) Mass loss rate.

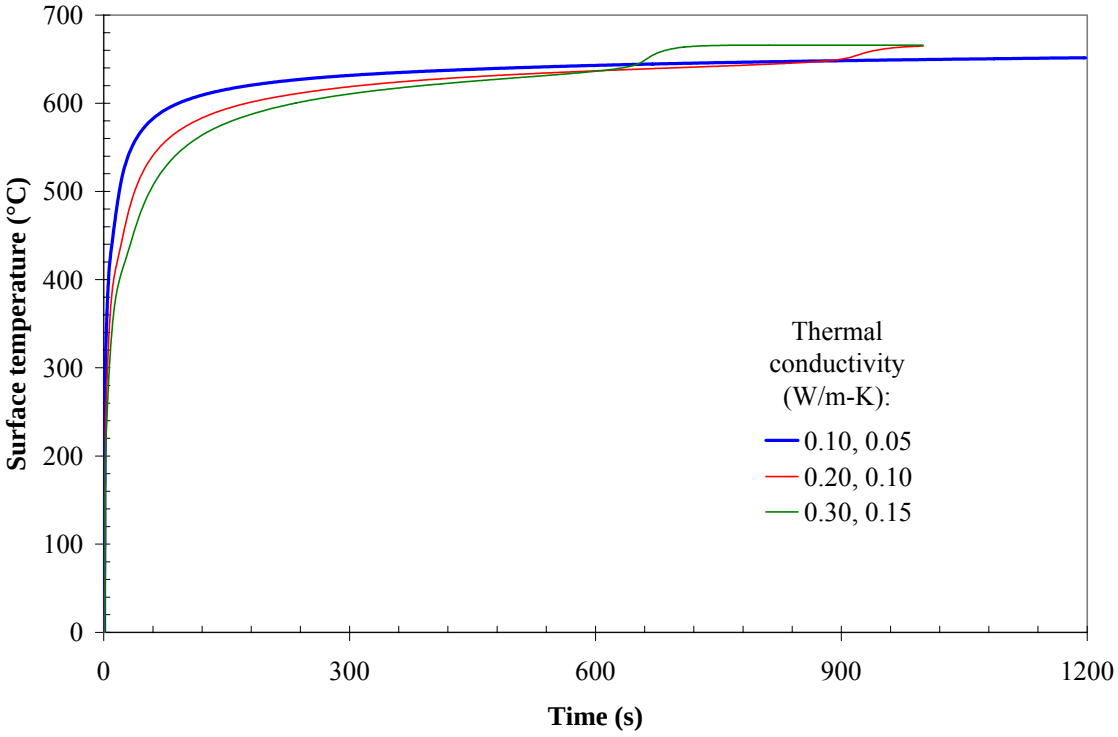

(a)

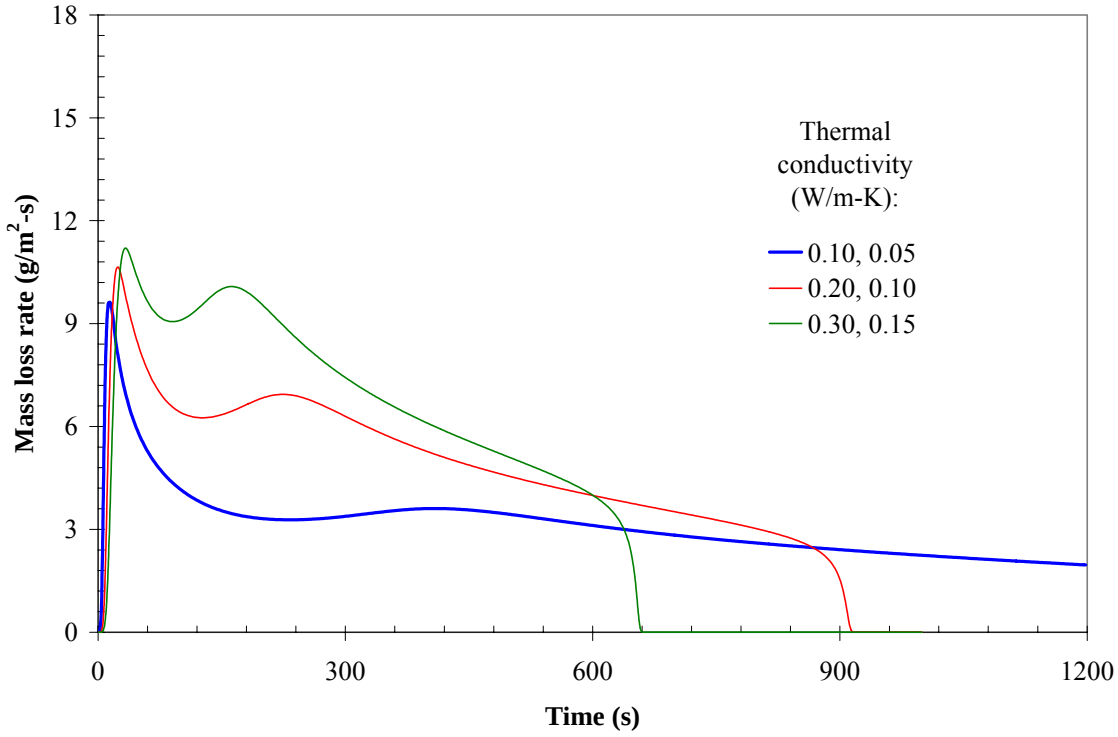

(b)

Figure 4.17. Effect of thermal conductivity on charring solid pyrolysis. (a) Surface temperature; (b) Mass loss rate.

4.10 Specific heat capacity

The effect of the specific heat capacity on the calculated surface temperature and mass loss rate curves is shown in Figure 4.18 for the hypothetical thermoplastic, and Figure 4.19 for the hypothetical charring solid. For the thermoplastic, the initial temperature rise is reduced as the specific heat capacity is increased, but the long–time surface temperatures are not strongly sensitive to the specific heat capacity. In the absence of reactions, the equilibrium (steady–state) surface temperature does not depend on the specific heat capacity. Thus, the minor differences in the surface temperature seen for the different specific heat capacities are caused by differences in the mass loss rate evident in Figure 4.18b. As expected, the mass loss rate decreases as the specific heat capacity is increased because the quantity of heat required to generate the volatiles is increased as the specific heat capacity is increased. The trends for the charring solid (Figure 4.19) are similar to those for the thermoplastic.

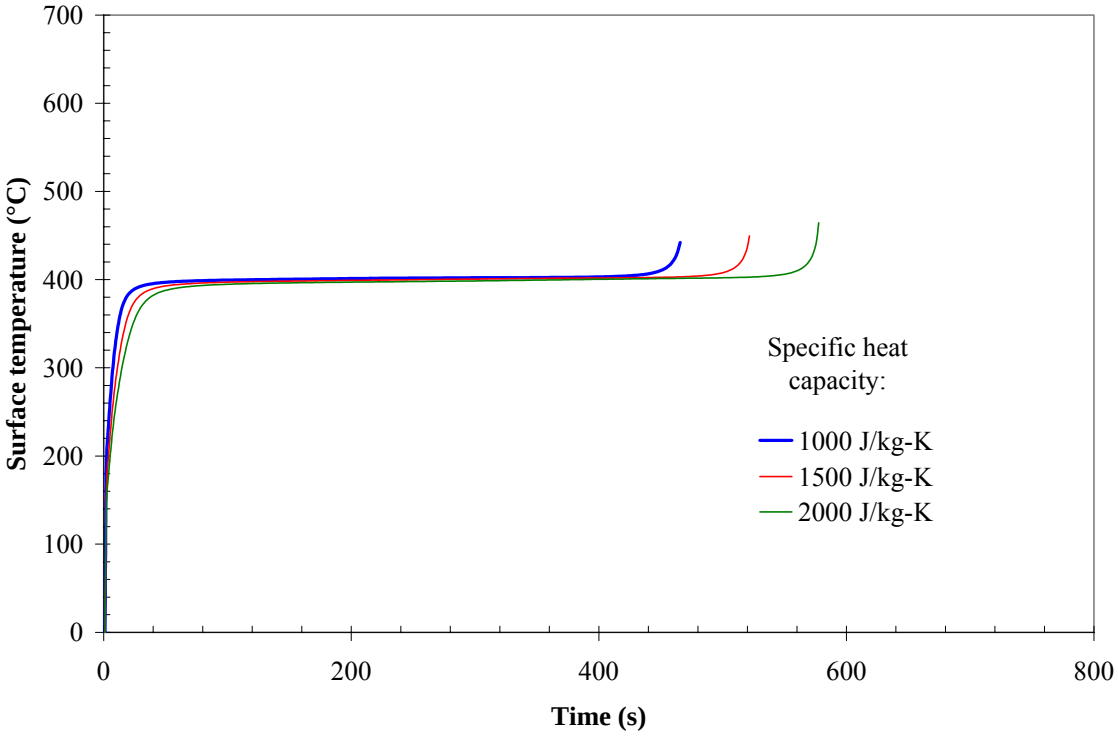

(a)

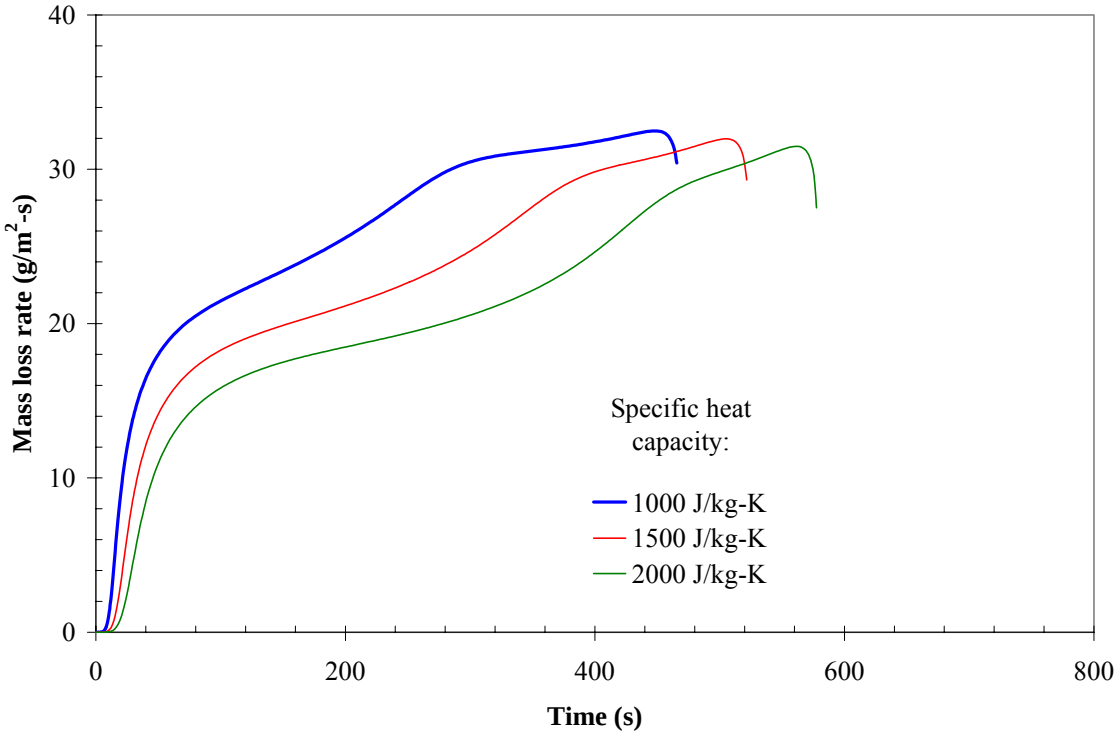

(b)

Figure 4.18. Effect of specific heat capacity on thermoplastic pyrolysis. (a) Surface temperature; (b) Mass loss rate.

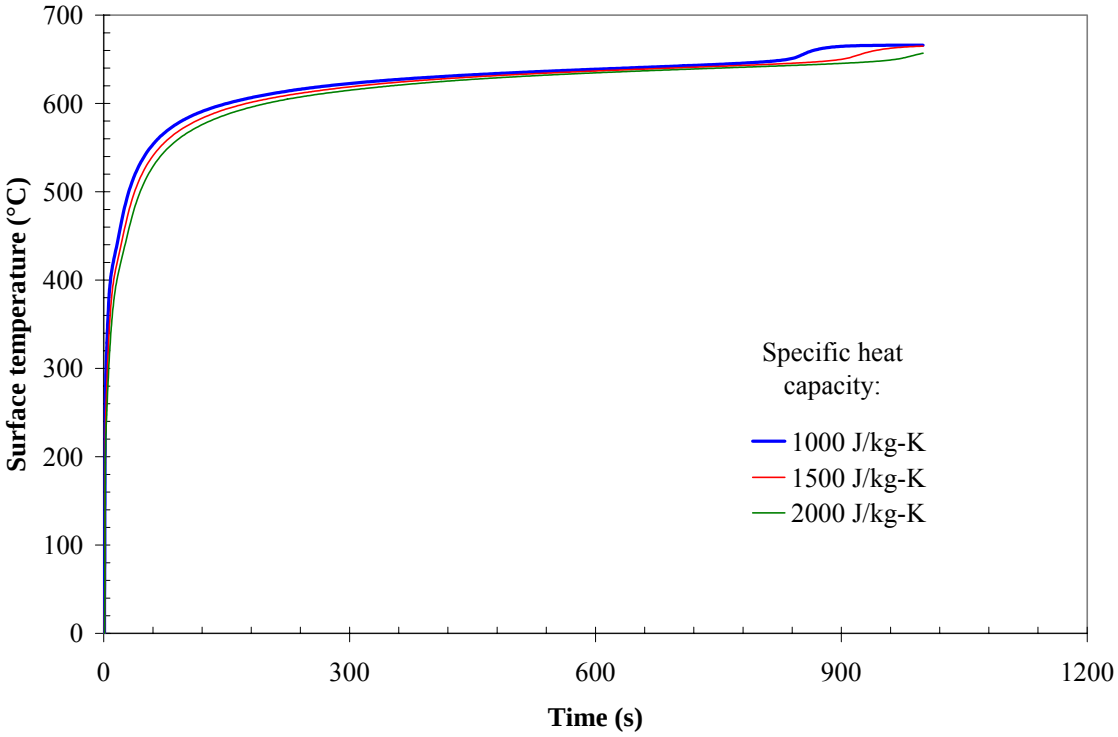

(a)

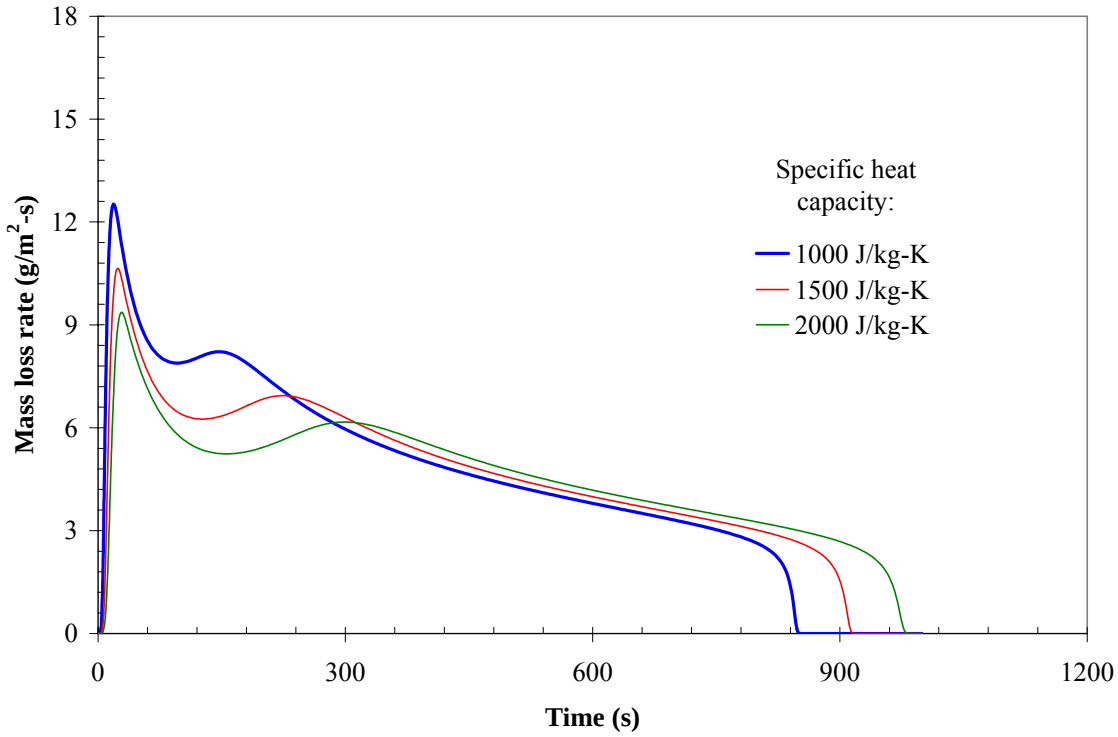

(b)

Figure 4.19. Effect of specific heat capacity on charring solid pyrolysis. (a) Surface temperature; (b) Mass loss rate.

4.11 Bulk density

The effect of bulk density on the calculated surface temperature and mass loss rate curves is shown in Figure 4.20 for the hypothetical thermoplastic material. Due to the reduction in the volumetric heat capacity as the bulk density is decreased, temperatures increase as the bulk density decreases. Due to the higher temperatures, the mass loss rate increases as the bulk density is decreased. An increase in bulk density also increases the area under the mass loss rate curve.

Analogous calculations are shown in Figure 4.21 for the charring solid. However, only the bulk density of the char is varied; the bulk density of the virgin phase is held constant at 500 kg/m^3. It can be seen from Figure 4.21a that the surface temperature depends only weakly on the char bulk density, increasing slightly as the char density is increased. However, the mass loss rate increases as the char bulk density is decreased, essentially because a larger fraction of the virgin fuel can be converted to gases for lower char densities.

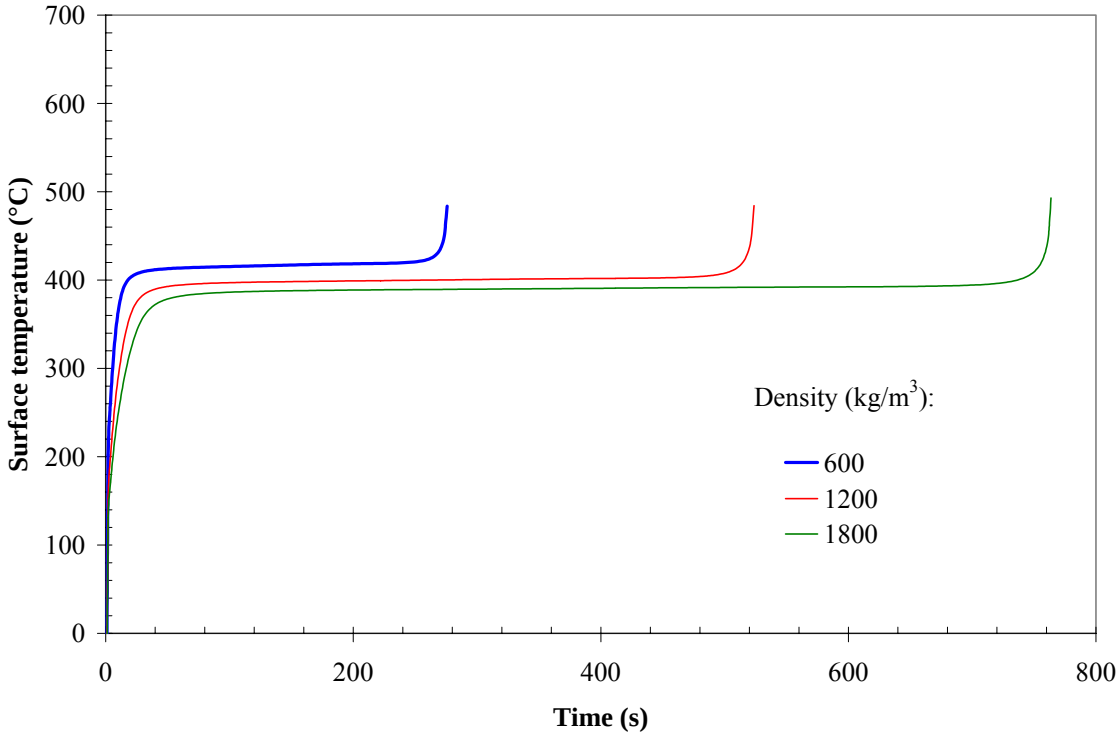

(a)

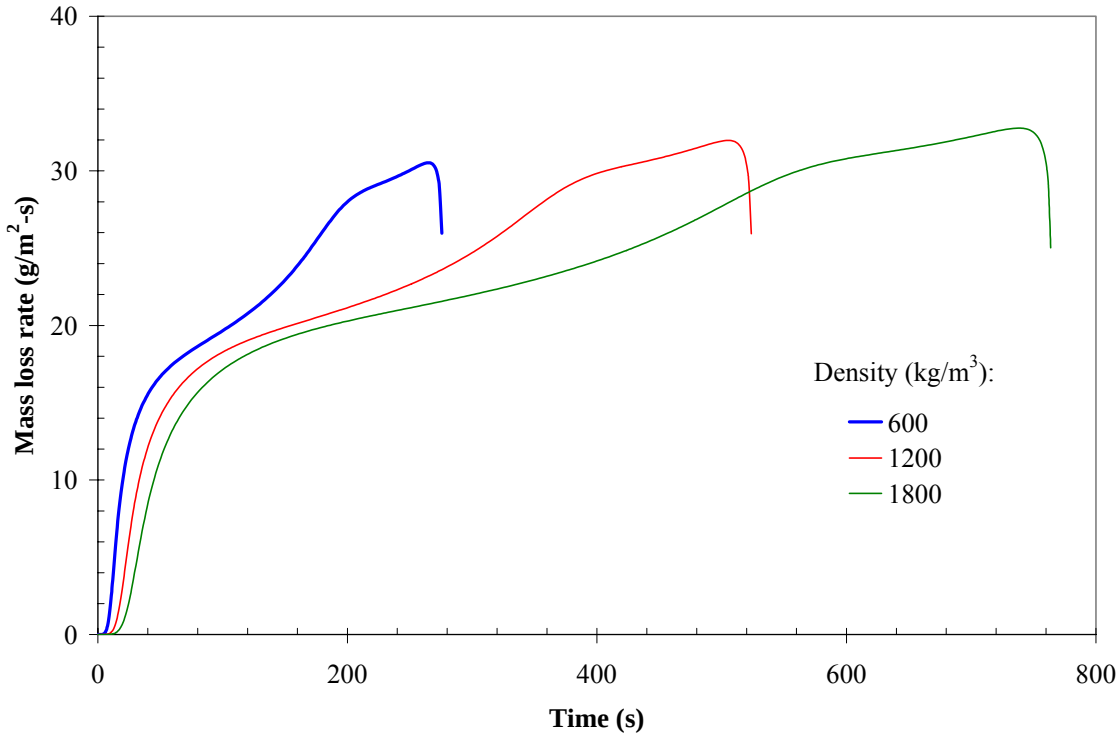

(b)

Figure 4.20. Effect of bulk density on thermoplastic pyrolysis. (a) Surface temperature; (b) Mass loss rate.

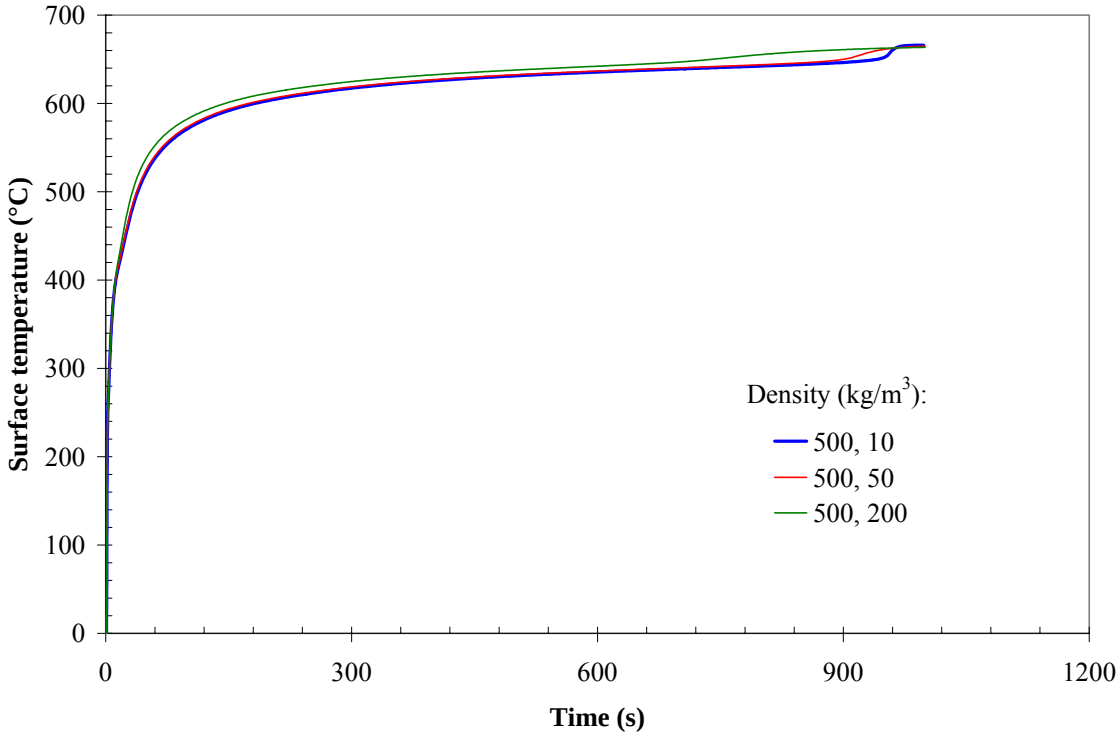

(a)

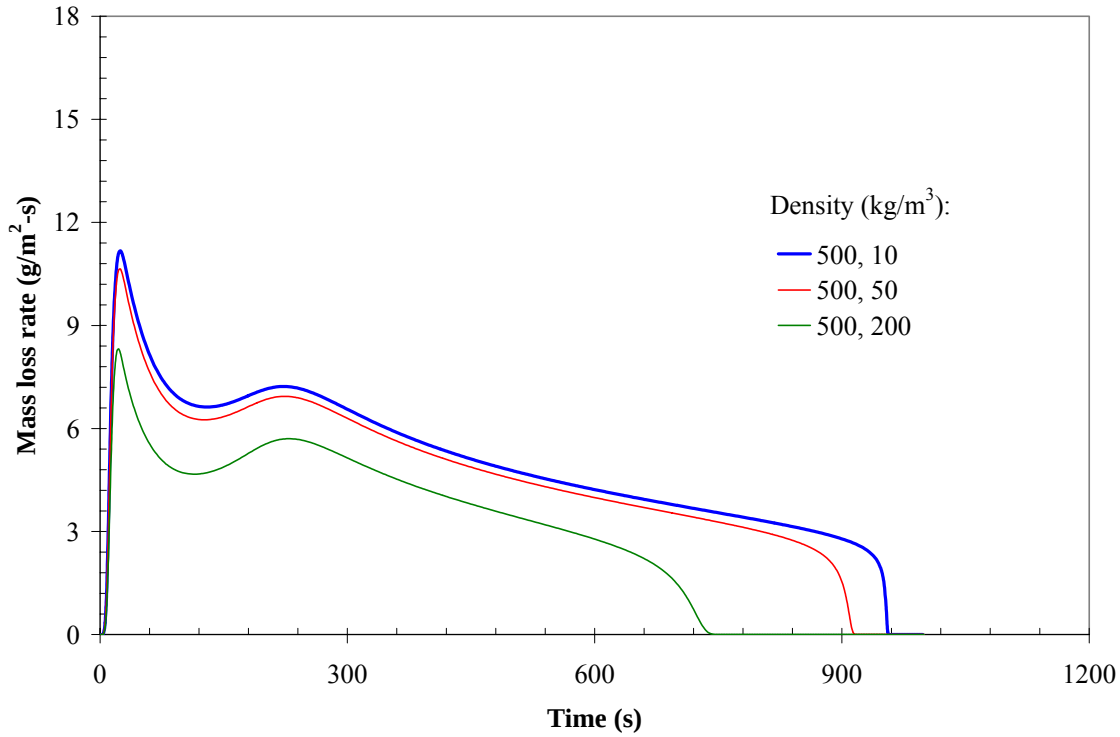

(b)

Figure 4.21. Effect of bulk density on charring solid pyrolysis. (a) Surface temperature; (b) Mass loss rate.

4.12 Front face convective heat transfer coefficient

Figures 4.22 and 4.23 show the effect of the front face heat transfer coefficient (h_c) on the calculated surface temperature and mass loss rate for the hypothetical thermoplastic and charring solid, respectively. Both the surface temperature and mass loss rate decrease as h_c is increased. For the thermoplastic, there are only minor differences between the curves for h_c = 0 W/m^2–K and h_c = 10 W/m^2–K. One reason for this is that at high temperatures, most of the surface heat losses are by radiation rather than convection. For a surface temperature of 400 °C and h_c = 10 W/m^2–K, the radiative heat losses are 11.2 kW/m^2 while the convective heat losses are only 3.7 kW/m^2 (assuming h_c is not affected by blowing). It is expected that at lower heat flux levels (here the applied heat flux level is 50 kW/m^2) the heat transfer coefficient will have a larger effect on the surface temperature because convective cooling will account for a larger fraction of the surface heat losses.

The calculated surface temperature and mass loss rates for the charring solid (Figure 4.23) show a similar sensitivity to h_c, but the surface temperature appears to be more sensitive to h_c than for the thermoplastic.

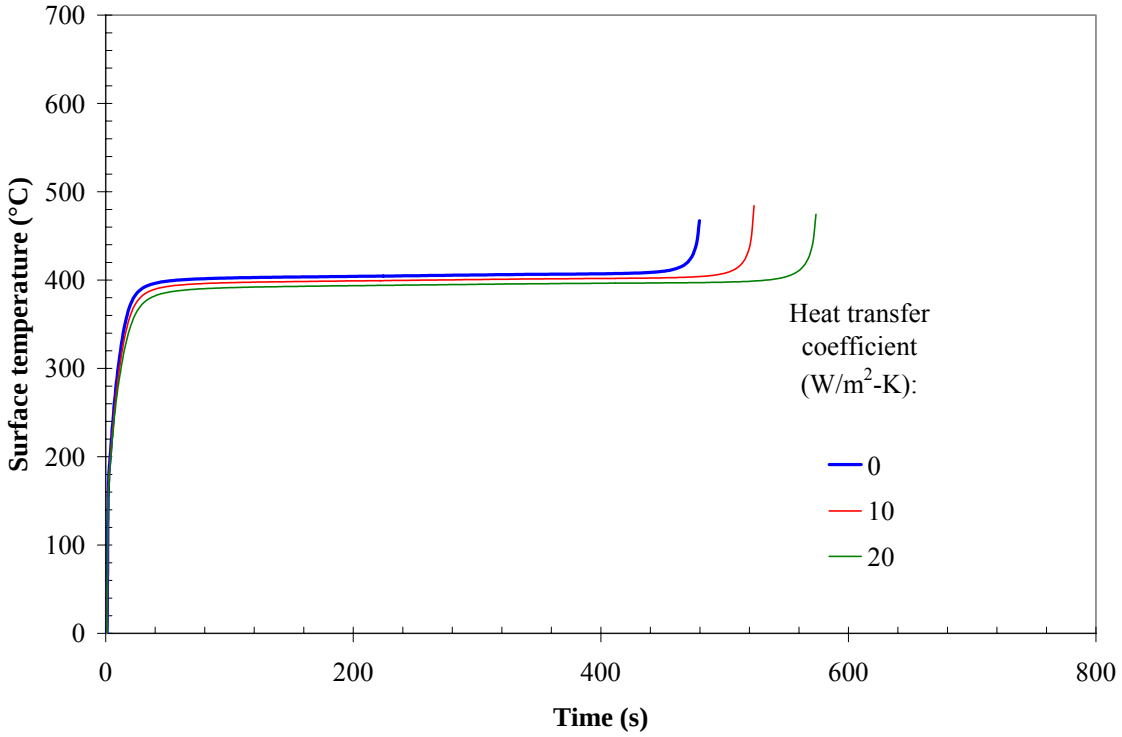

(a)

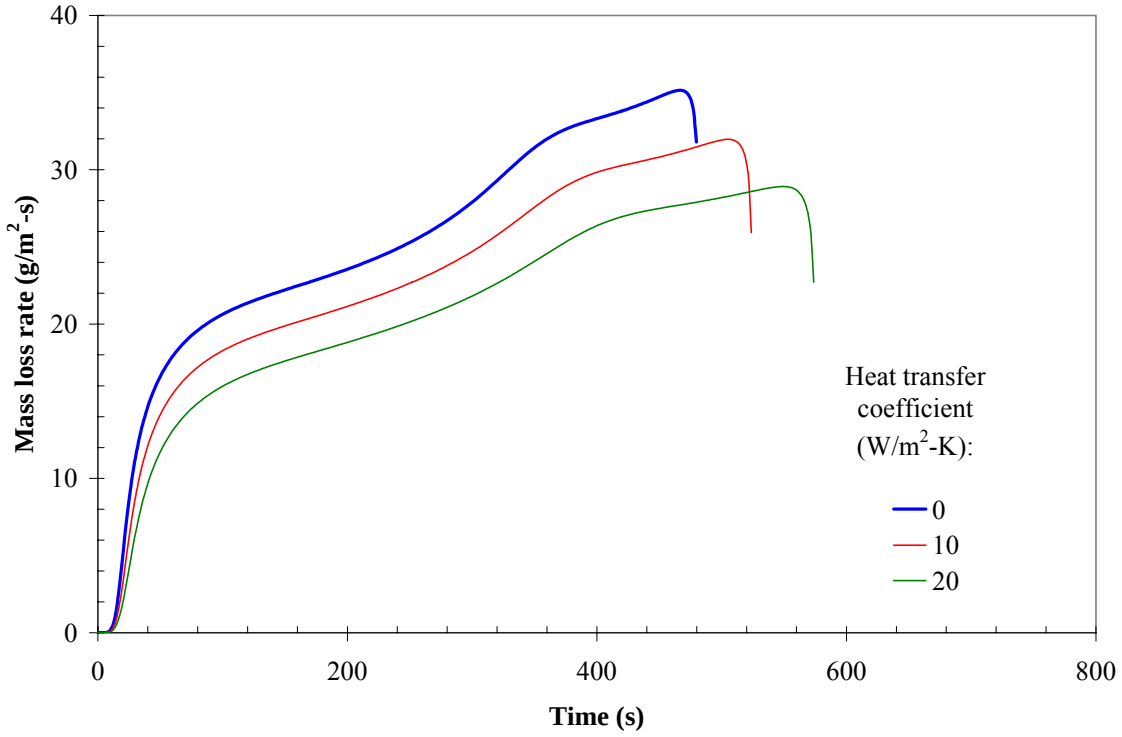

(b)

Figure 4.22. Effect of front face heat transfer coefficient on thermoplastic pyrolysis. (a) Surface temperature; (b) Mass loss rate.

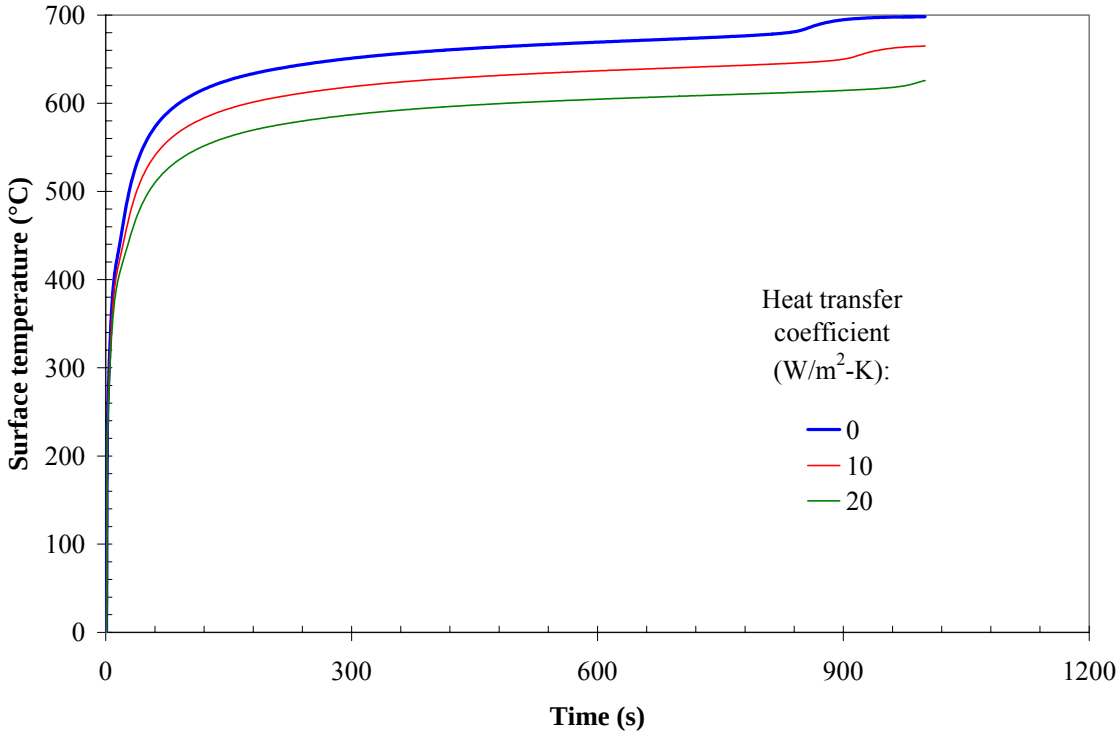

(a)

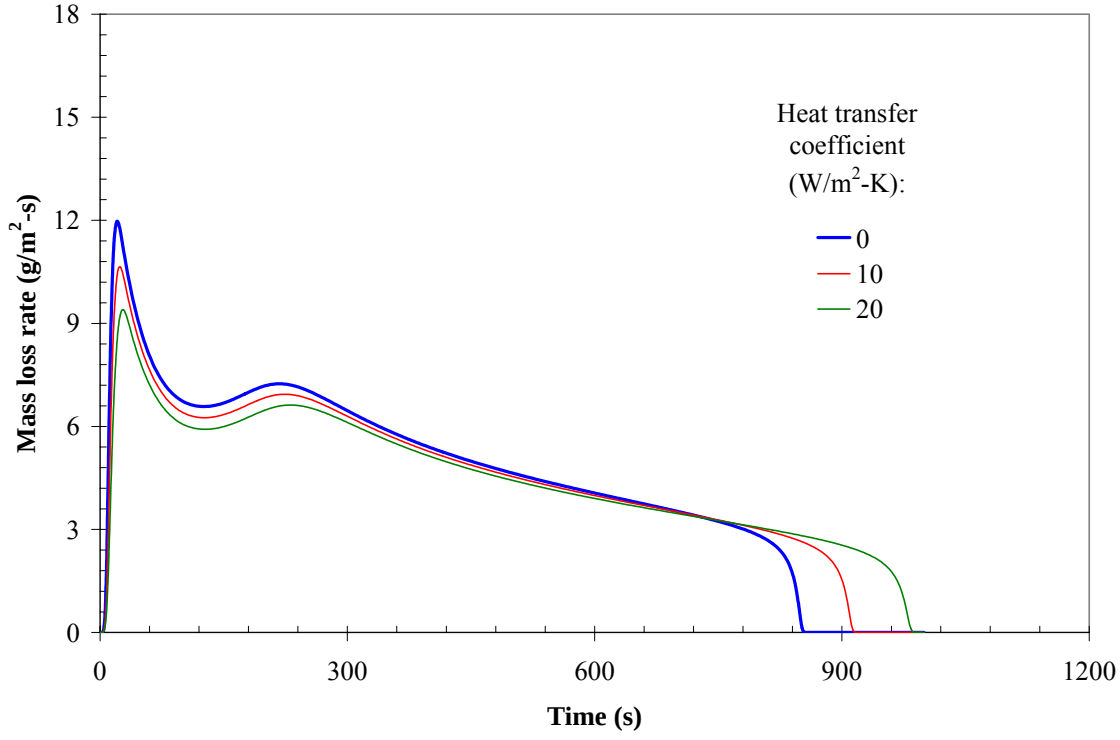

(b)

Figure 4.23. Effect of front face heat transfer coefficient on charring solid pyrolysis. (a) Surface temperature; (b) Mass loss rate.

In all of the preceding calculations, the convective heat transfer coefficient at the front face was fixed. In reality, the front face heat transfer coefficient is reduced as the mass loss rate increases due to blowing. The generalized pyrolysis model contains a simple Couette blowing factor (Equation 3.25) that can be enabled at the user's request.

A comparison of the calculated surface temperature and mass loss rate with and without blowing enabled (h_c = 10 W/m^2–K without blowing) is shown in Figure 4.24 for the thermoplastic solid. The surface temperature and mass loss rate increase when blowing is enabled due to the reduction in h_c. Analogous plots are given in Figure 4.25 for the charring solid. It can be seen that there are only minor differences in the calculated surface temperature and mass loss rate when the Couette blowing model is enabled. This is partly because h_c is not affected as much by blowing due to the lower mass loss rates for the charring solid.

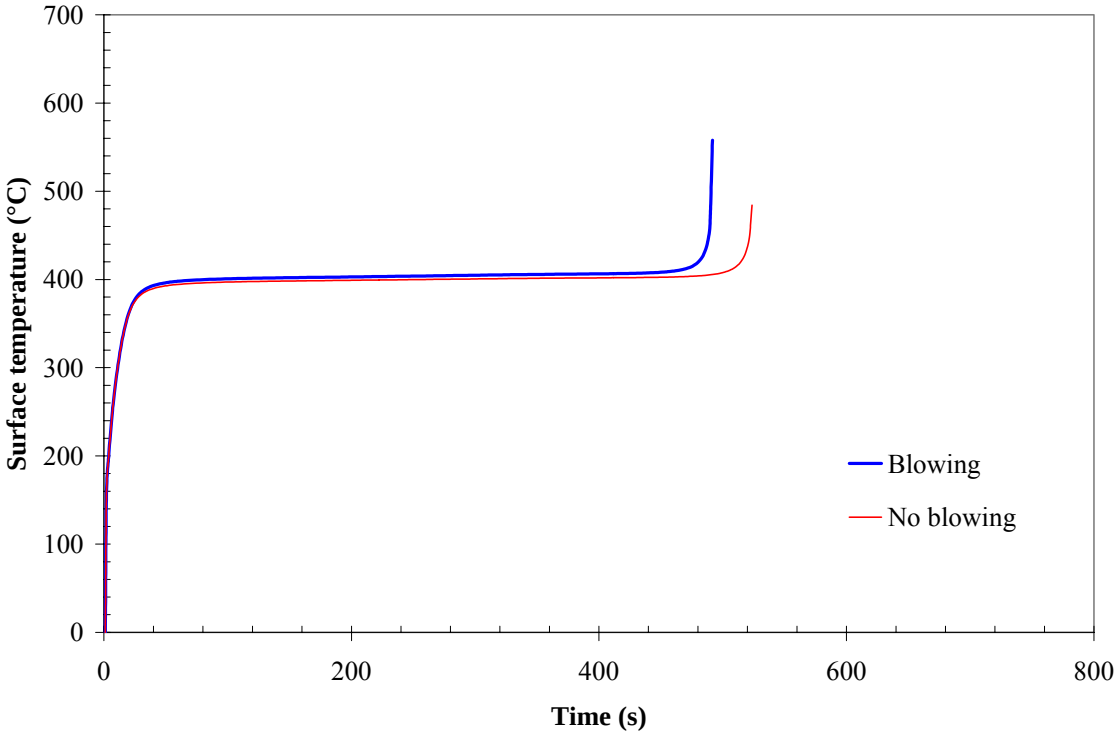

(a)

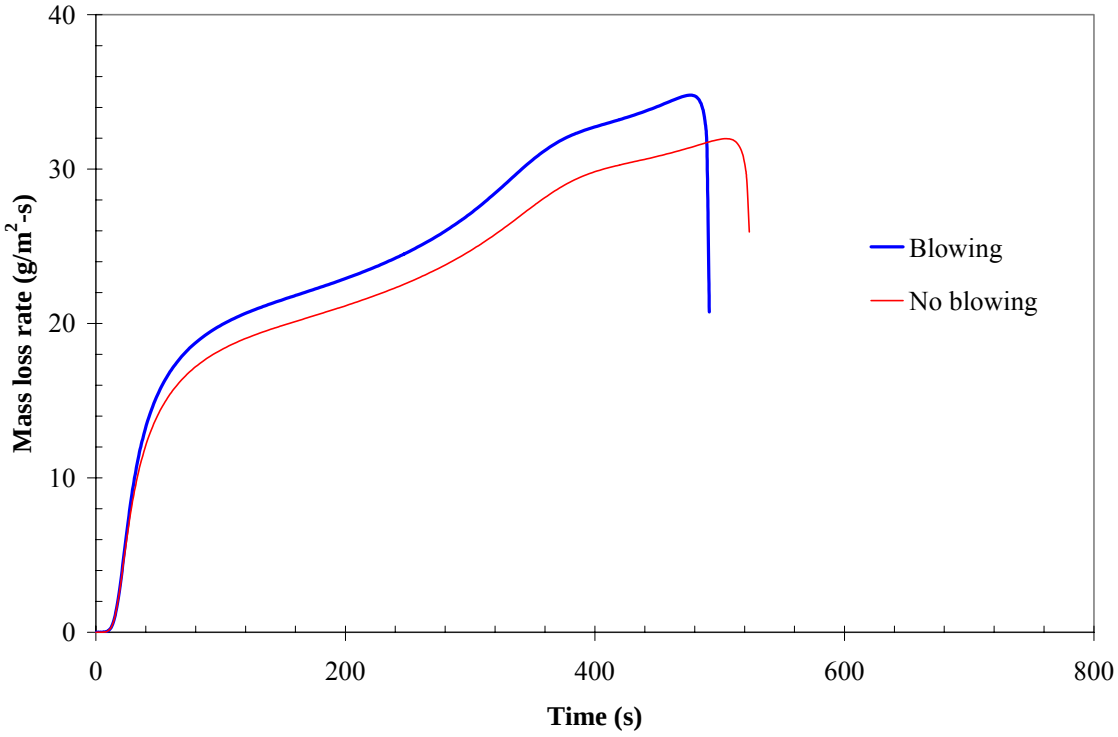

(b)

Figure 4.24. Effect of blowing on thermoplastic pyrolysis.
(a) Surface temperature; (b) Mass loss rate.

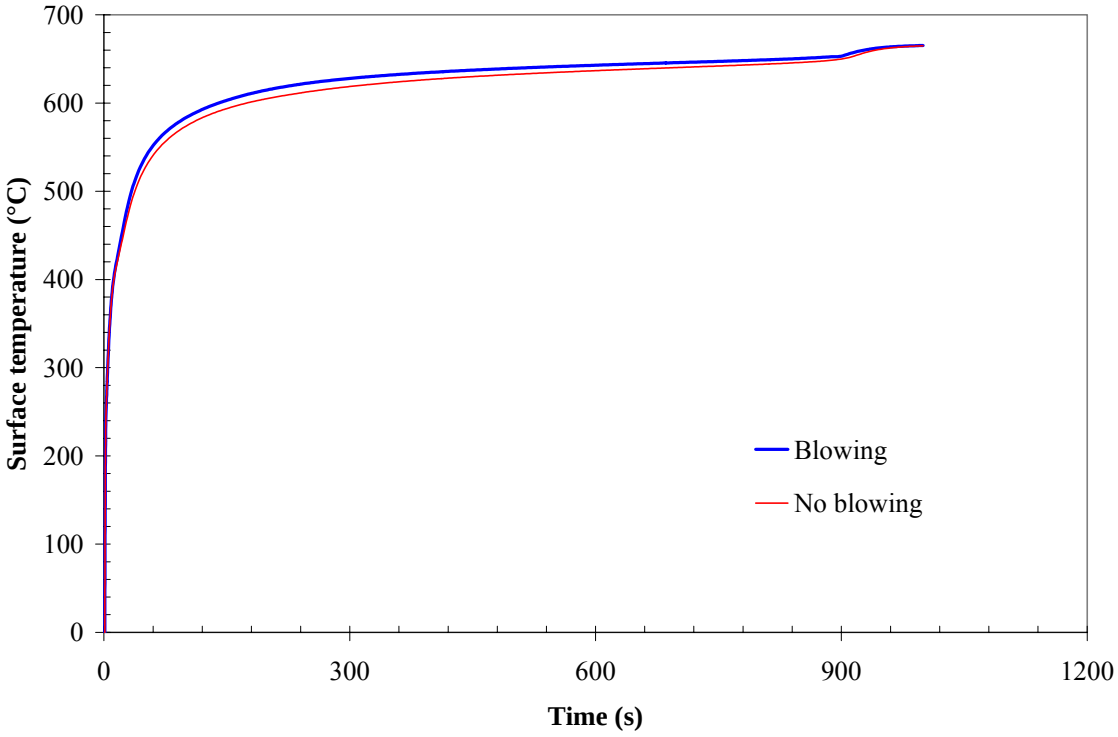

(a)

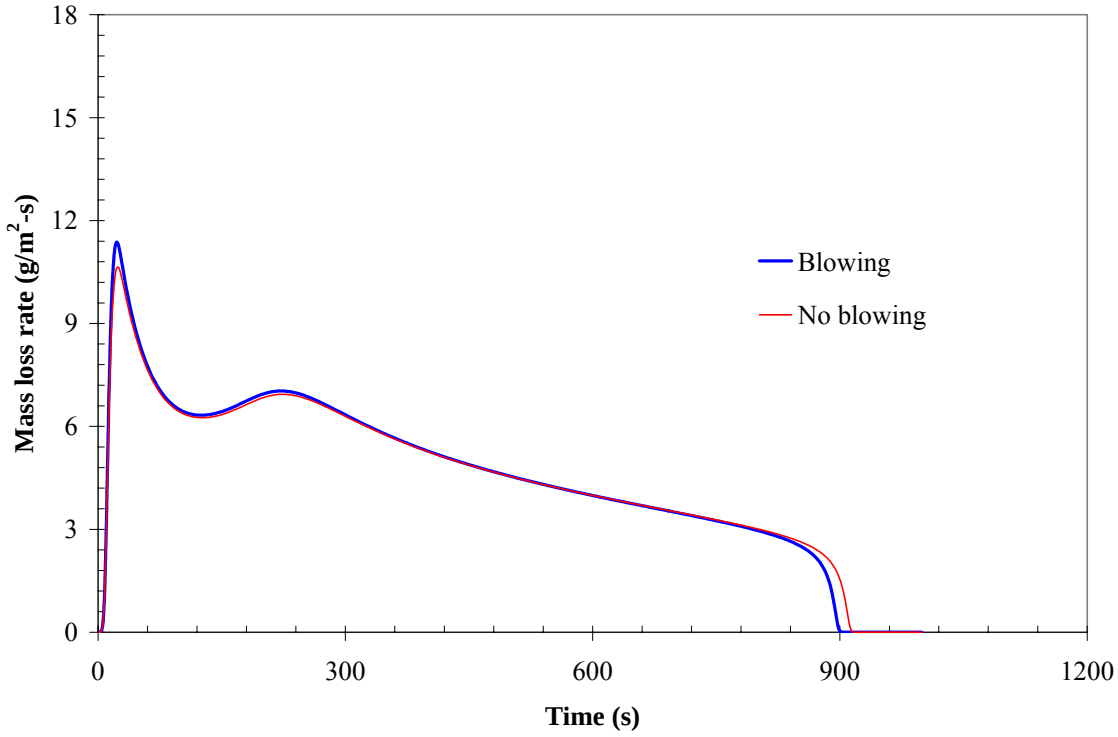

(b)

Figure 4.25. Effect of blowing on charring solid pyrolysis.
(a) Surface temperature; (b) Mass loss rate.

4.13 Back face heat transfer coefficient

The back face heat transfer coefficient affects the calculations after the thermal wave has penetrated to the back face and the pyrolysis zone "feels" the effect of the back face boundary condition. The highest mass loss rates occur for an insulated back face. Figure 4.26 shows the calculated surface temperature and mass loss rate for three different back face heat transfer coefficients: 0 W/m^2–K (insulated), 10 W/m^2–K, and 20 W/m^2–K. It can be seen from Figure 4.26 that for the thermoplastic material, differences in the calculated mass loss rate become apparent around 200 s. While the surface temperature in not sensitive to the back face heat transfer coefficient, the mass loss rate is somewhat sensitive.

From Figure 4.27 (charring solid), it can be seen that the calculated mass loss rates begin to diverge after ~120 s. The second peak in mass loss rate is observed only for the case of an insulated back face; when back face heat losses occur, the mass loss rate decreases monotonically after reaching its initial peak. Thus, the back face boundary condition has an important effect on the pyrolysis behavior of finite–thickness solids.

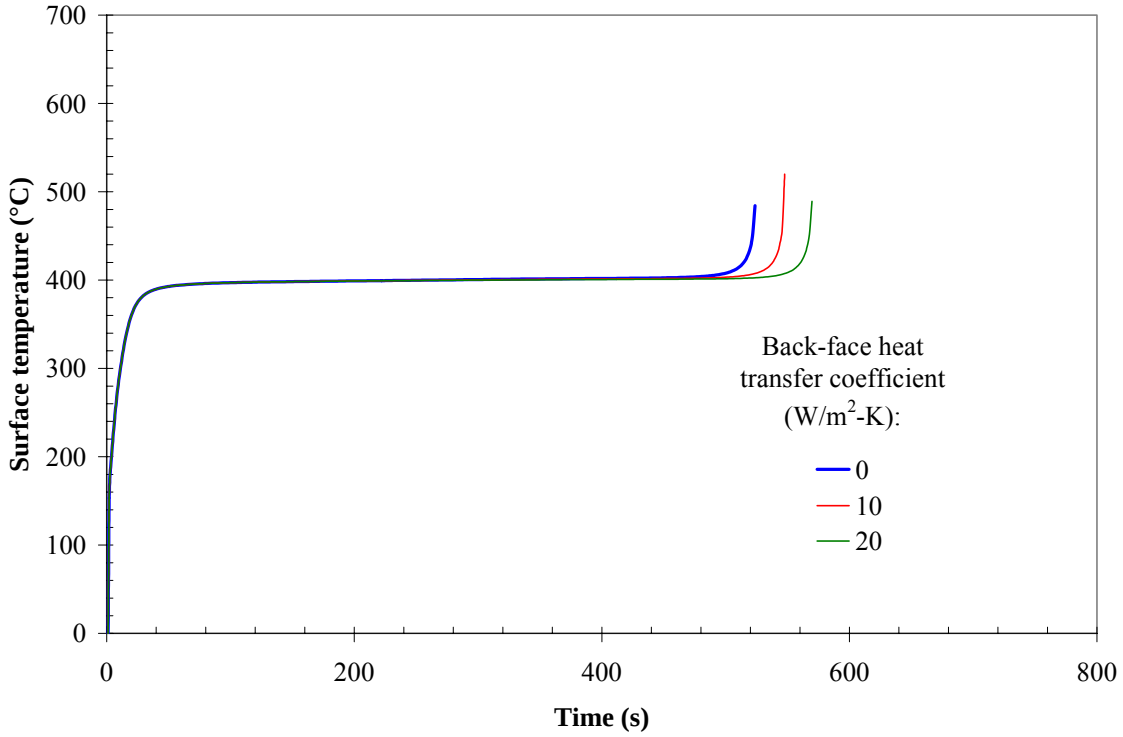

(a)

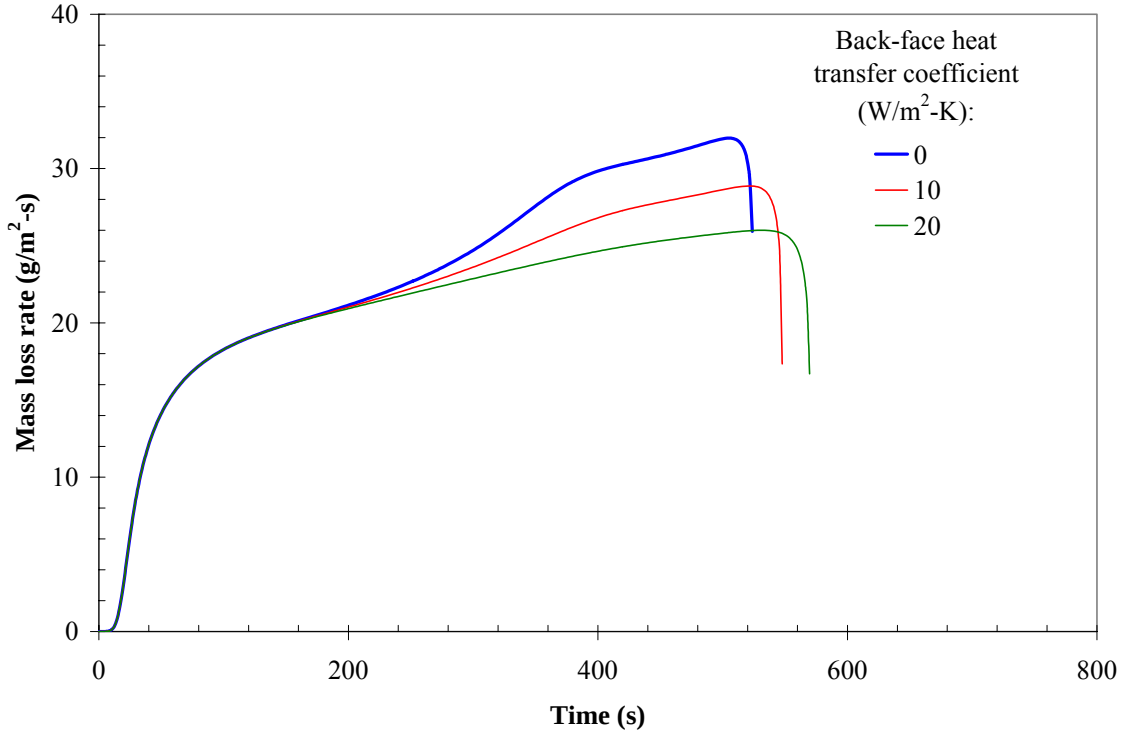

(b)

Figure 4.26. Effect of back face heat transfer coefficient on thermoplastic pyrolysis. (a) Surface temperature; (b) Mass loss rate.

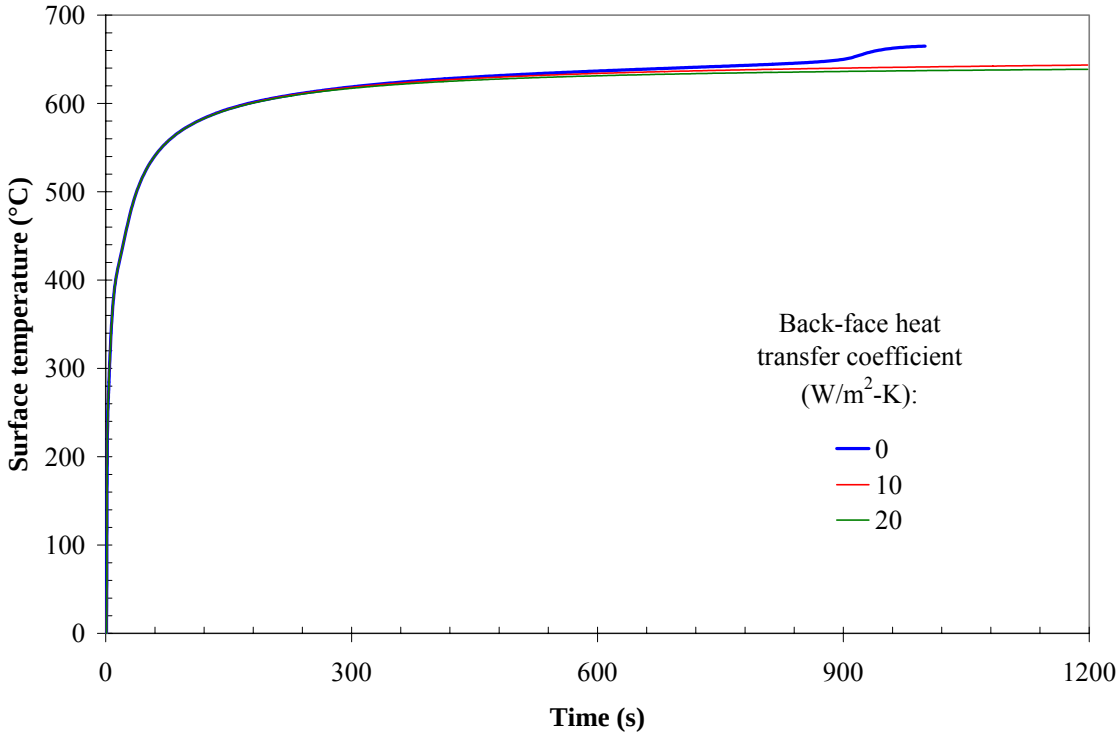

(a)

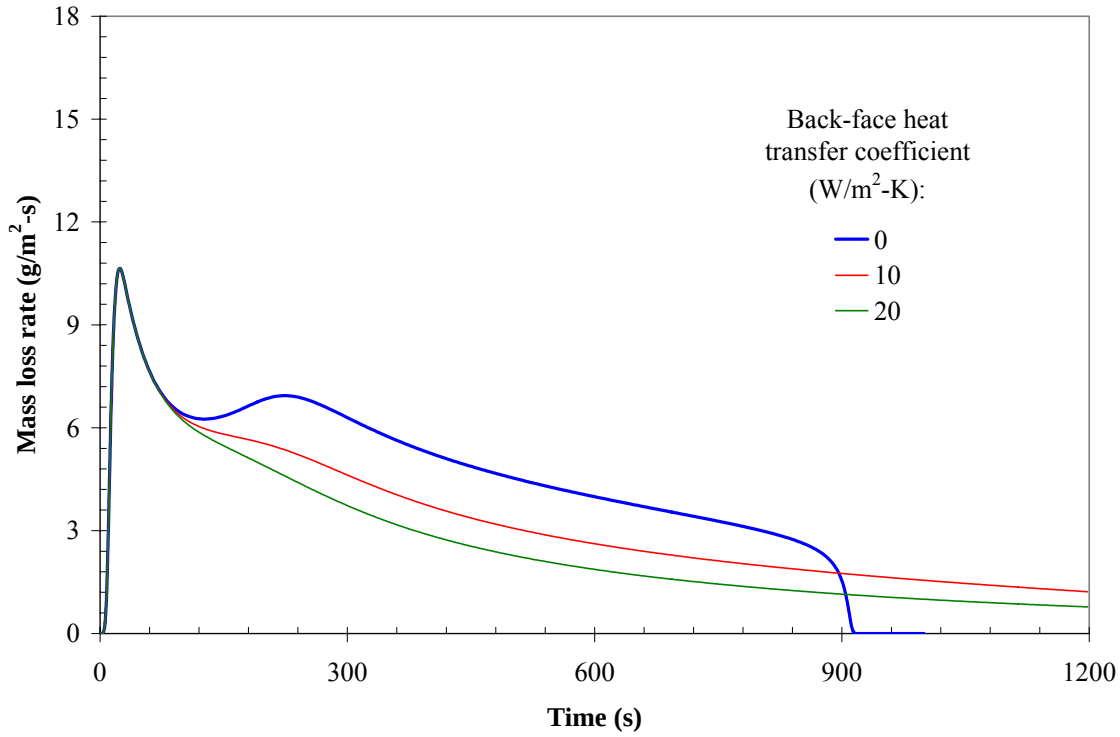

(b)

Figure 4.27. Effect of back face heat transfer coefficient on charring solid pyrolysis. (a) Surface temperature; (b) Mass loss rate.

4.14 Permeability

The preceding calculations were conducted without invoking the pressure solver. For the calculations shown below in this section, the pressure solver is invoked to assess the effect of the permeability. Only the charring solid is considered, and three different permeability values are investigated: 1×10^{-8} m^2, 1×10^{-10} m^2, and 1×10^{-12} m^2.

Extremely slight differences are apparent between the calculated surface temperatures and mass loss rates. When plotted in an analogous manner to the above plots, the simulation results appear visibly identical. However, significant differences can be seen in the calculated pressure profiles. Figure 4.28 (note logarithmic *y*–axis) shows the calculated pressure profile at a time of 240 s (close to the second "peak" in mass loss rate curve shown in Figure 4.25b). The peak overpressure is approximately 1,000 Pa for a permeability of 1×10^{-12} m^2, 10 Pa for a permeability of 1×10^{-10} m^2, and 0.1 Pa for a permeability of 1×10^{-8} m^2. The magnitude of the overpressure is approximately inversely proportional to permeability. However, the magnitude of the pressure inside the decomposing solid has little effect on the macro–scale mass loss rate or temperature distribution. The reason for this is that even for the case of a permeability of 1×10^{-12} m^2, the absolute pressure increases by only ~1%, from 101.3 kPa to 102.3 kPa. This increase in pressure slightly increases the storage of gases inside the decomposing solid (due to the increased density) but this effect is negligible for the present case.

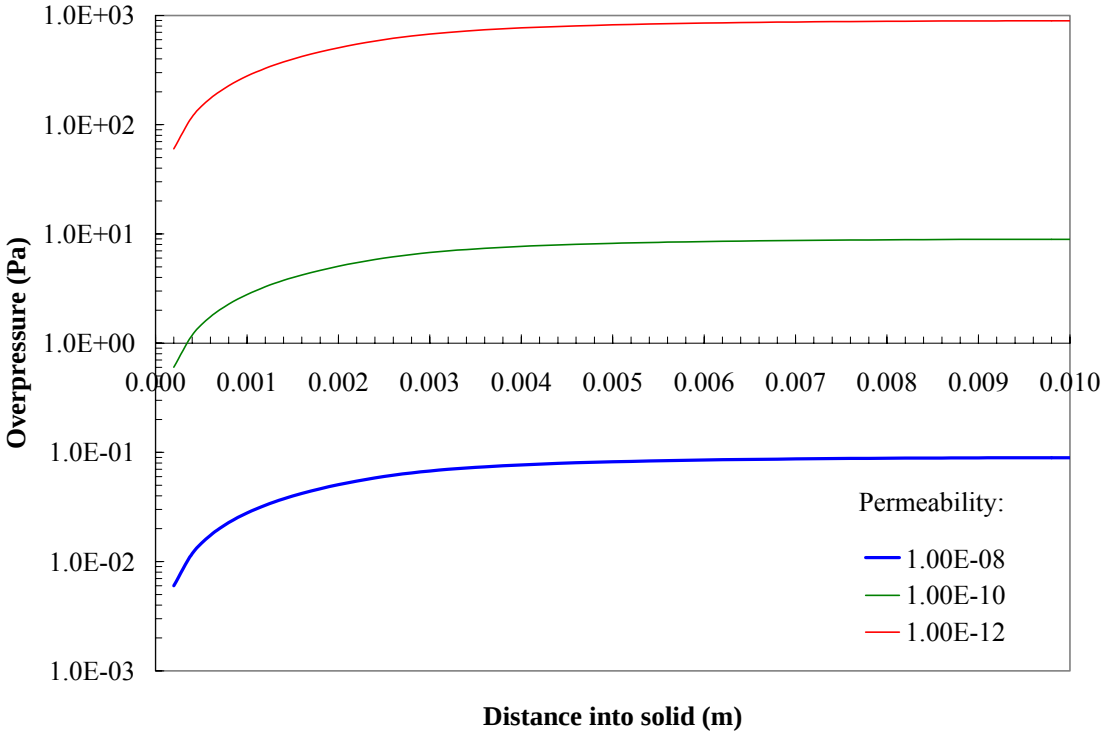

Figure 4.28. Effect of permeability on pressure profile in charring solid at *t* = 240 s.

5.0 GENETIC ALGORITHM FOR MATERIAL PROPERTY ESTIMATION

Chapters 3 and 4 showed several calculations that used the generalized pyrolysis model to simulate hypothetical materials. However, before the model can be applied to real–world combustible solids, the model input parameters required to characterize these materials must be established. Unfortunately, we have a limited ability to extract the required material properties from laboratory experiments such as the cone calorimeter [18], Fire Propagation Apparatus [178], thermogravimetric analysis, and differential scanning calorimetry. This is the biggest barrier preventing increased application of research–type pyrolysis models for practical purposes.

Although techniques have been developed to estimate several material fire properties from laboratory fire tests, there is a disconnect between the material properties needed for numerical pyrolysis modeling and those properties that can be determined with existing techniques (this will be discussed further in Section 5.2.1). It is for this reason that this chapter presents a methodology that uses an automated optimization method based on a genetic algorithm (GA) to extract the material properties needed for numerical pyrolysis modeling from laboratory experiments, particularly traditional bench–scale flammability tests (cone calorimeter, FPA) and small–scale thermal analysis (TGA). This chapter expands on a paper published in *Fire Safety Journal* [196].

Genetic algorithms are a class of search tools that use the principles of Darwinian evolution to seek an optimal solution to a problem. In contrast to many classical search methods, genetic algorithms can handle nonlinear problems and search spaces having high dimensionality, i.e. a large number of adjustable parameters. The proposed methodology involves simulating a laboratory test or tests with the generalized pyrolysis

model described earlier, and using a genetic algorithm to locate a set of model parameters (or "material properties") that provide optimal agreement between the model calculations and the experimental data, subject to the constraints imposed by the model and the experiments.

Optimization techniques based on genetic algorithms are "embarrassingly parallel", meaning that they can be easily divided into a large number of parallel tasks that can run on a separate CPU or core. The actual computer implementation of the genetic algorithm optimization methodology presented here has been parallelized using Message Passing Interface. The parallel code has been successfully run on Linux computer clusters at UC Berkeley using more than 60 CPUs. The code is massively parallel, meaning that it can use as many CPUs or cores as are available in a networked computer cluster.

The material properties found by the genetic algorithm will be close to the "actual" values provided: 1) the experimental measurements are sufficiently accurate and contain enough information to establish a unique set of model parameters, 2) the pyrolysis model is an adequate representation of the underlying physical processes, and 3) the specified boundary and initial conditions are an accurate representation of the experimental configuration. This approach is self–consistent in the sense that the same model that is used to estimate the material properties from small–scale experimental data can be coupled to a CFD code to model large–scale fire development.

5.1 Inadequacy of existing data reduction techniques

The simplest combustible solid is a homogeneous, opaque, noncharring, constant–property material with known emissivity and single–step first order Arrhenius

decomposition kinetics. This is an idealization, and such materials do not actually exist because real materials have temperature–dependent thermal properties, may exhibit multi–step (and sometimes oxygen–sensitive) decomposition kinetics, and may absorb radiation in–depth. Nonetheless, even for this highly simplified case, at least five unknown material properties are needed: thermal conductivity, specific heat capacity, pre–exponential factor, activation energy, and heat of volatilization/pyrolysis. At least three additional properties are needed to simulate an idealized charring material: char thermal conductivity, char specific heat, and char density. Even for these highly simplified and idealized materials, the required material properties cannot be directly estimated from laboratory tests.

Thermal ignition theories (e.g., Reference [197]) can be used to determine a material's apparent thermal inertia (the product $k\rho c$) by plotting ignition time data at multiple heat flux levels, but numerical pyrolysis models require individual thermal properties. Furthermore, the derived $k\rho c$ is an effective value that depends on the data reduction technique [179] and environmental conditions [86]. Being an effective value, it also includes the endothermicity of the pyrolysis reaction, which is treated explicitly in numerical models. Since the effective thermal inertia is derived from a thermally thick analysis using a linearized total heat transfer coefficient, it has limited usefulness for numerical modeling where nonlinear surface re–radiation is treated explicitly [198] and for non–thick materials. A perhaps more significant limitation is that although charring materials account for a large fraction of the materials encountered in practice, there are no procedures available to estimate the thermal conductivity, density, and specific heat capacity of the char phase from fire test data.

Similarly, there are currently no procedures available that use laboratory fire test data to estimate the Arrhenius pyrolysis rate coefficients. These coefficients are usually determined by thermogravimetric experiments that involve slowly heating very small samples with a mass of a few milligrams and measuring the resultant mass loss [103]. Since heat and mass transfer processes are expected to be different in milligram size samples and the bulk material's end–use configuration, the relevance of these measurements to the pyrolysis and combustion of large samples under fire–level heating rates is questionable. However, the use of traditional flammability tests in conjunction with thermal analysis experiments (TGA, DSC) for material property estimation is an approach deserving further consideration.

The heat of volatilization (sometimes called the heat of vaporization, heat of reaction, or heat of pyrolysis, see Section 2.2.2) is the amount of heat required to convert unit mass of solid material at its pyrolysis temperature to unit mass of pyrolysate at that same temperature. This is the appropriate quantity for characterizing the endothermicity of a pyrolysis reaction in a numerical pyrolysis model, but it cannot be directly determined from fire tests with existing procedures. Only the effective heat of gasification (the heat required to raise unit mass of material from its initial temperature to its pyrolysis temperature plus the heat of volatilization/vaporization/reaction/pyrolysis) can be estimated from fire test data [25]. Furthermore, it is not clear whether the heat of gasification concept can be effectively applied to charring materials that do not exhibit a steady–state burning phase.

Since existing data reduction techniques that are widely used to determine material fire properties are not appropriate for numerical pyrolysis modeling, one of the

primary contributions of this work is the development of a tool that can be used to establish the needed material properties from existing laboratory experiments. As described earlier, this involves simulating laboratory experiments with the generalized pyrolysis and using a genetic algorithm to optimize the input parameters until the model calculations provide an adequate fit of the available experimental data.

5.2 Simulating laboratory experiments

The pyrolysis model described earlier can be used to simulate both traditional flammability tests (cone calorimeter, FPA) as well as TGA experiments. When samples are instrumented with thermocouples, cone calorimeter and FPA experiments can provide information regarding a material's thermal properties, but probably cannot be used to establish detailed kinetics mechanisms. In comparison, TGA provides no information about a material's thermal properties, but provides detailed information about a material's decomposition kinetics. Although it has not been attempted in this work, differential scanning calorimetry or differential thermal analysis could potentially be used to infer specific heat capacity and heats of reaction. Due to the different types of information that can be obtained from flammability tests and thermal analysis experiments, both are potentially useful for material property estimation for pyrolysis modeling. Therefore, the procedure through which each type of test is simulated with the pyrolysis model will be described below.

5.2.1 Traditional flammability tests

The physical problem being modeled is the radiative heating, pyrolysis, and (sometimes) combustion of solid fuel slab. A simplified schematic is given in Figure 5.1.

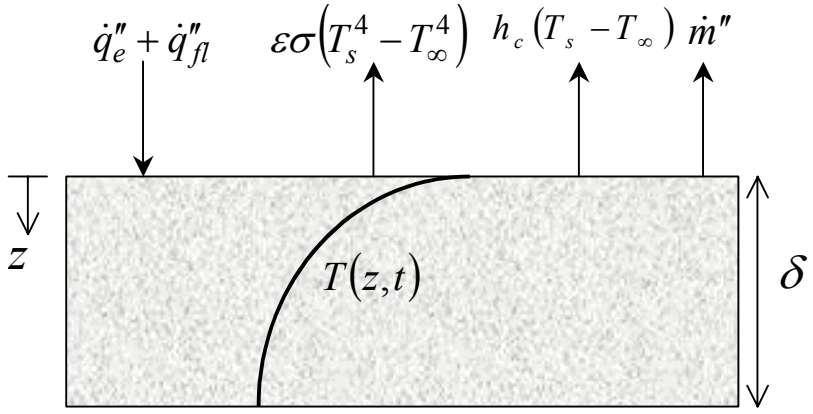

Figure 5.1. Simplified schematic of the physical problem.

The sample thickness δ is usually small in comparison with its length and width so edge effects are considered negligible and the problem is nominally one–dimensional. The irradiated face of the sample is located at $z = 0$, and its back face abuts a perfectly thermally insulating substrate at $z = \delta$. The solid fuel is approximated as spectrally gray. A particular laboratory experiment is modeled by applying a specific set of initial and boundary conditions that describe the initial state (T_0), the convective environment (h_c, T_∞), and the applied external radiation level ($\dot{q}''_e$).

Prior to ignition, the fuel is heated only by the externally applied radiation; if ignition occurs, it is also heated by heat feedback from the flame ($\dot{q}''_{fl}$). Thus, the flame heat flux is assumed negligible prior to ignition, instantaneously jumping to a constant value at the observed ignition time. In reality, the flame heat flux varies from apparatus to apparatus, and for a particular apparatus it depends on the fuel type, the instantaneous heat release rate, and environmental conditions (particularly ambient O_2 concentration). As a very rough approximation, it can be assumed that during flaming combustion in cone calorimeter type experiments in air that the flame heat flux is independent of fuel type, spatially uniform, temporally invariant, and equal to ~30 kW/m^2.

5.2.2 Thermogravimetric tests

Thermogravimetric experiments involve continuously weighing a very small sample of material, usually having a mass on the order of a few milligrams, while it exposed to an atmosphere having known composition (oxygen concentration) and temperature. The atmosphere may be isothermal or, more commonly, have a temperature that increases linearly with time. Due to the small sample size, gradients of temperature and species concentrations across the sample are in theory negligible.

Simulation of thermogravimetric tests is much more straightforward than simulation of traditional flammability tests because the sample can be treated as a "lumped" system. The ambient environment is characterized by its composition, initial temperature, and linear temperature ramp rate β (K/min). The initial state of the lumped system is characterized by specifying initial mass fractions of each condensed phase species. The mass (and mass time rate of change) of the lumped system is calculated using the equations presented in Section 3.1.10. This can then be directly compared to experimental data.

5.3 A genetic algorithm for automated optimization

In this section, a methodology is presented that can be used to estimate unknown model input parameters from experimental data. It involves using a genetic algorithm to find a set of model input parameters that provides near–optimal agreement between the calculations of the generalized pyrolysis model and experimental measurements from a laboratory test. However, this inverse problem is ill–posed. That is, the solution (the set of model input parameters) is not necessarily unique and it is not necessarily stable to small changes in the input data. The proposed methodology is heuristic, meaning that the

final solution is not necessarily the absolute optimal solution; however, the algorithm will find a solution that gives a near–optimal prediction of the experimental data given the constraints of the underlying physical model. That is, the results are almost as good as those that would be obtained with the optimal solution.

Genetic and evolutionary algorithms have been previously used in engineering. They have already been applied to the optimization of combustion and chemical kinetics problems, including heterogeneous [199] and homogeneous [200] reaction mechanisms. However, since the use of a GA to estimate solid phase material properties from fire test data is a specialized application, the algorithm used here is described in detail below. It is presented within the context of using cone calorimeter or FPA–type experiments for property estimation, but the basic methodology also applies to thermal analysis experiments (TGA, DSC, DTA). The reader desiring a general treatment of genetic or evolutionary algorithms is referred to several books covering the topic [201–203].

5.3.1 Initial population

The search process is initialized by randomly generating several candidate solutions (for the idealized charring material described earlier, this would be a vector of eight real numbers corresponding to k_v, c_v, Z, E, ΔH_{vol}, k_c, ρ_c, and c_c). Each candidate solution is referred to as an *individual* or a *chromosome*, and the terms are used interchangeably throughout the genetic algorithms literature. A single parameter of an individual (or chromosome) is referred to as a *gene*, for example the numerical value of the virgin phase thermal conductivity is one gene. The entire group of candidate solutions is referred to as a *population*. Typical population sizes range from tens to hundreds of individuals. Populations constantly evolve to form subsequent *generations*; the initial

population is the first generation, the offspring of the first generation make up the second generation, and so on.

This chapter adopts a separate nomenclature from the rest of the dissertation. Let $\{a_1, a_2 \ldots a_n\}$ denote the n parameters, or genes, that make up an individual, or chromosome. Here, a_1 may be associated with k_v, a_2 with c_v, and so on. For certain variables that may take on values over several orders of magnitude, it is convenient to have the gene represent the logarithm of that variable. Let $\{A^1, A^2 \ldots A^N\}$ denote the N individuals that make up the population. The nomenclature $A^I(\ell)$ is used to denote the I^{th} individual of generation ℓ. Similarly, $A_j^I(\ell)$ represents the j^{th} gene of the I^{th} individual of generation ℓ.

Begin by generating an initial population:

$$A_j^I(1) = a_{j,\min} + r_j^I\left(a_{j,\max} - a_{j,\min}\right) \tag{5.1}$$

The parameters $a_{j,max}$ and $a_{j,min}$ are the user–specified upper and lower bounds of each variable; all parameters are constrained by these values throughout the evolution process. In Equation 5.1, r_j^I is an N by n matrix of random real numbers distributed uniformly on the interval [0, 1]. The indices I and j are cycled from 1 to N and 1 to n, respectively.

5.3.2 Fitness

Next, the *fitness* of each individual is evaluated. Here, fitness is a measure of how well the candidate solution matches the experimental data. For demonstration purposes, it is assumed in the following discussion that the experimental data is obtained from a flammability test such as the cone calorimeter. It is also assumed that at a minimum, surface temperature and mass loss rate histories are available. Extension to additional

measurements (e.g., in–depth thermocouple temperature measurements) or experimental configurations (e.g., TGA) is straightforward. The residuals that measure the level of agreement between the measured surface temperature/mass loss rate histories and the predictions of individual *I* are:

$$E_{T_s}^I = \frac{1}{n_{\Delta t}} \sum \left(\frac{T_{s,exp}}{\left| T_{s,try}^I - T_{s,exp} \right| + \varepsilon_{T_s} T_{s,exp}} \right)^{\zeta} \tag{5.2a}$$

$$E_{\dot{m}''}^I = \frac{1}{n_{\Delta t}} \sum \left(\frac{\dot{m}''_{exp}}{\left| \dot{m}''^{\,I}_{try} - \dot{m}''_{exp} \right| + \varepsilon_{\dot{m}''} \dot{m}''_{exp}} \right)^{\zeta} \tag{5.2b}$$

Here, a subscript "exp" denotes the experimental data, and a subscript "try" denotes the trial solution generated by a certain set of parameters contained in the individual. The parameter ε is a user–specified small number that prevents the fitness from approaching infinity as the first term in the denominator approaches zero, and ζ is a user–specified exponent. Equation 5.2 is written as a summation, rather than an integral, because experimental measurements are obtained at discrete time intervals. In Equation 5.2a, the summation is performed for surface temperature measurements/predictions only before the experimentally determined ignition time, but in Equation 5.2b the summation for the mass loss rate measurements/predictions is carried out over the entire duration of the test. This choice was made because the accuracy of surface temperature measurement becomes more questionable after ignition.

Next, the weighted fitness of individual *I* is calculated as:

$$\tilde{f}^I = \phi_{T_s} E_{T_s}^I + \phi_{\dot{m}''} E_{\dot{m}''}^I \tag{5.3}$$

the ϕ factors are user–specified constants that determine the relative importance of each fitness metric. If experimental data are obtained at multiple heat flux levels (or heating

rates in the case of TGA experiments), then an individual's final fitness is considered to be the sum of the fitness values calculated at each heat flux level:

$$f^I = \sum_{n_{\dot{q}''_e}} \tilde{f}^I \tag{5.4}$$

where $n_{\dot{q}''_e}$ is the number of heat flux levels (or heating rates) at which data were obtained. The steps represented by Equations 5.2 through 5.4 are then repeated for all individuals to tabulate a numerical fitness value for each individual.

5.3.3 Selection for reproduction

The next generation is obtained through the reproduction process wherein parents' genes are combined to produce offspring. The likelihood that an individual reproduces is determined by its fitness. In this way, relatively bad candidate solutions die out, while relatively good solutions survive and propagate. This "natural selection" process is the basis of genetic algorithms' ability to exploit good solutions.

There are many different ways in which individuals can be selected for reproduction, but proportional selection [203] is used here for simplicity. The selection probability of individual *I* is:

$$p^I_{sel} = \frac{f^I}{\sum_{I=1}^{N} f^I} \tag{5.5}$$

Thus, the higher an individual's fitness, the greater the probability it will be selected for reproduction. In practice, the selection probability in Equation 5.5 is implemented by first sorting the current population in order of decreasing fitness, i.e. $f^I \geq f^{I+1}$. Then, for each individual, the following is calculated:

$$q^I = \sum_{i=I}^{N} p_{sel}^i \tag{5.6}$$

Note that by definition, $q^1 = 1$ and $q^N = p_{sel}^N$. Next, a random number r belonging to a uniform distribution is generated on the interval [0, 1]. Selection proceeds by comparing r with q: if $q^{I+1} < r \leq q^I$, then A^I is selected for reproduction. The selection process is repeated N times to choose N parents.

If one individual has a relative fitness much higher than the average fitness, it is likely that this individual will be selected several times for reproduction. To prevent premature convergence, a target (maximum) selection number S is used so that any individual may be selected for reproduction no more than S times per generation ($1 \leq S < N$). If an individual has reproduced S times and is selected again for reproduction, then a new individual is randomly selected from the population for reproduction. Low values of S preserve variability at the expense of convergence.

5.3.4 Reproduction

Once individuals have been selected for reproduction, offspring are generated through a linear combination of two parents. Denote $\{B\}$ as the subset of population $\{A\}$ that was selected for reproduction. As many as S copies of a single individual may belong to the set $\{B\}$. The offspring are stored in a temporary intermediate population denoted $\{C\}$. This is accomplished by generating a matrix of random numbers (denoted r_j^i where $i = 1 \ldots N/2$ and $j = 1 \ldots n$) belonging to a uniform distribution on the interval [–0.5, 0.5] and then producing offspring as linear combinations of the parents:

$$\begin{aligned} C_j^I &= r_j^i B_j^I + \left(1 - r_j^i\right) B_j^{I+1} \\ C_j^{I+1} &= r_j^i B_j^{I+1} + \left(1 - r_j^i\right) B_j^I \end{aligned} \quad \text{for } I = 1, 3, 5 \ldots N-1 \quad \text{where} \quad i = \frac{I+1}{2} \tag{5.7}$$

5.3.5 Mutation

After two parents have combined genes to produce a new individual, a process analogous to genetic mutation is used to introduce variability into the population, which ensures the entire search space is explored and that the solution does not become trapped at a local maximum. Mutation is accomplished by introducing random variations into one or more of an individual's genes. The probability that a gene is mutated is relatively low, perhaps 0.05. Mutation is performed on a gene–by–gene basis. At the start of the calculation, each parameter (gene) is assigned a user–specified mutation probability $p_{mut,j}$. Mutation is performed on the intermediate population $\{C\}$ and begins by generating a matrix of random numbers, denoted r_j^I (where $I = 1 \ldots N$ and $j = 1 \ldots n$) belonging to a uniform distribution on the interval [0,1]. Mutation occurs on individual I gene j if $r_j^I \le p_{mut,j}$. If a gene is selected for mutation, then one of two types of equiprobable mutation occur. In the first (Equation 5.8a) the gene is simply replaced with a randomly generated value. In the second, the gene is replaced with an excursion from its current value (Equation 5.8b):

$$C_j^I = a_{j,\min} + r\left(a_{j,\max} - a_{j,\min}\right) \tag{5.8a}$$

$$C_{\mathrm{j}}^I = C_{\mathrm{j}}^I + s\, v_{mut}\left(a_{j,\max} - a_{j,\min}\right) \tag{5.8b}$$

In Equation 5.8a, r is a random number on the interval [0, 1], and in Equation 5.8b s is a random number on the interval [–0.5, 0.5]. The user–specified parameter v_{mut} controls the severity of the mutation and is generally less than 1.

5.3.6 Replacement

The final step in the genetic algorithm is to replace the parents with the offspring. In the algorithm used here, the offspring (i.e., the individuals in the intermediate population) completely replace the parents:

$$A^I(\ell+1) = C^I(\ell) \quad \text{for } I = 1,2,3,\ \ldots\ N \tag{5.9}$$

The processes of selection, reproduction, and mutation and replacement are repeated until a predetermined number of generations has passed or the solution converges, meaning no further improvement of the solution occurs with subsequent generations.

5.4 Application to a synthetic material with known properties

To assess the methodology's capabilities, a hypothetical charring material with a thickness of 10 mm is used to generate a set of simulated experimental data under nonflaming conditions at 25 kW/m^2 and 75 kW/m^2 irradiance. A known set of input parameters is used to generate synthetic experimental data, i.e. real experimental data are not used. This represents a situation where the thermophysical properties of an idealized material are known exactly, and provides an opportunity to see how closely the genetic algorithm can match these known properties.

The overall fitness is evaluated from the surface temperature, back face temperature, mass loss rate, and cumulative mass loss. All eight ϕ values are set to 1, a value of $\varepsilon = 0.1$ is used, and the fitness exponent ζ is set to 2. In this case, the maximum attainable fitness is $8/\varepsilon^{\zeta} = 800$.

The evolution of the population–averaged fitness and the fitness of the best individual found at any point during the evolution process are shown in Figure 5.2. The

average fitness, an indication of the quality of the "gene pool", increases rapidly for the first ~40 generations but increases only slightly or plateaus thereafter. By 150 generations, the highest fitness found during in the evolution process reached over 600, or 75% of the maximum attainable fitness (800). For practical situations, it would have been adequate to stop the algorithm after ~150 generations.

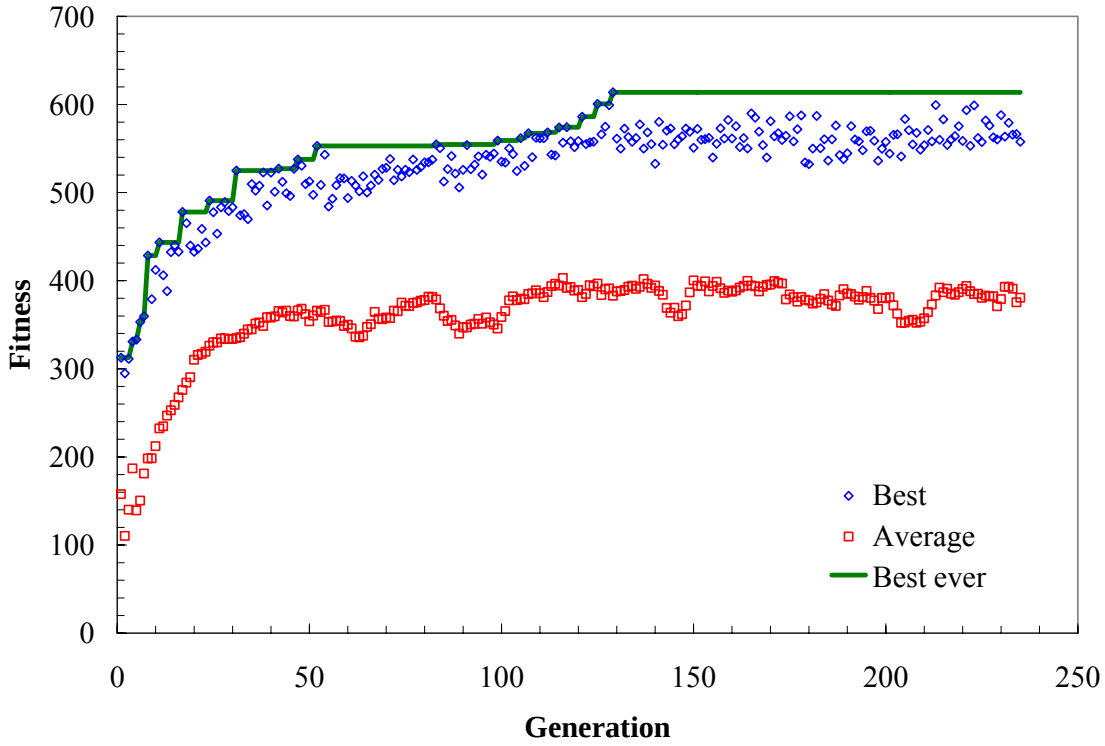

Figure 5.2. Evolution of average and best fitness to ~250 generations for simulated experimental data case.

Table 5.1 gives a comparison of the optimal values found by the genetic algorithm and the actual values used to generate the simulated experimental data. The algorithm matched 7 of 13 parameters within 10%. The biggest error was for the specific heat capacity temperature exponents. The lower value of the pre–exponential factor found by the genetic algorithm is compensated for by the slightly lower activation energy. This compensation effect between the pre–exponential factor and the activation energy has

long been observed to occur in the estimation of pyrolysis kinetics parameters from thermogravimetric analysis [126, 204]. Due to the kinetic compensation effect, the algorithm may not find the "true" values of the pre–exponential factor and the activation energy, but it will find values of these parameters that match the Arrhenius function over the temperature range within which pyrolysis occurs.

Table 5.1. Comparison of actual material properties used to generate simulated experimental data and material properties found with genetic algorithm.

Property	Actual	GA	% Error
Pre–exponential factor (s^{-1})	2.00×10^{11}	1.56×10^{10}	–92.2
Activation energy (kJ/mol)	142.0	130.4	–8.2
Reaction order (–)	2.00	1.90	–5.0
Char density (kg/m^3)	100.0	102.9	2.9
Heat of pyrolysis (J/kg)	5.00×10^5	5.21×10^5	4.1
Virgin conductivity @ 300 K (W/m–K)	0.200	0.207	3.6
Char conductivity @ 300 K (W–m–K)	0.060	0.095	59.0
Virgin conductivity temperature exponent (–)	0.500	0.397	–20.5
Char conductivity temperature exponent (–)	0.800	0.395	–50.6
Virgin specific heat @ 300 K (J/kg–K)	1400	1333	–4.8
Char specific heat @ 300 K (J/kg–K)	1600	1610	0.6
Virgin specific heat temperature exponent (–)	0.200	0.379	89.6
Char specific heat temperature exponent (–)	0.100	0.477	376.8

A comparison of the simulated experimental surface temperature, back face temperature, and mass loss rate with the model predictions using the optimal material properties found by the genetic algorithm is given in Figure 5.3. It is seen that the agreement is excellent, which verifies the methodology's capabilities to estimate material properties from experimental data.

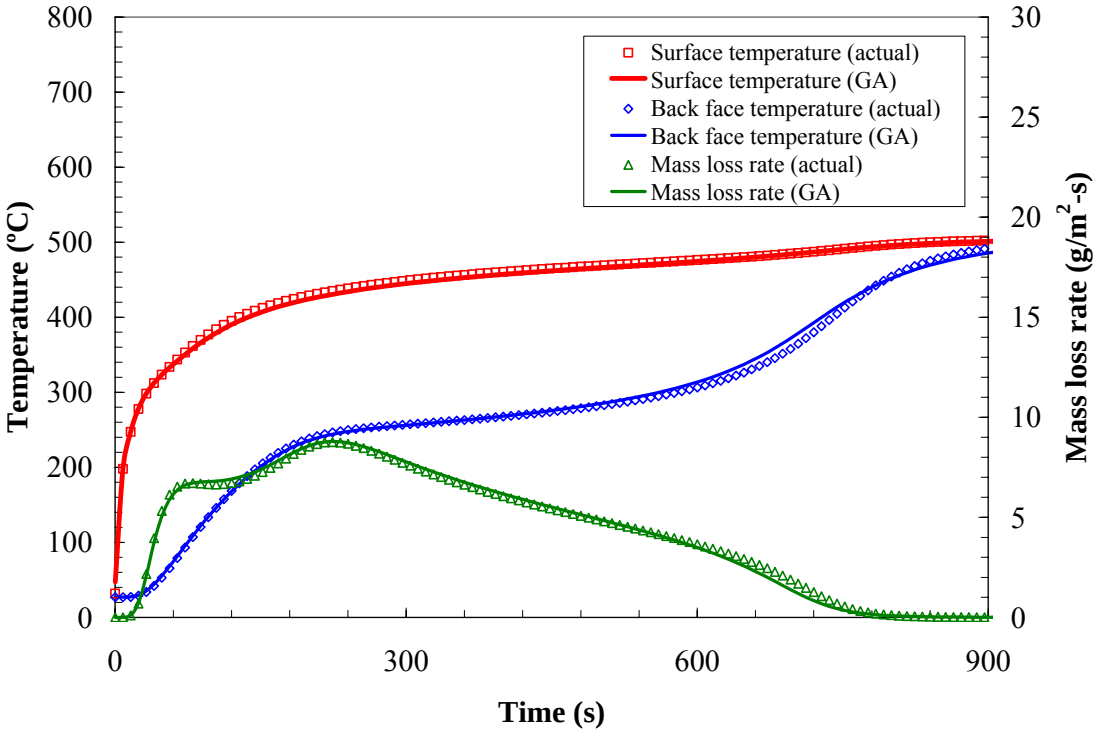

(a)

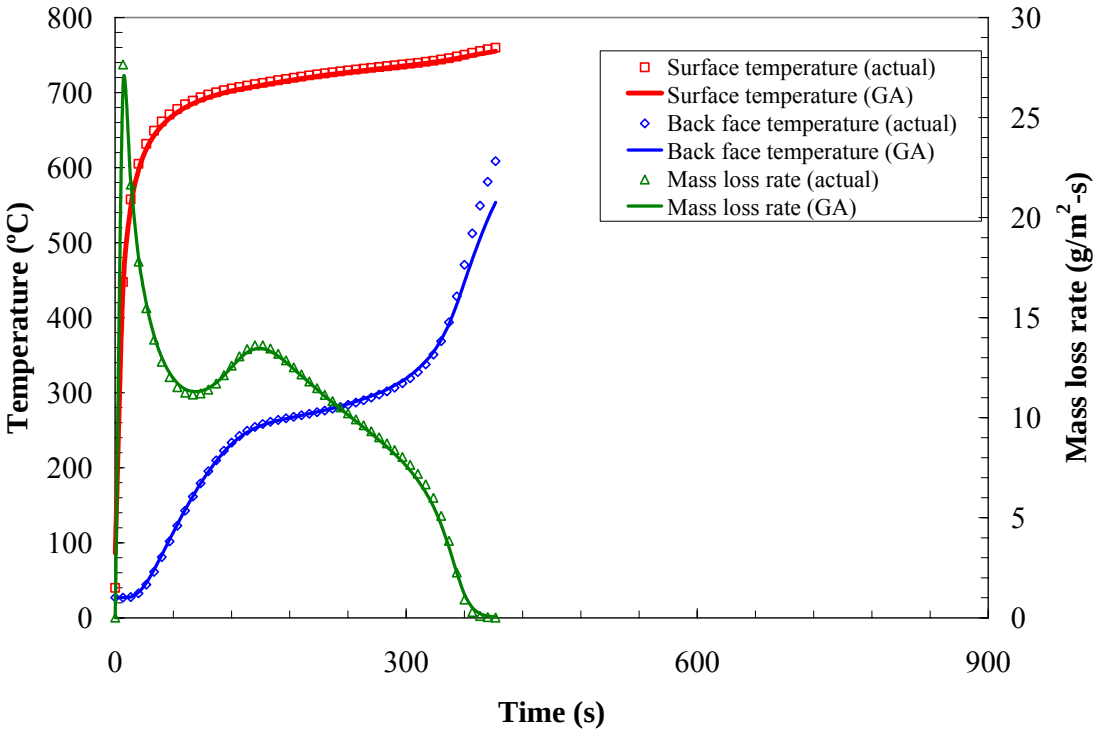

(b)

Figure 5.3. Comparison of simulated experimental data and model calculations using optimized material properties determined by GA. (a) 25 kW/m^2 irradiance; (b) 75 kW/m^2 irradiance.

6.0 APPLICATION OF MODEL TO REAL FUELS

In earlier chapters, the generalized pyrolysis model and genetic algorithm optimization methodology are applied only to hypothetical materials. In this chapter, calculations of the generalized pyrolysis model are compared with experimental data after using the genetic algorithm to estimate the required material properties. Specifically, the thermo–oxidative decomposition of a noncharring thermoplastic (PMMA) and a charring material (white pine) are modeled. Also simulated are the gasification and swelling of an intumescent coating and smolder wave propagation in polyurethane foam. The model's predictive capabilities are assessed by comparing its calculations to experimental data that were not used as part of the property estimation process.

In the simulations below, the initial grid spacing is 0.1 mm, except for the intumescent coating simulation where 0.025 mm is used. The time step is constant at 0.1 s. Except in the smolder simulation, the back face is impermeable to mass transfer and is perfectly insulated. In the smolder simulation, the back face temperature is directly specified to emulate the experimental ignition protocol. The front face boundary condition is a convective–radiative balance. For simulations where the pressure distribution is explicitly solved, all condensed phase species are assumed to have a permeability of 1×10^{-10} m^2. The gaseous specific heat is constant (independent of temperature) and equal to 1000 J/kg–K. Other gas properties (M, σ, and ε/k) are estimated from Bird *et al.* [193] wherever possible (*i.e.*, for oxygen and nitrogen).

6.1 Noncharring gasification – PMMA

PMMA decomposition kinetics and thermodynamics (as well as the composition of the volatiles generated) are sensitive to oxygen concentration. This has been

demonstrated by Kashiwagi and Ohlemiller [55] by measuring the mass loss rate of PMMA irradiated under nonflaming conditions at 17 and 40 kW/m^2 in atmospheres ranging from pure nitrogen to 40% oxygen by volume. They found that the mass loss rate increases with the oxygen content of the atmosphere, but the oxygen sensitivity is more noticeable at 17 kW/m^2 irradiance than 40 kW/m^2 (see Figure 2.3). They hypothesized that this may be caused by a reduction in oxygen concentration in the vicinity of the irradiated surface due to blowing. Since the mass loss rates are higher at 40 kW/m^2 irradiance, the blowing effect is greater and it is more difficult for oxygen to penetrate into the bubble layer.

This set of experiments has been previously modeled by Esfahani and co workers [111, 205] with good results. However, the effect of oxygen on the decomposition process was incorporated essentially by introducing a pre–exponential factor that varies with the freestream oxygen concentration. Diffusion of oxygen into the bubble layer was not explicitly modeled, so the blowing effect was not captured. This may explain why different pre–exponential factors and heats of volatilization were used to simulate the 17 kW/m^2 experiments [111] and the 40 kW/m^2 experiments [205]. In the modeling approach outlined below, diffusion of oxygen into the bubble layer is explicitly modeled and the input parameters do not depend on heat flux or oxygen concentration.

Two condensed phase species are considered in the simulations: pmma and bpmma. The latter is "bubbled" PMMA having a bulk density 95% of that of the virgin PMMA and a porosity of 5%. Penetration of ambient oxygen into the bubble layer is modeled by approximating the bubble layer as a porous medium. Oxidative reaction rates are related to the local oxygen concentration inside the decomposing solid, rather than the

freestream value. Four gaseous species are tracked, numbered as follows: 1) thermal pyrolysate; 2) oxygen; 3) nitrogen; 4) oxidative pyrolysate.

Three reactions are considered: 1) Transformation of pmma to bpmma in a condensed phase to condensed phase reaction; 2) Thermal pyrolysis of bpmma in the absence of oxygen to produce thermal pyrolysate (mostly MMA monomer); 3) Oxidation of bpmma to produce oxidative pyrolysate while consuming oxygen in the process. The assumed 3–step reaction mechanism is given in Equation 6.1:

$$\text{pmma} \rightarrow \text{bpmma} \tag{6.1.1}$$

$$\text{bpmma} \rightarrow \text{thermal pyrolysate} \tag{6.1.2}$$

$$\text{bpmma} + \nu_{O_2}\, O_2 \rightarrow \nu_{\text{opyro}}\ \text{oxidative pyrolysate} \tag{6.1.3}$$

Using Equations 3.53 and 3.54b – 3.54d to relate the ν coefficients in Equation 6.1 to the species yield matrix ($y_{s,j,k}$), it can be seen that $\nu_{O_2} \equiv -y_{s,3,3}$ and $\nu_{\text{opyro}} \equiv y_{s,4,3}$. That is, ν_{opyro} is equivalent to the species yield of the fourth gaseous species (oxidative pyrolysate) from the third reaction (Equation 6.1.3).

For these simulations, there is no melting ($\Delta H_m = 0$), and radiative heat transfer across pores is not modeled ($\gamma = 0$). However, in–depth radiation absorption is modeled by using a non–infinite absorption coefficient. The experiments were conducted under natural convection, and a convective heat transfer coefficient of 10 W/m^2–K is assumed for the simulations. The Couette model for blowing (Equation 3.25) is not used.

Model input parameters are estimated using genetic algorithm optimization from the experiments of Kashiwagi and Ohlemiller [55] at 40 kW/m^2 irradiance. After estimating the input parameters from the 40 kW/m^2 experimental data, the model is used with these input parameters to simulate the 17 kW/m^2 experiments [55]. This provides

insight into whether model input parameters optimized for one heat flux level are applicable to other heat flux levels. Tables 6.1 through 6.3 at the end of this section list the optimized model input parameters.

The 40 kW/m^2 experimental data and model calculations using the optimized input parameters are shown separately at all oxygen concentrations in Figure 6.1, and comparisons of the model calculations and experimental data at individual oxygen concentrations are shown in Figure 6.2. There is good agreement between the model calculations and the experimental data. The model correctly predicts the experimentally observed trend of decreasing surface temperature with increasing ambient oxygen concentration.

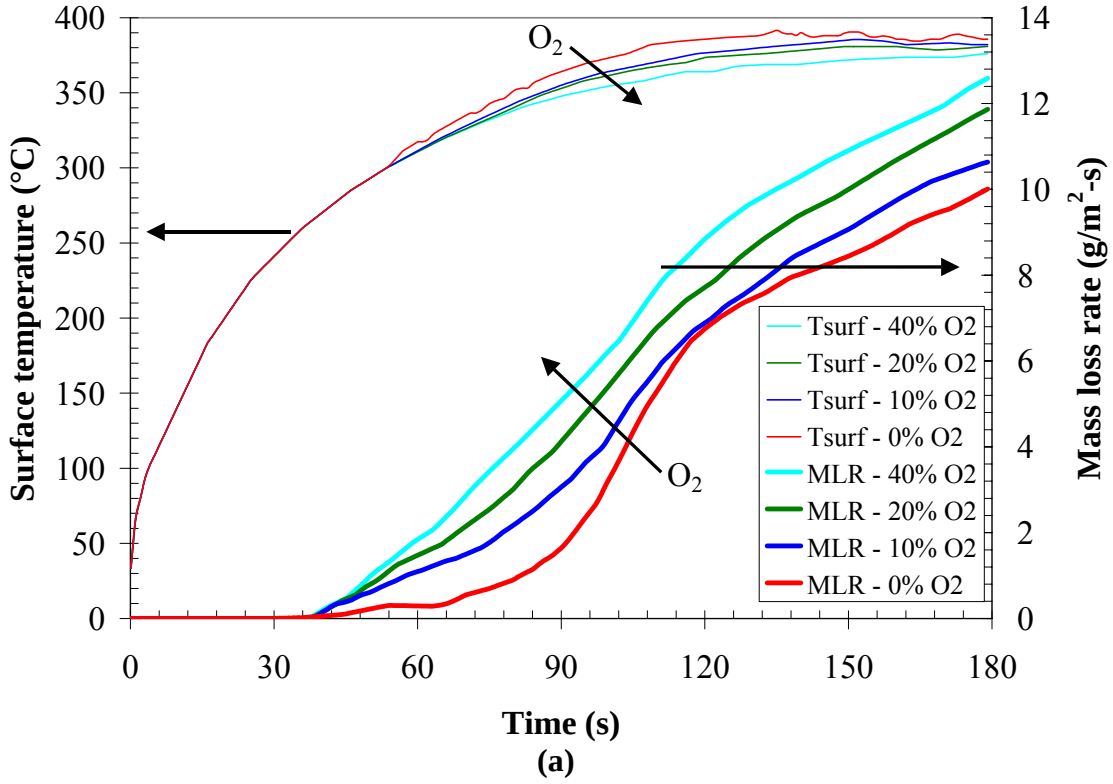

(a)

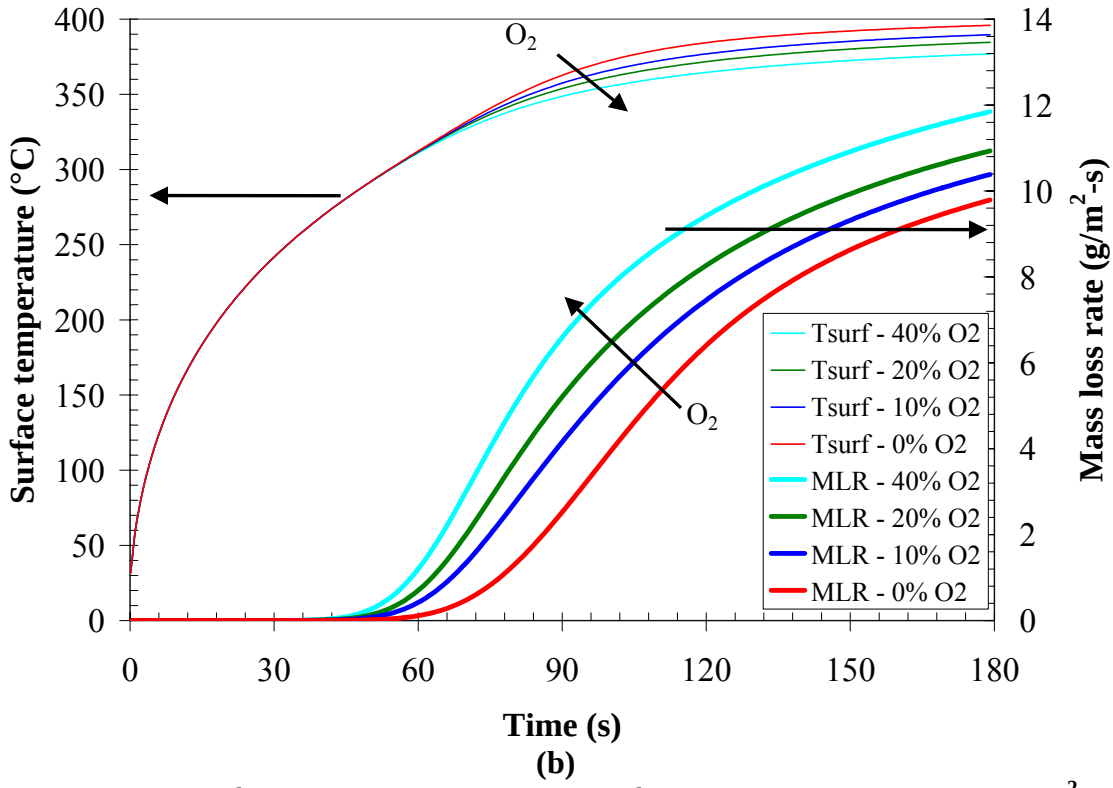

(b)

Figure 6.1. Surface temperature and MLR of PMMA irradiated at 40 kW/m^2. (a) Experimental data [55]; (b) Model.

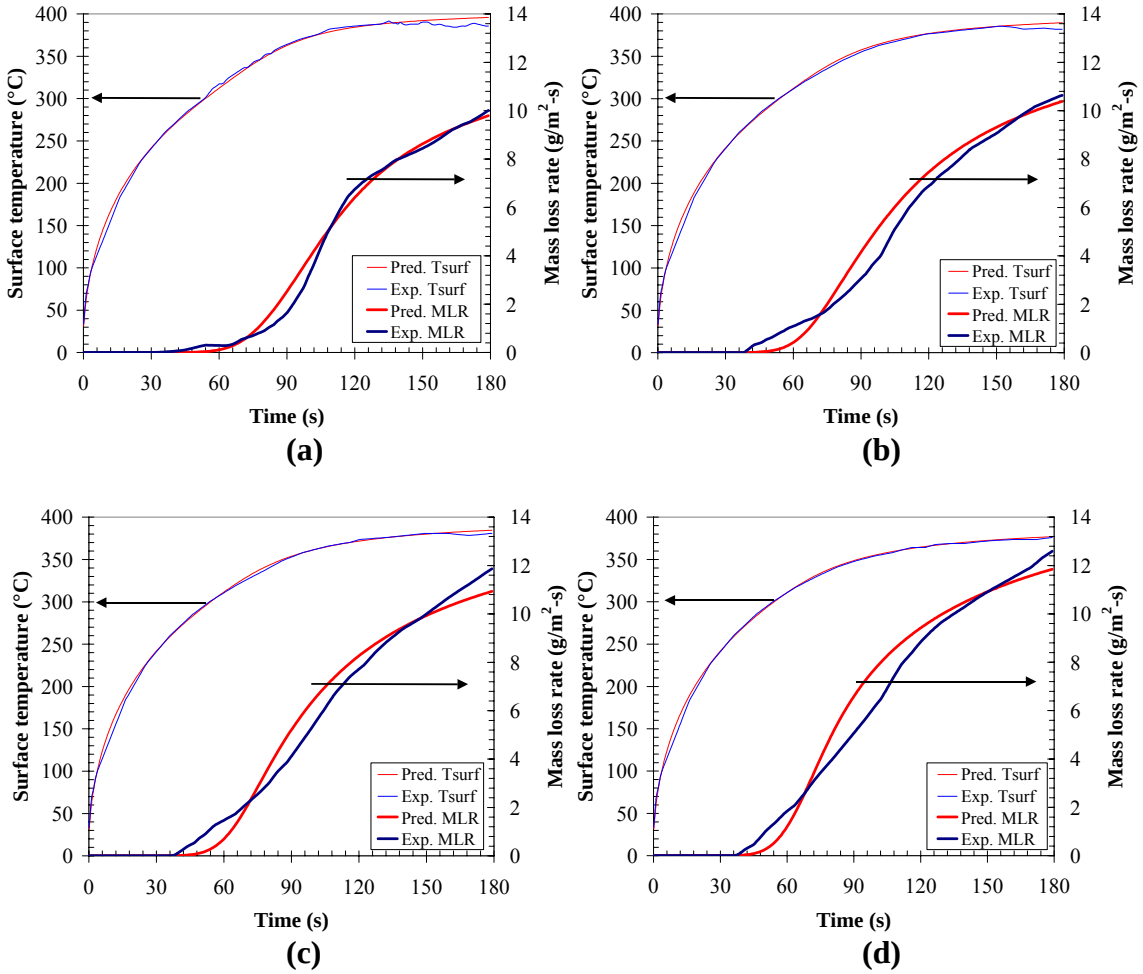

Figure 6.2. Comparison of experimental [55] and modeled surface temperature and mass loss rates of PMMA irradiated at 40 kW/m^2.
(a) N_2; (b) 10% O_2; (c) 20% O_2; (d) 40% O_2.

Since the parameters were optimized at a heat flux of 40 kW/m^2, the experiments at 17 kW/m^2 [55] are used to assess the model's predictive capabilities for experimental conditions not included in the property estimation process. The experimental results (at all oxygen levels) are shown in Figure 6.3a, and the model predictions are shown in Figure 6.3b. Detailed comparisons are shown in Figures 6.4a–6.4d.

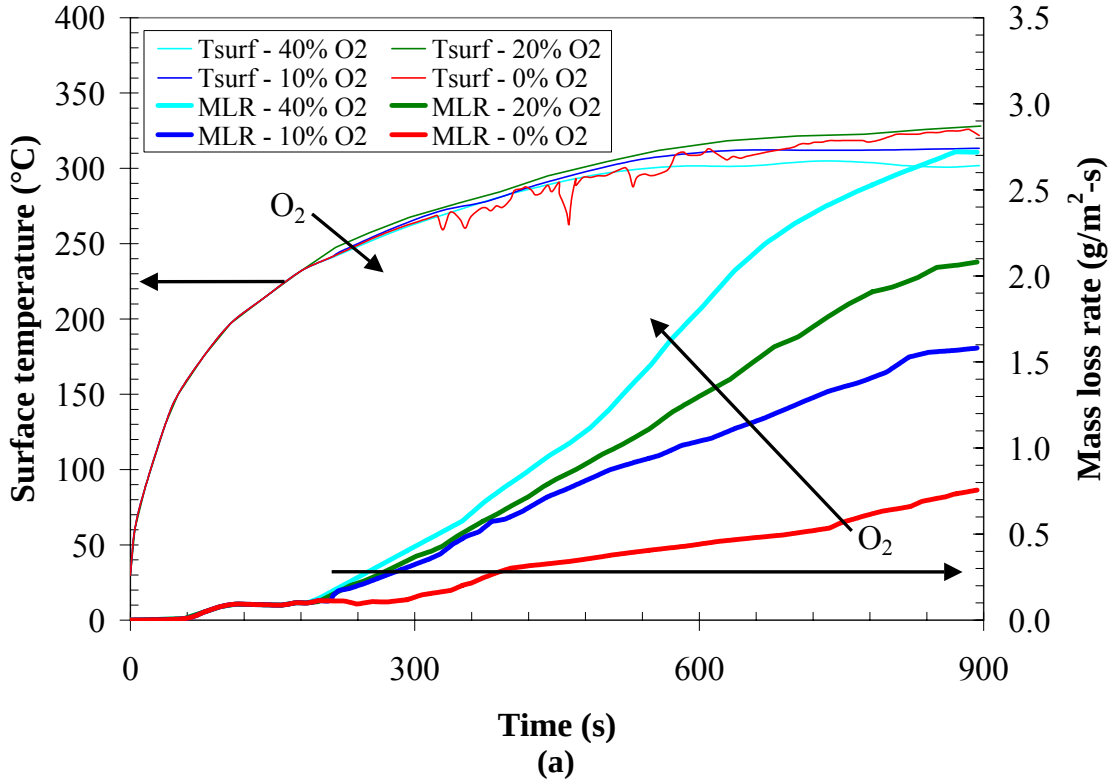

(a)

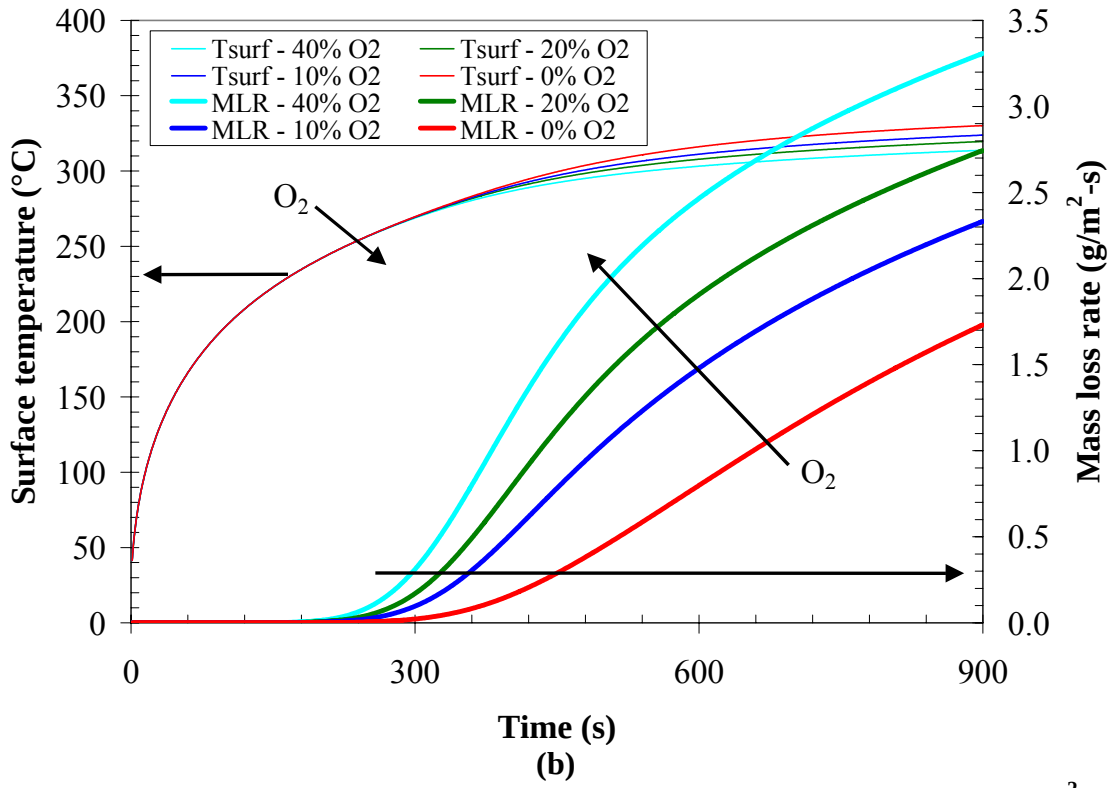

(b)

Figure 6.3. Surface temperature and MLR of PMMA irradiated at 17 kW/m^2. (a) Experimental data [55]; (b) Model.

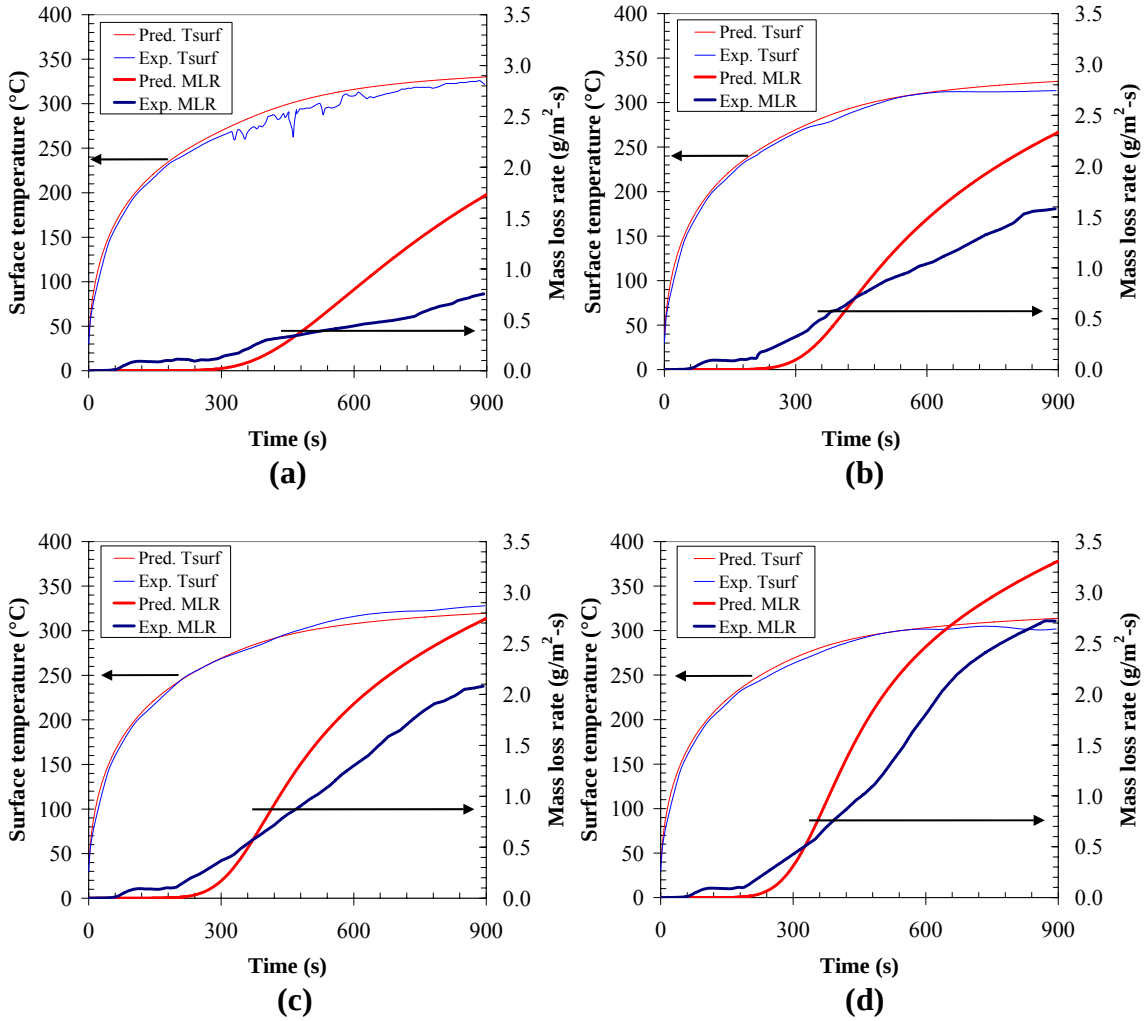

Figure 6.4. Comparison of experimental [55] and modeled surface temperature and mass loss rates of PMMA irradiated at 17 kW/m^2.
(a) N_2; (b) 10% O_2; (c) 20% O_2; (d) 40% O_2.

It can be seen from Figure 6.3 that the model correctly captures the experimentally observed increase in the oxygen sensitivity at 17 kW/m^2 irradiance compared to 40 kW/m^2. Figure 6.4 shows that the model predicts the surface temperatures well. Also, the mass loss rate is predicted reasonably well, but there is a bias toward over–prediction at later times.

Although it is possible to experimentally measure only the total mass loss rate, the model here tracks the mass loss rate due to generation of different gaseous species. In the

simulations, the pyrolysate is either thermal (forms in the absence of oxygen) or oxidative (forms in the presence of oxygen). Figure 6.5 shows the total mass loss rate, the mass loss rate due to generation of thermal pyrolysate, and the mass loss rate due to generation of oxidative pyrolysate. This type of information regarding the composition of the pyrolysate may be important when coupling to a CFD code that handles gas phase combustion, particularly if different volatiles produced during pyrolysis have different combustion characteristics.

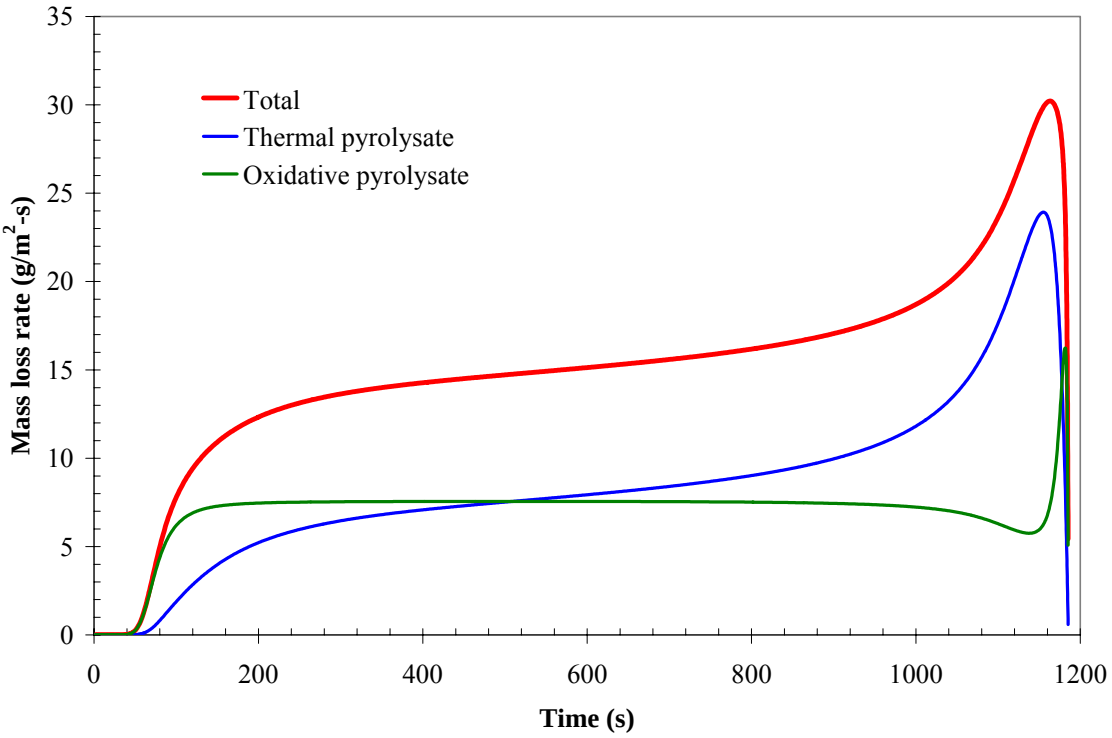

Figure 6.5. Total mass loss rate, mass loss rate due to generation of thermal pyrolysate, and mass loss rate due to generation of oxidative pyrolysate. Sample thickness is 15 mm, heat flux is 40 kW/m^2, and O_2 concentration is 40%.

Given an ignition criterion (such as critical surface temperature or critical mass loss rate) the model can calculate ignition times as a function of heat flux, oxygen concentration, sample thickness, etc. Drysdale and Thomson [206] measured the critical mass loss rate at ignition of two different types of PMMA (denoted FINN and PX). These

types of PMMA are slightly different from the PMMA used by Kashiwagi and Ohlemiller [55], so the model input parameters estimated here may not directly apply to the PMMA used by Drysdale and Thomson [206]. Nonetheless, Figure 6.6 shows a comparison of experimental ignition time data [206] and the model's predictions using a critical mass loss rate of 1.9 g/m^2–s as the ignition criterion. It can be seen that the model considerably over–predicts the ignition time. This may be due to differences in the PMMA used by Kashiwagi and Ohlemiller [55] and Drysdale and Thomson [206].

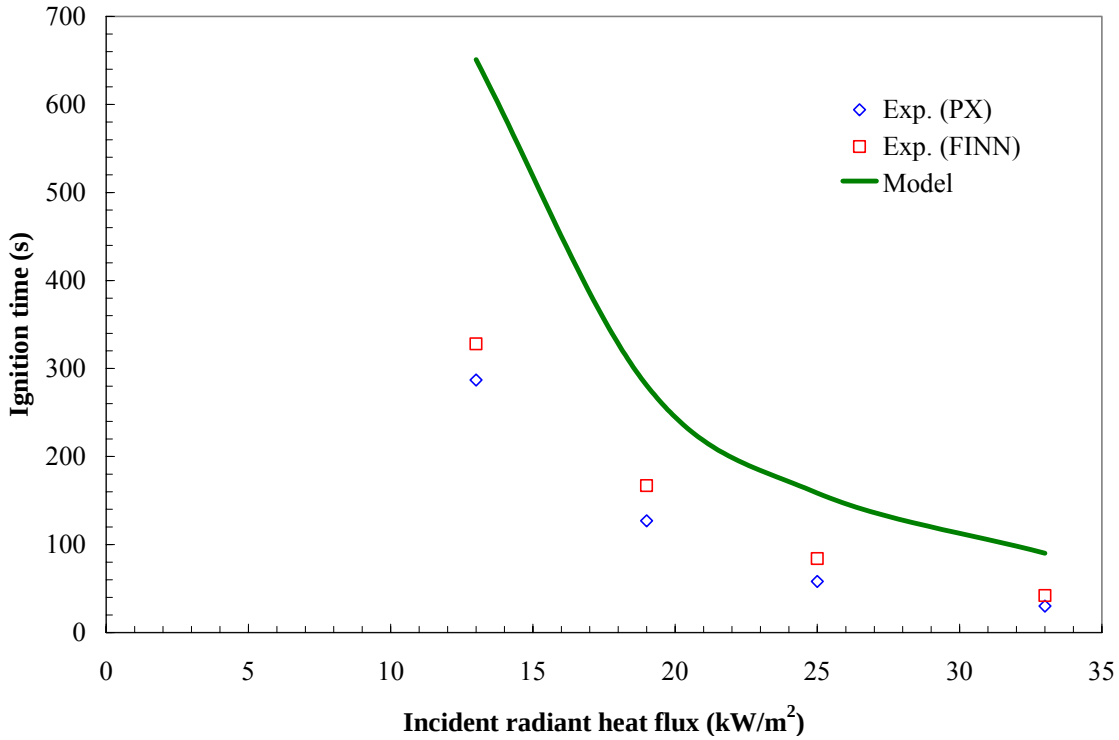

Figure 6.6. Comparison of experimental PMMA ignition time [206] and model predictions using 1.9 g/m^2–s as critical mass loss rate for ignition.

The parameters used in the simulations described above are listed in Tables 6.1 – 6.3. The in–depth absorption coefficients determined by the genetic algorithm are significantly higher than those reported by Manohar *et al.* [174] for PMMA (see Table 2.10). However, the surface emissivity (0.87 – 0.91) is close to the integrated absorptivity

reported by Hallman [166] for clear PMMA irradiated by a blackbody at 1000 K (0.85, see Table 2.8). The optimized heats of volatilization (506 kJ/kg for thermal pyrolysis and 418 kJ/kg for oxidative pyrolysis) are lower than the literature values reported earlier in Table 2.4 (550 kJ/kg under air and 687 – 1080 kJ/kg under nitrogen). Consequently, it is possible that use of these optimized heats of volatilization may over–predict mass burning rates. A comparison of the thermal conductivity and specific heat capacity found by genetic algorithm optimization to data reported by Steinhaus [152] is shown in Figure 6.7. The optimized thermal conductivity and specific heat capacity are generally within 25% of the literature data.

Figure 6.8 gives a comparison of the reaction rate, $Z\exp(-E/RT)$, calculated using the Z and E values located by the genetic algorithm with literature data from Hirata *et al.* [176]. The conventional way to plot Arrhenius reaction rates is the natural logarithm of the reaction rate as a function of inverse temperature, but for consistency with Figure 6.7, the reaction rates are plotted in Figure 6.8 as the base 10 logarithm of the reaction rate as a function of temperature. At 300 °C, the reaction rate from GA optimization is about 2.7 times that calculated from the literature data; at 330 °C it is approximately equal to that calculated from the literature data; at 350 °C it is about 0.7 times that calculated from the literature data; and at 400 °C it is about 0.2 times that calculated from the literature data. The reaction rate optimized by the genetic algorithm best matches that calculated from the literature data over the temperature range where most of the volatilization occurs.

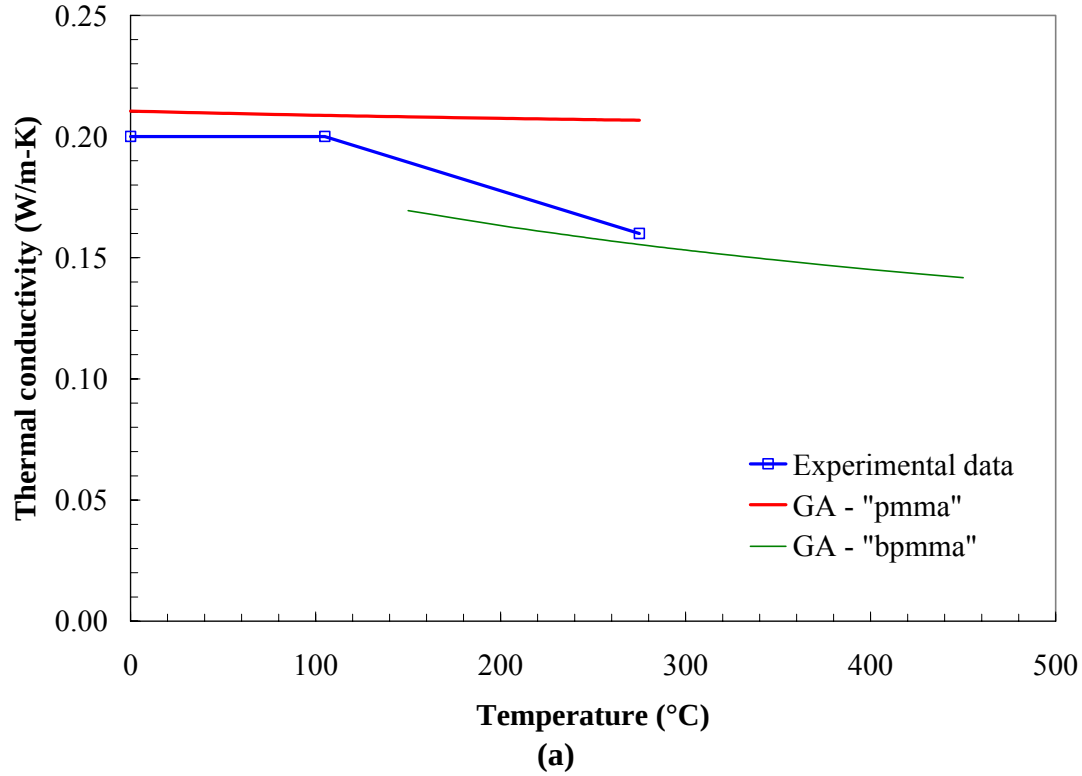

(a)

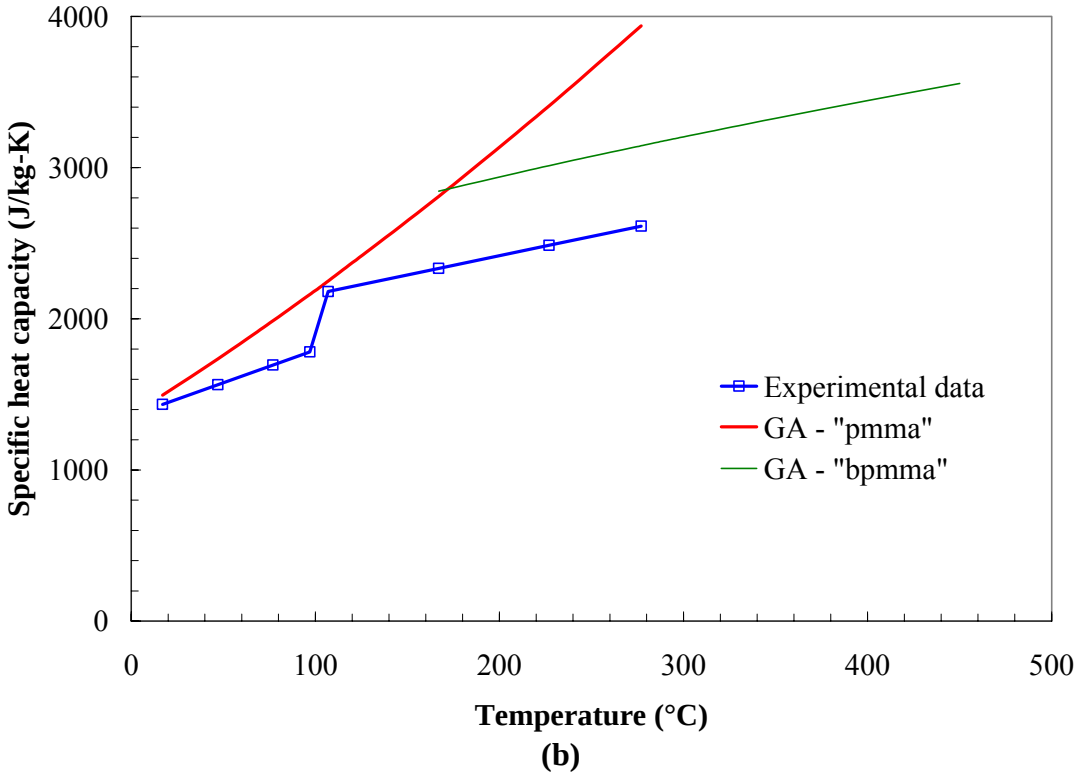

(b)

Figure 6.7. Comparison of temperature–dependent PMMA thermal properties determined by GA optimization and literature data [152]. (a) Thermal conductivity; (b) Specific heat capacity.

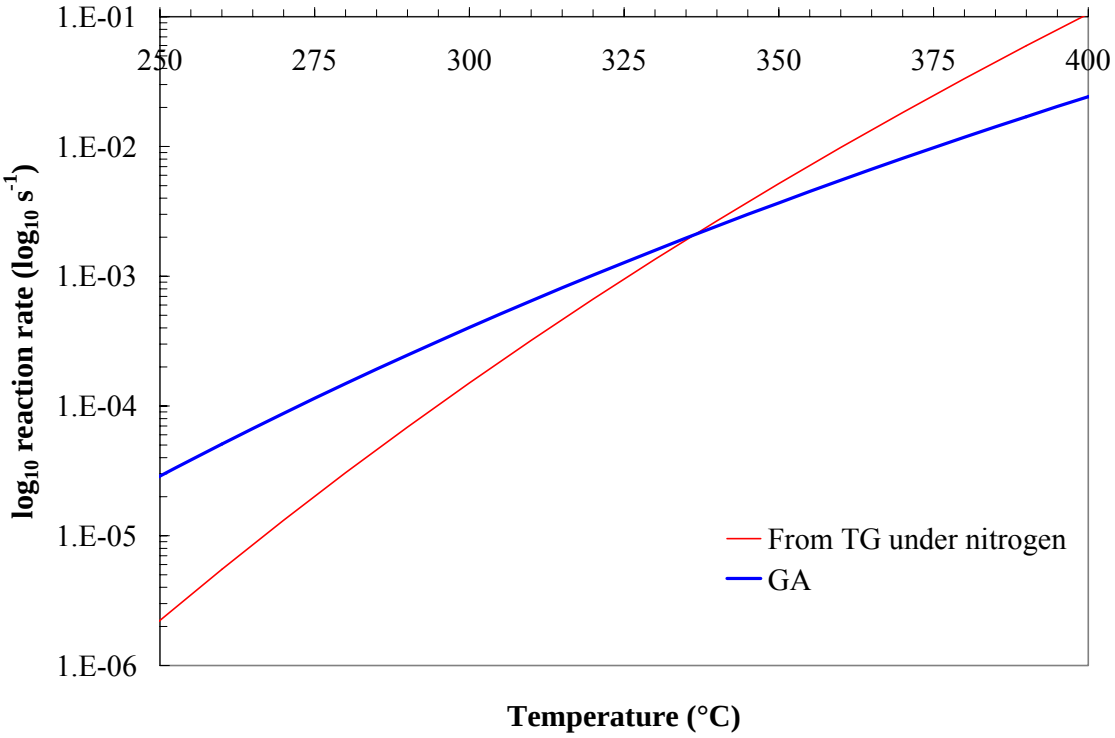

Figure 6.8. Comparison of PMMA reaction rate calculated from *Z* and *E* determined by GA optimization and literature data [176].

Table 6.1. Condensed phase parameters for PMMA simulations.

i	Name	k_0 (W/m–K)	n_k (–)	ρ_0 (kg/m^3)	n_ρ (–)	c_0 (J/kg–K)	n_c (–)	ε (–)	κ (m^{-1})	ρ_{s0} (kg/m^3)
1	pmma	0.21	–0.03	1190	–0.1	1573	1.51	0.87	3400	1190.1
2	bpmma	0.19	–0.33	1131	–0.1	2394	0.45	0.91	2950	1190.1

Table 6.2. Reaction parameters for PMMA simulations.

k	From	To	χ (–)	ΔH_{sol} (J/kg)	ΔH_{vol} (J/kg)	Z (s^{-1})	E (kJ/mol)	n (–)	n_{O2} (–)
1	pmma	bpmma	0	4.58×10^3	0	2.48×10^{10}	128.8	1.22	0
2	bpmma	gases	1	0	5.06×10^5	3.79×10^8	131.3	1.20	0
3	bpmma	gases	1	0	4.18×10^5	1.03×10^9	124.6	1.16	2.48

Table 6.3. Gaseous yields for PMMA simulations.

j \ k	1	2	3
1 (thermal pyrolysate)		1.00	
2 (oxygen)			–0.05
3 (nitrogen)			
4 (oxidative pyrolysate)			1.05

6.2 Charring gasification – white pine

Ohlemiller, Kashiwagi, and Werner [84, 207] experimentally studied the effects of ambient oxygen concentration on the nonflaming gasification of irradiated white pine. Reference [84] contains mass loss rate measurements at multiple heat flux levels and oxygen concentrations as well as surface and in–depth thermocouple temperature measurements. This comprehensive set of experimental data provides a challenging test case for the model. In the experiments, white pine cubes 3.8 cm on edge were irradiated at 25 kW/m^2 and 40 kW/m^2 in oxygen concentrations of 0% (pure nitrogen), 10.5%, and 21% (normal air) by volume. The initial pine density was approximately 380 kg/m^3, with an initial moisture content of ~5% by mass.

The experiments of Kashiwagi, Ohlemiller, and Werner [84] have been simulated by Jia *et al.* [60] and Weng *et al.* [208] using integral charring models. Jia *et al.* [60] modeled only the experiments [84] that were conducted in pure nitrogen because their model did not include exothermic char oxidation. Weng *et al.* [208] recently modeled the experiments [84] with a previously–developed integral model that was modified to explicitly consider char oxidation. Both groups obtained reasonably good agreement between their model calculations and the experimental data. However, neither group explicitly modeled the transport of oxygen from the ambient to the decomposing solid.

Here, the experiments are simulated in greater detail than in the earlier papers [60, 208]. Model parameters are estimated from experimental data in a two–step process. First, the genetic algorithm is used in conjunction with the experimental data obtained under nitrogen to estimate the values of the input parameters that do not involve oxygen (oxidative reactions and species formed by oxidative reactions are not considered). Next,

these parameters are held constant while the remaining parameters are determined by genetic algorithm optimization from the experimental data obtained in oxidative atmospheres at 40 kW/m^2. The model parameters determined by genetic algorithm optimization are listed in Tables 6.4 through 6.8 at the end of this section.

6.2.1 Thermal pyrolysis under nitrogen

The first stage of the property estimation process involves only non–oxidative (nitrogen) atmospheres. Three condensed phase species are considered: 1) wet wood, 2) dry wood, and 3) char. The gas phase is comprised of 3 species: 1) thermal pyrolysate, 2) nitrogen, and 3) water vapor. A two–step reaction mechanism is implemented:

$$\text{wet wood} \rightarrow \nu_{\text{dw}}\ \text{dry wood} + \nu_{\text{H}_2\text{O}}\text{H}_2\text{O} \tag{6.2.1}$$

$$\text{dry wood} \rightarrow \nu_{\text{char}}\ \text{char} + \nu_{\text{tp}}\ \text{thermal pyrolysate} \tag{6.2.2}$$

The first reaction is modeled after Atreya [209]. Due to mass conservation considerations, some of the coefficients in the above reaction mechanism are interrelated. Making use of Equations 3.53 (assuming $\chi = 1$, i.e. there is no swelling or shrinkage) and 3.54b – 3.54d, the following relations are obtained:

$$\nu_{\text{dw}} = \text{SF}_1 = \frac{\rho_{\text{dw}}}{\rho_{\text{ww}}} = 0.95$$

$$\nu_{\text{H}_2\text{O}} = 1 - \text{SF}_1 = 1 - \frac{\rho_{\text{dw}}}{\rho_{\text{ww}}} = 0.05$$

$$\nu_{\text{char}} = \text{SF}_2 = \frac{\rho_{\text{char}}}{\rho_{\text{ww}}}$$

$$\nu_{\text{tp}} = 1 - \text{SF}_2 = 1 - \frac{\rho_{\text{char}}}{\rho_{\text{ww}}}$$

where the bulk density of wet wood is ρ_{ww}, the bulk density of dry wood is ρ_{dw}, and ρ_{char} is the bulk density of char.

In the simulations, the thermal properties of all condensed phase species are assumed to vary with temperature. Radiative heat transfer across char pores is modeled, and condensed phase species have different emissivities to account for blackening of the surface as charring occurs. Thermal equilibrium between the condensed phase and the gas phase is assumed. The 25 unknown parameters are estimated by genetic algorithm optimization from the 40 kW/m^2 nitrogen experimental data.

A comparison of the model calculations using the optimized parameters and the experimental temperature data for the 40 kW/m^2 experiment is shown in Figure 6.9a. The calculated surface temperature is slightly higher than the experimental data, but the temperatures calculated at 5 mm and 10 mm match the experimental data well. A slight "water plateau" (caused by the endothermic evaporation of water) is evident in the 10 mm experimental temperature trace as the temperature approaches 100 ºC. This plateau is not captured in the model calculations, perhaps because in the model the drying reaction occurs over a temperature range that is too wide. This suggests that a higher activation energy and pre–exponential factor than are used here may be more appropriate to simulate drying.

The calculated mass loss rate (Figure 6.9b) matches the experimental data reasonably well, except that the peak mass loss rate calculated by the model is ~10% lower than the experimental data and occurs 20 s earlier than in the experiment. This level of accuracy is acceptable considering the complexity of the problem.

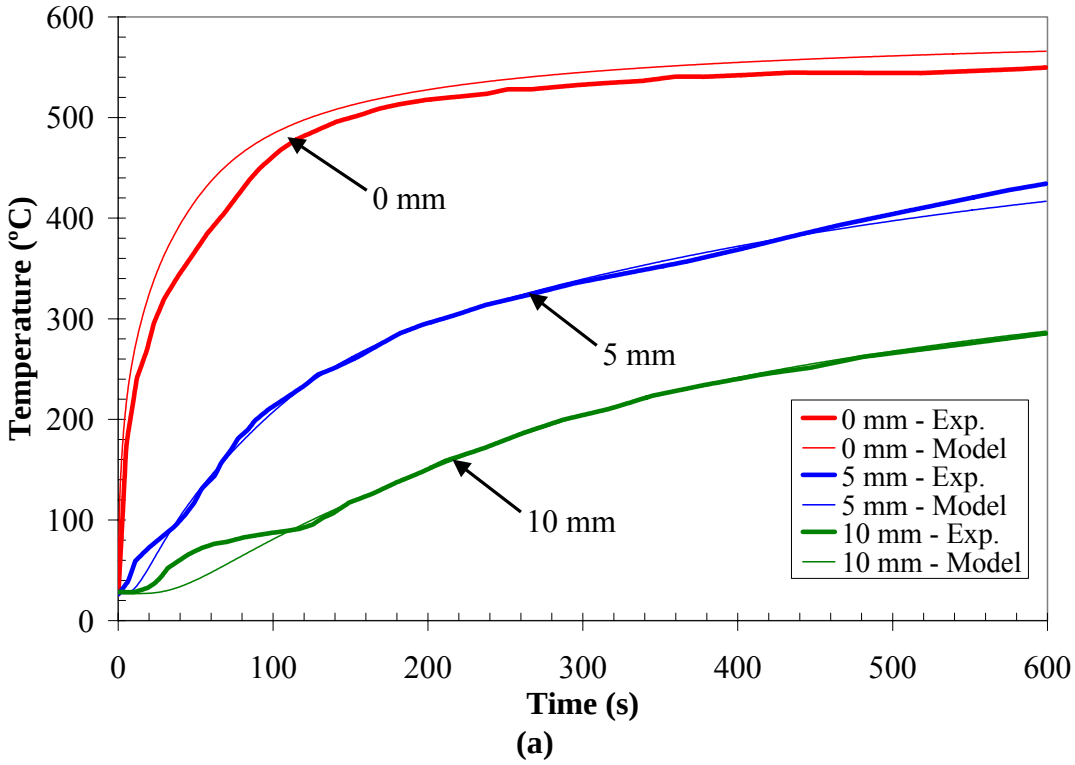

(a)

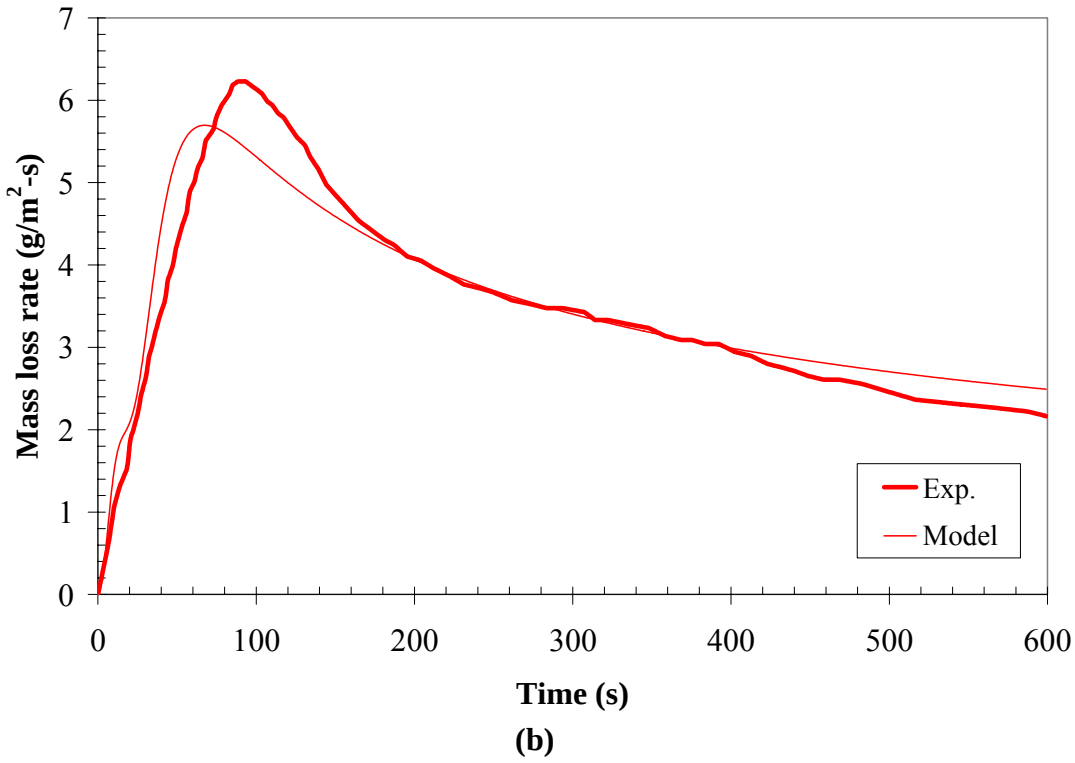

(b)

Figure 6.9. Comparison of optimized model calculations and experimental data [84] for pyrolysis of white pine at 40 kW/m^2 irradiance in nitrogen. (a) Temperature; (b) Mass loss rate.

The experimental data under nitrogen at an irradiance of 25 kW/m^2 were not used in the parameter estimation process. Therefore, they are used to assess the model's predictive capabilities for experimental conditions not included in the parameter estimation process. The model is used with the input parameters estimated from the 40 kW/m^2 experiment to simulate the 25 kW/m^2 experiment, and a comparison of the model predictions and the experimental data is give in Figure 6.10. It can be seen that the shapes of the curves match reasonably well, but the maximum mass loss rate is over–predicted by almost 20% and the peak occurs approximately 2 minutes earlier in the model than in the experiment.

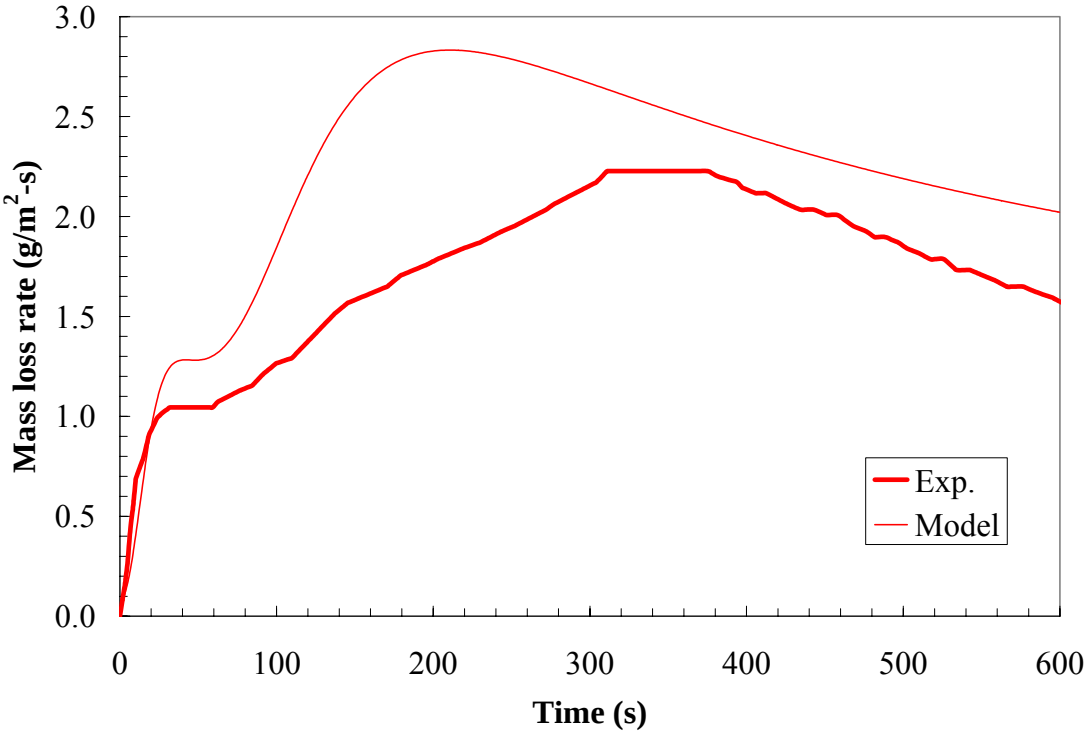

Figure 6.10. Comparison of modeled mass loss rate and experimental data [84] for pyrolysis of white pine at 25 kW/m^2 irradiance in nitrogen.

In this work, temperature–dependent specific heat capacity and thermal conductivities are used for each condensed phase species. Although Jia *et al.* [60] and

Weng *et al.* [208] simulated the same experiments, they used constant thermal properties. However, Yang *et al.* [75] simulated white pine pyrolysis using temperature dependent thermal properties. Also, in Section 2.3.1, temperature–dependent thermal properties are compiled for generic wood. Figures 6.11 and 6.12 compare the temperature–dependent thermal properties from Yang *et al.* [75] and generic wood properties from Section 2.3.1 with the optimized values located by the genetic algorithm. The generic wood property correlations are denoted "literature (generic)" and values used by Yang *et al.* [75] are denoted "literature (white pine)" in Figures 6.11 and 6.12.

In Figure 6.11a, the specific heat capacity of wet wood and dry wood used in this work are compared with the available literature data. It can be seen that the specific heat capacity of dry wood as determined by the genetic algorithm falls between the available literature data. The specific heat capacity of wet wood used in these calculations is within ~20% of the literature data. Figure 6.11b shows the specific heat capacity of char optimized by the genetic algorithm falls between the available literature data.

Figure 6.12 gives similar plots for thermal conductivity. It can be seen from Figure 6.12a that the thermal conductivity of both wet wood and dry wood optimized by the genetic algorithm is approximately a factor of two higher than the generic wood literature data, but it matches the white pine literature data within ~20%. Interestingly, Figure 6.12a shows the opposite trend for wood char, i.e. the thermal conductivity optimized by the genetic algorithm matches the generic wood literature data, particularly from 200 ºC to 400 ºC, but is only 20% to 50% that of the white pine literature data.

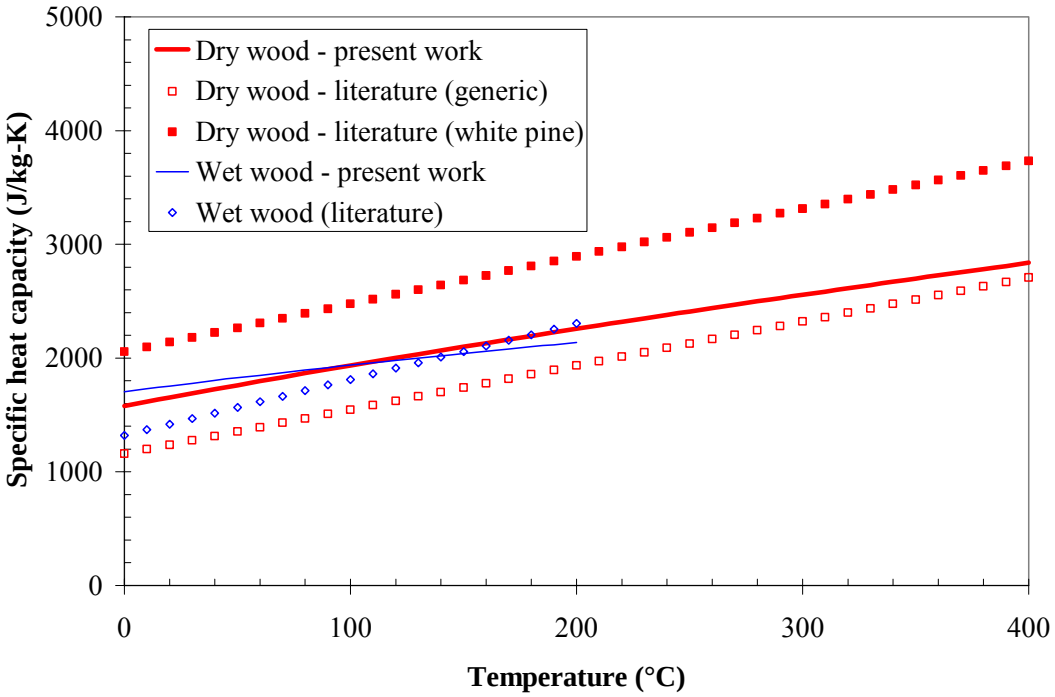

(a)

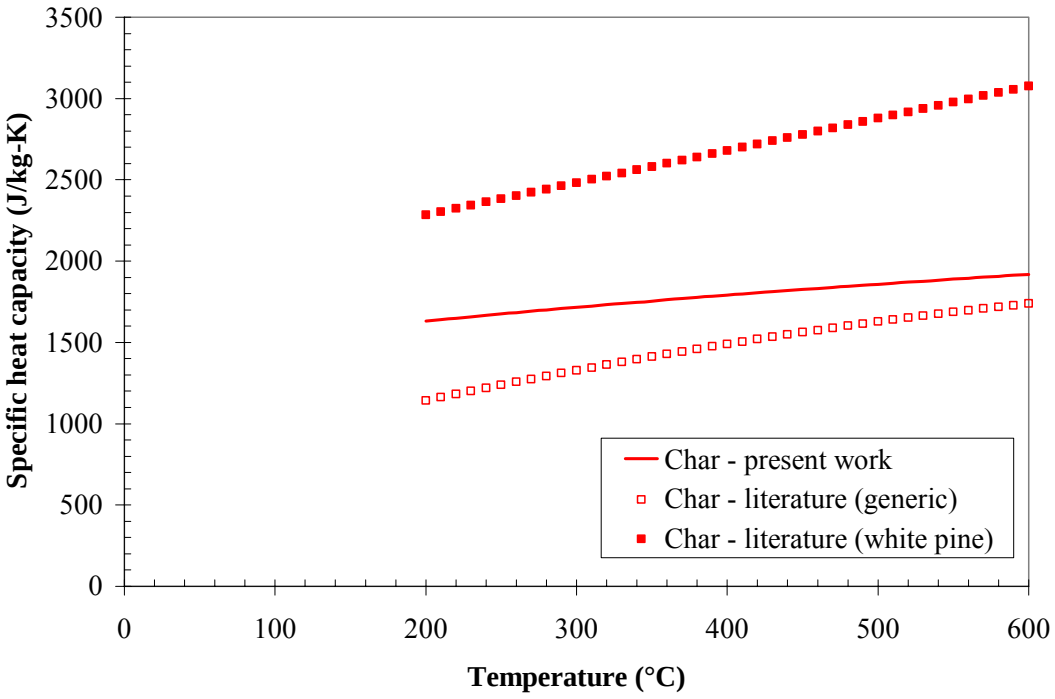

(b)

Figure 6.11. Comparison of white pine temperature–dependent specific heat capacity optimized by genetic algorithm with literature data. (a) Virgin wood; (b) Char.

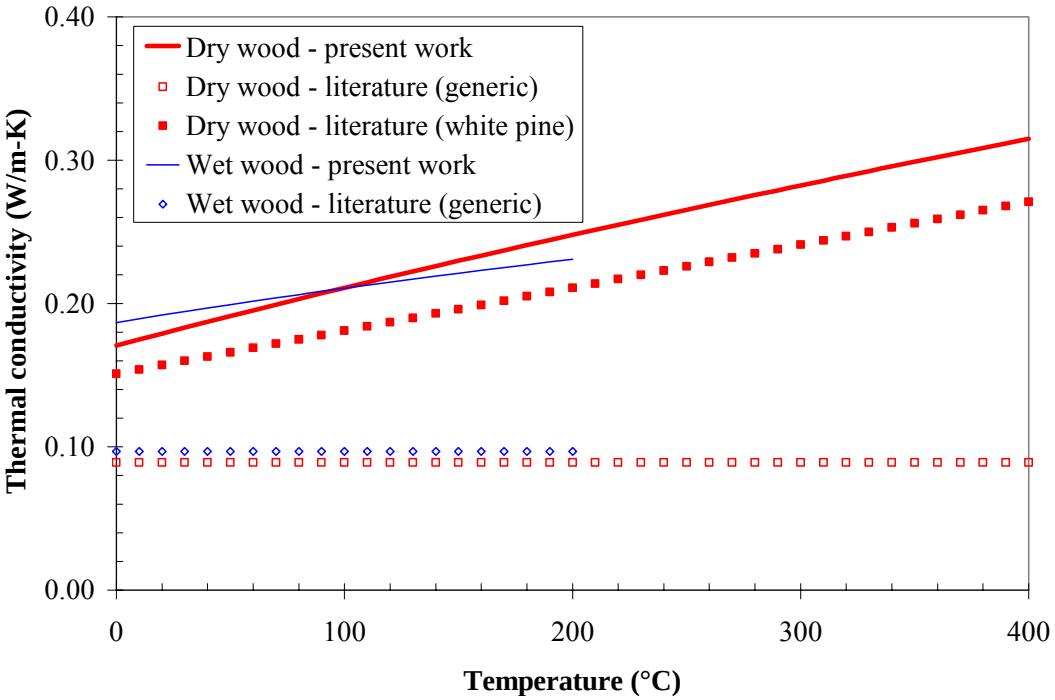

(a)

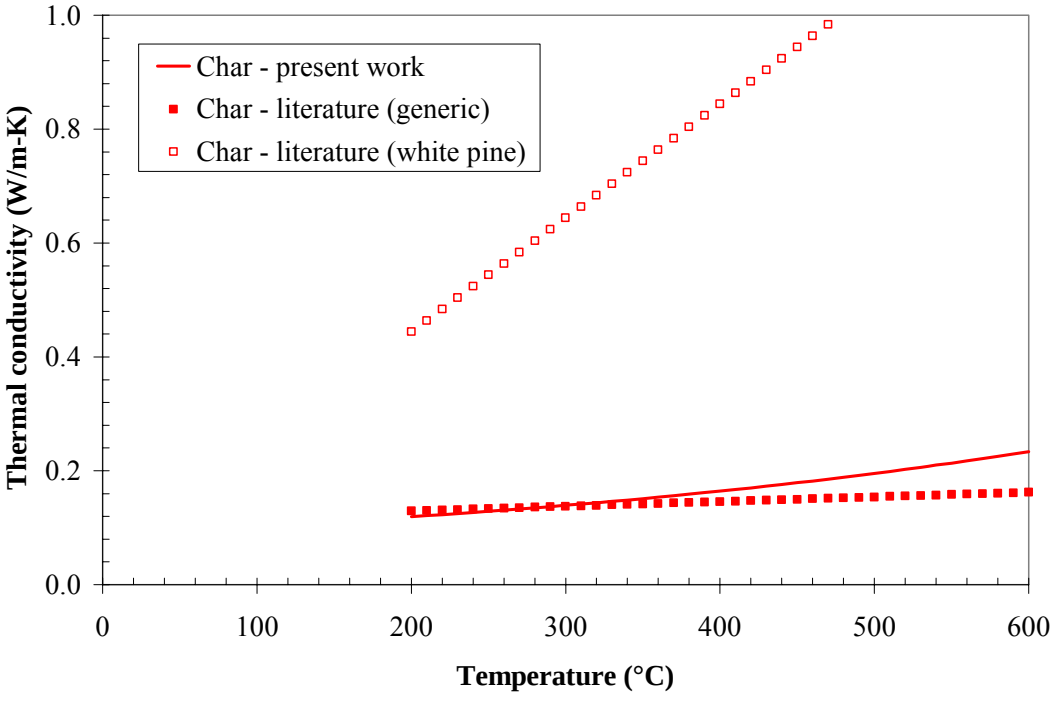

(b)

Figure 6.12. Comparison of white pine temperature–dependent thermal conductivity optimized by genetic algorithm with literature data. (a) Virgin wood; (b) Char.

6.2.2 Oxidative pyrolysis

The next set of simulations involves oxidative atmospheres (10.5% and 21% O_2 by volume). Thus, it is necessary to include oxidative reactions and species formed by oxidative reactions in the modeling approach. The model input parameters that were estimated from the nitrogen experiment in Section 6.2.1 are held fixed, and additional parameters associated with oxidative reactions are estimated from the experiments that were conducted in oxidative atmospheres.

Before this can be done, a reaction mechanism must be postulated. Char oxidation is normally viewed as a heterogeneous process occurring near the surface of a decomposing solid. For example, Weng *et al.* [208] and Boonme and Quintiere [210] modeled wood char oxidation by adding a heat flux to the front face boundary condition to account for exothermic reactions. In the present work, two heterogeneous reactions are added to the reaction mechanism presented earlier in Equation 6.2. These correspond to the oxidation of dry wood to form char plus gaseous oxidative pyrolysate, and the oxidation of char to form ash plus gaseous char oxidation products:

$$\text{dry wood} + \nu_{\text{O}_2\text{dw}}\,\text{O}_2 \rightarrow \nu_{\text{char}}\,\text{char} + \nu_{\text{op}}\,\text{oxidative pyrolysate} \tag{6.2.3}$$

$$\text{char} + \nu_{\text{O}_2\text{char}}\,\text{O}_2 \rightarrow \nu_{\text{ash}}\,\text{ash} + \nu_{\text{cop}}\,\text{char oxidation products} \tag{6.2.4}$$

The following relations result from mass conservation considerations, assuming $\chi = 1$ (no shrinkage or swelling):

$$\nu_{\text{O}_2\text{dw}} = -(1-\text{SF}_3)y_{s,4,3} = -\left(1-\frac{\rho_{\text{char}}}{\rho_{\text{ww}}}\right)y_{s,4,3}$$

$$\nu_{\text{op}} = (1-\text{SF}_3)y_{s,5,3} = \left(1-\frac{\rho_{\text{char}}}{\rho_{\text{ww}}}\right)y_{s,5,3}$$

$$\nu_{\text{ash}} = 1 - \text{SF}_4 = \left(1 - \frac{\rho_{\text{ash}}}{\rho_{\text{char}}}\right)$$

$$\nu_{\text{O}_2\text{char}} = -(1 - \text{SF}_4) y_{s,4,4} = -\left(1 - \frac{\rho_{\text{ash}}}{\rho_{\text{char}}}\right) y_{s,4,4}$$

$$\nu_{\text{cop}} = (1 - \text{SF}_4) y_{s,6,4} = \left(1 - \frac{\rho_{\text{ash}}}{\rho_{\text{char}}}\right) y_{s,6,4}$$

Here, all symbols have the same meaning as before, ρ_{ash} is the ash bulk density, and $y_{s,j,k}$ is the heterogeneous gaseous species yield matrix discussed earlier. The above relations show for a specific case how the ν coefficients are related to condensed phase bulk density ratios and the species yield matrix.

Considerable simplifications are inherent in this mechanism. Gaseous "pseudo" or "surrogate" species are used to represent complex gas mixtures. For example, a single gaseous species called "char oxidation products" is used to represent the gases that form via heterogeneous char oxidation (Equation 6.2.4). In reality, char oxidation products may include a mixture of CO, CO_2, H_2O, unburnt hydrocarbons, etc., but since little is known about the actual composition of these gases, they are tracked in the model by a single surrogate species. Another approximation stems from the formation of "char" by both thermal pyrolysis of dry wood (Equation 6.2.2) and oxidation of dry wood (Equation 6.2.3). In reality, the chemical composition of "char" formed by thermal pyrolysis of wood is not expected to be the same as that formed by oxidation of the wood. However, the complexity of the above mechanism would be significantly increased if a second char species (such as "oxidative char") were added.

Although char oxidation is conventionally viewed as a heterogeneous process, two homogeneous (gas–gas) reactions are also considered here:

$$\text{thermal pyrolysate} - y_{g,4,1}O_2 \rightarrow y_{g,7,1}\ \text{pyrolysate oxidation products} \qquad (6.3.1)$$

$$\text{oxidative pyrolysate} - y_{g,4,2}O_2 \rightarrow y_{g,7,2}\ \text{pyrolysate oxidation products} \qquad (6.3.2)$$

Here, $y_{g,j,\ell}$ is the homogeneous gaseous species yield matrix discussed earlier. Since thermal equilibrium between the condensed phase and the gas phase is assumed, any heat released by the two homogeneous reactions in Equation 6.3 is distributed directly to the condensed phase. As with the heterogeneous reactions, the homogeneous reactions are approximations. For example, thermal pyrolysate (which forms by the pyrolysis of dry wood in the absence of oxygen) and oxidative pyrolysate (which forms by the oxidation of dry wood) are treated as chemically distinct species. Thus, it is expected that their combustion products would be different. However, it can be seen from Equations 6.3.1 and 6.3.2 that the oxidation of both species forms "pyrolysate oxidation products". Again, this approximation is necessary to reduce the number of species that must be tracked.

To summarize, the four condensed phase species are numbered as follows: 1) wet wood, 2) dry wood, 3) char, 4) ash. Seven gaseous species are considered: 1) thermal pyrolysate, 2) nitrogen, 3) water vapor, 4) oxygen, 5) oxidative pyrolysate, 6) char oxidation products, and 7) pyrolysate oxidation products. A total of four condensed phase reactions are considered. Reaction 1 converts wet wood to dry wood and water vapor. Reaction 2 is the anaerobic conversion of dry wood to char plus thermal pyrolysate. Reaction 3 also converts dry wood to char, but consumes oxygen in the process to produce oxidative pyrolysate. Finally, reaction 4 converts char to ash, consuming oxygen in the process, and produces char oxidation products. In addition to the four heterogeneous reactions, two homogeneous gas phase reactions are considered: 1)

oxidation of thermal pyrolysate to form pyrolysate oxidation products, and 2) oxidation of oxidative pyrolysate to form pyrolysate oxidation products.

Due to the large number of species and reactions, there are 20 additional parameters associated with oxidative reactions and products that must be estimated via genetic algorithm optimization. As before, the experimental data at 40 kW/m^2 irradiance is used for property estimation. The 25 kW/m^2 oxidative data are not used as part of the genetic algorithm optimization process so that they can be used to assess the model's predictive capabilities for experimental conditions not included in the parameter estimation process.

A comparison of the experimental measurements and model calculations for a heat flux of 40 kW/m^2 in oxidative environments is given in Figures 6.13 – 6.14. Figure 6.13 compares the model's temperature calculations with the available experimental data at oxygen concentrations of 10.5% and 21%. The model correctly captures the increase in temperature with ambient oxygen concentration. The combined exothermicity of the heterogeneous and homogeneous reactions causes the temperature to increase as the ambient oxygen is increased. Figure 6.14 compares the calculated mass loss rate with the experimental data. Qualitatively, the calculated shapes of the mass loss rate curves are similar to the experimental data. Quantitatively, the model calculations match the experimental data well, although the calculated mass loss rate is slightly lower than the experimental data in the later stages of the experiment. This may be due to an under–estimated char oxidation rate, or perhaps another reaction that is not included in the simplified reaction mechanism (Equation 6.2).

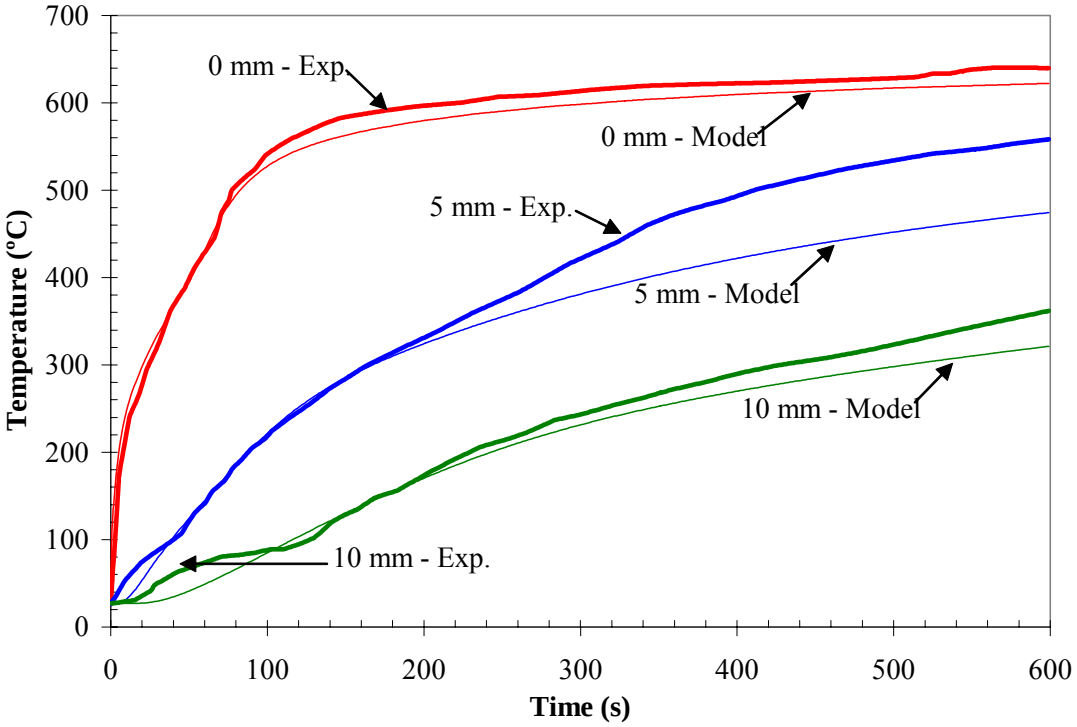

(a)

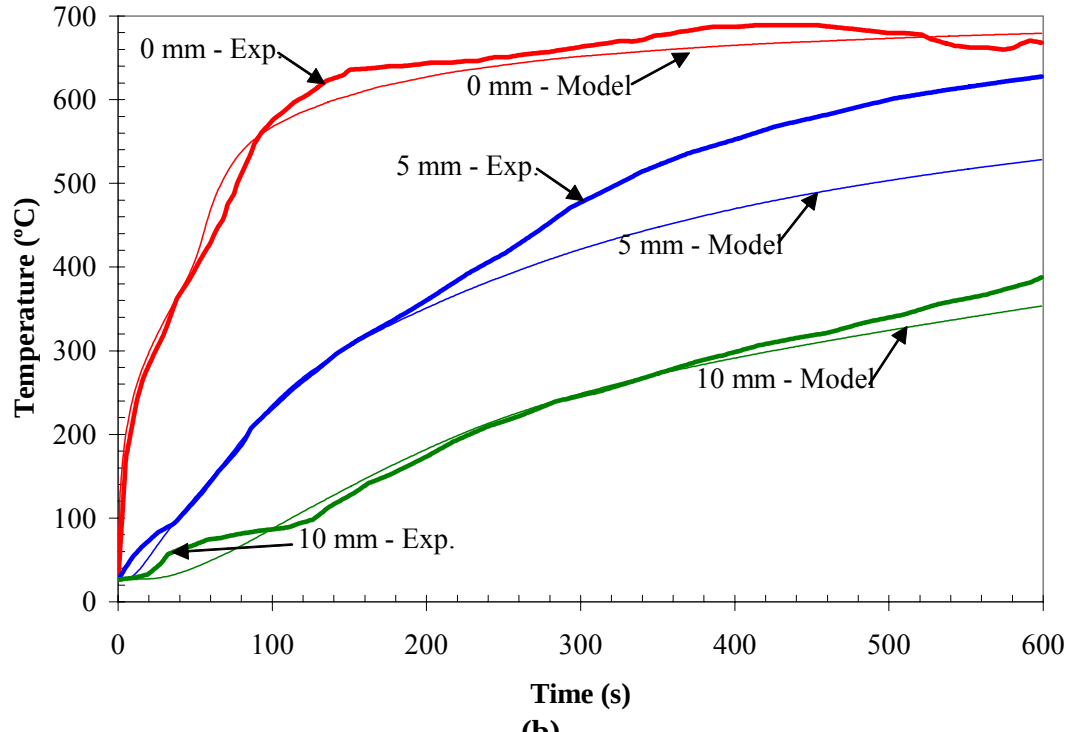

(b)

Figure 6.13. Comparison of experimentally measured [84] and modeled temperatures at several depths below the surface of white pine irradiated at 40 kW/m^2.
(a) 10.5% O_2 atmosphere; (b) 21% O_2 atmosphere.

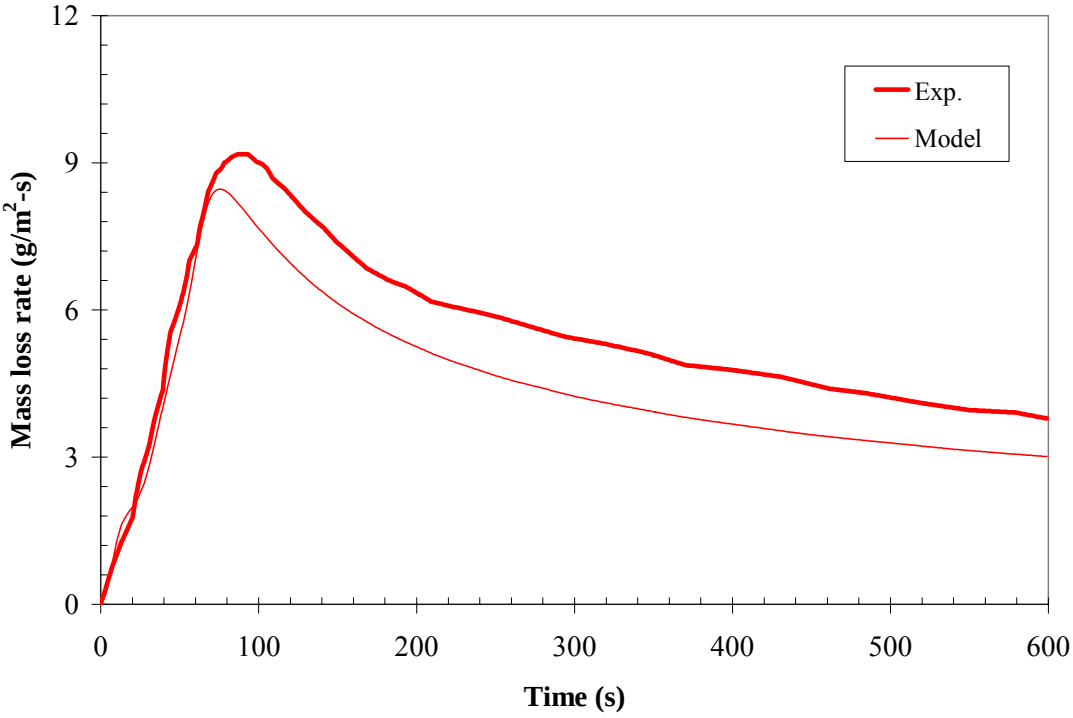

(a)

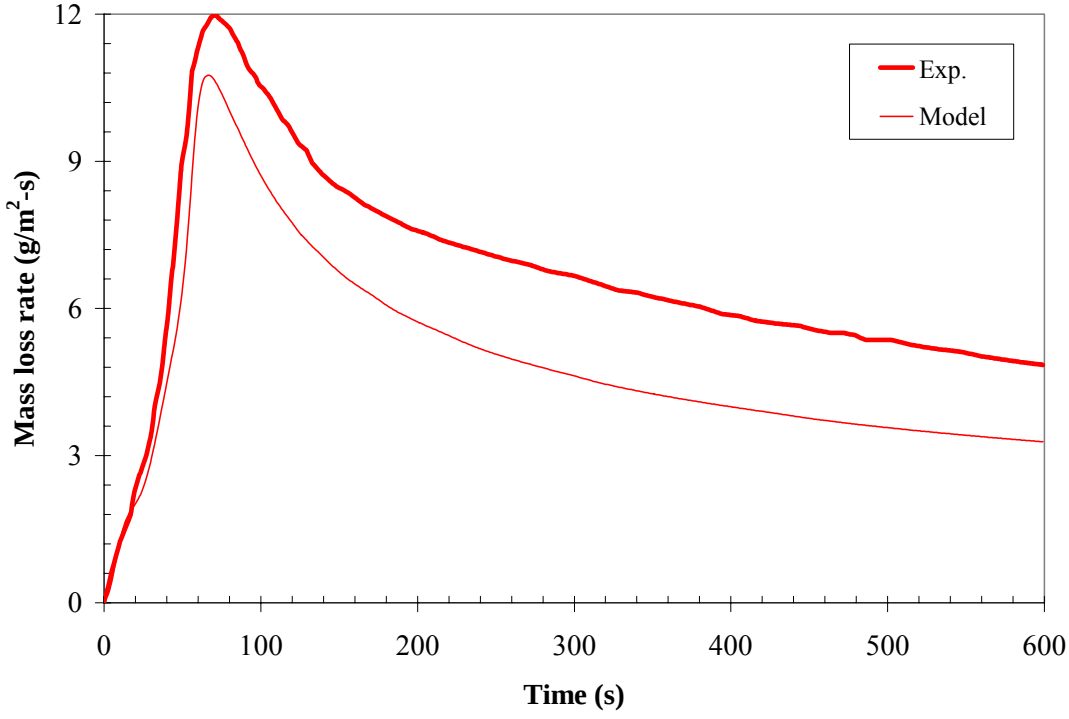

(b)

Figure 6.14. Comparison of experimentally measured [84] and modeled mass loss rate of white pine at 40 kW/m^2 irradiance.
(a) 10.5% O_2 atmosphere; (b) 21% O_2 atmosphere.

The model is next used to simulate the 25 kW/m^2 oxidative experiments (which were not used for property estimation). Figures 6.15 and 6.16 give a comparison of the model predictions and experimental data at a heat flux of 25 kW/m^2 and oxygen concentrations of 10.5% and 21% by volume. It can be seen from Figure 6.15 (temperatures at 25 kW/m^2 and 10.5% O_2) that the temperature calculations do not match the experimental data as well as at 40 kW/m^2 irradiance. However, the temperatures calculated at five locations in the decomposing pine slab are within ~50 ºC of the experimental data for the duration of the experiment. A comparison of the measured and modeled MLR (25 kW/m^2, 10.5% O_2 and 21% O_2) is shown in Figure 6.16. The shapes of the curves are well–predicted by the model, and the calculated MLRs match the experimental data within ~20% for the duration of the experiments. Considering the experimental uncertainty and the complexity of the problem, this is considered a good fit.

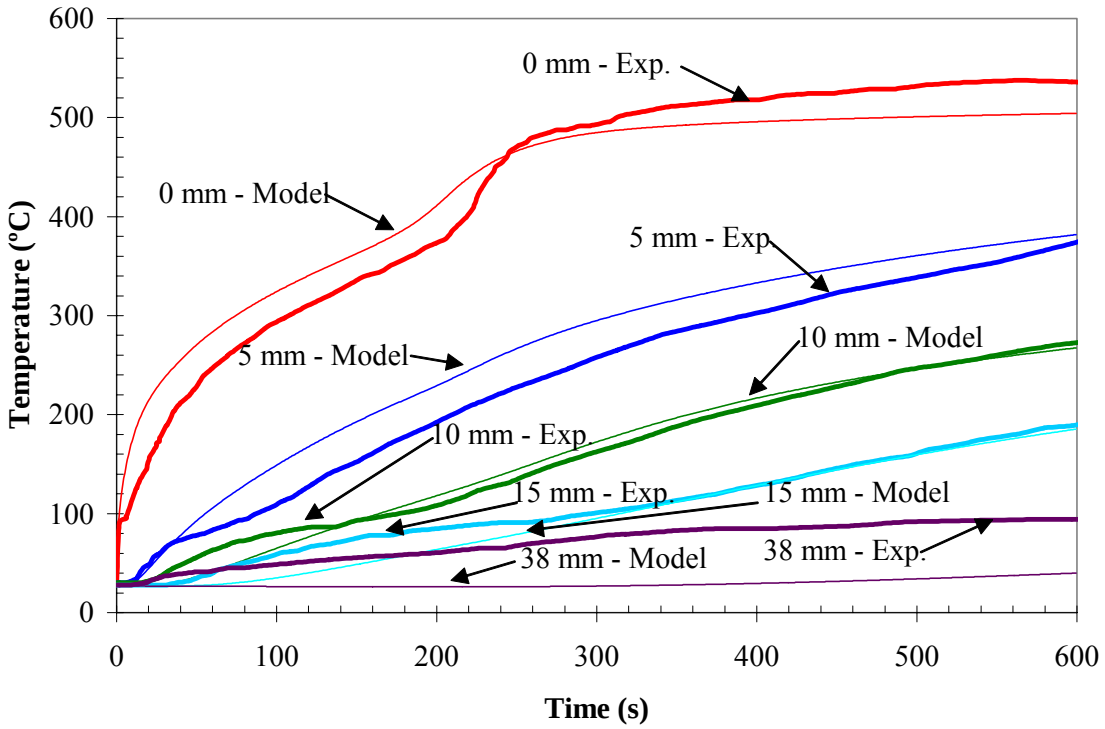

Figure 6.15. Comparison of experimentally measured [84] and modeled temperatures at several depths below the surface of white pine irradiated at 25 kW/m^2 in 10.5% O_2 atmosphere.

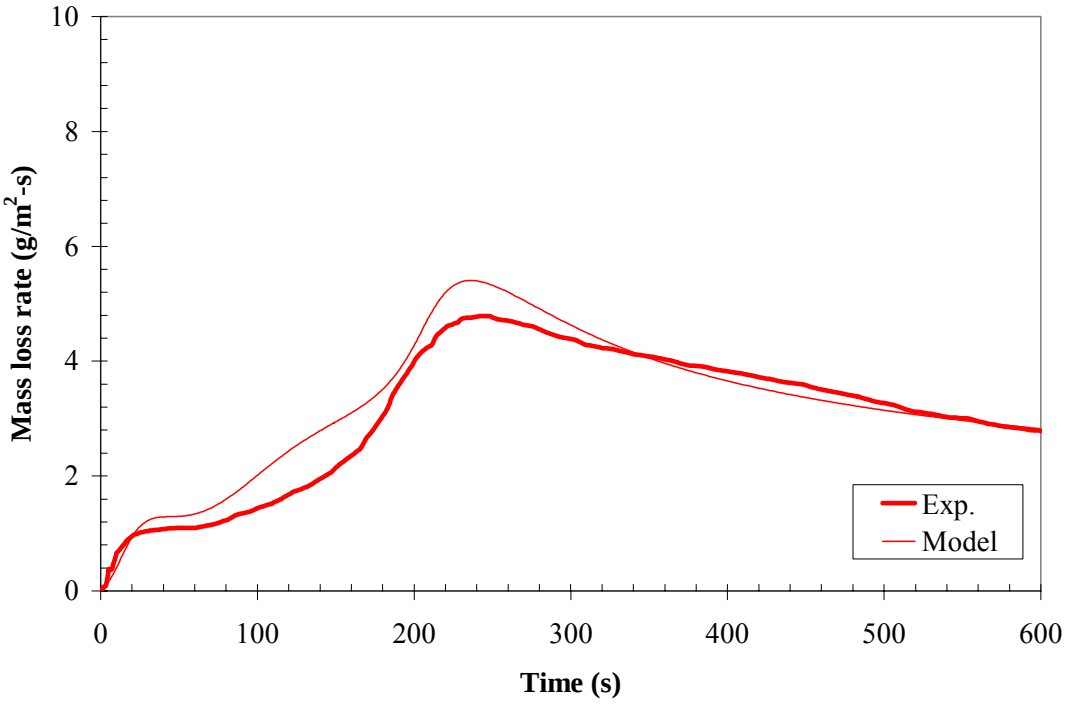

(a)

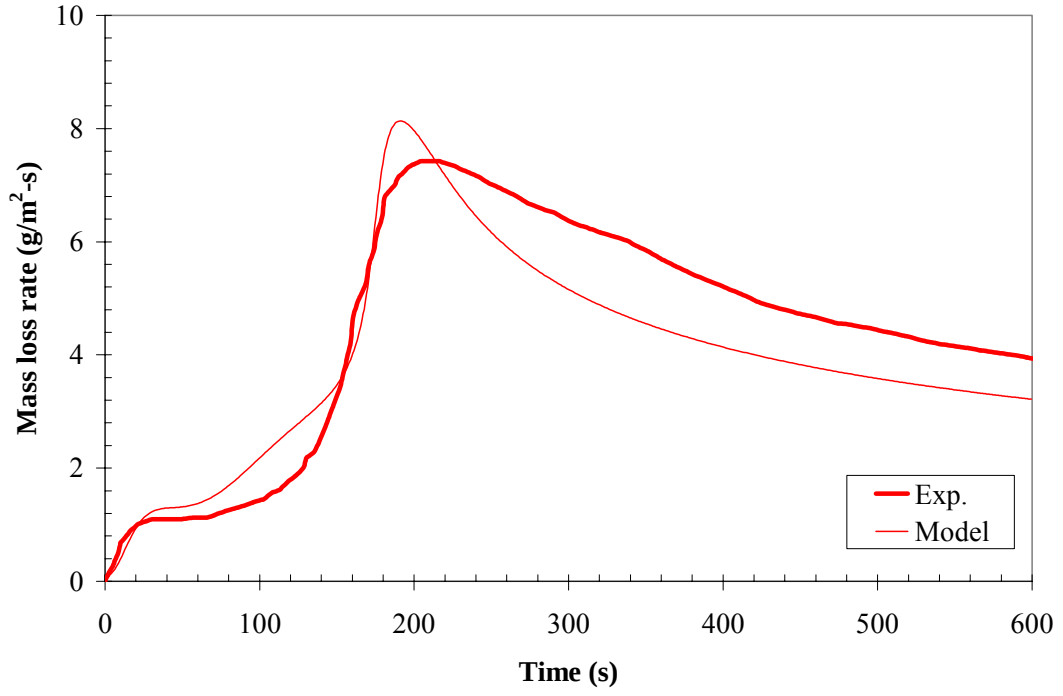

(b)

Figure 6.16. Comparison of experimentally measured [84] and modeled mass loss rate of white pine at 25 kW/m^2 irradiance.
(a) 10.5% O_2 atmosphere; (b) 21% O_2 atmosphere.

The preceding modeling results are encouraging, but it is evident that there is still room for improvement. This modeling is one of the most comprehensive attempts at simulating wood slab pyrolysis/oxidation for fire applications that has been conducted to date. Particularly novel is the treatment of oxidative exothermic reactions, which are accounted for by simulating diffusion of ambient oxygen into the decomposing solid and allowing this oxygen to participate in reactions. To put the preceding results into context, two recent studies are mentioned below to give a sense of current predictive capabilities for wood pyrolysis.

Shen *et al.* [211] recently modeled the pyrolysis of several different species of wet wood using 3 parallel reactions. Although they simulated cone calorimeter experiments conducted in air, all three reactions were modeled as endothermic. This is presumably because model calculations (and experimental data) were truncated at surface temperatures below 400 ºC, so oxidative reactions had very little influence. Shen *et al.* [211] obtained good agreement between measured and calculated temperatures (at the surface and in depth), but did not present a comparison of modeled and measured mass loss rates. Weng *et al.* [208] recently modeled the same set of experiments [84] that are modeled here. They included the effect of char oxidation through the surface boundary condition. The present modeling results match the experimental data more closely than the simulations of Weng *et al.* [208].

However, it should be emphasized that just because one set of simulations matches a set of experimental data better than another simulation, it does not necessarily mean that the physics are being more accurately modeled. The present simulations include both heterogeneous and homogeneous oxidative reactions. However, char

oxidation is conventionally viewed as a heterogeneous process. Consequently, it is not clear whether the homogeneous reactions included in the present simulations occur in reality. The effect of these homogeneous reactions on the simulation results was assessed by running calculations with only heterogeneous reactions, only homogeneous reactions, both types of reactions, and neither type of reaction. The results, shown in Figure 6.17, are particularly interesting. Comparing the surface temperature in Figure 6.17a for the case where both types of reactions occur (medium weight blue line) with the case where only heterogeneous reactions occur (thin red line) it can be seen that the homogeneous reactions start to have an effect as the surface temperature approaches 600 ºC.

In order to determine whether or not it is feasible that homogeneous gas phase reactions could start to have an appreciable effect at temperatures near 600 ºC, the characteristic time scale of homogeneous gas phase combustion reactions must be compared with the gas phase residence time in the hot char layer. If these time scales are of the same order of magnitude, it is conceivable that homogeneous gas phase combustion reactions could occur as combustible volatiles generated in–depth flow through the hot char layer and react with oxygen that is diffusing inward from the ambient. The order of magnitude of the volatiles' velocity near the surface is ~10 mm/s. This is estimated by dividing a mass loss rate of 7 g/m^2–s by a density of 0.7 kg/m^3 (calculated from the ideal gas law at 600 ºC assuming a mean molecular weight of 50 g/mol). Consequently, the residence time in the char layer, assuming it has a thickness of 5 mm, is approximately 0.5 s. Although low–temperature gas phase combustion chemistry is not all that well understood, experimental data [212] for the spontaneous ignition delay time of a lean propane/air premixture at 670 ºC (the lowest temperature at

which data were reported) is approximately 0.2 s. Thus, it seems that at temperatures above 600 ºC the gas phase combustion time scale could approach the residence time in a heated char layer. Consequently, it is possible that in oxidative environments, homogenous gas phase reactions could occur inside a radiatively heated solid and contribute to the overall heat release. However, no firm conclusions can be drawn at this point, and future work in this area is needed to unravel the physical mechanism of oxidative pyrolysis.

The present simulations include a simple Couette model for blowing (see Equation 3.25) that, while probably better than not accounting for blowing at all, may not accurately represent oxygen diffusion through the natural convection boundary layer in the experiments. The calculated surface temperature and mass loss rate for the 21% O_2 case are shown in Figure 6.18 with and without blowing enabled. It can be seen that the surface temperature is higher when blowing is disabled due to greater diffusion of oxygen to the surface. Blowing also has an appreciable effect on the calculated peak mass loss rate. Boonme and Quintiere [210] used the classical "stagnant layer" model (sometimes called the Stefan problem) to account for the effect of blowing through a Spalding mass transfer number (*B* number).

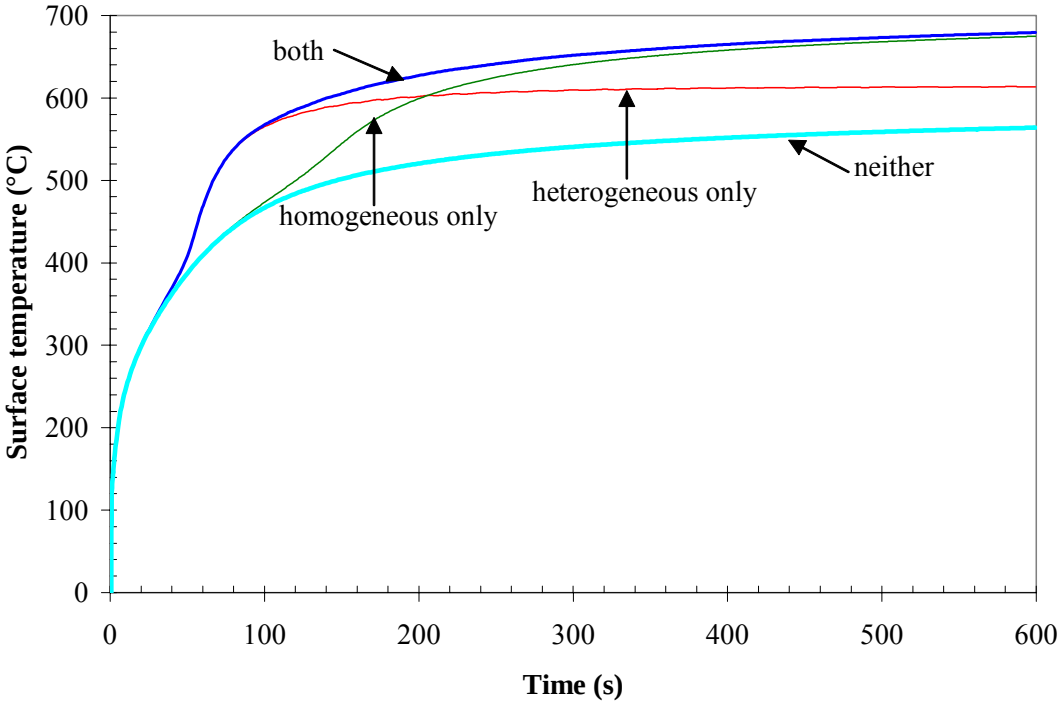

(a)

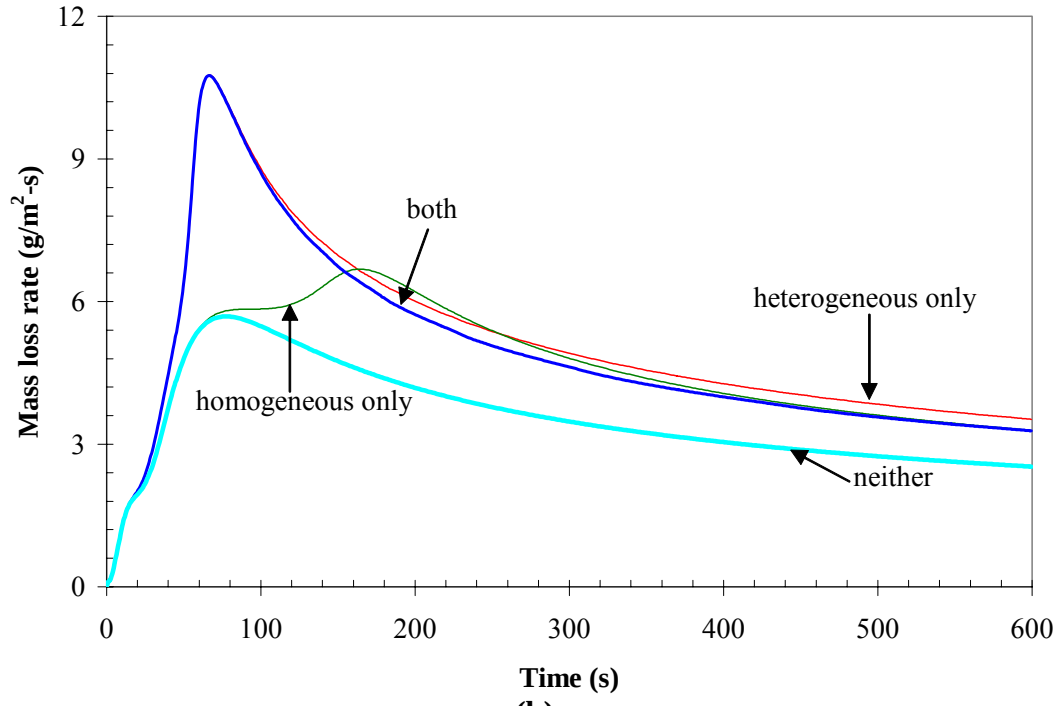

(b)

Figure 6.17. Effect of heterogeneous and homogeneous reactions on the oxidative pyrolysis of white pine at 40 kW/m^2 irradiance and 21% O_2.
Text in figures indicates reactions included in simulations.
(a) Surface temperature; (b) Mass loss rate.

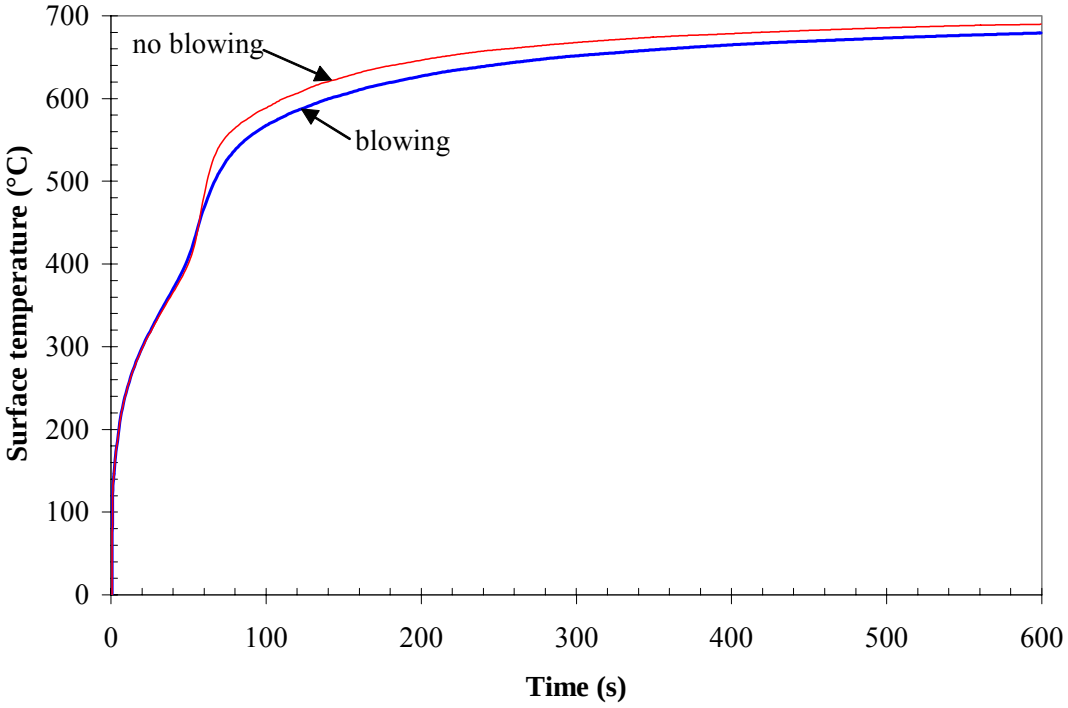

(a)

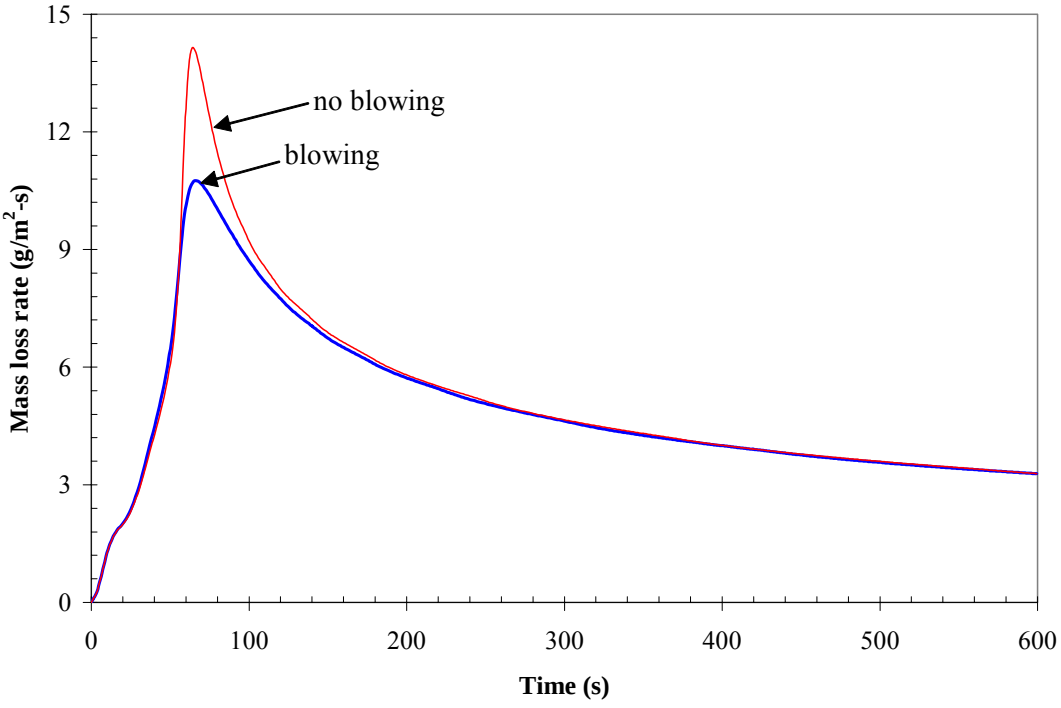

(b)

Figure 6.18. Effect of blowing on calculated mass loss rate of white pine at 40 kW/m^2 irradiance and 21% O_2.
(a) Surface temperature; (b) Mass loss rate.

Table 6.4. Condensed phase parameters for white pine simulations.

i	Name	k_0 (W/m–K)	n_k (–)	ρ_0 (kg/m^3)	n_ρ (–)	c_0 (J/kg–K)	n_c (–)	ε (–)	γ (m)	ρ_{s0} (kg/m^3)
1	wet wood	0.194	0.386	380	0	1772	0.411	0.755	0	380.1
2	dry wood	0.182	0.679	360	0	1680	0.649	0.757	0	380.1
3	char	0.089	0.304	88.5	0	1445	0.266	0.973	2.9×10^{-3}	380.1
4	ash	0.079	0.157	5.7	0	1229	0.226	0.973	7.1×10^{-3}	380.1

Table 6.5. Reaction parameters for white pine simulations.

k	From	To	χ (–)	ΔH_{sol} (J/kg)	ΔH_{vol} (J/kg)	Z (s^{-1})	E (kJ/mol)	n (–)	n_{O2} (–)
1	wet wood	dry wood	1	0	2.41×10^6	4.31×10^3	43.6	1.02	0
2	dry wood	char	1	0	6.74×10^5	3.14×10^9	135.4	5.42	0
3	dry wood	char	1	0	-9.15×10^5	3.14×10^9	126.7	5.42	1.31
4	char	ash	1	0	-3.05×10^7	9.02×10^{13}	192.6	1.51	1.91

Table 6.6. Gaseous yields for white pine simulations. Only nonzero yields are shown.

j \ k	1	2	3	4
1 (thermal pyrolysate)		1		
2 (nitrogen)				
3 (water vapor)	1			
4 (oxygen)			–0.1	–2.0
5 (oxidative pyrolysate)			1.1	
6 (char oxidation products				3.0
7 (pyrolysate oxidation products)				

Table 6.7. Homogeneous gaseous reaction parameters for white pine simulations.

k	Reactant 1	Reactant 2	p (–)	q (–)	b (–)	Z (kg–m^3 / mole^2–s)	E (kJ/mol)	ΔH (MJ/kg)
1	thermal pyrolysate	oxygen	1.0	1.0	0.0	6.76×10^9	163.2	-1.98×10^7
2	oxidative pyrolysate	oxygen	1.0	1.0	0.0	7.31×10^9	162.2	-1.92×10^7

Table 6.8. Homogeneous gaseous yields for white pine simulations. Only nonzero yields are shown.

j \ k	1	2
1 (thermal pyrolysate)	–1.0	
2 (nitrogen)		
3 (water vapor)		
4 (oxygen)	–1.6	–1.5
5 (oxidative pyrolysate)		–1.0
6 (char oxidation products)		
7 (pyrolysate oxidation products)	2.6	2.5

6.3 Heating and swelling of intumescent coating

Griffin *et al.* [100] experimentally studied the effect of atmospheric oxygen concentration on intumescent fire retardant coatings using thermogravimetry, differential thermal analysis, and cone calorimetry. In this section, the generalized pyrolysis model is used to simulate their "material A", an epoxy–based intumescent coating with inorganic filler consisting of glass/silica fibers. The experiments simulated include thermogravimetric tests conducted under nitrogen (heating rates of 10, 15, 20, and 30 ºC/min) and cone calorimeter tests conducted at an irradiance of 90 kW/m^2 in a "reduced O_2" atmosphere having an oxygen concentration between 8% and 10%. The intumescent coating tested in the cone calorimeter was applied manually onto mild steel plates having thickness of either 3 mm or 5 mm. The assembly was then mounted in a specially–designed calcium silicate sample holder that permits optical measurement of the coating thickness as it swells.

In this set of simulations, the effect of oxygen on the decomposition reactions is not explicitly modeled, so the gaseous species conservation equation and the pressure evolution equation are not solved. Instead, the pyrolysate mass flux is calculated from Equation 3.74, that gas phase mass conservation equation. Four condensed phase species are considered: virgin_coating, char, ash, and steel. Two reactions are considered: the first reaction converts species virgin_coating to char and gases. It is this reaction that causes intumescence. The second reaction converts char to ash and gases. The two–step reaction mechanism is represented as:

$$\text{virgin\_coating} \rightarrow \nu_{\text{char}}\ \text{char} + \nu_{\text{gas1}}\ \text{gases} \tag{6.4.1}$$

$$\text{char} \rightarrow \nu_{\text{ash}}\ \text{ash} + \nu_{\text{gas2}}\ \text{gases} \tag{6.4.2}$$

From Equations 3.53 and 3.54, the ν coefficients are related to the condensed phase density ratios and reaction solid fraction as follows:

$$\nu_{\text{char}} = \text{SF}_1 = 1 + \left(\frac{\rho_{\text{char}}}{\rho_{\text{virgin\_coating}}} - 1 \right) \chi_1$$

$$\nu_{\text{gas1}} = 1 - \text{SF}_1 = \left(1 - \frac{\rho_{\text{char}}}{\rho_{\text{virgin\_coating}}} \right) \chi_1$$

$$\nu_{\text{ash}} = \text{SF}_2 = \frac{\rho_{\text{ash}}}{\rho_{\text{char}}}$$

$$\nu_{\text{gas2}} = 1 - \text{SF}_2 = 1 - \frac{\rho_{\text{ash}}}{\rho_{\text{char}}}$$

In the simulations, the intumescent coating/steel plate system was modeled as two distinct layers. The top layer is the intumescent coating. It has a thickness of 2.7 mm and the initial mass fraction of condensed phase species virgin_coating was specified as 1.0 in this layer. The second layer is the steel plate, having a thickness of 3 mm. The initial mass fraction of condensed phase species steel is specified as 1.0 in this layer. The assumed inverse contact resistance between the intumescent coating and the steel plate is 100 W/m^2–K. In–depth absorption of radiation is not modeled ($\kappa \to \infty$), but radiation heat transfer across pores is considered. The density of the intumescent coating is not indicated in the experimental paper [100], so it is estimated (somewhat arbitrarily) at 1,000 kg/m^3.

As with the other simulations, the genetic algorithm optimization procedure is used to estimate the model parameters. The optimization is conducted in two stages. First, the kinetics parameters are estimated from the thermogravimetric data. In the second stage, the reaction kinetics are held fixed and the thermal properties and reaction

enthalpies are estimated from the cone calorimeter data. The resultant model parameters is listed in Tables 6.9 and 6.10 at the end of this section. Gaseous species yields are not given because the gas phase species conservation equation is not solved.

A comparison of the experimental differential thermogravimetric curves and those calculated with the model using the optimized parameters is shown in Figure 6.19, and Figure 6.20 gives a comparison of the experimental and modeled thermogravimetric (integrated) curves. The model captures the main features of these curves, but not all of the details. However, this is expected since only two reactions are considered.

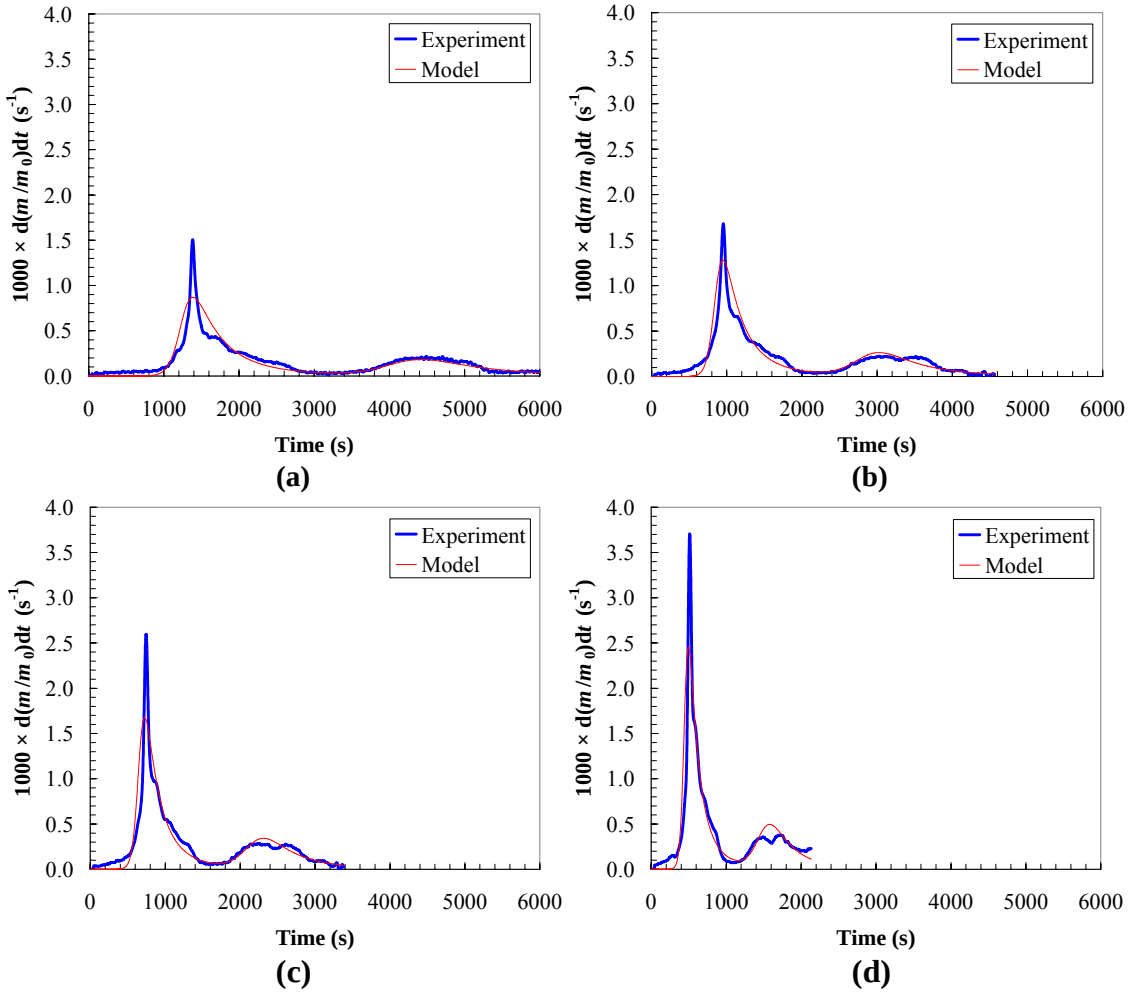

Figure 6.19. Comparison of experimentally measured (Material A from Ref. [100]) and modeled differential thermogravimetric curves of an intumescent coating. (a) 10 ºC/min; (b) 15 ºC/min; (c) 20 ºC/min; (d) 30 ºC/min.

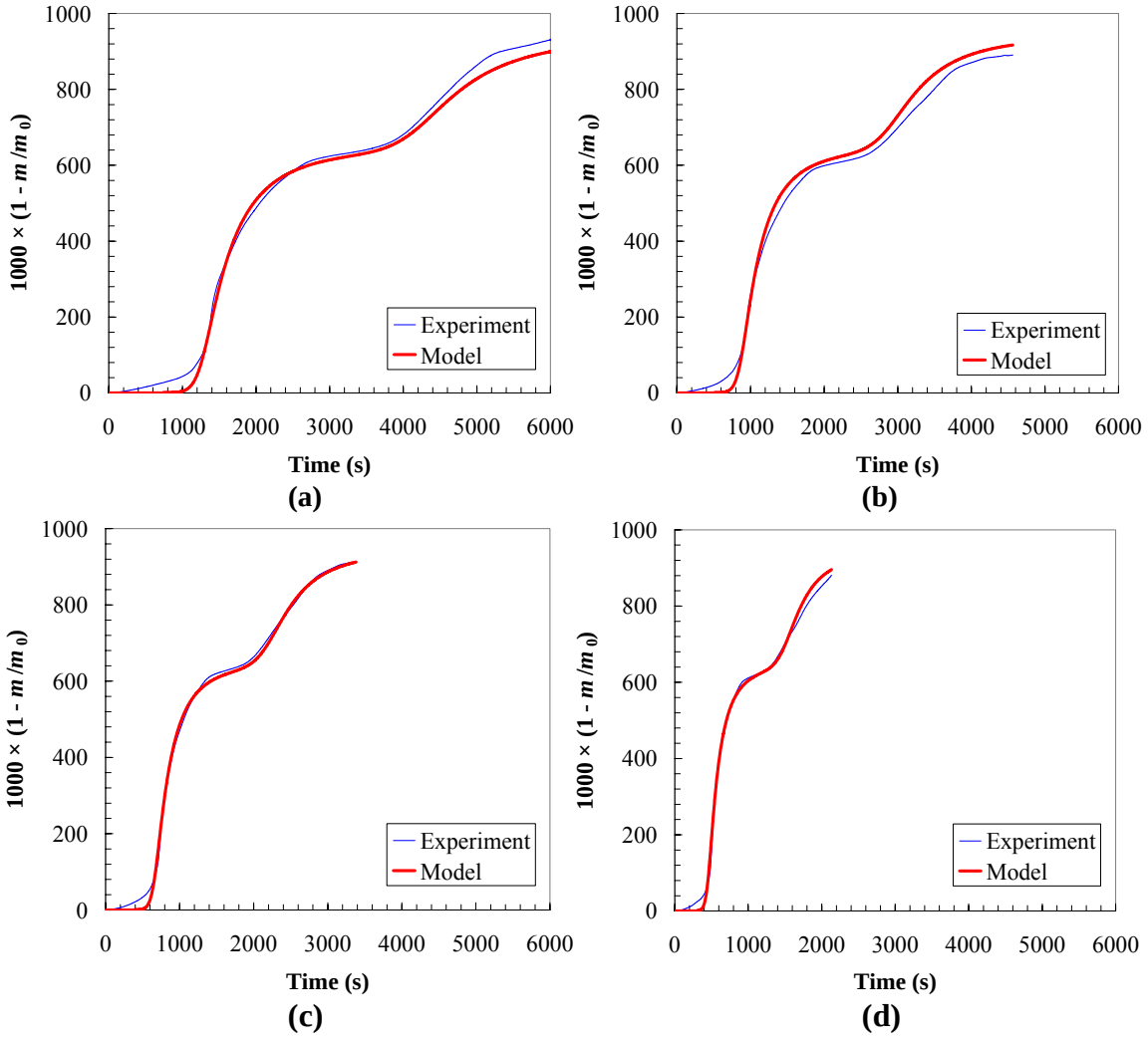

Figure 6.20. Comparison of experimentally measured (Material A from Ref. [100]) and modeled thermogravimetric curves of an intumescent coating. (a) 10 ºC/min; (b) 15 ºC/min; (c) 20 ºC/min; (d) 30 ºC/min.

Figure 6.21 gives a comparison of the modeled and experimentally measured substrate temperature and coating thickness. The modeled substrate temperature is taken as the temperature at the back face of the steel substrate. The substrate temperature calculated by the model matches the experimental data well, differing from the experimental data by no more than 50 °C over the 30 minute experiment. There is also good agreement between the measured and calculated transient thickness of the coating as it increases in thickness by a factor of almost 20.

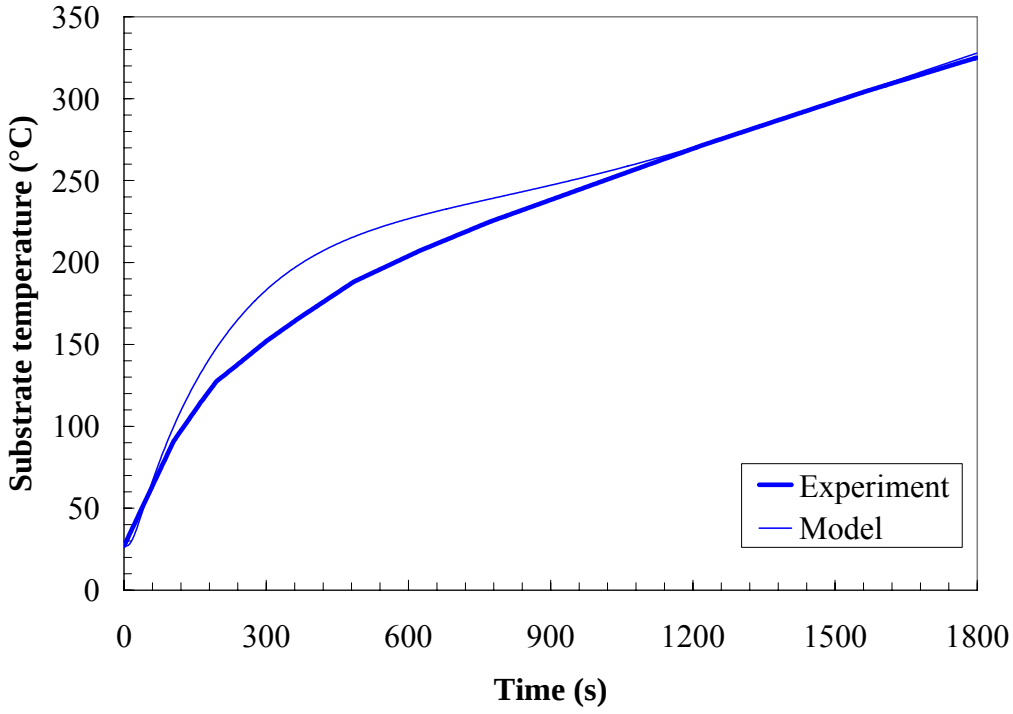

(a)

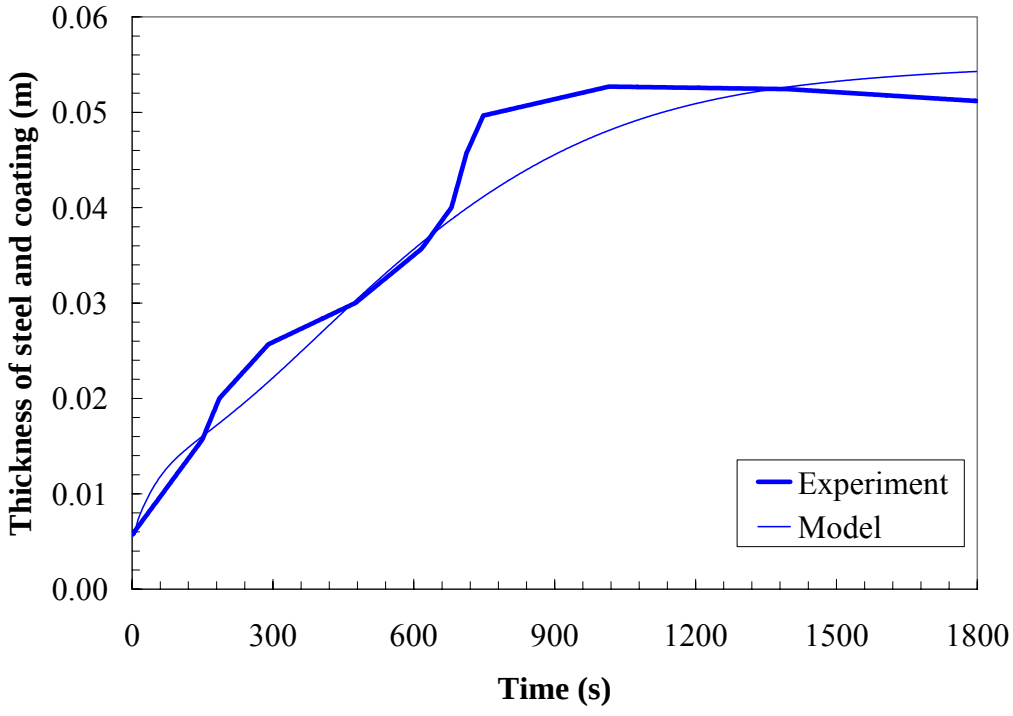

(b)

Figure 6.21. Comparison of experimental cone calorimeter data [100] and model calculations for intumescent coating.
Material A from Reference [100] irradiated at 90 kW/m^2 in reduced O_2 atmosphere.
(a) Substrate temperature; (b) Steel and coating thickness.

The calculated mass loss rate and surface temperature are shown in Figure 6.22. Experimental data for these quantities were not reported. It can be seen that the surface temperature initially increases rapidly, but later remains relatively constant. This is because the intumescent char that forms has a low bulk density and thermal conductivity. The mass loss rate reaches a peak early in the simulation, coinciding with the initial intumescence. Mass loss rates later in the simulation are retarded by the insulating effect of the intumescent char.

Figure 6.23 shows the calculated in–depth temperature profile at several times. Note that the first 3 mm is the steel substrate. This shows how the temperature profile is "stretched" as the intumescent coating expands. Due to the high thermal conductivity of the steel substrate, there is a small temperature gradient across the steel substrate. The discontinuity in the temperature at the interface between the steel plate and the intumescent coating is due to the assumed interfacial contact resistance.

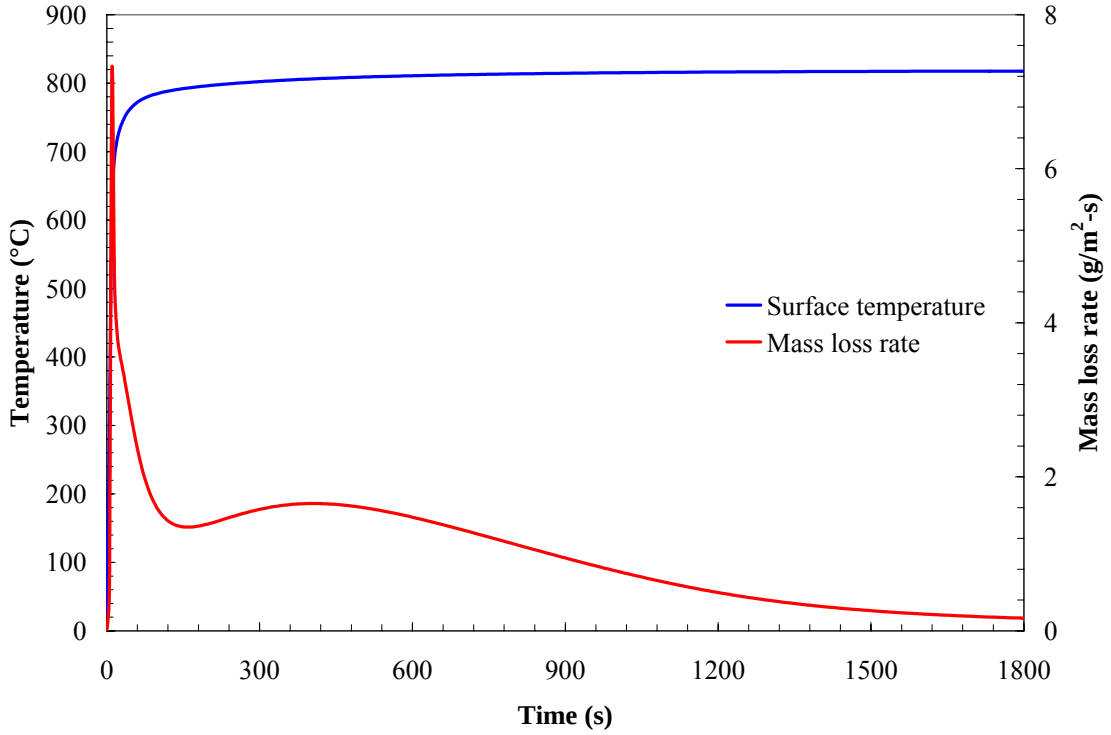

Figure 6.22. Calculated surface temperature and mass loss rate for intumescent coating in cone calorimeter.

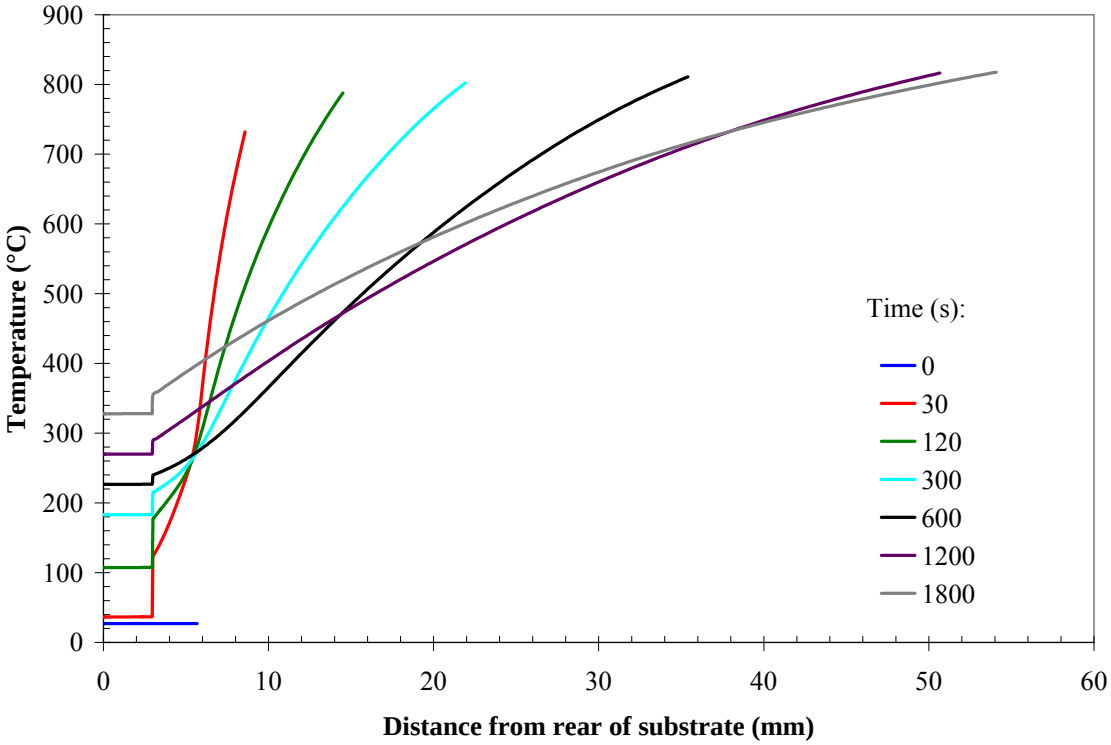

Figure 6.23. Calculated temperature profiles at several times for intumescent coating in cone calorimeter.

Although these simulations suggests that the model may have good predictive capabilities for thermal resistance of intumescent coatings, several uncertainties are inherent in these simulations. The initial coating density is unknown and was estimated as 1000 kg/m^3. The substrate thickness was not indicated in the paper and was therefore assumed to be 3 mm. Finally, the contact resistance between the intumescent coating and the steel substrate is not accurately known.

Table 6.9. Condensed phase parameters for intumescent coating simulations.

i	Name	k_0 (W/m–K)	n_k (–)	ρ_0 (kg/m^3)	n_ρ (–)	c_0 (J/kg–K)	n_c (–)	ε (–)	γ (m)
1	virgin_coating	0.205	0.401	1000	0	1659	0	0.83	0
2	char	0.036	0.467	17.6	0	1636	0	0.95	3.21×10^{-3}
3	ash	0.021	0.472	2.8	0	1677	0	0.96	6.09×10^{-3}
4	steel	56.0	–0.330	7833	0	465	0	0.90	0

Table 6.10. Reaction parameters for intumescent coatings simulations.

k	From	To	χ (–)	ΔH_{sol} (J/kg)	ΔH_{vol} (J/kg)	Z (s^{-1})	E (kJ/mol)	n (–)	n_{O2} (–)
1	virgin_coating	char	0.66	0	6.11×10^5	4.67×10^{12}	156.4	5.47	0
3	char	ash	1	0	-2.32×10^5	2.17×10^6	181.0	3.56	0

6.4 Smolder in polyurethane foam

The final experiment modeled here [213] is the forward propagation of a smolder wave through a polyurethane foam cylinder 12 cm in diameter and 14 cm in length. The experiments were conducted in microgravity on the NASA Space Shuttle (missions STS–105 and STS–108). Temperatures were measured with centerline thermocouples installed at eight axial locations. The smolder reaction was initiated with a porous igniter at one end of the cylinder. Air was forced into the foam sample at the igniter end so that the smolder wave propagated in the same direction as the airflow. While the igniter was energized (during the first 400 s of the experiment), the forced airflow velocity was

approximately 0.01 mm/s. The igniter was de–energized at 400 s, at which time the airflow was increased to its nominal value of either 3 mm/s or 5 mm/s. One experiment at each velocity was conducted.

Rein *et al.* [214] have already simulated these experiments with a smolder–specific model. Although their model is formulated slightly differently than the present model, their basic treatment of reaction kinetics is adopted here. Three condensed phase species (foam, char, and residue) are considered, and the reaction mechanism is:

$$\text{foam} \rightarrow \nu_{c,p}\ \text{char} + \nu_{g,p}\ \text{gas} \tag{6.5.1}$$

$$\text{foam} + \nu_{O_2,o} O_2 \rightarrow \nu_{c,o}\ \text{char} + \nu_{g,o}\ \text{gas} \tag{6.5.2}$$

$$\text{char} + \nu_{O_2,c} O_2 \rightarrow \nu_{r,c}\ \text{residue} + \nu_{g,c}\ \text{gas} \tag{6.5.3}$$

where the values of the ν coefficients are [214]:

$$\nu_{c,p} = 0.05$$
$$\nu_{g,p} = 0.95$$

$$\nu_{O_2,o} = 0.12$$
$$\nu_{c,o} = 0.40$$
$$\nu_{g,o} = 0.72$$

$$\nu_{O_2,c} = 0.62$$
$$\nu_{r,c} = 0.30$$
$$\nu_{g,c} = 1.32$$

It is not possible to directly implement the above reaction mechanism in the present model due to the definitions in Equation 3.53 and 3.54. The reason for this is that using $\nu_{c,p} = 0.05$ from the first reaction implies (for the present model) that the char bulk density is 5% that of the foam, but using $\nu_{c,o} = 0.40$ from the second reaction implies that

the char bulk density is 40% that of the foam. Thus, the reaction mechanism used by Rein *et al.* [214] cannot be applied to the present model in a self–consistent manner because it is over–specified when viewed from the present modeling framework. To circumvent this difficulty, it is assumed here that $\nu_{c,p} = \nu_{c,o} = 0.4$, and the pre–exponential factor of the first reaction is reduced by a factor of 0.40/0.05 = 8.

Based on the above reaction mechanism, three condensed phase species are tracked: 1) foam, 2) char, and 3) residue. The three reactions are given above in Equation 6.5, and the four gaseous species tracked by the code are: 1) pyrolysate, 2) nitrogen, 3) oxygen, and 4) char oxidation products.

In the simulations, the temperature at the igniter is specified for the duration of the experiment. Heat losses from the outflow end are approximated with a convective heat transfer coefficient of 10 W/m^2–K plus radiant emission. To account for radial heat losses, a volumetric heat loss coefficient of 25 W/m^3–K is assumed. This value was estimated by matching the slope of the predicted thermocouple temperatures after the smolder front has passed to the experimental data. The forced mass flux is 0.1 g/m^2–s for the first 400 s, linearly ramping to either 3.5 g/m^2–s (3 mm/s case) or 5.8 g/m^2–s (5 mm/s case) between 400 and 410 s.

Initial simulations using the exothermic heats of reaction from Rein *et al.* [214] resulted in unrealistically high peak smolder temperatures. For this reason, these heats of reaction were reduced by ~25% to –0.7 MJ per kg of foam oxidized and –3.6 MJ per kg of char oxidized. This corresponds to 5.8 MJ of heat released per kg of oxygen consumed (compared with the value of ~13 MJ released per kg oxygen consumed that is frequently

used in oxygen consumption calorimetry). A complete listing of the model parameters used in the simulations is given at the end of this section in Tables 6.11 – 6.13.

Figure 6.24 shows the calculated temperature profiles at several different times for the 3 mm/s airflow case. The smolder wave propagates from right to left (same direction as the airflow), with peak smolder temperatures around 450 ºC.

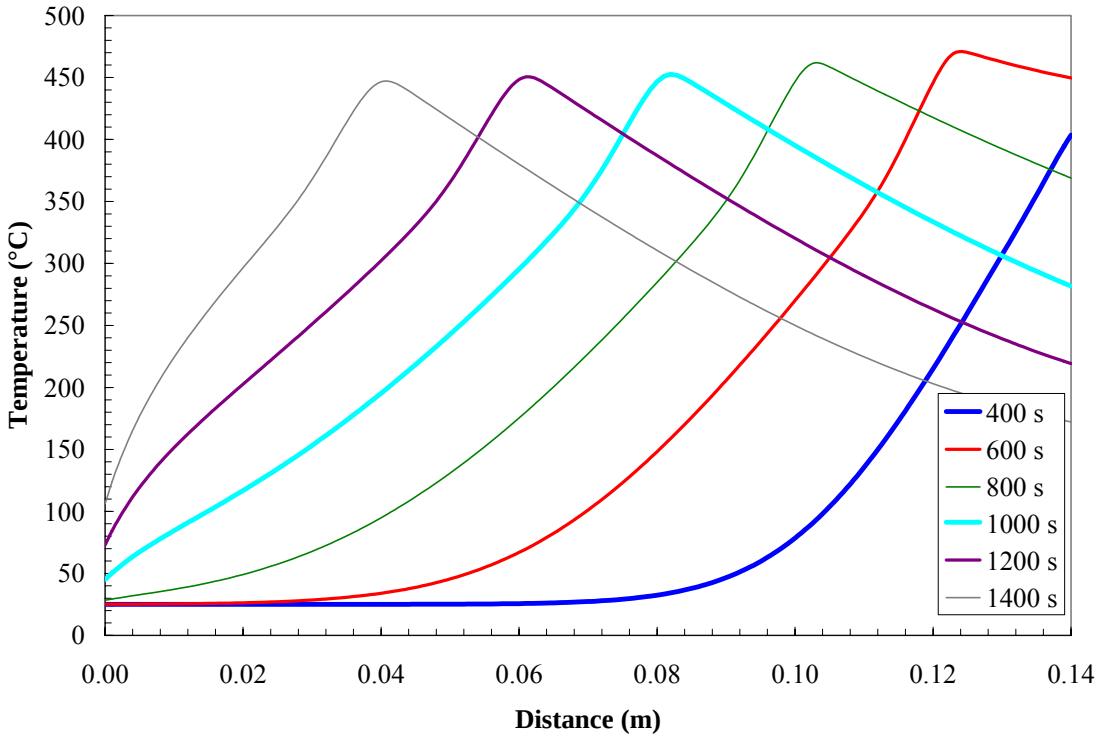

Figure 6.24. Calculated temperature profiles in smoldering polyurethane foam at several different times. Airflow is 3 mm/s.

The calculated gas phase oxygen mass fraction profile is shown in Figure 6.25a at several different times for the 3 mm/s airflow case. Again, airflow is from right to left. It can be seen that the oxygen concentration downstream of the smolder front approaches zero, implying that all available oxygen is completely consumed at the smolder front. The calculated condensed phase char mass fraction profile is shown in Figure 6.25b at several different times. The char mass fraction profile reaches a peak of ~0.9. This peak occurs

because char is produced by foam pyrolysis and oxidation, but the char oxidation reaction soon follows and converts the char to residue. To the left of this char mass fraction peak is virgin foam, and to the right of the peak is residue (generated by the third reaction).

Figure 6.26a gives a comparison of the model predictions and the experimental temperature data for the 3 mm/s airflow case, and Figure 6.26b gives the comparison for the 5 mm/s airflow case. In the 3 mm/s airflow case, the modeled smolder wave propagates at a steady rate of approximately 0.1 mm/s. This compares favorably with the propagation rate calculated by Rein *et al.* [214]. The experimentally–observed quenching of the smolder reaction is not predicted by the present model. The calculated smolder velocity for the 5 mm/s airflow case is 0.19 mm/s, compared with approximately 0.26 mm/s calculated by Rein *et al.* [214]. The solution bifurcation reported by Rein *et al.* [214] at 5 mm/s airflow velocity is not observed here.

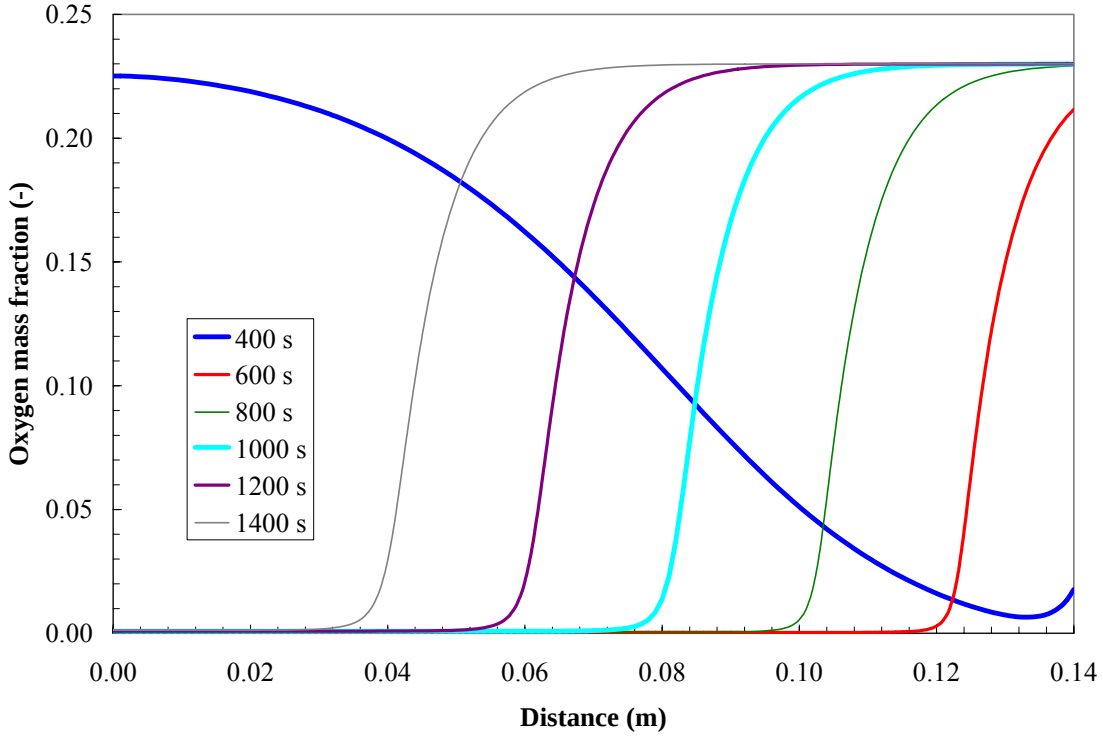

(a)

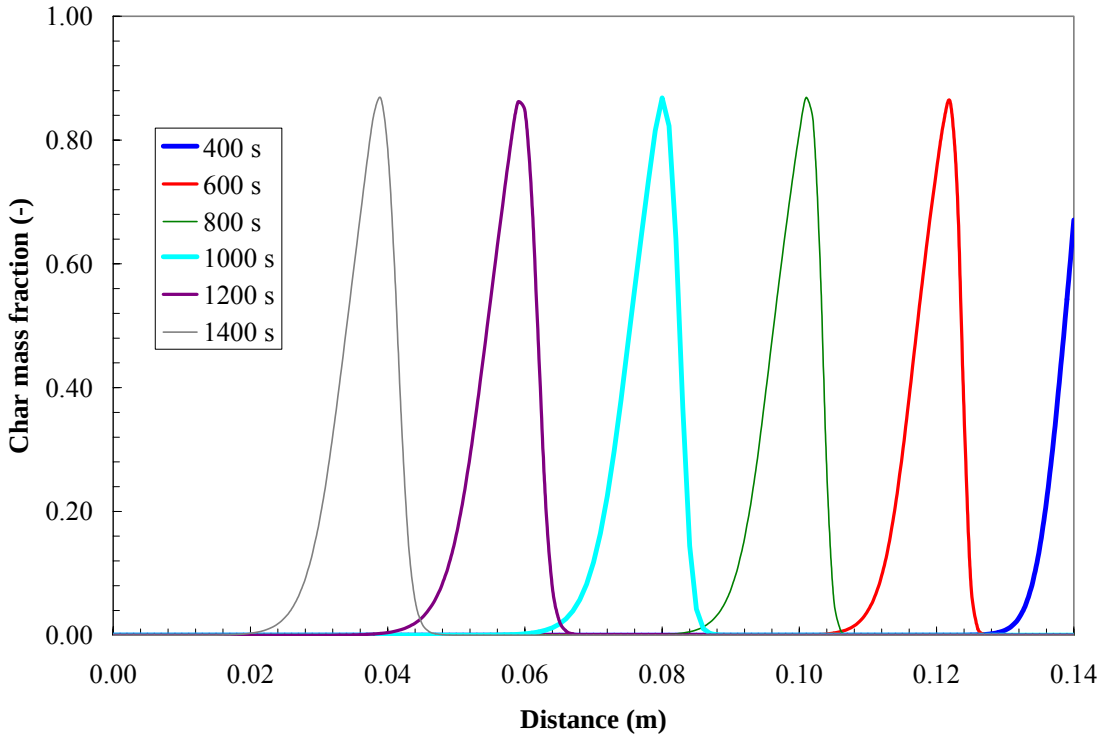

(b)

Figure 6.25. Calculated species profiles in smoldering polyurethane foam at several different times. Airflow is 3 mm/s.
(a) Gas phase oxygen mass fraction; (b) Condensed phase char mass fraction.

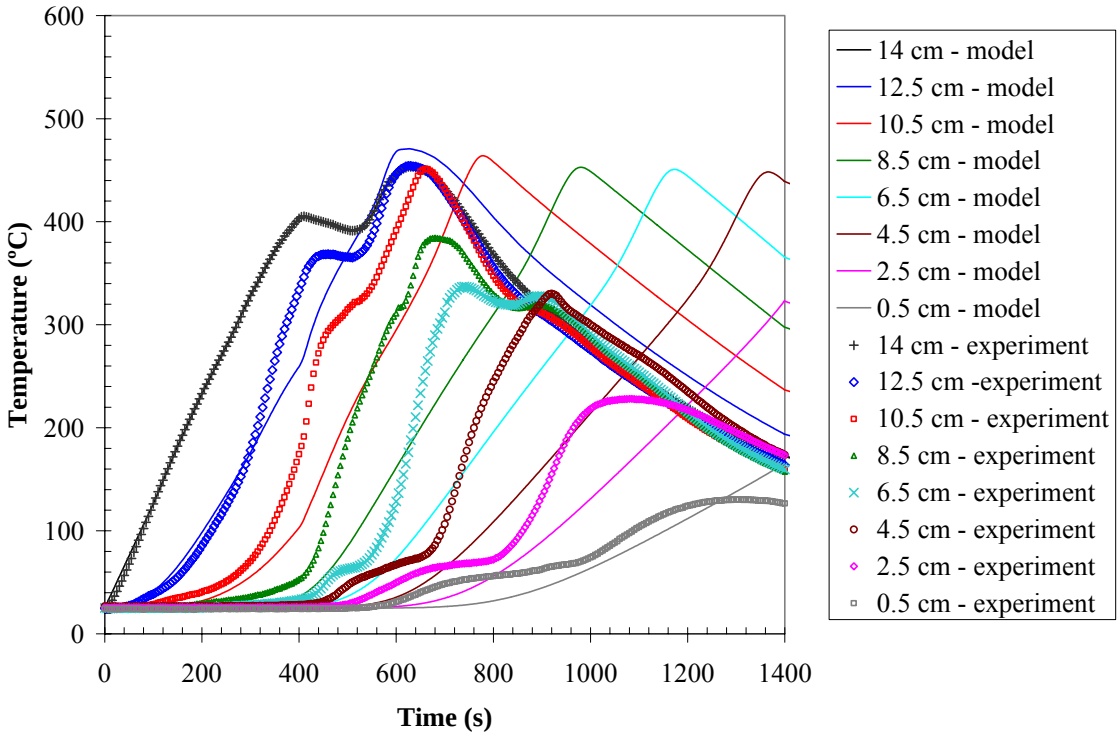

(a)

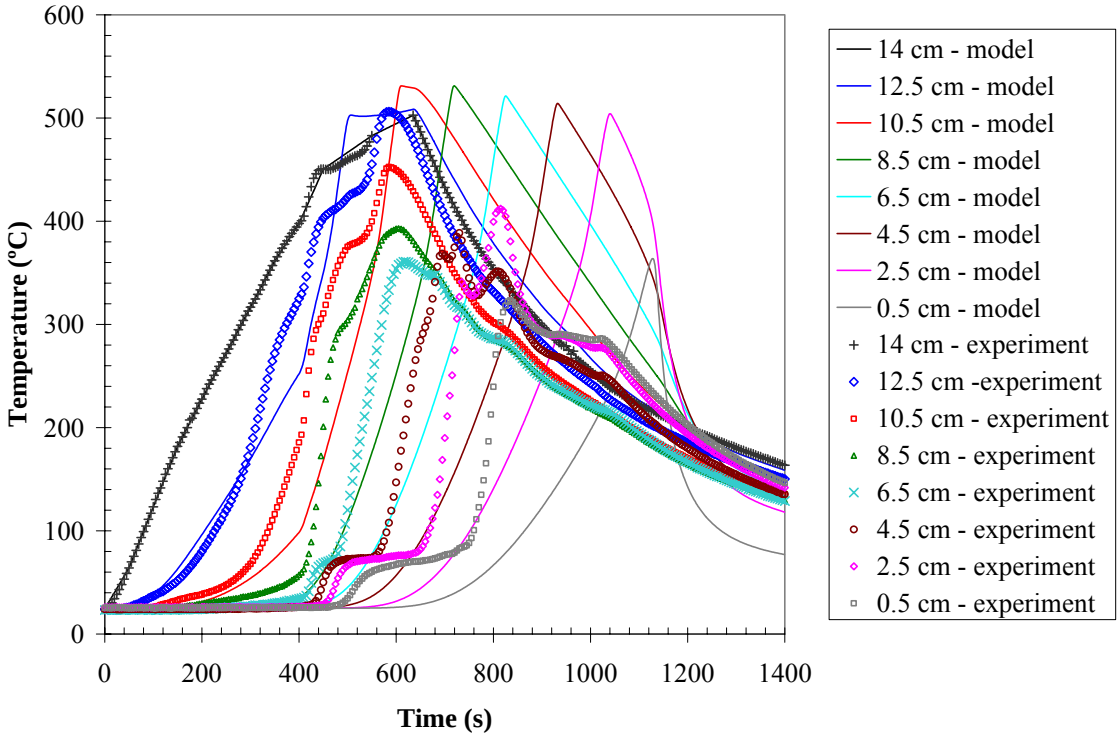

(b)

Figure 6.26. Comparison of experimentally measured [213] and modeled temperature in PU foam cylinder smolder in microgravity. (a) 3 mm/s airflow velocity; (b) 5 mm/s airflow velocity.

Table 6.11. Condensed phase parameters for smolder simulations.

i	Name	k_0 (W/m–K)	n_k (–)	ρ_0 (kg/m^3)	n_ρ (–)	c_0 (J/kg–K)	n_c (–)	γ (m)	K (m^2)	ψ (m^3/m^3)
1	foam	0.05	1.6	27.0	0	2000	0.7	0.003	5×10^{-9}	0.970
2	char	0.05	1.6	10.8	0	2000	0.7	0.006	5×10^{-9}	0.990
3	residue	0.05	1.6	3.2	0	2000	0.7	0.008	5×10^{-9}	0.995

Table 6.12. Reaction parameters for smolder simulations.

k	From	To	χ (–)	ΔH_{sol} (J/kg)	ΔH_{vol} (J/kg)	Z (s^{-1})	E (kJ/mol)	n (–)	n_{O2} (–)
1	foam	char	1	7.75×10^5	7.75×10^5	6.25×10^{14}	200	3	0
2	foam	char	1	-7.00×10^5	-7.00×10^5	2.00×10^{12}	155	1	1
3	char	residue	1	-3.58×10^6	-3.58×10^6	4.00×10^{13}	185	1	1

Table 6.13. Gaseous yields for smolder simulations.

j \ k	1	2	3
1 (pyrolysate)	1	1.2	
2 (nitrogen)			
3 (oxygen)		–0.2	–0.89
4 (char oxidation products)			1.89

7.0 CONCLUDING REMARKS

7.1 Contributions of this dissertation

The main contributions of this dissertation are: 1) Formulation of a simplified generalized pyrolysis model that can be applied to a wide variety of combustible solids; 2) Initial development and testing of a material property estimation technique that can be used to estimate the needed model input parameters from existing laboratory experiments using parallel processing; 3) Numerical implementation (coding) of all equations and making the subsequent software, source code, executable files, and associated documentation available electronically. In addition to these main contributions, several new concepts are introduced in this work.

A new method for handling volume change in a general way is developed. The treatment of heterogeneous reactions combined with the treatment of mass conservation allows grid cells to shrink or swell. Consequently, surface regression and intumescence can be simulated without complicated coordinate transformations or overly complex numerical solution techniques.

Although not emphasized in earlier chapters, some of the numerics presented here contain new ideas. For example, it is not a trivial process to extract temperature from weighted enthalpy for a general multi–component system having temperature–dependent specific heat capacities. In this model, temperature is extracted from weighted enthalpy in a computationally efficient way. This is accomplished by using assumed functional forms for the temperature dependency of thermophysical properties and treating melting as an increase in the apparent specific heat capacity distributed as a Gaussian peak. Also, wherever possible, the governing equations are cast in a form that facilitates numerical

solution with a highly efficient (recursive) tri–diagonal matrix algorithm (TDMA). Since the pressure evolution equation and the gaseous species and energy conservation equations are solved via TDMA, their solution can be included in calculations at minimal additional computational expense.

By solving the gas phase species and energy conservation equations, this work begins investigating (and provides a tool for future workers to further investigate) several phenomena that have not yet been given much attention by modelers. Most fire–related pyrolysis modeling work to date has focused on calculating the total mass loss rate of an irradiated solid, but the present model includes the ability to actually calculate the escaping volatiles' composition. This is an important consideration for fire growth simulations where a pyrolysis model is coupled to a CFD code that simulates the external gas phase because not all volatiles leaving the solid are combustible (H_2O, CO_2), and others may have widely varying heats of combustion (CO vs. gaseous hydrocarbons). Furthermore, fire retarded solids can actually produce volatiles containing halogenated compounds that inhibit gas phase combustion reactions.

Closely related to calculating the volatiles' composition, oxidative pyrolysis can be simulated by modeling the diffusion of ambient oxygen into a decomposing solid and its subsequent effect on various reactions. This was done in Section 6 for PMMA and white pine irradiated under nonflaming conditions. These simulations are one of the most comprehensive attempts at modeling oxidative pyrolysis of a solid fuel slab (i.e., a non–lumped system) that has been conducted to date.

7.2 Model capabilities and potential applications

The calculations reported in this dissertation represent a small fraction of the types of problems that can be simulated with the present code. With the exception of the intumescent coating/steel substrate system, all materials simulated here are homogeneous. However, the model can accommodate layered composition, including contact resistance between layers. This may be an important consideration in many practical materials (composites, fabric/foam upholstery systems, etc.).

The generalized treatment of reactions and reaction products makes it possible to calculate species production rates as a function of the composition of the ambient. Experimental data show that CO production rates increase when wood is pyrolyzed in an oxygen–vitiated atmosphere; this important phenomenon could be simulated with the present model given sufficient information about the controlling reactions. By coupling this pyrolysis model to a CFD code (earlier versions of this code were coupled to FDS 4 and work is presently underway to couple it to FDS 5) it is possible to simulate a number of fire phenomena that have not yet been modeled from first principles. In addition to simulating enhanced CO production rates in vitiated atmospheres, fire retardant solid combustibles could be simulated with condensed phase reaction mechanisms that produce gaseous diluents or free radical scavengers which in turn inhibit gas phase combustion reactions.

Although not reported in this dissertation, the code has recently been extended to two spatial dimensions. A fellow graduate student has used it to simulate 2D smolder in polyurethane foam with a seven–step reaction mechanism [9]. With the exception of condensed phase advection, the model includes most physics and chemistry

(heterogeneous and homogeneous gas phase reactions) required to simulate the transition from smolder to flaming. This problem has been widely studied in polyurethane foam, but the transition from smolder to flaming is a major vector for the propagation of wildfires. Embers lofted by fire plumes can land in dried vegetation (duff, litter, mulch, etc.) or combustibles inside attic spaces of houses and smolder for an extended period before transitioning to flaming. Although this process has been only sparsely studied experimentally and is far from being understood quantitatively, it could be simulated with the present model. Similarly, the self–heating and spontaneous combustion of oil–soaked rags causes many accidental fires in buildings and is not understood quantitatively, but could be simulated with the present model. Anisotropy (wood grain orientation, composite lamination effects, etc.) could be accounted for with the present model by introducing a permeability and thermal conductivity that vary with direction. Since the pressure distribution is calculated, the model could probably be extended to simulate concrete spalling.

The genetic algorithm optimization code discussed earlier has been parallelized using Message Passing Interface (MPI). This parallelization is very efficient due to the low network overhead associated with the algorithm. The genetic algorithm optimization code has been successfully run on a Linux cluster at UC Berkeley using more than 60 CPUs. This makes it possible to calculate the same number of trial solutions overnight that could be calculated in approximately one month on a single processor. The code is portable, and it has been run in parallel on a Linux cluster at WPI as part of a collaborative research project with WPI's Department of Fire Protection Engineering.

It is hoped that the general framework presented here will allow future workers to make much needed progress in the areas mentioned above. The code could also be used to help develop a deeper understanding of physical phenomena and controlling mechanisms relevant to pyrolysis of solid fuels as well as comprehensive models for specific materials. This is the primary motivation for developing a rudimentary user's guide (see Appendix B) and making all source code and software available.

7.3 Philosophical issues raised by this work

Central to this work is the use of an optimization technique (a genetic algorithm) to locate a set of model properties that provides good agreement between model calculations and experimental data. The "accuracy" of a calculation is then judged by how well model calculations match experimental data. This brings up an interesting philosophical question: If the calculations of a numerical pyrolysis model provide a close match to experimental data (e.g., temperatures and mass loss rate), does this necessarily mean that the physics embodied in the model are correctly simulated? Unfortunately, the answer is "no".

As the number of degrees of freedom or number of adjustable parameters increases, it is usually possible to obtain a reasonable match between model calculations and experimental data given enough time and computer power to optimize input parameters even if the underlying reaction mechanism or thermophysical properties are not accurate representations of the actual real–world system. For example, a surface emissivity that is too low or a specific heat that is too high could be compensated for by a fictitious exothermic reaction. By adding this fictitious reaction to a calculation, the simulation could potentially match the experimental data more closely than a simulation

that does not include this reaction, but this does not mean that the underlying physics are faithfully modeled.

Rather than trying to decide on an appropriate level of complexity (as measured by degrees of freedom or number of input parameters) to include in a simulation, this work provides a generalized model and leaves that decision to the user. At one end of the spectrum, the user is free to simulate a particular material as a constant–property opaque solid with a single–step first order decomposition kinetics, requiring specification of ~6 adjustable parameters (k, c, Z, E, ΔH_{vol}, ε). At the other end of the spectrum, the user can simulate a particular material as a multi–component semi–transparent solid with multiple heterogeneous and homogeneous gas reactions or arbitrary order, mass flux by Darcy's law, etc. requiring the specification of 100 or more adjustable parameters.

The "best" modeling approach is one which includes only essential physics and reactions, minimizes the number of adjustable parameters, and matches the experimental data within the desired accuracy over the range of conditions that are of interest (heat flux, oxygen concentration, etc.). Tradeoffs are always inherent in pyrolysis modeling. For example, is it "worth" adding two additional reactions to increase the R^2 coefficient between the measured and modeled mass loss rate from 0.96 to 0.99? By starting simple and adding complexity as needed, the user can make this decision and select a modeling approach that balances accuracy with complexity; this is an underlying theme of this work.

This discussion highlights some of the potential pitfalls that must be borne in mind when using a genetic algorithm, or any other optimization method, to extract model input parameters from bench–scale experimental data. In particular, before the

optimization process begins, the user must first postulate the reaction mechanism(s) and specify the physical phenomena to include in the simulations. Then, the genetic algorithm locates a set of model input parameters that that minimizes the difference between the model calculations and the experimental data subject to the specified reaction mechanism(s) and physical phenomena included in the simulations. The genetic algorithm cannot determine whether any relevant physics (e.g., diathermancy, melting, change in surface emissivity due to charring, etc.) have been omitted from the simulations, or if any imaginary physics or reactions are included in the simulations; all it does is attempt to find a set of model input parameters that best matches the experimental data given the modeling approach specified by the user. Particularly as the number of degrees of freedom (input parameters) increases, compensating effects often make it possible to match the experimental data even if extraneous physics are included or essential physics are excluded.

Despite the caveats noted above, it is felt that genetic algorithms (or other optimization approaches) are a reasonable way to estimate the input parameters needed for pyrolysis modeling from experimental data if used properly. First, reliable set of experimental data must be obtained. Ideally, this data set would include both TGA experiments (which could be used at a minimum to give an idea of the number of reactions that occur) as well as cone calorimeter or FPA–type experiments. The experimental data should span the range of conditions (oxygen concentrations and heat flux levels) over which predictions will be made because extrapolation beyond this range can lead to predictive errors. For example, experiments conducted under nitrogen contain no information about oxidative reactions that could occur in air, and experiments

conducted at low heat flux levels are probably not affected high–temperature reactions that may occur at higher heat flux levels.

From a modeling perspective, care must be taken to include only essential physics and reactions, and omit all nonessential physics or reactions. If a reasonable modeling approach is postulated, parameter optimization by genetic algorithm (or related) techniques should be able to provide a set of model input parameters that are adequate for engineering calculations given sufficiently broad and reliable experimental data. However, this type of property estimation process requires considerable engineering judgment. Due to the wide range of solid fuels encountered in fires, it is probably not possible to formalize or automate this process without additional research.

7.4 Recommendations for future work

At this point in time, our ability to model various pyrolysis phenomena for practical solid combustibles is particularly limited by our ability to determine the model input parameters controlling those phenomena. Thus, it seems that one of the biggest challenges associated with pyrolysis modeling is material property estimation, and it is therefore recommended that future work focus on this area.

In this work, a genetic algorithm is used to extract model input parameters from bench–scale experimental data (TGA and cone calorimeter/FPA–type experiments). However, it is very likely that there are more efficient optimization methods that could be applied. The genetic algorithm used here is an extremely simple self–developed code. It was occasionally susceptible to becoming trapped in local maxima, and it is not adept at fine–local tuning (that is, it can find a good solution, but there are better solutions nearby that may not be located). The literature is filled with examples of more complex (and

probably more efficient and robust) genetic algorithms and hybrid methods. It is possible that a hybrid method that combines some type of stochastic search (such as a genetic algorithm) with a Jacobian–based gradient climbing method may work well. It is recommended that more research be conducted to find (or develop) an optimization algorithm that could be used to extract pyrolysis model input parameters from experimental data.

One approach to material property estimation that was not explored in this work is the independent and separate measurement of all properties that contribute to a material's overall pyrolysis behavior using small–scale laboratory tests. This might involve extracting decomposition kinetics from thermogravimetric analysis, specific heat capacity and heats of reaction from differential scanning calorimetry, and thermal conductivity from specialized small–scale experiments. These measured properties would then be provided as input parameters to a pyrolysis model and used to simulate a slab pyrolysis experiment such as the cone calorimeter. The systematic measurement of all required properties from laboratory tests followed by faithful modeling of a bulk experiment has not yet been widely attempted. It is recommended that this line of material property estimation for pyrolysis modeling be further pursued.

Although this approach is definitely worth investigating, it involves significant challenges that must be overcome. TGA and DSC data obtained from small samples at low heating rates may not be directly applicable to pyrolysis of fuel slabs at high heating rates. Thermal properties are needed over a wide range of temperatures, including temperatures above the onset of pyrolysis. It is not clear that thermal properties of decomposing or partially decomposed solids can be accurately measured. It is also not

obvious how to characterize several parameters such as the in–depth radiation absorption coefficient (κ), the length scale that controls radiation heat transfer across pores (γ), or the temperature–dependent surface emissivity (particularly for solids that darken as they are heated). There may be so much uncertainty in the measured properties that some type of optimization similar to that presented earlier would be necessary, so a hybrid method that combines the two approaches may be the most logical way to proceed.

Modern bench–scale fire tests quantify a material's overall reaction to fire and can be used to estimate effective flammability properties (thermal inertia, ignition temperature, etc.), but they were never intended as a means to estimate the parameters for numerical pyrolysis modeling. Thus, an experimental apparatus that is specifically designed to provide the model input parameters needed for pyrolysis modeling is needed. The apparatus could combine different aspects of a small–scale thermal property measurement test with more traditional flammability tests. A step in this direction is the Thermal Decomposition Apparatus (TDA) used by Lattimer and Ouellette [215] to measure the thermal properties of a glass reinforced vinyl ester composite, and it is recommended that further development of this and similar devices be pursued.

In addition to highlighting the need for improved material property estimation techniques, this work also uncovered instances where improved understanding of underlying physical phenomena is needed. One area needing further study is oxidative reactions, and char oxidation in particular. In Section 6.2, the oxidative pyrolysis of white pine was simulated using both heterogeneous reactions (wood oxidation and char oxidation) and homogenous gas phase reactions (pyrolysate oxidation). In the simulations, both types of reactions contribute to the heat release that raises wood's

temperature in oxidative environments and increases its mass loss rate. However, the conventional view of char oxidation in the fire community is that it is a heterogeneous process, not a homogeneous gas phase oxidation process. Nonetheless, a comparison of the gas phase combustion time scale with the residence time of the volatiles in the heated char indicates that these time scales are of the same order of magnitude. It cannot be said with certainty that homogeneous gas phase reactions are or are not occurring, and further investigation is needed in this area. In particular, it may be fruitful to adapt concepts developed in the combustion community for coal combustion modeling. Related to oxidative reactions, improved techniques for modeling the diffusion of oxygen to the surface of the fuel are needed, including the reduction of the heat/mass transfer coefficient by blowing.

The model formulation could be improved by relaxing the assumption that porosity is a property of each condensed phase species. As was discussed in Section 3.1.1, this approximation considerably simplifies the model because the weighted porosity can be calculated from the local composition as $\overline{\psi} = \sum X_i \psi_i$. However, it has distinct disadvantages when modeling materials such as glass fiber composites that have a noncharring polymer matrix. As discussed in Section 3.1.1, for two composites having different glass concentrations, the porous glass matrix that remains behind after the noncharring resin is pyrolyzed away would have to be modeled as two separate species even though the glass is physically the same. This shortcoming could be eliminated by relaxing the approximation that porosity is a property of a particular condensed phase species and solving a separate porosity evolution equation. This is planned for future work.

REFERENCES

[1] Croce, P.A., "The FORUM for international cooperation on fire research: a position paper on evaluation of products and services for global acceptance," *Fire Safety Journal* **36**: 715–717 (2001).

[2] Gritzo, L.A., Senseny, P.E., Xin, Y., and Thomas, J.R., "The international FORUM of fire research directors: a position paper on verification and validation of numerical fire models," *Fire Safety Journal* **40**: 495–490 (2005).

[3] McGrattan, K., "Fire Dynamics Simulator (Version 4) technical reference guide," NIST Special Publication 1018–4, 2004.

[4] Lautenberger, C., Zhou, Y.Y., and Fernandez–Pello, A.C., "Numerical modeling of convective effects on piloted ignition of composite materials," *Combustion Science and Technology* **177**: 1231–1252 (2005).

[5] Lautenberger, C., McAllister, S., Rich, D., and Fernandez–Pello, C., "Modeling the effect of environmental variables on opposed–flow flame spread rates with FDS," *Fire Safety in Tall Buildings International Congress*, University of Cantabria, Santander Spain, October 18–20 2006.

[6] Lautenberger, C., McAllister, S., Rich, D., and Fernandez–Pello, C., "Effect of environmental variables on flame spread rates in microgravity," *45th AIAA Aerospace Sciences Meeting and Exhibit*, Reno, NV, January 2007, AIAA Paper 2007–383.

[7] Rich, D., Lautenberger, C., Torero, J.L., Quintiere, J.G., and Fernandez–Pello, C., "Mass flux of combustible solids at piloted ignition," *Proceedings of the Combustion Institute* **31**: 2653–2660 (2007).

[8] Lautenberger, C. and Fernandez–Pello, A.C., "Approximate analytical solutions for the transient mass loss rate and piloted ignition time of a radiatively heated solid in the high heat flux limit," *Fire Safety Science – Proceedings of the Eighth International Symposium*, Beijing China, September 2005, pp. 445–456.

[9] Dodd, A., Lautenberger, C., and Fernandez–Pello, C., "Numerical modeling of two–dimensional smolder structure," Paper C–02, 2007 Fall Technical Meeting of the Eastern States Section of the Combustion Institute, October 22, 2007.

[10] Di Blasi, C., "Modeling and simulation of combustion processes of charring and non–charring solid fuels," *Progress in Energy and Combustion Science* **19**: 71–104 (1993).

[11] Kashiwagi, T., "Polymer combustion and flammability–role of the condensed phase," *Proceedings of the Combustion Institute* **25**: 1423–1437 (1994).

[12] Fernandez–Pello, A.C., "The solid phase," in *Combustion Fundamentals of Fire*, Ed. G. Cox, pp. 31–100, Academic Press, New York, 1995.

[13] Di Blasi, C., "The state of the art of transport models for charring solid degradation," *Polymer International* **49**: 1133–1146 (2000).

[14] Lyon, R.E. and Janssens, M.L., "Polymer flammability," DOT/FAA/AR–05/14, 2005.

[15] Moghtaderi, B., "The state–of–the–art in pyrolysis modeling of lignocellulosic solid fuels," *Fire and Materials* **30**: 1–34 (2006).

[16] Lautenberger, C. and Fernandez–Pello, A.C., "Pyrolysis modeling, thermal decomposition, and transport processes in combustible solids," to appear in *Transport Phenomena in Fires*, Ed. M. Faghri and B. Sunden, WIT Press, 2008.

[17] Di Blasi, C., "Modeling chemical and physical processes of wood and biomass pyrolysis," to appear in *Progress in Energy and Combustion Science* (2008).

[18] ASTM E1354–03, "Standard test method for heat and visible smoke release rates for materials and products using an oxygen consumption calorimeter".

[19] ASTM E1321–97a, "Standard test method for determining material ignition and flame spread properties".

[20] Quintiere, J.G., "A simulation model for fire growth on materials subject to a room–corner test," *Fire Safety Journal* **20**: 313–339 (1993).

[21] Dembsey, N.A. and Williamson, R.B., "Coupling the fire behavior of contents and interior finishes for performance fire codes: evaluation of a fire spread model," *Journal of Fire Protection Engineering* **8**: 119–132 (1997).

[22] Lattimer, B.Y., Hunt, S.P., Wright, M., and Sorathia, U., "Modeling fire growth in a combustible corner," *Fire Safety Journal* **38**: 771–796 (2003).

[23] Zhang, J., Yang, F., Shields, T.J., Silcock, G.W.H., and Azhakesan, M.A., "Effects of surface flame spread of plywood lining on enclosure fire in a modified ISO room," *Journal of Fire Sciences* **21**: 67–83 (2003).

[24] Urbas, J., Parker, W.J., and Luebbers, G.E., "Surface temperature measurements on burning materials using an infrared pyrometer: Accounting for emissivity and reflection of external radiation," *Fire and Materials* **28**: 33–53 (2004).

[25] Tewarson, A. and Pion, R.F., "Flammability of plastics–I. Burning intensity," *Combustion and Flame* **26**: 85–103 (1976).

[26] Drysdale, D.D., *An Introduction to Fire Dynamics*, Second Edition, John Wiley & Sons, 1999.

[27] Tewarson, A., "Generation of heat and chemical compounds in fires," in *SFPE Handbook of Fire Protection Engineering*, Third Edition, Ed. DiNenno P., pp. 3–82 to 3–161, National Fire Protection Association, Quincy, MA, 2002.

[28] Brehob, E.G., Kim, C.I., and Kulkarni, A.K., "Numerical model of upward flame spread on practical wall materials," *Fire Safety Journal* **36**: 225–240 (2001).

[29] Tsai, K.–C. and Drysdale, D.D., "Using cone calorimeter data for the prediction of fire hazard," *Fire Safety Journal* **27**: 697–706 (2002).

[30] Karlsson, B., "Models for calculating flame spread on wall lining materials and the resulting heat release rate in a room," *Fire Safety Journal* **23**: 365–386 (1994).

[31] Vovelle, C., Akrich, R., and Delfau, J.–L., "Thermal degradation of solid materials under a variable radiant heat flux," *Proceedings of the Combustion Institute* **20**: 1647–1654 (1984).

[32] Mitler, H.E., "Predicting the spread rates of fires on vertical surfaces," *Proceedings of the Combustion Institute* **23**: 1715–1721 (1990).

[33] Mitler, H.E. and Steckler, K.D., "SPREAD – A model of flame spread on vertical surfaces," NISTIR 5619, National Institute of Standards and Technology, 1995.

[34] Babrauskas, V., "Heat release rates," in *SFPE Handbook of Fire Protection Engineering*, Third Edition, Ed. DiNenno P., pp. 3–11 to 3–37, National Fire Protection Association, Quincy, MA, 2002.

[35] Delichatsios, M.A. and Chen, Y., "Asymptotic, approximate, and numerical solutions for the heatup and pyrolysis of materials including reradiation losses," *Combustion and Flame* **92**: 292–307 (1993).

[36] Rhodes, B.T. and Quintiere, J.G., "Burning rate and flame heat flux for PMMA in a cone calorimeter," *Fire Safety Journal* **26**: 221–240 (1996).

[37] Hopkins, D. and Quintiere, J.G., "Material fire properties and predictions for thermoplastics," *Fire Safety Journal* **26**: 241–268 (1996).

[38] Staggs J.E.J, "A discussion of modelling idealised ablative materials with particular reference to fire testing," *Fire Safety Journal* **28**: 47–66 (1997).

[39] Jia, F., Galea, E.R., and Patel, M.K., "The numerical simulation of the noncharring pyrolysis process and fire development within a compartment," *Applied Mathematical Modeling* **23**: 587–607 (1999).

[40] Tsai, T.–H., Li, M.–J., Shih, I.–Y., Jih, R., and Wong, S.–C., "Experimental and numerical study of autoignition and pilot ignition of PMMA plates in a cone calorimeter," *Combustion and Flame* **124**: 466–480 (2001).

[41] Fernandez–Pello, A. and Williams, F.A., "A theory of laminar flame spread over flat surfaces of solid combustibles," *Combustion and Flame* **28**: 251–277 (1977).

[42] Vovelle, C., Delfau, J.–L., Reuillon, M., Bransier, J., and Laraqui, N., "Experimental and numerical study of the thermal degradation of PMMA," *Combustion Science and Technology* **53**: 187–201 (1987).

[43] Di Blasi, C., Crescitelli, S., Russo, G., and Cinque, G., "Numerical model of ignition processes of polymeric materials including gas phase absorption of radiation," *Combustion and Flame* **83**: 333–344 (1991).

[44] Brescianini, C.P, Yeoh, G.H., Chandrasekaran, V., and Yuen, R, "A numerical model for pilot ignition of PMMA in a cone calorimeter," *Combustion Science and Technology* **129**: 321–345 (1997).

[45] Staggs, J.E.J, "A theoretical investigation into modeling thermal degradation of solids incorporating finite–rate kinetics," *Combustion Science and Technology* **123**: 261–185 (1997).

[46] Staggs, J.E.J. and Whiteley, R.H., "Modeling the combustion of solid phase fuels in cone calorimeter Experiments," *Fire and Materials* **23**: 63–39 (1999).

[47] Staggs, J.E.J., "Modeling thermal degradation of polymers using single–step first–order kinetics," *Fire Safety Journal* **32**: 17–34 (1999).

[48] Staggs, J.E.J., "A simple model of polymer pyrolysis including transport of volatiles," *Fire Safety Journal* **34**: 69–80 (2000).

[49] Córdova, J.L. and Fernandez–Pello, A.C., "Convection effects on the endothermic gasification and piloted ignition of a radiatively heated combustible solid," *Combustion Science and Technology* **156**: 271–289 (2000).

[50] Zhou, Y.Y., Walther, D.C., and Fernandez–Pello, A.C., "Numerical analysis of piloted ignition of polymeric materials," *Combustion and Flame* **131**: 147–158 (2002).

[51] McGrattan, K., Hostikka, S., Floyd, J., Baum, H., and Rehm, R., "Fire Dynamics Simulator (Version 5) technical reference guide," NIST Special Publication 1018–5, 2007.

[52] Wichman, I.S., "A model describing the steady–state gasification of bubble–forming thermoplastics in response to an incident heat flux," *Combustion and Flame* **63**: 217–229 (1986).

[53] Butler, K.M., "A mixed layer pyrolysis model for polypropylene," *Fire Safety Science – Proceedings of the Sixth International Symposium*, pp. 313–324, 1999.

[54] Butler, K.M., "A numerical model for combustion of bubbling thermoplastic materials in microgravity," National Institute of Standards and Technology NISTIR 6331, 2002.

[55] Kashiwagi, T. and Ohlemiller, T.J., "A study of oxygen effects on nonflaming transient gasification of PMMA and PE during thermal irradiation," *Proceedings of the Combustion Institute* **19**: 815–823 (1982).

[56] Vovelle, C., Akrich, R., and Delfau, J.L., "Mass loss rate measurements on solid materials under radiative heating," *Combustion Science and Technology* **36**: 1–18 (1984).

[57] Wichman, I.S. and Atreya, A., "A simplified model for the pyrolysis of charring materials," *Combustion and Flame* **68**: 231–247 (1987).

[58] Chen, Y., Delichatsios, M.A., and Motevalli, V., "Material pyrolysis properties, part I: an integral model for one–dimensional transient pyrolysis of charring and non–charring materials," *Combustion Science and Technology* **88**: 309–328 (1993).

[59] Moghtaderi, B., Novozhilov, V., Fletcher, D., and Kent, J.H., "An integral model for the transient pyrolysis of solid materials," *Fire and Materials* **21**: 7–16 (1997).

[60] Jia, F., Galea, E.R., and Patel, M.K., "Numerical simulation of the mass loss process in pyrolyzing char materials," *Fire and Materials* **23**: 71–18 (1999).

[61] Spearpoint, M.J. and Quintiere, J.G., "Predicting the burning of wood using an integral model," *Combustion and Flame* **123**: 308–324 (2000).

[62] Spearpoint, M.J. and Quintiere, J.G., "Predicting the piloted ignition of wood in the cone calorimeter using an integral model – effect of species, grain orientation, and heat flux," *Fire Safety Journal* **36**: 391–415 (2001).

[63] Theuns, E., Vierendeels, J., and Vandevelde, P., "A moving grid model for the pyrolysis of charring materials," *International Journal of Numerical Methods for Heat & Fluid Flow* **12**: 541–559 (2002).

[64] Galgano, A. and Di Blasi, C., "Modeling wood degradation by the unreacted–core–shrinking approximation," *Industrial & Engineering Chemistry Research* **42**: 2101–2111 (2003).

[65] Galgano, A. and Di Blasi, C., "Modeling the propagation of drying and decomposition fronts in wood," *Combustion and Flame* **139**: 16–27 (2004).

[66] Theuns, E., Merci, B., Vierendeels, J., and Vandevelde, P., "Extension and evaluation of the integral model for transient pyrolysis of charring materials," *Fire and Materials* **29**: 195–212 (2005).

[67] Theuns, E., Merci B., Vierendeels, J. and Vandevelde, P., "Critical evaluation of an integral model for the pyrolysis of charring materials," *Fire Safety Journal* **40**: 121–140 (2005).

[68] Galgano, A. and Di Blasi, C., "Infinite– versus finite–rate kinetics in simplified models of wood pyrolysis," *Combustion Science and Technology* **177**: 279–303 (2005).

[69] Ji, J., Cheng, Y., Yang, L., Guo, Z., and Fan, W., "An integral model for wood auto–ignition under variable heat flux," *Journal of Fire Sciences* **24**: 413–425 (2006).

[70] Kung, H.–C., "A mathematical model of wood pyrolysis," *Combustion and Flame* **18**: 185–195 (1972).

[71] Kansa, E.J., Perlee, H.E., and Chaiken, R.F., "Mathematical model of wood pyrolysis including internal forced convection," *Combustion and Flame* **28**: 311–324 (1977).

[72] Fredlund, B., "Modelling of heat and mass transfer in wood structures during fire," *Fire Safety Journal* **20**: 39–69 (1993).

[73] Ritchie, S.J., Steckler, K.D., Hamins, A., Cleary, T.G., Yang, J.C., and Kashiwagi, T., "The effect of sample size on the heat release rate of charring materials," *Fire Safety Science–Proceedings of the Fifth International Symposium*, pp. 177–188, 1997.

[74] Novozhilov, V., Moghtaderi, B., Fletcher, D.F., and Kent, J.H., "Computational fluid dynamics modeling of wood combustion," *Fire Safety Journal* **27**: 69–84 (1996).

[75] Yang, L., Chen, X., Zhou, X., and Fan, W., "A modified model of pyrolysis for charring materials in fire," *International Journal of Engineering Science* **40**: 1011–1021 (2002).

[76] Yang, L., Chen X., Zhou, X., and Fan, W., "The pyrolysis and ignition of charring materials under an external heat flux," *Combustion and Flame* **133**: 407–413 (2003).

[77] Kuo, J.T., and Hsi, C.–L., "Pyrolysis and ignition of single wooden spheres heated in high–temperature streams of air," *Combustion and Flame* **142**: 401–412 (2005).

[78] Yang, L.Z., Guo, Z.F., Chen, X.J., and Fan, W.C., "Predicting the temperature distribution of wood exposed to a variable heat flux," *Combustion Science and Technology* **178**: 2165–2176 (2006).

[79] Trelles, J. and Lattimer, B.Y., "Modelling thermal degradation of composite materials," *Fire and Materials* **31**: 147–171 (2006).

[80] Yang, L., Guo, Z., Zhou, Y., and Fan, W., "The influence of different external heating ways on pyrolysis and spontaneous ignition of some woods," *Journal of Analytical and Applied Pyrolysis* **78**: 40–45 (2007).

[81] de Ris, J.L. and Yan, Z., "Modeling ignition and pyrolysis of solid fuels," *Proceedings of the Fifth International Conference on Fire and Materials*, pp. 111–121, 1998.

[82] Zhao, L. and Dembsey, N.A., "Uncertainty effects on measurement of fire characteristics of material systems," *Proceedings of Fire and Materials 2005*, pp. 37–49, 2005.

[83] Moghtaderi, B., Novozhilov, V., Fletcher, D.F., and Kent, J.H., "The effect of char oxidation on the flaming combustion characteristics of wood materials," *Journal of Applied Fire Science* **6**: 189–201 (1996).

[84] Kashiwagi, T., Ohlemiller, T.J., and Werner, K., "Effects of external radiant flux and ambient oxygen concentration on nonflaming gasification rates and evolved products of white pine," *Combustion and Flame* **69**: 331–345 (1987).

[85] Omrane, A., Ossler, F., Aldén, M., Svenson, J., and Pettersson, J.B.C, "Surface temperature of decomposing construction materials studied by laser–induced phosphorescence," *Fire and Materials* **29**: 39–51 (2005).

[86] Cordova, J.L., Walther, D.C., Torero, J.L., and Fernandez–Pello, A.C., "Oxidizer flow effects on the flammability of solid combustibles," *Combustion Science and Technology* **164**: 253–278 (2001).

[87] Boss, C.R. and Chien, J.C.W., "Oxygen diffusion limitation in auto oxidation of polypropylene," *Journal of Polymer Science: Part A–1* **4**: 1543–1551 (1966).

[88] Stuetz, D.E., Diedwardo, A.H., Zitomer, F., and Barnes, B.P., "Polymer combustion," *Journal of Polymer Science: Polymer Chemistry Edition* **13**: 585–621 (1975).

[89] Sorathia, U., Gracik, T., Ness, J., Durkin, A., Williams, F., Hunstad, M., and Berry, F., "Evaluation of intumescent coatings for shipboard fire protection," *Journal of Fire Sciences* **21**: 423–450 (2003).

[90] Zaikov, G.E. and Lomakin, S.M., "Ecological aspects of polymer flame retardancy," In *Fire Retardancy of Polymers: The Use of Intumescence*, Ed. Le Bras, M., Camino, G., Bourbigot, S., and Delobel, R., The Royal Society of Chemistry, Cambridge, pp. 421–447, 1998.

[91] Cagliostro, D.E. and Riccitiello, S.R., "Intumescent coating modeling," *Journal of Fire, and Flammability* **6**: 205–221 (1975).

[92] Anderson, C.E. and Wauters, D.K., "A thermodynamics heat transfer model for intumescent systems," *International Journal of Engineering Science* **22**: 881–889 (1984).

[93] Buckmaster, J., Anderson, C., and Nachman, A., "A model for intumescent paints," *International Journal of Engineering Science* **24**: 263–276 (1986).

[94] Henderson, J.B. and Wicek, T.E., "A mathematical model to predict the thermal response of decomposing, expanding polymer composites," *Journal of Composite Materials* **21**: 373–393 (1987).

[95] Shih Y.C., Cheung, F.B., and Koo, J.H., "Theoretical modeling of intumescent fire–retardant materials," *Journal of Fire Sciences* **16**: 46–71 (1998).

[96] Bourbigot, S., Duquesne, S., and Leroy, J.–M., "Modeling of heat transfer of a polypropylene–Based intumescent system during combustion," *Journal of Fire Sciences* **17**: 42–56 (1999).

[97] Di Blasi, C. and Branca, C., "Mathematical model for the nonsteady decomposition of intumescent coatings," *AIChE Journal* **47**: 2359–2370 (2001).

[98] Di Blasi, C., "Modeling the effects of high radiative heat fluxes on intumescent material decomposition," *Journal of Analytical and Applied Pyrolysis* **71**: 721–737 (2004).

[99] Wang, J., Yang, S., Li, G., and Jiang, J., "A mathematical model of heat transfer of a PU–based intumescent flame–retardant coating during combustion in a cabinet," *Polymer International* **52**: 1827–1832 (2003).

[100] Griffin, G.J., Bicknell, A.D., and Brown, T.J., "Studies on the effect of atmospheric oxygen content on the thermal resistance of intumescent, fire–retardant coatings," *Journal of Fire Sciences* **23**: 303–328 (2005).

[101] Ŝimon, P., "Single–step kinetics approximations employing non–Arrhenius temperature functions," *Journal of Thermal Analysis and Calorimetry* **79**: 703–708 (2005).

[102] Kim, S., Jang, E.–S., Shin, D.–H., and Lee, K.–H., "Using peak properties of a DTG curve to estimate the kinetic parameters of the pyrolysis reaction: application to high density polyethylene," *Polymer Degradation and Stability* **85**: 799–805 (2004).

[103] Vyazovkin, S. and Wight, C.A., "Isothermal and non–isothermal kinetics of thermally stimulated reactions of solids," *International Reviews in Physical Chemistry* **17**: 407–433 (1998).

[104] Agrawal, R.K., "On the use of the Arrhenius equation to describe cellulose and wood pyrolysis," *Thermochimica Acta* **91**: 343–349 (1985).

[105] Ŝimon, P., "Isoconversional methods fundamentals, meaning, and application," *Journal of Thermal Analysis and Calorimetry* **76**: 123–132 (2004).

[106] Parker, W.J., "Prediction of the heat release rate of Douglas Fir," *Fire Safety Science – Proceedings of the Second International Symposium*, pp. 337–346, 1989.

[107] Jinno, D., Gupta, A.K., and Yoshikawa, K., "Determination of chemical kinetic parameters of surrogate solid wastes," *Journal of Engineering for Gas Turbines and Power* **126**: 685–692 (2004).

[108] Senneca O., Chirone, R., and Salatino, P., "Oxidative pyrolysis of solid fuels," *Journal of Analytical and Applied Pyrolysis* **71**: 959–970 (2004).

[109] Westerhout, R.W.J., Waanders, J., Kuipers, J.A.M., and van Swaaij, W.P.M., "Kinetics of the low–temperature pyrolysis of polyethylene, polypropylene, and polystyrene modeling, experimental determination, and comparison with literature

models and data," *Industrial & Engineering Chemical Research* **36**: 1955–1964 (1997).

[110] Zimmermann, H. and Behnisch, J., "Thermogravimetric investigations on the kinetics of thermal degradation of polyoxymethylenes," *Thermochimica Acta* **59**: 1–8 (1982).

[111] Esfahani, J.A., "Oxygen–sensitive thermal degradation of PMMA: a numerical study," *Combustion Science and Technology* **174**: 183–198 (2002).

[112] Jun, H.C., Lee, H.P., Yi, S.–C., Yoo, K.O., and Oh, S.C., "A kinetic analysis of the thermal–oxidative decomposition of polypropylene," *Journal of Fire Sciences* **18**: 245–263 (2000).

[113] Peterson, J.D., Vyazovkin, S., and Wight, C.A., "Kinetic study of stabilizing effect of oxygen on thermal degradation of poly(methylmethacrylate)," *Journal of Physical Chemistry B* **103**: 8087–8092 (1999).

[114] Rein, G., Lautenberger, C., Fernandez–Pello, A.C., Torero, J.L., and Urban, D.L., "Application of genetic algorithms and thermogravimetry to determine the kinetics of polyurethane foam in smoldering combustion," *Combustion and Flame* **146**: 95–108 (2006).

[115] Ferriol, M., Gentilhomme, A., Cochez, M., Oget, N., and Mieloszynski, J.L., "Thermal degradation of poly(methylmethacrylate) (PMMA): modelling of DTG and TG curves," *Polymer Degradation and Stability* **79**: 271–181 (2003).

[116] Aracil, I., Font, R., and Conesa, J.A., "Thermo–oxidative decomposition of polyvinyl chloride," *Journal of Analytical and Applied Pyrolysis* **74**: 215–223 (2005).

[117] Leach, S.V., Rein, G., Ellzey, J.L., and Ezekoye, O.A., "Kinetic and fuel property effects on forward smoldering combustion," *Combustion and Flame* **120**: 346–358 (2000).

[118] Khalturinskij, N.A., Reshetnikov, I.S., Yablokova, M.Y., Rudakova, T.A., and Svistunov, V.S., "Microkinetics of high–temperature pyrolysis," *Fire and Materials* **22**: 47–54 (1998).

[119] Alves, S.S. and Figueiredo, J.L., "Pyrolysis kinetics of lignocellulosic materials by multistage isothermal thermogravimetry," *Journal of Analytical and Applied Pyrolysis* **13**: 123–134 (1988).

[120] Chan, W.–C. R., Kelbon, M., and Krieger, B.B., "Modeling and experimental verification of physical and chemical processes during pyrolysis of a large biomass particle," *Fuel* **64**: 1505–1513 (1985).

[121] Alves, S.S. and Figueiredo, J.L., "A model for pyrolysis of wet wood," *Chemical Engineering Science* **44**: 2861–2869 (1989).

[122] Gao, M., Zhu, K., Sun, Y.J., and Sun, C., "Thermal degradation of wood treated with amino resins and amino resins modified with phosphate in nitrogen," *Journal of Fire Sciences* **22**: 505–515 (2004).

[123] Gao, Z., Kaneko, T., Hou, D., Nakada, M., "Kinetics of thermal degradation of poly(methylmethacrylate) studied with the assistance of the fractional conversion at the maximum reaction rate," *Polymer Degradation and Stability* **84**: 399–403 (2004).

[124] Lyon, R.E. and Walters, R.N., "Pyrolysis combustion flow calorimetry," *Journal of Analytical and Applied Pyrolysis* **71**: 27–46 (2004).

[125] Vyazovkin, S. and Wight, C.A., "Model–free and model–fitting approaches to kinetic analysis of isothermal and nonisothermal data," *Thermochimica Acta* **340–341**: 53–68 (1999).

[126] Narayan, R. and Antal, M.J., "Thermal lag, fusion, and the compensation effect during biomass pyrolysis," *Industrial & Engineering Chemical Research* **35**: 1711–1721 (1996).

[127] Carrasco, F. and Pagès, P., "Thermogravimetric analysis of polystyrene: influence of sample weight and heating rate on thermal and kinetic parameters," *Journal of Applied Polymer Science* **61**: 187–197 (1996).

[128] Frederick, W.J. and Mentzer, C.C., "Determination of heats of volatilization for polymers by differential scanning calorimetry," *Journal of Applied Polymer Science* **19**: 1799–1804 (1975).

[129] Staggs, J.E.J., "The heat of gasification of polymers," *Fire Safety Journal* **39**: 711–720 (2004).

[130] Zhang, H. "Fire–safe polymers and polymer composites," DOT/FAA/AR–04/11, 2004.

[131] Janssens, M.L., "Modeling of the thermal degradation of structural wood members exposed to fire," *Fire and Materials* **28**: 199–207 (2004).

[132] Roberts, A.F., "The heat of reaction during the pyrolysis of wood," *Combustion and Flame* **17**: 79–86 (1971).

[133] Kung, H.–C. and Kalelkar, A.S., "On the heat of reaction in wood pyrolysis," *Combustion and Flame* **20**: 91–103 (1973).

[134] Gupta, A.K. and Müller, P., "Pyrolysis of paper and cardboard in inert and oxidative environments," *Journal of Propulsion and Power* **15**: 187–194 (1999).

[135] Zhou, Y.Y., Fernandez–Pello, A.C., Torero, J.L., and Ross, H.D., "Theoretical prediction of piloted ignition of polymeric fuels in microgravity at low velocity flows," *Microgravity Science and Technology* **XIV/1**: 44–50 (2003).

[136] Höhne, G.W.H, Hemminger, W.F., and H.–J. Flammersheim, *Differential Scanning Calorimetry*, Second Edition, Springer–Verlag, New York, 2003.

[137] Atreya, A., "Pyrolysis, ignition, and fire spread on horizontal surfaces of wood," Ph.D. Thesis, Harvard University, May 1983.

[138] Dakka, S.M., "TGA/DTA/MS of poly(methylmethacrylate) the role of the oxidative environment," *Journal of Thermal Analysis and Calorimetry* **73**: 17–24 (2003).

[139] Dakka, S.M., "TG/DTA/MS of poly(methylmethacrylate)," *Journal of Thermal Analysis and Calorimetry* **74**: 729–734 (2003).

[140] Lyon, R.E., "Plastics and rubber," in *Handbook of Building Materials for Fire Protection*, Ed. Harper, C.A., pp. 3.1–3.51, McGraw–Hill, New York, 2004.

[141] Orwoll, R.A., "Densities, coefficients of thermal expansion, and compressibilities of amorphous polymers," in *Physical Properties of Polymers Handbook*, Ed. Mark, J.E., pp. 81–89, American Institute of Physics Press, Woodbury, NY, 1996.

[142] Gaur, U. and Wunderlich, B., "Heat capacity and other thermodynamic properties of linear macromolecules. II. polyethylene," *Journal of Physical and Chemical Reference Data* **10**: 119–152 (1981).

[143] Gaur, U. and Wunderlich, B., "Heat capacity and other thermodynamic properties of linear macromolecules. III. polyoxides," *Journal of Physical and Chemical Reference Data* **10**: 1001–1049 (1981).

[144] Gaur, U. and Wunderlich, B., "Heat capacity and other thermodynamic properties of linear macromolecules. IV. polypropylene," *Journal of Physical and Chemical Reference Data* **10**: 1051–1064 (1981).

[145] Gaur, U. and Wunderlich, B., "Heat capacity and other thermodynamic properties of linear macromolecules. V. polystyrene," *Journal of Physical and Chemical Reference Data* **11**: 313–325 (1982).

[146] Gaur, U. Lau, S.–F., Wunderlich, B.B., and Wunderlich, B., "Heat capacity and other thermodynamic properties of linear macromolecules. VI. acrylic polymers," *Journal of Physical and Chemical Reference Data* **11**: 1065–1089 (1983).

[147] Gaur, U., Wunderlich, B.B., and Wunderlich, B., "Heat capacity and other thermodynamic properties of linear macromolecules. VII. other carbon backbone polymers," *Journal of Physical and Chemical Reference Data* **12**: 29–63 (1983).

[148] Gaur, U., Lau, S.–F., Wunderlich, B.B., and Wunderlich, B., "Heat capacity and other thermodynamic properties of linear macromolecules. VIII. polyesters and polyamides," *Journal of Physical and Chemical Reference Data* **12**: 65–89 (1983).

[149] Gaur, U., Lau, S.–F., and Wunderlich, B., "Heat capacity and other thermodynamic properties of linear macromolecules. IX. final group of aromatic and inorganic polymers," *Journal of Physical and Chemical Reference Data* **12**: 91–108 (1983).

[150] Zhang, X., Hendro, W., Fujii, M., Tomimura, T., and Imaishi, N., "Measurements of the thermal conductivity and thermal diffusivity of polymer melts with the short–hot–wire method," *International Journal of Thermophysics* **23**: 1077–1090 (2002).

[151] Zhang, X. and Fujii, M., "Measurements of the thermal conductivity and thermal diffusivity of polymers," *Polymer Engineering and Science* **43**: 1755–1764 (2003).

[152] Steinhaus, T., "Evaluation of the thermophysical properties of poly(methylmethacrylate): A reference material for the development of a flammability test for micro–gravity environments," MS Thesis. University of Maryland, Department of Fire Protection Engineering, 1999.

[153] MacLean, J.D., "Thermal conductivity of wood," *Transactions of the American Society of Heating and Ventilating Engineers* **47**: 323–354 (1941).

[154] TenWolde, A., McNatt, J.D., and Krahn, L., "Thermal properties of wood and wood panel products for use in buildings," USDA Forest Products Laboratory DOE/USDA–21697/1, 1988.

[155] Ragland, K.W. and Aerts, D.J., "Properties of wood for combustion analysis," *Bioresource Technology* **37**: 161–168 (1991).

[156] Suleiman, B.M., Larfeldt, J., Leckner, B., and Gustavsson, M., "Thermal conductivity and diffusivity of wood," *Wood Science and Technology* **33**: 465–473 (1999).

[157] Thunman, H. and Leckner, B., "Thermal conductivity of wood–models for different stages of combustion," *Biomass and Bioenergy* **23**: 47–54 (2002).

[158] Gupta, M., Yang, J., and Roy, C., "Specific heat and thermal conductivity of softwood bark and softwood char particles," *Fuel* **82**: 919–927 (2003).

[159] Janssens, M. and Douglas, B., "Wood and wood products," in *Handbook of Building Materials for Fire Protection*, Ed. Harper, C.A., pp. 7.1–7.58, McGraw–Hill, New York, 2004.

[160] Anderson, C.E., Ketchum, D.E, and Mountain, W.P., "Thermal conductivity of intumescent chars," *Journal of Fire Sciences* **6**: 390–410 (1988).

[161] Kantorovich, I.I., and Bar–Ziv, E., "Heat transfer within highly porous chars: a review," *Fuel* **78**: 279–299 (1999).

[162] Staggs, J.E.J., "Estimating the thermal conductivity of chars and porous residues using thermal resistor networks," *Fire Safety Journal* **37**: 107–119 (2002).

[163] Staggs, J.E.J., "Heat and mass transport in developing chars," *Polymer Degradation and Stability* **82**: 297–307 (2003).

[164] de Ris, J., "Fire radiation – a review," *Proceedings of the Combustion Institute* **17**: 1003–1016 (1979).

[165] Hallman, J.R., "Ignition characteristics of plastics and rubber," Ph.D. Dissertation, University of Oklahoma, 1971.

[166] Hallman, J.R., Welker, J.R., and Sliepcevich, C.M., "Polymer surface reflectance–absorptance characteristics," *Polymer Engineering and Science* **14**: 717–723 (1974).

[167] Hallman, J.R., Sliepcevich, C.M., and Walker, J.R., "Radiation absorption for polymers: The radiant panel and carbon arcs as radiant heat sources," *Journal of Fire & Flammability* **9**: 353–366 (1978).

[168] Wesson, H.R., Welker, J.R., and Sliepcevich, C.M., "The piloted ignition of wood by thermal radiation," *Combustion and Flame* **16**: 303–310 (1971).

[169] Janssens, M., "Piloted ignition of wood: a review," *Fire and Materials* **15**: 151–167 (1991).

[170] Modak, A.T. and Croce, P.A., "Plastic pool fires," *Combustion and Flame* **30**: 251–265 (1977).

[171] Börsch–Supan, W., Hunter, L.W., and Kuttler, J.R., "Endothermic gasification of a solid by thermal radiation absorbed in–depth," *International Journal of Heat and Mass Transfer* **27**: 1171–1182 (1984).

[172] Park, S.H. and Tien, C.L., "Radiation induced ignition of solid fuels," *International Journal of Heat and Mass Transfer* **33**: 1511–1520 (1990).

[173] Sohn, Y., Baek, S.W., and Kashiwagi, T., "Transient modeling of thermal degradation in non–charring solids," *Combustion Science and Technology* **145**: 83–108 (1999).

[174] Manohar, S.S., Kulkarni, A.K, and Thynell, S.T., "In–depth absorption of externally incident radiation in nongray media," *Journal of Heat Transfer* **117**: 146–151 (1995).

[175] Progelhof, R.C., Quintiere, J., and Throne, J.L., "Temperature distribution in semitransparent plastic sheets exposed to symmetric, unsymmetric, and pulsed radiant heating and surface cooling," *Journal of Applied Polymer Science* **17**: 1227–1252 (1973).

[176] Hirata, T., Kashiwagi, T., and Brown, J.E., "Thermal and oxidative degradation of poly(methylmethacrylate): weight loss," *Macromolecules* **18**: 1410–1418 (1985).

[177] Thomson, H.E. and Drysdale, D.D., "Flammability of plastics I: ignition temperatures," *Fire and Materials* **11**: 163–172 (1987).

[178] ASTM E 2058–03, "Standard test methods for measurement of synthetic polymer flammability using a Fire Propagation Apparatus (FPA)".

[179] Babrauskas, V. *Ignition Handbook*. Fire Science Publishers, Issaquah, WA, 2003.

[180] Kashiwagi T., Grulke, E., Hilding, J., Groth, K., Harris, R., Butler, K., Shields, J., Kharchenko, S., and Douglas, J., "Thermal and flammability properties of polypropylene/carbon nanotube nanocomposites," *Polymer* **45**: 4227–4239 (2004).

[181] Siegel, R. and Howell, J.R., *Thermal Radiation Heat Transfer*. Third Edition, Taylor & Francis, Washington, 1992.

[182] Kaviany, M., *Principles of Heat Transfer in Porous Media*. Second Edition. Springer–Verlag, New York, 1995.

[183] Strakhov, V.L., Garashchenko, A.N., Kuznetsov, G.V., Rudzinskii, "Mathematical simulation of thermophysical and thermochemical processes during combustion of intumescent fire–protective coatings," *Combustion, Explosion, and Shock Waves* **37**: 178–186 (2001).

[184] Puiroux, N., Prat, M., and Quintard, M., "Non–equilibrium theories for macroscale heat transfer: ablative composite layer systems," *International Journal of Thermal Sciences* **43**: 541–554 (2004).

[185] Duval, F., Fichot, F., and Quintard, M., "A local thermal non–equilibrium model for two–phase flows with phase–change in porous media," *International Journal of Heat and Mass Transfer* **47**: 613–639 (2004).

[186] Florio, J., Henderson, J.B., Test, F.L., and Hariharan, R., "A study of the effects of the assumption of local–thermal equilibrium on the overall thermally–induced response of a decomposing, glass–filled polymer composite," *International Journal of Heat and Mass Transfer* **34**: 135–147 (1991).

[187] Hastaoglu, M.A. and Berruti, F., "A gas–solid reaction model for flash wood pyrolysis," *Fuel* **68**: 1408–1415 (1989).

[188] Lee, C.K., Chaiken, R.F., and Singer, J.M., "Charring pyrolysis of wood in fires by laser simulation," *Proceedings of the Combustion Institute* **16**: 1459–1470 (1976).

[189] Zhang, T., Shields, T.J., and Silcock, G.W.H., "Effect of melting behavior on upward flame spread of thermoplastics," *Fire and Materials* **21**: 1–6 (1997).

[190] Butler, K.M., Ohlemiller, T.J., and Linteris, G.T., "A progress report on numerical modeling of experimental polymer melt flow behavior," *Interflam 2004*, pp. 937–948, 2004.

[191] Yang, J.C., Hamins, A., and Donnelly, M.K., "Combustion of a polymer (PMMA) sphere in microgravity," National Institute of Standards and Technology NISTIR 6331, 1999.

[192] Zhou, Y. and Fernandez–Pello, A.C., "An enthalpy–temperature hybrid method for solving phase–change problems and its application to polymer pyrolysis and ignition," *Combustion Theory and Modeling* **4**: 477–493 (2000).

[193] Bird, R.B., Stewart, W.E., and Lightfoot, E.N., *Transport Phenomena*, John Wiley & Sons, New York, 1960.

[194] Patankar, S.V., *Numerical Heat Transfer and Fluid Flow*, Hemisphere Publishing Corporation, New York, 1980.

[195] Mills, A.F., *Mass Transfer*, Prentice Hall, Upper Saddle River, NJ, 2001, pg. 161.

[196] Lautenberger, C., Rein, G., and Fernandez–Pello, C., "The application of a genetic algorithm to estimate material properties for fire modeling from bench–scale fire test data," *Fire Safety Journal* **41**: 204–214 (2006).

[197] Quintiere, J.G., "Simplified theory for generalizing results from a radiant panel rate of flame spread apparatus," *Fire and Materials* **5**: 52–60 (1981).

[198] Mowrer, F.W, "An analysis of effective thermal properties of thermally thick materials," *Fire Safety Journal* **40**: 395–410 (2005).

[199] Park, T.Y. and Froment, G.F., "A hybrid genetic algorithm for the estimation of parameters in detailed kinetic models," *Computers & Chemical Engineering* **22**: S103–S110 (1998).

[200] Elliott, L., Ingham, D.B., Kyne, A.G., Mera, N.S., Pourkashanian M., and Wilson, C.W., "Genetic algorithms for optimisation of chemical kinetics reaction mechanisms," *Progress in Energy and Combustion Science* **30**: 297–328 (2004).

[201] Goldberg, D., *Genetic Algorithms: In Search, Optimization & Machine Learning*. Addison–Wesley Publishing Company, Inc., Menlo Park, 1989.

[202] Michalewicz, Z., *Genetic Algorithms + Data Structures = Evolution Programs*. Springer–Verlag, New York, 1992.

[203] Dumitrescu D., Lazzerini B., Jain, L.C., and Dumitrescu A., *Evolutionary Computation*. CRC Press, New York, 2000.

[204] Liu, N., Wang, B., and Fan, W., "Kinetic compensation effect in the thermal decomposition of biomass in air atmosphere," *Fire Safety Science – Proceedings of the Seventh International Symposium*, Ed. Evans, D.D., pp. 581–592, 2003.

[205] Esfahani, J.A., Ayani, M.B., and Shirin, M.B., "A transient two–dimensional model of thermal and oxidative degradation of PMMA," *Iranian Journal of Science & Technology, Transaction B, Engineering* **29 B2**: 207–218 (2005).

[206] Drysdale, D.D. and Thomson, H.E., "Flammability of plastics II: critical mass flux at the firepoint," *Fire Safety Journal* **14**: 179–188 (1989).

[207] Ohlemiller, T.J., Kashiwagi, T., and Werner, K., "Wood gasification at fire level heat fluxes," *Combustion and Flame* **69**: 155–170 (1987).

[208] Weng, W.G., Hasemi, Y., and Fan, W.C., "Predicting the pyrolysis of wood considering char oxidation under different ambient oxygen concentrations," *Combustion and Flame* **145**: 723–729 (2006).

[209] Atreya, A., "Ignition of fires," *Philosophical Transactions of the Royal Society A: Mathematical, Physical, and Engineering Sciences* **356**: 2787–2813 (1998).

[210] Boonme, N. and Quintiere, J.G., "Glowing ignition of wood: the onset of surface combustion," *Proceedings of the Combustion Institute* **30**: 2303–2310 (2005).

[211] Shen, D.K., Fang, M.X., Luo, Z.Y., and Cen, K.F., "Modeling pyrolysis of wet wood under external heat flux," *Fire Safety Journal* **42**: 210–217 (2007).

[212] Freeman, G. and Lefebvre, A.H., "Spontaneous ignition characteristics of gaseous hydrocarbon–air mixtures," *Combustion and Flame* **58**: 153–162 (1984).

[213] Bar–Ilan, A., Rein, G., Fernandez–Pello, A.C., Torero, J.L., and Urban, D.L., "Forced forward smoldering experiments in microgravity," *Experimental Thermal and Fluid Science* **28**: 743–751 (2004).

[214] Rein, G., Bar–Ilan, A., Fernandez–Pello, A.C., Ellzey, J.L., Torero, J.L., and Urban, D.L., "Modeling of one–dimensional smoldering of polyurethane in microgravity conditions," *Proceedings of the Combustion Institute* **30**: 2327–2334 (2005).

[215] Lattimer, B.Y. and Ouelette, L., "Properties of composite materials for thermal analysis involving fires," *Composites: Part A* **37**: 1068–1081 (2006).

APPENDIX A. DERIVATION OF EXACT SOLUTION TO HEAT CONDUCTION EQUATION FOR FINITE–THICKNESS SOLID WITH IN–DEPTH RADIATION ABSORPTION

Consider a constant–property solid of thickness L initially at temperature $F(z)$ that is exposed to thermal radiation of intensity $\dot{q}''_e$. The back face (at $z = L$) is perfectly insulated. Of the total radiation incident at $z = 0$, some may be reflected, some may be absorbed at the surface, and some may pass through the surface where it may be attenuated (absorbed) in–depth. The radiation absorption process in the solid is modeled by the Beer–Lambert law and is characterized by the absorption coefficient $\kappa\,(\mathrm{m}^{-1})$. Heat losses are solely by convection to the ambient at temperature T_∞. In this regard, the convection coefficient h must be viewed as a linearized total heat transfer coefficient that accounts for surface reradiation.

The problem may be stated as:

$$\frac{\partial^2 T(z,t)}{\partial z^2} + \frac{1}{k} g(z) = \frac{1}{\alpha} \frac{\partial T(z,t)}{\partial t} \quad \text{for } 0 \le z \le L \tag{A.1a}$$

$$\left. \frac{\partial T}{\partial z} \right|_{z=L} = 0 \tag{A.1b}$$

$$-k \left. \frac{\partial T}{\partial z} \right|_{z=0} = \dot{q}''_1 - h\left(T - T_\infty\right)\Big|_{z=0} \tag{A.1c}$$

$$T\big|_{t=0} = F(z) \tag{A.1d}$$

where:

$g(z) = \dot{q}''_2 \kappa \exp(-\kappa z)$ = volumetric heat generation rate due to in–depth radiation absorption

$\dot{q}''_1 = (1 - r)\gamma \dot{q}''_e$ = radiation heat flux absorbed at surface $z = 0$

$\dot{q}_2'' = (1-r)(1-\gamma)\dot{q}_e''$ = radiation heat flux passing through surface $z = 0$

r = surface reflectivity

γ = fraction of nonreflected radiation absorbed at surface

$\dot{q}_e''$ = radiation incident at $z = 0$

κ = in–depth radiation absorption coefficient, m^{-1}.

Before this problem can be solved by separation of variables (combined with Green's function to handle the heat generation term attributed to in–depth radiation absorption), the boundary condition at the irradiated surface (Equation A.1c) must be made homogeneous. This is accomplished by transforming $T(z)$ to $\theta(\zeta)$, where θ and ζ are defined as:

$$\zeta = L - z \quad \text{i.e. } z = L - \zeta \tag{A.2a}$$

$$\theta(\zeta,t) = T(\zeta,t) - T_\infty - \frac{\dot{q}_1''}{h} \quad \text{i.e. } T(\zeta,t) = \theta(\zeta,t) + T_\infty + \frac{\dot{q}_1''}{h} \tag{A.2b}$$

The mathematical problem statement then becomes:

$$\frac{\partial^2\theta(\zeta,t)}{\partial\zeta^2} + \frac{1}{k}g(\zeta) = \frac{1}{\alpha}\frac{\partial\theta(\zeta,t)}{\partial t} \quad \text{for } 0 \le \zeta \le L \tag{A.3a}$$

$$\left.\frac{\partial\theta}{\partial\zeta}\right|_{\zeta=0} = 0 \tag{A.3b}$$

$$\left.\frac{\partial\theta}{\partial\zeta}\right|_{\zeta=L} + \frac{h}{k}\theta\Big|_{\zeta=L} = 0 \tag{A.3c}$$

$$\theta|_{t=0} = f(\zeta) \tag{A.3d}$$

where $g(\zeta) = \dot{q}_2''\kappa\exp(-\kappa(L-\zeta))$

Both boundary conditions in Equation A.3 are now homogeneous, so the problem can be solved by separation of variables using a Green's function. Since Equation A.3a is nonhomogeneous, the auxiliary homogenous problem (without heat generation) is solved to determine the Green's function, which (in ζ coordinates) is found to be:

$$G(\zeta,t\,|\,\zeta',\tau)=\sum_{m=1}^{\infty}\frac{2\lambda_m\exp\left(-\alpha\lambda_m^2(t-\tau)\right)}{\lambda_m L+\frac{1}{2}\sin(2L\lambda_m)}\cos(\lambda_m\zeta)\cos(\lambda_m\zeta') \tag{A.4}$$

The solution can be found by evaluating the integrals in Equation A.5:

$$\theta(\zeta,t)=\int_{\zeta'=0}^{L}G(\zeta,t\,|\,\zeta',\tau)f(\zeta')\,\mathrm{d}\zeta'+\frac{\alpha}{k}\int_{\tau=0}^{t}\mathrm{d}\tau\int_{\zeta'=0}^{L}G(\zeta,t\,|\,\zeta',\tau)g(\zeta')\,\mathrm{d}\zeta' \tag{A.5}$$

For the special case of $T\big|_{t=0}=T_0$ (i.e., $f(\zeta')=\theta_0=T_0-T_\infty-\dot{q}_1''/h$) the final solution (in z coordinates) is:

$$\begin{aligned}T(z,t)=\;& T_\infty+\frac{\dot{q}_1''}{h}+2\left(T_0-T_\infty-\frac{\dot{q}_1''}{h}\right)\sum_{m=1}^{\infty}\frac{\sin(\lambda_m L)\exp\left(-\alpha\lambda_m^2 t\right)}{\lambda_m L+\frac{1}{2}\sin(2L\lambda_m)}\cos(\lambda_m(L-z))+\\ &\frac{2\dot{q}_2''\kappa^2}{k}\sum_{m=1}^{\infty}\frac{1}{\lambda_m\left(\kappa^2+\lambda_m^2\right)}\frac{\cos(\lambda_m L)+\frac{\lambda_m}{\kappa}\sin(\lambda_m L)-\exp(-\kappa L)}{\lambda_m L+\frac{1}{2}\sin(2L\lambda_m)}\times\\ &\cos(\lambda_m(L-z))\left(1-\exp\left(-\alpha\lambda_m^2 t\right)\right)\end{aligned} \tag{A.6a}$$

with eigenvalues given by the relation:

$$\cot(\lambda_m L)=\frac{k}{h}\lambda_m \tag{A.6b}$$

The Fortran program used to calculate the temperature profiles (and ignition time given a critical surface temperature at ignition) is listed below.

```
      PROGRAM EIGENVALUES

      USE VARS
      USE IO
      USE FUNCS

      IMPLICIT NONE

      INTEGER :: IX, IT

      WRITE(*,*) 'Reading input file and initializing.'
      CALL READ_NAMELIST

      QE     = QE * 1D3
      Q1     = (1. - R) * GAMMA        * QE
      Q2     = (1. - R) * (1. - GAMMA) * QE
      ALPHA  = K / (RHO * C)
      NX     = L / DX
      NT     = TSTOP / DT

      ALLOCATE(X(0:NX)) ; X = 0D0
      ALLOCATE(T(0:NT)) ; T = 0D0
      ALLOCATE(BETA(0:NBETA)); BETA(:) = 0D0
      ALLOCATE(QEAR(1:1000)); QEAR(:) = 0D0
      ALLOCATE(TIG(1:1000)); TIG(:) = 0D0
      ALLOCATE(TMP   (            0:NX,0:NT)); TMP   (:,:)     = 0D0
      ALLOCATE(SERIES(0:0    ,1:2,0:NX,0:NT)); SERIES(:,:,:,:) = 0D0

      DO IX = 0, NX
         X(IX) = REAL(IX) * L / REAL(NX)
      ENDDO

      DO IT = 0, NT
         T(IT) = REAL(IT) * DT
      ENDDO

C Find first NBETA eigenvalues
      WRITE(*,*) 'Finding eigenvalues.'
      CALL FIND_EIGENVALUES

C Write eigenvalues to disk
      CALL DUMP_EIGENVALUES

      WRITE(*,*) 'Calculating temperature profile from series.'
C Calculate temperature profile
      CALL CALC_PROFILE

C Write temperature profile to disk
      CALL DUMP_PROFILE

      IF (QESTOP .LE. QESTART) STOP

      WRITE(*,*) 'Calculating ignition time as a function of heat flux.'
C Calculate ignition time
      CALL CALC_TIG

C Write ignition time to disk
      CALL DUMP_TIG

      END PROGRAM EIGENVALUES
```

```
      MODULE VARS
      IMPLICIT NONE

C Variables to be read in from namelist group:
      DOUBLE PRECISION :: L       !Sample thickness (m)
      DOUBLE PRECISION :: K       !Thermal conductivity (W/m-K)
      DOUBLE PRECISION :: RHO     !Density (kg/m3)
      DOUBLE PRECISION :: C       !Specific heat J/kg-K
      DOUBLE PRECISION :: H       !Heat transfer coeff (W/m2-K)
      DOUBLE PRECISION :: TMP0    !Initial temperature (K)
      DOUBLE PRECISION :: TMPINF  !Ambient temperature (K)
      DOUBLE PRECISION :: KAPPA   !In-depth absorption coefficient (1/m)
      DOUBLE PRECISION :: DX      !x-spacing in solid to write solution to disk
      DOUBLE PRECISION :: DT      !time step in solid to write solution to disk
      DOUBLE PRECISION :: TSTOP   !End time
      DOUBLE PRECISION :: R       !Reflectivity
      DOUBLE PRECISION :: GAMMA   !
      DOUBLE PRECISION :: QE      !Heat flux (kW/m2)
      DOUBLE PRECISION :: DBETA   !Find eigenvlues to this accuracy

      INTEGER          :: NBETA
      INTEGER          :: NX
      INTEGER          :: NT

      DOUBLE PRECISION :: TMPIG   !Ignition temperature (K)
      DOUBLE PRECISION :: QESTART !Starting value of heat flux (kW/m2)
      DOUBLE PRECISION :: QESTOP  !Ending value of heat flux (kW/m2)
      DOUBLE PRECISION :: DQE     !Heat flux "step" (kW/m2)

C Variables not read in but calculated or set elsewhere
      DOUBLE PRECISION :: ALPHA
      DOUBLE PRECISION :: Q1
      DOUBLE PRECISION :: Q2
      INTEGER :: NQE

C Parameters
      DOUBLE PRECISION, PARAMETER :: PI = 3.14159265358979323846264338
      INTEGER, PARAMETER :: LU5 = 5, LU101 = 101
      CHARACTER(60) :: FN

C Globals
      DOUBLE PRECISION, ALLOCATABLE, DIMENSION(:) :: X,T,BETA,QEAR,TIG
      DOUBLE PRECISION, ALLOCATABLE, DIMENSION (:,:)     :: TMP
      DOUBLE PRECISION, ALLOCATABLE, DIMENSION (:,:,:,:) :: SERIES

      END MODULE VARS
```

```
      MODULE IO
      USE VARS

      IMPLICIT NONE

      CONTAINS

C *****************************************************************************
      SUBROUTINE READ_NAMELIST
C *****************************************************************************

      NAMELIST /IGN/ L, K, RHO, C, H, TMP0, TMPINF, KAPPA, DX, DT,
     .               TSTOP, QE, DBETA, NBETA, R, GAMMA, QESTART,
     .               QESTOP, DQE, TMPIG

D     OPEN(LU5,FILE='input.data',FORM='FORMATTED',STATUS='OLD')
      READ(LU5,NML=IGN)
D     CLOSE(LU5)

      END SUBROUTINE READ_NAMELIST
C *****************************************************************************

C *****************************************************************************
      SUBROUTINE DUMP_EIGENVALUES
C *****************************************************************************

      INTEGER :: M

      FN = 'eigenvalues.csv'
     OPEN(UNIT=LU101,FILE=FN,FORM='FORMATTED',STATUS='REPLACE')
      WRITE(LU101,*) 'm,lambda_m'
      DO M = 1, NBETA
         WRITE(LU101,97) M, BETA(M)
      ENDDO
      CLOSE(LU101)

  97  FORMAT(I8,',', 4(F16.9,','))

      END SUBROUTINE DUMP_EIGENVALUES
C *****************************************************************************

C *****************************************************************************
      SUBROUTINE DUMP_PROFILE
C *****************************************************************************

      INTEGER :: IX, IT

      FN = 'Tprofile.csv'
     OPEN(UNIT=LU101,FILE=FN,FORM='FORMATTED',STATUS='REPLACE')
      WRITE(LU101,98) ','
      WRITE(LU101,99) (X(IX), IX = 0, NX)
      WRITE(LU101,*)

      DO IT = 0, NT
         WRITE(LU101,100) T(IT),(TMP(IX,IT),IX=0,NX)
         WRITE(LU101,*)
      ENDDO
      CLOSE(LU101)

  98  FORMAT(A$)
  99  FORMAT(F16.9,',',$)
 100   FORMAT(F16.9,',',$)

      END SUBROUTINE DUMP_PROFILE
C *****************************************************************************
```

```
C ********************************************************************************
      SUBROUTINE DUMP_TIG
C ********************************************************************************
      USE VARS

      INTEGER :: IQE

      FN = 'tig.csv'
     OPEN(UNIT=LU101,FILE=FN,FORM='FORMATTED',STATUS='REPLACE')
      WRITE(LU101,*) 'qe,tig,1/sqrt(tig)'

      DO IQE = 1, NQE
         WRITE(LU101,99) QEAR(IQE), TIG(IQE), 1D0/SQRT(TIG(IQE))
      ENDDO
      CLOSE(LU101)

 99   FORMAT(3(F16.9,','))

      END SUBROUTINE DUMP_TIG
C ********************************************************************************

      END MODULE IO

      MODULE FUNCS

      IMPLICIT NONE

      CONTAINS

C ********************************************************************************
      DOUBLE PRECISION FUNCTION COT(X)
C ********************************************************************************
      IMPLICIT NONE
      DOUBLE PRECISION, INTENT(IN) :: X
      COT = TAN(X)**-1D0
      END FUNCTION COT
C ********************************************************************************
```

```
C ******************************************************************************
      SUBROUTINE FIND_EIGENVALUES
C ******************************************************************************

      USE VARS

      DOUBLE PRECISION :: DIFF,RHS,LHS,BSTART,BSTOP,B
      INTEGER :: DIFFSIGN, DIFFSIGN_OLD, M
      LOGICAL :: FOUND

      DIFFSIGN_OLD = -1
      M = 0

      DO WHILE (M .LT. NBETA)
         BSTART = REAL(M) * PI/L
         BSTOP  = BSTART + PI/L
         B      = BSTART

         FOUND = .FALSE.
         DIFFSIGN_OLD = -1

         DO WHILE (FOUND .EQ. .FALSE. .AND. B .LE. BSTOP)
            B = B + DBETA
            LHS  = COT(B*L)
            RHS  = B/(H/K)
            DIFF = RHS - LHS

            IF (DIFF .LE. 0D0) DIFFSIGN = -1
            IF (DIFF .GT. 0D0) DIFFSIGN =  1

            IF (DIFFSIGN .NE. DIFFSIGN_OLD) THEN
                     M = M + 1
                     BETA(M) = B
               WRITE(*,199) 'Eigenvalue ', M, ': ', BETA(M)
               FOUND = .TRUE.
            ENDIF
         ENDDO

         DIFFSIGN_OLD = DIFFSIGN

         IF (B .GT. BSTOP) THEN
            WRITE(*,*) 'No root found.'
         ENDIF

      ENDDO

 199  FORMAT(A, I5, A, F10.2)

      END SUBROUTINE FIND_EIGENVALUES
C ******************************************************************************
```

```
C ***********************************************************************
      SUBROUTINE CALC_PROFILE
C ***********************************************************************

      USE VARS

      INTEGER :: M,IT,IX
      DOUBLE PRECISION :: MULT1, MULT2, DENOM1, DENOM2, NUMER1, NUMER2,
     .                    EXPTRM, FRAC1, FRAC2

      DO M = 1, NBETA
         DENOM1 = BETA(M) * L + 0.5D0 * SIN(2D0*L*BETA(M))
         DENOM2 = DENOM1 * BETA(M) * (KAPPA**2D0 + BETA(M)**2D0)
         NUMER1 = SIN(BETA(M) * L)
         NUMER2 = COS(BETA(M) * L) + (BETA(M)/KAPPA)*SIN(BETA(M)*L) -
     .            EXP(-KAPPA*L)

         DO IT = 0, NT
            EXPTRM = EXP(-ALPHA * T(IT) * BETA(M)**2)
            FRAC1 = NUMER1 * EXPTRM         / DENOM1
            FRAC2 = NUMER2 * (1D0 - EXPTRM) / DENOM2
            DO IX = 0, NX
               SERIES(0,1,IX,IT) = SERIES(0,1,IX,IT) +
     .                             FRAC1 * COS(BETA(M)*(L - X(IX)))
               SERIES(0,2,IX,IT) = SERIES(0,2,IX,IT) +
     .                             FRAC2 * COS(BETA(M)*(L - X(IX)))
            ENDDO
         ENDDO
      ENDDO

      MULT1 = 2D0*(TMP0 - TMPINF - Q1/H)
      MULT2 = 2D0 * Q2 * KAPPA * KAPPA / K
      TMP(:,:) = TMPINF + Q1/H + MULT1 * SERIES(0,1,:,:) +
     .                           MULT2 * SERIES(0,2,:,:)

      END SUBROUTINE CALC_PROFILE
C ***********************************************************************
```

```
C ********************************************************************************
      SUBROUTINE CALC_TIG
C ********************************************************************************
      USE VARS

      DOUBLE PRECISION :: MULT1, MULT2, DIFF
      INTEGER :: IQE, IT

      DQE     = DQE     * 1D3
      QESTART = QESTART * 1D3
      QESTOP  = QESTOP  * 1D3
      QE      = QESTART

      TIG(:) = -9D9
      IQE = 0
      DO WHILE (QE .LE. QESTOP)
         IQE = IQE + 1
         QEAR(IQE) = QE * 1D-3
         Q1     = (1. - R) * GAMMA        * QE
         Q2     = (1. - R) * (1. - GAMMA) * QE
         MULT1 = 2D0*(TMP0 - TMPINF - Q1/H)
         MULT2 = 2D0 * Q2 * KAPPA * KAPPA / K

         TMP(0,:) = TMPINF + Q1/H + MULT1 * SERIES(0,1,0,:) +
     .                              MULT2 * SERIES(0,2,0,:)
         DO IT = 0, NT
            DIFF = TMP(0,IT) - TMPIG
            IF (DIFF .GE. 0D0 .AND. TIG(IQE) .LT. 0D0) TIG(IQE) = T(IT)
         ENDDO

         QE = QE + DQE

      ENDDO

      NQE = IQE

      END SUBROUTINE CALC_TIG
C ********************************************************************************

      END MODULE FUNCS
```

APPENDIX B. USER'S GUIDE

The source code and software developed as part of this dissertation are freely available. Development of the code will continue through 2010 as part of NSF Award 0730556 "Tackling CFD Modeling of Flame Spread on Practical Solid Combustibles" (PI Prof. Carlos Fernandez–Pello). At the conclusion of that grant, the source code and executable files will be made available through a web hosting site such as Source Forge or Google Code. Until then, the source code and executable files will be distributed to by email (please send an email inquiry to clauten@me.berkeley.edu or chris.lautenberger@gmail.com).

For the time being, the software is distributed in a compressed rar archive named tdma_y.yyy.rar where y.yyy is the version number of the code. Within the rar archive are three root directories: src, linux, and vc8. The src directory contains the Fortran source files from which the code is compiled. A sample MS Excel front end file (more on this later) is located in the src folder, along with a file called "version_history.txt" that describes historical modifications to the code. The linux directory contains a simple build script (make.sh) and Makefiles for compiling the code under Linux environments. The Makefiles are set up to use Portland Group's Fortran 90 compiler but it should be possible to use almost any Fortran compiler. Finally, the vc8 (Visual C 8) directory contains Visual Studio .net 2005 Solution files and a directory structure that allows one to use the Microsoft Integrated Development Environment for modifying and debugging the code. If it is desired to use this development environment, then Visual Studio .net 2005 and Intel Visual Fortran 9.1 must be installed. The user should unrar the archive to

c:\tdma so that the file tdma.sln exists in c:\tdma\vc8\. Then, the solution file can be opened by double–clicking on tdma.sln from the Windows Explorer.

The Linux build script and Visual Studio .net Solution file are set up to compile two separate executable files. The file tdma_standalone_y.yyy (with the extension .exe if running under Windows is the standalone model. This binary file is used for running a simulation or sequence of simulations for a known set of model input parameters, initial conditions, and boundary conditions. The file tdma_ga_y.yyy (again with the .exe extension if running under Windows) is the executable file for the genetic algorithm optimization method that is used to extract a set of model input parameters from available experimental data. Since the genetic algorithm uses message passing libraries for parallelization, an MPI implementation (such as MPICH) must be correctly installed in order to compile the genetic algorithm code.

As eluded to above, a simple user interface (or "front end") is implemented though a Microsoft Excel spreadsheet. Visual Basic macros are used to automatically generate the ASCII input files that are read in by the code. This allows the user to specify material properties, reaction kinetics, etc. in spreadsheet form without being concerned with the syntax of the actual input files read in by the code. The input parameters for the standalone model as well as the genetic algorithm optimization code are all specified from the same front end. If the user prefers, it is possible to circumvent the spreadsheet–based front end and work directly with the text–based input files using any standard text editor.

From anywhere within the Excel–based front end, the input files required to run the model can be generated via the keystroke ctrl–g (for "go"). This executes a Visual

Basic macro that writes several input files to the current directory. The names of the input files are hard coded, so any input files that exist in the working directory will be over–written. Although the input files are usually created in a Windows environment, they are compatible with Linux file systems (there are no issues with dos/Unix carriage return/line feed conventions) so calculations can also be performed under *nix systems. In fact, all calculations reported in this dissertation were conducted on Linux clusters. Once the ASCII input files have been generated from the front end, the standalone pyrolysis model can be run by typing "tdma_standalone_y.yyy" (where y.yyy is a version number) from a dos prompt or Linux shell, or by double–clicking on the executable file from within a Windows environment. Similarly, the genetic algorithm optimization code can be run by typing tdma_ga_y.yyy or double–clicking on the executable file.

The standalone executable writes the main results to files named summary_0001.csv, summary_0002.csv, etc. These files contain surface and back face temperatures, mass loss rate, species fluxes, etc. For the genetic algorithm optimization executable, a comparison of the optimal model calculations and experimental data are written to a file called results_best.csv. Diagnostic information such as the fitness evolution is written to a file called summary.csv.

This is a research code. It is not user friendly, it takes a while to learn how to use, and very little error checking has been implemented. Thus, the code won't give a warning message if non–physical input parameters are specified. If you see strange behavior during a simulation, or if the code gives a run–time error such as a segmentation fault, this is often caused by nonphysical input parameters (negative thermal conductivities, inconsistent specification of species yields that create or destroy mass, etc.). It is the

user's responsibility to ensure that all input parameters are physically realistic and correctly specified through the front end. That being said, there are undoubtedly some bugs in the code. If you think you've found one, don't hesitate to send an email to clauten@me.berkeley.edu or chris.lautenberger@gmail.com.

In Section B.1, the front end worksheets associated with running the standalone model are described. The additional worksheets needed to run the genetic algorithm optimization routines are described in Section B.2.

B.1 Standalone model

The Excel–based front end is divided into several worksheets, i.e. the worksheet "sprops" contains info about solid properties, "rxns" is condensed phase reactions, and so on. Table B.1 below lists the worksheets that are associated with the standalone model and describes the types of parameters that are specified in each worksheet. The input parameters available through each of these worksheets are discussed individually below. A hypothetical charring material with completely fabricated properties is used to illustrate the input parameter specification process.

Table B.1. Front end worksheets associated with standalone pyrolysis model.

Worksheet name	Section	Description
sprops	B.1.1	Thermophysical properties of each solid (condensed phase) species. Includes k, ρ, c, ε, κ, T_m, γ, K, ρ_{s0}. Convergence criteria and miscellaneous options
rxns	B.1.2	Condensed phase (heterogeneous) reactions. Z, E, ΔH_{sol}, ΔH_{vol}, χ, n, n_{O2}
gprops	B.1.3	Gas properties (c_{pg}, Lennard–Jones parameters, initial conditions, etc.)
gyields	B.1.4	Heterogeneous reactions gaseous yields matrix ($y_{s,j,k}$)
layers	B.1.5	Layered composition (layer thickness, contact resistance, and initial condensed phase species mass fractions)
qe	B.1.6	Heat flux and environmental variables (ambient gaseous mass fractions, heat transfer coefficient, etc.)
hgrxns	B.1.7	Homogeneous gaseous reactions parameters–includes p, q, b, Z, E, ΔH
hgyields	B.1.8	Homogeneous reactions gaseous yields matrix ($y_{g,j,\ell}$)
general	B.1.9	Miscellaneous parameters–stuff that doesn't fit anywhere else
BCpatch	B.1.10	Boundary conditions patches–used when qe worksheet does not provide enough flexibility for boundary conditions

B.1.1 Solid properties – sprops worksheet

A screen–shot of the sprops (solid properties) worksheet is shown in Figure B.1. The first data entry section is from cells A1 to A10. Column A is user–specifiable values, column B is the corresponding variable name in the Fortran code, and column C gives a description of that particular variable. This general format is typical of some of the other worksheets that are part of the front end.

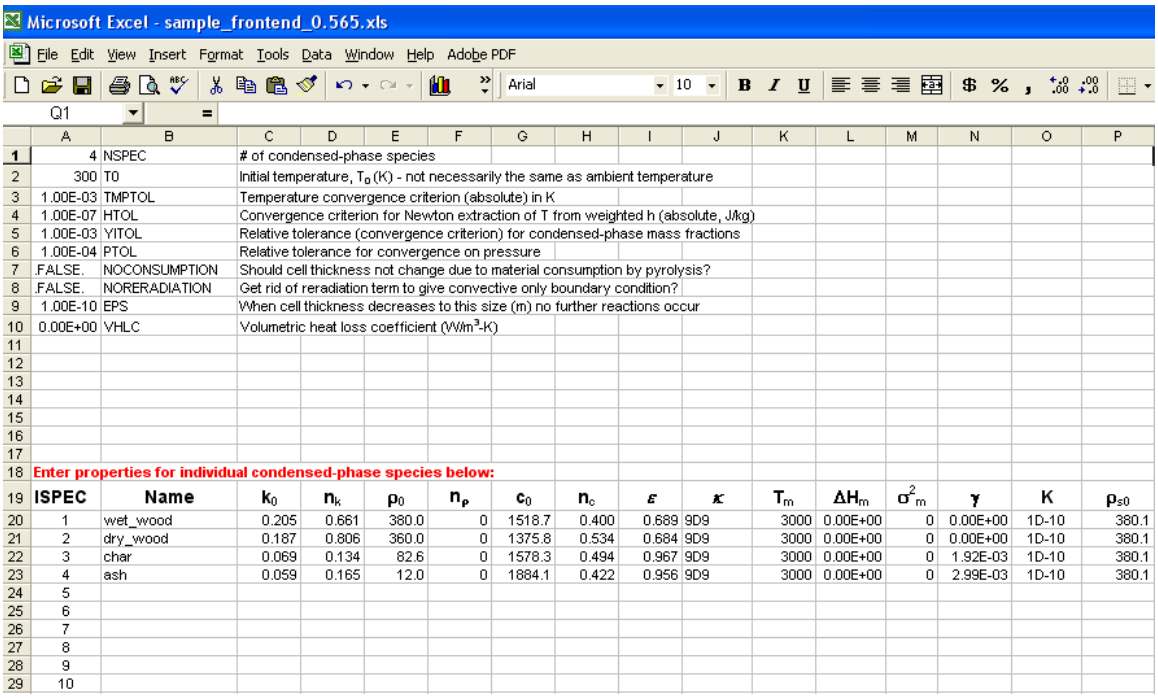

Microsoft Excel - sample_frontend_0.565.xls

File Edit View Insert Format Tools Data Window Help Adobe PDF

Arial 10

Q1 =

	A	B	C	D	E	F	G	H	I	J	K	L	M	N	O	P
1	4	NSPEC	# of condensed-phase species													
2	300	T0	Initial temperature, T_0 (K) - not necessarily the same as ambient temperature													
3	1.00E-03	TMPTOL	Temperature convergence criterion (absolute) in K													
4	1.00E-07	HTOL	Convergence criterion for Newton extraction of T from weighted h (absolute, J/kg)													
5	1.00E-03	YITOL	Relative tolerance (convergence criterion) for condensed-phase mass fractions													
6	1.00E-04	PTOL	Relative tolerance for convergence on pressure													
7	.FALSE.	NOCONSUMPTION	Should cell thickness not change due to material consumption by pyrolysis?													
8	.FALSE.	NORERADIATION	Get rid of reradiation term to give convective only boundary condition?													
9	1.00E-10	EPS	When cell thickness decreases to this size (m) no further reactions occur													
10	0.00E+00	VHLC	Volumetric heat loss coefficient (W/m^3-K)													
11																
12																
13																
14																
15																
16																
17																
18	Enter properties for individual condensed-phase species below:															
19	ISPEC	Name	k_0	n_k	ρ_0	n_ρ	c_0	n_c	ε	κ	T_m	ΔH_m	σ^2_m	γ	K	ρ_{s0}
20	1	wet_wood	0.205	0.661	380.0	0	1518.7	0.400	0.689	9D9	3000	0.00E+00	0	0.00E+00	1D-10	380.1
21	2	dry_wood	0.187	0.806	360.0	0	1375.8	0.534	0.684	9D9	3000	0.00E+00	0	0.00E+00	1D-10	380.1
22	3	char	0.069	0.134	82.6	0	1578.3	0.494	0.967	9D9	3000	0.00E+00	0	1.92E-03	1D-10	380.1
23	4	ash	0.059	0.165	12.0	0	1884.1	0.422	0.956	9D9	3000	0.00E+00	0	2.99E-03	1D-10	380.1
24	5															
25	6															
26	7															
27	8															
28	9															
29	10															

Figure B.1. Screen shot of sprops worksheet.

The number of solid species is the variable NSPEC, and the initial temperature of the material is T0 (the initial temperature is assumed uniform throughout). After NSPEC and T0 are several variables related to solution convergence. The variable TMPTOL is the absolute convergence criterion for the condensed phase energy equation, i.e. the solid phase energy equation is converged when the temperature changes by no more than TMPTOL (units of K) in any cell between iterations. Similarly, PTOL (units of Pa) is the absolute convergence criterion for the pressure evolution equation, YITOL is the relative convergence criterion for the condensed phase species conservation equations. HTOL is slightly different—it is the convergence criterion for the Newton iteration process whereby the temperature is extracted from the weighted enthalpy. That is, the local temperature in a cell is "found" when the difference between the enthalpy calculated from the energy conservation equation and the weighted enthalpy calculated from the

found temperature match within HTOL. It may be helpful to review the discussion of Newton iteration in Section 3.3.5.

By setting NOCONSUMPTION=.TRUE. (cell A7), the consumption of condensed phase reactants is prevented. This was sometimes used to eliminate surface regression in 2D flame spread simulations (in FDS) over thermoplastics when it was desirable to include 2D heat conduction. Related to surface regression, EPS is the cell size (in m) below which reactant consumption is no longer calculated. When a cell becomes very small due to reactant consumption, the absolute amount of gaseous fuel production in that cell also becomes very small. Preventing further reactions can eliminate convergence problems that may be encountered as grid cells become very small. A value of 10^{-10} m (0.1 nm, smaller than the hard–sphere diameter of a single atom) was found to work well for many simulations. The parameter NORERADIATION is used to eliminate surface reradiation. It is useful to set NORERADIATION=.TRUE. when comparing the model calculations to an analytical solution that includes Newtonian (convective) cooling but no surface reradiation.

The next input section, extending downward from row 19, is where the actual thermophysical properties of each condensed phase species are specified. Be sure that the number of condensed phase species for which you specify properties is the same as the value of NSPEC in cell A1! In column B, each species should be assigned a unique name (character string), e.g. wood, char, ash, glass_fibers, etc. Do not use spaces in the names (underscores can be used instead). Column C is k_0, the thermal conductivity of each species (in units of W/m–K) at the reference temperature T_r (which is specified in the "general" worksheet). Column D is the thermal conductivity exponent n_k. As discussed in

Section 3.1.1, the presumed temperature dependency is $k(T) = k_0(T/T_r)^{n_k}$ where T_r is the reference temperature. The functional form of the temperature dependency for the density and specific heat capacity is the same as for the thermal conductivity. Thus, columns E and F are ρ_0 and n_ρ, the analogous quantities for the density (kg/m^3), and columns G and H are c_0 and n_c, the analogous quantities for the specific heat capacity (J/kg–K).

The emissivity of each species is specified in column I. The effective surface emissivity used in the code is calculated as a volume–weighted average using the species volume fractions in the boundary cell. Thus, the code can account for the change in the emissive/absorptive characteristics that some materials exhibit as they pyrolyze (for example, the darkening of wood). Column J contains another radiative property: the absorption coefficient κ (m^{-1}). As with emissivity, the effective absorption coefficient used in the calculations is also a volume–weighted quantity. If the value of κ in the first cell is greater than 10^6 m^{-1}, then the code considers only surface absorption. Otherwise, the code calculates in–depth radiation absorption per Equation 3.28.

Melting parameters are specified in columns K, L, and M. T_m is the melting temperature (K), ΔH_m is the latent heat of melting (J/kg), and σ_m^2 (units of K^2) is the parameter in Equation 3.5c that controls the width of the Gaussian peak over which the latent heat of melting is distributed as an apparent specific heat capacity. Melting is handled in an extremely simple way through an increase in the specific heat capacity in the vicinity of the melting temperature. Other thermophysical properties (thermal conductivity, density) do not exhibit a discontinuity at the melting temperature, and a species above its melting temperature does not flow.

In column N, the parameter γ controls the radiative conductivity (attributed to radiative heat transfer across pores) and has units of length (See Equation 3.4). Essentially, for nonzero values of γ, a species is given a component of its effective thermal conductivity that varies proportional to T^3.

The final two properties (columns O and P) are permeability (K, units of m^2) and the density of a nonporous block of the species at temperature T_r (ρ_{s0}, units of kg/m^3). The latter is used only to calculate porosity ($\psi_i = 1 - \rho_i / \rho_{s0,i}$) which only plays a role in the gas phase species and energy conservation equations. Permeability only affects the gas phase momentum conservation equation through Darcy's law. The effective permeability and porosity used in the conservation equations are calculated as volume–weighted quantities.

B.1.2 Condensed phase reactions–rxns worksheet

The rxns worksheet is used to enter the parameters that control the condensed phase reactions (homogeneous gas phase reactions are entered through the worksheet hgrxns). A screen shot of the rxns worksheet is given in Figure B.2:

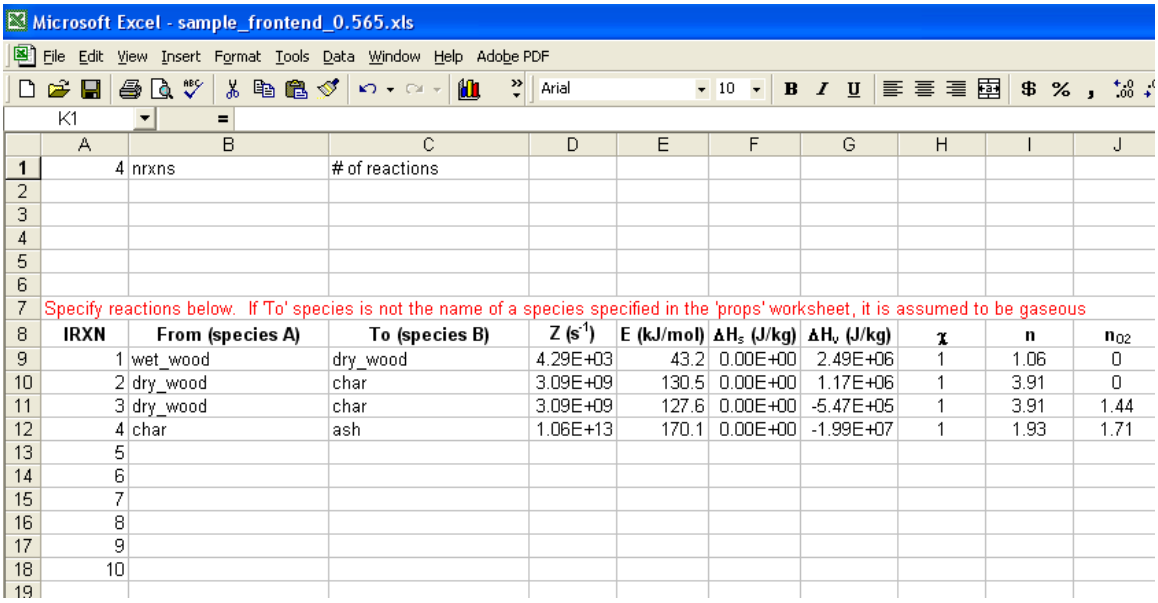

Microsoft Excel - sample_frontend_0.565.xls

File Edit View Insert Format Tools Data Window Help Adobe PDF

K1

	A	B	C	D	E	F	G	H	I	J
1	4	nrxns	# of reactions							
2										
3										
4										
5										
6										
7	Specify reactions below. If 'To' species is not the name of a species specified in the 'props' worksheet, it is assumed to be gaseous									
8	IRXN	From (species A)	To (species B)	Z (s^{-1})	E (kJ/mol)	ΔH_s (J/kg)	ΔH_v (J/kg)	χ	n	n_{O2}
9	1	wet_wood	dry_wood	4.29E+03	43.2	0.00E+00	2.49E+06	1	1.06	0
10	2	dry_wood	char	3.09E+09	130.5	0.00E+00	1.17E+06	1	3.91	0
11	3	dry_wood	char	3.09E+09	127.6	0.00E+00	-5.47E+05	1	3.91	1.44
12	4	char	ash	1.06E+13	170.1	0.00E+00	-1.99E+07	1	1.93	1.71
13	5									
14	6									
15	7									
16	8									
17	9									
18	10									
19										

Figure B.2. Screen shot of rxns worksheet.

The number of reactions to be considered should be entered in cell A1, and the parameters for each individual reaction are entered below row 8. Column B is name of the condensed phase reactant (the species that will be consumed) and column C is the name of the condensed phase product (the species that will be produced). Using the nomenclature from the main body of this dissertation, for reaction *k* the "From" species is A_k, and the "To" species is B_k. These names must correspond exactly to the name of a condensed phase species listed in the sprops worksheet, and the names are case–sensitive. If a "From" species specified in the rxns worksheet does not have an analogous definition in the sprops worksheet, the code will give an error message and shut down. However, if a "To" species is specified without an analogous definition in the sprops worksheet, the code does not treat this as an error. Instead, it will assume that reaction produces only gases, i.e. the reaction leaves behind no condensed phase residue. Be sure you do not inadvertently spell a species incorrectly in the "To" column and end up with a noncharring reaction when you intended to specify a charring reaction!

Column D is the pre–exponential factor (Z) for the pyrolysis reaction (s^{-1}), and column E is the activation energy (E) in units of kJ/mol. Column F is ΔH_{sol}, the latent enthalpy difference between the condensed phase product species and the condensed phase reactant species in units of J/kg (See Equation 3.64). A positive value gives an endothermic reaction and a negative value gives an exothermic reaction. Column G is ΔH_{vol} (sometimes called heat of volatilization, heat of vaporization, or heat of pyrolysis) in units of J/kg. It is the amount of heat required to volatilize unit mass of the condensed phase reactant at whatever temperature this volatilization occurs. A positive value of ΔH_{vol} implies an endothermic reaction, and a negative value implies an exothermic reaction. These quantities are specified on a J/kg of reactant produced basis. That is, ΔH_{vol} has units of Joules per kilogram of gases liberated from the condensed phase, and ΔH_{sol} has units of Joules per kilogram of condensed phase species B formed from condensed phase species A. A heat of reaction with units of Joules per kilogram of species A destroyed can be recovered by setting $\Delta H_{sol} = \Delta H_{vol}$. See the discussion after Equation 3.64 if this is confusing.

Intumescent reactions can be specified by setting the value of χ in column H to a value between 0 and 1. As discussed in Section 3.2.1, χ is the fraction of the density difference between the condensed phase reactant and the condensed phase product species that is realized as gases. A value of $\chi = 1$ means that all of the density difference caused by the formation of a lower density solid from a higher density solid will result in generation of gaseous species, and a value of $\chi = 0$ means that no gases will be generated and swelling will occur to conserve mass. Values of χ between 0 and 1 cause intumescence (swelling) to occur simultaneously with the release of gases.

The remaining two parameters are reaction orders. Column I is the reaction order (n) in the remaining solid, and column J is the reaction order in the local oxygen mass fraction (n_{O2}, see Equation 3.58). The user should set $n_{O2} = 0$ for reactions that are not affected by the local oxygen concentration.

B.1.3 Gas properties – gprops worksheet

All properties related to the gas phase are specified in the gprops worksheet, shown below in Figure B.3.

Microsoft Excel - sample_frontend_0.565.xls

File Edit View Insert Format Tools Data Window Help Adobe PDF

J1 =

	A	B	C	D	E	F	G	H	I
1	7	NGSPEC	# of gaseous species						
2	1	IBG	Species index of background gaseous species (for calculating diffusivity)						
3	4	IO2	Species index of oxygen						
4	1.00E-04	YITOL	Tolerance (relative) for convergence on gaseous species mass fractions						
5	0.10	HGTOL	Tolerance (absolute) for convergence on gaseous enthalpy (J/kg)						
6	5.00E+05	HCV	Volumetric heat transfer coefficient for solid-gas heat transfer, h_{cv} (W/m^3-K)						
7	1000	CPG	Specific heat capacity of gas (J/kg-K)						
8									
9									
10									
11									
12									
13									
14									
15	**IGSPEC**	**Name**	**Y_{j0}**	**M (g/mol)**	**σ (Å)**	**ε/k (K)**	**B (J/kg)**	**T_{onset}**	**T_{span}**
16	1	pyrolysate	0.000	44	5.061	254	0.00E+00	653	50
17	2	nitrogen	1.000	28	3.681	91.5	0.00E+00	653	50
18	3	water_vapor	0.000	18	3.737	32	0.00E+00	653	50
19	4	oxygen	0.000	32	3.467	107	0.00E+00	653	50
20	5	oxidative_pyrolysate	0.000	44	5.061	254	0.00E+00	653	50
21	6	char_oxid_products	0.000	44	3.941	195	0.00E+00	653	50
22	7	pyro_oxid_products	0.000	44	3.941	195	0.00E+00	653	50
23	8								
24	9								
25	10								

Figure B.3. Screen shot of gprops (gas properties) worksheet.

The gprops worksheet is set up similarly to the sprops worksheet. The number of gaseous species (NGSPEC) is specified in cell A1. This number should be set to a minimum of 1, even if the gaseous species conservation equation is not being explicitly solved. IBG (cell A2) is the gaseous species index of the background species, and IO2

(cell A3) is the gaseous species index corresponding to oxygen. IBG and IO2 are needed because the diffusion coefficient is calculated from Chapman–Enskog theory as the diffusivity of oxygen into the background species (recall that all species are assigned the same diffusivity). IO2 is also used by the code for heterogeneous reactions that are affected by the local oxygen concentration, i.e. reactions for which $n_{O_2,k} \neq 0$, see Equation 3.58. The variable YITOL (cell A4) is the (relative) convergence criterion for the gaseous species conservation equations. Cell A5 is HGTOL, the convergence criterion for the gas phase energy equation (in units of J/kg), i.e. the gas phase energy equation is converged when the solution in all cells changes by no more than HGTOL between iterations. In cell A6, HCV is the volumetric heat transfer coefficient (h_{cv} in Equation 3.26) that controls the rate of heat transfer between the gaseous and the condensed phases. For simplicity, it is assumed that HCV is invariant and does not depend on pore structure or Reynolds number. Finally, the specific heat of the gas phase (in units of J/kg–K) is specified in cell A7. It is assumed that all gases have the same specific heat capacity, independent of temperature.

Properties of individual gases are specified starting at row 16. The index of each gaseous species (IGSPEC) is specified in column A. Species should be numbered sequentially starting with 1. The next column is a character string that assigns a unique name to each species (do not use spaces). Column C is the initial mass fraction of each species, which does not vary spatially (i.e., from cell to cell). Column D is the molecular weight of each species in units of g/mol. Columns E and F are the Lennard Jones model parameters that determine species' diffusivity, see Equation 3.9. Note that σ is specified in units of Å, and ε / k has units of K. Recall that all species are assumed to have the

same diffusivity, taken as that of oxygen into the background species. Thus, the code only uses the values σ and ε / k for the background species (specified by IBG) and oxygen (specified by IO2). The values of these parameters for the other species do not affect the calculations, but must be specified to avoid i/o errors.

The last 3 parameters in columns G, H, and I are remnants from a simplified method of treating char oxidation. Although the code sections still remain, they have not been tested or verified and the user should set B = 0 (in column G); if this is done then the values of T_{onset} and T_{span} in columns H and I won't affect the calculations.

B.1.4 Heterogeneous reactions gaseous yields – gyields worksheet

In the code, the distinction is made between homogeneous gas phase reactions that involve only gaseous species, and heterogeneous gas phase reactions that involve the generation of gases from the condensed phase (and sometimes the consumption of gaseous species, as in the case of heterogeneous char oxidation where oxygen is consumed). The code uses a species yield matrix (see Equation 3.65) to specify the composition of the gases generated from a condensed phase (or heterogeneous) reaction. The species yield matrix is entered in the worksheet gyields (gaseous yields).

A screenshot of the gyields worksheet is shown in Figure B.4. For the matrix beginning at cell C18, each row corresponds to a gaseous species (specified in the gprops worksheet), and each column corresponds to a condensed phase reaction (specified in the rxns worksheet). As an example, the entry in the third row, second column is the yield for the third gaseous species (as specified in the grprops worksheet) from the second condensed phase reaction (as specified in the rxns worksheet). To conserve mass, all entries in a column must add to 1. Note that entries may be either positive or negative,

with a positive entry corresponding to production of a gaseous species, and a negative entry corresponding to consumption of a gaseous species. For the example shown in Figure B.4, the first reaction generates pure water vapor. The fourth reaction (char oxidation) consumes oxygen and produces a species called char_oxid_products. The code tracks not only the total mass loss rate, but also the composition of the volatiles that escape from the surface of the decomposing solid.

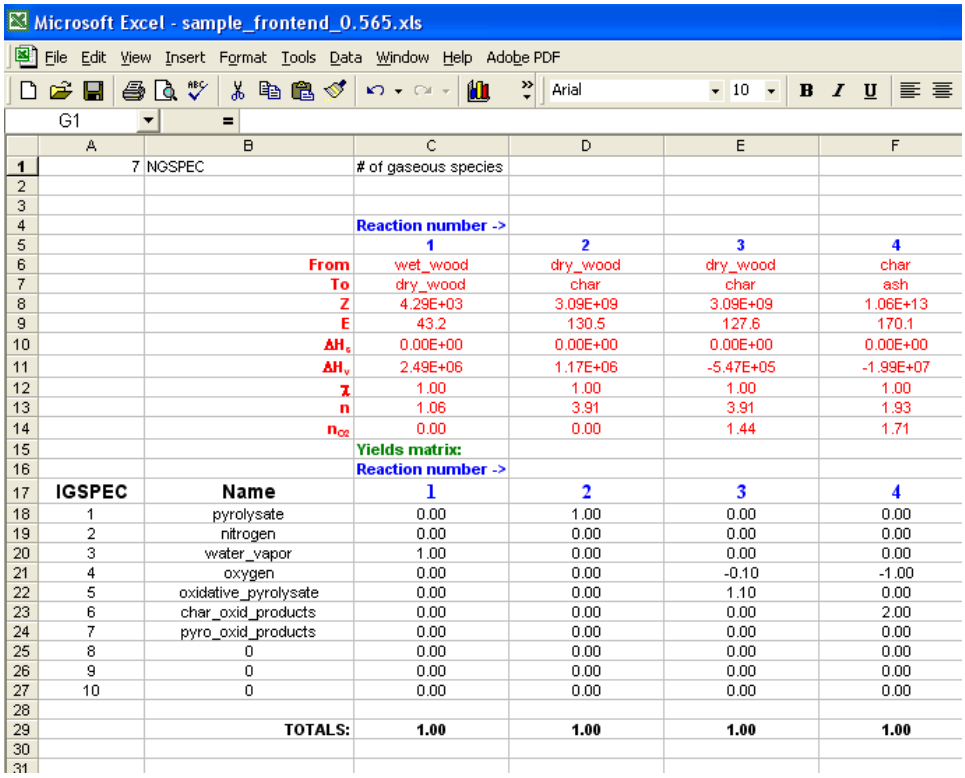

Microsoft Excel - sample_frontend_0.565.xls

File Edit View Insert Format Tools Data Window Help Adobe PDF

Arial 10 B I U

G1 =

	A	B	C	D	E	F
1	7	NGSPEC	# of gaseous species			
2						
3						
4			Reaction number ->			
5			1	2	3	4
6		From	wet_wood	dry_wood	dry_wood	char
7		To	dry_wood	char	char	ash
8		Z	4.29E+03	3.09E+09	3.09E+09	1.06E+13
9		E	43.2	130.5	127.6	170.1
10		ΔH_s	0.00E+00	0.00E+00	0.00E+00	0.00E+00
11		ΔH_v	2.49E+06	1.17E+06	-5.47E+05	-1.99E+07
12		χ	1.00	1.00	1.00	1.00
13		n	1.06	3.91	3.91	1.93
14		n_{oz}	0.00	0.00	1.44	1.71
15			Yields matrix:			
16			Reaction number ->			
17	IGSPEC	Name	1	2	3	4
18	1	pyrolysate	0.00	1.00	0.00	0.00
19	2	nitrogen	0.00	0.00	0.00	0.00
20	3	water_vapor	1.00	0.00	0.00	0.00
21	4	oxygen	0.00	0.00	-0.10	-1.00
22	5	oxidative_pyrolysate	0.00	0.00	1.10	0.00
23	6	char_oxid_products	0.00	0.00	0.00	2.00
24	7	pyro_oxid_products	0.00	0.00	0.00	0.00
25	8	0	0.00	0.00	0.00	0.00
26	9	0	0.00	0.00	0.00	0.00
27	10	0	0.00	0.00	0.00	0.00
28						
29		TOTALS:	1.00	1.00	1.00	1.00
30						
31						

Figure B.4. Screen shot of gyields worksheet.

B.1.5 Layered composition – layers worksheet

Layered (or laminated) composition is specified via the layers worksheet, shown in Figure B.5. The user specifies the number of layers in cell A1. Starting in row 15, the user lists the thickness, contact resistance, and condensed phase species initial mass fractions of each layer. The thickness (m) of each layer is specified in column B, and the number of cells that span that layer is specified in column C. However, this feature has

not yet been implemented in the code so at the present time column C is not used. Instead, it is assumed that the grid spacing in all layers is constant, uniform, and equal to the thickness in the qe worksheet divided by the number of cells specified in the qe worksheet. Column D is the inverse contact resistance (h_{cr}, W/m^2–K) between adjacent layers. This makes it possible to simulate layers that are not in perfect thermal contact with one another, with the rate of heat transfer between layers given as $h_{cr}\Delta T$ where ΔT is the temperature difference between layers. The user should set h_{cr} to a very high value (say 10^6) if perfect thermal contact between layers is desired. Convective heat losses from the last layer are calculated as $h_{cr}\Delta T$ where ΔT is the temperature difference between the last cell in the last layer and the ambient temperature. Thus, an adiabatic back face boundary condition can be specified by setting $h_{cr} = 0$ for the last layer (which, if there is only one layer, is also the first layer).

Along with the thickness and h_{cr} of each layer, the user must also specify the initial condensed phase species mass fractions in that layer. This is done starting in column E and moving to the right. That is, column E is the initial mass fraction of condensed phase species 1, column F is the initial mass fraction of condensed phase species 2, and so on. For the example shown in Figure B.5, the material has a single layer that initially consists of 100% species 1 (wet_wood as defined in the sprops worksheet).

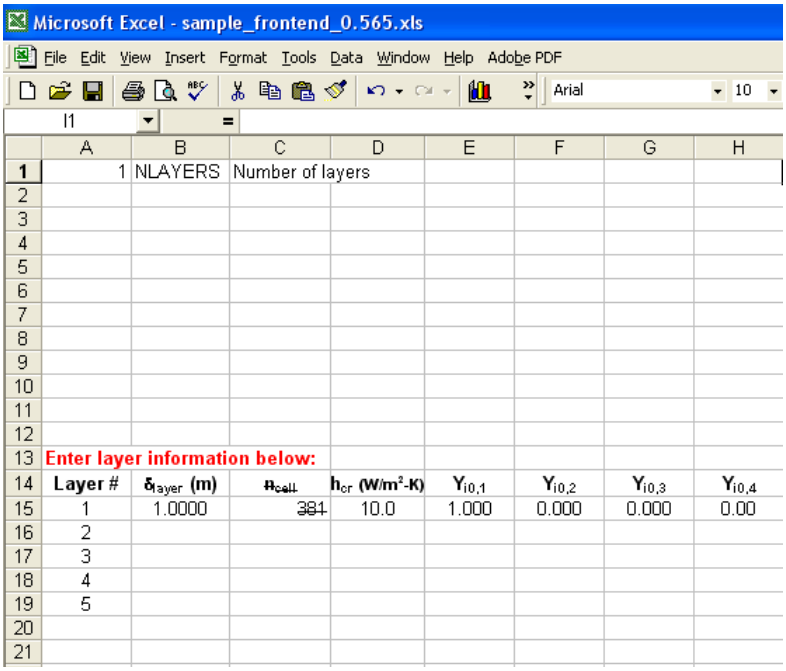

Microsoft Excel - sample_frontend_0.565.xls

File Edit View Insert Format Tools Data Window Help Adobe PDF

Arial 10

I1 =

	A	B	C	D	E	F	G	H
1	1	NLAYERS	Number of layers					
2								
3								
4								
5								
6								
7								
8								
9								
10								
11								
12								
13	Enter layer information below:							
14	Layer #	δ_{layer} (m)	~~n_{cell}~~	h_{cr} (W/m^2-K)	$Y_{i0,1}$	$Y_{i0,2}$	$Y_{i0,3}$	$Y_{i0,4}$
15	1	1.0000	~~381~~	10.0	1.000	0.000	0.000	0.00
16	2							
17	3							
18	4							
19	5							
20								
21								

Figure B.5. Screen shot of layers worksheet.

B.1.6 Heat flux and environmental variables – qe worksheet

The incident radiative heat flux and other environmental variables are specified in the qe worksheet, shown below in Figure B.6.

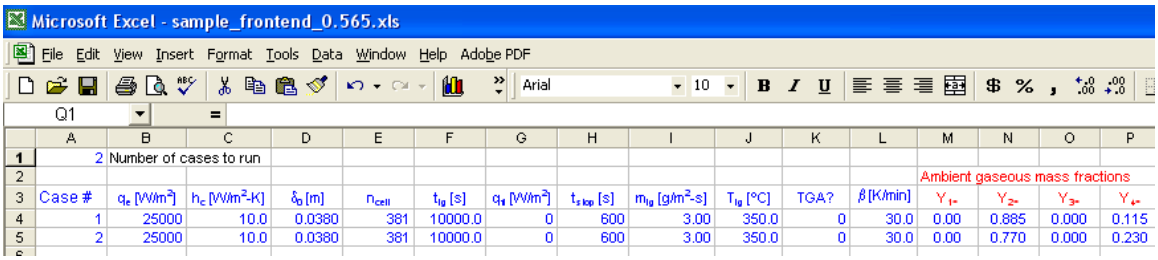

Microsoft Excel - sample_frontend_0.565.xls

File Edit View Insert Format Tools Data Window Help Adobe PDF

Arial 10

Q1 =

	A	B	C	D	E	F	G	H	I	J	K	L	M	N	O	P
1	2	Number of cases to run														
2													Ambient gaseous mass fractions			
3	Case #	q_e [W/m^2]	h_c [W/m^2-K]	δ_0 [m]	n_{cell}	t_{ig} [s]	q_f [W/m^2]	t_{skip} [s]	m_{ig} [g/m^2-s]	T_{ig} [°C]	TGA?	β [K/min]	$Y_{1\infty}$	$Y_{2\infty}$	$Y_{3\infty}$	$Y_{4\infty}$
4	1	25000	10.0	0.0380	381	10000.0	0	600	3.00	350.0	0	30.0	0.00	0.885	0.000	0.115
5	2	25000	10.0	0.0380	381	10000.0	0	600	3.00	350.0	0	30.0	0.00	0.770	0.000	0.230

Figure B.6. Screen shot of qe worksheet.

The number of cases to run is specified in cell A1. This allows multiple heat flux levels, thicknesses, heat transfer coefficients, oxygen concentrations, etc. to be run in batch mode. After the simulations run, the output file summary_0001.csv corresponds to case 1, summary_0002.csv corresponds to case 2, and so on. As is discussed below in the

"general" worksheet section, detailed profiles of various in–depth quantities can also be generated.

The environmental variables for each case are specified starting in row 4. Column A is the case number (cases should start at 1 and be numbered sequentially). Column B (q_e) is the incident radiant heat flux at the front face (W/m^2), and column C is the convective heat transfer coefficient without blowing (W/m^2–K). The initial thickness (δ_0) is specified in column D, and column E (n_{cell}) is the number of grid points spanning that thickness. A uniform grid spacing is used, i.e. grids are not clustered near the irradiated surface as in FDS. Also, the same grid spacing is used in all layers.

The ignition time (t_{ig}, units of seconds) is specified in column F. After the simulation time exceeds the ignition time, a constant flame heat flux (q_{fl}, specified in column G in units of W/m^2) is added to the applied radiant heat flux. Flame heat transfer can be eliminated by setting a zero value of q_{fl} or setting a value of t_{ig} that is greater than the simulation stop time, t_{stop}, which is specified in column H in units of seconds.

The critical mass loss rate for ignition (m_{ig}, g/m^2–s) and the critical surface temperature for ignition (T_{ig}, ºC) are specified in columns I and J. These are used by the code to calculate the ignition time based on either a critical mass loss rate or surface temperature ignition criterion. Note that no flame heat flux is added once these critical conditions for ignition are exceeded; if a flame heat flux is desired, then it is necessary to explicitly specify the ignition time in column F. The ignition times for each case based on the specified ignition criteria are written to the file tig_summary.csv along with a few other quantities. This provides a convenient way to calculate ignition delay curves based on both critical mass loss rate and surface temperature ignition criteria.

Columns K and L are used to simulate thermogravimetric experiments. In column K (labeled TGA), enter a value of 1 if the case is a TGA experiment, otherwise enter 0 and the code will simulate an irradiated solid (analogous to a cone calorimeter experiment). For a TGA experiment, also specify the heating rate in column L (units of K/min), and set ncell to 1 in column E. This directs the code to only solve for the species evolution and mass loss processes of a single "lumped" particle. Essentially, only the condensed phase species and mass conservation equations are solved, while the energy equations and the gaseous species and momentum conservation equations are bypassed. Thus, the temperature of the solid is determined by the specified linear ramp rate, and the mass fractions of gases inside the decomposing particle are assumed to equal the ambient values.

The ambient species mass fractions are specified starting in column M. That is, column M is the ambient mass fraction of gaseous species 1, column N is the ambient mass fraction of gaseous species 2, and so on. This is analogous to the way in which the initial mass fractions of the condensed phase species are specified in the layers worksheet.

For the example shown in Figure B.6, the code will simulate two experiments in which a 3.8 cm thick solid is irradiated at 25 kW/m^2 under nonflaming conditions in an atmosphere that is 11.5% oxygen by mass (case 1) and 23% oxygen by mass (case 2).

B.1.7 Homogeneous gaseous reactions – hgrxns worksheet

The parameters that control homogeneous gas phase reactions are specified in the hgrxns worksheet, shown below in Figure B.7. The number of homogeneous gas phase reactions is specified in cell A1, and the actual parameters for each reaction are specified

starting in row 9. The homogeneous gas phase reaction rates are calculated according to Equation 3.67. The first reactant is specified in column B, and in column C the second reactant is specified. The reaction rate is proportional to the molar concentration of reactant 1 raised to the power p (column D) multiplied by the molar concentration of reactant 2 raised to the power q (column E). Column F is the temperature exponent (b), column G is the pre–exponential factor (Z), and column H is the activation energy E in units of kJ/mol (refer to Equation 3.67). Finally, column I is the heat of reaction per unit mass of reactant 1 consumed (units of J/kg). This corresponds to ΔH_ℓ in Equation 3.70. Note that ΔH_ℓ should be negative for an exothermic reaction and positive for an endothermic reaction.

Units of kg, m^3, mole, and s are used for the pre–exponential factor (Z), but for dimensional consistency the actual units of Z vary with the specified values of p, q, and b. For p = 1, q = 1, and b = 0, the units of Z are kg–m^3/$mole^2$–s.

Microsoft Excel - sample_frontend_0.565.xls

File Edit View Insert Format Tools Data Window Help Adobe PDF

J1 =

	A	B	C	D	E	F	G	H	I
1	2	NHGRXNS	# of homogeneous gas-phase reactions						
2									
3									
4									
5									
6	Specify homogeneous gas-phase reactions below.								
7									
8	**IHGRXN**	**Reactant 1 (species A)**	**Reactant 2 (Species B)**	**p**	**q**	**b**	**Z**	**E (kJ/mol)**	**ΔH (kJ/kg)**
9	1	pyrolysate	oxygen	1.00	1.00	0.00	1.00E+10	151.1	-1.79E+07
10	2	oxidative_pyrolysate	oxygen	1.00	1.00	0.00	1.00E+10	166.1	-1.62E+07
11	3								
12	4								
13	5								
14	6								
15	7								
16	8								
17	9								
18	10								
19									

Figure B.7. Screen shot of hgrxns worksheet.

B.1.8 Homogeneous gaseous reactions yields – hgyields worksheet

The homogeneous gaseous reaction rates are determined according to the parameters specified in the hgrxns worksheet. The reaction rates are translated to formation or consumption of individual gaseous species by the "homogeneous gaseous species yield matrix" (see Equation 3.69) which is specified in the hgyields worksheet, shown below in Figure B.8. The specification of the yields for a homogeneous gaseous reaction is similar to the method for heterogeneous reactions, except here the sum of any column must add to zero (instead of 1). That is, there can be no net creation of gaseous mass by a homogeneous gas phase reaction. Negative entries correspond to the consumption of a species, and positive entries correspond to its production.

Microsoft Excel - sample_frontend_0.565.xls

File Edit View Insert Format Tools Data Window Help Adobe PDF

F1 =

	A	B	C	D	E
1	7	NGSPEC	# of gaseous species		
2					
3					
4			Reaction number ->		
5			1	2	3
6		Reactant 1	pyrolysate	oxidative_pyrolysate	0
7		Reactant 2	oxygen	oxygen	0
8		p	1.00	1.00	0.00
9		q	1.00	1.00	0.00
10		b	0.00	0.00	0.00
11		Z	1.00E+10	1.00E+10	0.00E+00
12		E	151.1	166.1	0.0
13		ΔH	-1.79E+07	-1.62E+07	0.00E+00
14					
15			Homogeneous gaseous reactions yields matrix:		
16			Reaction number ->		
17	IGSPEC	Name	1	2	3
18	1	pyrolysate	-1.00	0.00	0.00
19	2	nitrogen	0.00	0.00	0.00
20	3	water_vapor	0.00	0.00	0.00
21	4	oxygen	-1.60	-1.50	0.00
22	5	oxidative_pyrolysate	0.00	-1.00	0.00
23	6	char_oxid_products	0.00	0.00	0.00
24	7	pyro_oxid_products	2.60	2.50	0.00
25	8	0	0.00	0.00	0.00

Figure B.8. Screen shot of hgyields worksheet.

For the example shown in B.8, the first reaction corresponds to the combustion pyrolysate. For every 1 kg of pyrolysate consumed, there are 1.6 kg of oxygen consumed,

and 2.6 kg of "pyro_oxid_products" (pyrolysate oxidation products) generated. The second reaction corresponds to the combustion of oxidative pyrolysate which does not consume as much oxygen since it is already partially oxygenated.

B.1.9 Miscellaneous parameters– general worksheet

Parameters not specifically related to the other groups of properties described above are covered in the "general" worksheet, shown in Figure B.9. Parameters are categorized into loosely related groups, differentiated by font color. Each parameter is discussed separately below.

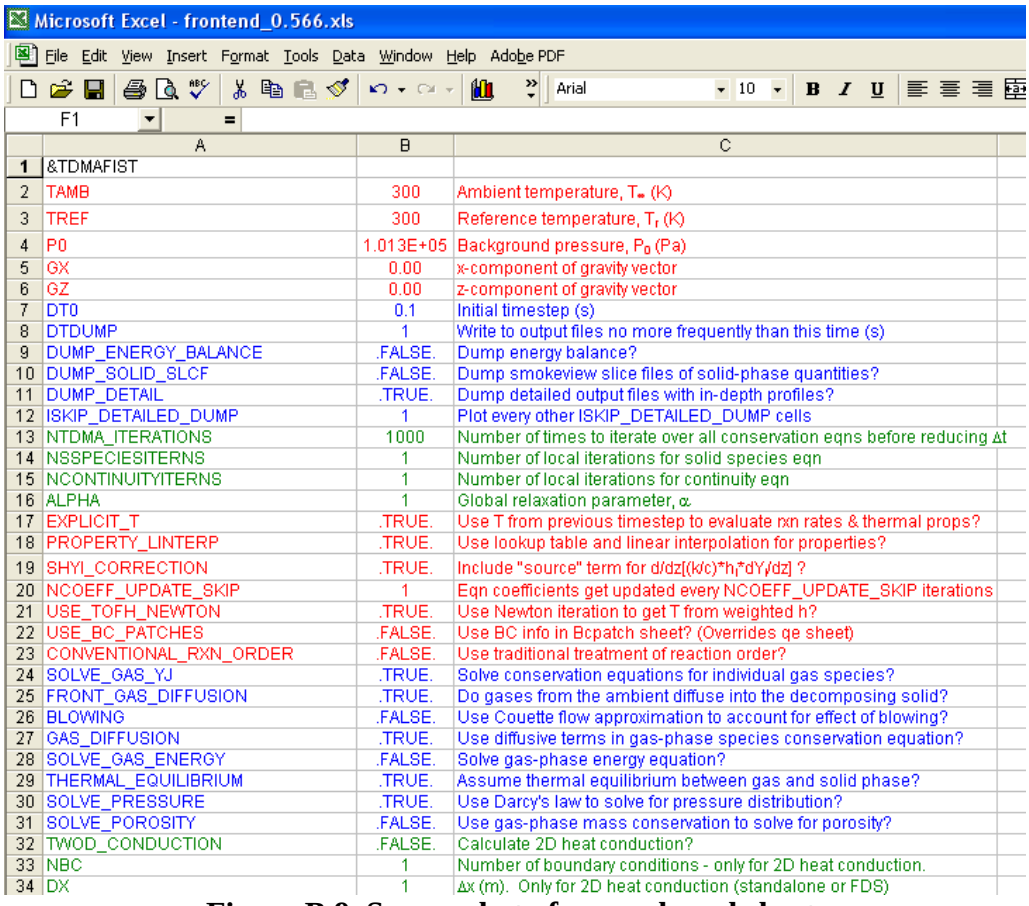

Microsoft Excel - frontend_0.566.xls

File Edit View Insert Format Tools Data Window Help Adobe PDF

F1

	A	B	C
1	&TDMAFIST		
2	TAMB	300	Ambient temperature, T_∞ (K)
3	TREF	300	Reference temperature, T_r (K)
4	P0	1.013E+05	Background pressure, P_0 (Pa)
5	GX	0.00	x-component of gravity vector
6	GZ	0.00	z-component of gravity vector
7	DT0	0.1	Initial timestep (s)
8	DTDUMP	1	Write to output files no more frequently than this time (s)
9	DUMP_ENERGY_BALANCE	.FALSE.	Dump energy balance?
10	DUMP_SOLID_SLCF	.FALSE.	Dump smokeview slice files of solid-phase quantities?
11	DUMP_DETAIL	.TRUE.	Dump detailed output files with in-depth profiles?
12	ISKIP_DETAILED_DUMP	1	Plot every other ISKIP_DETAILED_DUMP cells
13	NTDMA_ITERATIONS	1000	Number of times to iterate over all conservation eqns before reducing Δt
14	NSSPECIESITERNS	1	Number of local iterations for solid species eqn
15	NCONTINUITYITERNS	1	Number of local iterations for continuity eqn
16	ALPHA	1	Global relaxation parameter, α
17	EXPLICIT_T	.TRUE.	Use T from previous timestep to evaluate rxn rates & thermal props?
18	PROPERTY_LINTERP	.TRUE.	Use lookup table and linear interpolation for properties?
19	SHYI_CORRECTION	.TRUE.	Include "source" term for d/dz[(k/c)*h_i*dY$_i$/dz] ?
20	NCOEFF_UPDATE_SKIP	1	Eqn coefficients get updated every NCOEFF_UPDATE_SKIP iterations
21	USE_TOFH_NEWTON	.TRUE.	Use Newton iteration to get T from weighted h?
22	USE_BC_PATCHES	.FALSE.	Use BC info in Bcpatch sheet? (Overrides qe sheet)
23	CONVENTIONAL_RXN_ORDER	.FALSE.	Use traditional treatment of reaction order?
24	SOLVE_GAS_YJ	.TRUE.	Solve conservation equations for individual gas species?
25	FRONT_GAS_DIFFUSION	.TRUE.	Do gases from the ambient diffuse into the decomposing solid?
26	BLOWING	.FALSE.	Use Couette flow approximation to account for effect of blowing?
27	GAS_DIFFUSION	.TRUE.	Use diffusive terms in gas-phase species conservation equation?
28	SOLVE_GAS_ENERGY	.FALSE.	Solve gas-phase energy equation?
29	THERMAL_EQUILIBRIUM	.TRUE.	Assume thermal equilibrium between gas and solid phase?
30	SOLVE_PRESSURE	.TRUE.	Use Darcy's law to solve for pressure distribution?
31	SOLVE_POROSITY	.FALSE.	Use gas-phase mass conservation to solve for porosity?
32	TWOD_CONDUCTION	.FALSE.	Calculate 2D heat conduction?
33	NBC	1	Number of boundary conditions - only for 2D heat conduction.
34	DX	1	Δx (m). Only for 2D heat conduction (standalone or FDS)

Figure B.9. Screen shot of general worksheet.

The first group of properties are ambient and reference values. TAMB is the ambient temperature (T_∞, K), TREF is the reference temperature (T_r, K), and P0 is the background pressure (in units of Pa). The parameters GX and GZ are the x and z components of the gravity vector in units of m/s^2. They influence 2D calculations by inducing a buoyant flow. For now, only GZ has any effect on the calculations, i.e. it is assumed that the gravity vector has a component only in the z direction. GZ only has an effect when USE_BC_PATCHES = .TRUE.. Buoyancy is included in 2D simulations when GZ is set to a value other than 0, and the density at infinity is calculated at TAMB using the gas compositions specified in the qe worksheet. This is a new part of the code that has not yet been widely exercised, so it is recommended that GZ be set to 0.

The next group of properties are related to time and the dump routines. DT0 is the initial time step (s). If the code cannot obtain a converged solution, it will automatically decrease the time step as necessary until a converged solution is obtained. The parameter DTDUMP is the time between data dumps (in seconds), i.e. DTDUMP = 5.0 would tell the code to write to the output files after every 5 seconds of simulation time. If the user sets DUMP_ENERGY_BALANCE = .TRUE., then the code will dump a simplified instantaneous energy balance to disk. The parameter DUMP_SOLID_SLCF tells the code whether or not to write several NIST Smokeview files to disk. This allows 2D transient profiles of temperature, density, thermal conductivity, etc. to be visualized with Smokeview (by double–clicking on the .smv file that is created). If the user specifies DUMP_DETAIL = .TRUE., then the code will write detailed profiles of several quantities to disk. However, these files can take up a lot of space, so be careful! The parameter ISKIP_DETAILED_DUMP controls the fraction of the cells that get dumped

to disk. For example, if it is set to 1, then the value in every cell gets written to disk; if it is set to 5, then every fifth cell gets dumped, and so on. This is useful if, for example, you are using a 0.1 mm grid resolution but you are really only interested in seeing output data to the nearest 1 mm, in which case you would specify ISKIP_DETAILED_DUMP = 10. This parameter can also be used to ensure that all output fits within the 256 column limitation of some versions of MS Excel.

The next group of parameters (starting in row 11) is related to iterations and convergence. NTDMA_ITERATIONS is the maximum number of iterations that the code will take per time step in an attempt to obtain a converged solution. If it reaches this number of iterations and the solution hasn't yet converged (based on the convergence criteria specified elsewhere), then the code will decrease the time step and try again. The parameters NSSPECIESITERNS and NCONTINUITYITERNS are integers that control the number of sub–iterations for the condensed phase species and mass conservation equations, respectively. This is necessary because the way that the condensed phase mass and species conservation equations are solved numerically, the unknown value at the next time step depends on itself (see Equations 3.73 and 3.75) so local iterations can sometimes encourage convergence. However, both NSSPECITERNS and NCONTINUITYITERNS are normally set to 1. The parameter ALPHA is the relaxation factor. When it is set to 1, no relaxation is used; but for values of ALPHA between 0 and 1, solution relaxation is implemented according to Equation 3.132.

The next group of parameters (starting in row 15) can be used to reduce the total required amount of CPU time by optimizing some routines, neglecting expensive terms, or attempting to reduce the number of iterations for convergence. If EXPLICIT_T =

.TRUE. then the code uses the converged temperature from the previous time step to calculate the reaction rates and the thermal properties for the current iteration. The advantage of doing so is that the strong temperature dependency of the reaction rates (and secondarily, thermal properties) does not hinder convergence because the reaction rates are not changing from iteration to iteration due to the newly–calculated temperature profile. This can also reduce the required CPU time because the temperature part of the source terms must be calculated only once per time step rather than at every iteration. However, since the code formulation is fully implicit, technically the temperature at the current iteration should be used to evaluate the reaction rates and the thermal properties, so EXPLICIT_T should normally be set to .FALSE.. Doing so preserves the correct long–term (or steady–state) behavior as $\Delta t \to \infty$. However, the code usually marches forward in time using small time steps on the order of 0.1 s or smaller, and it was found that under most circumstances the results were not sensitive to the value of EXPLICIT_T. The logical parameter PROPERTY_LINTERP controls whether or not the code uses a lookup table in conjunction with linear interpolation to obtain the temperature–dependent thermophysical properties or whether they are calculated explicitly, e.g. from the relation $k(T) = k_0 (T/T_r)^{n_k}$. If it is set to .TRUE., then a lookup table with linear interpolation is used; this is considerably less CPU intensive than evaluating the exponentiation term in every cell at every time step. The logical parameter SHYI_CORRECTION controls whether the summation term in Equation 3.88a and b is included in the calculation of the conductive heat flux. Technically, this term is not really a "correction" but rather part of the proper definition of the conductive heat flux when it is expressed as an enthalpy gradient, so SHYI_CORRECTION should always be set to .TRUE.. However, this term

is expensive to calculate, sometimes slows down convergence, and may not have a significant impact on the overall results. For this reason, an option was added to disable this term (mostly for debugging purposes). The parameter NCOEFF_UPDATE_SKIP tells the code how frequently to update coefficients (thermal conductivities, specific heat capacity, etc.). If it is set to 1, then the coefficients are updated every iteration, if it is set to 5, they are updated every fifth iteration, and so on. The logical parameter USE_TOFH_NEWTON tells the code whether or not to use Newton iteration to extract the temperature from the weighted enthalpy and the condensed phase mass fractions. If it is set to .FALSE., then the code assumes the specific heat of each species does not depend on temperature and uses the explicit relation given in Equation 3.102 to calculate the temperature from the enthalpy (this is much faster than using Newton iteration). Otherwise, the Newton iteration is used to solve Equation 3.96 for *T*. The flag USE_BC_PATCHES tells the code whether or not to use the boundary condition "patches" specified in the BCpatch worksheet to override those specified in the qe worksheet. This is because the qe worksheet assumes a cone calorimeter type configuration, with radiation at the front face, convective heat losses etc. If more elaborate boundary conditions are desired, then the user should set USE_BC_PATCHES to .TRUE.. This directs the code to replace the heat flux, heat transfer coefficient, and ambient species' mass fractions in the qe worksheet with the potentially more general boundary conditions specified in the BCpatch worksheet (discussed in the next section). All other parameters in qe are unaffected. Also, for 2D simulations the user would normally set USE_BC_PATCHES = .TRUE. so that the "left" and "right" boundary conditions can be specified. This part of the code is relatively new and hasn't been

rigorously tested, so the user should proceed with caution! The flag CONVENTIONAL_RXN_ORDER is used to specify whether the code should use the conventional reaction order approach wherein $\left(\overline{\rho} Y_i \Delta z\right)_\Sigma$ in Equation 3.56 is replaced with $\left(\overline{\rho} \Delta z\right)\big|_{t=0}$.

The next group of parameters (starting in row 21) is logical flags that make it possible to enable or disable various parts of the code. Setting SOLVE_GAS_YJ = .TRUE. tells the code to solve the gas phase species conservation equation. If the gas phase species conservation equation is solved, then the logical parameter FRONT_GAS_DIFFUSION controls whether or not gases from the ambient diffuse into the decomposing solid. Similarly, the logical variable GAS_DIFFUSION tells the code whether or not to include the diffusive terms in the gaseous species conservation equations. Under some circumstances (high Peclet numbers), it may be sufficient to consider only the convective terms in the gaseous species conservation equations, but it was found that this sometimes leads to convergence problems. If the parameter BLOWING is set to .TRUE. then the code uses a Couette flow approximation (Equation 3.25) to account for the effect of blowing on the front face convective heat transfer coefficient; otherwise it is assumed to be constant.

If the logical parameter SOLVE_GAS_ENERGY is set to .TRUE., then the code will solve the gas phase energy equation (in this case, the user should also set SOLVE_GAS_YJ to .TRUE.). If THERMAL_EQUILIBRIUM = .TRUE., then the code assumes that thermal equilibrium exists between the gas phase and the condensed phase. Note that it is possible to have THERMAL_EQUILIBRIUM = .TRUE. without solving the gas phase energy equation. If the user sets both SOLVE_GAS_ENERGY = .TRUE.

and THERMAL_EQUILIBRIUM = .TRUE., then any heat release from homogeneous gas phase reactions is added to the condensed phase, rather than the gas phase. However, if SOLVE_GAS_ENERGY = .TRUE. and THERMAL_EQUILIBRIUM = .FALSE., then the code will calculate the rate of heat transfer between the gaseous and the condensed phase according to Equation 3.26, and any heat release from homogeneous gas phase reactions is distributed to the gas phase. This can drastically increase the number of iterations required for convergence and the required CPU time is increased considerably. The logical parameter SOLVE_PRESSURE tells the code whether or not to solve the pressure (momentum) equation. If SOLVE_PRESSURE = .FALSE., then the code uses gaseous mass conservation (Equation 3.18) to calculate the local convective mass flux per Equation 3.74; otherwise it is calculated from Equation 3.42. The flag SOLVE_POROSITY tells the code whether or not to solve a separate equation to determine the porosity. For now, this part of the code is non–functional, so the user should always set SOLVE_POROSITY = .FALSE. or non–physical results will occur!

The next group of parameters has to do with 2D heat conduction. NBC is the "number of boundary conditions". This name is somewhat misleading and is an artifact of coupling the pyrolysis model to FDS. NBC is normally 1, and this directs the code to perform a 1D calculation. However, 2D simulations can be conducted by setting NBC to a number greater than 1. For example, setting NBC = 200 tells the code that there are 200 adjacent 1D calculations. If the parameter TWOD_CONDUCTION is set to .TRUE. then the code will conduct a 2D simulation. In this case, the user should also specify DX (the x–direction grid spacing, Δx, in units of m). For example, if NBC = 200 and DX = 0.0001 m, then the code will perform a 2D calculation in a region 0.02 m in the x direction (200

cells 0.1 mm in thickness). The height of this domain in the z direction is dictated by the value of δ_0 specified in the qe worksheet. This will also cause the code to dump the 2D temperature profile every DTDUMP seconds.

B.1.10 Boundary condition patches – BCpatch worksheet

The BCpatch worksheet can be used when the boundary conditions available in the qe (h_c, q_e, Y_j^∞) and layers worksheet (h_{cr}) don't provide sufficient flexibility, or when a forced–flow boundary condition is desired. It allows the user to specify general time–dependent boundary conditions over a number of surface patches. In a 1D simulation, there are only 2 patches: the top face (at $z = 0$) and the bottom face (at $z = \delta$). However, in 2D simulations, the situation becomes more complex because the user must contend with boundary conditions at the top, bottom, left, and right faces. Furthermore, the boundary conditions at each face may vary temporally as well as spatially. For example, at $z = 0$ the boundary condition may be a fixed heat flux for $0 \le x \le a$, and a fixed temperature for $a < x \le b$, and the fixed heat flux and fixed temperature may both vary with time! The BCpatch worksheet provides the ability to specify such generalized boundary conditions.

To enable specification of boundary conditions via the BCpatch worksheet, the user should set USE_BC_PATCHES = .TRUE. in the "general" worksheet. This directs the code to override the boundary conditions specified in qe and layers with those specified in BCpatch. The reason for this is that at the present time, BCpatch provides no mechanism to specify boundary conditions for multiple cases. Although BCpatch may be used in conjunction with both the standalone and the genetic algorithm executable, they

can be applied only to a single case (IQE = 1). Another limitation is that at the present time, boundary condition patches are available only for solid energy conservation, gas momentum conservation, and gaseous species conservation. They have not yet been implemented for the gaseous energy conservation. Thus, "two temperature" simulations where the condensed phase and gas phase have separate temperatures cannot be conducted. Consequently, the user should set THERMAL_EQUILIBRIUM = .TRUE. (in the "general" worksheet) when using boundary condition patches.

The BCpatch worksheet, shown in Figure B.10, is divided into three main sections: condensed phase energy conservation boundary conditions, gas phase momentum conservation boundary conditions, and gas phase species conservation boundary conditions. The number of each type of boundary condition patch is specified in cells A1, A2, and A3.

Data entry for the condensed phase energy boundary conditions must begin in row 10. Make sure that the first boundary condition patch is specified in row 10 or the simple i/o routines in the Excel front end and the standalone executable will both complain loudly! Each patch is numbered sequentially in column A. In Column B, the user should specify a time. If the patch boundary condition is "static", meaning that it does not change with time, then enter 0 for the time (transient boundary conditions will be discussed in the next paragraph).

The x location of the patch is specified in Columns C and D, and the z location is specified in columns E and F. Either x_1 and x_2 must be equal, or z_1 and z_2 must be equal, but not both (since each patch must be planar). In the example below, the first boundary condition patch (row 10) is applied at the plane x = 0.00 m, from z = 0.00 m to z = 0.05

m. Two types of boundary conditions are available: fixed temperature, or radiative/convective surface heat balance. The externally applied heat flux is specified in column G, and the convective heat transfer coefficient is specified in column H. For the time being, it is assumed all patches see the same ambient temperature (equal to TAMB specified in the general worksheet). If the surface reradiates, then column I should be set to .TRUE.. Otherwise, if column I is .FALSE., the patch loses heat to the ambient only by Newtonian cooling. Finally, the fixed temperature of the patch is specified in column J. Specifying a value greater than 0 in column J overrides any boundary conditions specified in columns G–I. In other words, if a radiative/convective heat balance boundary condition is desired, specify a negative number for the fixed temperature in column J; if a fixed temperature boundary condition is desired, set that fixed temperature in column J.

If a boundary condition patch is transient, you will have to enter a time history for that patch. The code will linearly interpolate between the specified times. For example, assume the temperature of a patch ramps from 300 K to 400 K over 60 s, and then decreases back to 300 K in another 60 s. The user should specify three patches having the same x and z coordinates, but 3 different times: 0 s, 60 s, 120 s having respective temperatures of 300 K, 400 K, and 300 K. The patch temperature at intermediate times will be calculated by linear interpolation between specified time/temperature pairs.

Data entry for the gaseous momentum boundary conditions starts in row 13 plus the number of condensed phase energy conservation boundary conditions. That is, if you have 20 condensed phase energy boundary conditions (be sure to specify this number in cell A1!) then you should start specifying the gas phase momentum boundary conditions in row 33. Columns A–F are the same as for the condensed phase energy boundary

condition, and transient boundary conditions are specified in the same way. For the gas phase momentum equation, two types of boundary conditions are available: fixed mass flux and fixed pressure. If a fixed mass flux is desired, then put a negative number in column H, and specify the desired mass flux in Column G using units of g/m^2–s. The convention used is that a positive quantity denotes an inflow, and a negative quantity denotes an outflow. If a fixed pressure is desired, specify the absolute pressure in column H. Analogous to the condensed phase energy boundary conditions, specification of a positive pressure in column H overrides any mass flux specified in column G.

The last set of boundary condition patches (gas phase species) is specified beginning in row 16 plus the number of condensed phase energy patches plus the number of gas phase momentum patches. That is, if you have 12 condensed phase energy boundary condition patches and 9 momentum boundary condition patches, you should start data entry for the gas phase species patches in row 37. For the gas phase species patches, columns A–F are the same as for condensed phase energy and gas phase momentum, and transient boundary conditions are specified in the same way. Column G is the mass transfer coefficient in units of kg/m^2–s. If no diffusive transfer of gaseous species from the patch is desired, then set the mass transfer coefficient to 0. However, if diffusive species transfer is desired, then specify the desired mass transfer coefficient in column G, and specify the ambient species mass fractions that each patch "sees" beginning in column H. That is, column H is the ambient mass fraction of gaseous species 1, column I is the ambient mass fraction of gaseous species 2, and so on.

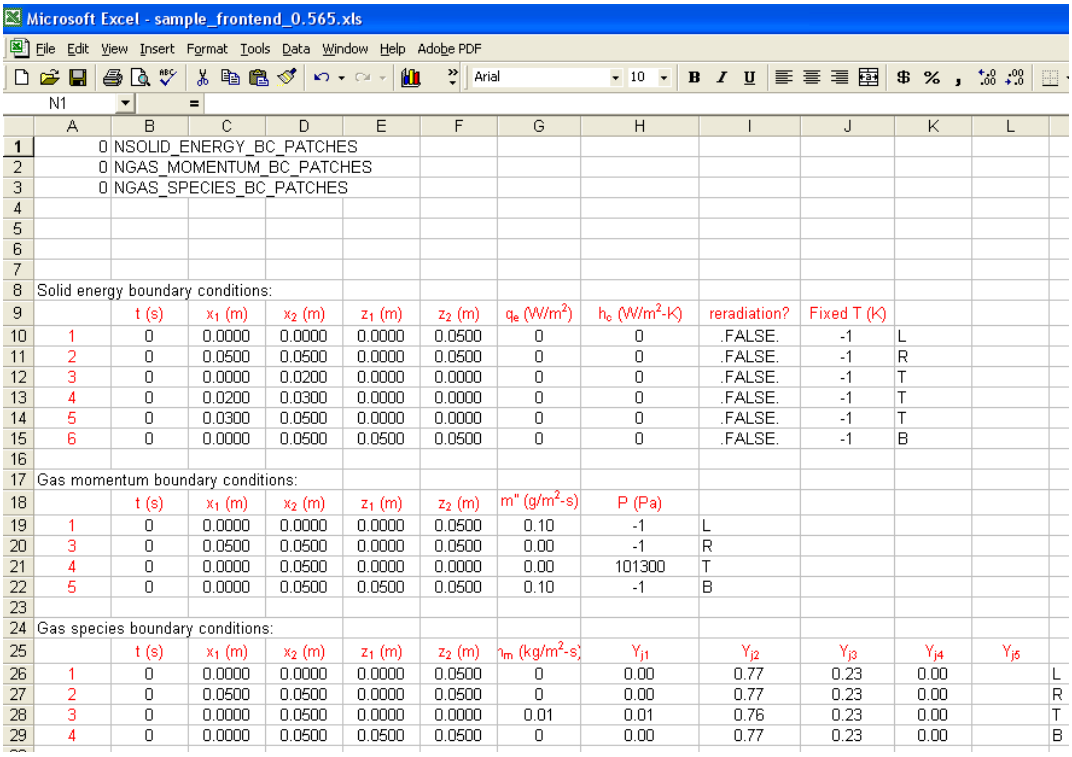

Microsoft Excel - sample_frontend_0.565.xls

File Edit View Insert Format Tools Data Window Help Adobe PDF

N1 =

	A	B	C	D	E	F	G	H	I	J	K	L
1	0	NSOLID_ENERGY_BC_PATCHES										
2	0	NGAS_MOMENTUM_BC_PATCHES										
3	0	NGAS_SPECIES_BC_PATCHES										
4												
5												
6												
7												
8	Solid energy boundary conditions:											
9		t (s)	x_1 (m)	x_2 (m)	z_1 (m)	z_2 (m)	q_e (W/m^2)	h_c (W/m^2-K)	reradiation?	Fixed T (K)		
10	1	0	0.0000	0.0000	0.0000	0.0500	0	0	.FALSE.	-1	L	
11	2	0	0.0500	0.0500	0.0000	0.0500	0	0	.FALSE.	-1	R	
12	3	0	0.0000	0.0200	0.0000	0.0000	0	0	.FALSE.	-1	T	
13	4	0	0.0200	0.0300	0.0000	0.0000	0	0	.FALSE.	-1	T	
14	5	0	0.0300	0.0500	0.0000	0.0000	0	0	.FALSE.	-1	T	
15	6	0	0.0000	0.0500	0.0500	0.0500	0	0	.FALSE.	-1	B	
16												
17	Gas momentum boundary conditions:											
18		t (s)	x_1 (m)	x_2 (m)	z_1 (m)	z_2 (m)	m" (g/m^2-s)	P (Pa)				
19	1	0	0.0000	0.0000	0.0000	0.0500	0.10	-1	L			
20	3	0	0.0500	0.0500	0.0000	0.0500	0.00	-1	R			
21	4	0	0.0000	0.0500	0.0000	0.0000	0.00	101300	T			
22	5	0	0.0000	0.0500	0.0500	0.0500	0.10	-1	B			
23												
24	Gas species boundary conditions:											
25		t (s)	x_1 (m)	x_2 (m)	z_1 (m)	z_2 (m)	γ_m (kg/m^2-s)	Y_{j1}	Y_{j2}	Y_{j3}	Y_{j4}	Y_{j5}
26	1	0	0.0000	0.0000	0.0000	0.0500	0	0.00	0.77	0.23	0.00		L
27	2	0	0.0500	0.0500	0.0000	0.0500	0	0.00	0.77	0.23	0.00		R
28	3	0	0.0000	0.0500	0.0000	0.0000	0.01	0.01	0.76	0.23	0.00		T
29	4	0	0.0000	0.0500	0.0500	0.0500	0	0.00	0.77	0.23	0.00		B

Figure B.10. Screen shot of BCpatch worksheet.

B.2. Genetic algorithm

All worksheets necessary to use the genetic algorithm property estimation program are also contained in the front end. There are three worksheets where the user specifies relevant parameters for the genetic algorithm: GA_GenInput, GA_phi, and GA_Vars. Each of these worksheets will be explained below. Additionally, there are a number of worksheets in which the experimental data must be specified. They are named 01, 02, 03 for experiment 1, 2, 3, and so on. The experimental data in these sheets must be laid out in a specific way, as will be described in detail below.

The genetic algorithm optimization routines were developed as part of a research code that is intended to be functional and efficient rather than user friendly (since for many years there was only one user!). The user is cautioned that there is even less error

checking in the genetic algorithm routines than in the standalone model, and the worksheets through which the data must be entered are somewhat more cryptic than for the standalone model. Thus, it is easy to make a mistake during data entry, and the user should carefully check the model output to make sure the code is doing what the user intended. Often, runtime errors result from erroneous data entry, but the actual cause can be difficult to track down, even when the code is run from within a debugger.

The genetic algorithm code can be run either in serial or in parallel, and the serial executable file is the same as the paraellel executable file. Parallelization is achieved using Message Passing Interface. The code has been successfully run in parallel on more than 60 CPUs, making it possible to do overnight what would take a single PC approximately one month. As with the standalone model, the input filenames are hardcoded. The serial executable can be run from a dos prompt or Linux shell by typing tdma_ga_y.yyy (where y.yyy is the version number). The parallel version has not been tested under Windows, but under Linux it is launched by issuing a command similar to the following: "nohup mpirun –np 32 –machinefile machines.linux –machinedir ./ /home3/clauten/bin/tdma_ga_y.yyy". The syntax may be slightly different with LAM MPI instead of MPICH MPI, but this example tells the code to run on 32 processors (–np 32), look up the machine names to run on in the file macines.linux (–machinefile machines.linux) located in the current directory (–machinedir ./), and execute the binary file called tdma_ga_y.yyy located in the /home3/clauten/bin directory. The code can be halted gracefully (important when running in parallel across multiple modes) by creating a file called "stop.stop" in the working directory. The code only checks for the existence of this file at the completion of a generation, so it may take several mintues (or even

several hours) for the code to shutdown after the file stop.stop is created. The contents of stop.stop are irrelevant, the code merely checks to see if it exists, and shuts down gracefully if it does.

B.2.1 Miscellaneous parameters – GA_GenInput worksheet

General parameters related to the genetic algorithm are specified in the GA_GenInput worksheet, shown below in Figure B.11. The parameter NGEN is the number of generations, or evolution steps, that will be taken (unless the user halts execution prematurely). NINDIV is the number of individuals (or chromosomes) in a population. These concepts are explained in Section 5.3.2. The parameter MAXCOPIES is the target (maximum) selection number described in Section 5.3.3.

If the code is run under Linux, then set LINUX = .TRUE.. This parameter isn't very important, all it does is delete the stop file which tells the code to shutdown gracefully by issuing the shell command "rm –f stop.stop" under Linux and "del stop.stop" under DOS.

The parameter SIMULATED_EXPERIMENTAL_DATA should normally be set to .FALSE.. If it is set to .TRUE., then the code generates a synthetic set of experimental data (instead of reading in actual experimental data) using the material properties specified in the front end. This feature was used during the development process to evaluate how well the genetic algorithm could perform for idealized scenarios, i.e. infinitely accurate experimental measurements with a computational model that is a perfect representation of the physical processes occurring.

FITMIN and FITCLIP are two parameters that come in to play only when an individual has a very bad fitness, or the solution does not converge. Normally, these are

set to zero. The variable FITEXPONENT is the parameter ζ in Equation 5.2. The last two parameters affect reproduction (whereby offspring are generated from parents). Normally, offspring are generated as linear combinations of parents (Equation 5.7). However, under some circumstances it may be useful to use the value of only one of the parents, i.e. an entire gene is used. This is analogous to setting r_j^i in Equation 5.7 to 1.0. The fraction of genes for which this is done is WHOLEGENEFRAC. The parameter RANDOM_CHILDREN indicates whether genes for the offspring should be generated randomly, rather than through the normal evolution process. Setting this parameter to .TRUE. essentially disables the genetic algorithm's ability to exploit promising solutions and the code reverts to a brute force search technique. During the search process, some solutions that do not converge for the specified initial time step may be encountered. The code can either reduce the time step until a converged solution is obtained (as would be done for a standalone simulation) or immediately kill the trial solution that did not converge. This is controlled by the parameter KILL_NONCONVERGED_SOLUTIONS. It is recommended that this parameter be set to .TRUE. because if it is set to .FALSE., then some simulations that do not converge could require a very small time step and consume a large amount of CPU time.

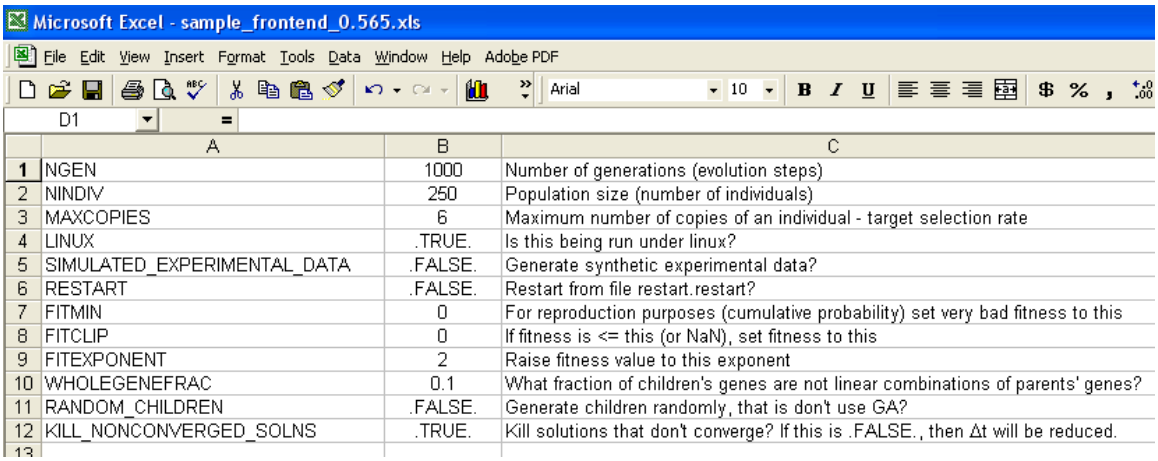

	A	B	C
1	NGEN	1000	Number of generations (evolution steps)
2	NINDIV	250	Population size (number of individuals)
3	MAXCOPIES	6	Maximum number of copies of an individual - target selection rate
4	LINUX	.TRUE.	Is this being run under linux?
5	SIMULATED_EXPERIMENTAL_DATA	.FALSE.	Generate synthetic experimental data?
6	RESTART	.FALSE.	Restart from file restart.restart?
7	FITMIN	0	For reproduction purposes (cumulative probability) set very bad fitness to this
8	FITCLIP	0	If fitness is <= this (or NaN), set fitness to this
9	FITEXPONENT	2	Raise fitness value to this exponent
10	WHOLEGENEFRAC	0.1	What fraction of children's genes are not linear combinations of parents' genes?
11	RANDOM_CHILDREN	.FALSE.	Generate children randomly, that is don't use GA?
12	KILL_NONCONVERGED_SOLNS	.TRUE.	Kill solutions that don't converge? If this is .FALSE., then Δt will be reduced.
13			

Figure B.11. Screen shot of GA_GenInput worksheet.

B.2.2 Fitness metric weightings – GA_phi worksheet

The fitness metric weightings, i.e. the ϕ values in Equation 5.3, are specified in the worksheet GA_phi, shown in Figure B.12. Each ϕ value multiplies a fitness function (Equation 5.2) that quantifies the level of agreement between model predictions and experimental data. In this way, certain experiments or measurements can be given greater importance than others.

The user should first specify the number of ϕ values (the number of experimental measurements) in cell A1, labeled NGA_PHI. In addition to the actual ϕ value (specified in column F) a few additional parameters must be given. The integer IQE (index of qe) in column B corresponds to the case # listed in the qe worksheet. For example, if IQE = 2, then the ϕ value specified is for case #2 in the qe worksheet.

Several types of experimental data can be used as fitness metrics: cumulative mass loss, mass loss rate, temperature, and thickness. The code is told what type of experimental data the ϕ value corresponds to in column C (TYPE). Here, the user enters one of four 3–character strings to indicate which type experimental data is being used:

TMP (temperature, ºC), MLR (mass loss rate, g/m^2–s), DLT (delta, or thickness, m), and CML (cumulative mass loss, g/m^2).

Column D is labeled "z_T". This column tells the code the depth (location) of a particular temperature measurement. For example, $z_T = 0$ indicates a surface temperature measurement, $z_T = 0.005$ indicates an in–depth temperature measurement 5 mm below the surface, and so on. Column D has meaning only if TMP is specified in column C.

Column E is labeled t_{stop}. This is a time in seconds that can be less than or equal to the simulation time specified in the qe worksheet. Setting a value of t_{stop} less than the simulation time directs the code to calculate the fitness metric only through a time of t_{stop}. This is convenient if, for example, the surface temperature was measured but deemed accurate only prior to ignition (at which point the presence of a flame can add uncertainty to temperatures measured via thermocouple or optical methods). By setting the value of t_{stop} for the ϕ value corresponding to the surface temperature to equal the observed ignition time, the code will only use the measured surface temperature before the ignition time when evaluating that part of the overall fitness. The actual ϕ value is specified in column F. There are no restrictions on the range of acceptable ϕ values, except that it doesn't make sense to have a negative ϕ value.

Finally, column G is a small number (ε) that prevents the fitness metric from approaching infinity when the model calculation is very close to the experimental data point. See Equation 5.2 for further explanation.

For the case shown in Figure B.12 there are ϕ values corresponding to 2 separate experiments (note that IQE ranges from 1 to 2). For both experiments the code will evaluate the fitness on the basis of a mass loss rate measurement (MLR in column C), 3

temperature measurements (TMP in column C), and a cumulative mass loss (CML in column C) measurement. For both experiments, the first temperature measurement is at a distance of 0 m (i.e., surface temperature), the second temperature measurement is at a depth of 0.005 m, and the third temperature measurement is at a depth of 0.01 m. Since t_{stop} = 600 s for all measurements, a comparison of the model calculations and the experimental data through 600 s is used to evaluate the fitness. Finally, the specified ϕ values range from 100 to 300 to give different weight to different measurements.

Microsoft Excel - sample_frontend_0.565.xls

File Edit View Insert Format Tools Data Window Help Adobe PDF

Arial 10 B I U

J1 =

	A	B	C	D	E	F	G	H	I
1	10	NGA_PHI							
2			**Valid types:**						
3			TMP	Temperature					
4			MLR	Mass loss rate					
5			DLT	delta (thickness)					
6			CML	Cumulative mass loss					
7	**Notes**	**Do not enter experimental data for CML - enter MLR instead and code will calculate CML**							
8		**z_T is only relevant for TMP type**							
9									
10									
11	**INDEX**	**IQE**	**TYPE**	**z_T**	**t_{stop}**	**ϕ**	**ε**		
12	1	1	MLR	0	600	1	0.1		
13	2	1	TMP	0.000	600	1	0.1		
14	3	1	TMP	0.005	600	1	0.1		
15	4	1	TMP	0.010	600	1	0.1		
16	5	1	CML	0	600	1	0.1		
17	6	2	MLR	0	600	1	0.1		
18	7	2	TMP	0.000	600	1	0.1		
19	8	2	TMP	0.005	600	1	0.1		
20	9	2	TMP	0.010	600	1	0.1		
21	10	2	CML	0	600	1	0.1		

Figure B.12. Screen shot of GA_phi worksheet.

B.2.3 Experimental data – 01, 02, 03, etc. worksheets

The experimental data must be pasted into worksheet 01 for case # (or IQE) 1, worksheet 02 for case # (or IQE) 2, and so on. Each ϕ value specified in GA_phi should have an analogous set of experimental data (with the exception of cumulative mass loss,

which the code automatically calculates by integrating the mass loss rate). The units for temperature measurements are ºC, mass loss rate is g/m^2–s, and thickness is m. For a TGA experiment, mass loss rate data should be entered as $1000 \times \mathrm{d}(m/m_0)/\mathrm{d}t$ where m is the sample mass and m_0 is the initial sample mass. Be sure to express this derivative as $\mathrm{d}/\mathrm{d}t$ and not $\mathrm{d}/\mathrm{d}T$ (time derivative instead of temperature derivative).

The experimental data must be entered according to a very specific layout, and in an order that corresponds to the order in which the ϕ coefficients are specified in the GA_phi worksheet. Column A is the time axis for the first experimental measurement for which a ϕ value was specified for that IQE in GA_phi. Column B is the corresponding experimental data at each time specified in column A. Column C is blank, and the next set of experimental measurements start in column D, i.e. column D is the time axis for the second experimental measurement, and column E is the analogous experimental data at each time. Column F is blank, and columns G and H would contain the next set of experimental data. Column I is blank, and columns J and K would contain the next set of experimental data, and so on. The order in which the experimental data is specified must correspond to the TYPE order specified in GA_phi. Do not specify experimental data for any cumulative mass loss measurements because this is calculated by integration from the mass loss rate. It is easy to make mistakes in this part of the data input process, and the input routines haven't been rigorously exercised, so be sure to check the output data to make sure that what the code has read in what you intended!

An example is shown in Figure B.13. Columns A and B are mass loss rate measurements in units of g/m^2–s. Columns D and E are the first temperature

measurement (temperatures are specified in ºC), columns G and H are the second temperature measurement, and columns J and L are the third temperature measurement.

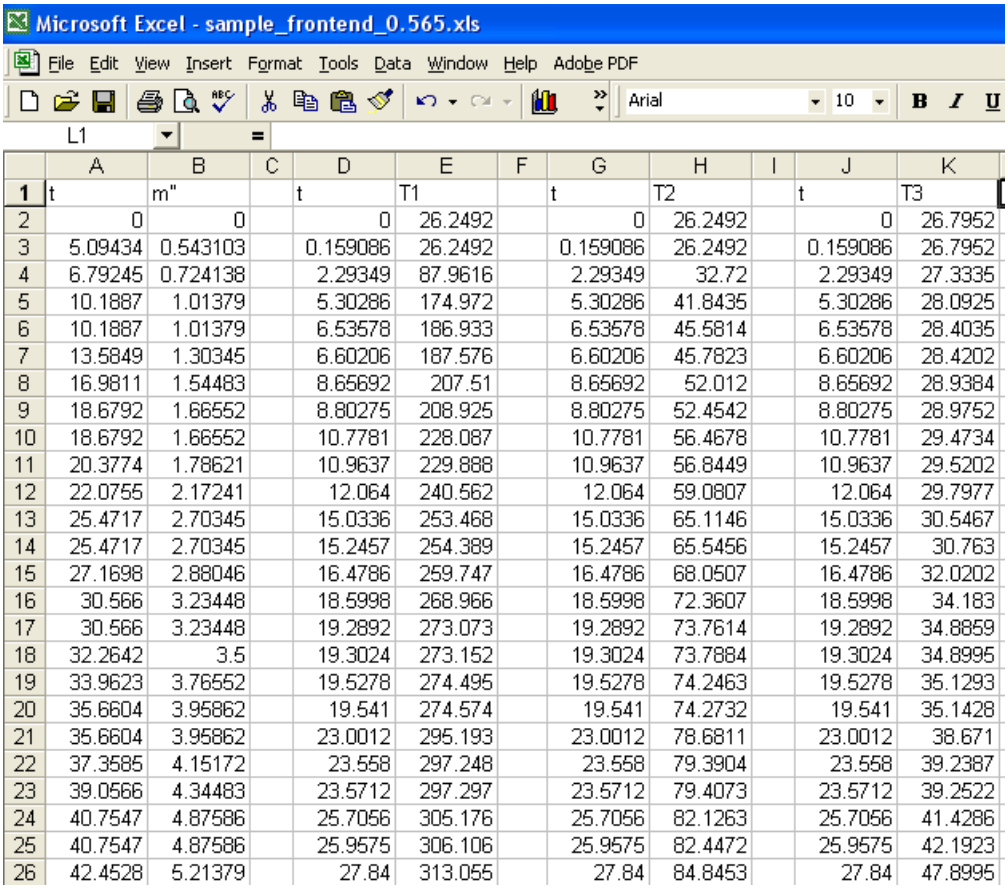

	A	B	C	D	E	F	G	H	I	J	K
1	t	m"		t	T1		t	T2		t	T3
2	0	0		0	26.2492		0	26.2492		0	26.7952
3	5.09434	0.543103		0.159086	26.2492		0.159086	26.2492		0.159086	26.7952
4	6.79245	0.724138		2.29349	87.9616		2.29349	32.72		2.29349	27.3335
5	10.1887	1.01379		5.30286	174.972		5.30286	41.8435		5.30286	28.0925
6	10.1887	1.01379		6.53578	186.933		6.53578	45.5814		6.53578	28.4035
7	13.5849	1.30345		6.60206	187.576		6.60206	45.7823		6.60206	28.4202
8	16.9811	1.54483		8.65692	207.51		8.65692	52.012		8.65692	28.9384
9	18.6792	1.66552		8.80275	208.925		8.80275	52.4542		8.80275	28.9752
10	18.6792	1.66552		10.7781	228.087		10.7781	56.4678		10.7781	29.4734
11	20.3774	1.78621		10.9637	229.888		10.9637	56.8449		10.9637	29.5202
12	22.0755	2.17241		12.064	240.562		12.064	59.0807		12.064	29.7977
13	25.4717	2.70345		15.0336	253.468		15.0336	65.1146		15.0336	30.5467
14	25.4717	2.70345		15.2457	254.389		15.2457	65.5456		15.2457	30.763
15	27.1698	2.88046		16.4786	259.747		16.4786	68.0507		16.4786	32.0202
16	30.566	3.23448		18.5998	268.966		18.5998	72.3607		18.5998	34.183
17	30.566	3.23448		19.2892	273.073		19.2892	73.7614		19.2892	34.8859
18	32.2642	3.5		19.3024	273.152		19.3024	73.7884		19.3024	34.8995
19	33.9623	3.76552		19.5278	274.495		19.5278	74.2463		19.5278	35.1293
20	35.6604	3.95862		19.541	274.574		19.541	74.2732		19.541	35.1428
21	35.6604	3.95862		23.0012	295.193		23.0012	78.6811		23.0012	38.671
22	37.3585	4.15172		23.558	297.248		23.558	79.3904		23.558	39.2387
23	39.0566	4.34483		23.5712	297.297		23.5712	79.4073		23.5712	39.2522
24	40.7547	4.87586		25.7056	305.176		25.7056	82.1263		25.7056	41.4286
25	40.7547	4.87586		25.9575	306.106		25.9575	82.4472		25.9575	42.1923
26	42.4528	5.21379		27.84	313.055		27.84	84.8453		27.84	47.8995

Figure B.13. Screen shot of experimental data worksheet.

B.2.4 Variables to optimize – GA_Vars worksheet

The model input parameters to be estimated from the available experimental data are specified in the GA_Vars worksheet, shown below in Figure B.14. Each variable to be optimized is called a gene, and the number of variables to be optimized is specified in cell A1. Each variable (gene) should be numbered sequentially in column A starting in row 11. In the next column, the name of the worksheet containing the variable to be optimized is specified. The valid choices are indicated in column B, rows 3–8. Note that variables from all sheets except "general" can be optimized. When optimizing variables

from the gyields or hgyields worksheets, the code performs normalization to ensure that the sum of all gyields add to 1 and that the sum of all hgyields add to 0, as is required for mass conservation. However, for this to work correctly, the user must include all nonzero yields as variables to be optimized. For example, if the column of the gyields matrix for a particular condensed phase reaction has four nonzero yields, then these four yields should be specified as variables to be optimized in the GA_Vars worksheet. The homogeneous gaseous yields are similar, except that it is not necessary to specify the yield of reactant 1 because it is always –1.

Column E is the variable (gene) type. The valid variable types for each sheet name are indicated in Column E from rows 3 to 9. For example, if sprops is specified in column B, then the valid variable types are K0 (thermal conductivity at reference temperature), NK (thermal conductivity exponent), and so on. If gyields or hgyields is specified in column B, then it is not necessary to specify a variable type because the code automatically knows that gene must correspond to a species yield.

Two indices are entered in columns D and E (called, very descriptively, Index 1 and Index 2). The role of these two integers depends on the sheet name specified in column B. For example, if the sheet name in column B is sprops, then column C (Index 1) is ISSPEC, the index of solid species as indicated in the sprops sheet. Similarly, if the sheet name in column B is rxns, then column C is IRXN, the index of the reaction (specified in the rxns worksheet). Index 2 does not matter for variables from worksheets sprops or gprops. However, for variables from worksheets gyields and hgyields, Index 1 is the index of the gaseous species, and Index 2 is the reaction number. Thus, if gyields is specified in column B, Index 1 is set to 2, and Index 2 is set to 3, then the gene

corresponds to the gaseous yield for the formation of gaseous species 2 from heterogeneous reaction 3.

Columns F and G (MinVal and MaxVal) are the lower and upper bounds of each variable, i.e. the values of $a_{j,min}$ and $a_{j,max}$ in Equation 5.1. These should be specified to limit the search space to physically realistic values, i.e. it is known that the thermal conductivity of wood isn't 1000 W/m–K. Column H is a logical parameter indicating whether the values of MinVal and MaxVal are the logarithm of the gene. For example, with a MinVal of 10 and a MaxVal of 12, if log is set to .TRUE. then the code will constrain the search from a minimum value 10^{10} to a maximum value of 10^{12}; but if log is set to .FALSE. then the code will search for values between 10 and 12.

The mutation probability (see Section 5.3.5) is specified in column I. The parameter v_{mut} in Equation 5.8b is specified in column J.

The integer in column K provides a convenient means to treat two genes as one parameter for reproduction purposes. For example, the logarithm of the pre–exponential factor and the activation energy are positively correlated, so it may be convenient to form offspring from two parents by applying the same weightings to both the log of the pre–exponential factor and the activation energy. This can be enabled by setting the value in column K to an integer greater than zero. Then, for reproduction purposes, the linear combination applied to the index of the gene specified in column K will also be applied to the current gene.

For solid properties, Index 2 is normally set to 0. However, if Index 2 is set to a solid species index (as specified in sprops) and both MinVal and MaxVal are negative, then the variable is actually the negative of the gene multiplied by the value of the

analogous variable of the solid species corresponding to Index 2. This is confusing and is best illustrated by an example: if Index 2 is set to 1, MinVal is set to –1, and MaxVal is set to –0.5, then the gene search space is between 0.5 and 1.0 multiplied by the value of the analogous gene for species 1. The same also applies to the rxns worksheet. Representing the genes in this way is convenient when it is known that one variable must be smaller or larger than another; for example, the thermal conductivity of a char is likely lower than the thermal conductivity of the virgin material from which it was formed, and the activation energy of an oxidative reaction may be lower than the activation energy of an analogous anaerobic reaction.

Microsoft Excel - sample_frontend_0.565.xls

File Edit View Insert Format Tools Data Window Help Adobe PDF

M1 =

	A	B	C	D	E	F	G	H	I	J	K	L
1	21	NVAR: NUMBER OF VARIABLES										
2		**Sheet names**	**Index 1**	**Index 2**	**Types**							
3		sprops	ISSPEC	isspec (optnl)	K0,NK,R0,NR,C0,NC,EMIS,KAPPA,TMELT,DHMELT,SIGMA2MELT,GAMMA,PERM,RS0							
4		rxns	IRXN	irxn (optnl)	Z, E, DHS, DHV, CHI, ORDER, O2ORDER							
5		gprops	IGSPEC	Not used	CPG, MW, SIGMA, EPSOK, B, TONSET, TSPAN							
6		gyields	IGSPEC	IRXN	Not used							
7		hgyields	IGSPEC	IHGRXN	Not used							
8		layers	ILAYER	ISSPEC	Not used							
9		hgrxns	IHGRXN	ihgrxn (optnl)	P, Q, B, Z, E, DH							
10	**Var #**	**From sheet name**	**Index 1**	**Index 2**	**Type**	**MinVal**	**MaxVal**	**Log**	**Pmut**	**Vmutmax**	**IvarPair**	
11	1	rxns	3	2	Z	-1	-1	.FALSE.	0.15	0.40	0	dry wood oxidation
12	2	rxns	3	2	E	-1	-0.85	.FALSE.	0.15	0.40	0	
13	3	rxns	3	2	ORDER	-1	-1	.FALSE.	0.15	0.40	0	
14	4	rxns	3	0	O2ORDER	1.2	3	.FALSE.	0.15	0.40	0	
15	5	rxns	3	0	DHV	-1.20E+06	-4.00E+05	.FALSE.	0.15	0.40	0	
16	6	rxns	4	0	Z	12.5	14.0	.TRUE.	0.15	0.40	0	char oxidation
17	7	rxns	4	0	E	150	200	.FALSE.	0.15	0.40	0	
18	8	rxns	4	0	ORDER	1	2	.FALSE.	0.15	0.40	0	
19	9	rxns	4	0	O2ORDER	1	2	.FALSE.	0.15	0.40	0	
20	10	rxns	4	0	DHV	-2.00E+07	-5.00E+06	.FALSE.	0.15	0.40	0	
21	11	sprops	4	3	EMIS	-1.00	-0.90	.FALSE.	0.15	0.40	0	ash
22	12	sprops	4	0	R0	10	30	.FALSE.	0.15	0.40	0	
23	13	sprops	4	3	K0	-1	-0.7	.FALSE.	0.15	0.40	0	
24	14	sprops	4	3	NK	-1.3	-0.7	.FALSE.	0.15	0.40	0	
25	15	sprops	4	3	C0	-1.2	-0.8	.FALSE.	0.15	0.40	0	
26	16	sprops	4	3	NC	-1.2	-0.8	.FALSE.	0.15	0.40	0	
27	17	sprops	4	3	GAMMA	-2.0	-1.0	.FALSE.	0.15	0.40	0	
28	18	hgrxns	1	0	E	140.0	170.0	.FALSE.	0.15	0.40	0	hgrxns
29	19	hgrxns	2	1	E	-1.10	-1.0	.FALSE.	0.15	0.40	0	
30	20	hgrxns	1	0	DH	-1.80E+07	-1.20E+07	.FALSE.	0.15	0.40	0	
31	21	hgrxns	2	0	DH	-1.80E+07	-1.20E+07	.FALSE.	0.15	0.40	0	

Figure B.14. Screen shot of GA_Vars worksheet.